

How humans use preview information in manual control

van der El, Kasper

DOI

[10.4233/uuid:cda9dd80-0a51-436e-9c70-ea174505692a](https://doi.org/10.4233/uuid:cda9dd80-0a51-436e-9c70-ea174505692a)

Publication date

2018

Document Version

Final published version

Citation (APA)

van der El, K. (2018). *How humans use preview information in manual control*. [Dissertation (TU Delft), Delft University of Technology]. <https://doi.org/10.4233/uuid:cda9dd80-0a51-436e-9c70-ea174505692a>

Important note

To cite this publication, please use the final published version (if applicable).
Please check the document version above.

Copyright

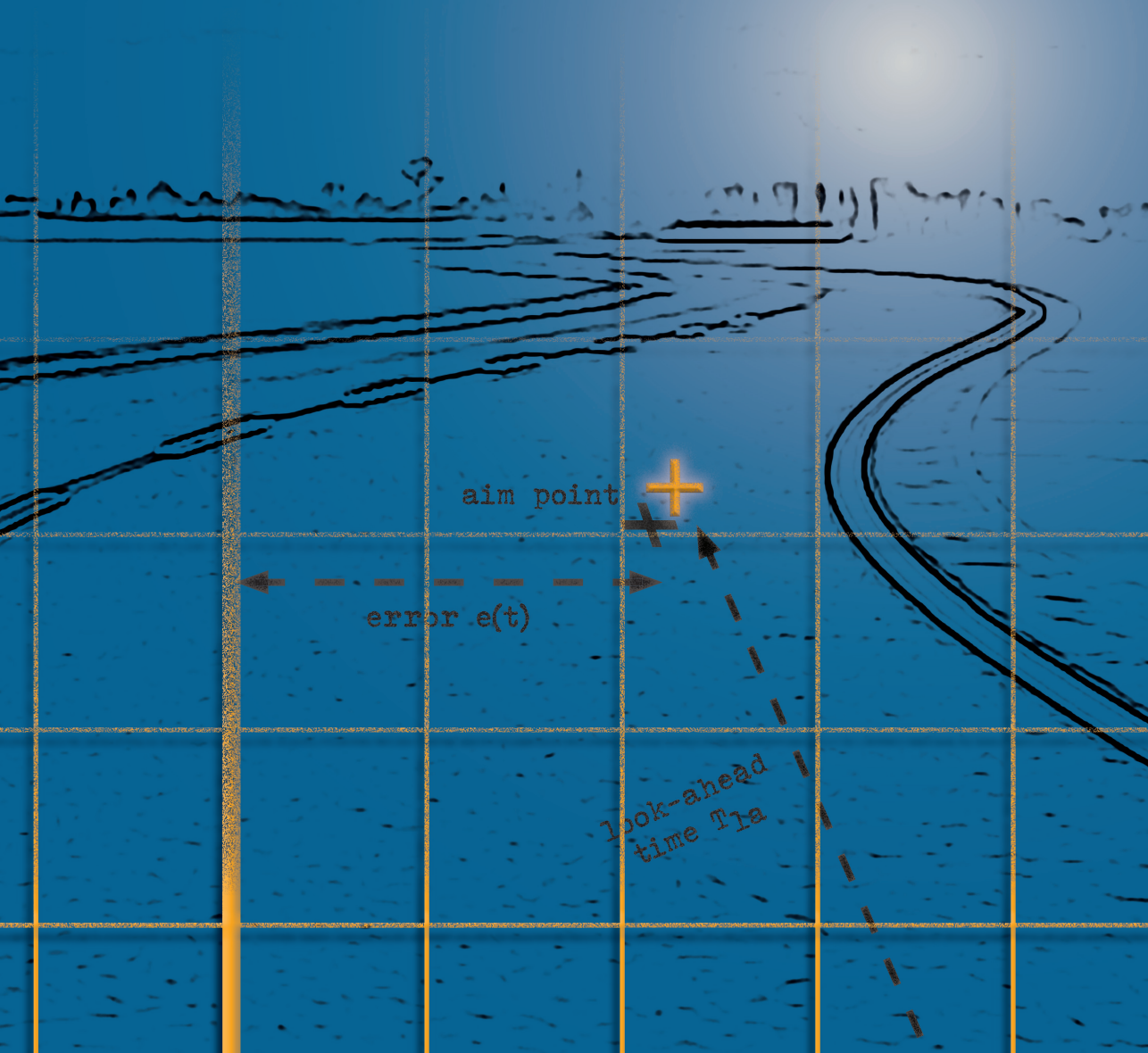
Other than for strictly personal use, it is not permitted to download, forward or distribute the text or part of it, without the consent of the author(s) and/or copyright holder(s), unless the work is under an open content license such as Creative Commons.

Takedown policy

Please contact us and provide details if you believe this document breaches copyrights.
We will remove access to the work immediately and investigate your claim.

KASPER VAN DER EL

HOW HUMANS USE PREVIEW INFORMATION IN MANUAL CONTROL



**HOW HUMANS USE PREVIEW
INFORMATION IN MANUAL CONTROL**

KASPER VAN DER EL

HOW HUMANS USE PREVIEW INFORMATION IN MANUAL CONTROL

Proefschrift

ter verkrijging van de graad van doctor
aan de Technische Universiteit Delft,
op gezag van de Rector Magnificus prof. dr. ir. T.H.J.J. van der Hagen,
voorzitter van het College voor Promoties,
in het openbaar te verdedigen op
donderdag 6 december 2018 om 15:00 uur

door

Kasper VAN DER EL

Ingenieur Luchtvaart en Ruimtevaart,
Technische Universiteit Delft, Nederland,
geboren te Capelle aan den IJssel

Dit proefschrift is goedgekeurd door de promotor:

Prof. dr. ir. M. Mulder

Copromotor:

Dr. ir. D.M. Pool

Samenstelling promotiecommissie:

Rector Magnificus,	voorzitter
Prof. dr. ir. M. Mulder,	Technische Universiteit Delft, promotor
Dr. ir. D.M. Pool,	Technische Universiteit Delft, copromotor

Onafhankelijke leden:

Prof. dr. ir. J. Schoukens	Vrije Universiteit Brussel, België
Prof. dr. ir. B. van Arem	Technische Universiteit Delft
Prof. dr. F.C.T. van der Helm	Technische Universiteit Delft
Prof. dr. N.A. Stanton	University of Southampton, UK
D.H. Klyde, M.Sc.	Systems Technology, Inc., US

dr. ir. M.M. van Paassen heeft in belangrijke mate aan de totstandkoming van het proefschrift bijgedragen.



Keywords: preview information, manual control, human behavior, tracking tasks, driver steering, system identification, parameter estimation

Printed by: Ipskamp Printing

Cover design: K. van der El

Copyright © 2018 by K. van der El

ISBN 978-94-6186-967-8

An electronic version of this dissertation is available at
<http://repository.tudelft.nl/>.

CONTENTS

Summary	xi
Samenvatting (Dutch summary)	xv
1 Introduction	1
1.1 Manual control in the age of automation.	3
1.2 An introduction to manual vehicular control.	4
1.2.1 Hierarchical categories of human control	4
1.2.2 An archetype example: Driver steering.	4
1.2.3 From sensory feedback to control	5
1.3 Manual preview control	6
1.3.1 Preview information	6
1.3.2 Feedforward and feedback control behavior	7
1.3.3 Humans as adaptive controllers	8
1.3.4 The preview portions used for control	8
1.4 Cybernetic control-theoretic models	9
1.4.1 Modeling compensatory tracking behavior.	9
1.4.2 Modeling preview control	11
1.5 Research goal	12
1.6 Research approach.	13
1.6.1 From compensatory tracking to curve driving	13
1.6.2 The cybernetic approach	16
1.7 Guidelines for the reader.	17
1.7.1 Outline of the thesis	17
1.7.2 Notes for the reader	19
I Fundamentals of manual preview control	21
2 Modeling human preview tracking behavior	23
2.1 Introduction	25
2.2 Background	26
2.2.1 The control task	26
2.2.2 Quasi-linear model for compensatory tracking.	26
2.2.3 Identification considerations.	28
2.2.4 Modeling considerations	29
2.3 Data acquisition	30
2.3.1 Measurement setup	30
2.3.2 Apparatus	31
2.3.3 Forcing functions	31
2.3.4 Subjects, instructions and procedure	32

2.4	Estimating operator control dynamics	33
2.4.1	Method	33
2.4.2	Results	34
2.5	Human controller model derivation	34
2.5.1	Controlled element output response	34
2.5.2	Target response	35
2.5.3	Model restructuring	38
2.5.4	Discussion	40
2.6	Parameter estimation and model validation	41
2.6.1	Methods	41
2.6.2	Results	42
2.7	Discussion	47
2.8	Conclusion.	48
3	The portions of preview used for control	49
3.1	Introduction	51
3.2	Background	52
3.2.1	The control task	52
3.2.2	Human controller model	52
3.2.3	The visual information that guides preview control	53
3.3	Method	54
3.3.1	Hypotheses	54
3.3.2	Experiment design	55
3.3.3	Data analysis.	57
3.4	Results.	58
3.4.1	Tracking performance and control activity	58
3.4.2	Eye-tracking results	60
3.4.3	System identification results	62
3.5	Discussion	66
3.6	Conclusion.	68
II	Human adaptation to task variables	69
4	Effects of controlled element dynamics	71
4.1	Introduction	73
4.2	Background	74
4.2.1	The control task	74
4.2.2	Classical approach and results	75
4.2.3	Human controller model	75
4.3	Offline model predictions	77
4.3.1	Perfect target-tracking.	78
4.3.2	Model simulations	78
4.4	Experimental validation: Method	82
4.4.1	Experiment design	82
4.4.2	Data analysis.	82
4.4.3	Hypotheses	84

4.5	Experimental validation: Results	85
4.5.1	Tracking performance and control activity	85
4.5.2	Open-loop dynamics	86
4.5.3	Human multiloop control dynamics	87
4.5.4	Model parameters	90
4.6	Discussion	92
4.7	Conclusion	93
5	Effects of preview time	95
5.1	Introduction	97
5.2	Background	98
5.2.1	The control task	98
5.2.2	Human controller model	98
5.3	Offline model predictions	100
5.3.1	Approach	100
5.3.2	Settings and procedure	101
5.3.3	Results	102
5.4	Experimental validation: Method	104
5.4.1	Hypotheses	104
5.4.2	Experiment design	104
5.4.3	Data analysis	105
5.5	Experimental validation: Results	106
5.5.1	Nonparametric results	106
5.5.2	Modeling results	109
5.6	Discussion	114
5.7	Conclusion	115
6	Effects of target trajectory bandwidth	117
6.1	Introduction	119
6.2	Background	120
6.2.1	The control task	120
6.2.2	Target trajectory bandwidth	120
6.2.3	Human controller model	122
6.3	Offline model predictions	123
6.3.1	Performance measures as motivation for adaptation	123
6.3.2	Human adaptation in compensatory tasks	123
6.3.3	Human adaptation in pursuit and preview tasks	124
6.3.4	Predicting human behavior adaptation	126
6.4	Experimental validation: Method	126
6.4.1	Hypotheses	126
6.4.2	Experiment design	128
6.5	Experimental validation: Results	129
6.5.1	Tracking performance	129
6.5.2	Human control behavior	132
6.6	Discussion	135
6.7	Conclusion	136

III	From preview tracking to curve driving	137
7	Effects of linear perspective	139
7.1	Introduction	141
7.2	Preview tracking and linear perspective	142
7.2.1	The control task	142
7.2.2	Perspective projection method	144
7.2.3	Perspective display gains.	144
7.3	Modeling and system identification	146
7.3.1	Human controller model for plan-view preview tracking	146
7.3.2	Nonparametric system identification.	148
7.3.3	Parameter estimation and model fitness	149
7.4	The experiment	150
7.4.1	Independent variables	150
7.4.2	Control variables.	152
7.4.3	Apparatus	153
7.4.4	Subjects and experimental procedure	153
7.4.5	Dependent measures.	153
7.4.6	Data processing	154
7.4.7	Hypotheses	154
7.5	Results.	155
7.5.1	Nonparametric results	155
7.5.2	Modeling results	158
7.5.3	Human controller adaptation	159
7.6	Discussion	162
7.7	Conclusion.	163
8	Effects of vestibular feedback	165
8.1	Introduction	167
8.2	Visual-vestibular manual control.	168
8.2.1	Compensatory tracking	168
8.2.2	Preview tracking.	170
8.2.3	Effects of motion feedback.	171
8.3	The experiment	172
8.3.1	Independent variables	172
8.3.2	Apparatus and control variables	172
8.3.3	Forcing functions	173
8.3.4	Experimental procedure	174
8.4	Data analysis.	174
8.4.1	Tracking performance and control activity	174
8.4.2	Open-loop dynamics.	175
8.4.3	Human multiloop control dynamics	175
8.4.4	Parameter estimation	176
8.4.5	Variance accounted for.	177
8.4.6	Parameter correlation matrix.	177

8.5	Nonparametric results	178
8.5.1	Tracking performance and control activity	178
8.5.2	Open-loop dynamics	179
8.5.3	Human multiloop control dynamics	181
8.6	Modeling results	181
8.6.1	Variance accounted for	181
8.6.2	Vestibular gain and time delay	183
8.6.3	Modeled control dynamics	184
8.6.4	Parameter correlation matrices	186
8.6.5	Visual response and neuromuscular system parameters	187
8.7	Discussion	188
8.8	Conclusion	189
9	Multiple visual feedbacks and outside visual field control	191
9.1	Introduction	193
9.2	Data acquisition	194
9.2.1	Control task	194
9.2.2	Independent variables	195
9.2.3	Apparatus	197
9.2.4	Road trajectory and wind-gust disturbances	197
9.2.5	Participants, instructions, and procedures	199
9.2.6	Data analysis	199
9.3	Multiloop dynamics estimation	200
9.3.1	System identification techniques	200
9.3.2	Results	201
9.3.3	Implications for drivers' control organization	205
9.4	Modeling driver multiloop steering behavior	206
9.4.1	Control-theoretic driver model	206
9.4.2	Model fits	208
9.4.3	Model analysis	211
9.5	From control theory to visual cues	213
9.5.1	Visual cues and perspective geometry	213
9.5.2	Relating control theory to perspective cues	216
9.5.3	Implications for driver steering	217
9.5.4	Single-loop optical cue control	218
9.6	Discussion	221
9.7	Conclusion	222
10	Boundary avoidance and restricted preview in driving	223
10.1	Introduction	225
10.2	Driving experiment	226
10.2.1	Independent variables	226
10.2.2	Apparatus and control variables	226
10.2.3	Participants, instructions, and procedure	226
10.2.4	Dependent measures	228
10.2.5	Hypotheses	230

10.3	Results	230
10.3.1	Nonparametric measures.	230
10.3.2	Modeling results	237
10.4	Discussion	242
10.5	Conclusion.	244
11	Conclusion and recommendations	245
11.1	Conclusion.	247
11.1.1	Part 1: Fundamentals of manual preview control.	247
11.1.2	Part 2: Human adaptation to task variables	248
11.1.3	Part 3: From preview tracking to curve driving.	251
11.1.4	General conclusion.	253
11.2	Recommendations	254
11.2.1	System identification of real-world preview control	255
11.2.2	Two-level driver steering behavior	255
11.2.3	Time-varying use of preview information	256
11.2.4	Connecting human gaze to preview control behavior.	256
11.2.5	Engineering applications.	257
	Appendices	259
A	Two interpretations of feedforward in manual control	261
A.1	Multi-channel manual control in pursuit tasks	263
A.1.1	Multi-channel pursuit control behavior	263
A.1.2	Model equivalence	264
A.1.3	Perfect target-tracking.	265
A.2	Example measurement data: Preview tracking	266
A.2.1	Control task and system identification techniques.	266
A.2.2	Frequency-response function estimates	267
A.2.3	Cybernetic modeling.	267
A.2.4	Modeling results	269
A.3	Conclusion.	272
B	Remnant data and modeling	273
B.1	Remnant power	275
B.2	Remnant modeling.	277
B.3	Conclusion.	279
	References	281
	Acknowledgements	299
	Curriculum vitæ	301
	List of publications	303

SUMMARY

HOW HUMANS USE PREVIEW INFORMATION IN MANUAL CONTROL

KASPER VAN DER EL

CONTROL of vehicles and devices is becoming increasingly automated, at the expense of traditional, *manual* control by humans. A clear example is the driving task, where lane-keeping assist, (adaptive) cruise control, and even “autopilot” systems are rapidly changing the way in which we interact with vehicles. Another example is the aerospace domain, where equivalents of these systems have been introduced during the past decades, and where the move towards increasing automation is still continuing today. The novel automation systems are intended to cooperate more intimately with the human operator than ever before. Obviously, the new technologies should *strengthen* and not accidentally *deteriorate* the combined human-automation system’s robustness and performance, especially compared to the case of only human manual control. To systematically optimize the potentially symbiotic relationship between humans and tomorrow’s automation systems, perhaps even *online* and *individualized*, a thorough quantitative understanding of the human’s manual control capabilities and limitations is essential.

Humans are extremely versatile manual controllers. Their behavior is typically a combination of anticipatory *feedforward* and stabilizing *feedback* control, which characteristics are difficult to quantify and predict in their full breadth. Nonetheless, it is well known that human controllers require *preview* to attain adequate performance in many manual control tasks. Preview is information about the trajectory to follow *in the future*, a familiar example of which is the road that is visible through the front windshield while driving a car. Preview allows humans to anticipate the target trajectory’s upcoming curves, while a lack of preview (e.g., due to fog or poor lighting) inhibits such anticipatory behavior and thus deteriorates target following accuracy. Despite the critical role of preview, it is safe to say that we poorly understand exactly *how humans use preview information in manual control*, that is, *what portions* of a previewed trajectory are used (the human inputs) and *how* (the human’s feedforward control dynamics). This lack of understanding is reflected by the state-of-the-art *driver steering* models, which include fundamentally different feedforward mechanisms to model the human’s preview response.

Without a doubt, manual control behavior is best understood in tasks where the available information is most *limited*, and where humans rely only on *feedback* control. In *compensatory* tracking tasks, for example, the displayed error signal is the only available feedback, forcing humans to adopt a *single-channel* feedback control organization. Consequently, a frequency-response function estimate of the error-response dynamics is easily obtained using *instrumental-variable*, black-box system identification techniques. This estimate then allows for formulating a control-theoretic model that does not only resemble humans' *input* and *output* signals, but also their *internal control dynamics*. Given an *invariant* task, the human's error-response dynamics are often fairly linear and time-invariant, and relatively simple, *quasi-linear* models suffice to capture the key control characteristics. The resulting model's parameters (e.g., gains and time delays) explain measured manual control behavior in much more detail than overt task performance measures. In addition, such a model facilitates *quantitative predictions* of the human's manual control behavior, providing an offline tool for optimizing the design of human-machine interfaces. This model-based analysis of manual control, using physically-interpretable parameters, is known as the *cybernetic* approach.

This thesis uses cybernetics to quantify and explain how humans use preview information in manual control. The key innovation is that *multiloop* frequency-response function measurements are obtained, to estimate both the human's *feedforward* and *feedback* responses. Estimates of the feedforward response are crucial for revealing how humans use the information of a previewed target trajectory for control. In addition, obtained frequency-response functions facilitate the formulation of a control-theoretic preview model which parameters provide physical insight into the human's preview control behavior. For this thesis, data was obtained in *eight* human-in-the-loop experiments that cover a wide range of preview control tasks. Experimental participants followed a *multisine* target trajectory, while simultaneously suppressing a *multisine* external disturbance. By designing these two multisine signals to be *uncorrelated*, they can be used as instrumental variables for estimating the human's feedforward and feedback response dynamics, without making any *a priori* assumptions.

The most relevant preview control task today is without a doubt driver steering on curved roads. Even with multiloop frequency-response function measurements, two fundamental challenges remain for understanding driver steering and their use of preview information. First, it is not trivial to disentangle the human's response to preview information from the variety of possible other response channels, which can be based on any of the wealth of available cues (e.g., visual, vestibular, somatosensory). Second, humans are known to effectively *adapt* their behavior to the characteristics of the control task, referred to as the *task variables*, to improve their performance, reduce workload, or improve on comfort. It is essential to also understand the factors that *underlie* human adaptation to critical task variables in order obtain a *general* theory of manual preview control. These challenges are resolved in this thesis in three steps:

- 1) Human preview control is studied in laboratory tracking tasks, where only the previewed trajectory is shown on a plan-view display together with the corresponding controlled element output, such that the human's preview (feedforward) response dynamics can be directly measured and modeled.

- 2) The effects of three key task variables – the controlled element dynamics, the preview time, and the target trajectory bandwidth – on manual preview tracking behavior are investigated, to reveal the factors that underlie human *adaptation*.
- 3) Elements that characterize real-life driving tasks are introduced stepwise into the preview tracking task, namely *linear perspective* scaling of the previewed target trajectory, *physical motion feedback*, *rotational visual feedback* with an outside visual display, and available *lane width* as opposed to error-minimizing tracking tasks. Measuring and modeling the effects of each element on the human's control behavior eventually leads to a profound understanding of the role of preview in driver steering on winding roads.

Experimental results from the single-axis tracking task with a plan-view preview display show that humans initiate *two* distinct feedforward responses, based on a “*near*” and a “*far*” viewpoint, respectively. These responses separate the tracking of the target trajectory into two distinct frequency regions. The main, low-frequency response is a *prospective* control response: error-minimizing feedback control based on a *future* target point (or *aim point*), namely the smoothed and scaled far viewpoint. To also follow the target trajectory at higher frequencies, human controllers additionally mechanize an auxiliary *open-loop* response with respect to the near viewpoint. A proposed quasi-linear control-theoretic model that resembles this dual-mode control behavior is shown to capture humans' *control output*, as well as their *feedback and feedforward control dynamics*. This model directly extends McRuer's seminal crossover model for compensatory tracking behavior, with an identical central error-minimization element.

Most importantly, the new model's physically interpretable parameters quantify and rationalize measured preview control behavior. Model fits indicate that human controllers position the near- and far-viewpoints 0.1-0.6 s and 0.6-1.2 s ahead, respectively. The other model parameters quantify the human's smoothing and scaling of the far viewpoint, the relative contribution of the near-viewpoint response, the error-response equalization dynamics, and the human's response time delay and neuromuscular activation dynamics. *Gaze* data, obtained in a dedicated second experiment, indicate that the estimated model's near-viewpoint position is correlated to the human's visual focus of attention. Moreover, by visually occluding parts of the future target trajectory, additional evidence is obtained that the estimated near- and far-viewpoints indeed reflect the crucial regions of preview that humans use for control.

Human adaptation to the controlled element dynamics, the preview time, and the target trajectory bandwidth is then predicted *offline* in computer simulations with the new preview model. The predictions are verified with data from three experiments, each focusing on variations within one of the three task variables. In general, it is concluded that human controllers adapt their far-viewpoint response predominantly to minimize the tracking error, but that adaptation of the near-viewpoint response depends also on task difficulty, as well as operator experience and motivation. Therefore, the model facilitates accurate offline predictions of the far-viewpoint response, that is, the human's *main* feedforward mechanism in preview tracking tasks, but not of the auxiliary near-viewpoint response.

Over the course of the final four experiments, the preview tracking task is transformed

into an ecologically realistic car steering task, in which the driver follows a winding road with full field-of-view visuals. The four experiments introduce linear perspective, physical motion feedback, rotational visual feedback and an outside visual view, and a road lane. In all these tasks, human controllers are found to mechanize an identical *prospective* – far-viewpoint driven – control response as in the basic preview tracking tasks. Evidence that human controllers also mechanize the auxiliary near-viewpoint response is increasingly scarce in the more realistic tasks. This suggests that a single viewpoint ahead suffices to model driver steering behavior with preview, which contradicts many driver models in the literature. Moreover, estimated model parameters in driving tasks indicate that the minimized error is a visual angle that is directly observable from the driver’s perspective view on the road ahead, namely the angle between the vehicle heading and the smoothed far viewpoint (the aim point). The steering models proposed in this thesis are thereby the first that capture both driver *preview control behavior* (i.e., control output and dynamics) and their *selection of feedbacks* from the wealth of available optical cues (i.e., inputs).

Considering how much the curve driving task differs from compensatory tracking, humans mechanize a *remarkably consistent* error-minimizing control response. The crucial difference between tasks is *which error* the human controller selects to minimize. Whereas the explicitly displayed error must be minimized in compensatory tracking tasks, preview allows the human controller to minimize an anticipated *future* error with respect to a selected aim point. This is the essence of effective preview control: responding to the target *ahead*, all phase lag in the control loop – primarily due to the human and the vehicle responses – are compensated for, and *performance improves without additional control effort*.

Because of the identical error-minimizing control strategy, human control behavior in widely varying control tasks is captured by a *single, unifying model*, with parameter adaptations to tune the model to a specific task. Most importantly, the model’s physically interpretable parameters allow for quantifying control processes *internal* to the human, to an extent that is currently not matched by any other method. The main modeled control mechanisms are: 1) the compensatory (error-minimizing) equalization dynamics, 2) the integration of multiple (visual or other) feedbacks, 3) what portions of the previewed trajectory are used for control, and 4) how the previewed trajectory is processed.

The results from this thesis can accelerate future research. For example, while eye-tracking measurements are often used to quantify the human’s visual focus of attention, this thesis shows that humans may not (only) use the visual information they directly aim their gaze at. With the proposed model, an alternative method is available for quantifying the optical cues that humans rely on in active preview control tasks, which can provide valuable support for traditional eye-tracking measurements. Moreover, the proposed preview control model can be used directly to optimize the design of automation systems for tomorrow’s vehicles, such as *shared* steering controllers for cars. By estimating the parameters of the proposed preview control model for a specific driver from online steering data, an *individualized* model is immediately available for implementation in the automatic part of the shared controller. Thereby, the automation is matched to the human driver’s steering behavior, leading to *avoidance* of conflicts and increased trust in the system.

SAMENVATTING

HOE MENSEN PREVIEWINFORMATIE GEBRUIKEN OM HANDMATIG TE STUREN

KASPER VAN DER EL

DE besturing van voertuigen wordt momenteel meer en meer geautomatiseerd, ten koste van traditionele handmatige besturing door mensen. Een spraakmakend voorbeeld is de autorijtaak, waar rijstrookondersteuning, (adaptieve) cruise-control, en zelfs “automatische-piloot” systemen de wisselwerking tussen mens en voertuig beïnvloedt. Equivalenten van zulke systemen zijn gedurende de afgelopen vijf decennia al geïntroduceerd in de luchtvaart en ook hier doet nieuwe automatisering nog steeds zijn intrede. Deze vernieuwde systemen leiden tot een samenspel tussen mens en machine dat intiemer is dan ooit tevoren. Het is evident dat nieuwe technologieën de robuustheid en prestaties van het gecombineerde mens-machine systeem moeten *verbeteren* en niet per ongeluk verslechteren, zeker vergeleken met puur handmatig sturen door mensen. Om de toekomstige, potentieel symbiotische relatie tussen de mens en de automatiseringssystemen te optimaliseren, mogelijk zelfs *online* en *geïndividualiseerd*, is een grondig begrip van de menselijke handmatige stuurcapaciteiten en -beperkingen essentieel.

Mensen zijn extreem veelzijdige bestuurders, wiens gedrag in al zijn facetten moeilijk te kwantificeren en te voorspellen is. Het is desalniettemin algemeen bekend dat *previewinformatie* vaak onmisbaar voor het adequaat uitvoeren van handmatige stuurtaken; specifiek betekent dit dat er informatie beschikbaar moet zijn over het te volgen *doeltraject* in de *nabije toekomst*. Een bekend voorbeeld van previewinformatie is de weg die zichtbaar is door de voorruit tijdens het autorijden. Door de aanwezigheid van preview kunnen mensen sturen door middel van een voorwaartskoppeling, waardoor effectief op aankomende bochten in het gewenste traject kan worden geanticipeerd. Bij een gebrek aan preview, bijvoorbeeld door mist of beperkt zicht, wordt de voorwaartsgekoppelde stuuractie bemoeilijkt en verslechteren de prestaties en de stabiliteit van het gecombineerde mens-machine systeem. Het is niettemin een feit dat we slecht begrijpen *hoe mensen previewinformatie precies gebruiken om handmatig te sturen*. Met name *welke delen* van een toekomstig traject worden gebruikt (de input naar de mens) en *hoe* deze worden gebruikt (de menselijke stuurdynamica) vormen een hiaat in de aanwezige kennis. Veelgebruikte stuurmodellen

voor autorijden reflecteren dit gebrek aan kennis met fundamentele verschillen in de wijze waarop het menselijk gebruik van previewinformatie is gemodelleerd.

Onze kennis van het menselijk stuurgedrag is zonder twijfel het verst ontwikkeld voor stuurtaken waarin de teruggekoppelde informatie het meest gelimiteerd is. Een voorbeeld hiervan is de visuele compensatie-volgtask, waarin mensen gedwongen worden zich te organiseren als een *enkel-kanaals* stuursysteem met terugkoppeling van *alleen* de getoonde stuurfout. De menselijke enkel-kanaals stuurdynamica kan direct gemeten worden door middel van *instrumentele-variabele*, "zwarte-doo's" systeemidentificatietechnieken. Voor invariante stuurtaken is er aangetoond dat de menselijke stuurdynamica meestal grotendeels lineair en tijdsinvariant is en uitstekend gemodelleerd kan worden in het *quasi-lineaire* raamwerk. De menselijke intrinsieke stuurdynamica wordt dan gevangen in modelparameters zoals versterkingsfactoren en tijdvertragingen, zodat deze modellen *fysiek* interpreteerbaar zijn en waardevol aanvullend inzicht geven bovenop openlijke prestatiemaatstaven. Daarnaast faciliteren deze modellen directe kwantitatieve voorspellingen van het menselijk stuurgedrag, waarmee het ontwerp van mens-machine interfaces geoptimaliseerd kan worden. Deze modelgebaseerde analyse van menselijk stuurgedrag door middel van fysiek interpreteerbare parameters staat bekend als de *cybernetische* aanpak.

Dit proefschrift gebruikt de cybernetische aanpak zowel om uit te leggen als te kwantificeren hoe mensen previewinformatie gebruiken om handmatig te sturen. Om precies te zijn wordt de dynamica van de menselijke stuurrespons op previewinformatie geschat door middel van zwarte-doo's systeemidentificatietechnieken. Hiervoor worden metingen gebruikt van een breed scala aan stuurtaken, verkregen in mens-in-de-lus experimenten. De belangrijkste vernieuwing van dit proefschrift is dat frequentierespons functies worden geschat van zowel de menselijke voorwaartskoppeling als de terugkoppeling. Deze geschatte responsies onthullen direct hoe mensen de previewinformatie van een toekomstig doeltraject gebruiken om te sturen *en* faciliteren het formuleren van meet- en regeltechnische modellen die de menselijke stuurdynamica in *meerdere* stimulus-respons kanalen dicht benaderen. Om zonder aannames schattingen te verwerven van de menselijke stuurdynamica volgden deelnemers tijdens de experimenten *multisinus* doeltrajecten, terwijl tegelijkertijd een externe *multisinus* verstoring moest worden onderdrukt. Door een *ongecorreleerd* ontwerp van deze twee multisinus signalen is het mogelijk om de dynamica van de menselijke terug- en voorwaartskoppelingen te scheiden met instrumentele-variabele systeemidentificatietechnieken gebaseerd op Fourier coëfficiënten.

Het uiteindelijke doel van dit proefschrift is om menselijk stuurgedrag te begrijpen in wat op dit moment de meest relevante preview-volgtask is, namelijk het sturen van een auto over een bochtige weg. Het is echter niet triviaal om in deze taak de menselijke respons op de previewinformatie te scheiden van de mogelijke andere menselijke stimulus-respons kanalen, die gebaseerd kunnen zijn op elk van de vele aanwezige bronnen van visuele, vestibulaire en somatosensorische terugkoppeling informatie. Bovendien is het bekend dat mensen hun gedrag effectief *aanpassen* aan de kenmerken van de gegeven stuurtaak, de zogenoemde *taakvariabelen*, om hun prestaties te verbeteren, de werkdruk te verlagen, of het comfort te vergroten. Om een *algemeen* model te verkrijgen dat menselijk preview-stuurgedrag beschrijft in een breed scala van stuurtaken, is het essentieel om ook de factoren te begrijpen die ten grondslag liggen aan de menselijke aanpassing aan

de taakvariabelen. Dit proefschrift lost deze uitdagingen op in drie stappen:

- 1) Menselijk preview-stuurgedrag wordt bestudeerd in display-volgtaken, waarin alleen een bovenaanzicht van het (toekomstige) doeltraject wordt gevisualiseerd, samen met de overeenkomstige bestuurd output, zodat de menselijke previewrespons accuraat gemeten en gemodelleerd kan worden.
- 2) De effecten van drie belangrijke taakvariabelen op het menselijk preview-volggedrag worden onderzocht (de systeemdynamica, de previewtijd en de bandbreedte van het doelsignaal), om te onthullen welke factoren ten grondslag liggen aan de menselijke gedragsaanpassing.
- 3) Elementen van autorij-stuurtaken worden stapsgewijs geïntroduceerd in de preview-volgtak, specifiek zijn dit: de *lineair perspectivische* schaling van het toekomstige doeltraject; de *terugkoppeling van fysieke bewegingen*; de *terugkoppeling van visuele rotaties* op een buitenzicht-display; en de aanwezigheid van een zekere *rijbaanbreedte*, in tegenstelling tot de gewenste fout-minimalisatie in volgtaken. Het meten en modelleren van de effecten van elk element op het menselijke preview-stuurgedrag leidt uiteindelijk tot het gewenste diepgaande begrip van het sturen van een auto over een slingerende weg.

Mens-in-de-lus data van de visuele, enkele-as preview-volgtaken laten zien dat mensen *twee* uitgesproken previewresponsies ontwikkelen, die gebaseerd zijn op een *nabij* en een *ver* zichtpunt op het doeltraject. Deze twee responsies scheiden het menselijke doeltraject-volggedrag in twee afzonderlijke frequentiegebieden. De voornaamste respons is die op lage frequenties en deze is gebaseerd op het (gladgestreken en geschaalde) verre zichtpunt. Dit is een zogenoemde “*aanstaande*” stuuractie: de *huidige* fout ten opzichte van het *toekomstige* gewenste doel wordt gebruikt als terugkoppelingsfout om te minimaliseren. Om ook de frequenties van het doeltraject te volgen boven de bandbreedte van de verre-zichtpunt respons, ontwikkelen mensen bovendien een *open-lus* respons ten opzichte van het nabije zichtpunt.

Een quasi-lineair model dat dit tweeledige stuurgedrag reflecteert vangt inderdaad zowel het menselijke *stuursignaal* als de geschatte terug- en voorwaartsgekoppelde *stuurdynamica*. De kern van het model is een fout-minimaliserende compensatie-respons die gelijk is aan het welbekende “crossover” model van McRuer. De aanpassing van deze dynamica is identiek in preview-volgtaken, resulterende in integrator open-lus dynamica rond de crossover frequentie. Geschatte modelparameters geven aan dat mensen het nabije en verre zichtpunt respectievelijk 0.1-0.6 sec en 0.6-1.2 sec vooruit positioneren. Schattingen van de overige modelparameters geven expliciet fysiek inzicht in de menselijke compensatie-respons dynamica; het afvlakken en schalen van de bewegingen van het verre zichtpunt; de bijdrage van de respons op het nabije zichtpunt; en de belangrijkste fysieke beperkingen (tijdvertraging en neuromusculaire activatiedynamica). Data van de menselijke kijkrichting, verzameld in een afzonderlijk tweede experiment, tonen aan dat de geschatte positie van het nabije zichtpunt gecorreleerd is aan de richting van de menselijke visuele aandacht. Met visuele occlusie technieken wordt bovendien aangetoond dat mensen gebruik maken van *substantiële delen* van het doeltraject rondom zowel het nabije als het verre zichtpunt, dus niet uitsluitend van de gemodelleerde punten zelf.

Het model wordt gebruikt om in computersimulaties te voorspellen hoe mensen hun stuurgedrag aanpassen aan de systeemdynamica, de previewtijd en de bandbreedte van het gewenste traject (de kritieke taakvariabelen). Data van drie nieuwe experimenten worden gebruikt om deze voorspelde aanpassingen te verifiëren voor geselecteerde combinaties van taakvariabelen. Een belangrijke bevinding is dat menselijke bestuurders hun respons op het verre zichtpunt zo aanpassen dat de optimale prestatie voor de gegeven taak benaderd wordt. Deze aanpassing van de belangrijkste previewrespons komt overeen met de voorspellingen (de computersimulaties), wat aantoont dat het voorgestelde model het menselijke stuurgedrag weerspiegelt voor een breed scala aan previewtaken. De aanpassing van de ondersteunende, nabije-zichtpunt respons richt zich echter niet alleen op het minimaliseren van de volgfout; deze respons is minder voorspelbaar en hangt af van de moeilijkheid van de gegeven taak, alsook de ervaring en motivatie van de bestuurder.

In de loop van vier aanvullende experimenten wordt het verkregen begrip van het handmatige preview-stuurgedrag uitgebreid naar een ecologisch realistische autorijtaak, waarin de bestuurder een slingerende weg volgt. De *aanstaande*, door het verre zichtpunt aangedreven stuurrespons, welke eerst werd gevonden in de enkele-lus, visuele preview-volgtaken, blijkt intact te blijven bij de introductie van lineair perspectief, fysieke bewegingen, visuele rotaties, buitenzicht, en een rijbaan. Echter, bewijs dat menselijke bestuurders ook de ondersteunende, door het nabije zichtpunt aangedreven stuurrespons toepassen is steeds zwakker naarmate de taak realistischer wordt. Dit suggereert dat een enkel zichtpunt volstaat om het menselijke sturen in autorijtaken met preview te modelleren, wat in tegenspraak is met bekende autorijmodellen uit de literatuur. In stuurtaken met visuele terugkoppeling van het volledige buitenzicht geven geschatte modelparameters aan dat de fout die bestuurders minimaliseren gelijk is aan de hoek tussen de lengteas van het voertuig en het (afgevlakte) verre zichtpunt; deze hoek is direct waarneembaar vanuit het zicht van de bestuurder op de weg vooruit. De stuurmodellen zoals voorgesteld in dit proefschrift zijn daarmee de eerste die zowel het *preview-stuurgedrag* van autobestuurders beschrijven, alsook hun *selectie van terugkoppelingen* vanuit de overvloed aan beschikbare optische informatie verklaren.

In acht nemend hoeveel de uitgevoerde stuurtaken van elkaar verschillen, van volgtaken met bovenaanzicht-displays tot autorijden over slingerende wegen, kan gesteld worden dat *mensen een opmerkelijk consistente fout-minimaliserende hoofd-stuuractie opzetten*. Het belangrijkste verschil in stuurgedrag tussen taken is *welke fout* er wordt geminimaliseerd. Waar mensen in compenserende-volgtaken gedwongen worden om de enkele, gevisualiseerde fout te minimaliseren, kan een geanticiperde fout ten opzichte van een vrij geselecteerd toekomstig doelpunt worden geminimaliseerd in previewtaken. Daardoor kan het menselijk stuurgedrag in alle geteste taken worden gevangen met een *enkel, unificerend model*, waarbij het model wordt afgestemd op een specifieke taak door middel van aanpassingen van modelparameters. De fysiek interpreteerbare modelparameters faciliteren het kwantificeren van *interne* menselijke stuurprocessen, met een hogere mate van detail dan reeds bestaande methoden. De belangrijkste menselijk stureigenschappen die gekwantificeerd kunnen worden zijn: 1) de compensatie-respons dynamica; 2) de integratie van meerdere (visuele of andere) terugkoppelingen; 3) de gebruikte delen van het toekomstige doeltraject; en 4) de verwerking van het toekomstige doeltraject.

De resultaten van dit proefschrift kunnen toekomstig onderzoek versnellen. Metingen van de menselijke kijkrichting worden bijvoorbeeld vaak gebruikt om de visuele aandacht te kwantificeren, terwijl dit proefschrift aantoont dat mensen niet (uitsluitend) de visuele informatie gebruiken waar direct naar gekeken wordt. Met het voorgestelde model is er een alternatieve methode beschikbaar om de optische elementen te kwantificeren die mensen gebruiken in actieve preview-stuurtaken, waarmee waardevolle ondersteuning kan worden geleverd aan oogvolgmetingen. De modellen die in dit proefschrift zijn voorgesteld kunnen bovendien direct gebruikt worden om het ontwerp van automatiseringssystemen voor toekomstige voertuigen te optimaliseren. Een voorbeeld is de *gedeelde* besturing van auto's, waarin zowel mens als machine tegelijkertijd een bijdrage leveren (bv. rijstrookondersteuning). Door de parameters van de voorgestelde previewmodellen te schatten voor een specifieke bestuurder vanuit stuurmetingen kan een *geïndividualiseerd* model beschikbaar worden gemaakt voor implementatie in het automatische deel van een gedeelde besturing. Hiermee kan de automatisering afgestemd worden op het gedrag van de menselijke bestuurder, waardoor conflicten met de machine worden vermeden en het menselijke vertrouwen in het systeem zal worden vergroot.

1

INTRODUCTION

What we've got here is

failure

to communicate

Guns N' Roses, Civil War

(adapted from the Captain's speech in Cool Hand Luke)

Parts of this chapter have been published as:

Title Measuring and Modeling Driver Steering Behavior: From Compensatory Tracking to Curve Driving

Journal Transportation Research Part F: Traffic Psychology and Behaviour, 2017, in press

Authors K. van der El, D.M. Pool, and M. Mulder

1.1. MANUAL CONTROL IN THE AGE OF AUTOMATION

MANUAL control is as old as the first man-made tools. Its importance has increased exponentially over the past centuries with the introduction of more – and more advanced – vehicles and devices. One of the most widespread manual control task today is car driving: the manipulation of the steering wheel and pedals to control the car’s trajectory [1]. But in addition, manually controlled motorcycles, trucks and bicycles also fill the roads [2–4], aircraft and helicopters the skies [5, 6], and ships and submarines the waters [7, 8]. Other examples of manual control include the pointing of devices such as video cameras and gun turrets, and the provision of inputs to digital computers and video games with mice, touch screens, and joysticks [9, 10]. Moreover, professionals remotely control vehicles and devices in extreme environments such as the deep ocean, outer space, and war zones [11–14]. Manual control tasks furthermore provide a tool for evaluating human skill, and are used, amongst others, to assess motor-skill degradation as a consequence of aging and neurological diseases [15–19]. These examples clearly illustrate that manual control is omnipresent in today’s society.

Yet, newspapers appear to report increasingly about more *autonomous* and *intelligent* technologies that can make manual control obsolete, including robots, artificial intelligence, and self-driving cars. The stakes are high, in particular in the driving domain, where *major* safety gains are possible. In 2015, road traffic accidents still accounted for more than 120,000 deaths in – the allegedly safest – high-income countries alone (18% of the world population) [20], and humans are the sole or contributing factor in 95% of the of road accidents [21]. Several of the worlds leading companies (e.g., Google, Apple, Uber, Daimler [22]) are designing self-driving vehicles to fully eradicate human-caused accidents. Although rarely advertised, they face a truly remarkable challenge. The paradox is that human drivers are *on average* extremely safe, being involved in a fatal accident only once in every two million hours of driving (the equivalent of 228 years, 24/7) [23].

With the current advances in digital technology, automatic controllers may supersede manual control in many tasks [24, 25]. Nonetheless, manual control will certainly remain relevant, also in a highly-automated world. Not technical, but *economic, psychological, and legal* factors may eventually favor manual over automatic control in certain tasks [26]: the difficulty of automating highly specialized, demanding control tasks can be economically unfeasible; humans like to be “in control”, a feeling that decreases with automation; and the issue of liability of autonomous vehicles is far from resolved. In addition, the advent of novel technologies also creates new applications of manual control, such as the interaction with (humanoid) robots [27], remote control of drones [28], and remote *backup* control to handle anomalies in autonomous vehicles [29].

Many of tomorrow’s control systems may in fact converge to a hybrid combination of manual *and* automatic control, exploiting each respective strengths [12, 25]. Illustrative is the current situation in aviation. Although automatic flight control systems were already sufficiently developed halfway the 20th century to result in the first *fully automatic* transatlantic flight in 1947 [30, 31], aircraft today are still controlled by pilots. Pilots are nonetheless supported by advanced technology that, for example, provides guidance information (flight director) or temporal automatic control of subtasks, such as keeping al-

titude (autopilot). However, pilots can regain manual control at any moment, and are even obliged to perform certain critical maneuvers manually, such as landing in adverse weather conditions. It is not difficult to imagine a similar future for many of today's manual control tasks, including driving. The division of subtasks – and the communication – between humans and technology may in fact become highly dynamic, to such an extent that both can even *share* the controls and control a system *simultaneously* [32–37].

Without a doubt, humans will work more closely together with tomorrow's automation systems. This leads to a major challenge for engineers, who are responsible for making a highly-automated future *safer*, instead of *more hazardous* than our current “manual” world. Unfortunately, there is ample evidence that increasing automation does not equate to safer systems *per se*, for example, from fatal accidents in commercial aviation and nuclear power plants [26, 38]. The *irony of automation* is that new types of *interaction* problems can emerge that do not occur with fully manual control [39]. For example, a lack of “hands-on” practice corrodes the human's manual control skills, which are still critical for backup control [24]. Moreover, the transition from automatic to manual control can be demanding and confusing [40]. As recently noted by Mindell [13]: “*It takes more sophisticated technology to keep humans in the loop than it does to automate them out*”. Paradoxically, the upcoming *age of automation* thus ask for a deeper understanding than ever before of the characteristics, dynamics, and limitations of *human manual control*.

1

1.2. AN INTRODUCTION TO MANUAL VEHICULAR CONTROL

1.2.1. HIERARCHICAL CATEGORIES OF HUMAN CONTROL

One of the fundamental truths of life is that we often want to be *somewhere else*. Traveling towards any destination typically involves tasks on three hierarchical levels: navigation, guidance, and control. *Navigation*, the highest level, is the selection of an overall route from the available alternatives. In case of automobile driving, navigating results in a particular set of highways, roads and streets that should be followed in sequence to reach the destination. The navigation task is now often automated using GPS-based services. On the second level, an explicit trajectory is planned over which to *guide* the vehicle in the near future, for example, to a desired *target* position that is visible ahead. For driving, this could be the exact spatio-temporal trajectory that is required to overtake another vehicle, to avoid a pedestrian, to change lanes, or to cut a tight corner. *Control* of the vehicle over the target trajectory is finally achieved through manipulation of the control effectors (e.g., gas pedal and steering wheel in automobiles).

1.2.2. AN ARCHETYPE EXAMPLE: DRIVER STEERING

A familiar example of a manual control task is the steering of a passenger car along a winding road, as illustrated in Fig. 1.1. Assume that the vehicle has constant forward velocity. The driver's task is then to follow road (i.e., the *target* trajectory) by providing inputs to the vehicle using only the steering wheel. The forward movement of the vehicle through the environment provides the driver with a continuously changing stream of

information (feedback) about the vehicle's state relative to the environment. Due to the road's curvature, steering inaccuracies, and external disturbances (e.g., wind-gusts), the vehicle will inevitably approach the road edges, and steering is required to remain on the road. Steering inputs again lead to a new position on the road, providing new incentives for steering, and the process repeats in a continuous *closed-loop* fashion, *ad infinitum*, or until the destination location is reached.

The closed-loop organization of Fig. 1.1 is representative for many manual vehicle control tasks. For example, for the pitch control of an aircraft in instrumental flight, the vehicle block is replaced by the aircraft's pitch response to yoke inputs. The target trajectory is the desired pitch angle and the aircraft's actual pitch angle is the vehicle output variable. Moreover, the human's role is then referred to as pilot, the control manipulator is a yoke, and the visual feedback is the artificial horizon on the primary flight display. Clearly, the overall control organization of the pitch task is identical to that of driver steering.

1.2.3. FROM SENSORY FEEDBACK TO CONTROL

In manual control, humans process sensory feedbacks to relevant control outputs. The sensory organs provide the human with information about egomotion and the environment (e.g., the target trajectory). Fig. 1.1 (bottom) shows two important feedbacks: visual (eyes) and physical motion (vestibular organ), but in principle *all* sensory feedbacks can be used for control. The sensory organs translate the external stimuli into neural spike

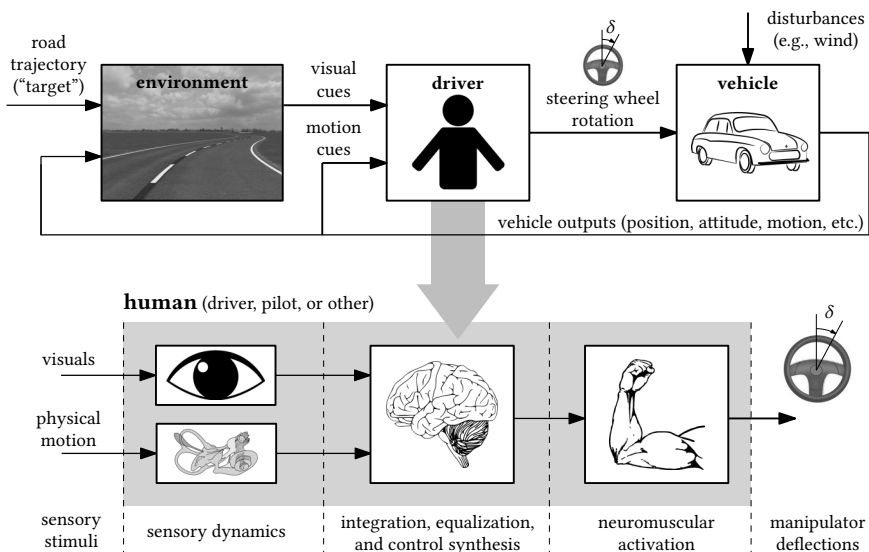


Figure 1.1: Illustration of the closed-loop task of driver steering on a winding road (top), with a detailed view of the three main stages in the human's stimulus-response relation: perception, control synthesis, and activation (bottom).

trains, which reach the central nervous system through afferent neurons [41]. Here, the sensory feedbacks are processed and integrated, before spike trains in efferent neurons signal the muscles to contract or relax, which thereby move the control manipulator.

The two-channel, visual-vestibular illustration of the human controller in Fig. 1.1 (bottom) is highly simplified. In practice, humans may not only mechanize additional control responses based on other sensory modalities, but each sensory channel itself may in fact reflect multiple responses. For example, the vestibular channel can include responses based on rotational and translational accelerations, while the visual channel may comprise responses to any of the salient features (e.g., road curves) and patterns (e.g., optic flow) that fall onto the eye's retina. Humans in ecological manual control tasks are thus in general *multi-channel controllers*. A major challenge in studying manual control behavior is to correlate a measured control output to a particular response channel [42–44].

1

1.3. MANUAL PREVIEW CONTROL

Exactly how much humans rely on various sensory feedbacks depends on the task and has been quantified mainly for simulator tracking tasks (e.g., see [45, 46]). Nonetheless, the critical role of vision for locomotion has long been recognized [1, 47] and is easily verified (although not recommended) by driving with closed eyes for several seconds, which is clearly an extremely dangerous feat [48]. Visual information is so important because it is the only sensory feedback that provides information about constraints on the trajectory to follow *in the future*. This future information is known as *preview* [49–52].

1.3.1. PREVIEW INFORMATION

A well-known example of preview information is the road that is visible through the front windshield while driving, as illustrated in Fig. 1.2a. It is also possible to present preview information on displays, such as a computer-generated perspective flight path display (Fig. 1.2a), or a plan-view tracking display (Fig. 1.2c). Specifically, if the target signal at current time t is given by $f_t(t)$ (see Fig. 1.2c), preview information is defined as $f_t(t+\tau)$, for all positive times τ *ahead*¹. In practical control tasks preview is often available for some finite *preview time* τ_p ahead $f_t([t, t + \tau_p])$. The trajectory beyond τ_p ahead is typically obscured by display edges, poor illumination, objects, or, ultimately, the horizon.

With sufficient preview, humans have been shown to be capable of following a target trajectory nearly perfectly [59, 60]. The importance of preview for adequate performance in various manual control tasks has been cleverly demonstrated using experimental occlusion techniques. For example, Ito and Ito [55] performed a laboratory tracking task with a display similar to that in Fig. 1.2c. Participants repeatedly performed the same tracking tasks, but with different preview times τ_p . The results, reproduced in Fig. 1.3a, show that increasing the preview time invariably leads to improved performance. Most importantly,

¹It could be more intuitive to express f_t as function of *position* ahead, instead of time. However, this thesis considers only control tasks with constant forward velocity, such that time and position are linearly related (small angle approximation), and it is equivalent to express all signals as function of either time or distance.

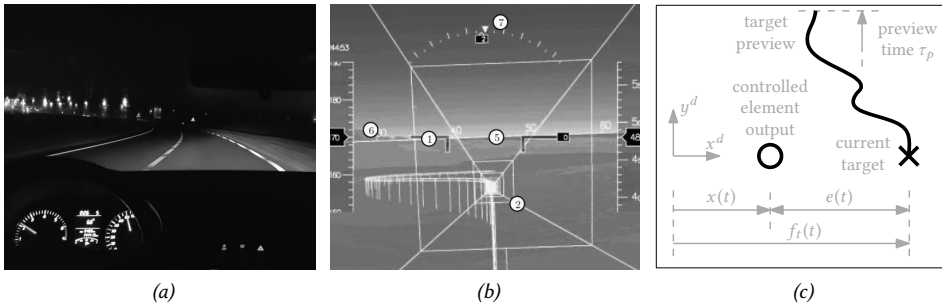


Figure 1.2: Three examples of preview information in manual control: the road trajectory that is visible through the front windshield while driving along a winding road (a); a computer-generated perspective flight path display for instrumental flight, adapted from [53] (b); and a plan-view, two-dimensional preview tracking display (c), which is commonly used in fundamental manual control research (e.g., in [49, 54–57]).

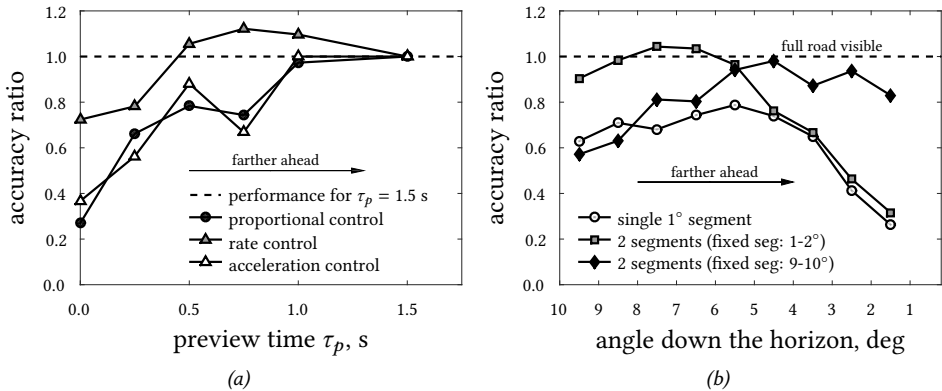


Figure 1.3: The effect of restricted preview on manual control performance (normalized). Results in (a) are reproduced from Ito and Ito [55] and are from a tracking task where all preview beyond the preview time was occluded (as in Fig. 1.2c). Results in (b) are reproduced from Land and Horwood [58] and are from a curve driving task (constant velocity, 16.9 m/s) where the full visual scene was occluded, except for selected one-degree vertical segments.

the performance improvement saturates beyond a certain *critical* preview time, which, from Fig. 1.3a, is concluded to be between 0.5 and 1 s.

1.3.2. FEEDFORWARD AND FEEDBACK CONTROL BEHAVIOR

The reason *why* substantial preview is required for adequate task performance is that preview allows humans to *anticipate* variations in the target trajectory. Without any preview humans are mostly restricted to *feedback* control [6] (in particular when the target trajectory is unpredictable). The human's response delay limits the manual control bandwidth,

and higher performance comes at the price of a less stable closed-loop system [6]. Preview of the target trajectory's future variations (i.e., road curves) supports humans in mechanizing an adequate *feedforward* control response [61]. Thereby, human controllers can effectively compensate for their own response delay and other lags in the system under control [55, 62], improving on their performance. In fact, it has been shown that humans track the target trajectory *perfectly* when their feedforward response resembles the inverse of the vehicle dynamics [42]. While the concept of feedforward is a generally accepted theory for preview control, it fails to explain exactly *what portions* of a previewed target trajectory are used for control (i.e., the inputs to the human) and *how* the different portions are relatively weighted (i.e., the human's control dynamics).

1

1.3.3. HUMANS AS ADAPTIVE CONTROLLERS

The most fundamental challenge in obtaining a general understanding of manual preview control is that, in the words of McRuer and Jex [6]: “*The human is a multimode, adaptive, learning controller capable of exhibiting an enormous variety of behavior*”. In other words, observed preview control behavior (i.e., previewed inputs, feedback and feedforward dynamics) can vary substantially depending on many, often subtle, factors. McRuer and Jex [6] defined four types of variables that provoke humans to adapt their control behavior. First and most importantly, the *task* variables are the characteristics of the control task and include, amongst others, the controlled element dynamics, the control manipulator, the forcing functions (i.e., the target trajectory and possible external disturbances), and the available sensory feedbacks. In tasks with preview the preview time is thus also a key task variable. Other elements that affect human control behavior were categorized as *operator-centered* variables (e.g., training, motivation), *environmental* variables (e.g., ambient temperature, vibration), and *procedural* variables (e.g., experimental instructions) [6].

The performance data in Fig. 1.3a clearly illustrate the human's adaptation in preview tracking tasks. The amount of preview required to achieve optimal performance in display tracking tasks (Fig. 1.3a) is approximately 1 s in proportional and acceleration control tasks, but only 0.5 s in rate control tasks. Critical task variables such as the controlled element dynamics thus affect *what portion* of the available preview information is used by the human for control. Formulating a *general* theory of manual preview control is therefore not possible without accounting for human *adaptation* to key task variables.

1.3.4. THE PREVIEW PORTIONS USED FOR CONTROL

Two methods in particular have led to substantial insight into the human's selection of optical cues for control (i.e., the human inputs), namely visual occlusion and eye-tracking [58, 63–70]. In the experiment of Land and Horwood [58, 66], drivers repeatedly steered their vehicle along the same winding road in a driving simulator under different visibility conditions. Fig. 1.3b shows that, when only a single one-degree vertical segment of the road was shown, drivers could never attain the same performance as with the full road visible (dotted line in Fig. 1.3b). In contrast, an additional, well-positioned second segment allowed participants to match or even improve on their own performance

compared to the full visibility condition. This strongly suggests that at least *two* distinct portions of the winding road that is visible ahead are used for control; these portions are referred to as the “near” and “far” visual field [51, 58, 66–69], but no consensus exists how “near” or “far” these portions actually lie ahead. This dual behavior in addition depends on the task variables, as only a single portion of the visual field suffices to attain adequate performance at low driving velocities (12.5 m/s) [58, 66], but not at 16.9 m/s (in Fig. 1.3b).

It has further been suggested that humans should “*look where they are going*” [71]. Consequently, eye-tracking data have been used to study the visual information used for control. Drivers in general tend to focus their gaze often on the *tangent point* of a curve in the road, or on a nearby *future path* point [65, 72–74]. However, results from both visual occlusion and eye-tracking experiments should be interpreted with care. Humans may cognitively “fill in” or estimate any occluded information (e.g., through interpolation), while they may not be using (only) the information that they are looking at for control [74]. Eye-tracking and occlusion data in addition fail to explain how humans translate the various portions of a previewed trajectory into a control response (i.e., the feedforward dynamics).

1.4. CYBERNETIC CONTROL-THEORETIC MODELS

It is clear now that overt human gaze, performance, and control output measurements generalize poorly to other tasks, and fail to systematically explain *the* crucial characteristic of manual control, namely human *adaptability* [6, 44, 75]. The empirical measures may differ markedly in the same task *between* individuals, and even temporally *within* an individual in the same task (e.g., due to fatigue). Consequently, the most successful approach to study the human’s low-level manual control skills is without a doubt through control-theoretic *modeling* [76, 77], as this allows for systematically quantifying human *adaptation*. The associated scientific field is known as *manual control cybernetics*².

1.4.1. MODELING COMPENSATORY TRACKING BEHAVIOR

The cybernetic models that are most *widely-accepted* are applicable to tasks where the human’s control behavior is most *restricted* [44]. The prime example is the behavior of well-trained human controllers in visual-only, single-axis compensatory tracking tasks with (quasi-)random perturbations, as illustrated in Fig. 1.4a. The compensatory tracking display shows only a single error variable, representing, for example, the difference between a vehicle’s actual and desired heading. Humans can respond only to this error and are forced to adopt a single-channel feedback control organization, resembling a classical single-input, single-output servomechanism [79]. Modeling of manual control typically focuses on the *linear* portion of the human response, $H_{o_e}(j\omega)$ in Fig. 1.4a. The remainder of the human’s control output is in general much smaller, and reflects nonlinear and time-

²A seductively simple alternative approach to study manual control could be proposed at this point, namely *introspection*: asking participants to verbally explain their control behavior. Unfortunately, introspection is rather unreliable and poorly *quantified*, because after initial familiarization with a manual control task, behavior is often *skill-based* and is performed mostly *unconsciously* [78]. It is extremely difficult to verbally explain our own unconscious behavior, such as our weighing of different portions of a previewed trajectory ahead.

varying behavior, and perception and motor noise. These effects are lumped together in Fig. 1.4a into the *remnant* $n(t)$, an approach known as *quasi-linear* modeling [6].

To model the linear error response, nonparametric Frequency-Response Function (FRF) estimates of $H_{o_e}(j\omega)$ can be obtained from experimental data using instrumental-variable (multisine) *system identification* techniques [80]. Such estimates (examples of which are shown in Fig. 1.4b,c), allowed McRuer *et al.* [6, 80] to propose the *simplified precision model*:

$$H_{o_e}(j\omega) = K_e \frac{1 + T_{L,e}j\omega}{1 + T_{l,e}j\omega} e^{-\tau_v j\omega}. \quad (1.1)$$

Here, τ_v reflects the human's input-output response time delay, a lumped combination of physical delays in the perception, cognition, neural transport, and neuromuscular activation stages, see Fig. 1.1. The gain K_e , and the lead ($T_{L,e}$) and lag ($T_{l,e}$) time-constants are adapted by the human to equalize the open-loop system dynamics to a single integrator in the crossover region [6]. This adaptation to the controlled element dynamics is summarized in the seminal *crossover model* [6].

For the example data in Fig. 1.4b,c, taken from an acceleration control task, the human's dynamics exhibit only lead and no lag equalization. The simplified precision model of Eq. (1.1) – extended with a second-order mass-spring-damper system $H_{nms}(j\omega)$ for the

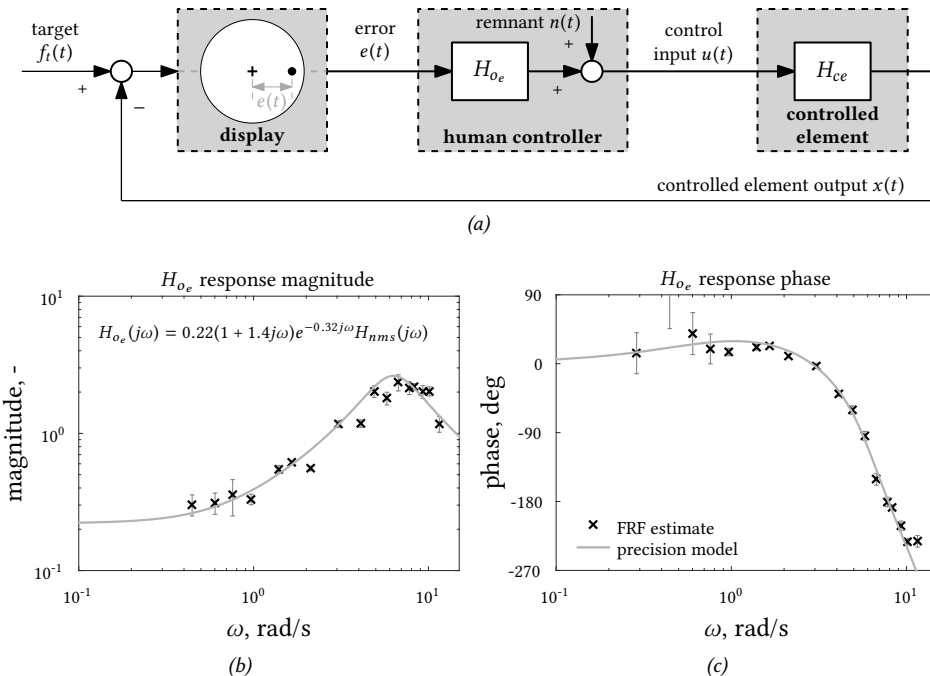


Figure 1.4: Control diagram of a human controller in a compensatory target-tracking task with a (quasi-)random target signal (a), and Bode plots of estimated response dynamics $H_{o_e}(j\omega)$ (b,c): nonparametric frequency-response functions (FRFs) and precision model fits.

arm neuromuscular system activation dynamics [44, 80] – captures the estimated FRF data in Fig. 1.4 very well. Most importantly, the *five* model parameters each quantify a distinct *physical* property of the human’s control behavior. For the data shown in Fig. 1.4, the control gain $K_e = 0.22$ and lead time-constant $T_{L,e} = 1.4$ s quantify how aggressive the human responded to the error and error rate, respectively; $\tau_v = 0.32$ s is the human’s input-output delay, and the neuromuscular system bandwidth and damping ratio are $\omega_{nms} = 6.33$ rad/s and $\zeta_{nms} = 0.38$, respectively. The direct physical interpretation of these model parameters facilitate a deep quantitative understanding of the otherwise black-box of human control, and provides insights beyond overt performance data, such as shown in Fig. 1.2. The crucial benefit of cybernetic models is that they provide a quantitative tool for *explaining* human manual control and *predicting adaptation thereof*, which can be used to systematically *optimize* human-machine interface designs [53, 81–83].

1

1.4.2. MODELING PREVIEW CONTROL

Motivated by the success of manual control models for compensatory tracking tasks, modeling efforts quickly shifted to the more general *pursuit* and *preview* tasks. These tasks provide the human controller with explicit information of the target trajectory to follow $f_t([t, t + \tau_p])$, up to preview time τ_p , and the corresponding controlled element output $x(t)$. Pure pursuit tasks are in fact identical to the more general preview tasks, but with a preview time τ_p equal to zero, such that only the *current* target value is available. As illustrated in Fig. 1.5, preview tasks allow humans to mechanize two responses in addition to the (compensatory) error response, namely *feedforward* based on the target $f_t([t, t + \tau_p])$ and feedback based on the controlled element output $x(t)$.

The stage for modeling preview control behavior was set by Sheridan [61] in 1966, who proposed three theoretical models for describing human manual preview control. Unfortunately, validating the proposed models proved difficult. Due to the fact that the three signals f_t , x , and e are *not* independent ($e = f_t - x$), FRF estimates can be obtained for only two of the three control responses [86, 87]. Even estimating two control responses is

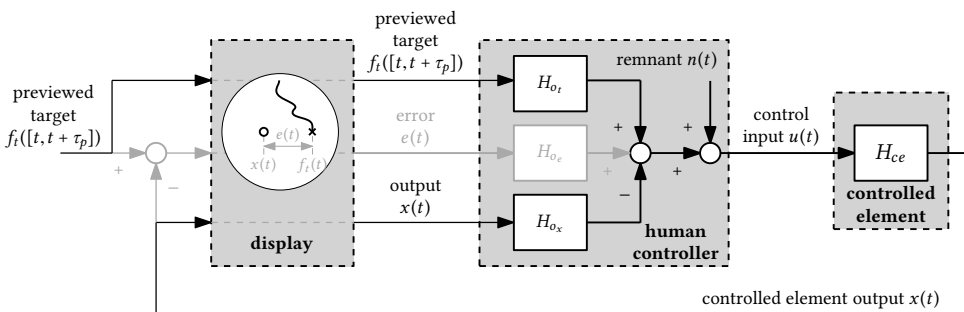


Figure 1.5: General control diagram for preview control that illustrates the multi-channel behavior of the human controller, adapted from [42, 62, 84, 85]. The single-loop compensatory response channel is shown in gray, pursuit pathways in black.

challenging, because a second uncorrelated perturbation (e.g., an external disturbance) is required besides the target signal [86, 87]. When Van Lunteren [56] in 1979 obtained the first (and so far only) multiloop FRF data of humans' feedforward and error responses in preview tracking tasks ($H_{o_i}(j\omega)$ and $H_{o_e}(j\omega)$ in Fig. 1.5), the interest in classical control models was already fading in favor of novel *optimal* control models. Dozens of preview control and driver steering models have been proposed in the five decades since the landmark paper of Sheridan [61] (see [88, 89] for recent reviews), yet not a single model's loop closures and response dynamics have ever been verified with multiloop FRF estimates. Consequently, no model for manual preview control is equally widely-accepted as the crossover and precision models for compensatory tracking tasks [6, 43].

Nothing illustrates the lack of comprehension of manual preview control behavior better than a comparison of some of the most-cited driver steering models, including those by McRuer *et al.* (1977) [90], Donges (1978) [91], MacAdam (1981) [92], Sharp *et al.* (2000) [93], Salvucci and Gray (2004) [94], and Saleh *et al.* (2013) [95]. The preview (feedforward) responses in these models are strikingly different. Different portions of preview are used as input, characterized by either one [90, 91], two [94, 95], or multiple [92, 93] points along the previewed trajectory ahead. The actual *information* used from the previewed trajectory ranges from its lateral position [92, 93] and curvature [90, 91] to optical visual angles that are available from the driver's perspective view on the road ahead [94, 95]. Because it is not clear whether the modeled inputs, (feedforward) control dynamics, and control organization match those of the actual human driver, the available models fail to reveal *how humans use preview information in manual control*.

1.5. RESEARCH GOAL

As shown, preview information is of critical importance for adequate performance and hence the *safety* of many manual control applications. Nonetheless, our understanding of the low-level skills involved in manual control with preview is very limited. It is as of yet unclear *what portions* of a previewed trajectory are used for control, how humans *integrate* and *respond* to the available preview information, and how this behavior is *adapted* to key task variables. To fill this gap, the goal of this thesis is defined as follows:

Goal of this thesis

Provide a qualitative and quantitative understanding of human behavior and adaptation in manual control with preview, through a cybernetic modeling approach.

Theories and models developed in this thesis are aimed to have a *general* validity, covering in principle *all* manual control task with preview. Because it is impossible to measure human behavior in each and every preview task, driver steering on winding roads is selected as the primary case study. Many people are familiar with this task and perform it on a daily basis. A variety of preview-related task variables characterize steering tasks (e.g., preview time, lane width, road trajectory) such that models of driver steering that account for human adaptation easily generalize to other tasks. Models of manual preview control

in driving can additionally contribute directly to the design and optimization of novel steering support technology; for example, in *shared* controllers, the automatic controller can be tuned to match the driver's steering dynamics to avoid conflicts [32, 34–37].

1.6. RESEARCH APPROACH

1.6.1. FROM COMPENSATORY TRACKING TO CURVE DRIVING

It is impossible to directly estimate the dynamics of *all* multimodal response channels that a human controller possibly mechanizes in a real-life control task such as curve driving [52], even with the multiloop FRF measurement technique as used by Van Lunteren [56]. Therefore, this thesis adopts a bottom-up approach, starting from the current state-of-the-art manual control models, those for the single-axis, visual compensatory tracking task (see Fig. 1.4a). The compensatory tracking task is equivalent to a driving task from which *only* the current lateral position error with respect to the road centerline is perceived by the driver. By stepwise introducing elements from a curve driving task into the compensatory tracking task, as schematically shown in Fig. 1.6, the additional (feedforward) response channels mechanized by human drivers are gradually introduced, and each response can be measured, interpreted, and modeled in isolation. The four major steps that bridge the gap between compensatory tracking and curve driving are: 1) pursuit and preview, 2) perspective viewing, 3) multiple feedback cues, and 4) boundary avoidance. The cover of this thesis illustrates the steps taken, connecting a compensatory display on the foreground (yellow grid) with the driver's view on a winding road in the background.

Step 1: Pursuit and preview

In contrast with compensatory tracking tasks, human controllers can adopt a *multi-channel* control organization in preview tasks, see Fig. 1.5 [62, 84]. Step 1 investigates how humans use preview for control in single-axis tracking tasks with pursuit and preview displays, comparable to Fig. 1.2c. Here, the human's control dynamics in response to a previewed trajectory can be studied without the “contaminating” effects of other control channels (i.e., due to multimodal feedback). In Step 1, multiloop FRF measurements are key to ex-

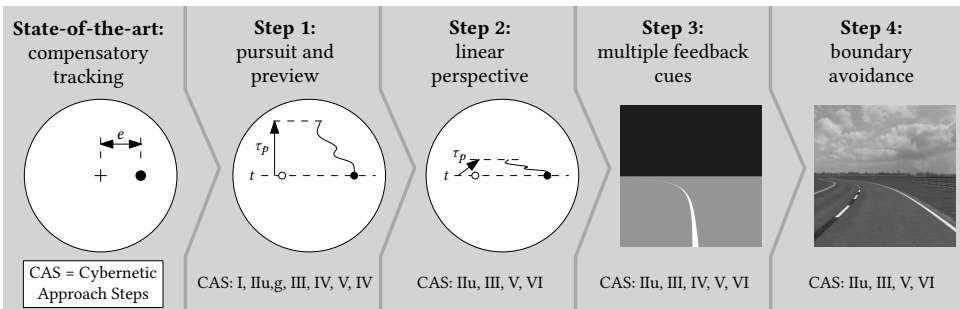


Figure 1.6: The roadmap that is being followed throughout this thesis, elements from a curve driving task (far right) are introduced stepwise into a compensatory tracking task (far left).

plicitly measure and model the human's feedforward, preview response [56].

Due to the human's versatile adaptive capabilities, proposing a *general* theory of manual pursuit and preview tracking requires understanding human *adaptation* to critical task variables. To tie in with the work on compensatory tracking by McRuer *et al.* [6, 43, 80], human adaptation to various controlled element dynamics and target trajectory bandwidths is investigated in Step 1. In addition, the effects of the preview time are of crucial importance in preview control tasks. Consequently, task variable variations along *three* dimensions are studied, which is illustrated in Fig. 1.7.

1

Step 2: Linear perspective

The viewing perspective in the real world differs markedly from that on the plan-view preview tracking displays of Step 1, as is obvious by comparing Fig. 1.2a,b with Fig. 1.2c. This has two major consequences for the information available to the human controller. First, linear perspective introduces a *nonlinear* compression of the previewed target trajectory as a function of the preview time ahead (see Fig. 1.6, Step 2). In contrast, the plan-view (orthographic projection) displays from Step 1 show the full previewed trajectory with a linear scaling independent of the preview time. It has never been explicitly investigated if and how linear perspective evokes adaptations in human preview control behavior, because this first requires a better understanding of human preview control (Step 1). The effects of linear perspective on human use of preview information are investigated in Step 2, using preview tracking tasks, but with a perspectively transformed previewed trajectory (see Fig. 1.6, Step 2).

Second, tracking displays have a marker that explicitly indicates the relevant controlled element output $x(t)$, but this is not the case for the (first-person) perspective view of

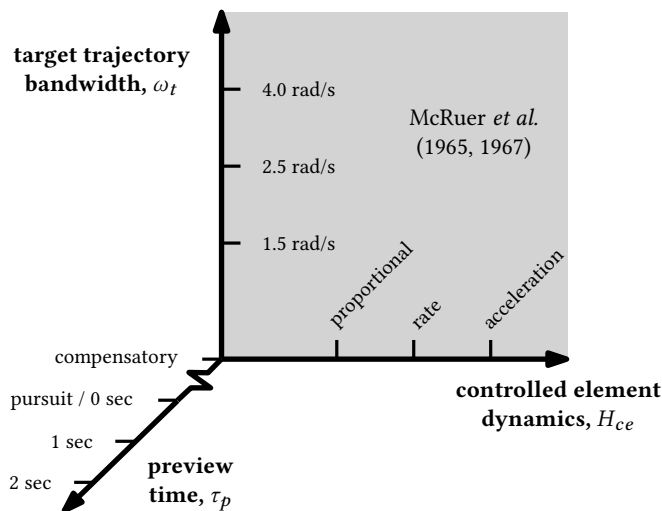


Figure 1.7: Illustration of the key task variable variations that are studied in preview tracking tasks, Step 1 in Fig. 1.6; the actual tested combinations are discussed in the respective chapters.

a human driver through the front windshield of a car. Information about $x(t)$ is only available *indirectly* from egocentric optical cues provided by the visual scenery ahead (i.e., as in the pictures of Steps 3 and 4 in Fig. 1.6). Features in the visual scene are related to the controlled element output by the perspective geometry [96, 97]. By first estimating the *lumped combination* of the perspective transformation *and* the human control dynamics, the perspective geometric relations can be used to isolate the human's control dynamics in a second step. Hereby, the exact features from the visual scene that humans select as feedbacks for control are also obtained. A similar approach has been adopted before in helicopter hovering tasks [64], piloting an aircraft through a tunnel-in-the-sky [53], aircraft pitch control tasks [98], and driver steering tasks on *straight* roads [90, 99].

Step 3: Multiple feedback cues

Real-world driving tasks provide humans with feedbacks through multiple sensory modalities, and, in addition, each modality itself can provide information about multiple controlled element outputs (e.g., lateral position, heading). Presented with these feedbacks, humans can close additional feedback loops, besides the single response to the controlled element output $x(t)$ in Steps 1 and 2. This is illustrated in Fig. 1.8. An inner-loop closure supports the main, lateral position outer-loop, by improving the suppression of external disturbances and by stabilizing unstable vehicle modes [50, 52, 100–105]. Feedback signals that provide *rate* information of the lateral position (the *main* controlled output) have been shown to be particularly useful as inner loop, alleviating the human driver from explicitly generating stabilizing lead on the lateral position [46, 86, 97, 106–112]. In driving, vestibular, proprioceptive, haptic, auditory and rotational visual cues (e.g., path/heading angle and rate) can all provide lateral velocity information and may thus be used as inner-loop feedback; none of these cues are available in Steps 1 and 2.

Studying how humans use each possible feedback variable, and correspondingly adapt their preview feedforward response, is practically infeasible within a single thesis. Step 3 therefore focuses on the two (arguably) most relevant additional feedbacks. First, *physical* motion feedback of $x(t)$ is provided in identical preview tracking tasks as in Step 1, using a motion-base simulator. Motion feedback is favored over feedback from other modalities,

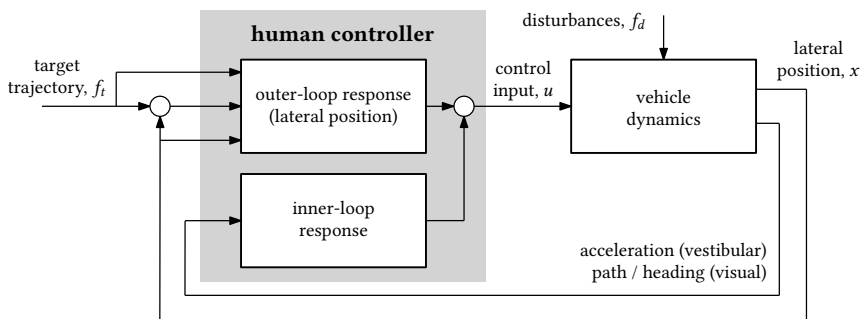


Figure 1.8: Illustration of the human as a multi-loop feedback controller, with a single inner-loop. In practice, the human may close a multiple inner loops using multimodal sensory feedback, or even using different cues from the same modality (e.g., the many outside visual cues).

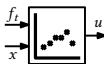
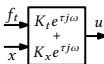
as it is well-known (and modeled) how humans use motion feedback in compensatory tracking tasks [45, 46] and because accelerations provide salient cues when negotiating curves in a car. Second, rotational *visual* feedback is introduced in a driving steering task (see Fig. 1.6, Step 3), by aligning the human's forward perspective (outside-visual) view with the vehicle heading, corresponding to a natural driving task. Consequently, the optical flow field provides information about heading and path angle (and rate) [47, 113–115], in addition to the translational, lateral position cues of Steps 1 and 2.

Step 4: Boundary avoidance

Finally, in real-world tasks such as driving, humans are typically not required to follow an exactly defined trajectory, as in the *tracking* tasks of Steps 1-3. Facilitated by available lane width, drivers may not continuously steer to keep their vehicle on the lane's centerline, but instead steer only when the vehicle approaches the lane edges [116, 117]. This behavior has been referred to as boundary-avoidance, error-neglecting, or satisficing control [90, 117]. Relative to tracking behavior, boundary-avoidance behavior is a less aggressive and possibly even *intermittent* mode of control [116, 118]. In Step 4, the multiloop, perspective preview tracking task from Step 3 is extended to an ecologically representative lane-keeping, curve driving task, see Fig. 1.6 (comparable, for example, to [52, 102, 116, 117, 119]).

1.6.2. THE CYBERNETIC APPROACH

In each of the investigated preview control tasks, human control behavior is rigorously quantified using the *cybernetic approach* [44], which comprises the following main steps:

- I: Offline predictions of human control behavior and adaption, given that a human controller model is available. 
- II: Acquisition of data in human-in-the-loop experiments, predominantly of the human's control output (u), occasionally augmented with gaze data (g). 
- III: Application of an instrumental-variable, multiloop system identification technique to obtain FRF estimates of the human's control dynamics in multiple response channels (feedforward and feedback). 
- IV: Control-theoretic modeling of the control dynamics observed in the estimated FRFs. 
- V: Application of a parametric system identification technique to fit the proposed model to the measured control data. 
- VI: Interpretation of the estimated control dynamics and model parameters, and adaptation thereof to the task variables, together with verification of any offline model predictions, if these were performed. 

The unique contribution of this thesis lies in Steps III and IV. Multiloop FRF measurements (Step III) yield objective estimates of the human's *feedback and feedforward (preview) control dynamics*, providing unmatched insight into human use of preview. Estimated FRFs further directly facilitate the formulation of *structurally-isomorphic* control-theoretic models in Step IV [85]. The model's parameters are *physically interpretable* and quantify the

key characteristics of manual preview control, identical as the parameters of the simplified precision model in Eq. (1.1) do for compensatory tracking tasks.

This thesis focuses predominantly on understanding the *linear, time-invariant* portion of the human's control dynamics, using *quasi-linear* models [6]. Humans typically exhibit fairly time-invariant, skill-based behavior when they are familiar with a particular control task [112]. Participants in the performed experiments (Step II) are therefore first trained to stable performance levels, before data is collected for analysis. Measured *steady-state* behavior is then compared *between* preview tasks with different task variables (Step VI), but temporal adaptations between tasks, or learning, are thus not investigated. Note that only human input-output response dynamics are analyzed with quasi-linear models, as opposed to *optimal control* models (e.g., see [49, 120–123]), which also quantify higher-level *goals* such as optimal performance and minimal control effort. However, optimal control models are overdetermined [124] so that their parameters are less suitable for quantifying the human's preview control behavior.

Besides the main *control behavioral* analysis, supporting eye-tracking measurement are occasionally gathered in Step II. These gaze data quantify the human's visual focus of attention along the previewed trajectory ahead, and provide supporting evidence for the portions of preview used for control (the human inputs). In addition, offline model analyses may be performed in Step I *before* the data acquisition (Step II) to explore beneficial adaptation strategies, effectively predicting human control behavior. To do so, previously proposed models are analyzed analytically or simulated in closed-loop on computers. The predictions are then verified with obtained human-in-the-loop data in Step VI. Because it is impossible to experimentally test all possible task variable combinations, such predictions are *indispensable* for obtaining a *general* theory of manual preview control that is valid beyond the experimental participants and task variable combinations.

1.7. GUIDELINES FOR THE READER

1.7.1. OUTLINE OF THE THESIS

This thesis consists of three parts, as illustrated in Fig. 1.9. In Part I, two tracking experiments are performed to obtain a basic understanding of manual preview control. These tasks are both part of Step 1 in Fig. 1.6. In Chapter 2, multiloop FRF measurements are used to derive a quasi-linear model for preview tracking tasks. Chapter 3 considers a similar task, but focuses particularly on the portions of preview that are used for control, by recording human gaze and by occluding selected regions of the target trajectory ahead.

Two appendices support Part I. First, as explained, FRFs can be estimated only for two of the three possible human response channels in preview tracking tasks (see Fig. 1.5). Whereas Chapter 2 shows only the identification and modeling results for the two-channel organization with feedforward and *controlled element output* feedback, Appendix A compares those results with the more common choice in literature for a two-channel feedforward and *error* feedback organization [42, 56, 61, 90, 91, 125–130]. Second, the remnant is not quantified in detail in the main chapters of this thesis, but models of the remnant spec-

Step 1, Fig. 1.6

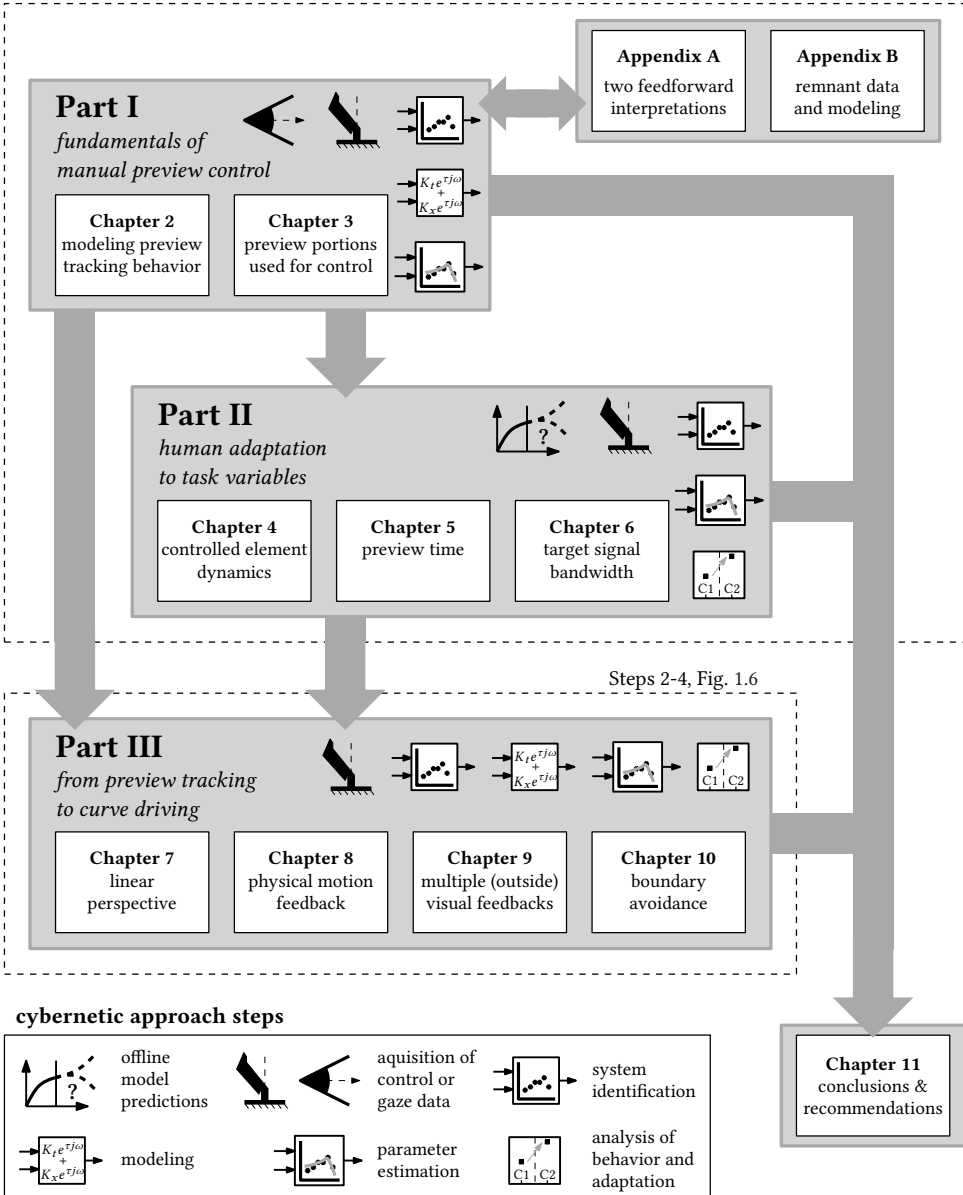


Figure 1.9: The outline of this thesis. Parts I and II correspond to Step 1 from the roadmap in Fig. 1.6, while Part III corresponds to Steps 2-4.

trum have been used together with linear models to predict human control behavior (e.g., see [83, 131–133]). To facilitate such predictions in preview tracking tasks, Appendix B provides the remnant data for the experiment of Chapter 2.

Part II of this thesis is an extension to Step 1 in Fig. 1.6, and comprehensively quantifies how humans *adapt* their preview control behavior to the three crucial task variables in Fig. 1.7. Each of Chapters 4–6 is dedicated to a specific task variable: the controlled element dynamics, the preview time, and the target trajectory bandwidth, respectively.

Part III of this thesis bridges the gap between single-axis preview tracking tasks and driver steering on winding roads. First, Chapter 7 and Chapter 8 investigate the effects of linear perspective and physical motion, respectively, on how humans use preview for control in single-axis tracking tasks. Next, Chapter 9 entails two steps: the basic preview tracking display is replaced by a real-world, outside view corresponding to the driver's forward view in a passenger car, and vehicle rotations are introduced, so that multiple feedbacks are available. Chapters 7–9 correspond to Steps 2 and 3 of the roadmap in Fig. 1.6.

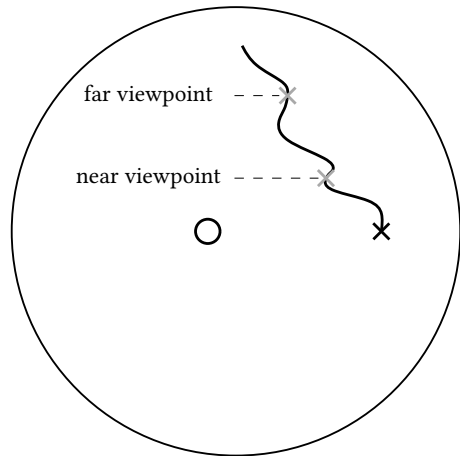
In Chapter 10, tracking and boundary-avoidance (lane-keeping) tasks are explicitly compared. The final lane-keeping task is designed to represent a real-world curve negotiation task as realistic as possible. Finally, this thesis ends with Chapter 11, which summarizes the main conclusions, presents recommendations for future work, and discusses several key implications for the design of tomorrow's human-machine interaction technology.

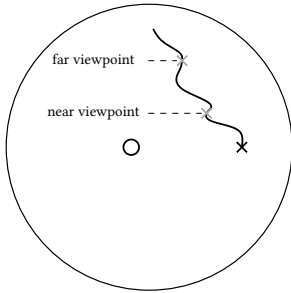
1.7.2. NOTES FOR THE READER

The chapters in this thesis have been written as stand-alone texts with the specific purpose to be published in international scientific journals. Each chapter can therefore be read independently. Chapters 2–5 and 7–9, as well as parts of this introduction have all been published in conference proceedings or in journals, details of which are supplied at the beginning of each chapter. Portions of Chapters 6 and 9 have been submitted for publication in journals and are currently (December 2018) under review. The exception that confirms the rule is Chapter 10, which directly extends (yet does not repeat) the models and theories introduced in Chapter 9 (which should thus be read first). Chapter 10 is planned to appear as a separate publication after the defense of this thesis.

PART I

FUNDAMENTALS OF MANUAL PREVIEW CONTROL



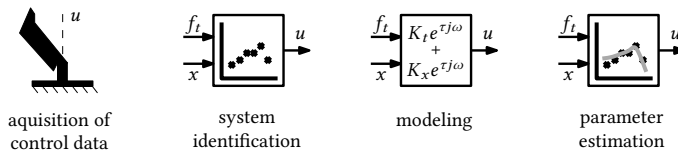


2

MODELING HUMAN PREVIEW TRACKING BEHAVIOR

Real-life control tasks often show preview information to the human controller about the future trajectory to follow. As explained in the introduction, preview allows a human controller to mechanize a feedforward response in addition to a feedback response. However, current state-of-the-art cybernetic models are limited and capture mainly the human's feedback response in zero-preview, compensatory tracking tasks. This chapter extends the widely-accepted crossover and simplified precision models for compensatory tracking tasks to pursuit and preview tracking tasks. A human-in-the-loop display tracking experiment is performed both without any preview (i.e., pursuit) and with 1 s of preview. Experimental data are analyzed with an instrumental-variable, multiloop frequency-domain system identification technique to estimate the dynamics of the human's feedforward (preview) and feedback control responses. The new model is then proposed in accordance with the observed control dynamics.

Steps of the cybernetic approach involved:



The contents of this chapter have been published as:

Title An Empirical Human Controller Model for Preview Tracking Tasks
Journal IEEE Transactions on Cybernetics, vol. 46, no. 11, pp. 2609–2621, Nov. 2016
Authors K. van der El, D.M. Pool, H.J. Damveld, M.M. van Paassen, and M. Mulder

2.1. INTRODUCTION

PREVIEW on the future track to follow is a dominant piece of information in many everyday manual control tasks. Examples include car driving along a winding road and landing an aircraft. The effect of this preview information on the behavior of the Human Controller (HC) is still relatively unknown. To study its contribution to HC behavior in isolation, other visual and motion cues that are simultaneously available are commonly removed, as well as the three-dimensional “real-world” visual perspective. In the two-dimensional *preview tracking task* that results, it is shown that tracking performance improves when the amount of preview increases [54–56, 134]. The question what control mechanisms underlie this accomplishment has not yet been answered.

Manual control behavior in simple tracking tasks *without* preview, such as the compensatory tracking task, is much better understood. The quasi-linear “crossover model”, as proposed by McRuer *et al.* [6, 80], plays a profound role in this. Derived from measurements in the frequency domain, after application of black-box system identification techniques, the crossover model reveals how HCs systematically adapt their control behavior and has become widely used in human-machine systems analysis and simulation. It would be extremely useful to also have a generic, widely applicable model for the more relevant tracking tasks with preview.

Unfortunately, research aimed at finding such a HC model for preview tracking has not been equally successful. Straightforward system identification as applied by McRuer *et al.* is impossible, due to the increased complexity of the task. Conceptual HC models for pure preview tracking tasks [54–56, 61, 62, 134, 135], and for real-life flying or driving tasks incorporating preview [63, 64, 90–92, 136–140], have been abundantly developed though; all using either one, two, or all points of the previewed target as inputs to the HC model. In general, multi-point models can describe HC behavior better than single point models. Nonetheless, which exact parts of the previewed target are used, and most importantly, *how* these parts are used by the operator for control, has remained inconclusive.

This chapter aims to derive a generic, empirical HC model for preview tracking tasks, without making *a priori* assumptions on the operator’s control mechanisms. To do so, the model is derived from measurements taken from twelve subjects and similar black-box system identification techniques are applied as used by McRuer *et al.* [80]. The measurements are collected in a combined target-tracking and disturbance-rejection task with no preview, the *pursuit* tracking task, and one second of full preview on the displayed target, *preview* tracking. In order for the model to be valid in a wide range of tasks, three basic types of controlled element (CE) dynamics are evaluated for each display: a gain, a single integrator and a double integrator.

The expected HC adaptation mechanisms on the effects of preview and CE dynamics are analyzed through an instrumental-variable, multiloop identification method using Fourier coefficients [87]. Based on this, the HC model structure is formulated and the model parameters are estimated. To assess the model validity, the coherence and Variance Accounted For (VAF) are calculated. For the first time, rigorous system identification is applied to allow the derivation of a mathematical description of the HC’s response to preview,

and to see whether there is any evidence for systematic adaptation mechanisms as found by McRuer *et al.* for compensatory tracking task.

This chapter is structured as follows. Section 2.2 provides some background regarding the identification of HC behavior and Section 2.3 explains the acquirement of measurement data of HC behavior in preview tracking tasks. Section 2.4 describes the applied system identification technique and results. The development of our empirical model will be extensively discussed in Section 2.5, followed by its validation in Section 2.6. The final two sections of this chapter contain the discussion and overall conclusions.

2.2. BACKGROUND

2

2.2.1. THE CONTROL TASK

The control task considered here is a combined target-tracking and disturbance-rejection task, illustrated in Fig. 2.1. The HC is instructed to track the target, $f_t(t)$, as accurately as possible, by generating control inputs, $u(t)$, while the CE (dynamics H_{ce}) is perturbed by disturbance $f_d(t)$. The HC minimizes tracking error, $e(t)$, defined as the difference between the target and CE output, $x(t)$:

$$e(t) = f_t(t) - x(t) \quad (2.1)$$

Additionally, preview information may be visible, visualizing a stretch of the future target, $f_t([t, t + \tau_p])$, up to time τ_p ahead. An example of a preview display is shown in Fig. 2.2a. The CE output (white marker) moves laterally over the screen, driven by the operator's control inputs and the disturbance. The previewed target (black curve) moves down over the screen with time, thereby laterally moving the current target (black marker). Note that, when only the current target is available, i.e., $\tau_p = 0$ s, a *pursuit* tracking task results.

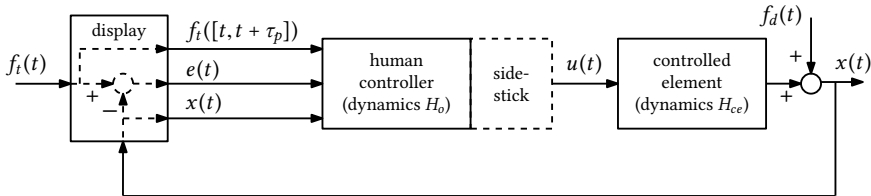


Figure 2.1: A human controller in a (preview) target-tracking and disturbance-rejection task.

2.2.2. QUASI-LINEAR MODEL FOR COMPENSATORY TRACKING

The goal of this chapter is to empirically derive a generic operator model for preview tracking tasks; an approach similar to the derivation of the model for compensatory tracking tasks by McRuer *et al.* [80]. Therefore, first some of their main methods and findings are discussed.

In compensatory tracking tasks, only the current error $e(t)$ is presented to the HC, see Fig. 2.2b. The HC model is characterized by a single-channel control diagram, Fig. 2.3,

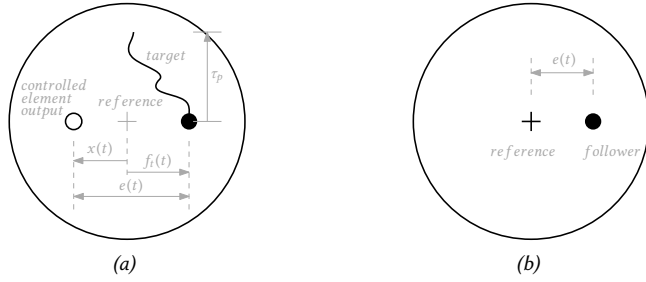


Figure 2.2: Layouts of pursuit/preview (a) and compensatory (b) displays.

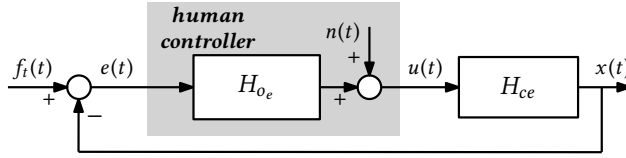


Figure 2.3: Control diagram of the crossover model for compensatory tracking [80].

hence only a target signal suffices to allow its identification. McRuer *et al.* proposed a quasi-linear model: a linear response to the error, $H_{oe}(j\omega)$, to which a remnant signal $n(t)$ is added to account for all nonlinearities in the HC's response. The target signal was a multisine with a limited number of components, which can be considered uncorrelated with the remnant at the input frequencies ω_t . The instrumental-variable identification method then yields an estimate of the HC describing function (DF) [80]:

$$\hat{H}_{oe}(j\omega_t) = \frac{S_{f_t u}(j\omega_t)}{S_{f_t e}(j\omega_t)}, \quad (2.2)$$

with S the spectral-density function of the respective subscripted signals.

For three important types of CE dynamics, a gain, a single integrator and a double integrator, McRuer *et al.* modeled the estimated DF as given in Table 2.1. Here, K_e , τ_v and $H_{nms}(j\omega)$ represent the HC's response gain, visual time delay and neuromuscular system (NMS) dynamics, respectively. HCs additionally generate lag for gain CE dynamics and lead for double integrator CE dynamics, characterized by lag and lead time-constants, $T_{l,e}$ and $T_{L,e}$. HCs thus systematically *adapt* their control dynamics, $H_{oe}(j\omega)$, to the CE

Table 2.1: Human response dynamics in compensatory tracking tasks [80].

CE dynamics	human describing function $H_{oe}(j\omega)$
K_{ce}	$K_e e^{-\tau_v j\omega} H_{nms}(j\omega) / (1 + T_{l,e} j\omega)$
$K_{ce} / j\omega$	$K_e e^{-\tau_v j\omega} H_{nms}(j\omega)$
$K_{ce} / (j\omega)^2$	$K_e e^{-\tau_v j\omega} H_{nms}(j\omega) (1 + T_{L,e} j\omega)$

dynamics in such a way that the open-loop DF approximates single integrator dynamics around the crossover frequency ω_c [80]:

$$H_{ol}(j\omega) = H_{o_e}(j\omega)H_{c_e}(j\omega) = \frac{\omega_c}{j\omega} e^{-j\omega\tau_v} \quad (2.3)$$

This model is known as the *crossover model*. Additional inclusion of the NMS, as in Table 2.1, extends the validity of the model to higher frequencies. In tracking tasks the NMS dynamics are typically modeled as [126, 128]:

$$H_{nms}(j\omega) = \frac{\omega_{nms}^2}{(j\omega)^2 + 2\zeta_{nms}\omega_{nms}j\omega + \omega_{nms}^2}, \quad (2.4)$$

with ω_{nms} and ζ_{nms} the natural frequency and damping ratio.

2.2.3. IDENTIFICATION CONSIDERATIONS

The instrumental-variable identification method applied here, discussed in detail in Section 2.4.1, allows for the identification of a number of DFs equal or smaller than the number of uncorrelated inputs to the system [56, 86, 87]. To identify the HC's response in the single-axis compensatory tracking task, this, obviously, yields no restriction.

Pursuit tracking

In pursuit tasks, the HC may respond to the CE output, the target, and the error, yielding the three DFs HC model shown in Fig. 2.4 (top) [42]. A maximum of two inputs can be inserted to the system in this particular task, the target and the disturbance, therefore, the

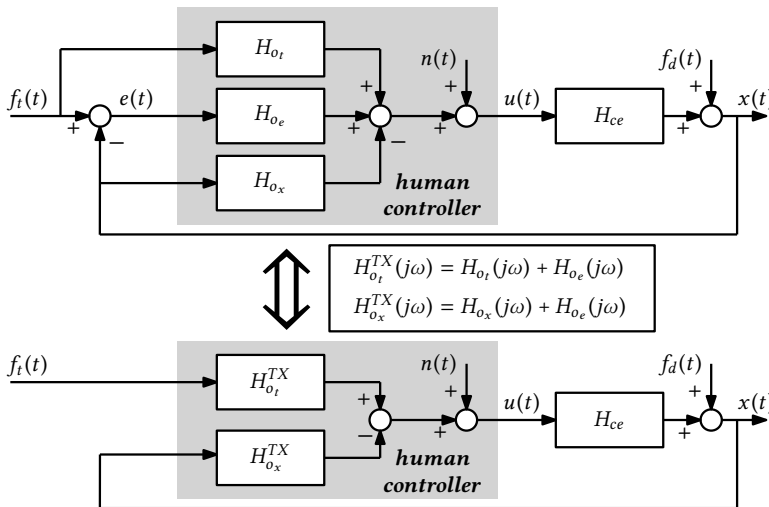


Figure 2.4: Control diagram of the general HC model for pursuit [42] and preview tracking tasks (top) and the equivalent TX two-channel model (bottom).

dynamics of only two operator DFs can be identified. Because of this constraint, no widely accepted, generic model has been identified to date [141].

A workaround is possible, by introducing a two-channel model as a *tool* to identify the HC dynamics, having either $f_t(t)$ and $x(t)$ (*TX*), $e(t)$ and $f_t(t)$ (*ET*) or $e(t)$ and $x(t)$ (*EX*) as inputs to the operator model. The *ET* model is commonly thought to be the most sensible choice, with $H_{o_e}(j\omega)$ assumed to be similar as in the crossover model and $H_{o_t}(j\omega)$ accounting for any additional feedforward control [42, 127, 128]. Wasicko *et al.* [42] showed that all three options are equally able to describe HC behavior.

This chapter uses the *TX* model, Fig. 2.4 (bottom), as it proved to be the structure in which key terms characterizing HC behavior were most easily recognized during our analysis. The two-channel *TX* model can be expressed in terms of the general, three-channel model:

$$H_{o_t}^{TX}(j\omega) = H_{o_t}(j\omega) + H_{o_e}(j\omega), \quad (2.5)$$

$$H_{o_x}^{TX}(j\omega) = H_{o_x}(j\omega) + H_{o_e}(j\omega), \quad (2.6)$$

which can be derived from the control diagrams in Fig. 2.4, for details see Appendix A. When there is no chance of confusion the *TX* superscript will be omitted in the following. Eqs. (2.5) and (2.6) show that the two DFs in the *TX* model are not the HC's *true* responses to the target and CE output, but rather lumped combinations of the true responses as defined in the general model, Fig. 2.4 (top).

Preview tracking

Extending the pursuit tracking task with preview of the target signal $f_t(t)$ allows the HC to also utilize the “infinite” number of points within the preview span for control. In theory, a unique DF $H_{o_t}(j\omega|\tau)$ can be defined with respect to each point a certain time τ ahead, $0 \leq \tau \leq \tau_p$. The control diagram is equal to that for pursuit tracking, Fig. 2.4, as all points of the previewed target are related, only differing by *negative* time “delay” τ . The total response to the target can then be expressed as:

$$H_{o_t}(j\omega) = \sum_{\tau=0}^{\tau_p} H_{o_t}(j\omega|\tau) e^{\tau j\omega} \quad (2.7)$$

Similar as for pursuit tracking, using Eqs. (2.5) and (2.6), the *TX* model can be obtained, to capture HC dynamics in preview tracking tasks. The identified dynamics can become rather complicated, however, as Eq. (2.7) shows that $H_{o_t}(j\omega)$ may contain a combination of many DFs.

2.2.4. MODELING CONSIDERATIONS

Most proposed HC models for preview tracking are based on one of the three fundamental types of models proposed by Sheridan [61]. As the aim of this chapter is to learn the actual HC model structure by recognition of individual responses in the lumped, identified DFs, such a restriction to an existing model is not made. It is interesting to see though, what the lumped responses in the *TX* model structure will be if the HC's control mechanisms are indeed as in one of Sheridan's proposals.

The extended convolution

The *ET* two-channel model, used in [54, 56, 90, 91, 136], was first introduced as the extended convolution model [61]. In addition to compensatory error control $u_e(t)$, feedforward control $u_t(t)$ is exerted:

$$u_t(t) = \int_{T_m}^{\tau_p} f_t(t + \tau) w_p(\tau) d\tau, \quad (2.8)$$

with $u(t) = u_e(t) + u_t(t)$, time T_m the HC's memory limit and $w_p(\tau)$ the target weighting function. The structure of Eq. (2.8) is similar to Eq. (2.7), however, contrary to our approach, the responses to the individual target points are explicitly related by $w_p(\tau)$. If HC behavior in preview tracking tasks is indeed characterized by the extended convolution model, $H_{o_i}(j\omega|\tau)$ in Eq. (2.7) is a series of gains that are related by $w_p(\tau)$.

CE output predictor models

In this type of model, the HC is hypothesized to predict the future CE output $\hat{x}(t + \tau)$ at some fixed time τ ahead [61, 63, 135, 139]. Together with the previewed target at the same time τ ahead, the HC can *internally calculate* a predicted error, $\hat{e}(t + \tau)$:

$$\hat{e}(t + \tau) = f_t(t + \tau) - \hat{x}(t + \tau), \quad (2.9)$$

which is corrected for with compensatory control. For example, if HCs apply linear prediction to calculate the error some time τ_{pr} ahead, $H_{o_x}(j\omega)$ in our *TX* model will equal $1 + \tau_{pr}j\omega$ and $H_{o_i}(j\omega|\tau)$ in Eq. (2.7) will equal 1 for $\tau = \tau_{pr}$ and 0 for $\tau \neq \tau_{pr}$. In practice HC's may utilize other prediction methods or predict the error at multiple future points.

A notable model related to the first two types of models is proposed in [55]. The HC is hypothesized to respond to an internally calculated, *current* error $e^*(t)$, based on a weighed average of the full previewed target into a single *current* target to steer to, $f_t^*(t)$:

$$e^*(t) = f_t^*(t) - x(t) = \int_0^{\tau_p} f_t(t + \tau) w_p(\tau) d\tau - x(t) \quad (2.10)$$

Optimal control models

Optimal control models [92, 134, 138, 140] assume the HC to steer in some "optimal" way. The optimum is the minimum of a cost function which generally weighs tracking error and control effort, but can include anything. Despite its intuitive structure its value is limited for this study, as explicit identification of the cost function is impossible [124].

2.3. DATA ACQUISITION

In this section, it is explained how the measurements, suitable for model-based analysis using system identification, were collected.

2.3.1. MEASUREMENT SETUP

A combined target-tracking and disturbance-rejection task was performed to allow identification of two operator DFs with the instrumental-variable method. Three different CE

dynamics and two different displays were evaluated, in order for the derived HC model to be valid for a wide range of tasks.

The three CE dynamics were chosen equal to the elementary dynamics evaluated by McRuer *et al.* in compensatory tracking [80]: a gain, a single integrator and a double integrator, representing position, velocity and acceleration control, respectively. Their gains, K_{ce} , were set to 0.8, 1.5 and 5, respectively. They were tuned such that the HC would never reach the stick deflection limits, yet could give small, accurate inputs.

The preview display that was used is shown in Fig. 2.2a, with the preview time τ_p equal to either 0 (pursuit) or 1 s. The latter was chosen sufficiently higher than the reported *critical* preview time for each CE dynamics: the preview time after which additional preview yields no further performance benefit [54–56, 134], suggesting constant “preview” control behavior.

2.3.2. APPARATUS

Measurements were collected in the Human-Machine Interaction Laboratory (HMI-Lab) at TU Delft, in a fixed-base part-task simulator. The display resolution was 1280 by 1024 pixels, the size 36 by 29.5 cm and the update rate 100 Hz. The display was positioned directly in front of the subjects, at approximately 75 cm, it had bright green lines and indicators on a black background and was projected with a time delay of approximately 20–25 ms. An electro-hydraulic servo-controlled side-stick with a moment arm of 9 cm, which could only rotate around its roll axis, was used to generate the control inputs. The torsional stiffness of the stick was 3.58 Nm/rad, the torsional damping 0.20 Nm·s/rad, the inertia 0.01 kg·m² and the gain 0.44 cm/deg.

2.3.3. FORCING FUNCTIONS

To analyze HC behavior with the instrumental-variable identification method, see Section 2.4.1, the target and disturbance signals were quasi-random sums of N_f sinusoids:

$$f(t) = \sum_{i=1}^{N_f} A_i \sin(\omega_i t + \phi_i), \quad (2.11)$$

with amplitude A_i , frequency ω_i and phase ϕ_i of the i^{th} sinusoid. ω_i were integer multiples k_i of the base frequency of 0.0524 rad/s, corresponding to a measurement time of 120 s. $N_f = 20$ sines were used for each forcing function; the resulting signals were considered to be unpredictable [142].

The power distribution of the target signal, as well as its total power, was chosen to be as close as possible to the signal used by McRuer *et al.*, with a bandwidth of approximately 1.5 rad/s [80]; the standard deviation σ_{f_t} was 1.27 cm (0.5 inch). The standard deviation of the disturbance signal, σ_{f_d} , was 0.51 cm (0.2 inch); both spectra are plotted in Fig. 2.5.

Double input frequency bands were used to allow for calculation of the coherence. Five realizations of f_t were used, differing only by the initial phases ϕ_i of the individual sine

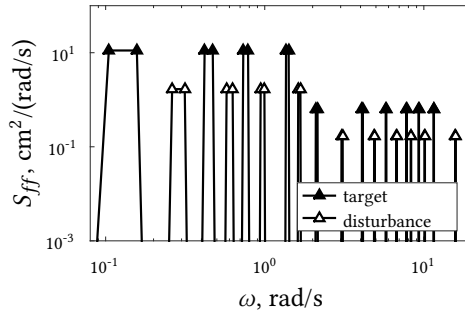


Figure 2.5: Single-sided power spectra of the target and disturbance signals.

2

components, to prevent subjects from recognizing parts of the signals because of repeated exposure. It was unlikely that subjects could memorize the disturbance signal, as it was not explicitly visible on the display, therefore a single realization was used. All forcing functions parameters are given in Table 2.2.

2.3.4. SUBJECTS, INSTRUCTIONS AND PROCEDURE

Twelve motivated, male volunteers were instructed to minimize tracking error $e(t)$. Each subject performed the six conditions in a single session, with breaks every 45 minutes.

Table 2.2: Amplitudes, frequencies, and phases of the experimental target and disturbance signals.

		target signals f_t						disturbance signal f_d			
k_t	A_t	ω_t	$\phi_{t,1}$	$\phi_{t,2}$	$\phi_{t,3}$	$\phi_{t,4}$	$\phi_{t,5}$	k_d	A_d	ω_d	ϕ_d
-	cm	rad/s	rad	rad	rad	rad	rad	-	cm	rad/s	rad
2	0.610	0.105	3.646	0.174	4.878	2.917	2.709	5	0.237	0.262	2.546
3	0.610	0.157	0.030	5.953	2.868	2.040	0.508	6	0.237	0.314	6.264
8	0.610	0.419	1.277	0.655	4.205	5.857	3.369	11	0.237	0.576	6.283
9	0.610	0.471	2.367	3.526	1.921	4.188	0.477	12	0.237	0.628	1.865
14	0.610	0.733	3.901	4.809	3.786	2.602	5.165	18	0.237	0.942	3.196
15	0.610	0.785	4.287	3.391	4.201	4.110	3.286	19	0.237	0.995	5.309
26	0.610	1.361	5.554	2.965	6.014	3.640	0.619	31	0.237	1.623	3.626
27	0.610	1.414	2.411	4.446	5.538	1.626	3.397	32	0.237	1.676	3.229
40	0.145	2.094	2.551	1.730	0.183	3.703	3.131	58	0.075	3.037	0.165
41	0.145	2.147	0.490	2.952	4.354	6.108	3.926	59	0.075	3.089	0.082
78	0.145	4.084	5.431	5.432	1.588	3.406	3.812	93	0.075	4.869	4.233
79	0.145	4.136	4.238	3.697	0.270	3.801	5.548	94	0.075	4.922	5.366
110	0.145	5.760	5.014	6.200	1.858	5.698	4.196	128	0.075	6.702	5.386
111	0.145	5.812	1.768	5.910	0.585	2.903	5.239	129	0.075	6.754	4.756
148	0.145	7.749	0.163	5.952	4.385	3.622	1.333	158	0.075	8.273	1.453
149	0.145	7.802	0.156	3.563	1.825	4.269	5.889	159	0.075	8.325	3.291
177	0.145	9.268	0.214	0.077	0.325	5.841	4.290	193	0.075	10.105	3.243
178	0.145	9.320	3.687	1.961	0.269	3.608	0.164	194	0.075	10.158	3.924
220	0.145	11.519	5.176	5.484	6.179	4.261	3.196	301	0.075	15.760	3.171
221	0.145	11.572	1.266	1.050	0.304	2.325	4.165	302	0.075	15.813	1.976

The total experiment lasted about 2.5 to 3.5 hours per subject, depending on the training required.

First, each condition was practiced to get the subject accustomed to the task. After that, the six conditions were performed consecutively in random order. When stable performance was achieved in a condition, generally after three to eight runs, the five actual measurement runs were recorded, after which subjects moved on to the next condition. After each run the root-mean-square of the error was reported to the subjects as a measure of their performance to motivate them.

Each run lasted 128 s, of which the first 8 s were used as run-in time; these data were not used for analysis. The remaining 120 s from the time traces of the error $e(t)$, the CE output $x(t)$, the operator's control actions $u(t)$, and the target and disturbance forcing functions were sampled at 100 Hz.

2.4. ESTIMATING OPERATOR CONTROL DYNAMICS

2.4.1. METHOD

The applied black-box, instrumental-variable, multiloop identification method is based on Fourier coefficients [87]. It is equivalent to the method based on spectral-density functions as used by McRuer *et al.* [80], see Eq. (2.2). For the TX two-channel HC model in Fig. 2.4, the Fourier transform of the operator's control actions at an arbitrary target input frequency ω_t is given by:

$$U(j\omega_t) = H_{o_t}(j\omega_t)F_t(j\omega_t) - H_{o_x}(j\omega_t)X(j\omega_t). \quad (2.12)$$

The capitals, U , F_t , and X , denote the Fourier transforms of the respective signals; remnant is neglected as its contribution can be assumed to be small at the input frequencies (see Appendix B). The two unknown operator DFs can be solved for by constructing a second equation, obtained by interpolating the same signals from the neighboring disturbance signal input frequencies ω_d to the considered ω_t . The resulting set of equations is:

$$\begin{bmatrix} U(j\omega_t) \\ \tilde{U}(j\omega_t) \end{bmatrix} = \begin{bmatrix} F_t(j\omega_t) & -X(j\omega_t) \\ \tilde{F}_t(j\omega_t) & -\tilde{X}(j\omega_t) \end{bmatrix} \begin{bmatrix} H_{o_t}(j\omega_t) \\ H_{o_x}(j\omega_t) \end{bmatrix}, \quad (2.13)$$

with the interpolated values denoted by a tilde. Solving Eq. (2.13) for the estimates of the operator DFs yields:

$$\hat{H}_{o_t}(j\omega_t) = \frac{\tilde{U}(j\omega_t)X(j\omega_t) - U(j\omega_t)\tilde{X}(j\omega_t)}{\tilde{F}_t(j\omega_t)X(j\omega_t) - F_t(j\omega_t)\tilde{X}(j\omega_t)}, \quad (2.14)$$

$$\hat{H}_{o_x}(j\omega_t) = \frac{\tilde{U}(j\omega_t)F_t(j\omega_t) - U(j\omega_t)\tilde{F}_t(j\omega_t)}{\tilde{F}_t(j\omega_t)X(j\omega_t) - F_t(j\omega_t)\tilde{X}(j\omega_t)}. \quad (2.15)$$

Mutatis mutandis, replacing ω_t for ω_d yields the operator DFs at the latter frequencies.

As the method poses no *a priori* assumptions on the dynamics in the DFs, the estimates can be regarded as the actual operator's control actions in the frequency domain for the chosen model inputs and outputs. The method has been successfully applied before to identify operator DFs in similar tasks involving multiloop HC behavior [56, 86, 115, 141].

2.4.2. RESULTS

A selection of typical identified operator DFs, averaged over the five runs in the frequency domain, is given in Figs. 2.6–2.8. Each figure shows four graphs: the magnitude (top) and the phase (bottom) of the HC's response to target (left) and to the CE output (right). The results for the preview (black triangles) and the pursuit (gray dots) conditions are drawn together, to illustrate the effects of preview on HC behavior.

In the next section, we will explain our approach to derive the model based on the data of the shown subjects/conditions combinations only. It equally applies to all measurements of all twelve tested subjects, which will be shown in Section 2.6. Two distinct different control strategies are found between subjects in single integrator CE dynamics tasks with preview, hence a representative example of each is given. For gain and double integrator CE dynamics conditions only a single representative subject is shown, as no structural between-subject differences are found.

2

2.5. HUMAN CONTROLLER MODEL DERIVATION

Here, the HC model that captures all identified DFs in Figs. 2.6–2.8 is derived, by first modeling the DF in each individual condition separately. These are combined into a single, comprehensive HC model towards the end of this section. For easier understanding by the reader, the order of individual model derivations is such that the conditions in which the simplest dynamics are obtained are explained first, advancing to more complex HC dynamics throughout this section.

2.5.1. CONTROLLED ELEMENT OUTPUT RESPONSE

For all evaluated CE dynamics, $|H_{o_x}(j\omega)|$ is similar in the pursuit and preview conditions. The magnitude slope is -1 in the mid-frequency range for gain CE dynamics, Fig. 2.7b, which can be modeled with a gain, K_x , and a lag term, $T_{l,x}$. For the single and double integrator CE dynamics, Fig. 2.6b, f and Fig. 2.8b show that $|H_{o_x}(j\omega)|$ has a slope of 0 and +1, respectively. These can be modeled by a gain K_x and a combination of a gain K_x with a lead term $T_{L,x}$. The HC's adaption to the CE dynamics is thus similar as in compensatory tracking [80], see Section 2.2.2. Additionally, the decrease in $|H_{o_x}(j\omega)|$ at the highest input frequencies indicates the presence of NMS dynamics. This is not clearly visible for gain CE dynamics though, possibly because here the subjects adopted a NMS break frequency well above the highest measured frequency. For all conditions, $\angle H_{o_x}(j\omega)$ at high frequencies shows the decreasing phase lag that characterizes a pure time delay; the HC's response

Table 2.3: Human CE output response dynamics.

CE dynamics	human describing function $H_{o_x}(j\omega)$
K_{ce}	$K_x H_{nms}(j\omega) e^{-\tau_v j\omega} / (1 + T_{l,x} j\omega)$
$K_{ce}/j\omega$	$K_x H_{nms}(j\omega) e^{-\tau_v j\omega}$
$K_{ce}/(j\omega)^2$	$K_x H_{nms}(j\omega) e^{-\tau_v j\omega} (1 + T_{L,x} j\omega)$

time delay, τ_v . The mentioned phenomena combined yield our model for $H_{o_x}(j\omega)$, see Table 2.3.

2.5.2. TARGET RESPONSE

The decrease of $|H_{o_t}(j\omega)|$ at high frequencies indicates the presence of the same NMS dynamics as in $H_{o_x}(j\omega)$. Contrary to $H_{o_x}(j\omega)$, the shape of $H_{o_t}(j\omega)$ is not similar in preview and pursuit tracking tasks; within preview tracking tasks even variations exist *between* subjects, see the estimates for single integrator CE dynamics in Fig. 2.6a, c, e and g. $H_{o_t}(j\omega)$ will therefore be modeled step by step.

Pursuit tracking tasks

For all considered CE dynamics, the shape of $|H_{o_t}(j\omega)|$ is very similar to that observed for $|H_{o_x}(j\omega)|$. They differ in magnitude though, which we model by the *target weighting gain*, K_f . The phase shift at the highest input frequencies is approximately equal in $H_{o_t}(j\omega)$ and $H_{o_x}(j\omega)$, see, for instance, Fig. 2.8c and d, suggesting that τ_v is equally large in both responses. So, in pursuit tracking tasks, $H_{o_t}(j\omega)$ is modeled with:

$$H_{o_t}^{PS}(j\omega) = K_f H_{o_x}(j\omega), \quad (2.16)$$

with $H_{o_x}(j\omega)$ as given in Table 2.3.

Preview tracking tasks

For Subject 2 and single integrator CE dynamics, $H_{o_t}(j\omega)$ is, at low frequencies, approximately equal to the pursuit condition, see Fig. 2.6e-h. Above 2 rad/s, $|H_{o_t}(j\omega)|$ reduces strongly with a break frequency that is too low to be caused by the NMS. Possibly, parts of the target signal's high frequencies were purposely ignored, facilitated by the available preview. We model this with a low-pass filter with lag time-constant $T_{l,f}$ in a filtering function $H_{o_f}(j\omega)$, which also incorporates the previously defined weighting gain K_f :

$$H_{o_f}(j\omega) = K_f \frac{1}{1 + T_{l,f}j\omega}. \quad (2.17)$$

The distinctive increasing phase lead at higher frequencies, see Fig. 2.6g, further indicates the presence of a *negative* time delay, suggesting that the subject is responding to the previewed target somewhere ahead. This *far-viewpoint* is located τ_f seconds ahead; subscript f is added to all parameters associated with it.

As the HC's response delay is now lumped with the negative ("look-ahead") time delay, it can no longer be uniquely determined from the DFs, which only capture the total input-output delay. We therefore assume that τ_v is equal to that in $H_{o_x}(j\omega)$ as was also found in the pursuit conditions. Summarizing, for Subject 2, $H_{o_t}(j\omega)$ is modeled by:

$$H_{o_t}^{SI-PR, S^2}(j\omega) = H_{o_x}(j\omega) H_{o_f}(j\omega) e^{\tau_f j\omega}. \quad (2.18)$$

Remember that the NMS dynamics and τ_v are incorporated in $H_{o_x}(j\omega)$, see Table 2.3. Eq. (2.18) is referred to as the *far-viewpoint response*, $H_{o_{r,f}}(j\omega)$.

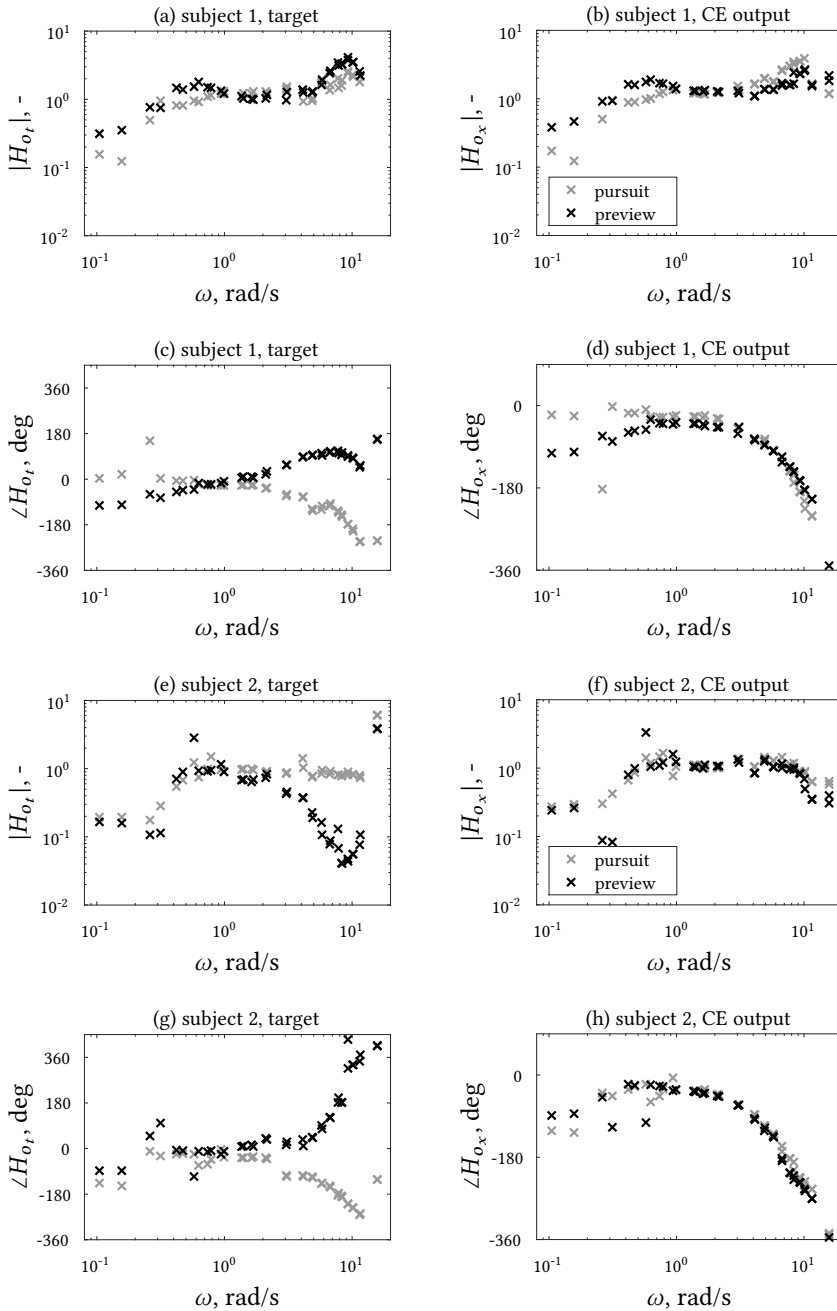


Figure 2.6: Operator DFs for single integrator CE: Subject 1 (a-d) and Subject 2 (e-h).

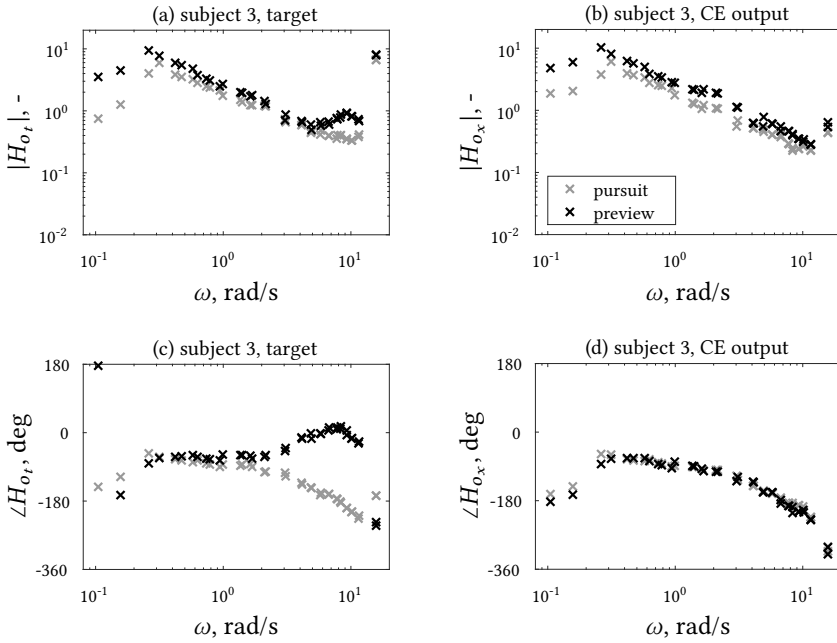


Figure 2.7: Operator DFs for gain CE: Subject 3.

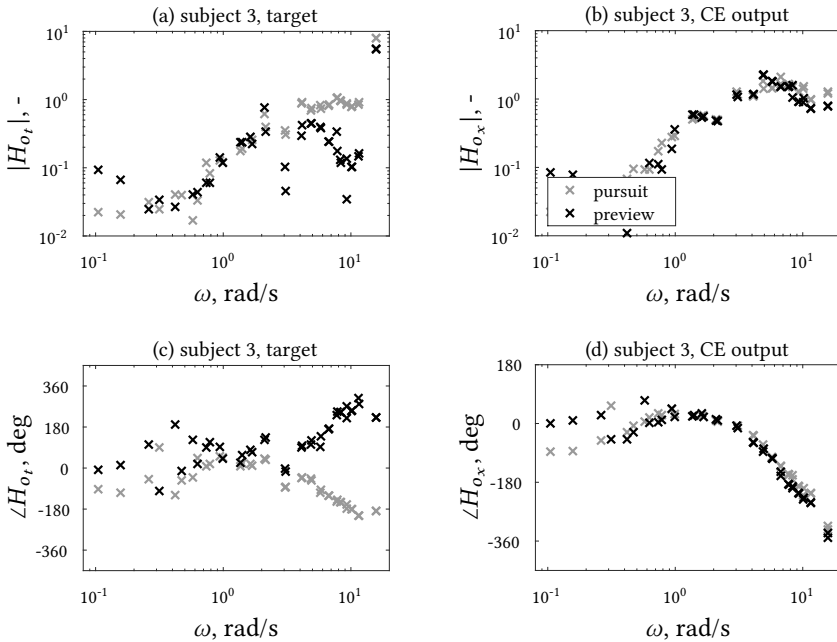


Figure 2.8: Operator DFs for double integrator CE: Subject 3.

Equation Eq. (2.18) can only partially capture the DFs for Subject 1, see Fig. 2.6a and c. Instead of the magnitude drop and increasing phase that were observed at high frequencies for Subject 2, here, a magnitude *peak* appears and the response phase flattens. This reveals the presence of more complex dynamics, i.e., a summation of (at least) two additive or parallel responses, each with its own negative time delay. This subject clearly uses multiple points of the previewed target for control.

The first response is assumed to be equivalent to Subject 2's far-viewpoint response, see Eq. (2.18). The flattening of $\angle H_{o_t}(j\omega)$ at high frequencies, Fig. 2.6c, indicates that the look-ahead time for the second response is lower than τ_f , hence it is named the *near-viewpoint response*, $H_{o_{t,n}}(j\omega)$. The point responded to is located τ_n seconds ahead.

As opposed to the low-pass filtered far-viewpoint response, the $H_{o_{t,n}}(j\omega)$ needs to be high-pass filtered, so it has a contribution only in the high-frequency region where the first response insufficiently describes the observed behavior. Again, we first define the *near-viewpoint filter* $H_{o_n}(j\omega)$:

$$H_{o_n}(j\omega) = K_n \frac{j\omega}{1 + T_{l,n}j\omega}, \quad (2.19)$$

with gain K_n and lag time-constant $T_{l,n}$. The NMS dynamics and visual response time delay are again assumed to be common with the other responses, therefore, $H_{o_{t,n}}(j\omega)$ becomes:

$$H_{o_{t,n}}(j\omega) = H_{o_n}(j\omega)e^{(\tau_n - \tau_v)j\omega}H_{nms}(j\omega). \quad (2.20)$$

Finally, the total target DF $H_{o_t}(j\omega)$ for Subject 1 is a summation of the near- and far-viewpoint responses:

$$H_{o_t}^{SI-PR,S1}(j\omega) = H_{o_{t,n}}(j\omega) + H_{o_{t,f}}(j\omega). \quad (2.21)$$

When $H_{o_{t,n}}(j\omega) = 0$, Eq. (2.21) is simply $H_{o_{t,f}}(j\omega)$, given by Eq. (2.18). Additionally, if $T_{l,f} = \tau_f = 0$ s, Eq. (2.18) further reduces into Eq. (2.16). Equation Eq. (2.21) thus simply *extends* the simpler models previously found for $H_{o_t}(j\omega)$.

For gain CE dynamics, no structural differences are observed between subjects. At high frequencies a similar magnitude peak and phase lead occurs as for Subject 1 for single integrator CE dynamics, see Fig. 2.7a and c. The combination of the near- and far-viewpoint responses in Eq. (2.21) is well capable to capture both these phenomena. Note that $H_{o_x}(j\omega)$ in the far-viewpoint response accounts for the HC's adaption to the CE dynamics.

Similar considerations apply for double integrator CE dynamics. For Subject 3, presented in Fig. 2.8, the ever-increasing phase at high frequencies suggests that only the far viewpoint is utilized. For a few other subjects the phase seems to flatten somewhat at high frequencies, although not as clearly as for conditions with single integrator CE dynamics. The derived two-point model can definitely capture these variations between subjects.

2.5.3. MODEL RESTRUCTURING

The two-channel model structure in Fig. 2.4, combined with the modeled $H_{o_x}(j\omega)$ and $H_{o_t}(j\omega)$ in Table 2.3 and Eqs. (2.16)–(2.21), respectively, yields a generic HC model for

pursuit and preview tracking, for gain, single integrator and double integrator CE dynamics. Fig. 2.9 (top) shows the complete model with all dynamics substituted into the control diagram. HC limitations, i.e., the NMS dynamics and time delay, are separated from $H_{o_x}(j\omega)$ for clarity. Moving all common elements to the right of the summation point and separating the summation in $H_{o_i}(j\omega)$ into two parallel blocks, the model structure at the bottom of Fig. 2.9 is obtained. Its structure intuitively explains how HCs perform pursuit and preview tracking tasks.

The bottom figure reveals that $H_{o_x}(j\omega)$ is in fact a response to the difference between the filtered far-viewpoint $f_{t,f}^*(t)$ and $x(t)$, hence to an *internally calculated error* $e^*(t) = f_{t,f}^*(t) - x(t)$. $H_{o_x}(j\omega)$ is therefore renamed to $H_{o_{e^*}}(j\omega)$. The target to steer to, $f_{t,f}^*(t)$ is obtained by *low-pass filtering* and *weighting* the far-viewpoint with $H_{o_f}(j\omega)$, Eq. (2.17); a possible visualization of this processing is illustrated in the display in Fig. 2.9.

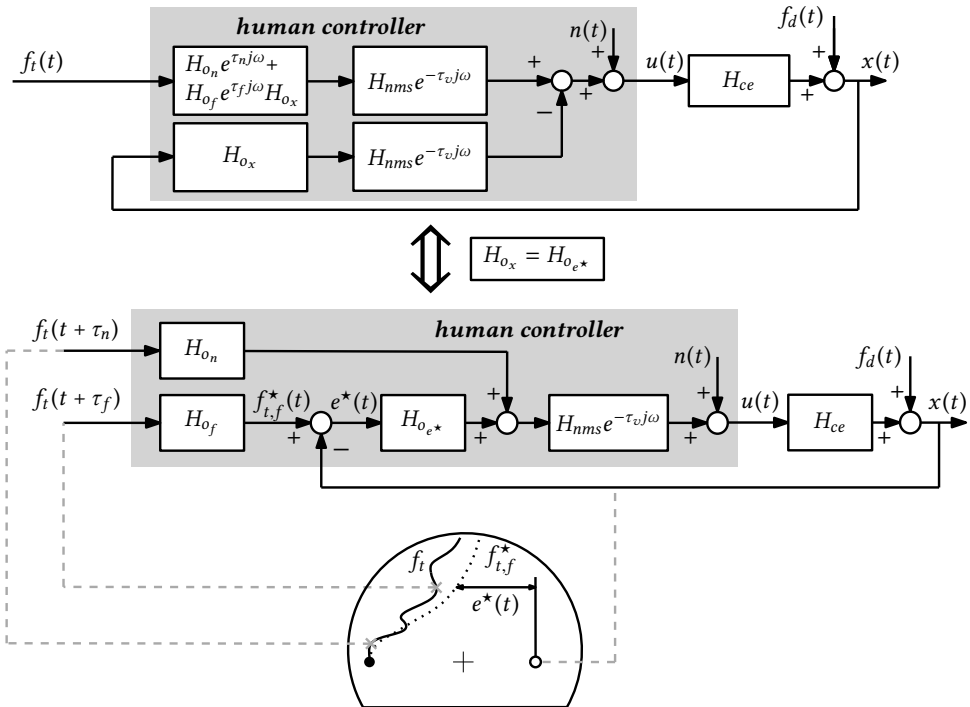


Figure 2.9: Control diagram of the derived HC model, restructured into a more intuitive form. The display at the bottom presents a possible physical interpretation of the modeled behavior.

2.5.4. DISCUSSION

Preview tracking

From the restructured model, the two governing mechanisms underlying the HC's control actions appear to be *feedback* and *pure feedforward*, as commonly suggested before [56, 61, 90, 91, 136, 137, 139], although never with all the key terms introduced here. The two responses do not only separate the HC behavior into two *spatial* regions, but also into two *frequency* regions, i.e., low-pass filtered feedback control with respect to a far-viewpoint and high-pass filtered feedforward control with respect to a near-viewpoint.

The feedforward $H_{o_n}(j\omega)$ is an open-loop control action, facilitated at the high frequencies because substantial parts of full periods of the target sine-components are instantly visible on the display. The expected function of the inverse of the CE dynamics, which would result in perfect target-tracking performance [42, 126, 128], is not found here though, possibly because the NMS dynamics also become effective at those frequencies where the contribution of the feedforward is large, hence interfering with it.

The preview visualizes a negligible portion of full periods of the target sine-components at low frequencies, so anticipating these is more difficult and feedback control is exerted. The mechanism behind this control is somewhat like the crossover model for compensatory tracking [80] with a similar adaptation to the CE dynamics. The definition of the error the HC responds to is rather different, however. The structure of the feedback response is more similar to the HC model as proposed by Ito and Ito [55], which is also an extension of the crossover model.

Previous findings that a minimum of two points of the target are needed as model inputs to adequately model the measured HC behavior [55, 64, 92, 134, 135, 138, 140] are only partially confirmed. Depending on the subject and the condition, either a response to a single point or to two points is initiated. The substantial differences between subjects are easily captured by the model.

Pursuit tracking

Recall that the pursuit tracking task is a special case of preview tracking task with $\tau_p = 0$ s. The fact that the derived model for pursuit tracking is also a reduced version of the model for preview tracking is therefore very intuitive. In pursuit conditions, $H_{o_n}(j\omega) = 0$ and $H_{o_f}(j\omega) = K_f$. The model thus explains what already followed from the identified DFs, namely that no pure open-loop response is initiated and that the feedback response is now based on to the *current* target, weighted by K_f . So, similar as in preview tracking, the HC is responding to an internally calculated error, $e^*(t)$.

Compensatory tracking

The derived model fits very well in the crossover model framework for compensatory tracking, derived by McRuer *et al.* [80]. In compensatory tracking, the HC can respond to the true error only, so $K_f = 1$ by definition. Substitution in Fig. 2.9 yields the exact same control model as in Fig. 2.3.

2.6. PARAMETER ESTIMATION AND MODEL VALIDATION

In this section the derived model will be validated, starting with a justification for the use of a quasi-linear HC model. The ability of the model to describe the measured HC control actions is quantified, and all model parameters are estimated and analyzed for consistency.

2.6.1. METHODS

Coherence

The coherence is a measure for the linearity between two signals, and has a value between 0 (completely nonlinear) and 1 (perfectly linear). A highly linear relation between the input forcing functions and the HC control actions can justify the use of a quasi-linear model. The coherence between the target signal and the HC's control output is given by [143]:

$$\Gamma(\tilde{\omega}_{f_i}) = \sqrt{\frac{|\tilde{S}_{f_i u}(\tilde{\omega}_{f_i})|^2}{\tilde{S}_{f_i f_i}(\tilde{\omega}_{f_i})\tilde{S}_{uu}(\tilde{\omega}_{f_i})}}. \quad (2.22)$$

The tilde indicates the average power-spectral density (\tilde{S}) at the average frequency ($\tilde{\omega}$) between the neighboring frequencies in a double band. The coherences at the disturbance signal input frequencies are calculated similarly.

Model fitting/parameter estimation

The parameters are estimated by fitting the model to the DFs in the frequency domain, using the two-channel TX model structure. The normalized error between, ϵ , is a measure for the quality of the fit, and is given for each parameter set Θ by:

$$\begin{aligned} \epsilon(\Theta) = & \sum_{i=1}^{2N_f} W \frac{|H_{o_t}^{DF}(j\omega_i) - H_{o_t}^{mod}(j\omega_i|\Theta)|^2}{|H_{o_t}^{DF}(j\omega_i)|^2} \\ & + \sum_{i=1}^{2N_f} W \frac{|H_{o_x}^{DF}(j\omega_i) - H_{o_x}^{mod}(j\omega_i|\Theta)|^2}{|H_{o_x}^{DF}(j\omega_i)|^2}, \end{aligned} \quad (2.23)$$

with $2N_f$ the total number of input frequencies and W a weighting vector $[0 \ 0 \ w_3 \ \dots \ w_{N-2} \ 0 \ 0]^T$. The two zeros at the upper and lower end of W ensure that the unreliable, extrapolated DF components at the lowest and highest input frequencies cannot affect the results. All other weights, w_3 to w_{N-2} , were determined based on the estimation reliability of the respective DF component. Weighting penalties were added to Eq. (2.23) for any negative parameter estimates and values of the NMS break frequency outside the measured frequency range. The parameter set that describes the operator's control behavior best was then calculated by minimizing the cost function ϵ :

$$\Theta_{opt} = \arg \min_{\Theta} \epsilon(\Theta). \quad (2.24)$$

Variance accounted for

The VAF is a measure for the similarity between two signals, and its highest value of 100% indicates that the two signals are exactly equal. Applied to compare the measured control

inputs $u(k)$ and the modeled control inputs $\hat{u}(k)$, it serves as a measure for the ability of the model to capture the HC's behavior. It is calculated by:

$$\text{VAF} = \left(1 - \frac{\sum_{k=1}^N |u(k) - \hat{u}(k)|^2}{\sum_{k=1}^N u^2(k)} \right) \times 100\%, \quad (2.25)$$

with N the number of samples in the time series. $\hat{u}(k)$ is obtained from time-domain simulation of the derived model with the target and CE output signals as inputs. The VAF is calculated per run, as time averaging is not possible due to the five different target signal realizations presented to the HC.

2

2.6.2. RESULTS

Coherence

Fig. 2.10 shows the average coherence per condition, calculated per run for all twelve subjects. The coherence between $f_i(t)$ and $u(t)$ is lower in preview tracking than in pursuit tracking at high frequencies. This corresponds to [54] and suggests that HCs exert less linear, perhaps time-varying control when preview is available. Except for the lowest input frequency, the mean coherence is well above 0.75 in all evaluated conditions, justifying the use of a quasi-linear model.

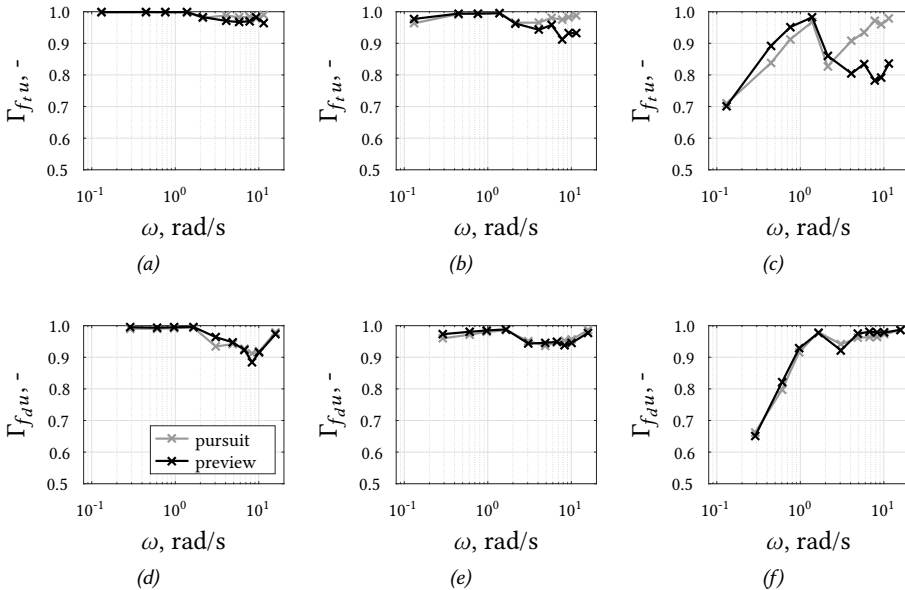


Figure 2.10: Coherence between the control inputs u and the target f_t (top) and disturbance f_d (bottom) inputs for gain (a,d), single integrator (b,e) and double integrator CE dynamics (c,f). To clarify, the pursuit data are shifted slightly to the left.

Model fits

The fitted models are drawn with solid lines in the DF Bode plots in Figs. 2.11–2.13, for the same CE dynamics and subjects as in Section 2.4. The model clearly captures the shape of the DFs for all CE dynamics.

For the preview condition, the HC's response to the far viewpoint, Eq. (2.18), and near viewpoint, Eq. (2.20), are also plotted individually to clarify their contributions to the total target response. Indeed, the magnitude plots show that the far-viewpoint response (black dashed line) always dominates $H_{o_t}(j\omega)$ at low frequencies. Depending on the condition and subject, the near-viewpoint response (gray dash-dotted line) can become the dominant contributor at high frequencies.

At low frequencies, the DFs are not very well captured by the (linear) model, especially for the double integrator CE. This is consistent with the fact that the coherence is also comparatively low at these frequencies (Fig. 2.10), indicating that the contribution of the remnant is high. As such, the weights w_i in Eq. (2.23) were low, resulting in a less tight fit to the DFs at these frequencies. Even for the double integrator CE the differences remain small, considering the visual magnification due to the logarithmic scale of the Bode plots.

Parameter estimates

The estimated model parameters are given in Table 2.4 for the same combination of subjects and conditions as the Bode plots in the previous sections. Estimates of the HC parameters that are also present in the model for compensatory tracking, namely K_{e^*} , T_{l,e^*} , T_{L,e^*} , τ_v , ω_{nms} and ζ_{nm} , see Table 2.1, are consistent with previous HC behavior studies, for example [6, 126, 128]. For conditions with gain CE dynamics, ω_{nms} is indeed well above the highest input frequency. Therefore it can not be estimated accurately and its estimate approaches our defined limit of 18 rad/s.

Table 2.4: Estimated human controller model parameters; PS = pursuit and PR = preview.

Subject #	K_{ce}		K_{ce}/s				K_{ce}/s^2	
	PS	PR	PS	PR	PS	PR	PS	PR
	3	3	1	1	2	2	3	3
K_{e^*} , -	3.85	6.62	1.43	1.11	0.85	1.07	0.14	0.14
T_{l,e^*} , s	2.06	2.39	-	-	-	-	-	-
T_{L,e^*} , s	-	-	-	-	-	-	2.54	2.22
τ_v , s	0.18	0.16	0.23	0.18	0.21	0.25	0.28	0.31
ω_{nms} , rad/s	17.9	18.0	11.2	10.2	7.89	7.66	6.15	5.33
ζ_{nm} , -	0.18	0.37	0.30	0.26	0.55	0.58	0.67	0.50
K_n , -	-	0.06	-	0.18	-	0.01	-	0.32
τ_n , s	-	0.08	-	0.34	-	0.00	-	0.00
$T_{l,n}$, s	-	0.06	-	0.04	-	0.94	-	5.89
K_f , -	1.21	1.11	0.95	1.12	1.01	0.93	0.54	0.63
τ_f , s	-	0.55	-	0.70	-	0.97	-	0.99
$T_{l,f}$, s	0.00	0.26	0.00	0.38	0.00	0.93	0.00	0.59
VAF, %	82.0	77.4	67.7	67.6	73.6	70.6	70.1	70.3

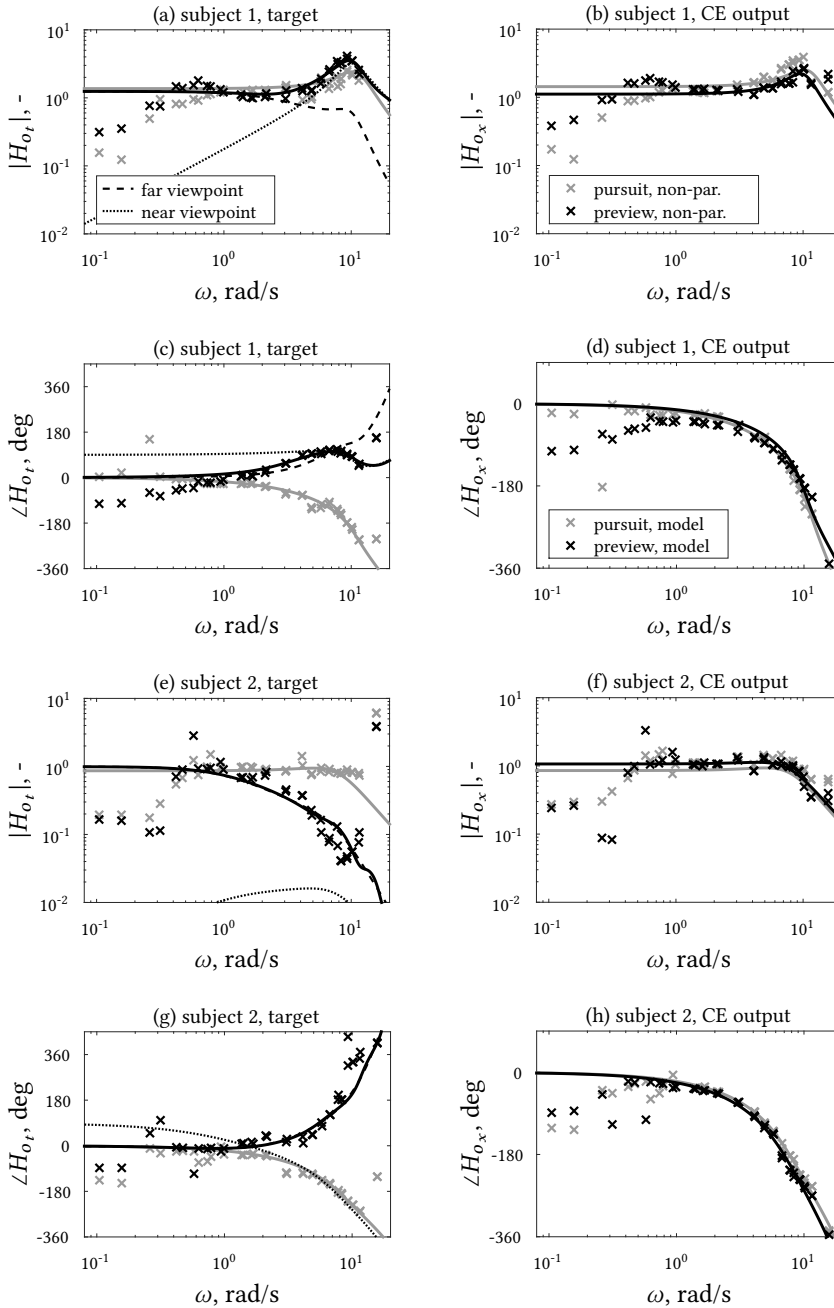


Figure 2.11: Model fits for single integrator CE dynamics; Subject 1 (a-d) and Subject 2 (e-h).

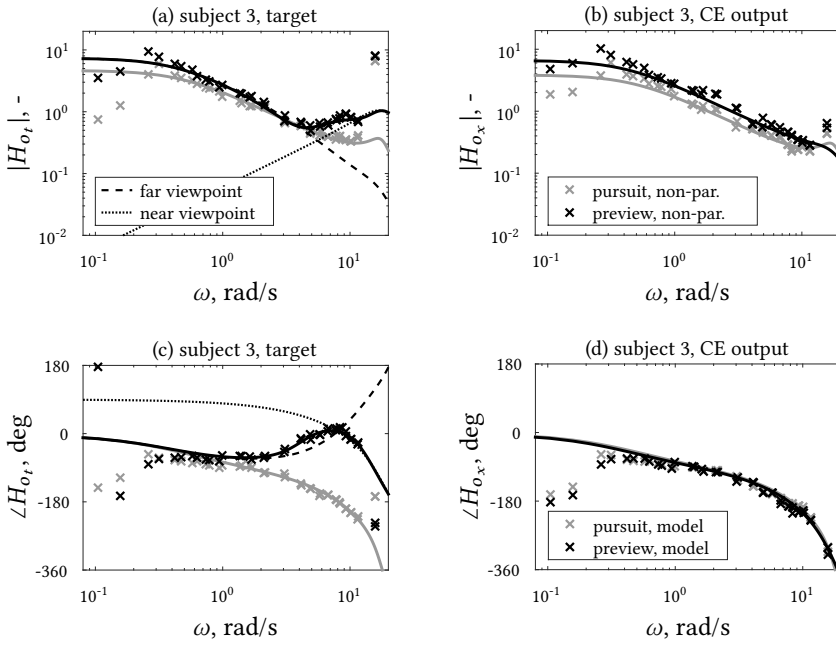


Figure 2.12: Model fits for gain CE dynamics; Subject 3.

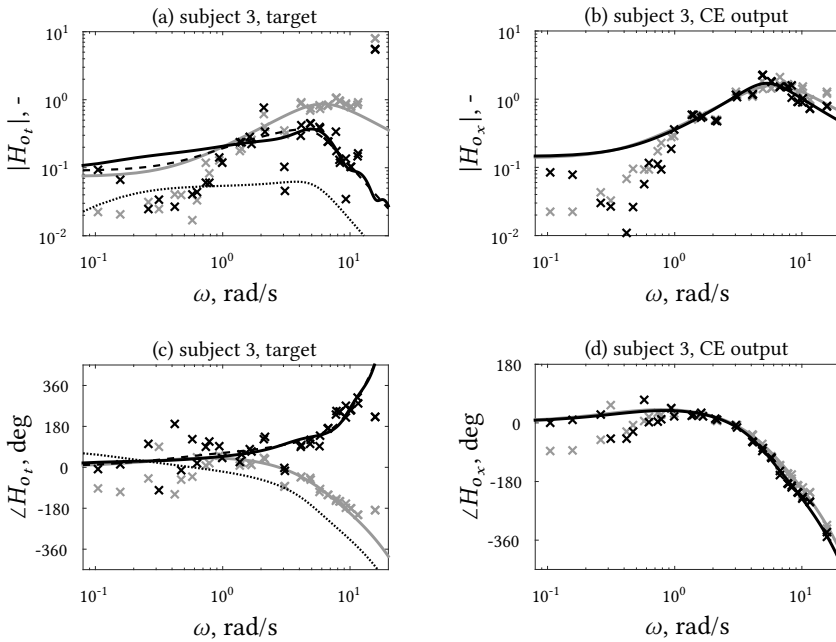


Figure 2.13: Model fits for double integrator CE dynamics; Subject 3.

For pursuit tracking tasks, the far-viewpoint low-pass filter was kept in the model during the estimation procedure. Table 2.4 shows that $T_{l,f}$ is estimated to be zero for all four cases, which is strong evidence that the filter can indeed be omitted and that $H_{o_f}(j\omega) = K_f$.

For single integrator CE dynamics, the average of the gain K_f is close to 1 in the pursuit condition. As the derived model closely resembles the crossover model for compensatory tracking when $K_f = 1$, the present study thus confirms previous results that HC behavior is very similar in pursuit and compensatory tracking tasks for single integrator CE dynamics [42, 141]. For conditions with double integrator CE dynamics, K_f is substantially lower than 1. K_f represents HCs' relative weighting of the target and the CE output in the calculation of $e^*(t)$, so this suggests that HCs prioritize stabilizing the CE output over tracking of the target.

Without being restricted in the estimation procedure, the look-ahead times τ_n and τ_f are both estimated to be lower than 1 s, so within the visually presented preview. They both increase when the CE dynamics become more difficult to control, supplying the HC with more phase lead to compensate for the larger inherent phase lag of the CE dynamics.

Especially in the preview tracking tasks with single integrator CE dynamics, the identified DFs were different *between* subjects. For Subject 2, K_n is indeed estimated to be approximately zero, confirming that this subject only uses the far viewpoint for control. Subject 1 clearly responds to an additional near viewpoint, indicated by a nonzero K_n .

Variance accounted for

The VAFs are generally between 65% and 85% for all twelve subjects in all conditions, see Fig. 2.14, indicating that the model output matches the measured control actions fairly well. Considered that the models are estimated on averaged frequency-domain data, while the related VAFs are calculated for each individual run in the time-domain, *before averaging*, makes these values particularly impressive. They roughly correspond to similar manual control modeling studies where data were averaged first to mitigate remnant effects, yielding higher VAFs [126, 128].

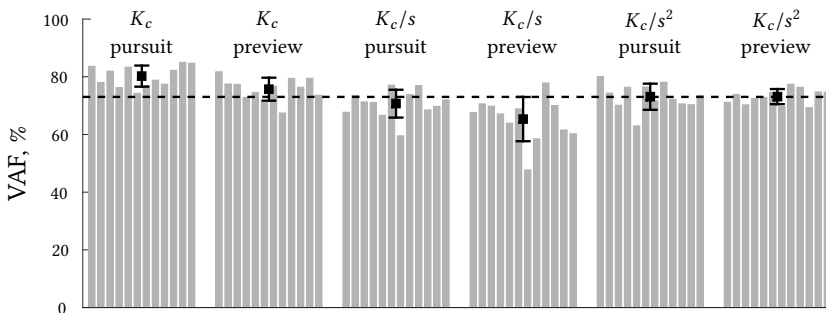


Figure 2.14: VAF per subject (gray bars), mean and standard deviation per condition (errorbars) and grand mean (dotted line).

2.7. DISCUSSION

In this chapter, a generic HC model for preview tracking tasks was derived from measurement data. For the first time, rigorous system identification was applied that allowed the identification of two independent operator responses. Based on the DFs, these two responses were modeled, followed by a restructuring of the HC model into a more intuitive form. The model parameters were estimated, after which the VAF and frequency-domain fits served as measures for the model validity. Additionally, the use of a quasi-linear operator model was justified by calculation of the coherence.

The resulting model is well capable of capturing the shape of the identified DFs for *all subjects in all measured conditions*. It describes the HC adaption to both the CE dynamics, by equalization in $H_{o_{e^*}}(j\omega)$, and to the display type, by optional feedforward control with a negative time delay (or look-ahead time). Additionally, the model captures the considerable variability in control behavior *between* subjects, which we demonstrated in particular for tasks with preview and single integrator CE dynamics.

The model helps to gain deeper insight in the underlying control mechanisms of manual tracking. A completely new view of HC behavior in pursuit tracking task emerges, which, according to the model, is very similar to compensatory tracking. Gain K_f by itself completely explains the difference, relatively weighting the contribution of the target and the CE output in HCs calculation of the *internal error*. Values of K_f lower than 1 suggest that HCs prioritize stabilizing the CE over tracking of the target, and *vice versa*.

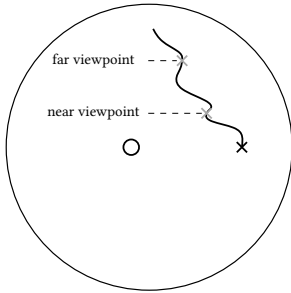
In conditions with preview, HC behavior becomes much more advanced. At low frequencies of the target, *feedback* control is applied with respect to the *far viewpoint*, while some subjects apply additional *feedforward* control with respect to the *near viewpoint* at high frequencies of the target. At high frequencies, entire periods of the target sinusoids are instantly observable. Recognizing these oscillations as such enables the HC to apply open-loop control with approximately the right timing to track the target. At low frequencies the periods of the target sinusoids are longer, so HCs can no longer recognize these as the oscillations they are and they revert to a feedback control strategy. By basing their feedback control on the target ahead, HCs *do* utilize the displayed preview though, generating extra phase lead to compensate for any lags in the loop.

Derived from measurements, our *empirical* model is not based on any previously proposed models. In hindsight, some remarkable similarities appear, however. In Ito and Ito's preview model [55], for example, the previewed target is also weighted to internally calculate a current error to compensate for, but without explicitly separating low- and high-frequency control and without feedforward control. Car drivers are commonly modeled using a combination of feedforward and feedback [91, 136], e.g., in the *two-point model* [139], which explicitly incorporates a near- and far-viewpoint. These models also lack the low and high frequency separation, as well as the relative target/CE output weighting. The similarities with other preview models are generally much smaller.

The model derived here surpasses other preview models on one other point: identifiability of the physically meaningful parameters. For the first time, it is possible to explicitly identify *how* the HC utilizes preview information for control.

2.8. CONCLUSION

A human operator model for preview tracking tasks is derived from measurement data by application of a black-box, instrumental-variable identification method. The derived model is an extension of the quasi-linear operator model for compensatory tracking tasks, with two points of the previewed target as inputs to the operator. The model is capable of describing the measured control behavior in conditions with both zero (pursuit) and one second of preview, and with gain, single integrator and double integrator controlled element dynamics. It also allows for considerable between-subject control behavior variations. The model provides a deeper insight into how humans utilize information on the future target for control. Two very distinct mechanisms split the response to the target both spatially and in frequency regions. Feedforward control is exerted with respect to a near viewpoint at the higher frequencies, while feedback control is exerted with respect to a far viewpoint at lower frequencies.

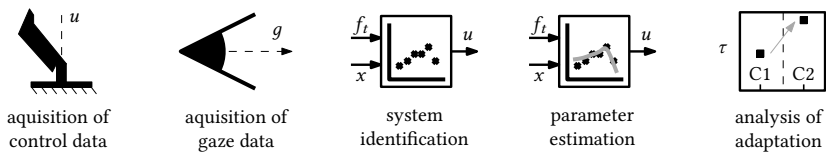


3

THE PORTIONS OF PREVIEW USED FOR CONTROL

It was shown in Chapter 2 that humans use preview to mechanize two distinct, parallel feed-forward responses. The inputs, the “near” and “far” viewpoints along the previewed trajectory ahead, were estimated directly from the measured human control data. This chapter investigates to what extent the near- and far-viewpoints represent the actual points, or portions, of the previewed trajectory that humans use for control. First, it is shown analytically why a two-viewpoint feedforward control strategy is beneficial in preview tracking tasks. Second, a new human-in-the-loop experiment is performed, where, in addition to the control output, the human’s visual focus of attention along the previewed trajectory ahead is recorded with an eye tracker. Gaze and control behavior adaptations are provoked by visually occluding the critical preview regions around the estimated model’s near- and far-viewpoints. The collected gaze data is then explicitly related to estimated model viewpoint positions.

Steps of the cybernetic approach involved:



Parts of this chapter have been published as:

Title Relating Human Gaze and Manual Control Behavior in Preview Tracking Tasks with Spatial Occlusion
Conference IEEE International Conference on Systems, Man, and Cybernetics, Miyazaki, Japan, 2018
Authors E. Rezenenko, K. van der El, D.M. Pool, M.M. van Paassen, and M. Mulder

3.1. INTRODUCTION

HUMAN Controllers (HCs) can *preview* the future trajectory they need their vehicle to follow in many manual control tasks [61]. A well-known example is driving, where the road ahead is visible [92, 136, 140, 144, 145]. To study how HCs use preview information for control, researchers commonly rely on laboratory tracking tasks that lack all control-related cues except the previewed trajectory, for example, see [49, 54, 55, 57] and Chapter 2. The experiment in Chapter 2 has provided evidence that HCs apply a *dual-mode* control strategy: open-loop feedforward control to track the high frequencies (fast changes) in the target trajectory, and combined feedback-feedforward control to follow the target's lower frequency components (slow changes). This dual behavior was captured in an identifiable quasi-linear model, in which two distinct “viewpoints” on the trajectory ahead are the inputs to the two control mechanisms. Together with all other model parameters, the viewpoint positions can be estimated directly from experimental data using system identification techniques. For example, in tasks with integrator Controlled Element (CE) dynamics, the near and far viewpoint were found to be positioned approximately 0.2-0.3 s and 0.6-0.8 s ahead, respectively, see Chapters 2 and 5.

Direct physical interpretation of these control responses and viewpoint positions, although tempting, is as of yet still perilous. Supporting evidence is restricted mainly to lumped Frequency-Response Function (FRF) estimates of HCs' input-output dynamics (i.e., from the displayed cues to applied manipulator deflections), the interpretation of which is not unique. Additional evidence for the human's visual inputs would be highly valuable to verify that the proposed control mechanisms and viewpoints from Chapter 2 indeed reflect the HC's true internal organization and perceptual cues. *Eye-tracking* measurements and *spatial occlusion* experiments can provide such evidence, and have already led to considerable understanding of human visual perception in many everyday tasks, like reading, sports, and driving [65, 146–154].

This chapter investigates the HC's near- and far-viewpoint control mechanisms, and in particular the visual preview information that guides each response. To do so, we combine three techniques that have never been combined before: spatial occlusion, eye tracking, and system identification. In a human-in-the-loop experiment, a baseline tracking task with 1.5 s of full preview was compared to three occlusion scenarios: 1) the region around the model's near viewpoint occluded (0-0.5 s), 2) the region around the far viewpoint occluded (0.35-0.85 s), and 3) zero preview, or *pursuit*. Measured control behavior is analyzed with system identification techniques, yielding multiloop FRF measurements and the parameters of the preview model from Chapter 2. The estimated viewpoint positions are explicitly related to the recorded gaze data; combined, these results provide unique insights in the way that HCs use different parts of a previewed trajectory for control.

This chapter is structured as follows. Section 3.2 introduces the HC preview model from Chapter 2 and discusses the visual inputs of the near- and far-viewpoint responses. Section 3.3 describes the performed experiment, and explains the applied system identification, eye tracking, and spatial occlusion techniques. Results are presented in Section 3.4, followed by a discussion in Section 3.5, and our main conclusions in Section 3.6.

3.2. BACKGROUND

3.2.1. THE CONTROL TASK

In the investigated preview control task, HCs are to follow a target trajectory $f_t(t)$, see Fig. 3.1, which is visible up to a preview time τ_p s ahead. The previewed trajectory $f_t([t, t + \tau_p])$ moves horizontally over the screen from right to left, forcing the current target marker (“+” in Fig. 3.1) to move vertically. The HC provides control inputs $u(t)$ to the CE to guide its output $x(t)$ (“○” in Fig. 3.1, restricted to vertical movements) over the target trajectory, minimizing the tracking error $e(t) = f_t(t) - x(t)$. In this chapter, the CE has integrator dynamics and is perturbed vertically by a disturbance $f_d(t)$, making this a combined target-tracking and disturbance-rejection, velocity control task. The target ($\sigma_{f_t} = 1.27$ cm) and disturbance ($\sigma_{f_d} = 0.51$ cm) signals were the sum of 20 sinusoids, with a 1.5 rad/s bandwidth, to facilitate analysis of measured HC behavior with frequency-domain system identification techniques. This same task was considered in Chapter 2.

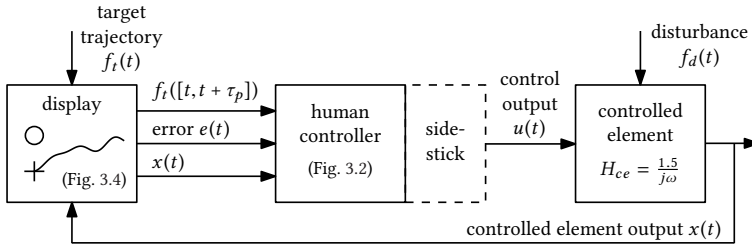


Figure 3.1: Schematic of the performed control task.

3.2.2. HUMAN CONTROLLER MODEL

Fig. 3.2 shows the quasi-linear HC model for preview tracking tasks from Chapter 2. The model’s inner-loop, which resembles the crossover model [6], includes the HC’s equalization dynamics (gain K_{e^*} for the integrator CE dynamics task considered here) and physical limitations such as a response delay (τ_v) and a second-order mass-spring-damper system for the arm’s neuromuscular activation dynamics (see Fig. 3.2).

HC use of preview is accounted for with two responses, which are based on a near- and a far-viewpoint, positioned τ_n and τ_f s ahead on the previewed trajectory, respectively (see also Fig. 3.3). The *far viewpoint* is the input to the compensatory inner-loop. However, whereas HCs minimize the true error $e(t)$ in compensatory tasks, the error $e^*(t)$ in preview tasks is an internally calculated signal. This error $e^*(t)$ equals the difference between the CE output and the target τ_f s ahead (i.e., the far viewpoint), smoothed by a first-order low-pass filter with time-constant $T_{l,f}$ and scaled by gain K_f . As such, HCs smoothly track only the lower frequencies (slow changes) of the target signal with the far-viewpoint response. Higher frequencies are captured by the faster, open-loop, *near-viewpoint* response, which dynamics resemble a pure differentiator. The near-viewpoint response is relatively weak compared to the far-viewpoint response, which manifests in a relatively low value of its gain K_n .

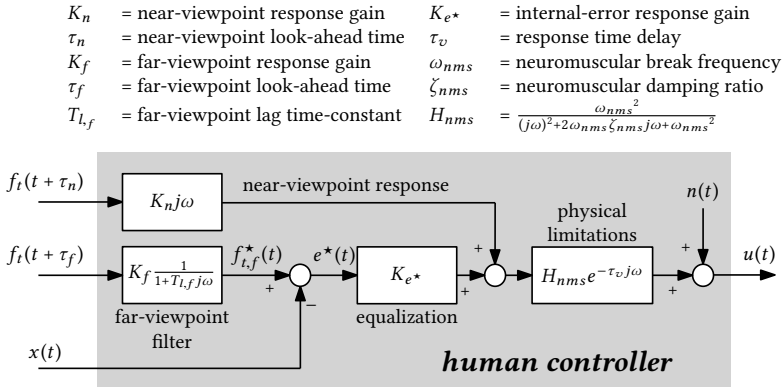


Figure 3.2: Quasi-linear human controller model for preview tracking tasks with integrator controlled element dynamics, proposed in Chapter 2. The near-viewpoint response dynamics lack the original model's first-order lag term, which is often not required to capture the HC's behavior, see Part II of this thesis for details.

3.2.3. THE VISUAL INFORMATION THAT GUIDES PREVIEW CONTROL

The preview model in Fig. 3.2 suggests that HCs use three explicit visual inputs: 1) the CE output $x(t)$, 2) the near viewpoint $f_t(t + \tau_n)$, and 3) the far viewpoint $f_t(t + \tau_f)$. These are drawn to scale in Fig. 3.3, together with the area that can be captured by the eye's foveola, that is, a one deg visual angle around the HC's gaze direction [148, 150, 155] (referred to as foveal vision in this thesis). Fig. 3.3 clearly shows that foveal vision is inadequate to sample the three model inputs simultaneously. This suggests that HCs periodically move their gaze, sampling each model input on average one third of the time. Alternatively, at least two model inputs may be perceived with extrafoveal vision, yielding reduced spatial perception accuracy, because visual acuity decreases by a factor two from its maximum in the foveola to the outer edge of the visual angle that covers all three model inputs (≈ 4 deg) [148].

Moreover, the HC's true visual sensory inputs may include other parts of the previewed trajectory besides the two modeled viewpoints. The far viewpoint $f_t(t + \tau_f)$ is in fact smoothed by a first-order low-pass filter, see Fig. 3.2 ($0.1 < T_{l,f} < 0.5$ s, see Chapter 2 and Part II). In the time-domain, this filter can be seen as the weighted average of the previewed trajectory up to the far viewpoint, with a weighting function equal to the filter's impulse response [55, 61], see the dashed line in Fig. 3.3 for a visualization. This suggests that HCs also use a substantial part of the previewed trajectory just before the far viewpoint. Indeed, the experiment in Chapter 5 shows that longer preview times (below the *critical* preview time) evoke higher values of $T_{l,f}$, which indicates that HCs use a longer portion of the previewed trajectory for smoothing.

The near-viewpoint response is also modeled to be driven by the single target point, $f_t(t + \tau_n)$. Although the modeled response dynamics lack a mechanism like the far-viewpoint's smoothing, HCs initiate a near-viewpoint response only when a part of the trajectory

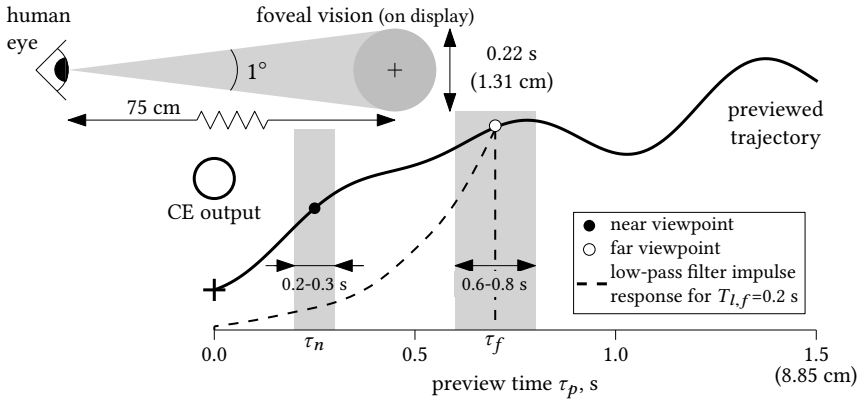


Figure 3.3: Regions of estimated near- and far-viewpoint locations (gray areas) in Chapters 4 and 5. Image is drawn to scale to indicate the part of the previewed trajectory that falls onto the eye's foveola, at 75 cm viewing distance (corresponding to the experimental setup in Chapter 2).

beyond τ_n is also visible [57] (see also Chapter 5). It has been suggested that HCs must first recognize a (high-frequency) pattern in the target signal, in order to activate the open-loop, feedforward control of the near-viewpoint response. For example, to recognize a sinusoidal oscillation in the target signal, a sufficient part of that sine wave must be visible. Consequently, the near- and far-viewpoints of the preview model in Fig. 3.2 may not fully characterize the true portions of the previewed trajectory that HCs use for control.

3.3. METHOD

To investigate what parts of the previewed trajectory truly guide the near- and a far-viewpoint control mechanism, we performed a human-in-the-loop experiment.

3.3.1. HYPOTHESES

Because HCs need to sample both model viewpoints to track a previewed trajectory, we hypothesize that:

H.I The model's viewpoint positions (τ_n and τ_f) correlate with the average HC gaze location, and viewpoint adaptations are accompanied by equivalent gaze adaptations.

Moreover, the modeled role of the near- and far-viewpoint responses in high- and low-frequency tracking, respectively, lead to following hypotheses:

H.II The "far preview region", just below and including the model's far-viewpoint (see Fig. 3.3), is essential for low-frequency target tracking (based on Chapter 2). Occluding this part of the trajectory evokes a weaker far-viewpoint response (lower K_f), and a shift of the far-viewpoint position (and corresponding gaze, H.I) to a

visible part of the trajectory (τ_f is either lower or higher). This control strategy is suboptimal compared to full preview, resulting in degraded performance.

H.III The “near preview region”, around the model’s near-viewpoint, is essential for high-frequency tracking (see Chapter 2). Occluding the trajectory in this region will prevent HCs from recognizing high-frequency target oscillations. Therefore, no open-loop near-viewpoint response can be applied and tracking performance reduces.

3.3.2. EXPERIMENT DESIGN

Independent variables

The experiment consisted of four conditions. In the baseline condition, 1.5 s *full preview* (PR) of the trajectory ahead was visible (see Fig. 3.4a). A zero-preview, *pursuit* (PS) condition was included to test H.I (Fig. 3.4b). Here, all control-relevant information is restricted to the current-target and CE output markers at $\tau=0$ s, and $\tau_n=\tau_f=0$ s by definition, such that a substantial gaze and viewpoint position shift is expected relative to the baseline PR condition. To test H.II, the full preview condition was repeated, but with the trajectory 0.35-0.85 s ahead occluded (*far occlusion*, FO, see Fig. 3.4c). Thereby, the expected far-viewpoint position is not visible, including the part of the trajectory that is strongly weighted by the low-pass filter in the far-viewpoint response. The expected near-viewpoint position (0.2-0.3 s ahead) remains visible. H.III was tested by occluding the trajectory 0-0.5 s ahead (*near occlusion*, NO, see Fig. 3.4d), covering the near viewpoint, but not the far viewpoint. Viewpoint and gaze adaptations in the FO and NO conditions are also used to support H.I.

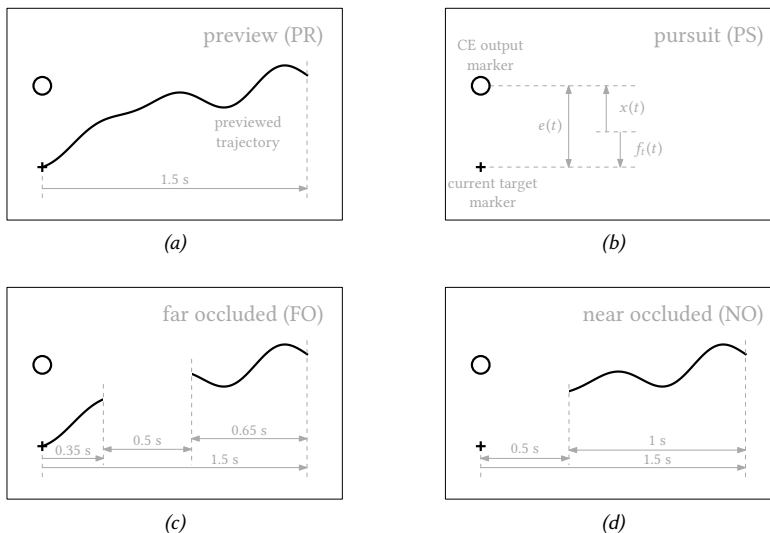


Figure 3.4: The four experimental displays, drawn to scale; only the black indicators were visible.

Apparatus

The experiment was performed in the fixed-base part-task flight simulator at TU Delft, shown in Fig. 3.5, see Chapter 2 for specifications. Subjects gave control inputs $u(t)$ with an electro-hydraulic servo-controlled side-stick (Fig. 3.5, d), which was configured to rotate only around the pitch axis; pitching the stick backwards moved the CE up and *vice versa*.

A non-intrusive, remote head- and eye-tracker system (faceLAB Seeing Machines) was used to measure the gaze-screen intersection position. Fig. 3.5 shows the eye-tracker's three infrared pods (a) positioned in a triangular shape around the display screen (c) to create reflections in the subjects' eyes, which were then measured by two cameras (b).

Subjects and experimental procedure

Eight motivated male volunteers participated in the experiment. After the experiment, the gaze data of two subjects were found to be of insufficient quality for meaningful analysis, and two additional volunteers performed the experiment as replacements.

Subjects were instructed to minimize the tracking error, using a strategy of their preference. Each subject was first familiarized with the task, by consecutively performing three PS, seven PR, two NO, and two FO runs. This rather long familiarization phase was indispensable, because it was not directly evident how to optimally use the remaining visible preview in the occlusion scenarios. Additionally, subjects had time to find a comfortable seating position, before the eye-tracking equipment was adjusted and calibrated for the measurement part of the experiment.

In the measurement part of the experiment, subjects performed a single condition until performance was stable in at least five runs, which were then used as data for analysis. The order of the four conditions was randomized according to a balanced Latin-square. To motivate subjects, the root-mean-square of the error was reported after each run as a measure of performance. The full experiment was completed in a single session and took between three and four hours per subject, depending on the training required. Breaks were scheduled after the familiarization phase and between each set of two tested conditions.

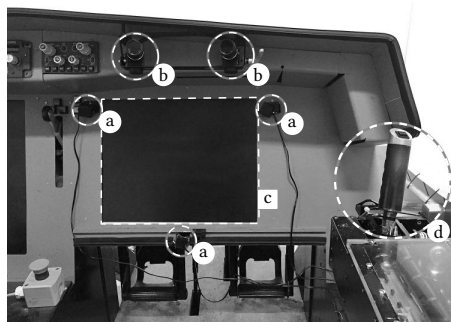


Figure 3.5: Experimental apparatus viewed from the subjects' perspective during the experiment. The eye tracker consists of three infrared pods (a) and two cameras (b). The preview display was presented on the screen (c), and control inputs were given with the side-stick (d).

The first 8 s of each 128 s long run were used as run-in time; the last 120 s were analyzed. Time-traces of the error $e(t)$, the CE output $x(t)$, and the stick deflections $u(t)$ were recorded at 100 Hz. The horizontal and vertical positions where subjects' gazes intersected with the display screen, $\chi_h(t)$ and $\chi_v(t)$, respectively, were logged synchronously.

3.3.3. DATA ANALYSIS

Tracking performance and control activity

The variance of the tracking error σ_e^2 was used as performance measure. It was calculated per run by integrating the error signal's power spectrum [156]. Individual contributions of the target and disturbance signal to the total tracking error were estimated by integrating only over each signal's respective input frequencies [157], while integrating over the remaining frequencies yielded the remnant contribution. Note that these estimates ignore the small remnant contribution at the target and disturbance input frequencies (see also Appendix B). The variance of the control output σ_u^2 was calculated similarly and was used as control activity measure.

Gaze positions

Distributions of horizontal gaze positions on the screen $\chi_h(t)$ were used as measure for the visual regions of interest along the previewed trajectory. These distributions were further quantified with their medians $\tau_{\chi_h^{med}}$ and inter-quartile ranges $\tau_{\chi_h^{iqr}}$. Gaze measurements were first filtered by removing the data points where subjects' eyes were nearly closed or that indicated a gaze position outside the 36×29.5 cm screen area (Fig. 3.5c). The horizontal gaze positions were then scaled to seconds of preview and compensated with the eye tracker's bias, which was estimated per subject in the pursuit condition as the difference between $\tau_{\chi_h^{med}}$ and $\tau=0$ s (the position of the CE and current-target markers).

Time traces of the vertical gaze positions $\chi_v(t)$ were used as measure for the synchrony of the vertical gaze with the target and CE output signals. These were further quantified with the time shifts (τ_{χ_v, f_t} and $\tau_{\chi_v, x}$) that maximize the cross-correlation function R , similar as in [158]. Between the target and vertical gaze signals, R_{χ_v, f_t} is given by:

$$R_{\chi_v, f_t}(\tau) = \int_{-\infty}^{\infty} \chi_v(t) f_t(t + \tau) dt. \quad (3.1)$$

The cross-correlation between the CE output and the vertical gaze position $R_{\chi_v, x}$ is defined similarly. Before analysis, vertical gaze position data were interpolated to a constant 100 Hz sampling frequency using shape-preserving piecewise cubic interpolation. Next, these data were smoothed using non-causal frequency-domain filtering, by explicitly setting the power at all frequencies higher than 16 rad/s (above the highest forcing function input frequency) to zero.

Human control behavior

Similar as in Chapter 2, the data were used to estimate a target FRF $H_{o_t}(j\omega)$ and a CE output FRF $H_{o_x}(j\omega)$. These FRFs are related to the preview model in Fig. 3.2 through:

$$\begin{aligned} U(j\omega) &= H_{o_t}(j\omega)F_t(j\omega) - H_{o_x}(j\omega)X(j\omega) + N(j\omega) \\ H_{o_x}(j\omega) &= K_{e^*}e^{-\tau_v j\omega}H_{nms}(j\omega) \\ H_{o_t}(j\omega) &= \left[\frac{K_f K_{e^*} e^{\tau_f j\omega}}{1 + T_{l,f} j\omega} + K_n j\omega e^{\tau_n j\omega} \right] e^{-\tau_v j\omega} H_{nms}(j\omega) \end{aligned} \quad (3.2)$$

$U(j\omega)$, $F_t(j\omega)$, $X(j\omega)$, and $N(j\omega)$ denote the discrete Fourier transform of the respective signals. Nonparametric estimates of the two FRF were obtained at the 40 input frequencies ω_i of the forcing functions, using a multiloop system identification technique, based on Fourier coefficients; see [86, 159] and Chapter 2 for details. Before estimating the FRFs, all measured signals were averaged in the frequency domain over each subject's five repeated runs per condition, to reduce effects of noise.

The model parameter vector Θ was estimated by minimizing the following Least-squares cost function:

$$\hat{\Theta} = \underset{\Theta}{\operatorname{argmin}} \sum_{i=1}^{40} |U(j\omega_i) - \hat{U}(j\omega_i|\Theta)|^2 \quad (3.3)$$

Here, $\Theta = [K_n \tau_n K_f T_{l,f} \tau_f K_{e^*} \omega_{nms} \zeta_{nms} \tau_v]^T$; $U(j\omega)$ is the five-run, frequency-domain average of the measured control output, and $\hat{U}(j\omega|\Theta)$ is the modeled HC control output, which is obtained from Eq. (3.2) with remnant $N(j\omega)=0$. A Nelder-Mead simplex algorithm was used to minimize Eq. (3.3). To reasonably guarantee that the global minimum of the nonlinear cost function was found, the best solution was selected from 100 randomly initialized optimizations. The two neuromuscular system parameters (ω_{nms} and ζ_{nms}) were not further analyzed; their values were often difficult to estimate from the obtained data and their adaptations are not critical for this chapter.

Statistical analysis

Statistically significant differences between conditions were investigated for all dependent measures, except the nonparametric FRF estimates. For each measure, the pursuit, near-occlusion, and far-occlusion conditions were individually compared to the full preview condition; a Bonferroni correction was applied for three comparisons such that the significance level was set to $p < .0167$. If the data in any of the two compared conditions violated Lilliefors normality test ($p < .05$), a Wilcoxon signed-rank test was performed, otherwise a paired-sample t-test was used.

3.4. RESULTS

3.4.1. TRACKING PERFORMANCE AND CONTROL ACTIVITY

Fig. 3.6a shows that tracking performance is best with full preview (PR), as indicated by a low total σ_e^2 . In the pursuit condition (PS), performance is significantly worse, mostly due to a higher error at the target signal input frequencies (white portions of the bars). Both

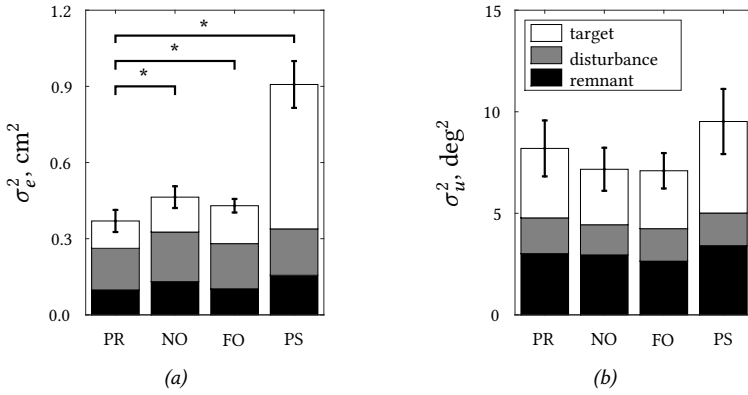


Figure 3.6: Mean variances of the error (a) and control output (b) of the eight subjects, at the target, disturbance, and remnant frequencies. Errorbars indicate the 95% confidence intervals on the total, compensated for between-subject variability; significant total effects are indicated by a “*” symbol.

Table 3.1: Statistical test results, significant differences relative to the full preview condition ($p < .0167$) are indicated by a “*” symbol.

	near occluded		far occluded		pursuit	
	t(7)/W(7)	sig.	t(7)/W(7)	sig.	t(7)/W(7)	sig.
σ_e^2	W = 0	*	W = 0	*	t = 9.68	*
$\sigma_e^2(f_t)$	W = 0	*	t = 4.69	*	t = 14.5	*
$\sigma_e^2(f_d)$	t = 6.14	*	W = 0	*	t = 1.98	-
$\sigma_e^2(n)$	t = 1.74	-	t = 1.51	-	W = 11	-
σ_u^2	t = -1.13	-	t = -2.36	-	t = 1.10	-
$\sigma_u^2(f_t)$	W = 5	-	W = 6	-	W = 4	-
$\sigma_u^2(f_d)$	W = 1	*	W = 8	-	W = 7	-
$\sigma_u^2(n)$	t = -0.11	-	t = -2.11	-	t = 0.47	-
$\tau_{\chi_h^{med}}$	W = 6.5	-	t = 0.29	-	t = 3.47	*
$\tau_{\chi_h^{iqr}}$	W = 9.5	-	W = 18	-	t = -2.58	-
$\tau_{\chi_v^{ft}}$	t = -0.02	-	t = -0.84	-	t = -10.71	*
$\tau_{\chi_v^{x}}$	t = 1.17	-	t = -0.33	-	t = 0.62	-
τ_n	W = 7	-	W = 18	-	W = 0	*
K_f	t = 0.73	-	t = -0.59	-	t = 18.5	*
K_n	t = -0.31	-	t = 0.37	-	t = -8.81	*
K_f	t = -3.87	*	t = -3.48	*	W = 0	*
$T_{l,f}$	t = -0.03	-	t = -0.37	-	t = -6.49	*
τ_v	t = 2.07	-	t = 0.36	-	t = 0.55	-
K_{e^*}	t = -3.18	*	t = -1.39	-	t = 0.08	-

occlusion scenarios (NO and FO) yield worse total performance than full preview, due to contributions of the target and disturbance (all significant effects, see Table 3.1).

Fig. 3.6b shows the variance of the control inputs. Compared to the full preview condition, pursuit evokes slightly higher control activity, especially at the target frequencies (not significant, see Table 3.1). Both occlusion scenarios show consistently lower control activity than the full preview condition; however, the only significant reduction occurs at the disturbance frequencies when the near preview region is occluded (see Table 3.1).

3.4.2. EYE-TRACKING RESULTS

Horizontal gaze

Fig. 3.7 shows the distributions of the measured horizontal gaze positions on the screen, along the previewed trajectory, while Fig. 3.8 shows the distributions' medians and inter-quartile ranges. In the pursuit condition (PS, Fig. 3.7d), the median of each subject's distribution is exactly at $\tau=0$ s, the horizontal position of the current-target and CE output markers, because we compensated the gaze data with the bias measured in this condition. The inter-quartile range reflects the combined noise of the eye-tracking measurement equipment and oculomotor "variability", due to nystagmus, drifts, and microsaccades [147].

In the full preview condition (PR), the median gaze position shifts to approximately 0.15 s ahead, see Fig. 3.8a, which is significantly different from the pursuit condition. The inter-quartile range is only slightly higher with full preview (not significant, Table 3.1), indicating that subjects focused their gaze roughly on the same point ahead throughout the measurement runs, and seldom shifted their gaze to other parts of the previewed trajectory. The positive skew of the mean distribution in Fig. 3.7a reflects the between-subject spread of visual attention along the previewed trajectory.

When the near preview region is occluded (NO), subjects generally focus their gaze farther ahead than in the full preview condition (see Fig. 3.8a). However, the distribution median is not significantly different (Table 3.1). The inter-quartile range is identical as in full preview tasks, and Fig. 3.7b shows that the gaze is most of the time focused directly into the occluded region (0-0.5 s ahead). Subjects apparently attempt to simultaneously observe the CE marker at $\tau=0$ s (required for disturbance rejection), and the previewed trajectory ahead at $\tau>0.5$ s (target-trajectory anticipation), without directly focusing their gaze on either point.

Occluding the far preview region (FO) yields distribution medians and inter-quartile ranges that are identical to the full preview condition. The wider spread of the distributions' medians in Fig. 3.8a suggests that different subjects adapt their gaze differently relative to full preview. Fig. 3.7c shows that the gaze is often focused on the part of the previewed trajectory before ($\tau<0.35$ s) and seldom beyond ($\tau>0.85$ s) the occluded region.

It must be noted that the measured horizontal gaze positions suffered from some drift throughout the experiment, likely due to subject posture changes. An example is the single gaze median that is to the left of the CE and target markers ($\tau<0$ s, Fig. 3.8a, FO), where in fact no information is shown on the screen. These biases on average cancel out

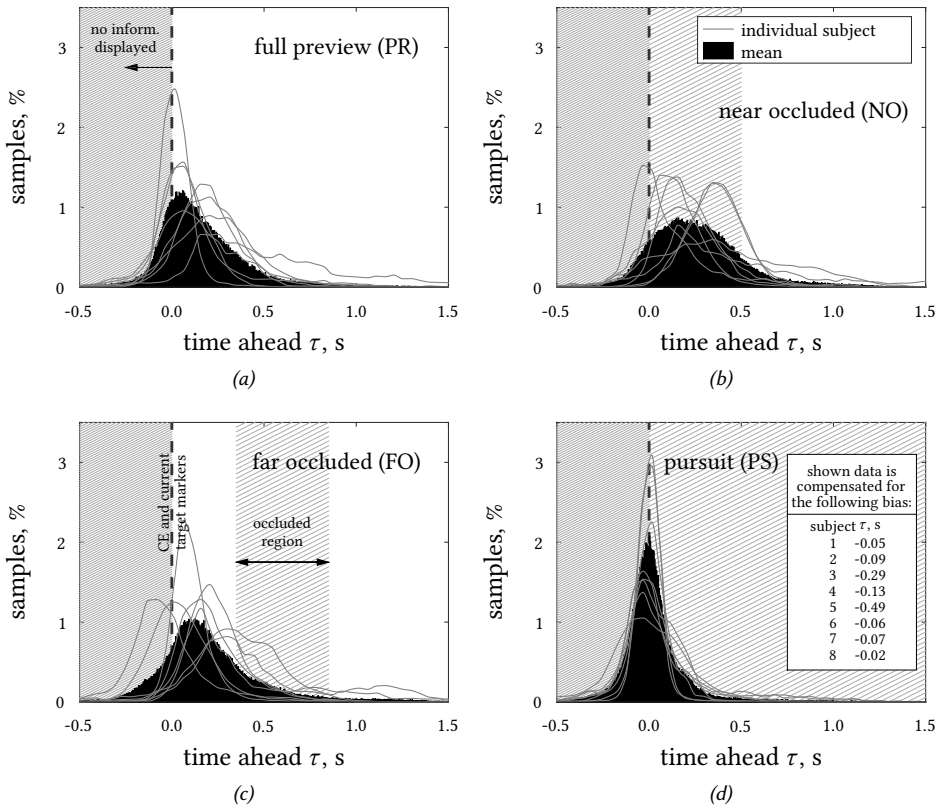


Figure 3.7: Horizontal gaze position distributions, based on 1 pix. (0.0048 s) bins, in the preview (a), near-occluded (b), far-occluded (c), and pursuit (d) conditions.

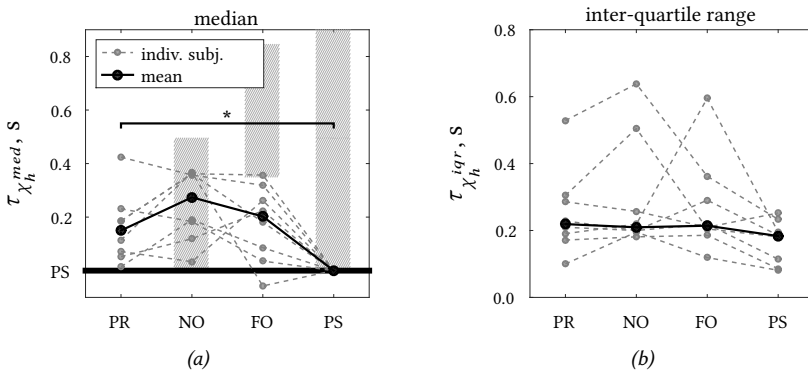


Figure 3.8: Horizontal gaze distribution medians (a) and inter-quartile ranges (b).

between subjects, partly due to the experiment's balanced Latin-square design, hence they do not affect our main findings.

Vertical gaze

Fig. 3.9 shows time traces of a representative sample of the vertical gaze and CE output positions relative to the target trajectory. Both the CE output and the vertical gaze clearly lag behind the target signal in pursuit tasks, but these lags disappear with preview.

Fig. 3.10 shows the time shifts that maximize the cross-correlation function R (corresponding to the correlation coefficient ρ in Fig. 3.9). In the pursuit condition, the vertical gaze lags the target and CE output signals by approximately 0.5 and 0.05 s, respectively, which indicates that subjects focus their gaze mainly on the CE output and not on the target. The gaze signal's lag on the target signal reduces to 0.1 s with preview (significant effect, see Table 3.1), while the lag relative to the CE remains constant at 0.05 s. As such, the vertical gaze data suggest that subjects focus their visual attention mainly on the CE output marker's vertical motions and not on the (future) target trajectory.

3

3.4.3. SYSTEM IDENTIFICATION RESULTS

Control dynamics

Fig. 3.11 shows an example of identified HC target and CE output response dynamics in the near-occlusion condition (NO). The combined model matches the shape of the non-parametric FRF estimates well, which verifies that the preview model from Chapter 2 can indeed capture the measured control behavior. This example is representative for all conditions and subjects. The preview model's far-viewpoint response captures the initial phase lead in $H_{o_t}(j\omega)$ at lower frequencies, while the phase drop at higher frequencies (>8 rad/s) is captured by the near-viewpoint response.

Fig. 3.12 compares the estimated control dynamics between conditions. Whereas the CE response $H_{o_x}(j\omega)$ is roughly invariant between conditions, the target response $H_{o_t}(j\omega)$ is adapted strongly. Compared to the characteristic response delay (i.e., phase roll-off) in the pursuit condition, full preview yields substantial phase lead in $H_{o_t}(j\omega)$, especially at higher frequencies, because subjects respond to the trajectory ahead. The shape of the target response phase with full preview in fact closely matches the dynamics that would yield zero-error, or "perfect" target tracking, $H_{o_t}^P(j\omega)$ in Fig. 3.12, the detailed derivation of which is treated in Chapter 4.

Occlusion induces several characteristic adaptations in the target response. By occluding the near region, the phase lead at the higher frequencies increases compared to full preview, indicating a response to the target farther ahead. The increase occurs mainly in the frequency region where the near-viewpoint response is expected. Additionally, the magnitude of the target response is lower, indicating a less aggressive response that corresponds to the lower control activity (Fig. 3.6).

Compared to full preview (PR), occluding the far region (FO) yields less phase lead in the target response between 2 and 8 rad/s. In this frequency region, both the near- and far-viewpoint responses contribute substantially. It is likely that both responses are adapted,

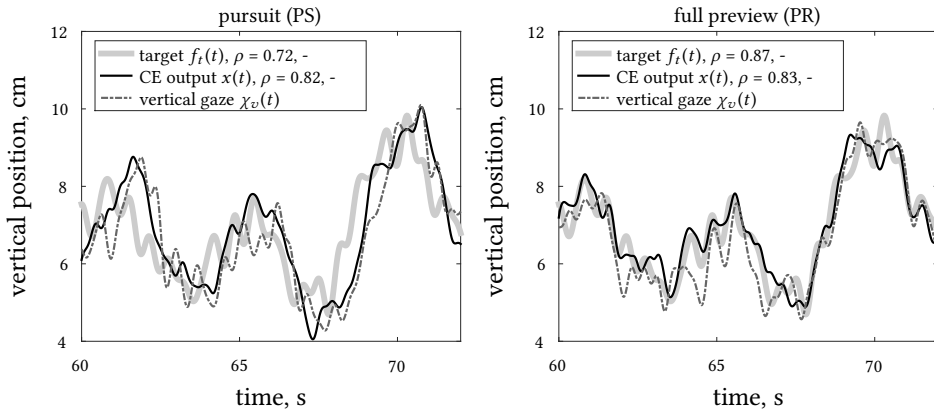


Figure 3.9: Vertical gaze position, target, and CE output time-traces from a run where the gaze data were relatively low noise. The Pearson correlation coefficients ρ indicate the signals' correlation with the vertical gaze position.

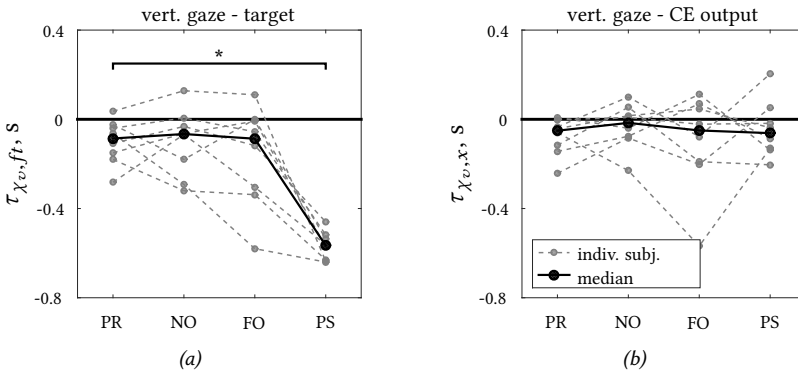


Figure 3.10: Time shifts τ that maximize the cross-correlation function $R(\tau)$ between the vertical gaze and the target (a) and the CE output (b) signals.

because, as discussed in Section 3.2, preview information in the occluded far region (0.35-0.85 s) is important for initiating both the near- and the far-viewpoint response. The lack of phase adaptation below 2 rad/s reflects the insensitivity of the low-frequency phase response to changes in viewpoint positions (i.e., τ_f and τ_n). Occluding the far region also evokes a lower target response magnitude, corresponding to the lower control activity in Fig. 3.6.

Near- and far-viewpoint positions

Fig. 3.13 shows the estimated near- and far-viewpoint positions, characterized by the look-ahead time parameters τ_n and τ_f , respectively. With full preview, subjects position their near- and far-viewpoints around 0.25 and 0.8 s ahead, respectively. The occluded regions in the NO (0-0.5 s) and FO (0.35-0.85 s) conditions thus indeed obscured the intended parts

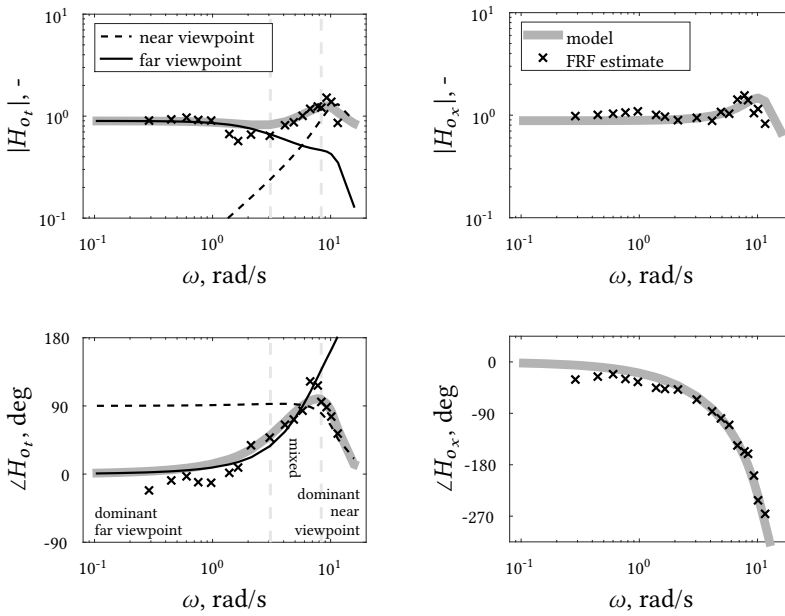


Figure 3.11: Bode plots of estimated target and CE output response dynamics in the near-occluded condition; single-subject data.

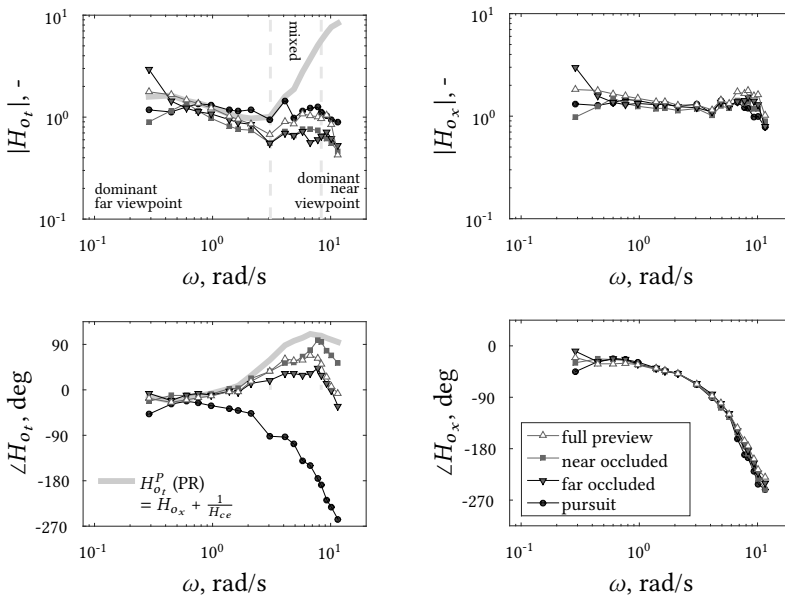


Figure 3.12: Bode plots of the nonparametric target and CE output FRF estimates, mean of all subjects. The $H_{O_t}^P(j\omega)$ dynamics reflect perfect, zero-error target tracking (see Chapter 4 for a derivation).

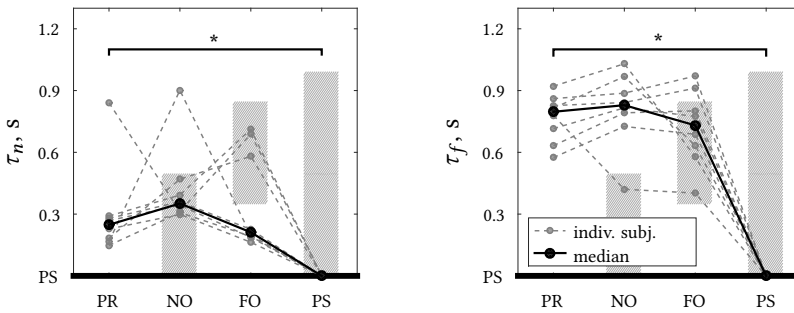


Figure 3.13: Estimated near- (τ_n) and far-viewpoint (τ_f) positions on the previewed trajectory ahead.

of the trajectory from the subjects' view. Several outliers are visible in τ_n , indicating that these subjects initiated no, or only a very weak, near-viewpoint response (see Chapter 4 for a detailed explanation).

Occluding the near preview region (NO) induces a shift of the near-viewpoint position slightly farther ahead along the previewed trajectory (not significant, see Table 3.1), which corresponds to the larger phase lead in the target FRF at high frequencies (Fig. 3.12). Nonetheless, the near viewpoint is estimated to be positioned well within the occluded region, similar to subjects' horizontal gaze (see Fig. 3.7b). As expected, near occlusion does not impact the far-viewpoint position.

Occluding the far region (FO) motivated several subjects to move their far viewpoint substantially closer ahead, whereas others move it farther ahead. This is consistent with the observed wider variety in gaze strategies (see Fig. 3.8) and suggests that finding the "optimal" control strategy is not evident. For most subjects the far viewpoint is still positioned well inside the occluded region. More subjects (three) than in any other condition initiate only a very weak, or no near-viewpoint response at all. Moreover, despite that far occlusion does not hide the near viewpoint from view, subjects position their near viewpoint slightly closer ahead compared to the full preview condition (not significant). This indicates that the far preview region, beyond 0.35 s ahead, provides subjects with essential information about the target signal's high-frequency oscillations, on which near-viewpoint response relies.

Other model parameters

Fig. 3.14 shows that both occlusion scenarios yield a lower far-viewpoint response gain, compared to full preview (significant effects), which corresponds to the lower target FRF magnitude (Fig. 3.12) and control activity (Fig. 3.6b). Remarkably, the near-viewpoint response gain and the far-viewpoint filter time-constant are not significantly affected by occlusion, despite their critical contribution to the near- and far-viewpoint responses. The response time delay τ_v (≈ 0.25 s) is slightly higher in both occlusion conditions, compared to full preview (not significant). Occluding the near preview region yields a significantly lower error response gain K_{e^*} , indicating that subjects respond less aggressively overall.

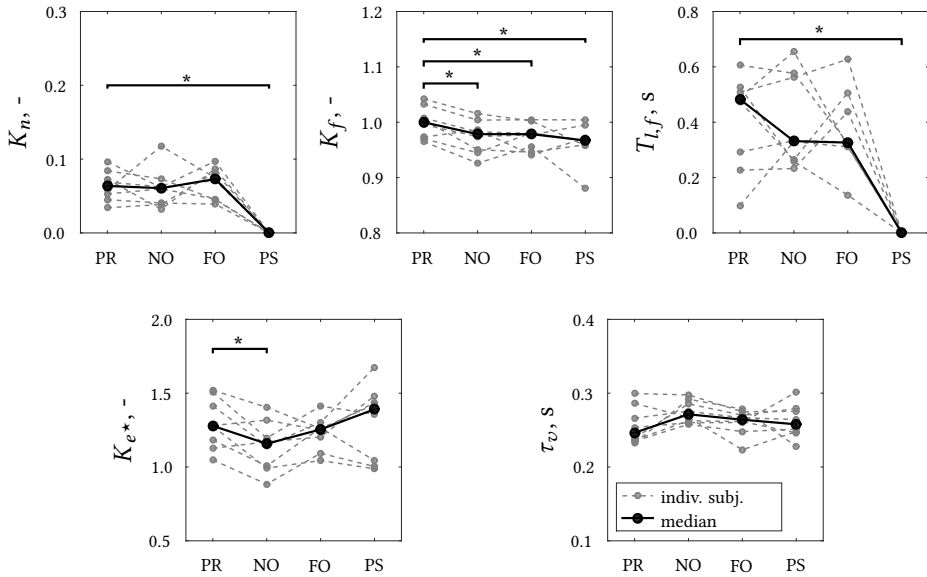


Figure 3.14: Estimated near-viewpoint gain K_n , far-viewpoint gain K_f , far-viewpoint lag time-constant $T_{l,f}$, error response gain K_{e^*} , and time delay τ_v .

3.5. DISCUSSION

This chapter investigated the HC's near- and far-viewpoint preview control mechanisms, and in particular the parts of the previewed trajectory that guide each response. We presented a unique combination of gaze and control-behavioral data, including estimated parameters from the preview control model from Chapter 2.

Our *first hypothesis* was that adaptations of gaze and model viewpoint positions are related. Fig. 3.15 shows a correlation plot of these parameters. Whereas the gaze median and viewpoint positions are by definition at $\tau=0$ s in pursuit tasks, both are clearly nonzero in preview tasks, indicating that HCs both respond to and focus their gaze on the trajectory ahead. This confirms our first hypothesis. Fig. 3.15 further shows that the horizontal gaze position median correlates very well with the near-viewpoint position. HCs seldom aim their gaze at the far viewpoint (≈ 0.8 s), which is positioned considerably beyond the third quartile of the gaze distribution (≈ 0.4 s, Fig. 3.15).

A possible reason for the predominant visual attention on the near region is that the open-loop near-viewpoint response depends on HCs to accurately recognize the low-amplitude, high-frequency target signal oscillations. Moreover, substantial visual attention is drawn to the CE output marker (at $\tau=0$ s), the movement of which provides the only feedback of effects of the external disturbances f_d . HCs in general aim their gaze vertically at the CE output marker (Fig. 3.10), and, when preview is present, to the right of the CE output marker towards the previewed trajectory (Fig. 3.8). The CE output marker is in fact

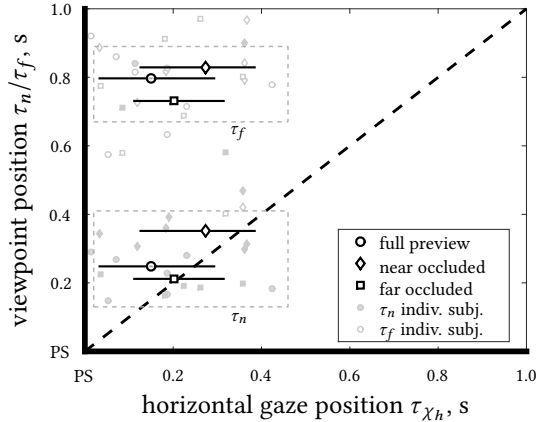


Figure 3.15: Correlation between horizontal gaze and near- and far-viewpoint positions. Data correspond to Figs. 3.8 and 3.13, errorbars on horizontal gaze positions indicate the distributions' inter-quartile ranges.

often in such close proximity to the near viewpoint that both can be sampled simultaneously with foveal vision. HCs' visual attention can be expected to shift towards the far viewpoint in other control tasks, where: 1) no explicit information is obtained from the CE output marker (e.g., "inside-out" viewing perspective in driving), and 2) no near-viewpoint response is initiated (e.g., following a low-frequency target trajectory with a double integrator CE, see Part II of this thesis).

Contrary to our expectations, viewpoint and gaze positions were not always found to fully shift to a visible part of the previewed trajectory in the occlusion scenarios. This lack of adaptation may be explained by the invariance of the "perfect" target-tracking dynamics, which are matched fairly well with full preview. Consequently, HCs resist behavior adaptations, even when parts of the previewed trajectory are occluded. In order to still respond to the "optimal" viewpoints, HCs must first make an estimate of the occluded part of the trajectory. To do so, it is essential that a part of the trajectory *beyond* the occluded region is visible, either to *memorize* the approaching trajectory, or to *interpolate* between the visible regions that surround the occluded part.

Our *second hypothesis* was that the "far preview region", just below and including the model's far-viewpoint, is critical for low-frequency target tracking. Occlusion of the trajectory in this region (0.35-0.85 s) indeed yields a weaker far-viewpoint response (lower K_f), worse tracking performance, and an adaptation of the HC's target FRF phase at the expected, lower frequencies (2-8 rad/s). Thereby, we consider our second hypothesis to be confirmed, despite a lack in viewpoint and gaze direction adaptations.

Our *third hypothesis* was that the "near preview region", around the model's near-viewpoint, is critical for high-frequency target tracking. Occluding the trajectory in this region (0-0.5 s) yields a consistent shift of the horizontal gaze positions forward along the previewed trajectory. The resulting reduction of visual attention around the CE out-

put marker leads to a less aggressive response (lower K_{e^*}) and, consequently, inferior disturbance-rejection performance. Moreover, the far-viewpoint response gain is lower, and the target FRF phase is adapted exactly at the frequencies where the near-viewpoint response is dominant (>8 rad/s). Nonetheless, we consider our third hypothesis only partially confirmed, because HCs still apply a near-viewpoint response when the region around the model's near viewpoint is occluded. The preview region just beyond τ_n (>0.25 s) in fact appears to be most critical for high-frequency target tracking, allowing HCs to recognize patterns in the target signal, which is required for effective open-loop control.

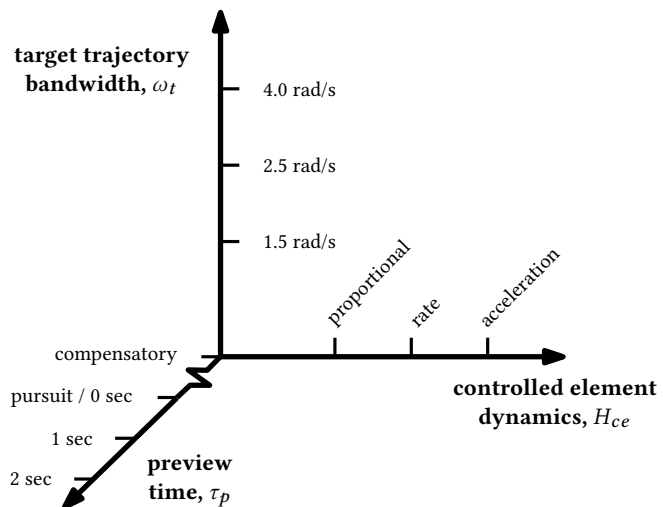
Future work should further investigate the relation between gaze data and model viewpoints. Task variables such as the controlled element dynamics affect the model's viewpoint positions (see Part II), but it is unknown whether HCs adapt their gaze correspondingly. Moreover, to truly connect human gaze to control behavior, it is essential to establish a temporal relation between gaze and model viewpoints, opposed to the averaging approach adopted in this chapter. Such a relation may allow for augmenting or even replacing control-behavioral measurements with gaze measurements, which could benefit human perception and control research, or (online) identification of preview control behavior for use in personalized monitoring and shared-control technologies (e.g., see [33]).

3.6. CONCLUSION

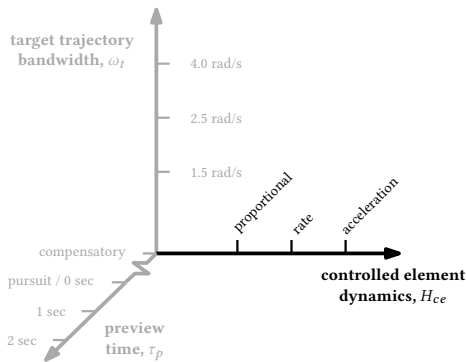
This chapter presented a unique combination of gaze and control-behavioral data from a human-in-the-loop preview tracking experiment, to improve our understanding of the (visual inputs of) humans' near- and far-viewpoint responses. Explicit evidence was presented that the preview region just beyond the estimated model's near viewpoint is essential for high-frequency target-tracking, while the region around the far viewpoint is important for following lower frequencies. Even with these critical preview regions occluded, humans typically still mechanize the near- and far-viewpoint responses, confirming humans' versatile adaptation capabilities. For the first time gaze data were related to estimated parameters of a control-theoretic model; results indicate that humans focus their gaze predominantly around the model's near-viewpoint position, and seldom at the far viewpoint. Establishing the relation between gaze and control behavior in a wide range of tasks may increase the implications drawn from future eye-tracking measurements, and facilitate the (online) identification of preview control behavior from gaze data.

PART II

HUMAN ADAPTATION TO TASK VARIABLES



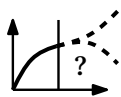
4



EFFECTS OF CONTROLLED ELEMENT DYNAMICS

In Part I of this thesis, a novel cybernetic model was proposed for human manual control behavior in pursuit and preview tracking tasks. To allow for rationalizing and predicting human preview control behavior (including their interaction with technology) in a wide range of control tasks, a quantitative understanding of human adaptation to crucial task variables is also essential. To this end, this chapter investigates how previewing humans adapt their control behavior to the controlled element dynamics. First, the preview control model proposed in Part I is used in offline computer simulations to predict the optimal near- and far-viewpoint control responses for tasks with various controlled element dynamics. The predictions are verified with data from a human-in-the-loop preview tracking experiment, in which gain, single-, and double-integrator controlled element dynamics are tested.

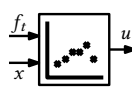
Steps of the cybernetic approach involved:



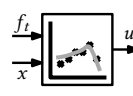
offline model predictions



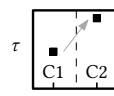
acquisition of control data



system identification



parameter estimation



analysis of adaptation

The contents of this chapter have been published as:

Title Effects of Preview on Human Control Behavior in Tracking Tasks with Various Controlled Elements

Journal IEEE Transactions on Cybernetics, vol. 48, no. 4, pp. 1242-1252, Apr. 2018

Authors K. van der El, D.M. Pool, M.M. van Paassen, and M. Mulder

4.1. INTRODUCTION

HUMANS are highly effective *adaptive* controllers [75]. The seminal work of McRuer and his coworkers [6] shows that Human Controllers (HC) systematically adapt their control response to the dynamics of the Controlled Element (CE), the display type, and the characteristics of the target signal to be tracked. The HC's adaptation mechanisms are relatively well-understood in simple error-compensation tasks [80]; however, few practical control tasks are purely compensatory. Instead, *preview* information of the target trajectory is often visible, commanding the HC were to steer to in the near future. Driving a car over a road is perhaps the best known example [92, 136, 140], but most vehicle control tasks involve preview, as well as many everyday motor control tasks [160, 161].

It has been shown that preview information helps HCs to improve task performance, compared to zero-preview (pursuit) tasks [54, 55, 92, 134, 140]. In tracking tasks, the amount of preview needed for maximum performance depends, at least, on the CE dynamics, and increases from about 0.5 to 1 s from position to acceleration control tasks [54, 55, 134]. To extrapolate these results to yet untested preview control tasks, many cybernetic models have been proposed (e.g., see [55, 61, 92, 134, 140, 162]). Although several models accurately replicate the human's control outputs, they are unsuitable to systematically study HC adaptation, because the proposed model inputs and multiloop control dynamics were never shown to resemble those of the actual HC with objective measurements.

Recently, we measured the HC's control dynamics in preview tracking tasks using a multi-loop frequency-domain system identification technique (see Chapter 2). Based on this, we extended McRuer *et al.*'s [6, 80] quasi-linear model for compensatory tracking tasks with two distinct responses that are based on a "near" and a "far" viewpoint on the previewed target ahead. The model's physically interpretable parameters, like the viewpoints' locations, can be explicitly estimated from measurement data. Thereby, this model may finally allow for quantifying HC control adaptation in preview tracking tasks, similar as established previously for compensatory tracking [6, 75, 80]. Unfortunately, the model's near- and far-viewpoint responses are still poorly understood: while HCs always apply a far-viewpoint response, the presence of a near-viewpoint response appears to depend strongly on the tested subject and CE dynamics (see Chapter 2). It is unclear when and why it is beneficial to respond to either one or two points on the previewed target ahead.

The goal of this chapter is to explain how HCs use preview for control in manual tracking tasks with various CE dynamics. First, the roles of the near- and far-viewpoint responses are investigated through offline simulations with the new preview model from Chapter 2, with gain, single-, and double-integrator CE dynamics. Second, these offline predictions are verified with measurements from a human-in-the-loop experiment, in which subjects performed a combined target-tracking and disturbance-rejection task with these same CEs, both in tasks with zero preview (i.e., pursuit) and 1 full second of preview. These experimental data were also used to derive the preview model in Chapter 2; however, in this chapter, a variety of new measures is presented. Effects of preview are quantified with measures for tracking performance and control activity, and with input-to-error and open-loop dynamics. The HC's underlying control behavior is investigated by estimating their multiloop response dynamics, together with the new preview model's parameters.

This chapter is structured as follows. Section 4.2 summarizes important aspects of HC behavior in preview tracking tasks, including the HC model from Chapter 2. Offline model analyses are presented in Section 4.3. The performed experiment and data analysis procedures are presented in Section 4.4, followed by the experimental results in Section 4.5. The final two sections then discuss these results and present the main conclusions.

4.2. BACKGROUND

4.2.1. THE CONTROL TASK

The general layout of a combined target-tracking and disturbance-rejection control task is illustrated in Fig. 4.1. In these tasks, HCs are to minimize the tracking error:

$$e(t) = f_t(t) - x(t), \quad (4.1)$$

which is the difference between the current values of the target signal $f_t(t)$ and the CE output $x(t)$. HCs generate control inputs $u(t)$ to minimize this tracking error. At the same time, the CE is perturbed by disturbance signal $f_d(t)$, for which the HC must also compensate. In *pursuit* tasks, only the current target at time t is presented on the display, together with the CE output (see Fig. 4.2a). In *preview* tasks, an additional stretch of the future target $f_t([t, t + \tau_p])$ is visible, up to preview time τ_p ahead (see Fig. 4.2b).

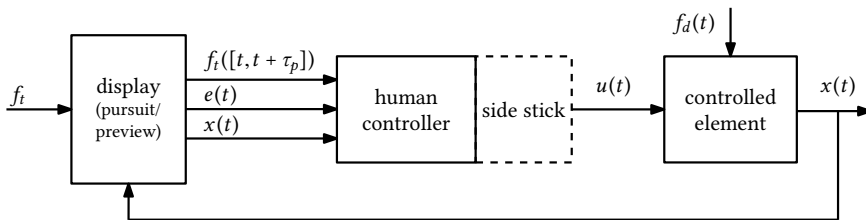


Figure 4.1: The human controller in a target-tracking and disturbance-rejection task.

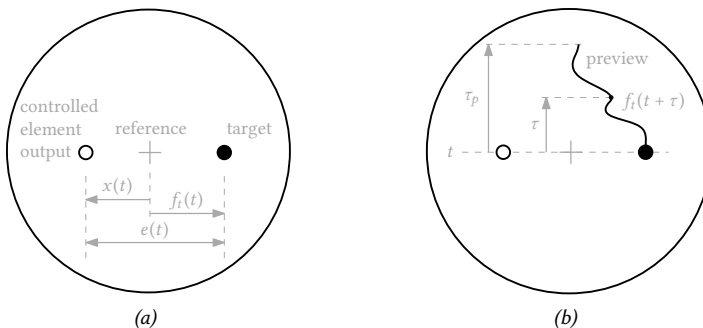


Figure 4.2: Layout of the pursuit (a) and preview (b) displays.

4.2.2. CLASSICAL APPROACH AND RESULTS

HCs can adopt a *multi-channel* control organization in pursuit and preview tracking tasks, initiating an independent response to the target, the CE output, and the error, and in preview tasks also to the target ahead [6, 42, 62, 141]. Because explicit identification of all individual response dynamics is impossible [42, 141] (see also Appendix A), HC behavior in these tasks has been traditionally analyzed by identifying *lumped* response dynamics [42, 54, 55, 141]. Ito & Ito [55], for example, measured the closed-loop dynamics from the target to the CE output:

$$H_{cl,t}(j\omega) = \frac{X(j\omega)}{F_t(j\omega)}, \quad (4.2)$$

with X and F_t the Fourier transforms of the respective signals. Perfect target-tracking is achieved when $X(j\omega)=F_t(j\omega)$, or equivalently, when $|H_{cl,t}(j\omega)|=1$ and $\angle H_{cl,t}(j\omega)=0$ deg. Ito & Ito's results (partly reproduced in Fig. 4.3) reveal that preview yields improved closed-loop characteristics, compared to the pursuit task, as the phase of $H_{cl,t}(j\omega)$ is closer to zero. The closed-loop magnitude does not show a clear improvement. Preview thus primarily helps HCs to better synchronize the CE output with the target. In tasks with lower-order CE dynamics (e.g., a gain), HCs extend the region where the closed-loop phase approximates zero to higher frequencies [55]. Unfortunately, the (lumped) closed-loop dynamics obscure exactly *how* HCs use the available preview information, and also how they adapt their control response to the CE dynamics.

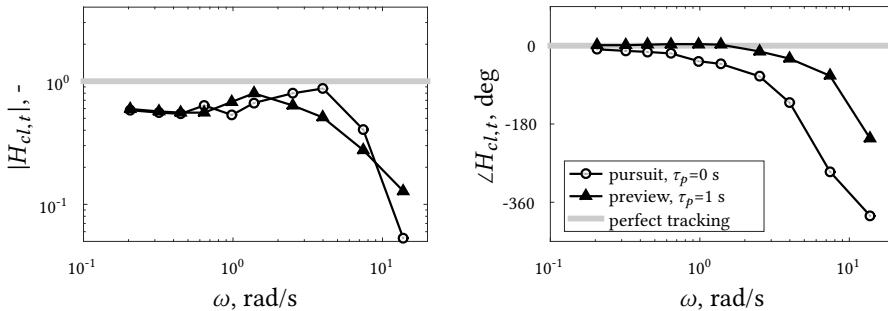


Figure 4.3: Closed-loop dynamics in a double-integrator task with and without preview, average of two subjects (reproduced from [55]).

4.2.3. HUMAN CONTROLLER MODEL

In Chapter 2, a new model for pursuit and preview tracking tasks was proposed that separates the HC's responses to the different input signals. Thereby, this model provides deeper insights in the human's underlying control mechanisms.

The model for pursuit tracking

The HC model for pursuit tasks (see Fig. 4.4a) extends McRuer *et al.*'s *simplified precision model* for compensatory tracking [80]. The model is also *quasi-linear*, which means that

linear describing functions account for the linear portion of the HC's response. Possible nonlinear and time-varying behavior are not explicitly modeled, nor are perception and motor noise; these are injected together as filtered white noise through the *remnant* $n(t)$.

The pursuit model involves a response to an error $e^*(t)$, with response dynamics $H_{o_{e^*}}(j\omega)$ that are equal to McRuer's simplified precision model (see [80] and Chapter 2):

$$H_{o_{e^*}}(j\omega) = K_{e^*} \frac{1 + T_{L,e^*}j\omega}{1 + T_{l,e^*}j\omega}. \quad (4.3)$$

K_{e^*} is the error response gain and T_{L,e^*} and T_{l,e^*} are the lead and lag time-constants, respectively. Similar as in compensatory tracking, HCs adapt to the CE dynamics by generating lead or lag in $H_{o_{e^*}}(j\omega)$, to establish a fair stretch of integrator-like dynamics around the open-loop crossover frequency (ω_c): $|H_{o_{e^*}}H_{ce}| \approx \omega_c/j\omega$ [42] (see also Chapter 2).

The error $e^*(t)$, a signal internal to the HC, is defined as the difference between the filtered target f_t^* and the CE output:

$$E^*(j\omega) = F_t^*(j\omega) - X(j\omega) = H_{o_f}(j\omega)F_t(j\omega) - X(j\omega). \quad (4.4)$$

In pursuit tasks, $H_{o_f}(j\omega)$ was modeled as a simple gain, $H_{o_f}(j\omega) = K_f$ (see Chapter 2). When $K_f = 1$, Eq. (4.4) shows that $e^*(t) = e(t)$, hence that HCs respond to the true error and that they effectively exhibit a single-channel "compensatory" control organization [79]. A non-unity value of K_f implies a "pursuit" control organization [79], or the presence of a feedforward response. Higher values of K_f indicate a more aggressive response to the target, while $K_f = 0$ means that the HC completely ignores the target and focuses only on disturbance rejection. Single-subject data in Chapter 2 showed that $K_f < 1$ for an (unstable) double integrator CE, $K_f \approx 1$ for an integrator CE, and $K_f > 1$ for a (highly stable) gain CE, which suggests that K_f reflects an important control-adaptation mechanism.

The model also incorporates the HC's most dominant physical limitations. Visual response delay τ_v combines perceptual, cognitive and transport delays, and $H_{nms}(j\omega)$ represents the combined neuromuscular system (NMS) and side-stick dynamics:

$$H_{nms}(j\omega) = \frac{\omega_{nms}^2}{(j\omega)^2 + 2\zeta_{nms}\omega_{nms}j\omega + \omega_{nms}^2}, \quad (4.5)$$

with ω_{nms} and ζ_{nms} the natural frequency and damping ratio.

The model for preview tracking

Fig. 4.4b shows the HC model for preview tasks, which extends the pursuit model. Two responses, each initiated with respect to a different viewpoint, can capture the HC's response to the *entire* previewed target (see Chapter 2). A *far viewpoint* $f_{t,f}(t)$ feeds the "pursuit" control-loop, while an additive, parallel feedforward channel describes the HC's response to a *near viewpoint* $f_{t,n}(t)$. The near- and far-viewpoints are located τ_n and τ_f s ahead on the previewed target:

$$f_{t,n}(t) = f_t(t + \tau_n), \quad f_{t,f}(t) = f_t(t + \tau_f). \quad (4.6)$$

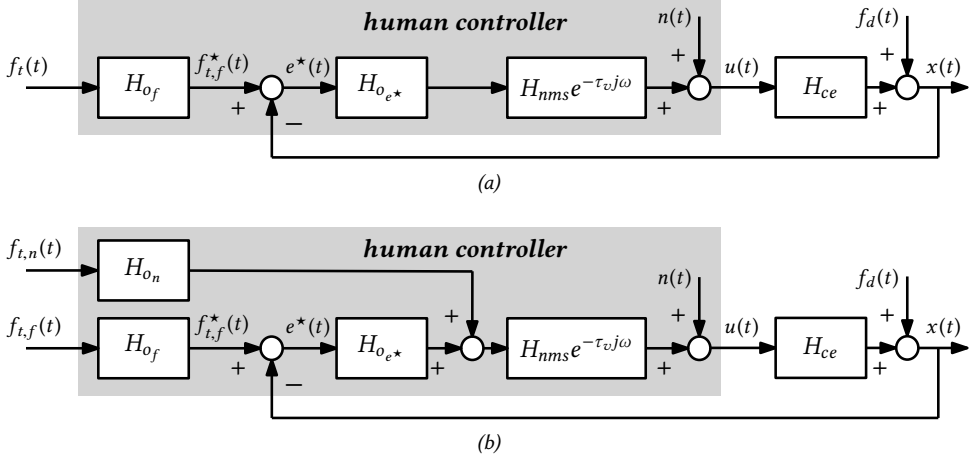


Figure 4.4: Control diagrams of the human controller model for pursuit (a) and preview (b) tracking tasks, as proposed in Chapter 2.

As the HC can select which points to respond to, based on the task specifics, both τ_n and τ_f are free model parameters. Note that these viewpoints do not necessarily correspond to the two levels, or two points, used in many driver steering models (e.g., [91, 95]).

In preview tracking tasks, HCs were found to smooth the target in the far viewpoint, so $H_{o_f}(j\omega)$ includes a low-pass filter (see Chapter 2):

$$H_{o_f}(j\omega) = K_f \frac{1}{1 + T_{l,f} j\omega}. \quad (4.7)$$

The far-viewpoint response thus only describes low-frequency target-tracking behavior, with the reciprocal of the time constant $T_{l,f}$ as cut-off frequency. The HC's response to higher frequencies in the target signal was modeled as an open-loop response $H_{o_n}(j\omega)$ with respect to the near viewpoint (see Chapter 2):

$$H_{o_n}(j\omega) = K_n \frac{j\omega}{1 + T_{l,n} j\omega}, \quad (4.8)$$

with gain K_n and high-pass filter time-constant $T_{l,n}$. The limited data provided in Chapter 2 suggests that not all subjects apply a near-viewpoint response in tasks with single- and double-integrator CE dynamics.

4.3. OFFLINE MODEL PREDICTIONS

The roles of the near- and far-viewpoint responses are not yet fully understood. To gain more insight, we next mathematically derive the HC dynamics that yield “perfect” target-tracking, and we investigate the contributions of both responses with model simulations.

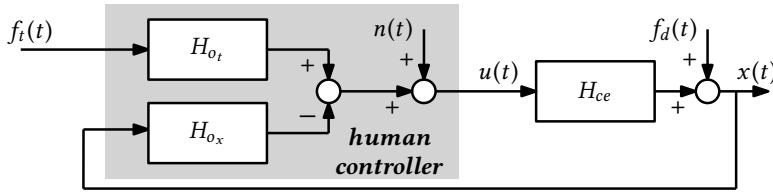


Figure 4.5: Two-channel equivalent control diagram of the human controller.

4.3.1. PERFECT TARGET-TRACKING

The introduced HC model (Fig. 4.4) can be restructured into the mathematically equivalent two-channel model of Fig. 4.5 (see Chapter 2). Here, the HC is modeled to respond to the target and the CE output, with lumped dynamics $H_{o_t}(j\omega)$ and $H_{o_x}(j\omega)$:

$$H_{o_t} = [H_{o_f}H_{o_{e^*}}e^{\tau_f j\omega} + H_{o_n}e^{\tau_n j\omega}]H_{nms}e^{-\tau_v j\omega}, \quad (4.9)$$

$$H_{o_x} = H_{o_{e^*}}H_{nms}e^{-\tau_v j\omega}. \quad (4.10)$$

In Eqs. (4.9) and (4.10) the dependency on $j\omega$ is left out for better readability. Using Fig. 4.5, the target closed-loop can be written as

$$H_{cl,t}(j\omega) = \frac{X(j\omega)}{F_t(j\omega)} = \frac{H_{o_t}(j\omega)H_{ce}(j\omega)}{1 + H_{o_x}(j\omega)H_{ce}(j\omega)}. \quad (4.11)$$

Substituting $X(j\omega)/F_t(j\omega)=1$ (i.e., perfect target-tracking), and solving for $H_{o_t}(j\omega)$, yields the perfect target-tracking dynamics $H_{o_t}^P(j\omega)$:

$$H_{o_t}^P(j\omega) = H_{o_x}(j\omega) + \frac{1}{H_{ce}(j\omega)}. \quad (4.12)$$

Because the form of the response function $H_{o_x}(j\omega)$ is identical in tasks with and without preview for a given CE (see Chapter 2), the form of $H_{o_t}^P(j\omega)$ is also fixed. For example, $H_{o_x}(j\omega)$ typically approximates a gain for integrator CE dynamics. $1/H_{ce}(j\omega)$ is then a pure differentiator, which has a negligible magnitude at low frequencies, but a much higher magnitude than $H_{o_x}(j\omega)$ at high frequencies. $H_{o_t}^P(j\omega)$ is thus dictated by $H_{o_x}(j\omega)$ at low frequencies and by $1/H_{ce}(j\omega)$ at high frequencies. The modeled HC target response in Eq. (4.9) has a similar form; for integrator CE dynamics, it is dictated by gain $K_f K_{e^*}$ at low frequencies and by differentiator $K_n j\omega$ at higher frequencies. This suggests that HCs attempt to approach perfect target-tracking when preview is available.

4.3.2. MODEL SIMULATIONS

Two key aspects of the model are essential for the difference between pursuit and preview tasks: 1) the point on the target ahead that is the input to the HC's "pursuit" response (characterized by τ_f), and 2) the presence and strength of the additive open-loop near-viewpoint response (characterized mostly by K_n , but to a lesser extent also by the other model parameters). Next, we investigate these two aspects for gain, single-, and double-integrator CE dynamics.

Settings

For tasks with 0 and 1 s of preview, estimated model parameters (single-subject data) are reproduced from Chapter 2 in Table 4.1; these are used as baseline settings in the simulations. The used target ($\sigma_{f_t}=1.27$ cm) and disturbance ($\sigma_{f_d}=0.51$ cm) signals are each the sum of 20 sines, with a square amplitude spectrum (1.5 rad/s bandwidth), augmented with a high-frequency shelf where the amplitudes are attenuated (see Chapter 2 for details). No remnant is included.

Analysis of the far-viewpoint location

We stepwise increase the value of τ_f from 0 s (i.e., pursuit tracking) to 1.5 s, while keeping all other parameters fixed at the pursuit settings in Table 4.1. Fig. 4.6a shows that the variance of the tracking error reduces substantially when τ_f increases, for all CE dynamics. Doing so, the target response exhibits phase lead that compensates for the CE's inherent lag, and the HC's NMS lag and visual response delay. The phase becomes markedly closer to $H_{o_t}^P(j\omega)$, especially at mid-frequencies, as shown for integrator CE dynamics in Fig. 4.6e. Responding to the target ahead requires no additional control activity (constant σ_u^2 in Fig. 4.6a), because a pure delay like τ_f only affects the phase of the target response (all $|H_{o_t}(j\omega)|$ lines overlap in Fig. 4.6c). Fig. 4.6a also shows that it is beneficial to respond to the target farther ahead for higher-order CEs, to compensate for its larger inherent lag.

Analysis of the near-viewpoint response

We stepwise increase the value of K_n from 0 and 0.6, keeping all other parameters fixed at the preview settings in Table 4.1. Fig. 4.6b shows that only a small performance improvement is possible by increasing K_n , which comes at the cost of a substantially higher control activity. For some subjects no near-viewpoint response was found in Chapter 2; possibly, these subjects aimed for lower control activity, instead of slightly better performance. The Bode plots (Fig. 4.6 d and f) show that an additional near-viewpoint response mainly affects the high frequencies of $H_{o_t}(j\omega)$, which resembles $H_{o_t}^P(j\omega)$ better in both magnitude and phase if K_n is nonzero. In particular, the characteristic increasing phase

Table 4.1: Simulation conditions and model parameter settings, adapted from Chapter 2.

H_{ce} K_{ce} , -	K_{ce} 0.8		K_{ce}/s 1.5		K_{ce}/s^2 5	
	0	1	0	1	0	1
τ_p , s abbreviation	GNPS	GNPR	SIPS	SIPR	DIPS	DIPR
K_{e^*} , -	3.85	6.62	1.43	1.11	0.14	0.14
T_{l,e^*} , s	2.06	2.39	-	-	-	-
T_{L,e^*} , s	-	-	-	-	2.54	2.22
τ_v , s	0.18	0.16	0.23	0.18	0.28	0.31
ω_{nms} , rad/s	17.9	18.0	11.2	10.2	6.15	5.33
ζ_{nms} , -	0.18	0.37	0.30	0.26	0.67	0.50
K_n , -	-	0.06	-	0.18	-	0.32
τ_n , s	-	0.08	-	0.34	-	0.00
$T_{l,n}$, s	-	0.06	-	0.04	-	5.89
K_f , -	1.21	1.11	0.95	1.12	0.54	0.63
τ_f , s	-	0.55	-	0.70	-	0.99
$T_{l,f}$, s	-	0.26	-	0.38	-	0.59

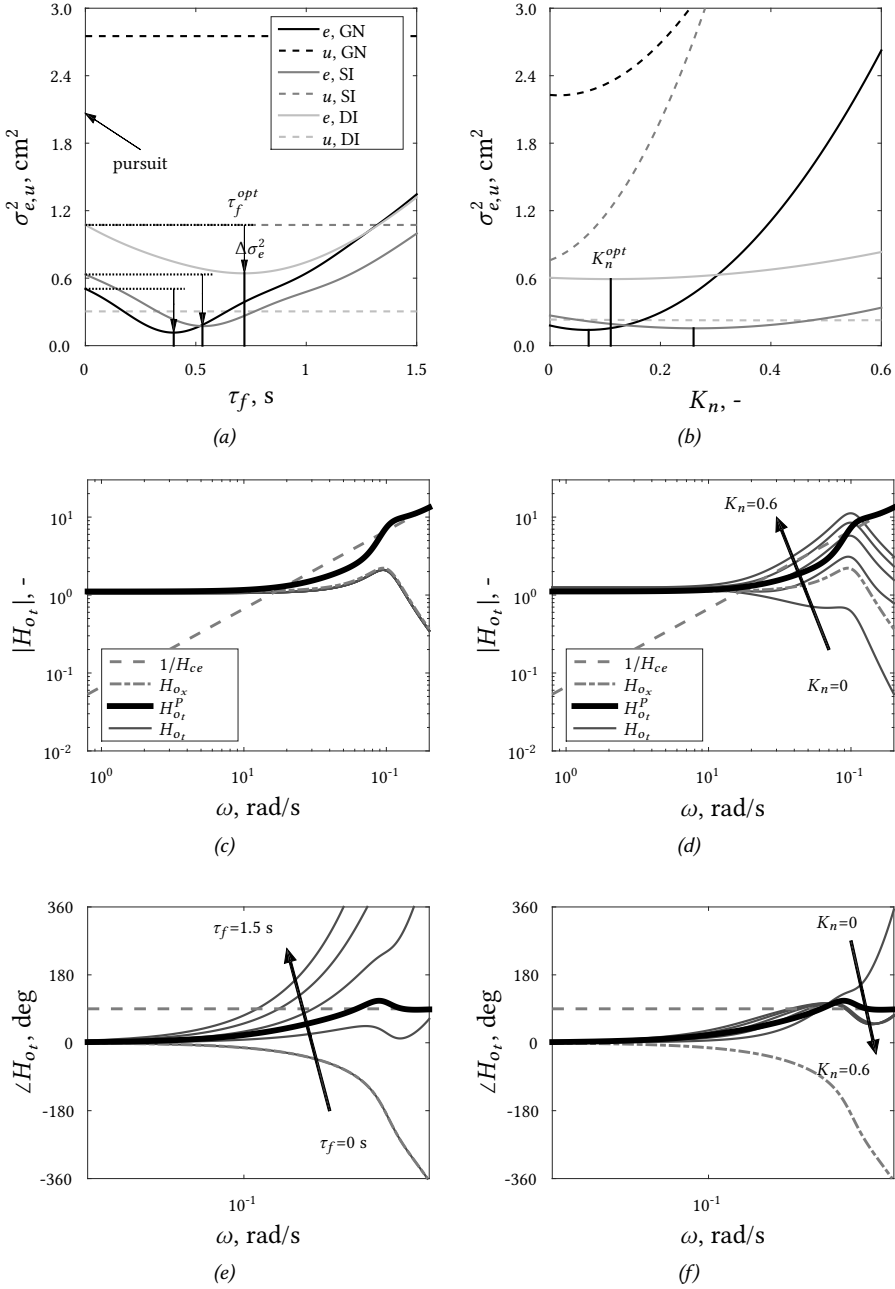


Figure 4.6: Simulated effects of τ_f (a, c, and e), and K_n (b, d, and f); Bode plots (c-f) show the effects for integrator CE dynamics only.

lead that results from responding to a far viewpoint (due to negative delay τ_f) disappears, even with low values of K_n .

Analysis of time traces

The simulated CE output is calculated with Eq. (4.11) for both the pursuit and preview parameters in Table 4.1, with the disturbance set to zero. Fig. 4.7 shows that the CE output follows the target signal much better with preview, lagging less behind, which is consistent with Fig. 4.6. Still, the fast oscillations, or high frequencies, are not completely reproduced; the CE output often remains on the inside of the target signal “corners”, reflecting corner-cutting behavior. This corresponds well with $|H_o(j\omega)|$ at high frequencies (Fig. 4.6d), which is smaller than than required for perfect target-tracking when K_n is small. With double integrator CE dynamics the target’s high frequencies are hardly tracked at all (Fig. 4.7c).

Fig. 4.7d shows the contributions of the near- and far-viewpoint responses when tracking with preview and integrator CE dynamics. The near-viewpoint response accounts for an output ($X_n = H_{o_n} H_{nms} e^{-\tau_v} F_{t,n}$) that is identical to the high-frequency sinusoids in the tar-

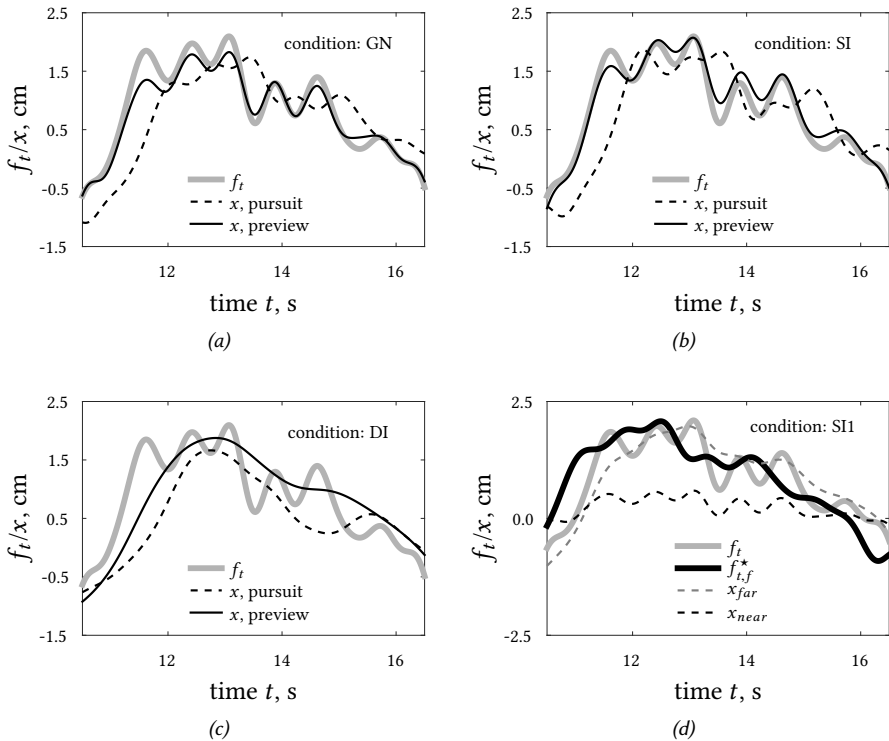


Figure 4.7: Simulated time-traces of the CE output: the benefit of preview (a-c), and the contributions of the near- and far-viewpoint responses (d).

get signal. The filtered far-viewpoint ($F_{t,f}^* = H_{of} F_{t,f}$) lacks exactly these high frequencies; tracking it results in an output (X_f , obtained from closed-loop simulation with K_n , τ_n and $T_{l,n}$ all set to zero) that approximates the target signal's low frequencies.

4.4. EXPERIMENTAL VALIDATION: METHOD

Next, the model simulations are verified with experimental data. Details of the experiment and the data analysis procedures are presented in this section.

4.4.1. EXPERIMENT DESIGN

Twelve subjects performed a combined target-tracking and disturbance-rejection task. Two independent variables were varied, the display and the CE dynamics. The display (see Fig. 4.2) showed either 0 (i.e., pursuit) or 1 s of preview; the CE had gain, integrator, or double integrator dynamics. All subjects performed the full factorial of the two independent variables in a randomized order. The six experimental conditions are summarized in Table 4.1; full details of the experimental settings, procedure, and apparatus are given in Chapter 2.

4.4.2. DATA ANALYSIS

Error and control output variance

The variances of the tracking error and the control output are used as measures for the achieved tracking performance and the applied control activity, respectively. The individual contributions due to the target, disturbance, and HC remnant are estimated by integrating the error and control output auto spectral-density functions only over the respective signal's input frequencies [157].

Input-to-error dynamics

The target-to-error and disturbance-to-error dynamics, $H_{f_t,e}(j\omega_t)$ and $H_{f_d,e}(j\omega_d)$, respectively, quantify the error amplification/attenuation, relative to the respective input signal, in the frequency domain. Each is estimated at either the target or the disturbance signal's input frequencies, ω_t or ω_d , as follows:

$$H_{f_t,e}(j\omega_t) = \frac{E(j\omega_t)}{F_t(j\omega_t)}, \quad H_{f_d,e}(j\omega_d) = \frac{E(j\omega_d)}{F_d(j\omega_d)}. \quad (4.13)$$

Open-loop dynamics

In the frequency domain, performance and stability are characterized by the open-loop crossover frequency ω_c and phase margin ϕ_m , respectively. The performed combined target-tracking and disturbance-rejection task allows for formulating two open-loop dy-

namics, $H_{ol,t}(j\omega)$ for the target and $H_{ol,d}(j\omega)$ for the disturbance [157]:

$$\begin{aligned} H_{ol,t}(j\omega_t) &= \frac{X(j\omega_t)}{E(j\omega_t)} \\ &= \frac{H_{o_t}(j\omega_t)H_{ce}(j\omega_t)}{1 + [H_{o_x}(j\omega_t) - H_{o_t}(j\omega_t)]H_{ce}(j\omega_t)}, \end{aligned} \quad (4.14)$$

$$\begin{aligned} H_{ol,d}(j\omega_d) &= -\frac{X(j\omega_d) - F_d(j\omega_d)}{X(j\omega_d)} \\ &= H_{ce}(j\omega_d)H_{o_x}(j\omega_d). \end{aligned} \quad (4.15)$$

Crossover occurs at the frequency ω_c for which $|H_{ol}(j\omega)|=1$, the corresponding phase margin ϕ_m is $180 + \angle H_{ol}(j\omega_c)$ deg.

Nonparametric multiloop system identification

Nonparametric estimates of $H_{o_t}(j\omega)$ and $H_{o_x}(j\omega)$ in Fig. 4.5 are used to objectively quantify the HC's multiloop control dynamics. Both responses can be estimated simultaneously with an instrumental-variable system identification technique based on Fourier coefficients [86]. From Fig. 4.5 it follows that the modeled control output is:

$$U(j\omega) = H_{o_t}(j\omega)F_t(j\omega) - H_{o_x}(j\omega)X(j\omega) + N(j\omega). \quad (4.16)$$

Two equations, needed to solve for the two unknown dynamics, are obtained by evaluating Eq. (4.16) both at the input frequencies ω_t of target signal, and by interpolating the signals F_t , X , and U in the frequency domain from the disturbance frequencies ω_d to these same ω_t (yielding \tilde{F}_t , \tilde{X} , and \tilde{U}). Assuming zero remnant, it follows that

$$\begin{bmatrix} U(j\omega_t) \\ \tilde{U}(j\omega_t) \end{bmatrix} = \begin{bmatrix} F_t(j\omega_t) & -X(j\omega_t) \\ \tilde{F}_t(j\omega_t) & -\tilde{X}(j\omega_t) \end{bmatrix} \begin{bmatrix} H_{o_t}(j\omega_t) \\ H_{o_x}(j\omega_t) \end{bmatrix}. \quad (4.17)$$

Eq. (4.17) can be solved for $H_{o_t}(j\omega_t)$ and $H_{o_x}(j\omega_t)$. Similarly, estimates can be obtained at the disturbance signal input frequencies, by evaluating Eq. (4.17) at ω_d , after interpolating from ω_t to ω_d .

Model parameter estimation

Estimates of the model parameters are used to explicitly quantify human control behavior, including the characteristics of the near- and far-viewpoint responses. The model parameters are estimated by minimizing a least-squares cost function J , which is based on a frequency-domain error E_u between the measured and modeled control outputs U and \hat{U} :

$$E_u(j\omega|\Theta) = U(j\omega) - \hat{U}(j\omega|\Theta), \quad (4.18)$$

$$J(\Theta) = \sum_{l=1}^{N_l} |E_u(j\omega_l|\Theta)|^2. \quad (4.19)$$

N_l is the number of frequency bins below a cut-off frequency, which is here selected at 25 rad/s; this is well above the highest forcing function input frequency (15.8 rad/s), while even higher frequencies can be considered as pure noise, which should not affect the estimation. The five-run frequency-domain average of the measured control output signals

is used to reduce effects of the remnant on the parameter estimates. The modeled control output is obtained from Eq. (4.16) with remnant N set to zero. The parameter vector Θ is $[K_{e^*} T_{l,e^*} T_{L,e^*} \tau_v \omega_{nms} \zeta_{nms} K_f \tau_f T_{l,f} K_n \tau_n]^T$. Because the break frequency of the near-viewpoint high-pass filter was generally well above measured frequency range in Chapter 2, $T_{l,n}$ is removed from the model here, such that Eq. (4.8) simplifies to a pure differentiator. NMS natural frequencies above the highest input frequency (about 15 rad/s) are difficult to estimate accurately; for subjects where this applies ω_{nms} is fixed at 15 rad/s. A Nelder-Mead simplex algorithm is used to minimize J , constrained only to avoid solutions that contain negative parameters. The best solution is selected from 100 randomly initialized optimizations.

Data processing

All nonparametric measures are calculated per run, and then averaged over the five measurement runs. Crossover frequencies and phase margins are calculated from the fitted HC model, which allows for better estimates of crossover frequencies outside the range of input frequencies. A repeated-measures two-way ANOVA is applied to test for significant differences in performance and control activity, crossover frequency, and phase margin; results are compensated with a conservative Greenhouse-Geisser correction when the assumption of sphericity is violated. Errorbars on the results in the next section always represent 95% confidence intervals, corrected for between-subject variability.

4

4.4.3. HYPOTHESES

Preview is information about the future target signal, so we expect that it affects only the *target-tracking*, and not the disturbance-rejection part of the task. This leads to the following hypotheses:

- I: Target-tracking performance improves with preview, in accordance with [54, 55, 134] and our offline model predictions; this will manifest in a lower error variance at the target frequencies and higher target crossover frequencies and phase margins;
- II: Disturbance-rejection behavior is similar in pursuit and preview conditions, resulting in similar control output variances and $H_{o_x}(j\omega)$ dynamics, hence similar parameters K_{e^*} , T_{l,e^*} , T_{L,e^*} , τ_v , ω_{nms} , and ζ_{nms} .

Based on the offline model analyses (Section 4.3.2) we further hypothesize that:

- III: Subjects respond to the target ahead to improve performance (characterized by τ_n and τ_f); furthermore, the two viewpoints are farther ahead in conditions with higher-order CE dynamics, to generate more compensating phase lead for the CE's larger inherent phase lag;
- IV: Subjects initiate a weak near-viewpoint response, reflected by a small but nonzero value of K_n , to better match the phase required for perfect target-tracking, without substantially increasing control activity.

4.5. EXPERIMENTAL VALIDATION: RESULTS

4.5.1. TRACKING PERFORMANCE AND CONTROL ACTIVITY

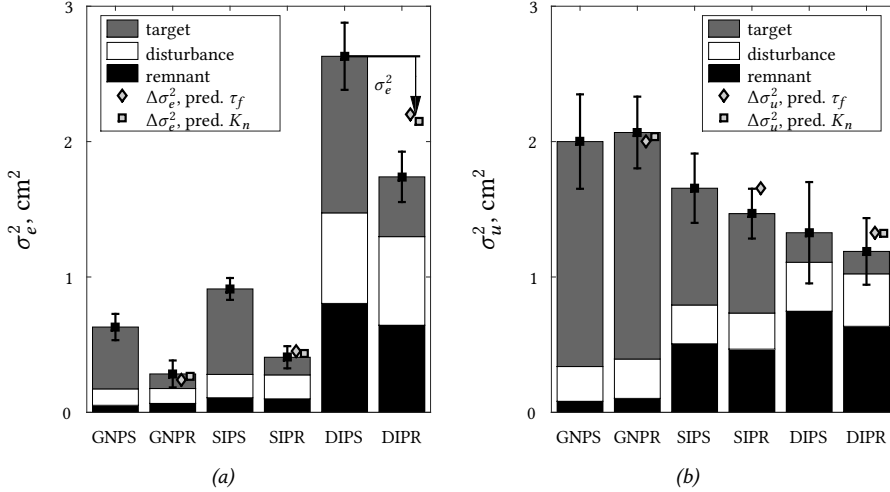


Figure 4.8: Variances of the tracking error (a) and the control output (b).

Fig. 4.8a shows that tracking performance is substantially better (lower σ_e^2) in conditions with preview, which corresponds to results in [54, 55, 134]. Especially target-tracking performance improves (gray part of the bars), but the slight performance increase due to reduced HC remnant is also significant (see Table 4.2). Neither disturbance-rejection performance nor control activity (Fig. 4.8b) are significantly different with preview. Fig. 4.8

Table 4.2: Error and control output ANOVA results. Symbols “**”, “*”, and “-” indicate highly significant ($p < .01$), significant ($p < .05$), and non-significant ($p > .05$) results, respectively.

		error, e			control output, u		
		df	F	sig.	df	F	sig.
σ^2	display	(1,11)	127	**	(1,11)	1.31	-
	dynamics	(1.07,11.8)	213	**	(1.23,13.6)	8.4	**
	disp. \times dyn.	(1.05,11.5)	13.5	**	(2,22)	0.91	-
σ_t^2	display	(1,11)	305	**	(1,11)	1.44	-
	dynamics	(1.16,12.8)	83.3	**	(2,22)	197	**
	disp. \times dyn.	(1.11,12.3)	14.5	**	(2,22)	0.95	-
σ_d^2	display	(1,11)	0.22	-	(1,11)	0.81	-
	dynamics	(1.01,11.1)	138	**	(1.08,11.9)	2.30	-
	disp. \times dyn.	(1.03,11.3)	0.20	-	(1.36,15.0)	0.79	-
σ_r^2	display	(1,11)	1.43	*	(1,11)	1.34	-
	dynamics	(1.03,11.3)	135	**	(1.16,12.7)	14.2	**
	disp. \times dyn.	(1.08,11.8)	7.98	*	(2,22)	1.10	-

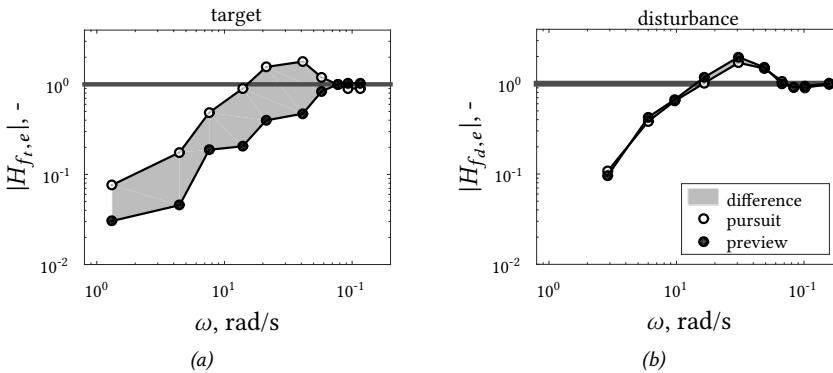


Figure 4.9: Nonparametric estimates of the target-to-error (a) and the disturbance-to-error (b) dynamics for integrator CE conditions, single-subject data.

4

also shows that the performance improvement predicted by the model simulations in Section 4.3.2 matches reasonably well with the experimental results.

With higher-order CE dynamics, tracking performance is substantially worse (Fig. 4.8a). However, this effect is smaller when preview is available, especially at the target and remnant frequencies (significant interaction effects). Increasing the order of the CE dynamics markedly affects the control activity distribution: the target component decreases significantly, while the remnant component increases significantly.

The estimated input-to-error dynamics are shown in Fig. 4.9 for integrator CE dynamics. The characteristic error-amplification peak, caused by the HC's response time delay [80], is clearly present in disturbance rejection, both with and without preview (indicated by $|H_{f,d,e}| > 1$ in Fig. 4.9b). In target tracking (Fig. 4.9a) this peak is only visible in pursuit tasks. With preview, $|H_{f,e}|$ is always smaller than one, so the error is attenuated at all input frequencies. This is evidence that preview enables HCs to compensate for their own response delays.

4.5.2. OPEN-LOOP DYNAMICS

In pursuit conditions, the measured target open-loop dynamics (Fig. 4.10, gray markers/line) resemble an integrator with a time delay around crossover, in accordance with [42, 163]. For double integrator CE dynamics subjects managed to generate integrator magnitude characteristics in only a minor region around crossover, due to the difficulty of this condition. All disturbance open-loop dynamics (not shown) have a similar shape, both in pursuit and preview conditions. With the introduction of preview, the magnitude of the target open-loop dynamics increases below the crossover frequency, and then drops off with a slope larger than that of an integrator (black markers/line, Fig. 4.10); additionally, the characteristic pure delay is not visible in the open-loop phase.

The target crossover frequency (Fig. 4.11a) and phase margin (Fig. 4.11c) are both higher

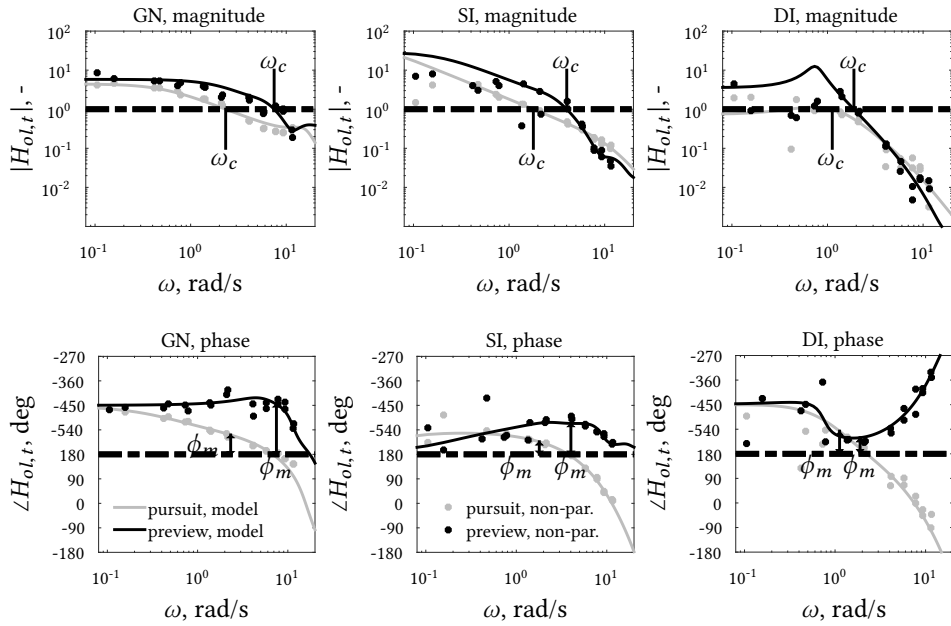


Figure 4.10: Target open-loop dynamics, single-subject data.

in conditions with preview (significant effect, Table 4.3), pointing to improved target-tracking performance and stability. The average target phase margins are between the values predicted by the near- and far-viewpoint model simulations (Section 4.3.2), suggesting that a combination of both responses is active (except in double integrator tasks). Note that the measured crossover frequencies are slightly lower than the idealized predictions. The disturbance crossover frequency (Fig. 4.11b) and phase margin (Fig. 4.11d) are similar in pursuit and preview conditions. Only for gain CE dynamics the disturbance crossover frequency is slightly lower with preview, yielding a significant display effect; however, this crossover frequency was difficult to estimate, due to the relatively low control activity at disturbance frequencies in gain CE conditions (see Fig. 4.8b).

The measured crossover frequencies (except target tracking with preview) are relatively low: they are in the region where *crossover regression* occurs in compensatory tracking tasks ($0.8\omega_c < \omega_i$ [6, 164]), as illustrated in Fig. 4.11. Little is known of this phenomenon in pursuit and preview tasks. The relative invariance of these low crossover frequencies with CE dynamics was reported earlier in similar pursuit tracking tasks [42, 128].

4.5.3. HUMAN MULTILoop CONTROL DYNAMICS

Fig. 4.12 shows Bode plots of the estimated $H_{o_r}(j\omega)$ and $H_{o_x}(j\omega)$ dynamics. As shown before in Chapter 2, the model fits (solid lines) coincide well with the nonparametric identification results (markers). Note that a similar equalization is visible as in compensatory

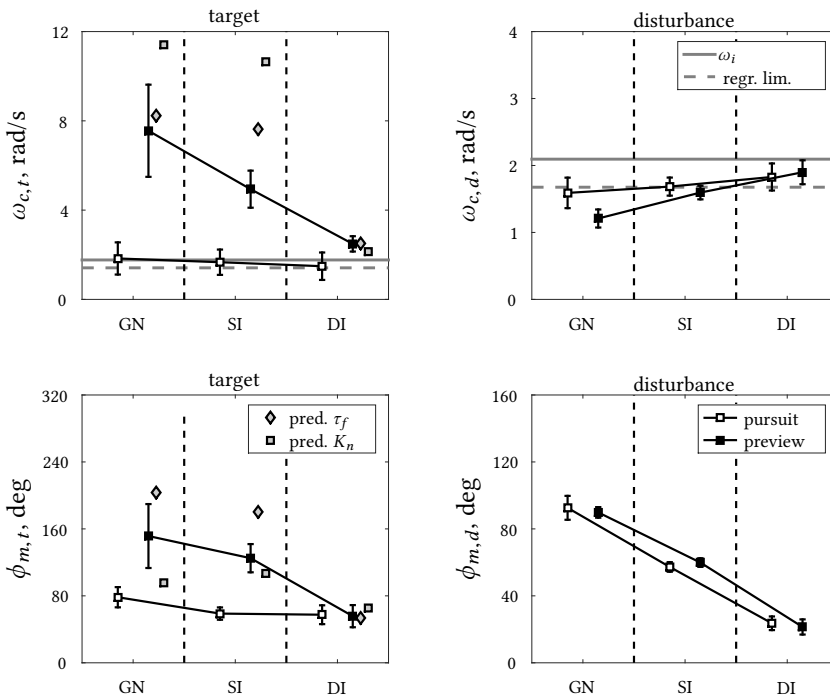


Figure 4.11: Crossover frequencies and phase margins, predictions indicate the change relative to the corresponding pursuit task.

Table 4.3: Crossover frequency and phase margin ANOVA results. Symbols “**”, “*”, and “-” indicate highly significant ($p < .01$), significant ($p < .05$), and non-significant ($p > .05$) results.

		target			disturbance		
		df	F	sig.	df	F	sig.
ω_c	display	(1,11)	35.7	**	(1,11)	7.80	*
	dynamics	(1.20,13.2)	19.7	**	(1.27,14.0)	8.35	**
	disp. × dyn.	(1.23,13.5)	12.1	**	(2,22)	8.69	**
ϕ_m	display	(1,11)	37.7	**	(1,11)	0.41	-
	dynamics	(1.58,17.4)	19.9	**	(1.20,13.1)	316	**
	disp. × dyn.	(1.17,12.9)	8.32	**	(1.33,14.7)	1.40	-

tracking tasks [80]; both $H_{o_t}(j\omega)$ and $H_{o_x}(j\omega)$ exhibit a -1, 0, and +1 mid-frequency magnitude slope for gain, single-, and double-integrator CE dynamics, respectively.

The target response in pursuit conditions (as well as the CE output response in all conditions), shows the characteristic high-frequency phase roll-off caused by the HC’s response delay and NMS lags. In the preview conditions such phase lag is not present in $H_{o_t}(j\omega)$; instead, *phase lead* is generated, similar as in the simulations in Section 4.3.2. The result-

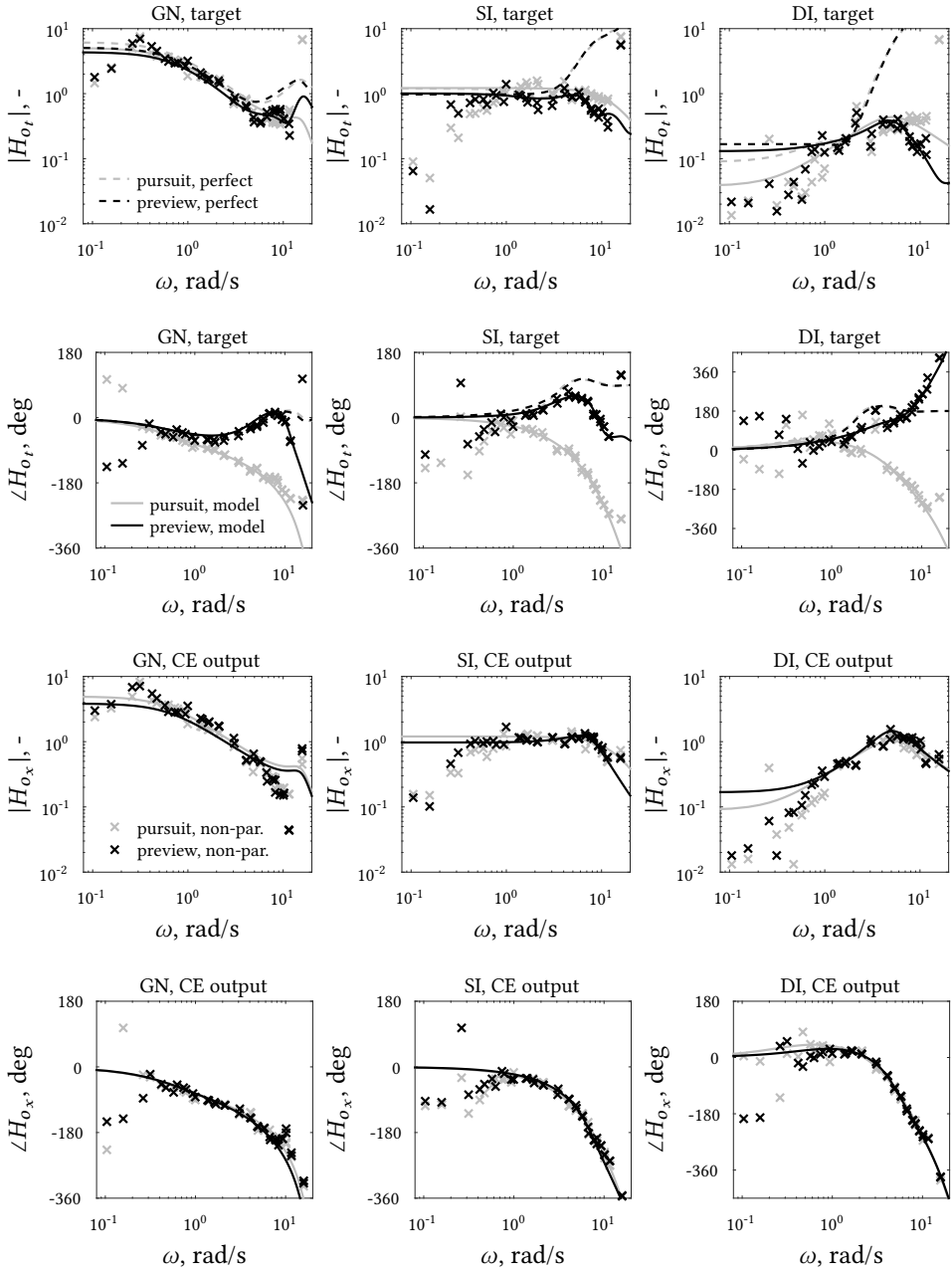


Figure 4.12: Bode plots of the target (top 2 rows) and CE output (bottom 2 rows) response dynamics: nonparametric estimates, model fits, and perfect target-tracking; single-subject data.

ing phase characteristics resemble perfect target-tracking much better, so subjects clearly apply control actions that cancel most of the lag from their own response and the CE dynamics. At higher frequencies and for higher-order CE dynamics the perfect target-tracking phase is matched less well.

Fig. 4.12 also shows that the magnitude of the target response at high frequencies is lower than that required for perfect target-tracking. This indicates *corner-cutting* behavior, and corresponds to the simulations with low values of the near-viewpoint gain K_n (Section 4.3.2).

4.5.4. MODEL PARAMETERS

Internal-error response

In gain CE conditions, both K_{e^*} and T_{l,e^*} increase slightly with preview (Fig. 4.13). As a result, the error-response dynamics have a higher magnitude at the lowest frequencies, but remain similar over most of the measured frequency range. Similarly, preview yields slightly higher K_{e^*} and T_{l,e^*} in double integrator conditions, which also points to a higher low-frequency magnitude. For integrator CE tasks, K_{e^*} is identical with and without preview.

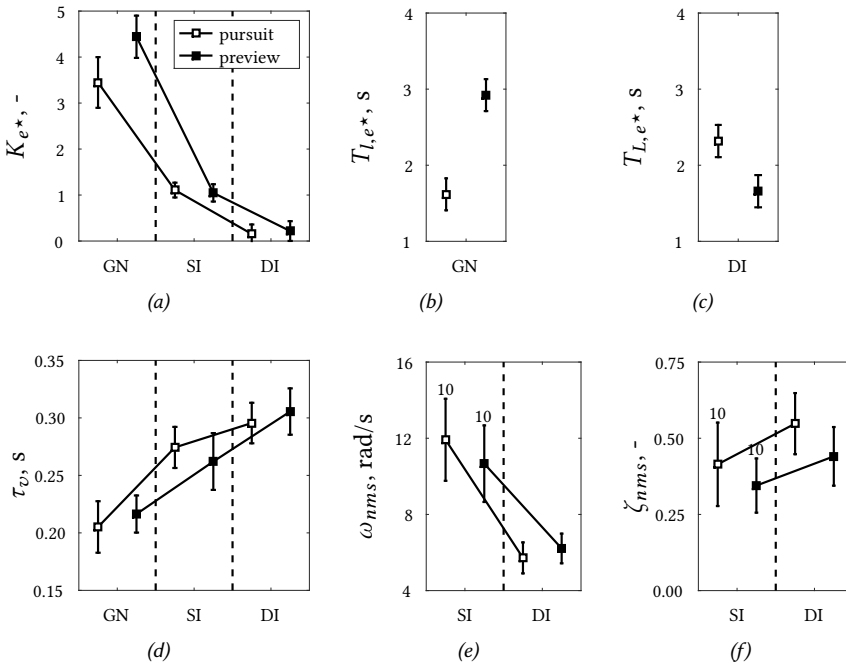


Figure 4.13: Estimated internal-error response (a-c) and physical limitation (d-f) parameters. For GN and SI the NMS could be estimated for 0 and 10 subjects, respectively.

Physical limitations

τ_v , ω_{nms} , and ζ_{nms} (Fig. 4.13) are not systematically adapted when preview becomes available. Only the NMS damping ζ_{nms} appears to be slightly lower with preview. Increasing the order of the CE dynamics yields more pronounced effects: the visual-response delay τ_v increases, while the NMS bandwidth (ω_{nms}) decreases; such adaptations have been measured before in [6, 42, 128, 163].

Far-viewpoint response

Fig. 4.14 shows the estimated far-viewpoint parameters. τ_f is larger for higher-order CE dynamics, indicating that subjects respond to the target farther ahead, to generate more compensating phase lead. For double integrator CE dynamics, τ_f is approximately at the limit of the presented preview (1 s), suggesting that the tracking performance in this condition may further improve with more preview. The far-viewpoint filter time-constant $T_{l,f}$ is also larger for higher-order CEs, such that less of the target's high frequencies are tracked through the far-viewpoint response. To compensate for the phase lag introduced by the low-pass filter, the measured values of τ_f are consistently higher than predicted in Section 4.3.2, where this low-pass filter was not considered (i.e., $T_{l,f}=0$ s).

For gain and integrator CE dynamics, the target weighting gain K_f is similar in pursuit and

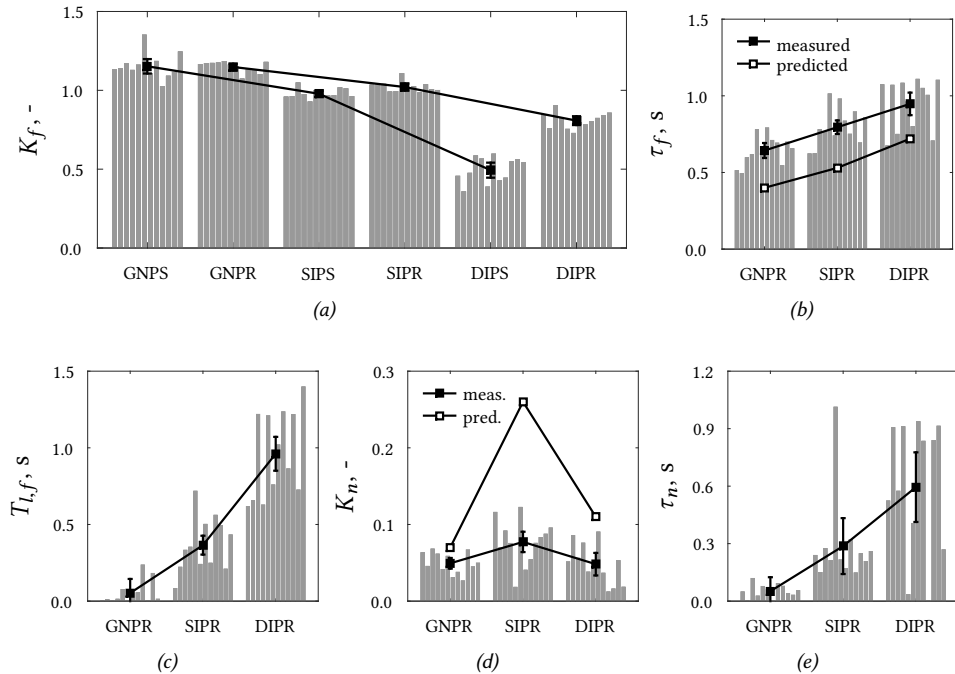


Figure 4.14: Estimated preview parameters: far-viewpoint gain K_f (a), far-viewpoint look-ahead time τ_f (b), far-viewpoint lag time-constant $T_{l,f}$ (c), near-viewpoint gain K_n (d), and near-viewpoint look-ahead time τ_n . Gray bars represent the individual subjects.

preview conditions. For double integrator CE dynamics, K_f is much larger with preview, indicating that subjects are responding more aggressively to the target signal. The difficulty of the pursuit task with double integrator CE dynamics likely forced subjects to prioritize stabilizing the CE's output, so less effort was put in target tracking. This is consistent with the generally lower values of K_f with higher-order CEs, and also with the lower control activity at the target frequencies (Fig. 4.8).

Near-viewpoint response

Fig. 4.14 also shows the estimated near-viewpoint parameters. K_n is small but always nonzero, suggesting that most subjects initiated a near-viewpoint response; however, this does not correspond to the Bode plots in Fig. 4.12. For example, for double integrator CE dynamics the increasing high-frequency phase of $H_{o_i}(j\omega)$ suggests that no near-viewpoint response is present, while K_n is estimated at 0.05. For single integrator CE dynamics, the phase flattening of $H_{o_i}(j\omega)$ at high frequencies does suggest that a near-viewpoint response is initiated, while K_n is estimated at 0.08. It is thus difficult to determine whether a subject initiated a near-viewpoint response, or not, merely from K_n . The adaptation of K_n to the CE dynamics is similar as predicted by the model simulations (Section 4.3.2), with the highest value of K_n found in single integrator conditions. As the estimated values of K_n are lower than predicted, it appears that subjects prioritize a low control activity over enhanced performance.

τ_n is larger for higher-order CE dynamics, similar as τ_f . However, between-subject variations are large, especially for double integrator CE dynamics. Likely, these variations (and the outlier for Subject 5 with single integrator CE dynamics) point to a negligible contribution of the near-viewpoint response. Consequently, it is impossible to obtain a meaningful estimate of τ_n .

4.6. DISCUSSION

This chapter explained how HCs use preview for control in manual tracking tasks with various CE dynamics, using both offline model analyses and experimental data. The hypothesized performance improvement with preview, in accordance with [54, 55, 134], was confirmed, predominantly in *target tracking* (H.I). Model simulations predicted the attained performance improvement remarkably well, especially considering that no remnant was included, and no parameter interactions were investigated. As hypothesized (H.II), disturbance-rejection behavior and performance were similar with and without preview.

Fitting the model to the experimental data allowed us to peek inside the black-box of human control, decomposing their behavior into several characteristic responses and physically interpretable parameters. Thereby, we confirmed that subjects respond to the target farther ahead in tasks with higher-order CE dynamics (as suggested before in Chapter 2), to compensate for the CE's larger phase lag (confirming H.III). The adopted far-viewpoint location was anticipated quite accurately with the offline model simulations, establishing the model's capability to predict HC behavior.

At the highest input frequencies, HCs cannot invert the CE dynamics, as required to attain perfect target-tracking, with just their far-viewpoint response. The role of the additive

near-viewpoint response is to better match the perfect target-tracking dynamics at these high frequencies, and to further increase the target crossover frequency. The hypothesized low but nonzero values for K_n (H.IV) were found in the experiment for most subjects, but these were not always supported by a clearly visible near-viewpoint response in the corresponding nonparametric estimate of the target response. The estimated value of K_n is a poor indicator for the presence of a near-viewpoint response, hence we cannot confidently confirm H.IV. The near-viewpoint response varies substantially between subjects, likely because it can yield only a marginal performance benefit, at the cost of substantially more control activity. For adequate task performance, the far-viewpoint response is much more important than the near-viewpoint response.

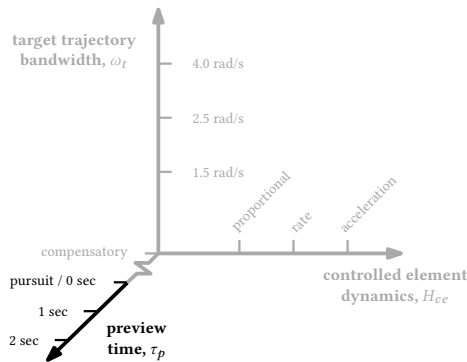
To better illustrate human adaption between pursuit and preview tracking tasks, and to the CE dynamics, we now propose a first set of verbal adjustment rules. 1) Similar as in compensatory tracking tasks [6], HCs equalize their internal error response $H_{o_e^*}(j\omega)$ to the given CE dynamics such that their combination exhibits integrator-like dynamics. 2) In pursuit and preview tasks, HCs apply feedforward control by adapting the relative target-tracking/CE-stabilization priority through K_f , with more emphasis on target tracking (higher K_f) in tasks with lower-order CEs. 3) In preview tasks, HCs anticipate the target signal's changes by basing their "pursuit" response on the far viewpoint τ_f s ahead, which is positioned farther ahead for higher-order CEs. Hereby, the response phase (hence performance) improves at lower frequencies but deteriorates at higher frequencies. 4) HCs filter these high frequencies from the previewed target signal by adapting $T_{l,f}$; they filter away more high frequencies (higher $T_{l,f}$) for higher-order CEs. 5) Optionally, performance can be enhanced slightly more by also tracking the target signal's high frequencies with an additive, parallel near-viewpoint response, which ideally resembles the inverse of the CE dynamics. With a near-viewpoint response, HCs sacrifice some phase margin in favor of a higher crossover frequency. These adjustment rules can be refined and extended by quantifying HC adaptation to other task variables, such as the preview time and the forcing functions' characteristics, which is the focus of the next two chapters.

4.7. CONCLUSION

This chapter explained how humans use preview for control in tracking tasks with various controlled element dynamics. Offline analyses with a quasi-linear human controller model and results from a human-in-the-loop experiment were presented, to establish the roles of the human's near- and far-viewpoint responses. Preview allows humans cancel their own and the controlled element's lags, up to relatively high frequencies, by basing their far-viewpoint, pursuit response on the target signal ahead; this requires no additional control activity. The optional open-loop near-viewpoint response helps to synchronize the output with the target signal at higher frequencies, but at the cost of substantially more control activity. Target-tracking performance improves primarily due to the far-viewpoint response mechanism, while the benefit from the near-viewpoint response is small. The adopted control-theoretic approach provided unique quantitative insights into human control adaptation in preview tasks, which can explain human behavior observed in other preview control tasks, like driving.

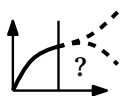
5

EFFECTS OF PREVIEW TIME



In Part I of this thesis, a novel cybernetic model was proposed for human manual control behavior in pursuit and preview tracking tasks. To allow for rationalizing and predicting human preview control behavior (including their interaction with technology) in a wide range of control tasks, a quantitative understanding of human adaptation to crucial task variables is also essential. Chapter 4 already quantified human adaptation to the controlled element dynamics. This chapter focuses on a second crucial task variable: the preview time, which indicates the limit up to which the previewed trajectory is visible ahead. More distant portions of preview are typically obscured from the human's view due to, for example, poor lighting, objects, or display edges. Similar to Chapter 4, human adaptation to the preview time is first predicted offline, using the human controller preview model proposed in Part I. The predicted adaptations are then verified with data from a human-in-the-loop experiment, in which eight preview time settings between 0 and 2 s are tested.

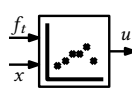
Steps of the cybernetic approach involved:



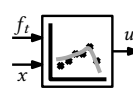
offline model
predictions



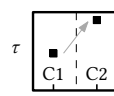
acquisition of
control data



system
identification



parameter
estimation



analysis of
adaptation

The contents of this chapter have been published as:

Title Effects of Preview Time in Manual Tracking Tasks

Journal IEEE Transactions on Human-Machine Systems, vol. 48, no. 5, pp. 486-495, Oct. 2018

Authors K. van der El, S. Padmos, D.M. Pool, M.M. van Paassen, and M. Mulder

5.1. INTRODUCTION

PREVIEW information about a future trajectory to follow is present in many manual control tasks. A clear example of preview is the road that is visible ahead when driving [137]. The extent of the visible preview is always limited by the horizon, fog, poor lighting, objects, or display edges. The *preview time* is the time required to reach the farthest visible point on the previewed trajectory at the current velocity. It has been shown that Human Controllers (HCs) can better follow a target trajectory when the preview time increases, in tasks ranging from display tracking [54–57, 61, 134] to car driving [58, 59, 62, 136]. However, task performance is typically stable when the preview time exceeds a certain minimum, or *critical preview time*, which is known to range between 0.3–1.5 s, depending on the control task [54–56, 59, 134]. To assure safe manual operation in control tasks with restricted preview, it is essential to quantify and, if possible, predict the critical preview time and the performance degradation at lower preview times.

The effects of preview time on HC behavior are as of yet not fully understood. Task characteristics (or variables) such as the Controlled Element (CE) dynamics and target trajectory bandwidth also evoke HC behavior adaptations [6, 44], and influence the effects of preview, including the critical time [134] (see also Chapter 4). Attempts to quantify the effects of preview time through control-theoretic modeling of driver steering [92, 137, 139, 140, 165] and manual tracking [54, 61, 134] account for HCs' use of preview in fundamentally different ways. A new quasi-linear model for preview tracking tasks was proposed in Chapter 2, which captures measured HC multiloop control dynamics in tasks with 0 s (pursuit) and 1 s of preview. Preliminary experimental results suggest that this model can also capture HC adaptation to preview time [57], but this was only shown for rate (velocity) control tasks with preview times between 0 and 1 s. The model's physically interpretable parameters can be directly estimated from experimental data using system identification, yielding novel *quantitative* insights into *how HCs use preview*. This already led to an initial set of “verbal adjustment rules” that cover HC adaptation to the CE dynamics in preview tracking tasks (Chapter 4). Unfortunately, we currently lack the understanding and experimental data that are required to formulate similar rules for the effects of other task variables, such as available preview time [44].

The goal of this chapter is to quantify the effects of preview time in manual tracking tasks; in particular focusing on the critical preview time and changes in task performance and HC control behavior. Because Chapter 4 showed that the CE dynamics strongly affect HCs' use of preview, we investigate the effects of preview time with both Single Integrator (SI, rate control) and Double Integrator (DI, acceleration control) CE dynamics.

First, the quasi-linear preview model from Chapter 2 is used to theoretically predict the effects of preview time offline, by finding the model parameters (i.e., the HC's behavior) that minimize the tracking error in closed-loop model simulations. Second, these predictions are verified with measurements from a human-in-the-loop experiment, in which eight participants performed the same target-tracking and disturbance-rejection task, with eight different preview times between 0 and 2 s (well above reported critical preview times [54–56, 59, 134]). To explicitly quantify HCs' adaptation to preview time, a nonparametric, multiloop system identification technique is applied [86], and a least-squares fit is made

of the preview model to the measurement data, to estimate the model's parameters.

This chapter is structured as follows. First, Section 5.2 introduces the considered preview tracking task and the preview control model from Chapter 2. Predictions of the effects of preview time are presented in Section 5.3, followed by the experimental method and the applied identification techniques in Section 5.4. Section 5.5 summarizes the experiment results and compares them to the predictions. The chapter ends with a discussion and our main conclusions in Sections 5.6 and 5.7, respectively.

5.2. BACKGROUND

5.2.1. THE CONTROL TASK

Fig. 5.1 illustrates the considered control task and shows the principal terminology used throughout this chapter. The HC's task is to give control inputs $u(t)$ to the CE such that the CE output $x(t)$ (white circle on the display, Fig. 5.1a) horizontally follows the target signal $f_t(t)$ (black cross) as closely as possible, while the CE output is simultaneously perturbed by a disturbance signal $f_d(t)$. In other words, the HC should minimize the horizontal tracking error $e(t) = f_t(t) - x(t)$. On the displays (Fig. 5.1a), the target signal $f_t([t, t + \tau_p])$ ahead is also visible (winding line) up to the preview time τ_p s ahead. The previewed target signal can be used by the HC to anticipate the future horizontal movements of the current target marker. When τ_p is zero, only the current target is visible and a classical pursuit task is obtained [62].

5.2.2. HUMAN CONTROLLER MODEL

The model of HC behavior in preview tracking tasks from Chapter 2 is depicted in Fig. 5.1c. The model is quasi-linear, with linear time-invariant transfer functions $H(j\omega)$ that account for the majority of the HC's behavior, and a remnant signal $n(t)$ that captures the remaining time-variations, nonlinearities, and noise. HC use of the full previewed target is modeled with two responses. The main, low-frequency, *far-viewpoint* response allows for most performance improvement relative to zero-preview, pursuit tasks, while the auxiliary, high-frequency, *near-viewpoint* response improves performance slightly more at a cost of a substantial increase in control effort (see Chapter 4). The far-viewpoint response involves an identical feedback control-strategy as in compensatory tracking tasks [6]; however, the error $e^*(t)$ that is minimized is not the true error $e(t)$, but the difference between the filtered target at the far viewpoint τ_f s ahead and the CE output: $E^*(j\omega) = H_{o_f}(j\omega)e^{\tau_f j\omega}F_t(j\omega) - X(j\omega)$, with the capital letters denoting the Fourier transforms of the respective signals. The low-pass smoothing filter $H_{o_f}(j\omega)$ is given by:

$$H_{o_f}(j\omega) = K_f \frac{1}{1 + T_{l,f}j\omega}, \quad (5.1)$$

with target weighting gain K_f and time constant $T_{l,f}$. HCs completely ignore the target signal variations when $K_f = 0$, while $K_f = 1$ indicates a response to the true advanced error, at least at those frequencies sufficiently below the smoothing filter cutoff $1/T_{l,f}$. In the

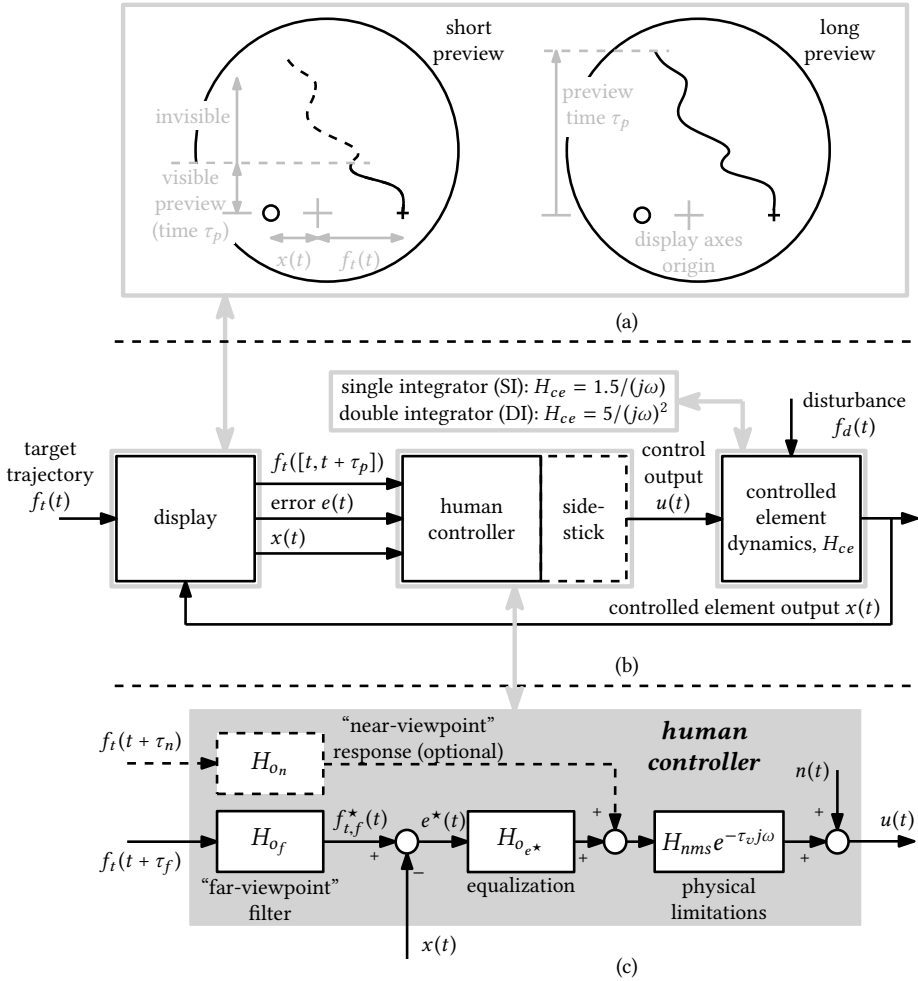


Figure 5.1: Preview displays with different preview times (a), illustration of the control task (b), and the model for human preview tracking behavior from Chapter 2 (c).

time domain, the low-pass filter in Eq. (5.1) can be interpreted as the weighted average of the previewed target up to the far viewpoint, such that τ_f is the most distance point on the previewed trajectory that is used by the HC, while $T_{L,f}$ quantifies the portion of the visible preview that is used for smoothing the trajectory.

The modeled error response $H_{oe^*}(j\omega)$ is a reduced form of the *precision model* [80]:

$$H_{oe^*}(j\omega) = K_{e^*}(1 + T_{L,e^*}j\omega). \tag{5.2}$$

Here, K_{e^*} is the error response gain and T_{L,e^*} is the lead time-constant. Possible lag equalization is omitted in Eq. (5.2), as such behavior is normally absent in SI and DI tasks [6]. In

SI tasks no lead equalization is required and Eq. (5.2) reduces to $K_e^*{}^1$. The HC's physical limitations are also included in this inner loop: τ_v is the response time delay and $H_{nms}(j\omega)$ represents the neuromuscular activation dynamics [166], modeled here as a second-order mass-spring-damper system:

$$H_{nms}(j\omega) = \frac{\omega_{nms}^2}{(j\omega)^2 + 2\zeta_{nms}\omega_{nms}j\omega + \omega_{nms}^2}, \quad (5.3)$$

with a break frequency ω_{nms} and damping ratio ζ_{nms} .

The open-loop, near-viewpoint response $H_{o_n}(j\omega)$, although not always initiated by all HCs, is used in parallel with the far-viewpoint response to better track the highest frequencies of the target signal (see Chapter 4 for details). Whether HCs apply a near-viewpoint response likely depends on their motivation to attain optimal performance (Chapter 4 showed that mechanizing a near-viewpoint response requires substantial control effort), and familiarity with the task's CE dynamics and target signal, which is essential for applying an open-loop feedforward control strategy effectively. Longer preview times may trigger the near-viewpoint response, as the HC's knowledge of the target signal improves. With 1 s of preview, most participants in Chapter 4 were found to apply a near-viewpoint response in SI tasks, but not in DI tasks, as accurate feedforward control with these unstable dynamics is difficult [128, 167]. Although not all subtleties of the near-viewpoint response are yet understood, its dynamics appear to approximate a simple differentiator:

$$H_{o_n}(j\omega) = K_n j\omega, \quad (5.4)$$

with gain K_n , and the target τ_n s ahead as the input. In the following, we will analyze two models: the "Full Model" (FM) and a "Reduced Model" (RM). The FM has parameter vector $\Theta = [K_n \tau_n K_f T_{l,f} \tau_f K_e^* T_{l,e^*} \omega_{nms} \zeta_{nms} \tau_v]^T$, while the RM omits the near-viewpoint response (i.e., no K_n and τ_n).

5.3. OFFLINE MODEL PREDICTIONS

In this section, we use the preview model from Chapter 2 to predict the effects of preview time on HC behavior and tracking performance. Two scenarios are investigated: a Reduced Model Prediction (RMP) and a Full Model Prediction (FMP), obtained with the RM ($H_{o_n}(j\omega)=0$) and FM ($H_{o_n}(j\omega)$ is used) versions of the model, respectively.

5.3.1. APPROACH

Humans are known to be adaptive controllers that optimize their control gains [6, 92, 121, 168]. This adaptation can be expressed mathematically with an optimality criterion that reflects the HC's goals, like a weighted combination of optimized performance and

¹Note that preview tasks with SI dynamics may evoke some low-frequency lag-lead behavior, which will also be shown in detail in Chapter 7; as this behavior was mostly absent in the current experiment, the lag-lead dynamics are excluded from the SI model in this chapter.

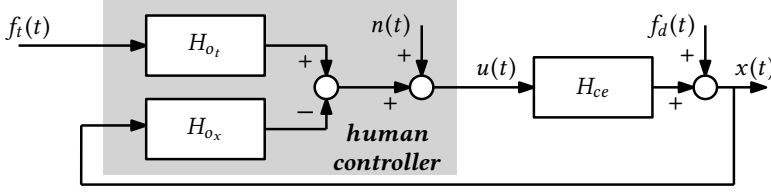


Figure 5.2: Two-channel equivalent control diagram of the human controller, which includes a feed-forward response $H_{o_t}(j\omega)$ and a feedback response $H_{o_x}(j\omega)$, identical to Chapter 2.

minimized control effort. Motivated HCs typically aim mainly for optimal tracking performance [6, 168], so a good prediction of the model parameter vector Θ is obtained by minimizing the variance of the error, $\sigma_e^2(\Theta)$. The variance can be calculated in the frequency domain by integrating the power spectral density function of the error signal [157].

To calculate the tracking error, we first lump the modeled HC dynamics from the previous section into two describing functions $H_{o_t}(j\omega)$ and $H_{o_x}(j\omega)$, which represent the HC's total response to the target and CE output signals (see Fig. 5.2 for the corresponding equivalent control diagram, see Chapter 2 for details):

$$H_{o_x} = H_{o_{e^*}} H_{nms} e^{-\tau_v j\omega}, \quad (5.5)$$

$$H_{o_t} = [H_{o_n} e^{\tau_n j\omega} + H_{o_f} e^{\tau_f j\omega} H_{o_{e^*}}] H_{nms} e^{-\tau_v j\omega}. \quad (5.6)$$

Here, the $j\omega$ terms are dropped for brevity. Expressing $X(j\omega)$ as a function of the external inputs $F_t(j\omega)$, $F_d(j\omega)$, and $N(j\omega)$ using Fig. 5.2, and substituting the result into $E(j\omega) = F_t(j\omega) - X(j\omega)$, yields for the tracking error [42]:

$$E = \frac{(1 + H_{ce}(H_{o_x} - H_{o_t}))F_t - F_d - H_{ce}N}{1 + H_{o_x}H_{ce}}. \quad (5.7)$$

5.3.2. SETTINGS AND PROCEDURE

HC adaptation to variations in τ_p between 0 and 2 s is predicted by minimizing $\sigma_e^2(\Theta)$, subject to a minimum phase margin constraint of 20 deg. The preview time is varied with a 0.01 s resolution, and at each preview time the near- and far-viewpoint locations are constrained to the visible preview region, that is $0 \leq \tau_n \leq \tau_p$ and $0 \leq \tau_f \leq \tau_p$. The human's limitation parameters and lead time-constant are kept fixed, their values are based on the preview tracking data obtained in Chapter 4 (see Table 5.1). For the RMP, the error variance is optimized for the remaining four model parameters: K_{e^*} , K_f , τ_f , and $T_{l,f}$. For the FMP, the error variance is optimized for K_n , τ_n , and $T_{l,f}$, while K_{e^*} , K_f , and τ_f are fixed at the optimal values found in the RMP, as their interaction with the desired near-viewpoint response is small (see Chapter 4). However, $T_{l,f}$ is again free to allow for an attenuated far-viewpoint response at high frequencies, which may improve the effectiveness of the near-viewpoint response. The predicted performance is compared to human-in-the-loop data from previous experiments for verification, see Table 5.2.

Table 5.1: Offline model simulations parameter settings.

	$H_{ce}(j\omega)$	T_{L,e^*}, s	$\omega_{nms}, \text{rad/s}$	$\zeta_{nms}, -$	τ_v, s
SI	$1.5/(j\omega)$	-	10.5	0.35	0.26
DI	$5/(j\omega)^2$	1.5	8	0.45	0.3

Table 5.2: Previous preview tracking experiments.

	CE	dist. added	forcing function	bandwidth, rad/s	no. subj.
Reid [54]	SI	no	filt. noise	-	6
Ito [55]	SI, DI	no	multisine	2.5	2
Tomizuka [134]	SI, DI	no	filt. noise	1.5	3
Van der El [57]	SI	yes	multisine	1.5	6

The target signal is a multisine composed of 20 sinusoids:

$$f_t(t) = \sum_{i=1}^{20} A_t[i] \sin(\omega_t[i]t + \phi_t[i]), \quad (5.8)$$

with amplitude $A_t[i]$, frequency $\omega_t[i]$, and phase $\phi_t[i]$ of the i^{th} sinusoid. The disturbance signal is defined identically, whereas remnant is set to zero. The target and disturbance signals have mutually exclusive frequencies, which are distributed logarithmically between 0.1 and 16 rad/s at integer multiples of the 0.0524 rad/s ($=2\pi/120$) fundamental frequency, corresponding to a 120 s measurement time. Both signals have a square amplitude spectrum, with a 1.5 rad/s bandwidth beyond which the amplitudes are attenuated. The variance of the target $\sigma_{f_t}^2$ and disturbance $\sigma_{f_d}^2$ signal is 1.61 cm^2 and 0.26 cm^2 , respectively. Both signals are identical to those used in Chapters 2 and 4, see Chapter 2 for the exact values of A_t , ω_t , and ϕ_t .

5.3.3. RESULTS

Fig. 5.3 shows that both the RMP and FMP predict an improved tracking performance with increasing preview time τ_p , as the normalized error variance $\sigma_e^2/(\sigma_{f_t}^2 + \sigma_{f_d}^2)$ decreases. In SI and DI tasks the RMP predicts that optimal performance is reached with approximately 0.6 and 1.15 s of preview, respectively. Additional preview beyond this critical preview time is not necessary for optimal performance, hence invariant HC behavior is predicted (the gray areas in Fig. 5.3). Below the critical preview time (white areas), HCs can benefit from additional preview by adapting their control behavior. The FMP predicts that a near-viewpoint response can considerably reduce the critical preview time. However, actual HCs can likely initiate this open-loop feedforward response only at higher preview times, when full periods of the high-frequency target sinusoids' are explicitly visible within τ_p , as explained in Chapter 3.

Fig. 5.3 shows that various previous human-in-the-loop experiments [54, 57, 134] indeed

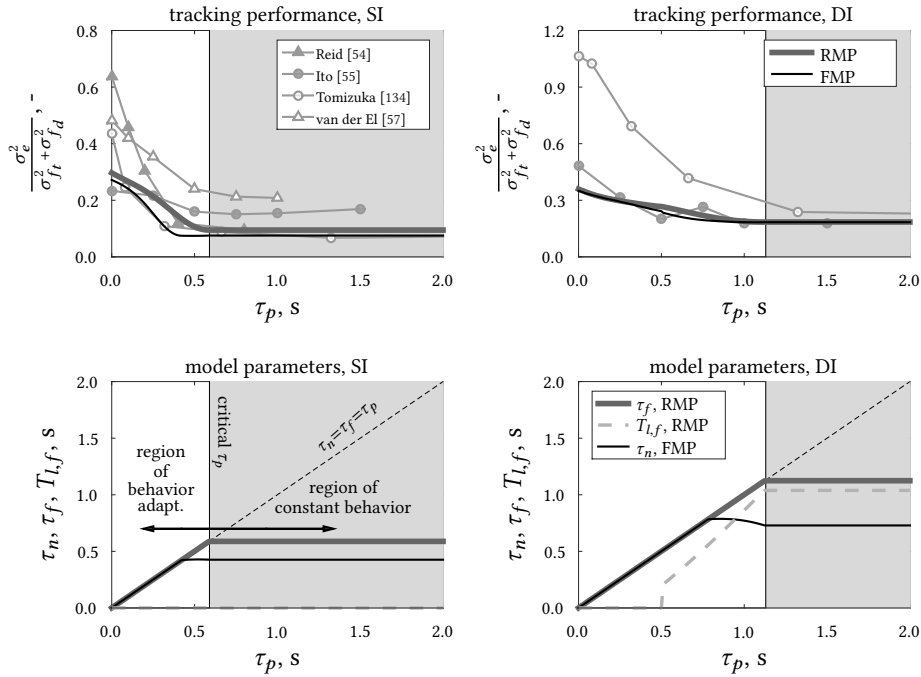


Figure 5.3: Predicted tracking performance as compared to previous experiments (top), and the optimal model parameters (bottom); the transition to the gray region indicates the predicted critical preview time.

measured optimal performance around our predicted critical preview time, both in SI and DI tasks. Only Ito & Ito [55] found a somewhat lower critical preview time, which may be due to the higher bandwidth of their target signal (2.5 rad/s, see Table 5.2). The predicted performance variations with preview time are also similar to the previous measurements [54, 55, 57, 134]. However, the predictions with the HC preview model generally yield better overall performance, as no remnant is included.

The RMP shows that a large performance benefit is possible by only adapting the far-viewpoint response. In particular, it is beneficial to keep the far viewpoint located at the endpoint of the previewed target signal (i.e., $\tau_f = \tau_p$ in Fig. 5.3) when more preview becomes available below the critical preview time. Moreover, $T_{l,f}$ increases in DI tasks, such that more of the high frequencies are cognitively filtered from the target signal with additional preview, as a longer portion of the trajectory is used for smoothing. Predicted adaptations of the other RMP parameters, K_e^* and K_f , are presented together with the experimental measurements in Section 5.5.

The FMP shows that, at short preview times, the near viewpoint's ideal position is also at the endpoint of the previewed target (i.e., $\tau_n = \tau_f = \tau_p$ in Fig. 5.3). This indicates a single-viewpoint control strategy, as the near- and far-viewpoint responses are based on the

same point on the target ahead. However, as explained before, it is unlikely that actual HCs initiate a near-viewpoint response at low preview times. At higher preview times (but still below the critical preview time), τ_n is predicted to be smaller than τ_f , which suggests that a two-viewpoint control strategy can yield improved performance. In this preview region it is more likely that actual HCs apply a near-viewpoint response, because there is additional preview beyond τ_n that can be used to plan this open-loop feedforward control. As shown before in Chapter 4, only a marginal performance improvement can be achieved relative to a far-viewpoint control strategy only. With sufficient preview, the optimal near-viewpoint position is around 0.4 and 0.7 s ahead in SI and DI tasks, respectively.

5.4. EXPERIMENTAL VALIDATION: METHOD

The predicted effects of varying preview time are verified with a human-in-the-loop experiment. Details of this experiment are presented here, together with the system identification techniques that are applied to analyze the measurements.

5.4.1. HYPOTHESES

We expect that the offline model predictions, which assume that HCs aim only for optimal performance, accurately reflect actual HC control adaptation to preview time. This leads to the following three hypotheses:

- I: Below the critical preview time, HCs adapt their control behavior (characterized by estimated preview model parameters) to increasing preview time to improve tracking performance. Most importantly, they position their far viewpoint as far ahead as possible ($\tau_f \approx \tau_p$).
- II: Beyond the critical preview time, HC behavior and tracking performance are invariant with preview time.
- III: The critical preview times in SI and DI tasks are 0.6 s and 1.15 s, respectively.

No hypothesis is formulated about the near-viewpoint response, because its possible contribution is only small (see Section 5.3); in addition, Chapter 4 has shown that it is often difficult to detect if the near-viewpoint response is active from experimental data.

5.4.2. EXPERIMENT DESIGN

Independent variables

In the experiment, eight preview times between 0 and 2 s were tested, in both SI and DI tasks (their dynamics were equal as in the offline analysis). The tested preview times included 0 and 1 s to allow for direct comparison with the data in Chapters 2 and 4, while preview times of 0.25, 0.5 and 0.75 s were added inbetween for a sufficient resolution in the predicted “region of behavior adaption” (see Fig. 5.3). In addition, preview times of 1.33, 1.66 and 2 s were included to ensure sufficient data in the “region of constant behavior”. The full factorial of the two independent variables was tested, yielding 16 conditions.

Control variables and apparatus

The experiment was conducted in the fixed-base simulator in the Human-Machine Interaction Laboratory (HMI-Lab) at TU Delft. The setup was identical to the preview tracking experiments in Chapters 2–4. Participants were seated directly in front of the screen on which the preview display of Fig. 5.1 was shown with dark green lines and indicators on a black background. Participants gave control inputs with a side-stick at their right-hand side (0.45 cm/deg input scaling), which was configured to only rotate around its roll axis. The target and disturbance forcing functions were also identical to those used in Chapters 2–4. Five different phase realizations of the target signal were used to prevent participants from recognizing parts after repeated exposure.

Participants, instructions, and procedure

Eight male volunteers participated in the experiment. They were aged between 23 and 54, with an average of 32 years, and their tracking experience ranged from novice to experienced. Participants were instructed to minimize the tracking error, and the RMS value of this error was reported to the participants after every run to motivate them to keep improving their performance.

To reduce effects of fatigue, the experiment was divided over two sessions, which took place on different days. Half of the participants performed the SI conditions first, while the other half of the participants performed the DI conditions first. The eight different preview times for each CE were performed in a single session. The conditions were presented to the participants in a random order following a Latin-square design. Before starting each experimental session, participants could familiarize themselves with the CE and all eight preview times, each being presented once in descending order from 2 to 0 s. Next, the participants performed a single condition until at least 8 runs were completed and performance was stable in the last five consecutive runs, which were then saved for later analysis. Then participants moved on to the next condition. Each run lasted 128 s, but only the last 120 s were used for analysis, the first 8 s were used as run-in time. Breaks of around 15 minutes were scheduled after completion of each two conditions, yielding a total time per session of approximately 4 hours, depending on the training required.

5.4.3. DATA ANALYSIS

The use of two multisine forcing functions, see Eq. (5.8), both with 20 input frequencies that are integer multiples of the measurement base frequency ($\omega_b=2\pi/120$ rad/s), facilitates the following frequency-domain analysis.

Tracking performance

The variance of the error σ_e^2 was used as measure of tracking performance. The variance was calculated per measurement run in the frequency domain by integrating the power spectral density function [157]. The contribution of the target and disturbance signals to the error variance were obtained by integrating only over the respective forcing function input frequencies, while the remainder was considered to be due to remnant. Hereby, the small remnant contribution at the input frequencies was neglected (see also Appendix B).

Human controller dynamics estimation

First, frequency-responses functions were estimated of the $H_{o_t}(j\omega_i)$ and $H_{o_x}(j\omega_i)$ blocks in Fig. 5.2, at the input frequencies ω_i of the target and disturbance signals. An instrumental-variable multiloop system identification technique was used, based on Fourier coefficients [86, 169]. The same method was used to derive the preview tracking model, see [86] or Chapter 2 for a complete derivation.

Second, following the same procedure as in Chapters 2–4, the model parameter vector Θ was estimated by minimizing a least-squares criterion based on the modeling error ϵ :

$$\hat{\Theta} = \underset{\Theta}{\operatorname{argmin}} \sum_{i=1}^{40} |\epsilon(j\omega_i|\Theta)|^2, \quad (5.9)$$

$$\text{where: } \epsilon(j\omega_i|\Theta) = U(j\omega_i) - \hat{U}(j\omega_i|\Theta). \quad (5.10)$$

$U(j\omega_i)$ is the measured control output, averaged over the five measurement runs in the frequency domain. The modeled control output $\hat{U}(j\omega_i|\Theta)$ is obtained from open-loop simulations of the model in Fig. 5.2, that is, $\hat{U}(j\omega_i|\Theta) = \hat{H}_{o_t}(j\omega_i|\Theta)F_t(j\omega_i) - \hat{H}_{o_x}(j\omega_i|\Theta)X(j\omega_i)$. To minimize Eq. (5.9) a Nelder-Mead simplex algorithm was used, constrained only to avoid solutions with negative parameters. The best estimate of Θ (given by the lowest criterion value) was selected from 100 randomly initialized optimization runs. In a few cases, when the best solution yielded clear outliers in the parameters, the second best solution was manually selected.

The Variance Accounted For (VAF) was used as measure for the model's quality-of-fit: $\text{VAF} = \left[1 - (\sigma_\epsilon^2/\sigma_u^2)\right] \times 100\%$ [170]. A VAF of 100% reflects that the modeling error ϵ is zero and that model perfectly describes the measurements.

Perfect target-tracking

HCs track the target perfectly when $X(j\omega)/F_t(j\omega)=1$. This condition is satisfied when the target frequency response ($H_{o_t}(j\omega)$ in Fig. 5.2) equals the “perfect” target response dynamics $H_{o_t}^P(j\omega) = H_{o_x}(j\omega) + 1/H_{ce}(j\omega)$, see Chapter 4 for a detailed derivation. $H_{o_t}^P(j\omega_i)$ was calculated based on the nonparametric frequency-response function estimate of $H_{o_x}(j\omega_i)$.

5.5. EXPERIMENTAL VALIDATION: RESULTS

5.5.1. NONPARAMETRIC RESULTS

Tracking performance

Fig. 5.4 shows that the measured tracking performance improves when more preview becomes available, both in SI and DI tasks. Performance improves mainly at the target frequencies, although the remnant frequencies also contribute slightly (especially in DI tasks); differences at the disturbance input frequencies are small, which corresponds to Chapter 4. Remarkably, in DI tasks, a minor performance degradation is observed when τ_p is increased from 1.66 to 2 s. Possibly, the additional information distracts the HC or evokes a reduced-effort control strategy. Fig. 5.4 shows that subjects attain most of the total performance improvement already with 0.5-0.75 s (SI) and 1-1.66 s (DI) of preview.

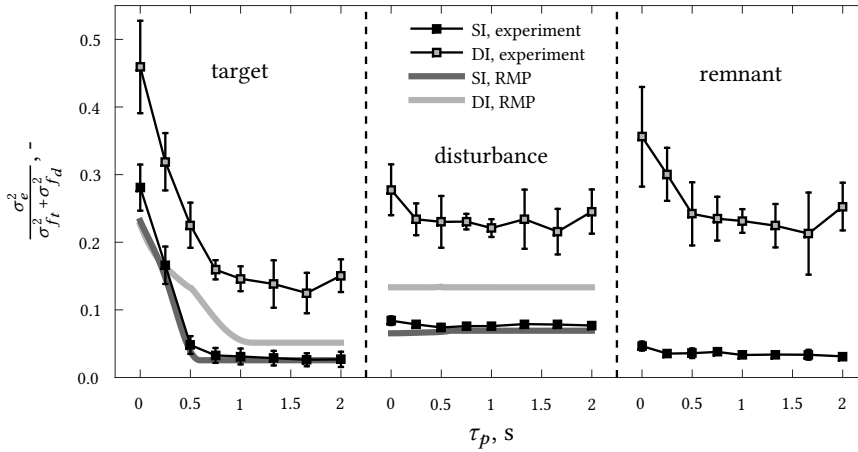


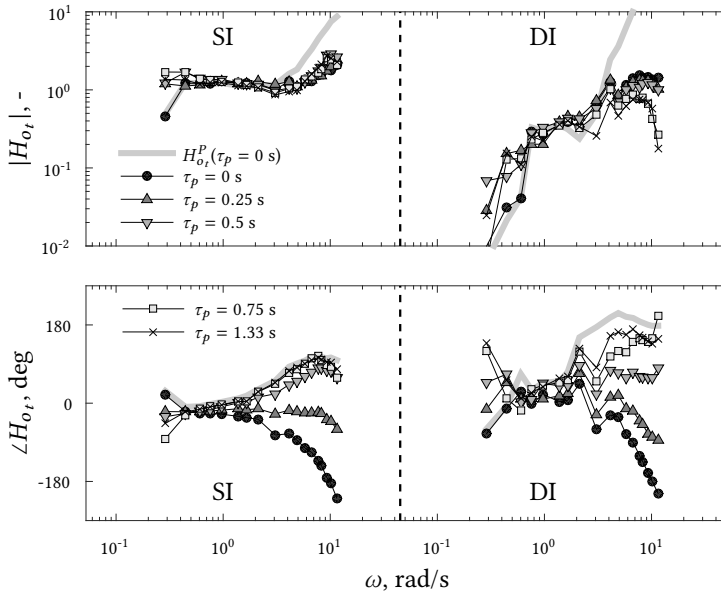
Figure 5.4: Experimental tracking error variance, separated into contributions at the target, disturbance, and remnant frequencies; average over eight subjects and 95% confidence intervals, corrected for between-subject variability. The offline model predictions (RMP) are also shown for comparison.

In SI tasks, the experimental performance at target and disturbance frequencies matches the RMP almost perfectly. In DI tasks, the RMP consistently predicts better performance than measured experimentally. Likely, the lack of damping in the CE led to increased remnant and a less linear response (see also Chapters 2 and 4), resulting in suboptimal performance. Nonetheless, the exponential trend of improving performance with increasing preview time is almost identical in the RMP and the experiment, and the predicted critical preview times (0.6 s for SI and 1.15 s for DI) are in the same range where the experimental performance stabilizes.

Target response dynamics

Fig. 5.5 shows estimates of the HCs' target frequency-response function $H_{o_t}(j\omega)$. In both SI and DI tasks, longer preview times yield markedly more phase lead in $H_{o_t}(j\omega)$, which thereby better matches the response required for perfect target-tracking $H_{o_t}^P(j\omega)$ (solid gray line). When the preview time exceeds 0.5 and 0.75 s in SI and DI tasks, respectively, $H_{o_t}(j\omega)$ approximates $H_{o_t}^P(j\omega)$ up to frequencies around 4 rad/s, which is well above the target signal bandwidth (1.5 rad/s). As such, all low-frequency, high-amplitude sinusoids are tracked well and the target-tracking performance improvement saturates with higher preview times, see Fig. 5.4. In DI tasks, more preview additionally evokes a decreased magnitude of $H_{o_t}(j\omega)$ at higher frequencies, corresponding to the predicted increase of the low-pass filter time-constant (see Fig. 5.3).

Whereas the frequency-response function estimates are a smooth function of frequency in SI tasks, the estimates in DI tasks are more variable. This is visible from the standard errors shown in Fig. 5.6, and is a consequence of both the larger remnant (see Fig. 5.4), and a general ignorance to track the higher frequencies of the target signal in DI tasks.



5

Figure 5.5: The experimental target response dynamics (average of all subjects). $H_{ot}^P(j\omega)$ is only shown for $\tau_p=0$ s, as it is identical at all preview times due to invariance of $H_{ox}(j\omega)$ (not shown).

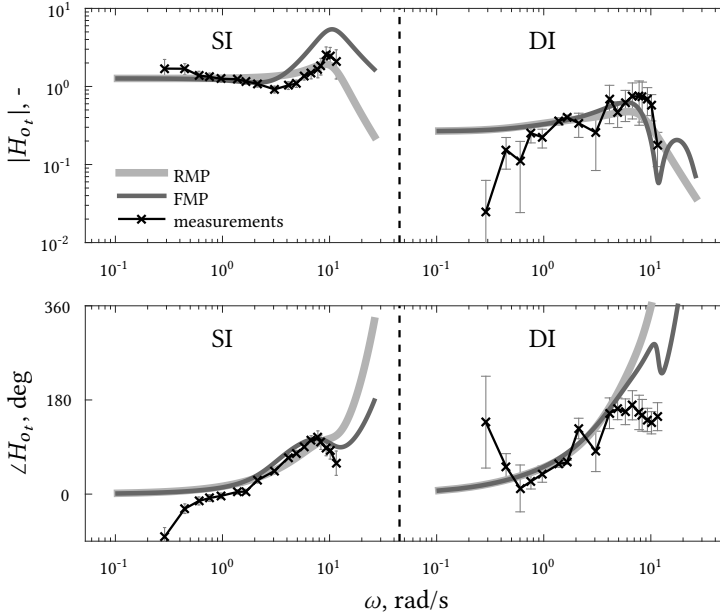


Figure 5.6: Comparison of experimental and predicted target response dynamics for $\tau_p=0.75$ s (SI) and $\tau_p=1.33$ s (DI). Measurements are the average over the eight subjects and the standard error.

Fig. 5.6 also shows the dynamics predicted by the offline model optimization. Overall, the experiment data matches the predictions reasonably well, although neither RMP nor FMP match the data perfectly. In SI tasks, the measured magnitude peak at the higher frequencies is higher than the RMP, but below the FMP, which suggests that at least several subjects initiated a near-viewpoint response. In DI tasks, the measurements match best with the FMP, both in phase and magnitude, but the difference between RMP and FMP is small. Fig. 5.6 also reveals some low-frequency lag in the measurements for SI tasks, which are not captured by the predictions; such lag been observed before in Chapter 2 (and will be investigated in more detail in Chapter 7), but is not explicitly included in the model here for simplicity.

5.5.2. MODELING RESULTS

Variance accounted for

Both RM and FM fits yield average VAFs well above 85% in SI tasks, and well above 75% in DI tasks (see Fig. 5.7). The VAF in DI tasks is lower than in SI tasks because of a larger remnant contribution (see Fig. 5.4), which is not captured by the linear model. The FM provides a consistently higher VAF than the RM, but at the cost of two additional model parameters (K_n and τ_n). With increasing τ_p the improvement in VAF from RM to FM increases, indicating a stronger near-viewpoint response. With short preview times, below 0.5 s for SI dynamics and 0.75 s for DI dynamics, the RM and FM describe the data equally well. Therefore, we will not further consider the FM fit results (nor the FMP) at these lower preview times in the remainder of this chapter.

RM fits: Internal-error response and physical limitations

Fig. 5.8 shows the model's (RM) estimated feedback parameters. In SI tasks, the experimental error response gain K_{e^*} is approximately invariant, while a 25% decrease was predicted below the critical preview time. The response time delay τ_v decreases from around 0.3 to 0.2 s. In DI tasks, K_{e^*} increases from 0.15 to 0.28, and while the response delay decreases only slightly, substantially less lead is generated (T_{L,e^*} drops from 2.7 to 1.5 s). These trends suggest that longer preview times evoke a more aggressive (higher gain)

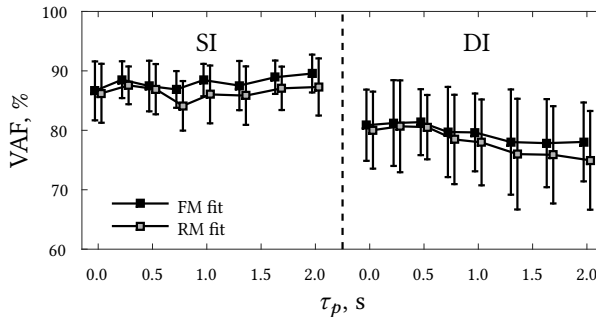


Figure 5.7: Model VAFs, average over eight subjects and standard deviations.

internal-error response at low frequencies, which corresponds to Fig. 5.5. The neuromuscular break frequency ω_{nms} is in general invariant with preview time, but the damping ratio ζ_{nms} decreases approximately 20-30%.

RM fits: Far-viewpoint response

In Fig. 5.9, the black markers show the estimated far-viewpoint parameters and the gray solid line represents the RMP; these match almost perfectly, especially in SI tasks. As predicted, below the critical preview time, subjects position their far viewpoint as far ahead as possible ($\tau_f \approx \tau_p$), see Fig. 5.9a. Although we estimated the model parameters without applying constraints, τ_f is always estimated lower than the preview time (gray shaded area in Fig. 5.9a), or only slightly higher. As such, τ_f indeed appears to accurately reflect the farthest point ahead along the previewed trajectory that subjects use for control.

When the preview time is above 0.75 s (SI) and 1 s (DI) the experimental τ_f data stabilize. Some subjects (presented with markers in Fig. 5.9) select a far viewpoint near τ_p even beyond the critical preview time, which was also reported in [57] for a SI task. However, with the highest preview time of 2 s all but one subject (in the DI task) set their τ_f close to the predicted values. Slightly more preview than the critical preview time thus induces HCs to position their far viewpoint at the visually salient endpoint of the winding preview line, opposed to the “optimal” position. This behavior appears to depend on the display scaling, because subjects focused even more on the trajectory’s endpoint while using the smaller preview displays in the experiments in Chapters 2 and 4.

In DI tasks, the estimated far-viewpoint gain K_f increases with preview time, as predicted (Fig. 5.9b). However, most subjects adopt a K_f well below the unity value of the RMP beyond the critical preview time, which explains why the attained tracking performance is worse than predicted (see Fig. 5.4). In SI tasks, subjects adopt a K_f close to unity, which corresponds to the RMP above the critical preview time. With short preview times the RMP predicted a lower K_f ; the difference is approximately 25% for $\tau_p=0$ s, which is equal but opposite to the error in the K_{e^*} prediction, such that the total target response gain $K_f K_{e^*}$ was in fact predicted accurately.

The far-viewpoint lag time-constant $T_{l,f}$ (Fig. 5.9c) increases with preview time, especially in DI tasks, which indicates that subjects respond less to the target’s higher frequencies when τ_p increases. Equivalently, a higher $T_{l,f}$ suggests that subjects use a longer region of the target signal for smoothing, which is indeed facilitated by the visible preview. Fig. 5.9c shows that, as expected, $T_{l,f}$ is typically smaller than τ_p . In SI tasks, the measured $T_{l,f}$ values around 0.1 s imply a break frequency of approximately 10 rad/s, which is near the highest forcing function excitation frequency; the effect of the estimated filter on the model output is thus small. This corresponds roughly with the RMP, which predicts that $T_{l,f} \approx 0$ s. In DI tasks, a higher $T_{l,f}$ was expected from the RMP. Likely, for the less aggressive target response gain K_f adopted by the subjects relative to our model predictions, it is rewarding to attenuate less of the high frequencies with the low-pass filter.

FM fits

Fig. 5.9 also shows the far-viewpoint parameters estimated with the FM, while Fig. 5.10 shows the two additional near-viewpoint parameters. Estimated values for τ_f and K_f differ only marginally between RM and FM fits and the trend with changes in preview time is

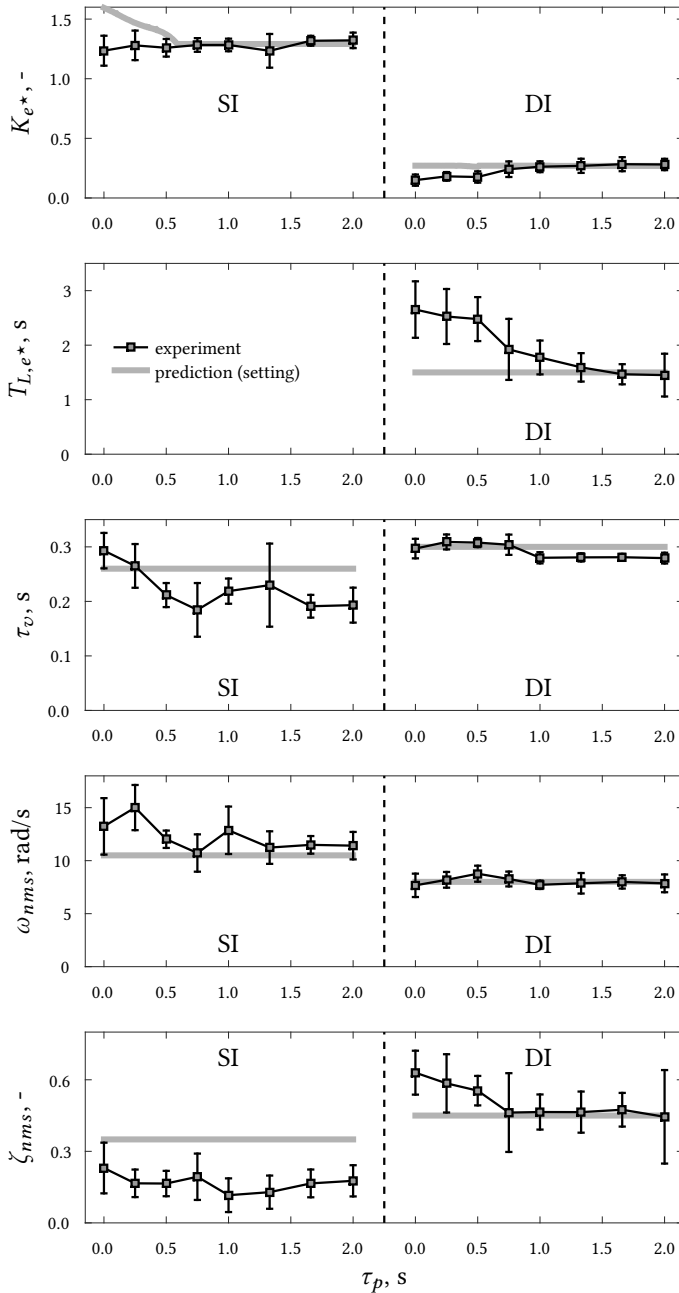


Figure 5.8: Internal-error response and physical-limitation parameters obtained from RM fits (FM fits yield similar results), average over eight subjects and 95% confidence intervals, corrected for between-subject variability. The offline predictions are also shown for comparison.

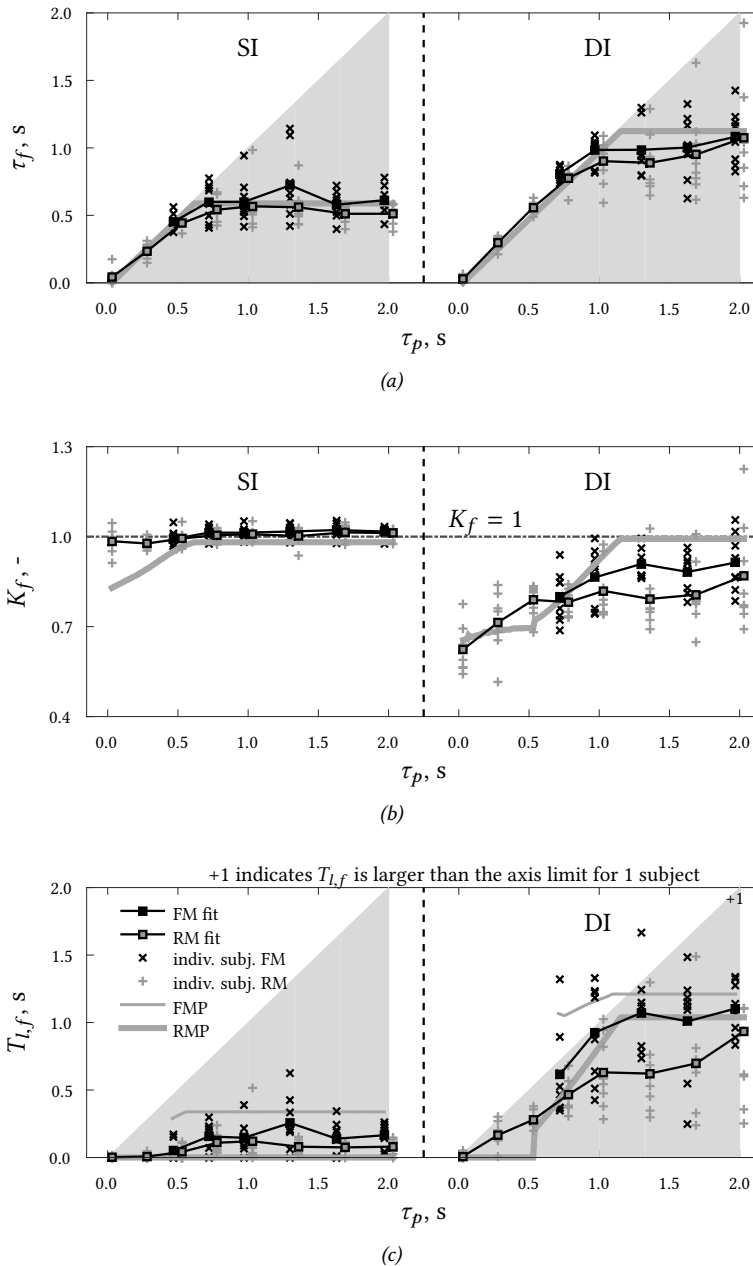


Figure 5.9: Estimated far-viewpoint parameters (means and individual subjects) compared to the predictions. Different results are slightly shifted horizontally to prevent overlapping. FM fits (and predictions) are omitted for low preview times because their VAFs are similar to the RM fits.

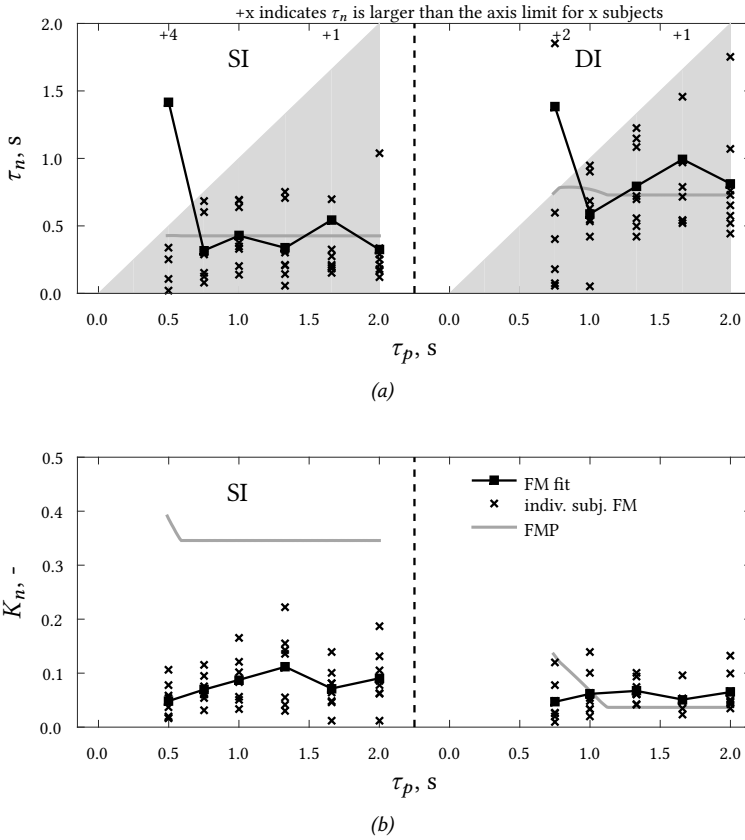


Figure 5.10: Estimated near-viewpoint parameters (means and individual subjects) compared to the predictions. Results for low preview times are omitted, because the VAFs of the RM and FM fits are very similar here.

identical. $T_{l,f}$ is in general higher in the FM fit, compared to the RM fit, because the HC's high-frequency target response can be captured by the model's near-viewpoint response.

The near-viewpoint position (τ_n , Fig. 5.10a) is occasionally estimated to be far beyond the shown preview (i.e., $\tau_n \gg \tau_p$). Such physically impossible values of τ_n occur when no near-viewpoint response is in fact present, as this effectively makes τ_n a free, and ineffectual, parameter. Disregarding the estimates well beyond the preview time limit, τ_n is approximately invariant with preview time, and stabilizes on average around the predicted values of 0.4 and 0.7 s in SI and DI tasks, respectively. Substantial between-subject differences are, however, visible: while most subjects select a near viewpoint that is clearly closer ahead on the previewed target than the far viewpoint, several other subjects select their two viewpoints very close together (i.e., $\tau_n \approx \tau_f$), which suggests that these subjects in fact apply a single-viewpoint preview control strategy.

The experimental near-viewpoint response gains K_n (Fig. 5.10b) are also approximately

constant above the critical preview time. Clearly, the FMP predicted a much higher K_n compared to the experimental measurements, especially in SI tasks and at lower preview times. This corresponds to results in Chapter 4, where it was also shown that a higher value of K_n yields improved performance, but also increased control activity. It thus appears that our subjects also aimed for limited control effort, and not just optimal performance, as was assumed in the offline predictions.

5.6. DISCUSSION

The goal of this chapter was to quantify and model human control adaptation to variations in available preview time, between 0 and 2 s. To this end, the preview tracking model from Chapter 2 was used both to make offline predictions and to analyze measurements from a human-in-the-loop experiment.

Corresponding to previous results [54–59, 61, 62, 134, 136], evidence supporting our first hypothesis was found that, below the critical preview time, HCs *adapt* their control behavior with increasing preview to improve tracking performance. HCs reposition their far viewpoint to the endpoint of the previewed target (i.e., $\tau_f \approx \tau_p$). Moreover, especially in DI tasks, HCs respond more aggressively to the target (higher K_f) with more preview, while using the longer preview span to better smooth the target signal (higher $T_{l,f}$), effectively ignoring more of the high frequencies.

Just below the critical preview time, more compelling evidence for the presence of a near-viewpoint response occurs. The FM, which includes the near-viewpoint response, captures the measured HC behavior more accurately than the “far-viewpoint only” RM, and the near viewpoint’s position is estimated within the range of visual preview for more subjects (i.e., $\tau_n \leq \tau_p$). HCs initiate a near-viewpoint response only when the preview time exceeds approximately 0.5 s (SI) and 0.75 s (DI), with average τ_n values around 0.2 s (SI) and 0.6 s (DI). The preview time needed for an effective near-viewpoint response approximately equals a full period (0.54 s) of the target signal’s highest frequency component ($\omega_t = 11.57$ rad/s). This suggests that the near-viewpoint response is in fact not a response to a single point ahead, but to a full sinusoid that is recognized from the target signal. When initiated, the near-viewpoint dynamics are mostly invariant with preview time.

Our second hypothesis was that HC behavior and tracking performance are *invariant* beyond the critical preview time. This was confirmed, but with two caveats. First, several subjects need markedly more preview than the critical preview time to move their far viewpoint away from the endpoint. Second, in DI tasks, tracking performance degraded slightly when the preview time increased from 1.66 s to 2 s. However, no consistent, explanatory adaptation of model parameters was found, so more measurements are required to establish whether the additional preview distracts HCs, evokes a subtle adaptation to a lower effort control strategy, or is an artifact of our modest sample size.

The *critical preview time*, the transition from adaptive to invariant HC behavior (and performance), was measured to be 0.5–0.75 s (SI) and 1–1.66 s (DI). This is in the same range as the 0.6 s (SI) and 1.15 s (DI) predicted offline, confirming our third hypothesis. Note that these values are *not universal*: the perfect target-tracking dynamics $H_{o_t}^P(j\omega)$ reveal

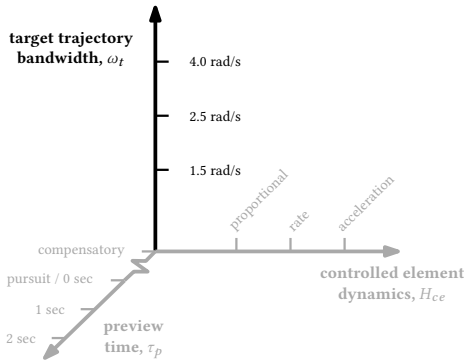
that the critical preview time depends not only on the *CE dynamics*, but also on the *HC's feedback response*. For example, a high (feedback) gain K_{e^*} leads to a lower critical preview time because the CE output intercepts the target signal faster. This lack of critical preview time invariance corresponds to measurements in previous preview tracking experiments [54–57, 134], and driving tasks [58, 59].

Compared to similar preview tracking experiments ([57] and Chapter 4), our subjects on average displayed more skilled, proficient manual control behavior, including better tracking performance, a lower response delay τ_v and a higher control gain K_{e^*} . Possible causes include that our subjects performed more tracking runs (eight conditions per CE) and that the experimental preview display was slightly larger compared to [57] and Chapter 4, which are both known to allow for superior performance. While the presented performance and critical preview times may not be representative for a general population (our subjects were eight relatively young males) and for other tasks, the observed low-level control adaptations to preview time *are generalizable*, and *can be predicted offline* for other populations and tasks using the preview model from Fig. 5.1.

5.7. CONCLUSION

This chapter investigated the effect of preview time in manual tracking tasks, using a combination of offline model predictions and human-in-the-loop measurements. Increasing the preview time results in better tracking performance, and larger “look-ahead” time model parameters, indicating that subjects respond to a part of the previewed trajectory farther ahead. Beyond a certain “critical” preview time, both tracking performance and control behavior stabilize, and effects of additional preview are small. The critical preview time is not invariant; in tasks with single- and double-integrator controlled element dynamics humans use around 0.6 and 1.15 s of preview, respectively. Measured control adaptations were predicted accurately with the quasi-linear manual control modeling framework. This approach promises to provide insight into human performance limitations due to restricted preview, including the critical preview time, also in other control tasks.

6

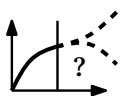


EFFECTS OF

TARGET TRAJECTORY BANDWIDTH

In Part I of this thesis, a novel cybernetic model was proposed for human manual control behavior in pursuit and preview tracking tasks. To allow for rationalizing and predicting human preview control behavior (including their interaction with technology) in a wide range of control tasks, a quantitative understanding of human adaptation to crucial task variables is also essential. Chapters 4 and 5 already showed how humans adapt their control behavior to the controlled element dynamics and the preview time, respectively. This chapter quantifies human adaptation to a third crucial task variable: the target trajectory bandwidth (which is known to provoke marked adaptations in compensatory tracking tasks). Similar to Chapters 4 and 5, human adaptation to the target trajectory bandwidth is first predicted offline using the human controller preview model that was proposed in Part I. The predicted adaptations are verified with data from a human-in-the-loop experiment, in which tracking tasks are performed with target trajectory bandwidths of 1.5, 2.5, and 4 rad/s.

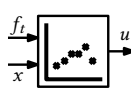
Steps of the cybernetic approach involved:



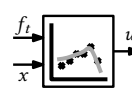
offline model predictions



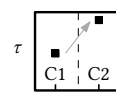
acquisition of control data



system identification



parameter estimation



analysis of adaptation

The contents of this chapter are currently under review to be published as:

Title Effects of Target Trajectory Bandwidth on Manual Control Behavior in Pursuit and Preview Tracking

Journal IEEE Transactions on Human-Machine Systems

Authors K. van der El, D.M. Pool, M.M. van Paassen, and M. Mulder

6.1. INTRODUCTION

HUMANS exhibit highly adaptive behavior when manually controlling vehicles and devices [44]. Four task variables profoundly affect the Human Controller's (HC's) behavior: the Controlled Element (CE) dynamics, display configuration, control manipulator, and forcing functions [6, 75]. HC adaptation to these task variables is well-understood in compensatory tracking tasks, for which the seminal *crossover model*, together with its *verbal adjustment rules*, quantifies the HC's compensatory control behavior and adaptation [6].

Most real-life manual control tasks, however, provide the HC with *pursuit*-type information, that is, feedback of a certain CE output variable together with the corresponding target value, possibly with additional preview of the future target trajectory. The available target information allows HCs to apply feedforward control. Feedforward does not only provide superior tracking performance relative to compensatory tasks, but also facilitates a myriad of new strategies to adapt to the task variables [42, 126, 128]. To systematically predict and analyze HC behavior (and adaptation) in these much more relevant pursuit and preview tracking tasks, an extension to the crossover model was proposed in Chapter 2. This new model has been shown to be capable of accurately predicting HC adaptation to the CE dynamics in Chapter 4 and to the preview time in Chapter 5.

We currently still lack an equal understanding of HC adaptation to key characteristics of the target trajectory, such as predictability, bandwidth, and frequency spectrum [126, 142, 171, 172]. The only characteristic to which HC adaptation has been quantified, and only in compensatory tracking tasks, is the target trajectory *bandwidth*. Here, HCs track higher-bandwidth target trajectories by increasing their control gain, so the open-loop crossover frequency remains well above the input bandwidth [80]. Ultimately, when a further increase in gain would lead to a loss of stability, HCs instead severely reduce their control gain, which is known as *crossover regression* [80, 164, 173, 174]. McRuer's crossover model has been instrumental in explaining and predicting these behavior adaptations [80, 164, 173, 174]. Due to the lack of a good model, subsequent analyses failed to provide an equally clear explanation for HC adaptation to target bandwidth in pursuit [42, 163] and preview [49, 129] tracking tasks. The goal of this chapter is to explain HC adaptation to target trajectory bandwidth in these latter tasks, through a similar model-based analysis that proved successful in compensatory tracking.

Beneficial adaptation strategies are first explored offline, using the cybernetic HC model for pursuit and preview tracking tasks from Chapter 2. Predictions are made for seven target signal bandwidths (0.4-7.5 rad/s), two CE dynamics (single- and double-integrator), and five display configurations (compensatory, pursuit, and limited (2) and full preview). These predictions are then verified with data from a human-in-the-loop experiment, in which a double integrator tracking task was performed with target signals with bandwidths of 1.5, 2.5, and 4 rad/s (matching the experiment by McRuer *et al.* [80]). The experiment was performed both with a pursuit and a preview display, as well as with a compensatory display to tie in with [80, 164, 173, 174]. The HC model for preview tracking is fit to the data to quantify exactly how HCs adapt to target bandwidth, providing insight beyond the overt performance effects that are often provided in the literature [42, 49, 129, 163].

This chapter is structured as follows. Sections 6.2 and 6.3 first review how HCs adapt their behavior to the target trajectory bandwidth in compensatory tracking tasks, and extend this to pursuit and preview tracking in an offline analysis with the model from Chapter 2. Next, Section 6.4 explains the performed experiment, of which the results are presented, and compared to the offline predictions, in Section 6.5. Section 6.6 then discusses the implications of these results, and conclusions are drawn in Section 6.7.

6.2. BACKGROUND

6.2.1. THE CONTROL TASK

In tracking tasks, HCs are to minimize the tracking error $e(t) = f_t(t) - x(t)$ between a target trajectory $f_t(t)$ and the corresponding CE output variable $x(t)$. In compensatory tasks only this tracking error is available for the HC to respond to, see Fig. 6.1 for an example compensatory display. In addition to the tracking error, pursuit tasks explicitly show both the target and the CE output, for example through two separate markers on a display (see Fig. 6.1). The future target trajectory ahead may also be visible, up to the preview time τ_p ; in pursuit tasks $\tau_p = 0$ s by definition, in preview tasks $\tau_p > 0$ s. Additionally, disturbances $f_d(t)$ may perturb the CE, yielding a combined target-tracking and disturbance-rejection control task.

6

6.2.2. TARGET TRAJECTORY BANDWIDTH

To characterize the target signal that an HC is to follow, researchers typically report the signal's power and bandwidth. The power (or variance) is given by $\sigma_{f_t}^2 = \frac{1}{\pi} \int_0^\infty S_{f_t f_t}(\omega) d\omega$, with $S_{f_t f_t}(\omega)$ the target signal's power-spectral density function [175]. The bandwidth ω_t is defined as the highest frequency at which the target signal has significant power. Fig. 6.2 shows the spectra and time traces of the three target signals tested by McRuer *et al.* in compensatory tasks [6, 80], which have bandwidths of 1.5, 2.5 and 4 rad/s and equal power. At frequencies beyond the bandwidth, indicated with

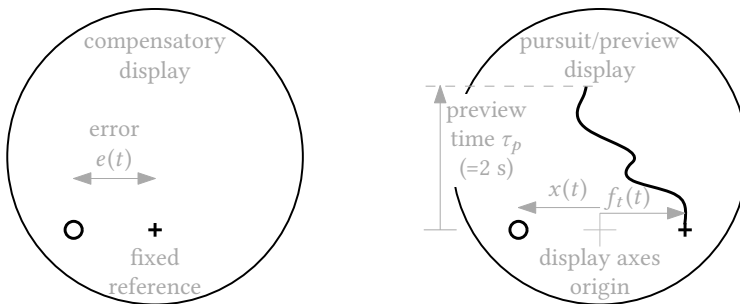


Figure 6.1: Displays used in the experiment, gray text and markers were not visible to the subjects (note that $\tau_p = 0$ s in pursuit tasks).

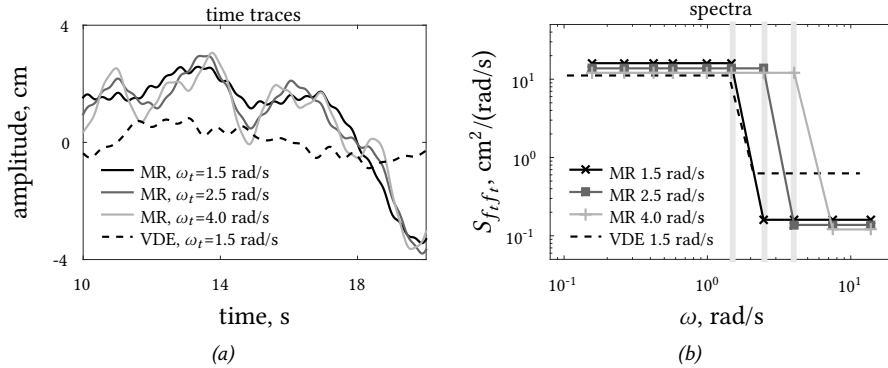


Figure 6.2: Target signal time-traces (a) and spectra (b), used by McRuer *et al.* [6] (MR) and Van der El *et al.* (VDE) in Chapters 4 and 5, $\sigma_{f_i} = 1.27 \text{ cm}$ ($= 0.5 \text{ inch}$).

vertical gray lines in Fig. 6.2b, the amplitudes are strongly attenuated, but still nonzero to allow for measuring the HC’s behavior over the full frequency range of interest [176].

The power and bandwidth do not fully characterize a target signal [175]. Low-pass filtered white noise and sum-of-sinusoid signals with identical bandwidths have both been used in human-in-the-loop experiments [175]. The advantage of sum-of-sinusoids is that they can be used as instrumental variables for estimating the HC’s control dynamics with frequency-domain system identification techniques [80, 86, 156, 175]. However, care must be taken to include enough sine-components for the signal to be sufficiently random-appearing, to avoid HCs from exploiting predictable patterns in the target signal through “precognitive” open-loop control [175]. The target signals used by McRuer *et al.* (see Fig. 6.2) therefore included ten sinusoids, each characterized by frequency ω_i , amplitude A_i , and phase ϕ_i :

$$f_t(t) = \sum_{i=1}^{10} A_i \sin(\omega_i t + \phi_i). \quad (6.1)$$

Signals with equal power and frequencies but different bandwidths (e.g., the three signals tested by McRuer) yield different amplitudes for the individual sinusoids (see Fig. 6.2b), such that measuring HC adaptation to one characteristic in isolation is impossible.

Apparently small changes in signal power, bandwidth, number of sinusoids, frequencies, amplitudes, and phases can severely affect the signal’s time-domain appearance, and hence the HC’s behavior. For example, the target signal that was used in the pursuit and preview tracking experiments in Chapters 4 and 5 is also shown in Fig. 6.2, and this signal’s spectrum matches the 1.5 rad/s bandwidth signal by McRuer *et al.* fairly well. Nonetheless, opposed to McRuer’s 10 sinusoids, this signal is composed of 20 sinusoids, and the high-frequency amplitudes are larger (to avoid HCs from ignoring these sine components, which are explicitly visible in preview tasks). Fig. 6.2a shows that the time-domain realization of these two signals appear very different to the HC, despite their equal total power and bandwidth.

It is safe to say that we still poorly understand exactly what characteristics of the target signal affect HC behavior [175]. To tie in with previous work on compensatory tracking [6, 164], this chapter also focuses on the effects of *bandwidth* in pursuit and preview tasks, and on the same range of input bandwidths that are representative for many realistic vehicle control tasks (1.5-4 rad/s).

6.2.3. HUMAN CONTROLLER MODEL

Fig. 6.3 shows the quasi-linear HC model for manual preview tracking, adapted from Chapter 2. The control output $u(t)$ provided by the HC in preview tasks is based on a point τ_f s ahead on the target trajectory, which is weighted (through K_f) and smoothed (through $T_{l,f}$) before being compared to the CE output to yield an “internal” error $e^*(t)$. In pursuit tasks, the lack of preview ($\tau_p = 0$ s) inhibits HCs from using the trajectory ahead for control, such that $\tau_f = T_{l,f} = 0$ s. HCs can still respond to both the target and the CE output, which relative weighting manifests in the parameter K_f . The model can also capture HC behavior in compensatory tracking tasks; by setting $K_f = 1$ and $\tau_f = T_{l,f} = 0$ s it follows that $e^*(t) = e(t)$ and the input to the HC is the true error. Regardless of the display configuration, HCs select an error (e or e^*) to use for compensatory-like control, with response dynamics $H_o^{comp}(j\omega) = H_{o_{e^*}}(j\omega)H_{nms}(j\omega)e^{-\tau_v j\omega}$ that include the equalization $H_{o_{e^*}}(j\omega)$, neuromuscular activation $H_{nms}(j\omega)$, and a time delay τ_v [6].

The model can be rewritten to obtain the total response to the target $H_{o_t}(j\omega)$ and the CE

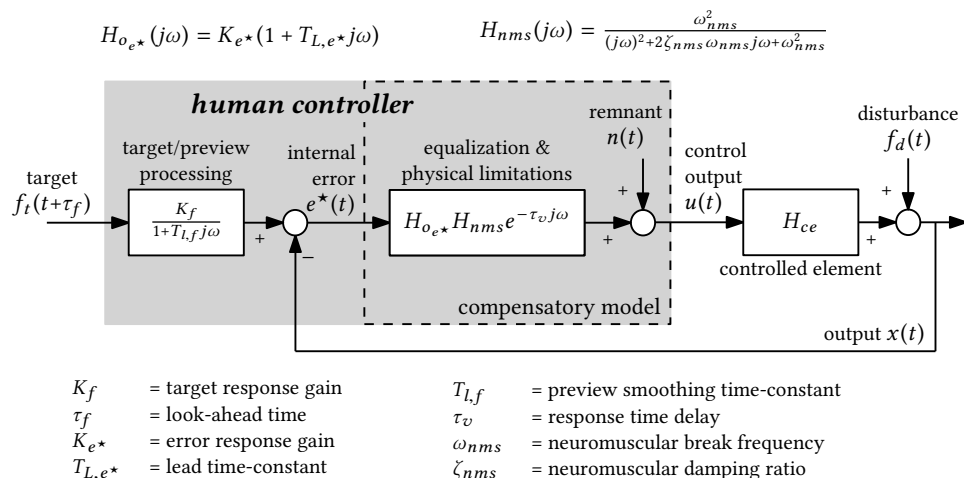


Figure 6.3: The human controller model for compensatory, pursuit, and preview tracking tasks from Chapter 2. The “near-viewpoint” response is omitted for simplicity, because it only captures the relatively weak, high-frequency target-tracking behavior.

output $H_{o_x}(j\omega)$, as follows (see Chapter 2 for details):

$$H_{o_x}(j\omega) = H_o^{comp}(j\omega), \quad (6.2)$$

$$H_{o_t}(j\omega) = K_f \frac{1}{1 + T_{l,f}j\omega} e^{\tau_f j\omega} H_o^{comp}(j\omega). \quad (6.3)$$

In accordance with the derivation in Chapter 4, the target response $H_{o_t}(j\omega)$ that yields “perfect”, zero-error target-tracking is then given by $H_{ce}^{-1}(j\omega) + H_{o_x}(j\omega)$.

6.3. OFFLINE MODEL PREDICTIONS

6.3.1. PERFORMANCE MEASURES AS MOTIVATION FOR ADAPTATION

HC control behavior, and adaptation thereof, is typically motivated by maximizing performance, while accounting for sufficient stability margins and avoiding excessive control effort [6]. The variance of the tracking error $\sigma_e^2 = \frac{1}{\pi} \int_0^{\infty} S_{ee}(j\omega) d\omega$, is a measure for performance, with $S_{ee}(j\omega)$ the power-spectral density of the error signal:

$$S_{ee}(j\omega) = |H_{f_t,e}(j\omega)|^2 S_{f_t,f_t}(j\omega) + |H_{f_d,e}(j\omega)|^2 S_{f_d,f_d}(j\omega) + |H_{n,e}(j\omega)|^2 S_{nn}(j\omega). \quad (6.4)$$

The input-to-error transfer functions $H_{f_t,e}(j\omega)$, $H_{f_d,e}(j\omega)$, and $H_{n,e}(j\omega)$ characterize the HC’s error-suppression proficiency of errors induced by the target $S_{f_t,f_t}(j\omega)$, disturbance $S_{f_d,f_d}(j\omega)$, and remnant $S_{nn}(j\omega)$, respectively. Using the HC model in Fig. 6.3, the input-to-error transfer functions can be written as follows (see Chapter 4 for details):

$$H_{f_t,e}(j\omega) = \frac{1 + H_{ce}(j\omega)(H_{o_x}(j\omega) - H_{o_t}(j\omega))}{1 + H_{ce}(j\omega)H_{o_x}(j\omega)}, \quad (6.5)$$

$$H_{f_d,e}(j\omega) = \frac{-1}{1 + H_{ce}(j\omega)H_{o_x}(j\omega)}, \quad (6.6)$$

$$H_{n,e}(j\omega) = \frac{-H_{ce}(j\omega)}{1 + H_{ce}(j\omega)H_{o_x}(j\omega)}. \quad (6.7)$$

For pursuit and preview tracking tasks, in which the target signal is explicitly visible, mainly the target-to-error dynamics $H_{f_t,e}(j\omega)$ are of interests.

Other common measures for performance (and stability) are the open-loop crossover frequency ω_c and phase margin ϕ_m [6]. The target and disturbance open-loop transfer functions are $H_{o_l,t}(j\omega) = H_{f_t,e}^{-1}(j\omega) - 1$ and $H_{o_l,d}(j\omega) = H_{f_d,e}^{-1}(j\omega) - 1$, respectively [156]. For manual tracking, errors due to each respective input signal are generally suppressed at all frequencies that are well below the crossover frequency [6, 164].

6.3.2. HUMAN ADAPTATION IN COMPENSATORY TASKS

The magnitude of the target-to-error transfer function $|H_{f_t,e}(j\omega)|$ is plotted for compensatory tasks in Fig. 6.4a. At low frequencies, $|H_{f_t,e}(j\omega)| \ll 1$ for the baseline HC dynamics

(black line), so the tracking errors are small and the target signal is tracked well. However, due to the HC's response delay τ_v , $|H_{f_t,e}(j\omega)| > 1$ is seen between 1.5 and 6 rad/s, yielding errors that exceed the magnitude of the target signal and poor tracking performance.

From Eq. (6.4) it is clear that not only $|H_{f_t,e}(j\omega)|$, but also the target signal input spectrum $S_{f_t}(j\omega)$ contributes directly to the tracking error. A target signal with $\omega_t < 1.5$ rad/s bandwidth (left gray vertical line in Fig. 6.4a) is tracked well with the baseline HC behavior, as the tracking errors are suppressed at all these frequencies. However, higher frequencies in the target signal (e.g., 4 rad/s, see Fig. 6.4a) excite the error amplification peak of $H_{f_t,e}(j\omega)$ and thus yield a strong decrease in tracking performance. By adapting their control behavior HCs can change the shape of $H_{f_t,e}(j\omega)$ to avoid excessive error-amplification at frequencies where the target signal's power is concentrated. To do so, HCs can typically adapt their response gain K_{e^*} and lead equalization T_{L,e^*} , their response time delay τ_v , or the properties of their neuromuscular system (ω_{nms} or ζ_{nms}). The effect of lowering the response gain K_{e^*} is shown in Fig. 6.4a: the error amplification peak reduces, but also becomes wider.

Fig. 6.4b shows how each frequency contributes to the error. At 1.5 rad/s target bandwidth, the baseline behavior still gives the best performance (the thick black line is lowest at 1.5 rad/s). However, at 2.5 rad/s, baseline control behavior results in a sharp increase in tracking error, and an increased gain strategy provides the best performance (e.g., $K_{e^*}=0.35$ in Fig. 6.4b). At 4 rad/s also the high-gain strategy leads to substantial tracking errors, and a severe reduction of the control gain (e.g., to $K_{e^*}=0.1$) is beneficial. Such a reduced control gain typically leads to regression of the open-loop crossover frequency to a value below the target signal bandwidth [6, 164]. The actual input bandwidth at which crossover regression occurs varies somewhat between performed experiments, but is roughly between 3 and 4 rad/s [6, 80, 164, 173], which agrees well with Fig. 6.4b.

6.3.3. HUMAN ADAPTATION IN PURSUIT AND PREVIEW TASKS

In pursuit tasks, HCs can additionally adapt their target response gain K_f to improve error suppression. Similar as reducing K_{e^*} , a lower K_f leads to a reduced error amplification peak, at the cost of inferior low-frequency tracking performance, see Fig. 6.4c. When K_f is zero, the HC completely ignores the target signal's movements; nothing of the target signal is fed into the compensatory loop, and the error is identical to the target ($|H_{f_t,e}(j\omega)| = 1$). Fig. 6.4d shows that low-gain pursuit control behavior (e.g., $K_f = 0.4$) yields relatively low errors for high-bandwidth target signals (e.g., 4 rad/s), much lower in fact than for any of the crossover-regressed compensatory-only control strategies in Fig. 6.4b. An additional benefit of reducing K_f is that the error response $H_o^{comp}(j\omega)$ can remain intact to adequately suppress disturbances and the remnant.

In preview tasks, HCs can respond to the trajectory ahead, which allows for adapting the model's τ_f and $T_{L,f}$ parameters. Fig. 6.4e shows that nonzero values of τ_f and $T_{L,f}$ help to suppress tracking errors at all frequencies below approximately 6 rad/s. The error amplification peak disappears completely when τ_f and $T_{L,f}$ are sufficiently high (≈ 1 s), which suggests that a reduced-gain control strategy is not required to attain adequate performance in tracking high-bandwidth target signals.

baseline (BL) model parameters (taken from the experiment in Chapter 5)

H_{ce}	$K_{e^*}, -$	T_{L,e^*}, s	τ_v, s	$\omega_{nms}, \text{rad/s}$	$\zeta_{nms}, -$	$K_f, -$	$T_{l,f}, s$	τ_f, s
$\frac{5}{(j\omega)^2}$	0.3	1.5	0.28	8.5	0.45	1	0	0

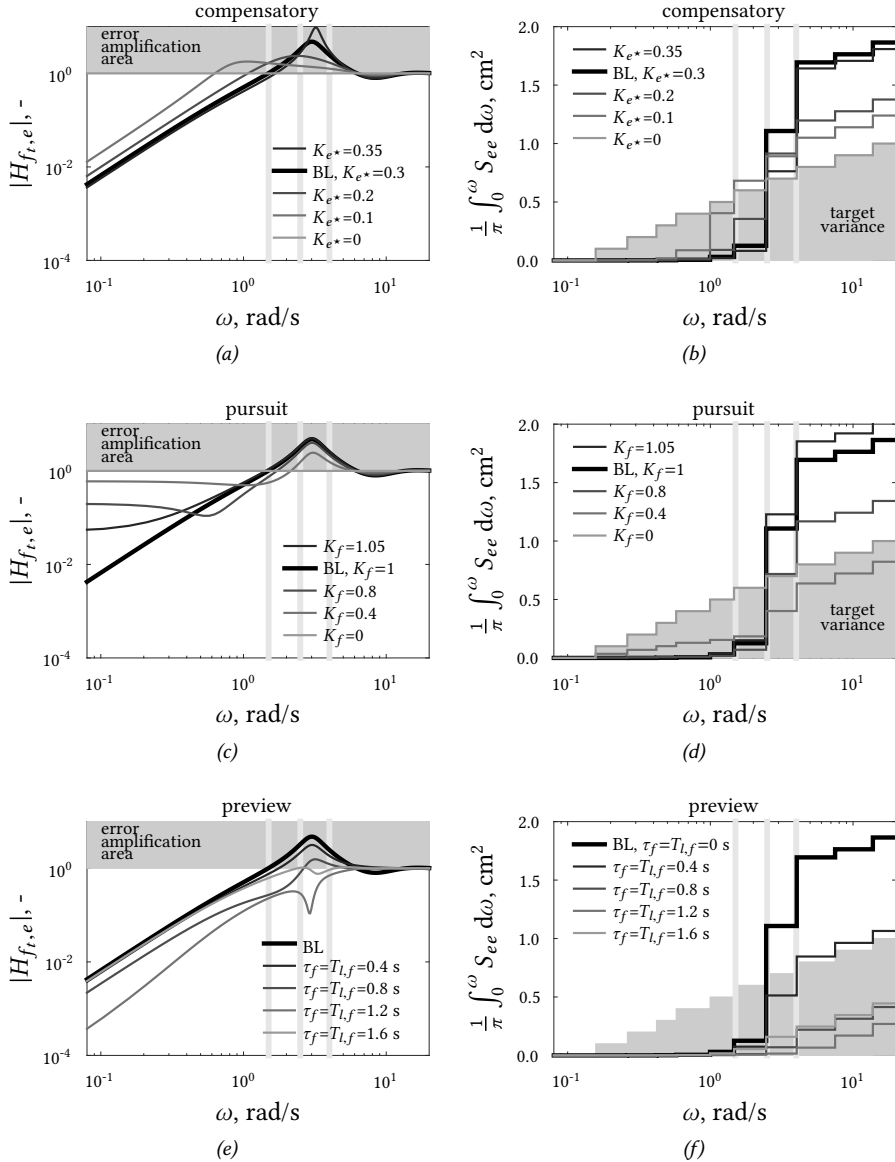


Figure 6.4: Effects of model parameters on the target-to-error dynamics (a,c,e) and cumulative performance (b,d,f), for a rectangular amplitude-spectrum sum-of-ten-sines target signal ($\sigma_{f_t}^2 = 1 \text{ cm}^2$) and double integrator CE dynamics.

6.3.4. PREDICTING HUMAN BEHAVIOR ADAPTATION

HC adaptation to target trajectory bandwidth variations is predicted by minimizing the tracking error variance in Eq. (6.4) for the model parameters K_{e^*} , T_{L,e^*} , K_f , $T_{l,f}$, and τ_f . Predictions are made for seven target signal bandwidths (0.4-7.5 rad/s), two CE dynamics (single- and double-integrator), and five display configurations (compensatory, pursuit, and limited (2) and full preview). The HC's physical limitation parameters are assumed to remain constant, with τ_v , ω_{nms} , and ζ_{nms} fixed at representative values of 0.2 s, 12 rad/s, and 0.2 (single integrator) and 0.28 s, 8.5 rad/s, and 0.45 (double integrator), respectively (these values were measured in the experiment in Chapter 5). Stability was guaranteed by constraining the phase margin $\phi_m > 20$ deg and a limit of $\omega_c > 0.5$ was enforced to avoid a zero-output control strategy; lead equalization was limited to $T_{L,e^*} < 3$ s. The simulated target signals differed only in the individual sinusoids' amplitudes; all signals consisted of 10 sinusoids and had equal power ($1.61 \text{ cm}^2 / 0.25 \text{ inch}^2$). The seven signals had 3-9 low-frequency high-amplitude sinusoids, augmented with a high-frequency shelf; the three signals with 6, 7, and 8 low-frequency, high-amplitude sinusoids correspond to the 1.5, 2.5 and 4 rad/s bandwidth signals in Fig. 6.2. No remnant was included in the simulations. The disturbance signal was the sum of ten sinusoids with a bandwidth of 1.5 rad/s, and its power was scaled to 16% of the power of the target signal to yield predominantly a *target-tracking* task; the same disturbance signal was used in all simulations. Predictions in tasks with limited preview were obtained by restricting $\tau_f < \tau_p$ and $T_{l,f} < \tau_p$ for τ_p equal to 0.2 and 0.4 s (single integrator) or 0.3 and 0.6 s (double integrator).

6

Fig. 6.5 shows that the maximum attainable performance deteriorates when the target signal bandwidth increases for all five display configurations. However, performance decreases markedly less with a pursuit display as compared to a compensatory display. Full preview yields the best performance, which is almost invariant with the target trajectory bandwidth. In compensatory tracking tasks, a reduced-gain K_{e^*} strategy is beneficial at bandwidths higher than 4 rad/s (single integrator) and 2.5 rad/s (double integrator), which corresponds well with previous experimental results [80, 164]. To track higher-bandwidth target signals on a pursuit display, it is better to attenuate the target response (lower K_f) and keep the error-response gain K_{e^*} constant, both in tasks with single- and double-integrator dynamics. When more preview becomes available, a higher target response gain K_f (closer to 1) is beneficial, especially in higher-bandwidth tasks. In fact, with full preview, only minor behavior adaptations are required to optimally follow various-bandwidth target trajectories, as indicated by the approximately constant values of K_f and τ_f . The optimal lead time-constant T_{L,e^*} and target smoothing time-constant $T_{l,f}$ are approximately equal for all bandwidths; these are shown together with the experimental results in Section 6.5.

6.4. EXPERIMENTAL VALIDATION: METHOD

6.4.1. HYPOTHESES

First, corresponding to the offline model predictions, we hypothesize that:

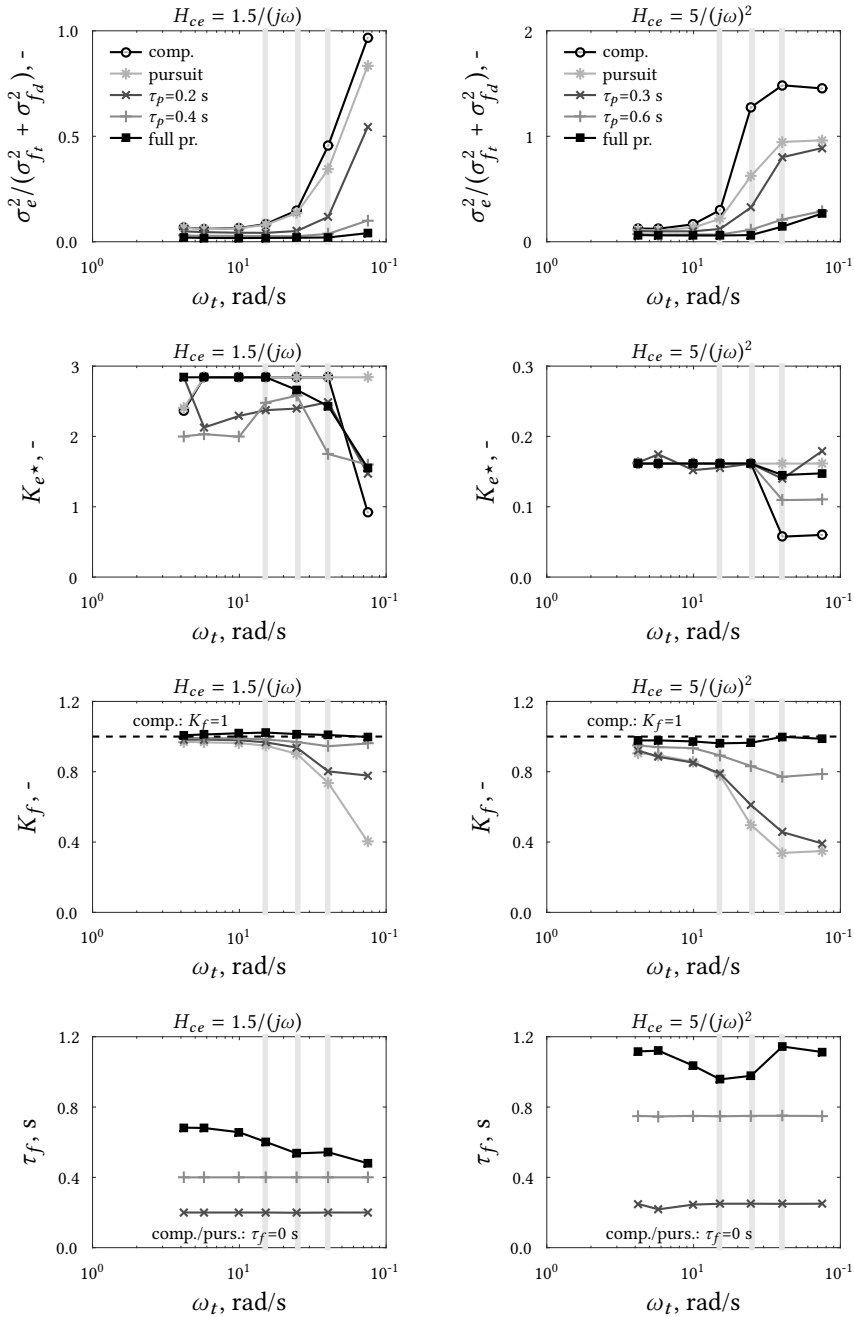


Figure 6.5: Optimized performance and corresponding model parameters, single integrator results are on the left and double integrator results on the right.

- I: Task performance decreases when tracking higher-bandwidth target signals, independent of the experimental display. However, performance decreases slower when using pursuit as compared to compensatory displays, and even slower when preview is available.

Second, to confirm previous experimental results from compensatory tracking tasks [80, 164], we hypothesize that:

- II: In compensatory tasks, HCs first increase their control gains to increasing bandwidth of the target signal, in order to maintain a crossover frequency well above the input bandwidth. When a further increase in crossover frequency leads to instability, increased target signal bandwidths instead evoke crossover regression.

Furthermore, based on the offline model predictions, we hypothesize that HCs adapt their behavior to increasingly high-bandwidth target signals in pursuit and preview tracking tasks as follows:

- H.III: In pursuit tasks, HCs attenuate their target response (lower K_f) and hold their error response constant (K_{e^*} and T_{L,e^*} invariant).
- H.IV: In preview tasks, HC behavior is roughly invariant; the control gains remain constant (K_{e^*} , T_{L,e^*} and K_f), while slight adaptations of τ_f and $T_{L,f}$ may occur to emphasize error-suppression at frequencies of the additional high-amplitude sinusoids.

6.4.2. EXPERIMENT DESIGN

To test these hypotheses and verify the offline model predictions, an experiment was performed in the fixed-base simulator in the Human-Machine Interaction Laboratory (HMI-Lab) at TU Delft. Subjects were seated directly in front of the display screen and gave control inputs with a side-stick at their right-hand side, which was configured to only rotate around its roll axis. The experimental setup was equal to the previously performed preview tracking experiments, see Chapters 2, 4 and 5 for details.

Independent variables

Only a selection of the simulated task variable variations (see Section 6.3) was experimentally tested, to avoid excessive measurement times. Double integrator CE dynamics were used throughout the experiment, as the predicted control behavior adaptation trends are largely identical, but more pronounced, as compared to single integrator tasks (see Fig. 6.5). Compensatory, pursuit, and preview ($\tau_p=2$ s) display configurations were tested; their layouts correspond to Fig. 6.1. The tested target signal bandwidths were 1.5, 2.5, and 4 rad/s, which corresponds to the signals tested by McRuer *et al.* [80] in compensatory tasks (see Fig. 6.2b). To avoid subjects from memorizing parts of the target signal after repeated exposure, five different phase realizations were used. The phases were generated randomly, but excessively low and high crest factors were avoided according to the method by Damveld *et al.* [175]. The experiment comprised the full factorial of the two independent variables (display and target bandwidth), yielding nine conditions.

Participants, instructions, and procedure

Nine volunteers participated in the experiment, all students and staff of TU Delft. Participants signed for informed consent prior to the experiment. The main instruction was to minimize the tracking error, of which the RMS value was reported to participants after every measurement run. The experiment had a within-subjects design and the order of the conditions was randomized according to a balanced Latin-square. The experiment started with a familiarization phase, during which subjects performed each experimental condition once. Then, the actual experiment commenced. A single condition was repeated until performance and control activity were stable in five runs. These five runs were used as measurement data, while all other runs were considered “training” and were not used for further analysis. Subjects then moved on to the next condition. The full experiment took around five hours per subject, and was performed in two separate sessions on different days. Breaks were taken between every two condition, during which subjects stepped out of the simulator. A single experimental run lasted 128 s, of which the last 120 s were used for analysis and the first 8 s were used as run-in time.

Dependent measures

A number of measures were used to quantify the tracking performance: the variance of the error σ_e^2 , the open-loop crossover frequency ω_c and phase margin ϕ_m , and the target-to-error dynamics $H_{f_t,e}(j\omega)$. Estimates of the $H_{o_t}(j\omega)$ and $H_{o_x}(j\omega)$ dynamics and the model parameters were used as measure for subjects’ control behavior. The definition of these measures was given in Section 6.3; see Chapters 2, 4 and 5 for details on their calculation from experimental data.

6.5. EXPERIMENTAL VALIDATION: RESULTS

6.5.1. TRACKING PERFORMANCE

Error variance

Fig. 6.6 shows that a higher target signal bandwidth leads to a lower total tracking performance, regardless of the display. Performance deteriorates much more in compensatory tasks than in pursuit tasks, and more in pursuit tasks than in preview tasks, which corresponds well with the offline predictions. The target, disturbance, and remnant frequencies all contribute to the performance reduction, so both target-tracking and disturbance-rejection performance are worse, while errors due to remnant injection also increase. Note that especially the key point of interest, the *target-tracking performance* in pursuit and preview tasks, yields an excellent match between the predictions and the measurements.

Target-to-error dynamics

Fig. 6.7 shows the estimated target-to-error dynamics. In compensatory tasks, higher bandwidths lead to a lower, but wider error amplification peak, while error suppression deteriorates at low frequencies. These effects correspond well to the reduced-gain K_{e^*} control strategy that was explored in Fig. 6.4a. In pursuit tasks, the target-to-error amplification peak also reduces with higher bandwidths. However, contrary to compensatory tasks, the peak’s width does not increase, which corresponds well to the effects of a reduced target response gain K_f control strategy, see Fig. 6.4c. In preview tasks, no error

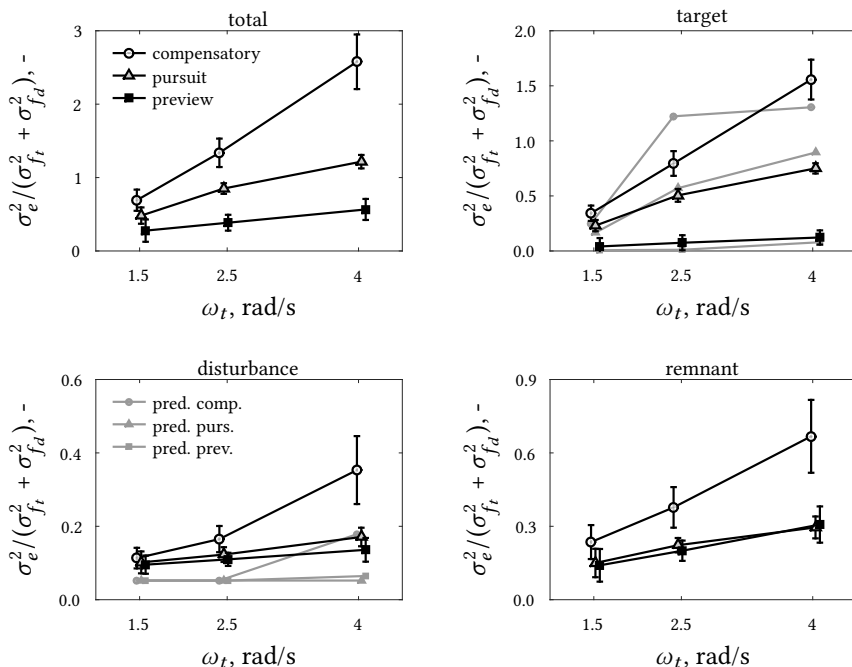


Figure 6.6: Total tracking performance and the separate contributions due to the target, disturbance and remnant inputs; average over nine subjects and 95% confidence intervals, corrected for between-subject variability.

amplification peak is visible for any target signal bandwidth, which indicates that subjects responded to the trajectory ahead (nonzero τ_f and $T_{l,f}$, Fig. 6.4e). In higher-bandwidth tasks, subjects suppress the errors due to the sinusoids at 2.5 and 4 rad/s slightly better when preview is available.

Crossover frequency and phase margin

Fig. 6.8 shows the crossover frequencies ω_c and phase margins ϕ_m . In compensatory tasks, higher bandwidths yield a lower target crossover frequency $\omega_{c,t}$ and, especially at 2.5 rad/s, a higher phase margin $\phi_{m,t}$, corresponding to a reduced-gain and more stable control strategy [6, 164]. In fact, in 2.5 and 4 rad/s bandwidth tasks, $\omega_{c,t}$ is lower than the bandwidth of the target signal, which indicates that not all of its high-amplitude sinusoids are tracked well. The target crossover frequency $\omega_{c,t}$ is around 2.5 rad/s at the lowest two bandwidths; comparable experiments have reported substantially higher values (≈ 3.5 rad/s) [6, 164, 173], possibly because no disturbance signal f_d was included in these experiments [163]. Note that the disturbance open-loop equals the target open-loop in compensatory tasks, so $\omega_{c,t} = \omega_{c,d}$ and $\phi_{m,t} = \phi_{m,d}$.

In pursuit tasks, the target crossover frequency $\omega_{c,t}$ reduces with increasing bandwidth. $\omega_{c,t}$ is approximately 0.2 rad/s lower and the phase margin $\phi_{m,t}$ is 20-60 deg higher as

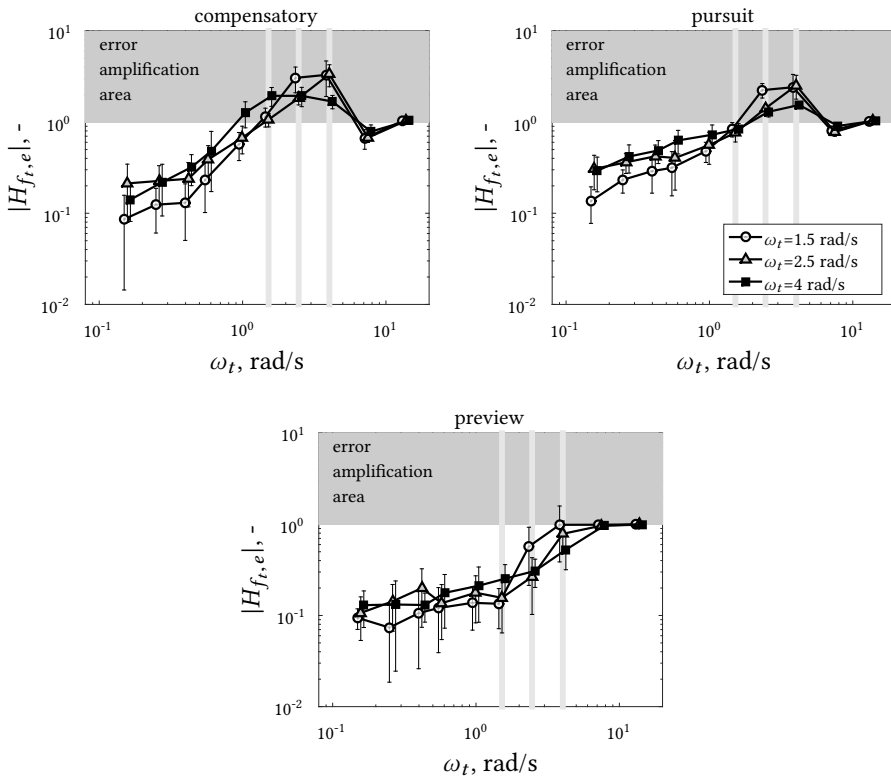


Figure 6.7: Target-to-error dynamics, average over nine subjects and standard deviations. Results are shifted slightly horizontally to reduce overlap.

compared to compensatory tasks, suggesting that subjects applied a more conservative and stable control strategy. The disturbance crossover frequency $\omega_{c,d}$ also decreases with increasing target bandwidth, which contradicts the predicted invariance in the offline analysis (gray lines in Fig. 6.8). However, this decrease is smaller than that observed in compensatory tracking, which is visible in the 4 rad/s task, where $\omega_{c,d}$ is still higher than the disturbance signal bandwidth in pursuit tasks, but $\omega_{c,d}$ is well below the disturbance bandwidth in compensatory tasks.

In preview tracking tasks, the target crossover frequency $\omega_{c,t}$ is around 4 rad/s for all input bandwidths. This indicates that all frequencies below the target signal bandwidth are tracked well, which corresponds to Fig. 6.7. Additionally, the target phase margin $\phi_{m,t}$ is very high (100-150 deg) due to the phase lead generated by responding to the trajectory ahead (see Chapter 4). Contrary to compensatory and pursuit tasks, the disturbance crossover frequency $\omega_{c,d}$ and phase margin $\phi_{m,d}$ are identical with all three bandwidths.

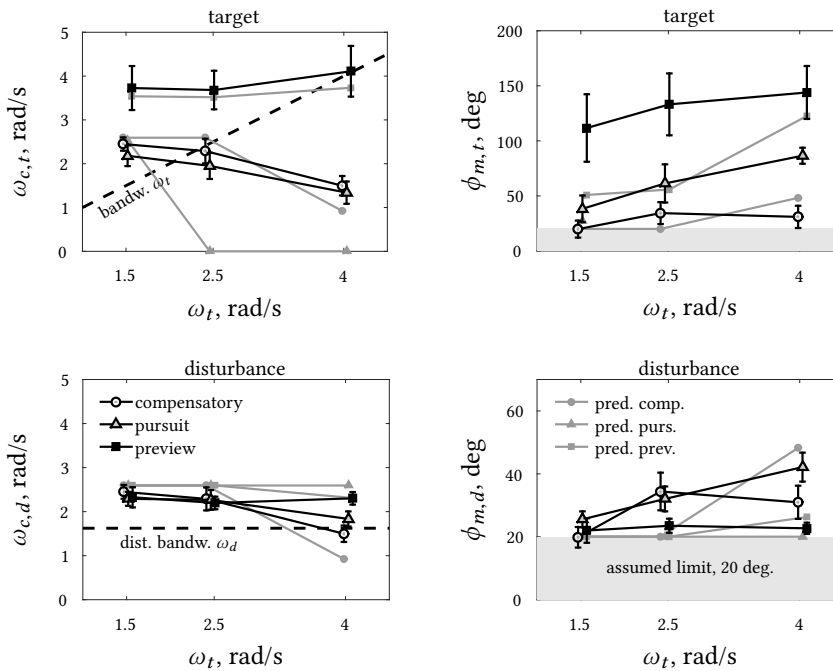


Figure 6.8: Crossover frequencies and phase margins; average over nine subjects and 95% confidence intervals, corrected for between-subject variability.

6

6.5.2. HUMAN CONTROL BEHAVIOR

Fig. 6.9 shows the estimated model parameters. In compensatory tasks, participants adapt their behavior from 1.5 to 2.5 rad/s tasks by reducing their control gain K_{e^*} , and increasing their lead time-constant T_{L,e^*} , both by a factor of around two. This corresponds to the almost identical $\omega_{c,t}$ and the increase in $\phi_{m,t}$ in Fig. 6.8. On the contrary, from 2.5 to 4 rad/s tasks, participants increase K_{e^*} (although only by approximately 25%), while again reducing T_{L,e^*} to the original value just above 1 s, which leads to clear crossover regression, see Fig. 6.8. Furthermore, participants consistently adapt to higher bandwidths by reducing their time delay τ_v , increasing their neuromuscular break frequency ω_{nms} , and reducing the neuromuscular damping ζ_{nms} .

In pursuit tasks, the response delay τ_v and neuromuscular damping ζ_{nms} decrease, while the neuromuscular break frequency ω_{nms} increases in higher-bandwidth tasks, identical as in compensatory tasks. However, contrary to compensatory tasks, the error response gain K_{e^*} and lead time-constant T_{L,e^*} are roughly invariant, and the target response gain K_f decreases from around 0.75 to 0.5. This adaptation corresponds well to the offline model predictions, although an even stronger reduction of the gain K_f was expected. The estimated HC control dynamics in Fig. 6.10 support these parameter adaptations, or invariants. The “compensatory” control dynamics $H_{o_x}(j\omega)$ (see Fig. 6.3) remain approxi-

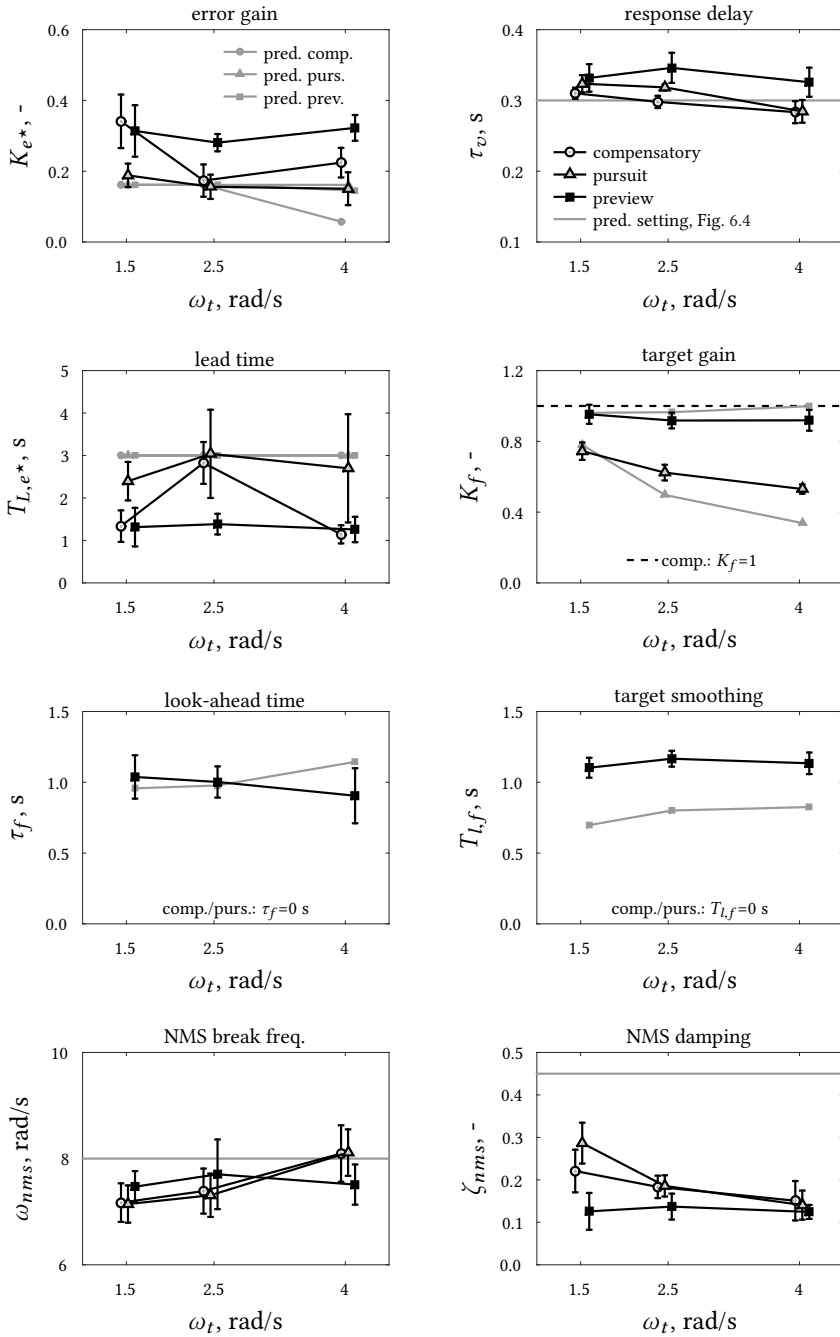


Figure 6.9: Estimated model parameters, average over nine subjects and 95% confidence intervals, corrected for between-subject variability.

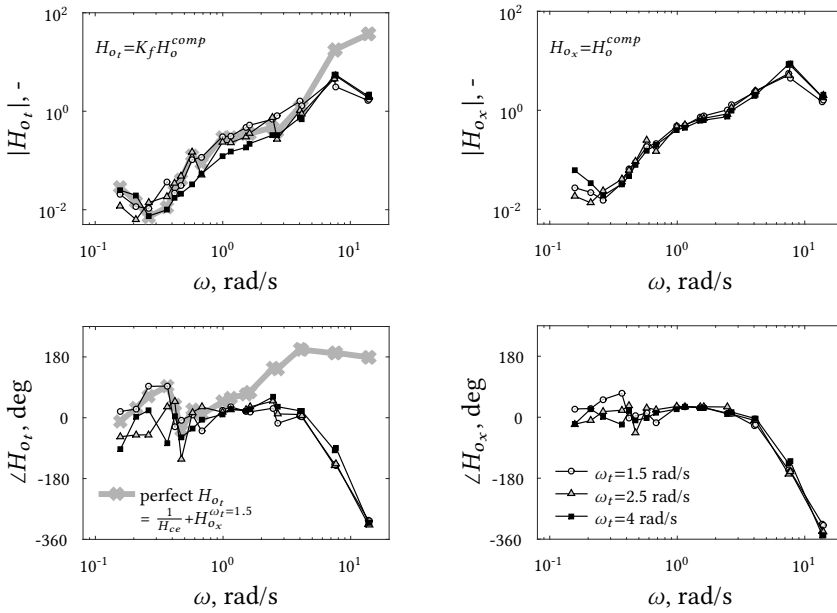


Figure 6.10: Bode plot of estimated HC dynamics in the pursuit tasks; single-subject data.

6

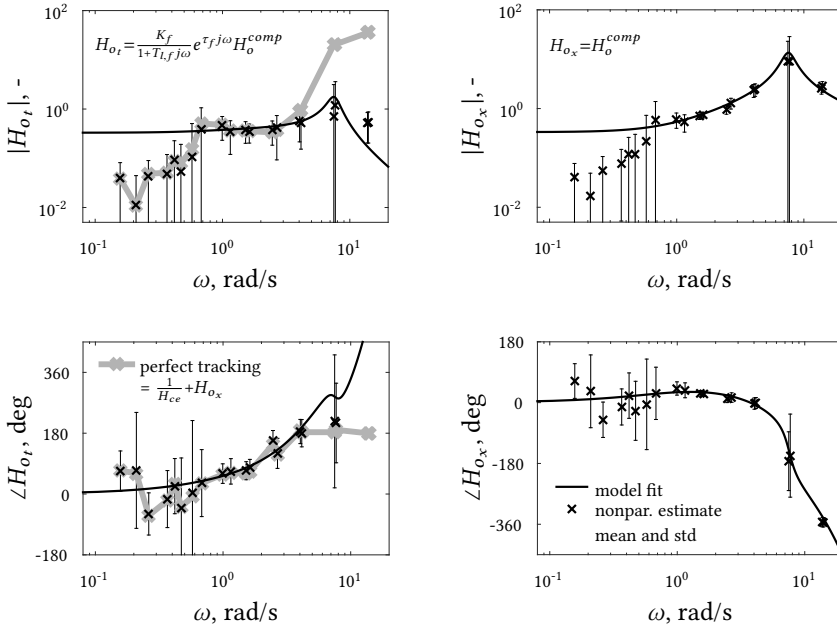


Figure 6.11: Bode plot of estimated HC dynamics in the preview tasks with a 4 rad/s bandwidth target signal; single-subject data.

mately constant, while the magnitude of $H_{o_t}(j\omega)$ decreases with increasing target bandwidth. The HC's actual target response lags behind the response that would yield perfect target-tracking (gray line in Fig. 6.10), resulting in tracking errors, especially at higher frequencies. Exactly these frequencies are more strongly excited by higher-bandwidth target signals, so HCs reduce their response gain K_f to avoid amplifying these tracking errors.

In preview tasks, bandwidth changes yield only minor adaptations in the model parameters, see Fig. 6.9. Only the average look-ahead time τ_f decreases slightly with bandwidth, from around 1.05 to 0.9 s, but with substantial between-subject variability, as indicated by the overlapping confidence intervals for τ_f in Fig. 6.9. Alternatively, the lower τ_f may reflect a subtle adaptation that leads to smaller errors due to the additional high-amplitude sinusoids at 2.5 and 4 rad/s, see also Fig. 6.7. In general, however, the way subjects used the previewed trajectory for control is not affected by the target signal bandwidth: the target response gain ($K_f \approx 0.95$) and lag time-constant ($T_{l,f} \approx 1.15$ s) are approximately invariant. The estimated control dynamics in Fig. 6.11 show that the target trajectory is tracked almost perfectly at all frequencies below 4 rad/s. Therefore, different-bandwidth target signals provide no incentive for HCs to severely adapt their control behavior with a preview display.

6.6. DISCUSSION

This chapter investigated how HCs adapt their control behavior to target trajectory bandwidth in pursuit and preview tracking tasks. Two approaches, an offline analysis with a quasi-linear HC model and a human-in-the-loop experiment, both yielded matching results, and analysis of the model parameters provided explicit insight into the HC's adaptation mechanisms, surpassing overt performance measures.

Our first hypothesis (H.I) was that higher bandwidth target signals lead to reduced tracking performance, but relatively less so in pursuit and preview tasks. This hypothesis is *confirmed*. Consequently, it is particularly beneficial to use preview displays in high bandwidth manual tracking tasks: the error variance in 4 rad/s bandwidth tasks is approximately five times higher with a compensatory display than with a preview display.

In compensatory tasks, the effects of target signal bandwidth have been quantified before [80, 164, 173, 174]. Corresponding to the literature, and as hypothesized (H.II), *crossover regression* was predicted and measured in double integrator CE tasks with high-bandwidth target signals. However, opposed to the literature, regression occurred already at a relatively low bandwidth of 2.5 rad/s. This is a direct consequence of the relatively low overall crossover frequencies of our participants in compensatory tasks. In accordance with one of the “verbal adjustment rules” by McRuer and Jex [6]: crossover regression occurs when the target signal bandwidth is higher than 80% of the crossover frequency. Our relatively low crossover frequencies are possibly the result of our more demanding task, which includes an additional disturbance signal for system identification purposes.

In pursuit tasks, the HC's dominant adaptation mechanism in tracking higher-bandwidth target signals is to attenuate their target response (lower K_f), which *confirms* our third hypothesis (H.III). As opposed to compensatory tracking, HCs maintain identical equal-

ization dynamics in their internal error response (K_{e^*} and T_{L,e^*} are adapted only slightly). Thereby, crossover regression occurs mainly in target-tracking, while stabilizing feedback control remains intact for disturbance-rejection.

In preview tasks, HCs do not consistently adapt their control behavior to the target trajectory bandwidth. Near-perfect target-tracking dynamics are adopted up to relatively high frequencies (≈ 4 -6 rad/s), while retaining a very high phase margin; therefore, there is no incentive for behavior adaptation, besides a slightly shifted emphasis to better suppress the errors at the frequencies of the additional high-amplitude sinusoids. This *confirms* our fourth hypothesis (H.IV).

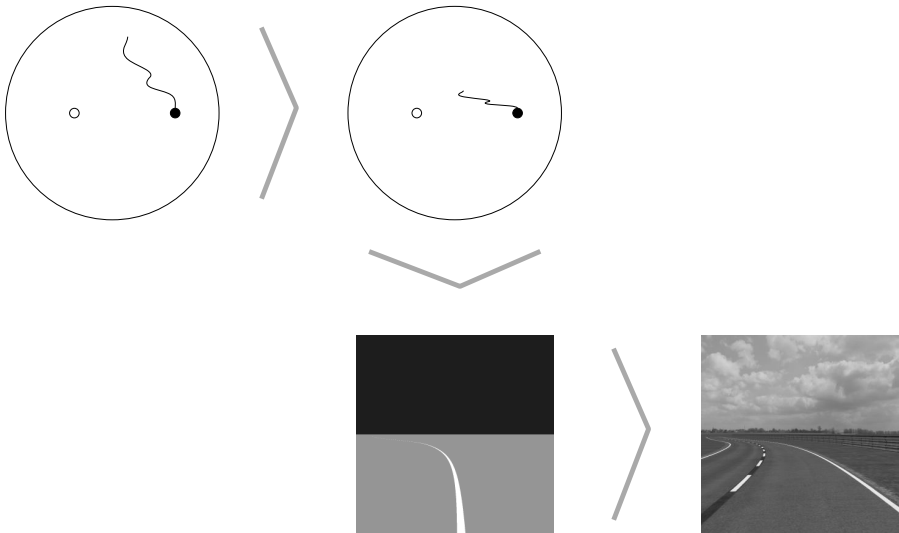
In this chapter, we predicted the effects of target trajectory bandwidth offline, for a wide range of tasks with bandwidths between 0.4 and 7.5 rad/s, compensatory, pursuit, and preview displays (with three settings from zero to unrestricted preview), and for single- and double-integrator CE dynamics. However, experimental validation was restricted to a limited number of tasks. In addition to our three experimental bandwidths between 1.5 and 4 rad/s, which are particularly interesting for manual control [6], future work should focus on validating the predictions for lower and higher bandwidths. Bandwidths below 1.5 rad/s may be relevant for understanding driver steering, as road “target” trajectories typically lack high frequencies. In contrast, tracking of signals with bandwidths beyond 4 rad/s may motivate humans to initiate a second, *near-viewpoint response*, to also match the perfect target-tracking dynamics at higher frequencies (e.g., see Chapter 4). Moreover, experimental data is required to verify the predicted HC behavior invariance with target trajectory bandwidth also in tasks with single-integrator CE dynamics, and to quantify HC adaptation to the bandwidth in tasks with restricted preview (i.e., between 0 and 2 s).

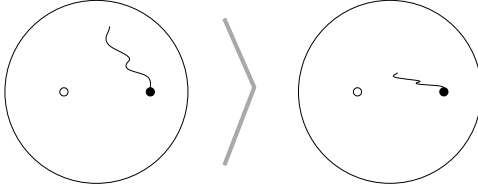
6.7. CONCLUSION

This chapter investigated the effects of target trajectory bandwidth on manual control behavior in pursuit and preview tracking tasks. Offline analysis with a quasi-linear human controller model accurately predicted human-in-the-loop measurements. Opposed to adapting their feedback control behavior in compensatory tracking tasks, humans adapt to higher-bandwidth target trajectories in pursuit tasks mainly by reducing their feed-forward, target response gain. In preview tasks, human control behavior is found to be largely invariant to target bandwidth variations between 1.5 and 4 rad/s. With these results, human control adaptation to the most critical task variables in pursuit and preview tracking tasks has now been quantified, facilitating offline predictions of human tracking behavior in tasks with various controlled element dynamics, preview times, and target signal bandwidths.

PART III

FROM PREVIEW TRACKING
TO CURVE DRIVING



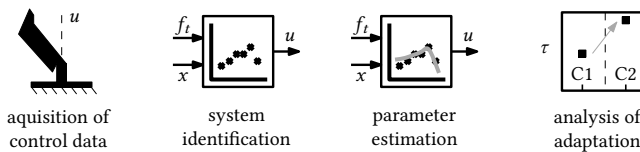


7

EFFECTS OF LINEAR PERSPECTIVE

Parts I and II of this thesis proposed a novel human controller model for preview tracking tasks, and used this model to quantify how humans adapt their control behavior to crucial task variables. The experiments in Parts I and II used plan-view displays, which show the full previewed target trajectory with a linear scaling, independent of the distance ahead. In contrast, the apparent size of a previewed target trajectory in the real world decreases with distance ahead due to linear perspective. By quantifying how humans adapt their control behavior to nonlinear, perspective scaling of the previewed trajectory, this chapter extends the obtained understanding (and model) of Parts I and II to a wider range of realistic preview control tasks. In a human-in-the-loop experiment, identical preview tracking tasks are performed with plan-view and perspective displays. Human control behavior adaptations are quantified both by estimating the human's feedforward and feedback dynamics with instrumental-variable, multiloop system identification techniques, and by analyzing estimated parameters of the proposed, plan-view preview model.

Steps of the cybernetic approach involved:



The contents of this chapter have been published as:

Title Effects of Linear Perspective on Human Use of Preview in Manual Control
Journal IEEE Transactions on Human-Machine Systems, vol. 48, no. 5, pp. 496-508, Oct. 2018
Authors K. van der El, D.M. Pool, M.M. van Paassen, and M. Mulder

7.1. INTRODUCTION

HUMANS rely heavily on visual information in many manual control tasks. An important visual cue is *preview*, information about the future reference trajectory, or target, to follow. Examples of preview include the road ahead when driving [95, 137, 140] or cycling [3], and an artificially displayed tunnel-in-the-sky when piloting a helicopter [177] or aircraft [97]. Preview enables humans to anticipate upcoming trajectory changes through feedforward control [61].

To study the human controller's (HC) use of preview information, simplified tracking tasks are often performed with a plan-view (i.e., two-dimensional or top down) display, for example in [54, 55, 134] and Parts I and II of this thesis. Removal of all other control-related cues, like physical motion and optic flow, then allows for explicit measuring and identification of the HC's response to preview information. Recent modeling efforts (Part I) and subsequent analysis (Part II) suggested that HCs apply a *dual-mode* preview control strategy: open-loop control based on a point on the target close ahead, the *near viewpoint*, and closed-loop control based on a point farther ahead, the *far viewpoint*.

The novel preview model from Chapter 2 extends McRuer *et al.*'s [6, 80] famous crossover model for compensatory tracking; as such, it may facilitate a similar structured, quantitative approach to design and evaluate human-machine systems (e.g., interfaces), but for more realistic control tasks. However, general vehicle control tasks differ markedly from the preview tracking experiments in Parts I and II, as the target trajectory is often viewed from a point within the visual scene, like a camera on a remote vehicle or the human eye. First, due to *linear perspective*, the previewed target trajectory appears increasingly compressed with distance ahead, while the target in the plan-view tracking experiments is displayed equally large nearby and far ahead. Second, the visual flow field provides additional cues of the viewpoint's rotations and translations [47, 115]. The HC's excellent adaptive capabilities [6, 75] make it difficult to predict if and how these two factors affect HC behavior.

This chapter focuses on the effects of linear perspective, because the reducing visual stimuli from the target farther ahead, and the corresponding magnification of parts nearby, may severely affect the near- and far-viewpoint responses adopted by the HC. On the one hand, it was shown in compensatory tracking tasks that smaller visual stimuli evoke less aggressive control behavior and larger response time delays [178, 179]. This would suggest that the HC's response to preview far ahead, which is strongly affected by perspective, will be weaker in perspective tasks (compared to plan-view tasks). On the other hand, perception research has shown that the human's visual system compensates visual stimuli with simultaneously sensed depth cues [180]; as such, HC perception (and hence control) of a previewed target might still be equal in plan-view and perspective tasks.

Perspective displays have been extensively studied, and applied, as they allow for intuitive three-dimensional spatial information transfer (e.g., see [181–183]). Unfortunately, these studies did not measure – and thus did not increase our understanding of – the HC's underlying control behavior. The HC's control dynamics were measured in other perspective control tasks, like driving and flying, but these tasks lacked preview informa-

tion [178, 184], or did not explicitly reveal the effects of linear perspective on the HC's near- and far-viewpoint responses [3, 97, 137, 140, 165].

The goal of this chapter is to explicitly quantify how linear perspective affects HC use of preview information, and specifically the near- and far-viewpoint response mechanisms. Measurements from a human-in-the-loop experiment are analyzed, in which eight subjects performed a tracking task with integrator controlled element (CE) dynamics, and 2 s of preview. The preview was shown either in plan-view, or with the horizontal and vertical perspective deformations along the previewed trajectory applied separately, as well as combined. First, objective measures are calculated to quantify tracking performance, control activity, and coherence. Next, a nonparametric, multiloop, frequency-domain system identification method is applied [87], and the parameters of the HC model for plan-view preview tracking tasks from Chapter 2 are estimated. The obtained HC dynamics and model parameters explicitly characterize how HCs adapt their control behavior between plan-view and perspective tasks.

This chapter is structured as follows. Section 7.2 introduces the preview control task and the concept of linear perspective. Sections 7.3 and 7.4 explain the methods: the HC model for plan-view preview tracking tasks from Chapter 2, the applied system identification techniques, and the performed experiment. Results are presented in Section 7.5, followed by a discussion and the main conclusions in the final two sections.

7.2. PREVIEW TRACKING AND LINEAR PERSPECTIVE

7.2.1. THE CONTROL TASK

This chapter considers a single-axis, lateral position tracking task, identical to those in Parts I and II. The HC is required to minimize the lateral tracking error $e(t)$, which is the difference between the target signal $f_t(t)$ and the CE output $x(t)$:

$$e(t) = f_t(t) - x(t), \quad (7.1)$$

at current time t . The HC gives control inputs $u(t)$ to the CE, which is simultaneously perturbed by a disturbance signal $f_d(t)$. The task, illustrated in Figs. 7.2 and 7.1, is thus *two-fold*: target tracking *and* disturbance rejection.

In preview tracking tasks, the target ahead $f_t([t, t + \tau_p])$ is visible up to preview time τ_p . A plan-view of the previewed target is shown in Fig. 7.2a; this view corresponds to looking

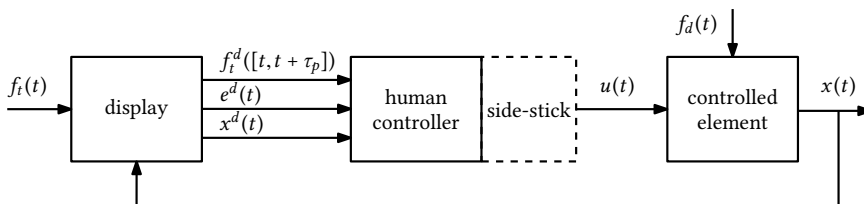


Figure 7.1: The human controller in a target-tracking and disturbance-rejection task.

straight down from a point high above the previewed target (i.e., 90° elevation in Fig. 7.2c). Due to the viewpoint's movement parallel to world frame axis X^w , the previewed target moves down over the screen and forces the current target (cross) left and right. Note that, in the considered forced-pace (fixed velocity) task, time and distance are linearly related, so all signals can be written with time as the independent variable without loss of generality.

The same scene observed from 10° elevation yields a perspective view (see Fig. 7.2b). Viewed from this particular point, the displayed target trajectory is compressed in vertical display direction V and magnified in horizontal display direction U . Vertical display coordinate v_a is much smaller on the perspective display than on the plan-view display, for the same point a on the previewed target τ_a s ahead. Horizontally, the display coordinate u_b is larger on the perspective display for any arbitrary point b on the previewed target. Clearly, the displayed signals (f_t^d , e^d , and x^d in Fig. 7.1), hence the visual stimuli from the previewed target, are markedly different in plan-view and perspective tasks.

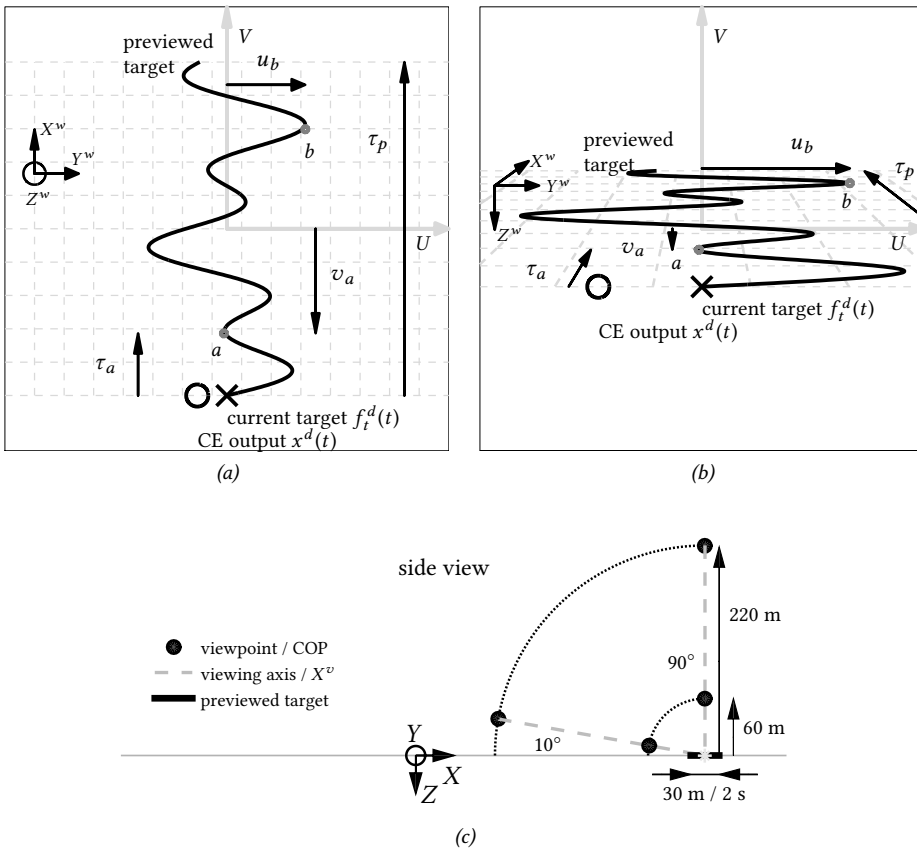


Figure 7.2: Plan-view (a) and perspective (b) preview displays, obtained by viewing the target from points “ $90^\circ/220\text{ m}$ ” and “ $10^\circ/60\text{ m}$ ”, respectively (c).

7.2.2. PERSPECTIVE PROJECTION METHOD

Central projection is a technique to map a three-dimensional visual scene to a two-dimensional display surface [185]. The basic principle is similar to that of a camera, which produces a picture (i.e., a two-dimensional representation) of a three-dimensional visual scene. The center of projection (COP), or viewpoint, is the location from which the visual scene is supposedly observed (see Fig. 7.3). Light rays, or projectors, emanate from each point in the visual scene to converge in the COP. When a certain viewplane is defined at finite distance κ from the COP, the intersection of passing light-rays with this viewplane yields a two-dimensional image: the perspective projection. Alternatively, when κ is infinite, a parallel projection is obtained, yielding a plan-view. The COP is the origin of the view reference frame (superscript v), with the central viewing axis X^v defining the viewing direction. The boundaries of the visualized volume are characterized by the horizontal and vertical field of view (FOV):

$$\text{HFOV} = 2 \arctan \left(\frac{w}{2\kappa} \right), \quad \text{VFOV} = 2 \arctan \left(\frac{h}{2\kappa} \right), \quad (7.2)$$

with w and h the viewplane's width and height, respectively. For an arbitrary point a in the visual scene, the corresponding viewplane coordinates u_a and v_a are obtained from:

$$u_a = \kappa \frac{y_a^v}{x_a^v}, \quad v_a = -\kappa \frac{z_a^v}{x_a^v}, \quad (7.3)$$

with x_a^v , y_a^v and z_a^v the coordinates of point a in the view reference frame.

7.2.3. PERSPECTIVE DISPLAY GAINS

HC task performance depends on the appearance of a perspective scene, as demonstrated by Kim *et al.* [181] for three-axis pursuit tracking tasks. It is possible to use the perspec-

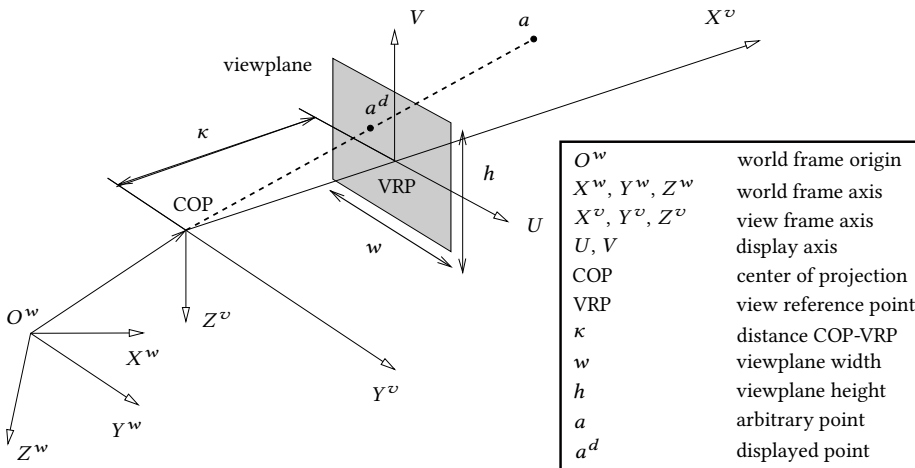


Figure 7.3: The perspective projection method and its principal terminology.

tive projection's parameters (like FOV and elevation) to compare the appearances of perspective scenes; however, when analyzing HC behavior, it is more convenient to express perspective deformations as display scaling gains, as a function of time τ along the previewed trajectory ahead. In horizontal display direction, we define display gain $K_{d,u}(\tau)$ as the ratio of the display and world coordinates of an arbitrary point a in the visual scene:

$$K_{d,u}(\tau) = \frac{u_a(\tau)}{y_a^w(\tau)}. \quad (7.4)$$

In vertical display direction, we define gain $C_{d,v}(\tau)$ as the ratio of the displayed and real (i.e., in world coordinates) lengths of an element with length $d\tau$ as:

$$C_{d,v}(\tau) = \frac{v_a(\tau + d\tau) - v_a(\tau)}{y_a^w(\tau + d\tau) - y_a^w(\tau)}. \quad (7.5)$$

Notations K and C are adopted to emphasize the task's controlled and non-controlled directions: HCs can only control the CE laterally, so in horizontal display direction.

As an example, consider the situation in Fig. 7.2c: a target trajectory is visible for 30 m ahead, corresponding to 2 s of preview at a velocity of 15 m/s. Fig. 7.4 shows the display gains for all four COP's, for a κ of 75 cm. Looking straight down from 220 m height, each point on the previewed target is approximately equally far away from the COP, yielding a near-uniform scaling in both horizontal and vertical display directions with a ratio of $1:\kappa/220$, or $1:0.0035$ (black solid lines in Fig. 7.4). This projects the 30 m of preview to about 10 cm on the display, which corresponds roughly to the plan-view preview tracking task in Parts I and II of this thesis. Fig. 7.4 shows that a smaller object distance (i.e., moving the COP down vertically) yields higher display gains in both directions (gray solid line). For large object distances this magnification is nearly uniform, as all points of the previewed target remain approximately equally far from the COP.

Viewed from a non-vertical elevation, the object distance to the nearer part of the previewed target (small τ) is smaller than that of far parts (large τ). Therefore, the horizontal

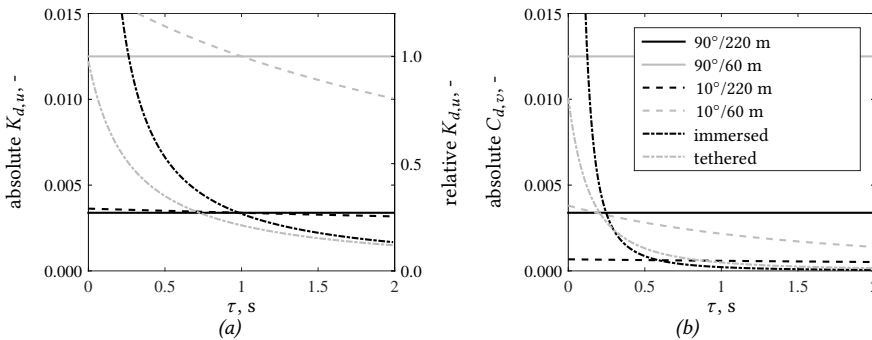


Figure 7.4: Horizontal (a) and vertical (b) display scaling gains for various viewpoints, as a function of time τ along the previewed trajectory ahead.

and vertical display gains will be larger for near points compared to far points, as illustrated for an elevation angle of 10° in Fig. 7.4 (black and gray dashed lines). This effect is more pronounced when the COP is closer to the previewed target, because the relative difference in object distance between near and far parts increases.

Fig. 7.4 also shows the display gains for an immersed and a tethered viewpoint, for a κ of 5 cm. The immersed viewpoint corresponds to a view from a car or bicycle, at 1 m height above the start of the previewed target (at $\tau=0$ s), yielding display gains that are a strong nonlinear function of τ (black dash-dotted line). The display gains increase asymptotically to infinity for points close ahead (small τ), as these parts are outside the (forward aimed) viewing volume. A tethered viewpoint located 3.5 m above and behind the start of the previewed target yields similar display gains, but with the near points still in sight (gray dash-dotted line). Our experiment will include the display gains from this tethered view. For comparison, the right axis in Fig. 7.4a shows the horizontal display gains relative to that of the tethered view at $\tau=0$ s.

7.3. MODELING AND SYSTEM IDENTIFICATION

To investigate how linear perspective affects HC use of preview information, experimental data are analyzed with system identification techniques, in combination with a quasi-linear cybernetic model. This approach is explained here.

7.3.1. HUMAN CONTROLLER MODEL FOR PLAN-VIEW PREVIEW TRACKING

The HC model for plan-view preview tracking tasks from Chapter 2 is shown in Fig. 7.5, together with a display model. The display gains $K_{d,u}(\tau)$ scale the previewed target horizontally at the indicated time τ ahead. The relative display gains are used, such that the CE output $x(t)$ (located at $\tau=0$ s) has unity scaling, as $K_{d,u}(0)=1$. It is mathematically equivalent to use the absolute display gains from Fig. 7.4, but this changes the interpretation of the gains in the HC model and inhibits comparisons with previous work.

The HC model extends McRuer *et al.*'s [6, 80] *crossover model* for compensatory tracking tasks, with two viewpoints on the previewed target as inputs. It was found that this

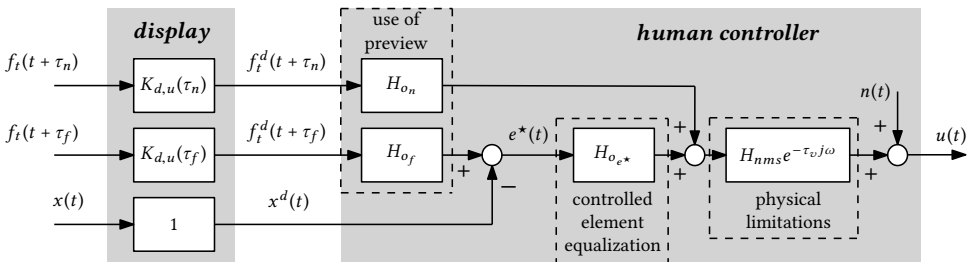


Figure 7.5: Control diagram of the human controller model for preview tracking tasks, adapted from Chapter 2 and augmented with a simple display model.

two-viewpoint model structure is sufficient to account for the HC's total response to a previewed target (see Parts I and II). A *far viewpoint* $f_t(t+\tau_f)$ is the input to a feedback model for compensatory control behavior (similar as in the model by Modjtahedzadeh & Hess [186]), while a *near viewpoint* $f_t(t+\tau_n)$ is the input to a parallel, additive open-loop response. The near- and far-viewpoints are located τ_n and τ_f s ahead on the previewed target, respectively. The model is *quasi-linear*, so linear functions describe most of the HC's behavior. Neither nonlinear and time-varying behavior, nor perception and motor noise are explicitly modeled; these are injected together as filtered white noise through the *remnant* $n(t)$.

Central to the model is the feedback response to an internal error $e^*(t)$: a hypothetical, *cognitively calculated* signal, which cannot be measured. Fig. 7.5 shows that $e^*(t)$ is the difference between the target in the far viewpoint, low-pass filtered by $H_{o_f}(j\omega)$, and the CE output:

$$E^*(j\omega) = H_{o_f}(j\omega)F_t^d(\tau_f, j\omega) - X^d(j\omega). \quad (7.6)$$

The signals written in capitals denote the Fourier transform of the respective time domain signals, and $H_{o_f}(j\omega)$ is the following low-pass filter:

$$H_{o_f}(j\omega) = K_f \frac{1}{1 + T_{l,f}j\omega}. \quad (7.7)$$

The time constant $T_{l,f}$ characterizes the bandwidth of the far-viewpoint response. It models the HC's cognitive elimination of the target signal's high frequencies from the far-viewpoint response, facilitated by the preview (see Chapter 4). Gain K_f reflects the HC's ability to respond relatively more aggressive to the target ($K_f > 1$) or to the CE output ($K_f < 1$). When $K_f = 1$ and $T_{l,f} = \tau_f = 0$ s, Eq. (7.6) and Eq. (7.7) show that $e^*(t) = e(t)$, so that the HC responds to the real error.

The internal error response $H_{o_{e^*}}(j\omega)$ is identical to the simplified precision model [80]:

$$H_{o_{e^*}}(j\omega) = K_{e^*} \frac{1 + T_{L,e^*}j\omega}{1 + T_{l,e^*}j\omega}, \quad (7.8)$$

with K_{e^*} the error response gain, and T_{L,e^*} and T_{l,e^*} the lead and lag equalization time-constants, respectively. In compensatory tracking tasks, humans apply only proportional control when the CE has integrator dynamics [6] (as considered in this chapter); however, estimated human control dynamics in the preview task in Chapters 2, 4 and 5 point to some low-frequency lag-lead equalization.

At the target signal's high frequencies the far-viewpoint response is attenuated by the low-pass filter in $H_{o_f}(j\omega)$. Here, HCs predominantly apply open-loop control, which is captured in the model by the near-viewpoint response $H_{o_n}(j\omega)$. A gain K_n with a differentiator generally suffices to describe these control dynamics (see Part II):

$$H_{o_n}(j\omega) = K_n j\omega. \quad (7.9)$$

A near-viewpoint response is not always clearly present in preview tasks, and some HCs do not apply this control mechanism at all (see Part II).

The model also includes the HC's main physical limitations. Visual response time delay τ_v combines perceptual, cognitive and transport delays, while $H_{nms}(j\omega)$ represents the combined side-stick and HC neuromuscular system (NMS) dynamics [166]:

$$H_{nms}(j\omega) = \frac{\omega_{nms}^2}{(j\omega)^2 + 2\zeta_{nms}\omega_{nms}j\omega + \omega_{nms}^2}, \quad (7.10)$$

with ω_{nms} and ζ_{nms} the natural frequency and damping ratio.

7.3.2. NONPARAMETRIC SYSTEM IDENTIFICATION

The HC dynamics can be estimated without making any assumptions, besides the model's inputs and outputs, using an *instrumental-variable*, nonparametric system identification technique based on Fourier coefficients [87]. The resulting estimates, called describing functions, can validate the parametric model structure from the previous section.

Forcing functions

Nonparametric system identification allows for the estimation of an equal number of describing functions as there are uncorrelated external inputs, called forcing functions [86]. To closely resemble common control tasks, only two forcing functions can be inserted in the considered preview tracking task: a target and a disturbance. By choosing multisine forcing functions (here with 20 sines each) high signal-to-noise ratio's are obtained at the input frequencies:

$$f_t(t) = \sum_{i=1}^{20} A_t[i] \sin(\omega_t[i]t + \phi_t[i]), \quad (7.11)$$

$$f_d(t) = \sum_{i=1}^{20} A_d[i] \sin(\omega_d[i]t + \phi_d[i]), \quad (7.12)$$

with amplitude $A[i]$, frequency $\omega[i]$ and phase $\phi[i]$ of the i^{th} sinusoid (see Section 7.4 for the values used in the experiment). Selecting different input frequencies for the target and disturbance is sufficient for these two signals to be uncorrelated.

Model restructuring

The two forcing functions allow for the identification of only two describing functions, so the model in Fig. 7.5 must first be converted to a two-channel model. The structure in Fig. 7.6 is convenient, as it separates the target-to-control dynamics $H_{f_t}^u(j\omega)$ from the CE-output-to-control dynamics $H_x^u(j\omega)$ (see Parts I and II). These dynamics can be expressed in terms of the HC dynamics and the display gains using block diagram algebra (for details, see Chapter 2):

$$H_{f_t}^u(j\omega) = \left[K_{d,u}(\tau_f)H_{o_f}(j\omega)H_{o_{e^*}}(j\omega)e^{\tau_f j\omega} + K_{d,u}(\tau_n)H_{o_n}(j\omega)e^{\tau_n j\omega} \right] H_{nms}(j\omega)e^{-\tau_v j\omega}, \quad (7.13)$$

$$H_x^u(j\omega) = H_{o_{e^*}}(j\omega)H_{nms}(j\omega)e^{-\tau_v j\omega}. \quad (7.14)$$

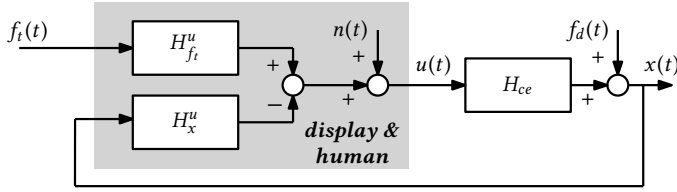


Figure 7.6: Two-channel model used for system identification, in which the display and HC are lumped.

Note that the HC dynamics and the display gains must be lumped in Eq. (7.13) and Eq. (7.14), as the visual stimulus provided by the perspective transformed, displayed target f_t^d is unsuitable for linear frequency-domain analysis. The HC and display gains in Eq. (7.13) can be lumped together into effective gains:

$$K_{n,eff} = K_{d,u}(\tau_n)K_n, \quad K_{f,eff} = K_{d,u}(\tau_f)K_f, \quad (7.15)$$

to easily compare results from plan-view and perspective tasks.

Multiloop describing function estimation

Using Fig. 7.6, the control output can be written as:

$$U(j\omega) = H_{f_t}^u(j\omega)F_t(j\omega) - H_x^u(j\omega)X(j\omega) + N(j\omega). \quad (7.16)$$

A second equation is required to solve for the two unknown describing functions. Evaluating Eq. (7.16) only at the target signal input frequencies ω_t , a second equation can be obtained by interpolating the measured signals (U , F_t , X) in the frequency domain from the disturbance input frequencies ω_d to these same ω_t (indicated by \tilde{U} , \tilde{F}_t , \tilde{X}). Neglecting the remnant, which is small compared to the HC's response to the forcing functions at the input frequencies, it follows that [86, 87]:

$$\begin{bmatrix} U(j\omega_t) \\ \tilde{U}(j\omega_t) \end{bmatrix} = \begin{bmatrix} F_t(j\omega_t) & -X(j\omega_t) \\ \tilde{F}_t(j\omega_t) & -\tilde{X}(j\omega_t) \end{bmatrix} \begin{bmatrix} H_{f_t}^u(j\omega_t) \\ H_x^u(j\omega_t) \end{bmatrix}. \quad (7.17)$$

Solving Eq. (7.17) for $H_{f_t}^u(j\omega_t)$ and $H_x^u(j\omega_t)$ yields the describing function estimates at ω_t . Replacing ω_t by ω_d in Eq. (7.17), and interpolating all signals from ω_t to ω_d , yields the describing functions at ω_d .

7.3.3. PARAMETER ESTIMATION AND MODEL FITNESS

Parameter estimation

The HC model parameters can be estimated in the frequency domain by minimizing a criterion J that is based on the difference between the measured and the modeled control outputs (see Chapter 4):

$$J(\hat{\Theta}) = \sum_{l=1}^{N_l} |U(j\omega_l) - \hat{U}(j\omega_l|\hat{\Theta})|^2. \quad (7.18)$$

The modeled output $\hat{U}(j\omega_l|\Theta)$ is given by Eq. (7.16) with remnant $N=0$; the model parameter vector Θ is $[K_{f,eff} \tau_f T_{l,f} K_{n,eff} \tau_n K_{e^*} T_{L,e^*} T_{l,e^*} \tau_v \omega_{nms} \zeta_{nms}]^T$. N_l is the number of measured frequencies below a chosen cut-off frequency, here 25 rad/s. A Nelder-Mead simplex algorithm is often used to minimize J , constrained only to avoid solutions with negative parameters. Selecting the best solution from many randomly initialized optimizations (here we use 100) yields a high chance to find the global minimum. In a second step, the display gains $K_{d,u}(\tau)$ can be calculated at the estimated τ_n and τ_f , which can then be used to calculate the HC gains K_n and K_f with Eq. (7.15).

Variance accounted for

The Variance Accounted For (VAF) is a measure for the similarity of two signals; its maximum, 100%, indicates that two signals are equal. When applied to compare the measured and the modeled control output the VAF inherently quantifies the model's ability to describe the measured HC behavior [187]. Because a signal's variance is equal to its integrated power-spectral density, the VAF can be calculated as follows:

$$\text{VAF} = \left(1 - \frac{\sum_{l=0}^{N_s-1} P_{\epsilon_u \epsilon_u}(l\omega_b)}{\sum_{l=0}^{N_s-1} P_{uu}(l\omega_b)} \right) \times 100\%, \quad (7.19)$$

with N_s the number of samples in the measured time-traces and ω_b the fundamental radial frequency. P is the estimated periodogram of the subscripted signals, and ϵ_u is the difference between the measured and modeled control outputs:

$$\epsilon_u(j\omega) = U(j\omega) - \hat{U}(j\omega|\Theta). \quad (7.20)$$

7

Coherence

The coherence is a measure for the linear relationship between two signals. A high coherence between the external input signals and the HC's control output can justify using a quasi-linear HC model to analyze the experimental data [187]. The value of the coherence is always between 0 (no linear relation) and 1 (perfect linear relation). The coherence $\Gamma_{f_t u}$ between the target signal and the control output is given by:

$$\Gamma_{f_t u}(\tilde{\omega}_t) = \sqrt{\frac{|\tilde{P}_{f_t u}(\tilde{\omega}_t)|^2}{\tilde{P}_{f_t f_t}(\tilde{\omega}_t)\tilde{P}_{uu}(\tilde{\omega}_t)}}, \quad (7.21)$$

The tilde indicates the average periodogram between the neighboring frequencies in a double band of input frequencies [187]. The coherence between the disturbance input signal and the HC output is calculated similarly.

7.4. THE EXPERIMENT

7.4.1. INDEPENDENT VARIABLES

The experiment had two independent variables, namely horizontal and vertical display scaling. Each had two levels: constant (plan-view) and perspective scaling. This design

allows to investigate the difference in HC behavior between plan-view and perspective tasks, while separating the individual effects of horizontal and vertical perspective deformations. The full factorial of the two independent variables was tested, yielding four conditions: 1) constant scaling, or no perspective (NP), 2) horizontal perspective with constant vertical scaling (HP), 3) vertical perspective with constant horizontal scaling (VP), and 4) horizontal and vertical perspective combined (HVP).

The applied perspective scaling was in accordance with the tethered view in Fig. 7.4, so the entire previewed target was visible on the display. The plan-view's vertical scale was set to 5.08 cm/s of preview, which was similar as in Parts I and II, and corresponds to the "90°/220 m" condition in Fig. 7.4. The plan-view had unity horizontal scaling, equal to the tethered view at $\tau=0$ s (see Fig. 7.4), yielding an equally large displayed error $e^d(t)$ in all four conditions; thereby, any measured changes in control behavior must be due to linear perspective. Pictures of all four displays are shown in Fig. 7.7.

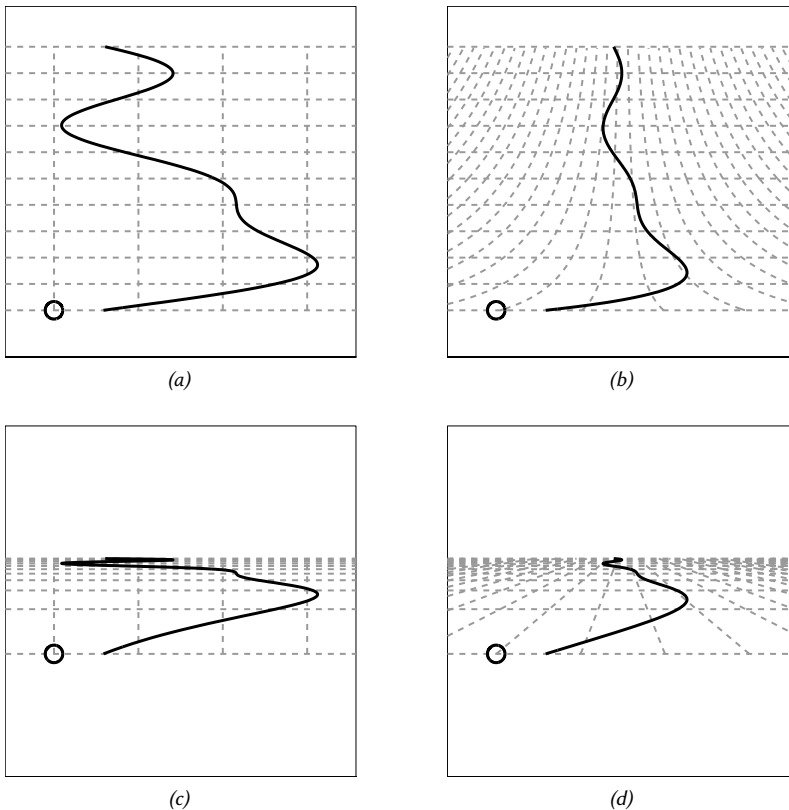


Figure 7.7: Layout of the four experimental displays: NP (a), HP (b), VP (c), and HVP (d); the grid was not visible during the experiment.

7.4.2. CONTROL VARIABLES

Controlled element: The CE had integrator dynamics, $H_{ce}(j\omega)=1.5/s$, with its gain of 1.5 tuned such that the operator could give accurate inputs, but would not reach the stick deflection limits during a normal run.

Display: The display showed the previewed target trajectory and the CE output in white, on a brown background. Grid lines, as included in Fig. 7.7 for clarification, were not shown. The CE output (circle) was a two-dimensional overlay, so subjects could only distinguish between conditions from the previewed target.

Preview time: The visual preview time τ_p was set to 2 s, well beyond reported critical preview times for integrator CE dynamics, according to [54, 55, 134] and Chapter 5.

Forcing functions: The target and disturbance signals' input frequencies were chosen such that an integer number k of their sinusoid periods exactly fitted the measurement time of 120 s. Double bands of input frequencies were used, to allow calculation of the coherence. The bandwidth of both signals was approximately 1.5 rad/s, above which the sinusoids' amplitudes were attenuated 20 dB. The target and disturbance signals standard deviations were 1.27 cm and 0.508 cm, respectively. Five different realizations of the target signal were used during the experiment to prevent subjects from remembering it, after repeated exposure. All forcing function parameters are given in Table 7.1.

Table 7.1: Forcing functions parameters, five target signals and one disturbance signal.

k_t	target signals f_t							disturbance signal f_d			
	A_t cm	ω_t rad/s	$\phi_{t,1}$ rad	$\phi_{t,2}$ rad	$\phi_{t,3}$ rad	$\phi_{t,4}$ rad	$\phi_{t,5}$ rad	k_d	A_d cm	ω_d rad/s	ϕ_d rad
-								-			
2	0.630	0.105	5.017	5.185	2.676	4.473	4.483	5	0.252	0.262	0.939
3	0.630	0.157	4.313	0.570	1.602	1.772	2.604	6	0.252	0.314	2.487
8	0.630	0.419	0.000	1.297	3.207	0.721	4.614	11	0.252	0.576	5.016
9	0.630	0.471	3.158	4.984	5.360	0.904	4.954	12	0.252	0.628	1.985
14	0.630	0.733	6.193	4.283	5.540	1.954	0.557	18	0.252	0.942	1.359
15	0.630	0.785	0.044	2.953	4.250	2.709	3.057	19	0.252	0.995	1.105
26	0.630	1.361	0.257	5.641	4.175	0.208	4.215	31	0.252	1.623	4.734
27	0.630	1.414	0.650	2.567	6.001	5.051	5.770	32	0.252	1.676	1.821
40	0.063	2.094	3.791	4.138	2.878	1.891	3.604	58	0.025	3.037	4.937
41	0.063	2.147	0.290	6.022	5.151	2.129	3.005	59	0.025	3.089	5.563
78	0.063	4.084	2.651	1.896	3.165	0.190	5.865	93	0.025	4.869	4.183
79	0.063	4.136	2.236	4.554	6.094	5.892	1.513	94	0.025	4.922	0.350
110	0.063	5.760	4.384	4.724	3.065	1.727	2.292	128	0.025	6.702	5.330
111	0.063	5.812	2.281	1.166	4.500	1.281	4.865	129	0.025	6.754	4.830
148	0.063	7.749	2.039	3.571	0.499	4.448	1.819	158	0.025	8.273	6.123
149	0.063	7.802	4.257	0.384	2.712	1.652	1.398	159	0.025	8.325	3.631
177	0.063	9.268	3.665	4.293	4.570	5.477	1.165	193	0.025	10.105	5.327
178	0.063	9.320	1.511	4.202	2.161	0.959	2.601	194	0.025	10.158	5.996
220	0.063	11.519	2.355	0.843	4.464	4.042	2.919	301	0.025	15.760	2.593
221	0.063	11.572	1.286	5.611	3.022	1.221	2.209	302	0.025	15.813	3.733

7.4.3. APPARATUS

The experiment was conducted in the part-task simulator of the Human-Machine Interaction Laboratory (HMI-Lab) at TU Delft. Subjects were seated directly in front of the screen on which the display was shown, at a distance of approximately 75 cm. The screen was 36 by 29.5 cm, had a resolution of 1280 by 1024 pixels, and an update rate of 100 Hz. The image generator time delay was in the order of 20-25 ms. To generate control inputs, subjects used an electro-hydraulic servo-controlled side-stick, positioned at their right-hand side. It had a moment arm of 9 cm and could only rotate around its roll axis. The side-stick's torsional stiffness was 3.58 Nm/rad, its torsional damping 0.20 Nm-s/rad, its mass moment of inertia 0.01 kg-m², and its gain 0.44 cm/deg.

7.4.4. SUBJECTS AND EXPERIMENTAL PROCEDURE

The experiment was performed by eight motivated, male volunteers; their tracking experience ranged from novice to experienced. We explained that the experimental goal was to investigate the effect of linear perspective on HC behavior, without giving further information about the individual conditions. Subjects were simply instructed to track the target as well as possible, hence to always minimize the current tracking error $e(t)$. They were informed of their rights and agreed to these by signing a consent form.

The experiment was divided in two sessions of two conditions. Each session took place on a different day to reduce fatigue effects. To get subjects accustomed with the task and the displays, each condition was practiced at least twice before the measurements were started. Then the conditions were presented to the subjects in an order dictated by a balanced Latin-square design. When stable performance was achieved in a condition, generally after three to eight (128 s long) runs, the five actual measurement runs were recorded, after which subjects moved on to the next condition. On the second day, all four conditions were practiced once before the final two conditions were tested.

After each run the subjects were informed of the root-mean-square of their tracking error in that run, to motivate them to optimize their performance. The total experiment lasted about 3.5 hours per subject, approximately evenly distributed over the two sessions. In-between each two conditions a 15 minute break was taken to further reduce fatigue effects.

The time traces of the error $e(t)$, the CE output $x(t)$, and the operator's control actions $u(t)$ were recorded during the experiment at 100 Hz. From the 128 s of each of the recorded time-traces only the last 120 s were used for our analysis; the first 8 s, which contained most of the subjects' transient response, were used as run-in time.

7.4.5. DEPENDENT MEASURES

First, time traces of the control output were used to compare control behavior between conditions. Second, the variances of the error σ_e^2 and the control output σ_u^2 were used as measures for tracking performance and control activity, respectively. Third, the coherence was used as a measure for the linearity of the subjects' response. Fourth, nonparametric describing functions were used to compare HC behavior in the frequency domain. Fifth,

the describing functions were compared to the model fits to validate the model's ability to describe the HC's dynamics. Sixth, the VAF was used as a second measure for the model's fitness. Finally, the subjects' control behavior was quantified with the model parameters, the response gains K_n and K_f , and the vertical display coordinate v responded to.

7.4.6. DATA PROCESSING

The error and control output variances and the coherence were calculated per run. Before applying system identification, all signals were averaged over the five runs in the frequency domain to reduce the remnant contribution in the estimates [87]. Statistics were used to test for significant effects on the error and control output variances, and the model parameters. To reflect within-subject effects only, 95% confidence intervals were calculated after removing between-subject variability, by compensating each subject's data both with that subject's mean over the four condition and the grand mean over all subjects. A repeated-measures two-way ANOVA was used to deal with the experiment's two categorical independent variables: horizontal and vertical display scaling. Each dependent measure was analyzed with a separate test. For some measures, the collected samples in specific conditions were not normally distributed, thereby violating the normality assumption for parametric statistical tests. With no nonparametric equivalent test for a two-way repeated-measured ANOVA, and ANOVAs' known robustness against violations of the normality assumption [188], the ANOVA was still performed.

7.4.7. HYPOTHESES

Due to linear perspective, the previewed target trajectory ahead is horizontally compressed by $K_{d,u}(\tau)$ (see Section 7.2). Considering that the task involves lateral control, HCs can adapt to horizontal perspective by increasing their control gains K_n and K_f . Although ideally the HC inverts the display gains (so the closed-loop dynamics remain equal as in plan-view tasks), subjects in compensatory control tasks increased their control gains insufficiently to compensate for smaller displayed errors, while also increasing their response delay τ_v [178, 179]. Therefore, we hypothesize that:

- I: From constant to perspective horizontal scaling, HCs increase their response gains K_n and K_f , but insufficiently to invert the display gain ($K_{n,eff}$ and $K_{f,eff}$ decrease); HCs also increase their response delay τ_v [178, 179].

Linear perspective also compresses the previewed target ahead vertically, by $C_{d,v}(\tau)$. Assuming that this vertical compression does not affect perception, we hypothesize that:

- II: With and without vertical perspective scaling HC behavior is similar: subjects select the same two viewpoints on the previewed target ahead (characterized by τ_n and τ_f); due to the perspective transformation, however, these correspond to other vertical display coordinates v .

7.5. RESULTS

7.5.1. NONPARAMETRIC RESULTS

Control output

Fig. 7.8 shows representative time-traces of the measured control outputs. At low frequencies (slow, large amplitude oscillations) the control outputs are similar in all conditions, but at high frequencies (fast, small amplitude oscillations) the control outputs have different amplitudes and are out-of-phase.

Performance and control activity

Fig. 7.9 shows the tracking performance and control activity, the corresponding ANOVA results are given in Table 7.2. Overall, task performance is good, considering that the target signal's variance was 1.61 cm^2 . The total tracking performance decreases significantly when either horizontal or vertical perspective is added to the plan-view task (NP). However, when horizontal perspective is already present and vertical perspective is added (HP to HVP), performance improves (significant interaction effect). The total control activity is slightly lower when horizontal perspective is present (not significant).

At the disturbance input frequencies (black bars in Fig. 7.9), both performance and control activity are identical in all conditions (although some differences are significant, see Table 7.2). At the target and remnant frequencies performance drops markedly with horizontal perspective, while control activity decreases at the target frequencies and increases at the remnant frequencies (all significant effects); this suggests that subjects apply a less consistent and less effective control strategy. Similar as for the total performance, vertical perspective has a negative effect on performance at the target and remnant frequencies when added to plan-view tasks (NP to VP), but a positive effect when horizontal perspective is already present (HP to HVP; significant interaction effect).

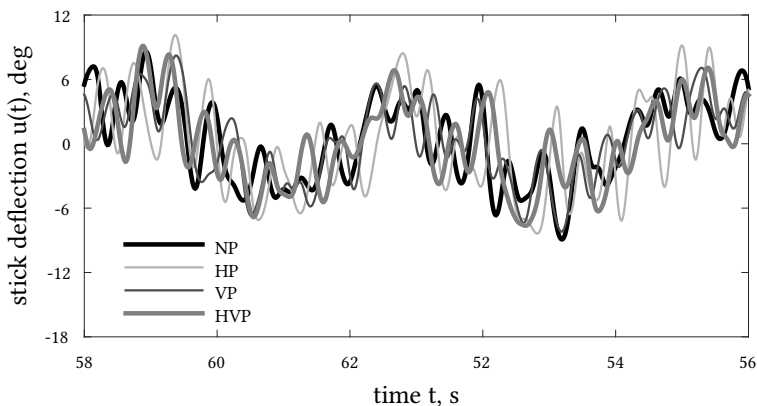


Figure 7.8: Measured control outputs for a representative subject, single-run data.

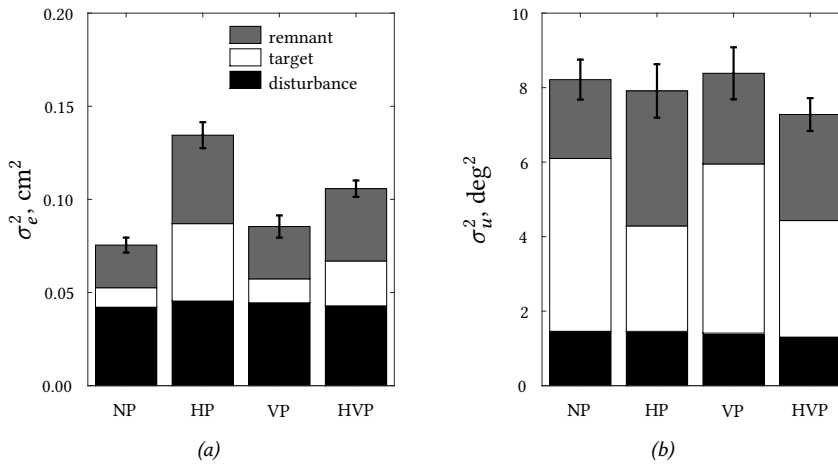


Figure 7.9: Variances of the error (a) and the control output (b), average over eight subjects; errorbars indicate 95% confidence intervals (corrected for between-subject variability).

Table 7.2: Error and control output ANOVA results. NV is the number of samples that violate the Lilliefors normality test ($p < .05$). Symbols “**”, “*”, and “-” indicate the result is highly significant ($p < .01$), significant ($p < .05$), and not significant ($p > .05$), respectively. Degrees of freedom (df) is always (1,7).

		NV	horizontal		vertical		hor. × vert.	
			F	sig.	F	sig.	F	sig.
error, e	total	0	174	**	8.04	*	180	**
	target	1	29.0	**	21.4	**	30.4	**
	disturb.	0	1.04	-	0.01	-	6.28	*
	remnant	1	49.6	**	2.04	-	36.5	**
	total	2	4.18	-	0.44	-	6.55	*
control output, u	target	0	49.0	**	0.40	-	1.97	-
	disturb.	0	2.47	-	21.5	**	11.0	*
	remnant	3	49.0	**	0.40	-	1.97	-

Coherence

The average coherence (Fig. 7.10) between the input signals and the control output is often close to 1, and always above 0.7. The closed-loop human-machine system is thus predominantly linear, even in perspective tasks, which justifies using a quasi-linear model to analyze the experimental data. Especially at frequencies below 2 rad/s the coherence is high. Here, the input signals’ amplitudes were large (see Section 7.4) and well visible, allowing for little observation noise. At higher frequencies, the input signals’ amplitudes were 10 times smaller; consequently, more observation noise is present and the coherence drops. With horizontal perspective scaling, the displayed excursions farther ahead are attenuated even more, yielding a lower coherence in the HP and HVP conditions. In these conditions where the coherence is low, the remnant is typically large (see Fig. 7.9b).

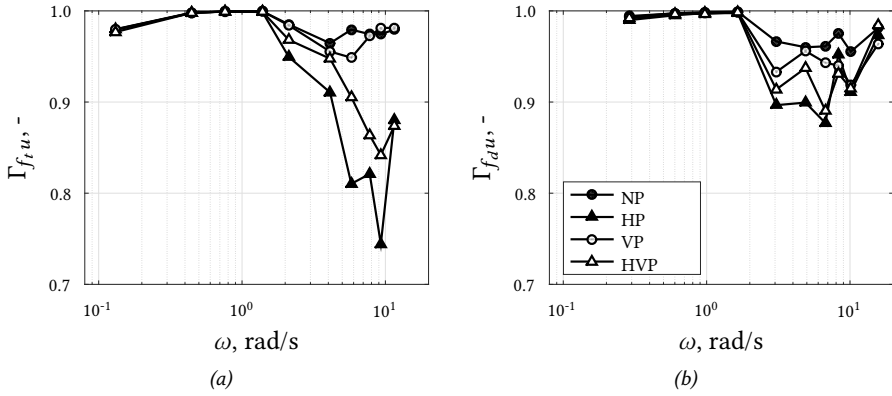


Figure 7.10: Coherence between the target (a) and disturbance (b) input forcing functions, and the HC control outputs; average over eight subjects.

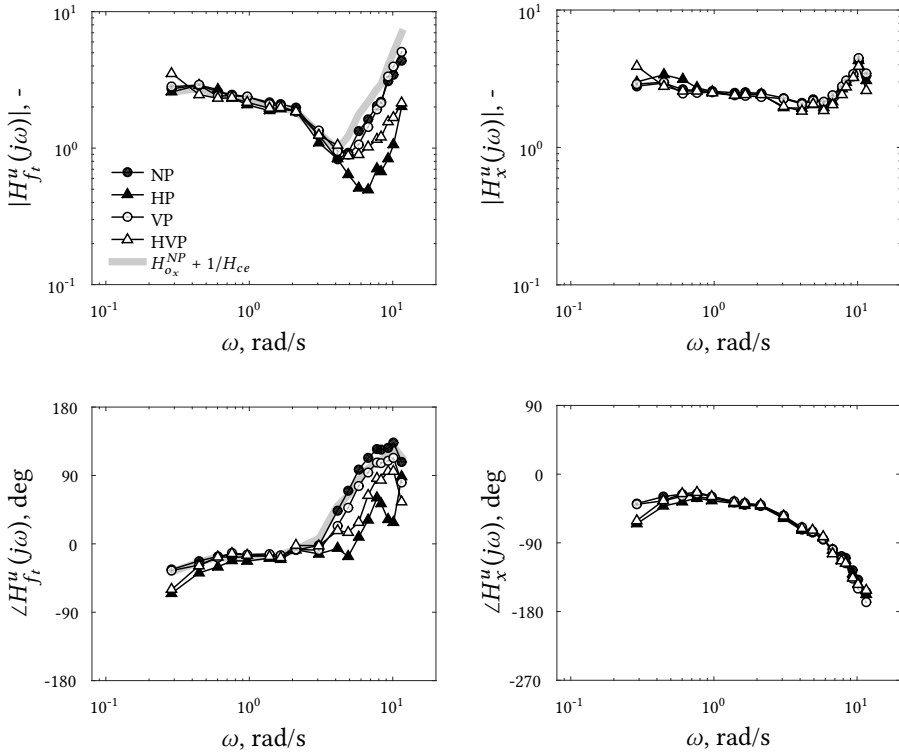


Figure 7.11: Nonparametric describing function estimates, average over eight subjects.

Describing functions

Fig. 7.11 shows the nonparametric describing function estimates. $H_x^u(j\omega)$ is similar in all conditions over the full input frequency range, which indicates that subjects hardly adapted their neuromuscular dynamics, response time delay, and internal-error feedback dynamics, see Eq. (7.14). In plan-view tasks (NP), $H_{f_t}^u(j\omega)$ approximates the dynamics that result in perfect target-tracking (gray line; $H_x^u(j\omega) + 1/H_{ce}(j\omega)$, see Chapter 4). Because $H_x^u(j\omega)$ is identical in all conditions (see Fig. 7.11b and d), the perfect target-tracking dynamics are also similar. With horizontal perspective (HP and HVP) the phase and magnitude required to perfectly track the target signal are matched less well, especially at high frequencies; this corresponds to the lower target-tracking performance in Fig. 7.9a.

7.5.2. MODELING RESULTS

Model fits

Fig. 7.12 shows both the nonparametric describing function estimates (markers) and the model fits (lines) for a representative subject. The full model fits (including lag-lead equal-

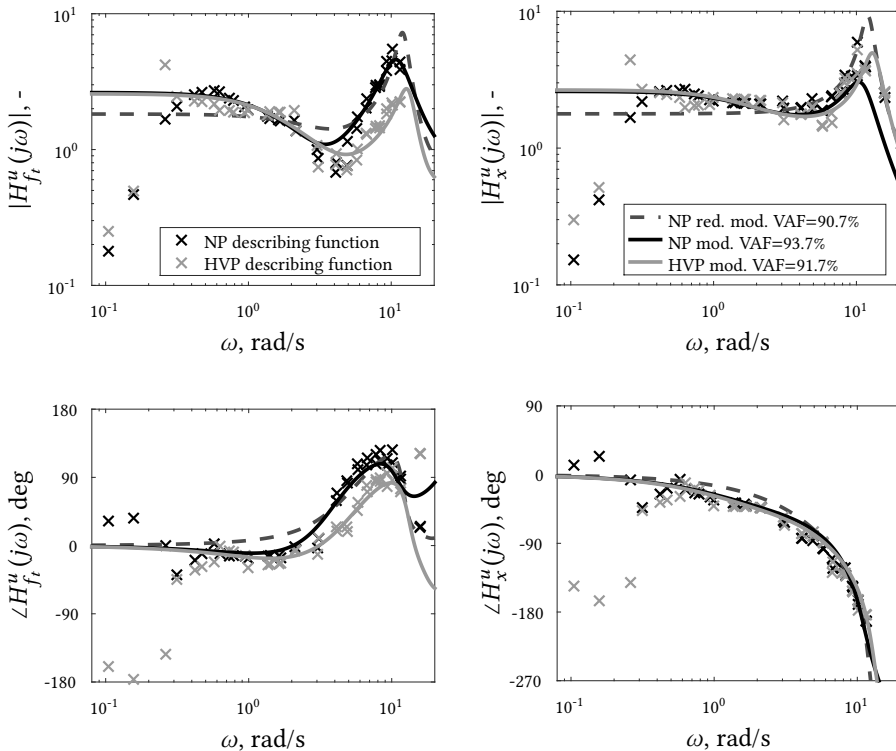


Figure 7.12: Estimated describing functions and model fits, single-subject data. The reduced model lacks the internal error response lead-lag equalization.

ization) coincide well with the estimated describing functions, which indicates that the model captures most of the subject's control dynamics, also in perspective tasks. A fit with the original model from Chapter 2, which lacked lag-lead equalization in integrator tasks (i.e., $H_{o_{e^*}}(j\omega) = K_{e^*}$), clearly matches the shape of the describing functions less well, and has a consistently lower VAF than the full model.

Variance accounted for

For most subjects, the model VAFs (Fig. 7.13a) are between 80% and 95%, which is higher than in Parts I and II and similar manual control modeling attempts [126]. In the HP condition the VAFs are slightly lower, which is in line with the larger remnant (see Fig. 7.9b). The consistently high VAFs indicate that the model describes all subjects' control behavior well, even in perspective tasks.

Model parameters

Fig. 7.13 also shows the estimated model parameters, corresponding ANOVA results are given in Table 7.3. The far-viewpoint response gain $K_{f,eff}$ (Fig. 7.13d) is most consistently affected by linear perspective; this was expected, as perspective deformations are largest far ahead. $K_{f,eff}$ is substantially lower with horizontal perspective (significant effect). The smaller visual stimulus in control direction thus evokes less aggressive control behavior, similar as in compensatory tracking tasks [178, 179]. Vertical perspective results in a higher $K_{f,eff}$, but only when horizontal perspective is already present (HP to HVP; significant interaction effect). Higher values of $K_{f,eff}$ correspond closely to a better tracking performance (see Fig. 7.9a). Effects of linear perspective on the effective near-viewpoint gain $K_{n,eff}$ (Fig. 7.13e) are similar to $K_{f,eff}$, but due to larger between-subject variations the statistical results are less pronounced. No systematic adaptation is visible for the near- and far-viewpoint look-ahead times, τ_n and τ_f (Figs. 7.13h and 7.13g), nor for the low-pass filter time-constant $T_{l,f}$ (Fig. 7.13j).

The internal-error response gain K_{e^*} (Fig. 7.13f) is slightly lower in all three perspective tasks (compared to NP), but this effect is only significant for vertical scaling. The lead and lag equalization time-constants, T_{L,e^*} and T_{l,e^*} (Figs. 7.13b and 7.13c), are both significantly lower with horizontal perspective. The lag time-constant is always about twice as large as lead time-constant, reflecting the low-frequency lag-lead equalization visible in Fig. 7.12. The response time delay τ_v (Fig. 7.13i) is slightly, but not significantly, higher in all conditions with perspective scaling, compared to the NP condition, which is similar as in compensatory tracking tasks where the error is displayed smaller [178, 179]. Finally, subjects also adapt the properties of their neuromuscular system, but only to horizontal perspective; here, the neuromuscular break frequency ω_{nms} is significantly higher (Fig. 7.13k), while the neuromuscular damping ratio ζ_{nms} (Fig. 7.13l) is significantly lower.

7.5.3. HUMAN CONTROLLER ADAPTATION

Horizontal display direction

The effective gains $K_{n,eff}$ and $K_{f,eff}$ (Figs. 7.13e and 7.13d) are lumped combinations of the HC and the display gains, see Eq. (7.15). To better illustrate HCs' control adaptation to horizontal perspective, Fig. 7.14a shows the separate contributions of the far-viewpoint

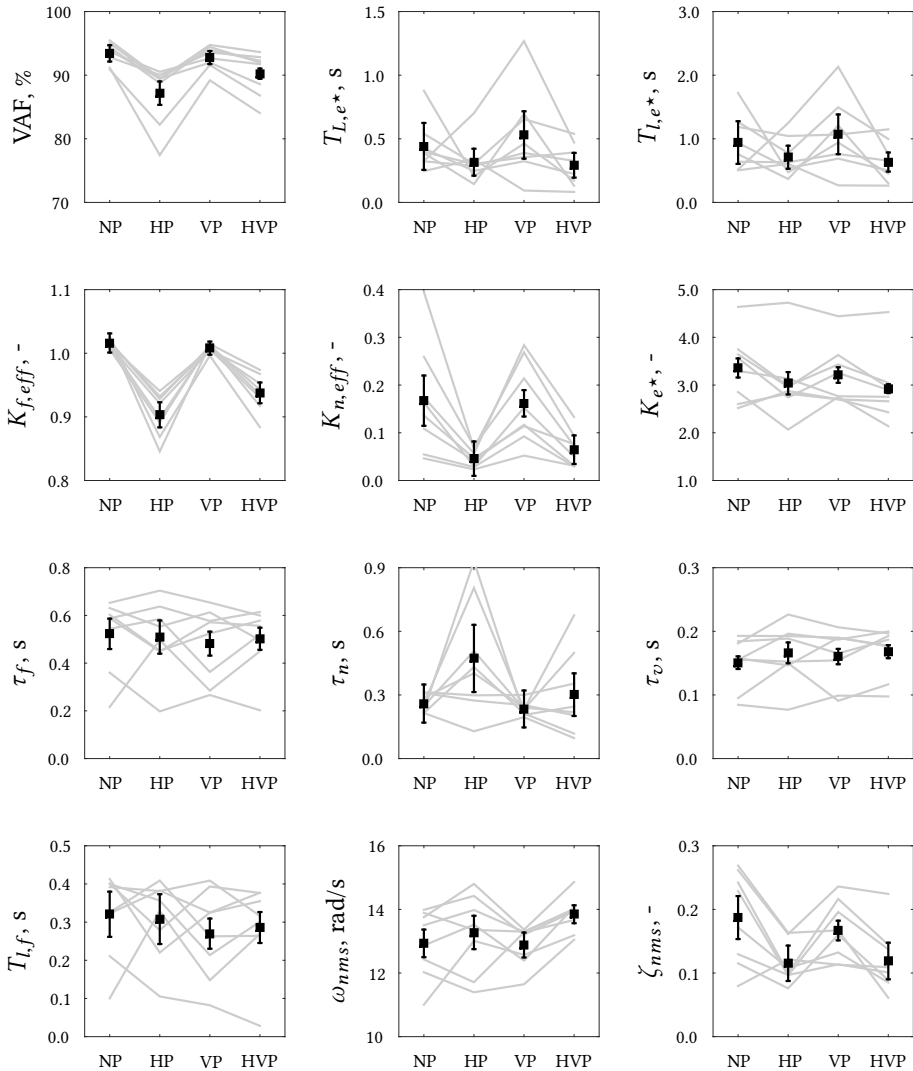


Figure 7.13: Estimated model parameters: individual-subject data (gray lines), and average over eight subjects with 95% confidence intervals (corrected for between-subject variability).

gains K_f , $K_{f,eff}$, and $K_{d,u}(\tau_f)$, which are most strongly affected by perspective. HCs more than double their response gain K_f (black markers) to compensate for the reduced display gains $K_{d,u}(\tau_f)$ (white markers) with horizontal perspective. In other words, subjects respond much more aggressively to the reduced visual stimulus. This adaptation is still less than required to fully invert the display gains, as the *combined* gain $K_{f,eff}$ is consistently lower with horizontal perspective (HP and HVP conditions). Results for the near-viewpoint gains are similar, see also Fig. 7.13.

Table 7.3: Estimated parameters ANOVA results. NV is the number of samples that violate Lilliefors normality test ($p < .05$). Symbols “**”, “*”, and “-” indicate the result is highly significant ($p < .01$), significant ($p < .05$), and not significant ($p > .05$), respectively.

	NV	horizontal		vertical		hor. × vert.	
		F	sig.	F	sig.	F	sig.
$K_{f,eff}$	0	80.7	**	3.77	-	17.6	**
τ_f	1	0.01	-	1.67	-	0.65	-
$T_{l,f}$	1	0.00	-	2.60	-	0.47	-
$K_{n,eff}$	0	17.2	**	0.21	-	1.23	-
τ_n	0	3.54	-	5.54	-	2.93	-
K_{e^*}	2	5.50	-	6.34	*	0.08	-
T_{L,e^*}	1	7.90	*	0.23	-	0.46	-
T_{l,e^*}	0	8.53	*	0.06	-	0.47	-
τ_v	1	3.28	-	0.81	-	0.53	-
ω_{nms}	1	11.2	*	1.26	-	3.04	-
ζ_{nms}	0	15.2	**	0.32	-	1.85	-

Vertical display direction

Due to the perspective transformation, the same point on the previewed target ahead corresponds to a different vertical display location in plan-view and perspective conditions. Fig. 7.14b shows the points on the display that subjects responded to, which clearly illustrates the substantial adaptation required to compensate for vertical perspective deformations. With the introduction of vertical perspective (NP and HP to VP and HVP), subjects shift their near-viewpoint from about 3.5 to 1.5 cm below the screen center, and their far-viewpoint from about 3 to 0.5 cm below the screen center. Moreover, the viewpoints' locations shift from about 25% above the start of the previewed target (at $\tau=0$ s in Fig. 7.14b) to about 25% below the end of the previewed target (at $\tau=2$ s).

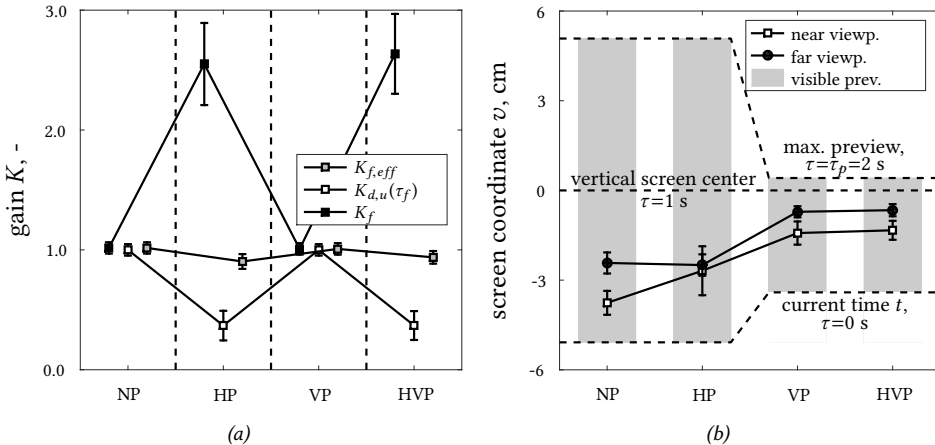


Figure 7.14: Estimated far-viewpoint response gain adaptation (a) and the vertical locations of the near- and far-viewpoints on the display (b).

7.6. DISCUSSION

In the experiment, it was measured how linear perspective affects HC use of preview information. With horizontal perspective scaling, the hypothesized increase of the response gains K_n and K_f (H.I) was indeed found. Subjects thus responded more aggressively to lower amplitude of the displayed target ahead, but, as expected, not aggressively enough to completely invert the display gain ($K_{n,eff}$ and $K_{f,eff}$ were lower than in the plan-view task). HCs also slightly increased their response time-delay τ_v , *confirming* H.I. HC adaptation to perspective scaling of a previewed target trajectory appears to be similar to their adaptation to a reduced scaling of the visual error in compensatory tracking tasks, which also evokes a less aggressive, and more delayed response [178, 179]. Due to the wider variety of HC behavior compared to compensatory tracking, we recommend future preview tracking investigations to test more than the eight subjects used here, to avoid normality violations and improve confidence in the results.

We further hypothesized that vertical perspective scaling would not affect HC behavior (H.II). Indeed, subjects selected approximately the same viewpoints τ_n and τ_f s ahead on the previewed target in conditions with and without vertical perspective, despite their different vertical locations v on the display. However, H.II cannot be fully confirmed, as the results point to a substantial interaction between horizontal and vertical perspective. When vertical perspective is added to a task where horizontal perspective is already present (HP to HVP), subjects reduce their remnant, respond with a higher gain $K_{f,eff}$, and improve their tracking performance. Comparison of the displays in Figs. 7.7b and 7.7d yields a possible explanation: the “unnatural” exponential magnification of the approaching previewed target in the HP condition is likely more difficult to anticipate on than the familiar full linear perspective in the HVP condition.

7

The results in the plan-view condition differ from those in Chapters 4 and 5, where a similar experiment with integrator dynamics was performed. Compared to those experiments, here, the forcing functions contained less high-frequency power, and the displayed signals were magnified horizontally (to keep the target far ahead well visible in perspective conditions). Amongst others, this resulted in a much more aggressive internal error response, as visible from the magnitude of $H_x^u(j\omega)$, which is about two times higher than in Chapters 4 and 5. Likely, the higher horizontal display scaling evoked the more aggressive control behavior, which again emphasizes the importance of proper display scaling in manual control tasks.

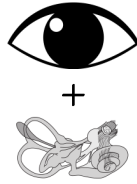
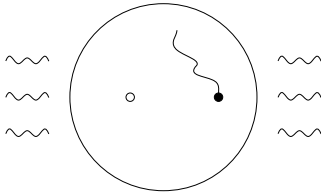
The model for plan-view preview tracking tasks from Chapter 2 accurately described the measured behavior, also in our perspective tasks. For such perspective tasks, it is convenient to lump the linear perspective transformation and the HC dynamics, so the model is mathematically equivalent as for plan-view tasks. Although the lumped model’s inputs are no longer the visual stimuli as sensed by the HC, but the actual target and CE output signals before the perspective transformation, the effective gains can be interpreted similar as the HC gains in plan-view tasks.

All subjects were found to apply lag-lead equalization at the lower frequencies, opposed to the pure proportional control strategy often observed in compensatory tracking tasks

with integrator CE dynamics [6]. While it was not yet recognized as such, similar lag-lead equalization is visible in the preview tracking results in Chapter 2. Preview information seems to evoke such behavior, which is perhaps best explained as “waiting” (i.e., lagging) for the low-frequency portion of the cognitively calculated, internal error to build up, before responding to it. Future investigations into preview tracking tasks with integrator CE dynamics can include the lag-lead equalization in the error response model.

7.7. CONCLUSION

This chapter quantified how linear perspective affects human use of preview information in manual control tasks, using experimental results and both nonparametric and parametric system identification techniques. The compression of the trajectory ahead due to linear perspective evokes less aggressive control behavior and inferior task performance, mainly due to reduced visual stimuli in the control direction (i.e., horizontal perspective scaling). Perspective deformations in the non-controlled (vertical) direction affect human control behavior only marginally. We conclude that humans adopt similar near- and far-viewpoint response mechanisms in plan-view and perspective preview tracking tasks, for perspective transformations that approximate the view on the road during driving or cycling. The validity of the previously derived quasi-linear model for preview tracking tasks is extended to perspective tasks, and can thereby be used to design and evaluate man-machine systems in such more realistic control tasks.

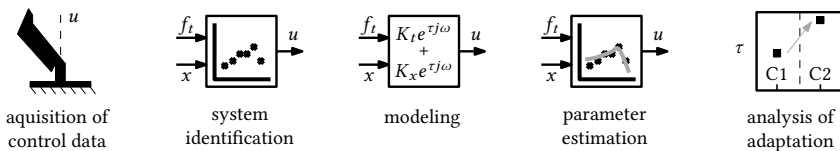


8

EFFECTS OF VESTIBULAR FEEDBACK

Part I of this thesis proposed a novel model for preview tracking tasks, and Part II used this model to quantify how humans adapt their control behavior to crucial task variables. Without exception, these tasks provided only visual feedback, while real-world control task may provide a wealth of multimodal sensory feedbacks. To extend the obtained model and our understanding of preview tracking behavior to a wider range of control tasks, this chapter quantifies how humans use physical motion feedback for control in preview tasks, a cue that is often available due to vehicle accelerations. A human-in-the-loop experiment is performed in a motion simulator, with the motion feedback switched either on or off. The human's visual feedforward and (lumped) visual-vestibular feedback control dynamics are estimated, and, based on this, a combined visual-vestibular preview control model is proposed. Estimated model parameters then explicitly quantify the human's, otherwise lumped, visual preview and vestibular feedback control responses.

Steps of the cybernetic approach involved:



Parts of this chapter have been published as:

Title The Effects of Motion Feedback in Manual Preview Tracking Tasks
Conference AIAA Modeling and Simulation Technologies Conference, Denver, Colorado, 2017
Authors K. van der El, J. Morais Almeida, D.M. Pool, M.M. van Paassen, and M. Mulder

8.1. INTRODUCTION

HUMANS are *multimodal* controllers, who integrate various *visual* and *vestibular* cues when controlling a vehicle [189]. Such multimodal cues are reproduced in simulators (e.g., for driving or flying) to give the human controller (HC) the sensation of the actual control task, while providing a safe and efficient environment for training and research. For many control tasks, however, it not fully understood how HCs use and weight the different modalities in determining their control actions. As such, it is not clear whether extensive simulator hardware (like a large motion system) is required to evoke realistic HC behavior, and to achieve effective training.

The only task where the HC's response to visual and vestibular cues has been extensively measured is *single-axis compensatory tracking* [45, 46, 111, 112, 189, 190]. Compensatory displays show a single error signal, like the offset between an aircraft pitch and the glide slope while landing. Using multiloop system identification, a separate Frequency-Response Function (FRF) can be obtained for the human's control dynamics with respect to each sensory input (e.g., the visual error and the vestibular acceleration). Modeling of the such observed dynamics has led to fundamental new insights in HC behavior, and facilitated quantifying the importance of motion feedback in vehicle control [111, 190], quantifying human skill development in motion simulators [112], and improvements in simulator motion cueing [157]. Unfortunately, few practical control tasks are purely compensatory, and generalization of the effects of motion feedback to more practical control tasks is essential for further improving our understanding of HC behavior, and improving simulators and training practices.

In most everyday control tasks HCs can anticipate the *future* target trajectory the vehicle needs to follow, for example through visual *preview* of the runway or road ahead [61, 90, 91, 94]. Such preview of the target trajectory facilitates feedforward control, through which experienced HCs can compensate for their own response delay, leading to superior performance over feedback-only tasks like compensatory tracking (see [191] and Parts I and II of this thesis). As of yet, it is unclear whether and how HCs use physical motion feedback for control in tasks with preview.

Perhaps the only technique available to unambiguously measure whether and how HCs use motion feedback, is frequency-domain, *multiloop* system identification [86, 87]. Unfortunately, the number of HC responses that be separately measured (i.e., disentangled) is limited to the number of uncorrelated external excitation signals, the "forcing functions". In most vehicle control tasks HCs are to follow a certain trajectory, or target (e.g., a glide slope or road), with their vehicle, while simultaneously mitigating effects of disturbances like wind gusts [45, 90]. These two forcing functions allowed for disentangling the visual (error) response and vestibular response in compensatory tracking tasks [190], and the feedback and feedforward responses in preview tracking tasks (in Parts I and II of this thesis). In visual-vestibular preview tasks, HCs likely initiate *three* separate responses: feedforward, visual feedback, and vestibular feedback. This yields a fundamental measurement problem, as only *two* forcing functions are available. Consequently, in preview tracking tasks it is only possible to measure *lumped combinations* of the HC's responses.

The goal of this chapter is two-fold: first, to quantify the effects of motion feedback on HC behavior in preview tracking tasks, and, second, to model this HC behavior. Measurements are presented from a human-in-the-loop experiment in the SIMONA Research Simulator (SRS) at TU Delft, in which subjects performed the same target-tracking and disturbance-rejection yaw control task with and without motion feedback, both with a compensatory and a preview display. First, the effects of motion feedback are quantified nonparametrically, using measures for task performance and control activity, and estimated open-loop dynamics. Moreover, two FRFs are estimated using multiloop system identification; because it is not possible to independently identify the presence and dynamics of HCs' vestibular response in visual-vestibular preview tasks, as opposed to compensatory tasks, the two tasks are explicitly compared to quantify effects of motion feedback. Second, a model is proposed for HC behavior in visual-vestibular preview tracking tasks, which extends previous models for visual-vestibular compensatory tracking [6, 190] and visual-only preview tracking (from Chapter 2). Model parameters are estimated to explicitly quantify HC behavior, including the relative contributions of the visual and vestibular response channels to the HC's control output. Finally, the model is verified with measures for its quality-of-fit and its parameter correlations.

This chapter is structured as follows. Section 8.2 introduces manual control in tracking tasks with compensatory and preview displays, and with motion feedback. The performed human-in-the-loop experiment is explained in Section 8.3, followed by the frequency-domain data analysis techniques (i.e., system identification) in Section 8.4. Experimental results are presented in Sections 8.5 and 8.6, split between the nonparametric and model fitting results, respectively. This chapter ends with a discussion and our main conclusions in Sections 8.7 and 8.8.

8.2. VISUAL-VESTIBULAR MANUAL CONTROL

8

In this chapter, a combined target-tracking and disturbance-rejection yaw control task is considered, comparable to rotating a helicopter or gun-turret around its vertical axis. The yaw axis was used as rotations in the horizontal plane do not lead to effects of gravity, which would otherwise need to be corrected for. HCs give control inputs $u(t)$ to follow the target trajectory $f_t(t)$ as well as possible, while the vehicle, or Controlled Element (CE) is simultaneously perturbed by disturbance $f_d(t)$. The CE dynamics are fixed to a double integrator, that is, $H_{ce}=5/(j\omega)^2$, because these typically evoke a strong vestibular response from the HC due to the required lead equalization [45, 46, 111, 112, 189, 190, 192, 193]. The CE output $x(t)$ is the yaw angle.

8.2.1. COMPENSATORY TRACKING

In compensatory tracking tasks, HCs are only presented with the error $e(t)$ between the target signal and the CE yaw angle: $e(t)=f_t(t)-x(t)$, see Fig. 8.1a. Fig. 8.1c shows a control diagram of the task, with two channels that account for HCs' visual response $H_{o_e}(j\omega)$ and vestibular (or motion) response $H_{o_m}(j\omega)$ [190]. This model extends the *crossover model* for visual-only compensatory tracking tasks [6] with a vestibular channel. In this "quasi-

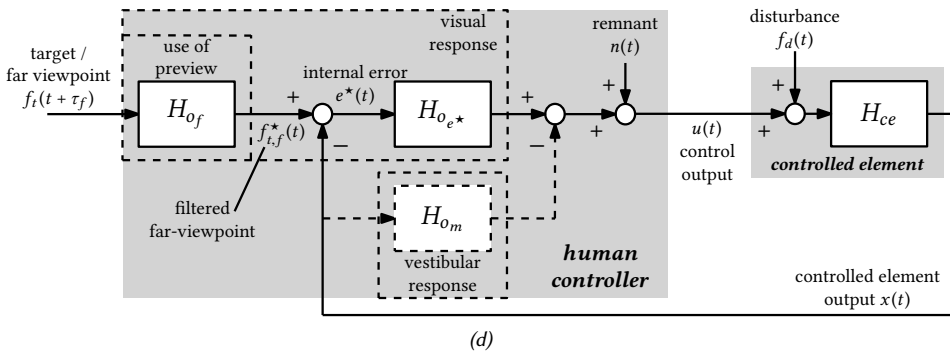
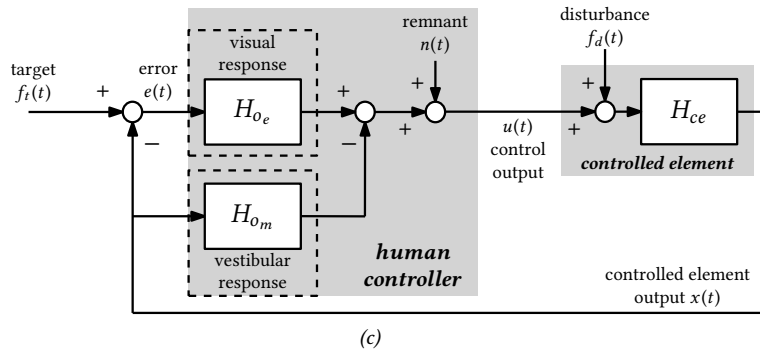
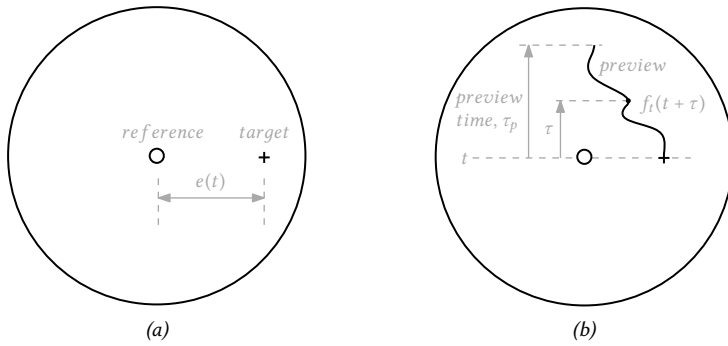


Figure 8.1: Compensatory (a) and preview (b) displays, and control diagrams of HC models for compensatory (c) and preview tasks (d). The compensatory model has visual and vestibular feedback channels, and is adapted from [190]. The preview model is identical to the visual-only preview tracking model from Part I, augmented with a vestibular feedback channel, which is connected with dashed paths to emphasize that it is as of yet unclear whether HCs actually initiate this response.

linear” modeling framework, nonlinear and time-varying HC behavior, and perception and motor noise are lumped together and accounted for by the *remnant* $n(t)$.

In tasks with double integrator CE dynamics, the (linear) visual-error response dynamics are accurately captured by a model that includes a response gain K_e , time delay τ_v , and lead time-constant $T_{L,e}$ [6]:

$$H_{o_e}(j\omega) = K_e(1 + T_{L,e}j\omega)e^{-\tau_v j\omega}H_{nms}(j\omega). \quad (8.1)$$

The HC’s neuromuscular system dynamics $H_{nms}(j\omega)$ are often represented as an underdamped second-order mass-spring-damper system, with natural frequency ω_{nms} and damping ratio ζ_{nms} [111]:

$$H_{nms}(j\omega) = \frac{\omega_{nms}^2}{(j\omega)^2 + 2\zeta_{nms}\omega_{nms}j\omega + \omega_{nms}^2}. \quad (8.2)$$

The HC’s vestibular response dynamics in the considered rotational acceleration control task can be modeled as [194]:

$$H_{o_m}(j\omega) = (j\omega)^2 H_{scc}(j\omega) K_m e^{-\tau_m j\omega} H_{nms}(j\omega), \quad (8.3)$$

where K_m and τ_m are the vestibular response gain and delay, respectively. $H_{scc}(j\omega)$ represents the semicircular canal (scc) dynamics, which sensory input (the yaw *acceleration*) is obtained by the double differentiation operation $(j\omega)^2$ on the $x(t)$, yaw *angle* input to the HC (see Fig. 8.1c). The semicircular canal dynamics can be approximated by [193]:

$$H_{scc}(j\omega) = \frac{5.97(0.11j\omega + 1)}{(5.9j\omega + 1)(0.005j\omega + 1)}. \quad (8.4)$$

8.2.2. PREVIEW TRACKING

8

In preview tasks, the future target trajectory is visible ahead, up to preview time τ_p . The display used in this study is shown in Fig. 8.1b: the previewed target moves down over the screen, allowing HCs to anticipate the lateral movements of the cross which represents the current target yaw angle. The display is oriented “inside-out” such that the stationary white circle corresponds to the CE’s current yaw angle $x(t)$.

The model we propose for visual-vestibular preview tracking tasks is shown in Fig. 8.1d. It contains the model for visual-only preview tracking tasks from Part I, extended with the vestibular response that was found in compensatory tracking tasks. The visual-only preview model extends the classic compensatory model by accounting for HC use of preview with prefiltering dynamics $H_{o_f}(j\omega)$. The model assumes that HCs use preview by responding to the target signal τ_f s ahead (around 1 s in tasks with double integrator CE dynamics (see Chapter 4), after smoothing the target signal in this *far viewpoint* first:

$$H_{o_f}(j\omega) = K_f \frac{1}{1 + T_{l,f}j\omega}, \quad (8.5)$$

with K_f the response gain and $T_{l,f}$ the low-pass filter time-constant. From the resulting filtered far-viewpoint $f_{t,f}^*(t)$ HCs calculate an “internal” error $e^*(t)$, to which they respond

with identical dynamics $H_{o_{e^*}}(j\omega)$ as in compensatory tasks, see Eq. (8.1). The error $e^*(t)$ is thus not equal to the error in the compensatory model, but to:

$$E^*(j\omega) = F_{i,f}^*(j\omega) - X(j\omega) = H_{o_f} e^{\tau_f j\omega} F_i(j\omega) - X(j\omega), \quad (8.6)$$

with the capital denoting the Fourier transforms of the respective signals. Note that the preview model is identical to the compensatory model in Fig. 8.1c when $e^*(t)=e(t)$, that is, when $K_f=1$ and $T_{i,f}=\tau_f=0$ s (zero seconds of preview).

The far-viewpoint low-pass filter in Eq. (8.5) reflects that HCs eliminate the higher frequencies from the target signal, which oscillate rapidly and are therefore difficult to track. Some HCs, however, also attempted to track these high frequencies in the experiments of Parts I and II, using an additive, parallel, open-loop *near-viewpoint* response. The near-viewpoint response is typically weak in tasks with double integrator CE dynamics, so it is safe to neglect it here (it is not included in Fig. 8.1d).

8.2.3. EFFECTS OF MOTION FEEDBACK

Effects of physical motion feedback have been elaborately studied for compensatory tracking task [45, 46, 111, 112, 189, 190, 192, 193]. Hosman [193] summarized the benefits of a vestibular-loop closure as follows: “*With the lead information supplied by the motion cues, the operator does not need to supply as much visual lead [...]. He can also increase his gain and achieve a higher crossover frequency because his effective time delay is reduced.*”

Eq. (8.3) shows that responding to the motion cues indeed yields lead information on the CE output, as H_{scc} approximate integrator dynamics between 0.1 and 10 rad/s, the frequency region where most manual control occurs. Thereby, the information perceived by the HC from the semicircular canals is in fact $(j\omega)^2 H_{scc}(j\omega) X(j\omega) \approx K_{scc} s X(j\omega)$, which is proportional to the *derivative* of $x(t)$, hence providing *lead* information. Moreover, vestibular motion perception has a shorter delay than the visual loop [112, 193] (i.e., $\tau_m < \tau_v$). This is beneficial especially when lead equalization is required, as visual observation of the displayed error’s velocity typically leads to a higher visual perception delay [6, 42]. As a result of the vestibular loop closure, HCs can generate less visual lead (lower T_{L,e^*}), and increase their visual control gain K_{e^*} [45, 46, 111, 112, 189, 190, 192, 193].

These adaptations to *motion feedback* yield improved task performance, both in target-tracking *and* disturbance rejection [45, 46, 111, 112, 189, 190, 192, 193]. A compilation of ten studies in [195] shows that the disturbance crossover frequency typically increases when motion feedback becomes available, but that the disturbance phase margin, the target crossover frequency, and the target phase margin are approximately invariant.

Availability of *preview information* mainly benefits target tracking, yielding far higher crossover frequencies and phase margins as compared to zero-preview tracking tasks (see Chapters 4 and 6). Interestingly, similar to having physical motion available, longer preview times also evoke a decrease in the visual lead time-constant T_{L,e^*} and an increase in the gain K_{e^*} (Chapter 5); the disturbance crossover frequency and phase margin are invariant, however (Chapter 4). These different benefits, and different control mechanisms involved, lead to the following hypothesis: *HCs use physical motion feedback in preview*

tracking tasks to close a similar vestibular feedback-loop as they do in compensatory tasks. An experiment was performed to test this hypothesis.

8.3. THE EXPERIMENT

8.3.1. INDEPENDENT VARIABLES

The experiment had two independent variables: the visual display and the presence of physical motion. The two tested displays were the compensatory and preview displays of Figs. 8.1a and 8.1b. For the latter, the preview time τ_p was set to 2 s, well above the critical preview time (see Chapter 5), beyond which HC behavior is invariant with preview time variations. Both displays were tested without motion feedback (static task) and with one-to-one motion feedback, yielding a total of four conditions.

8.3.2. APPARATUS AND CONTROL VARIABLES

The experiment was conducted in the SIMONA Research Simulator (SRS), Fig. 8.2, which has a hexapod motion base with a maximum yaw rotation of ± 41.6 deg. Subjects were seated in the right seat of the simulator; rotations were applied around this position to minimize perceived surge and sway acceleration, and no compensation for specific forces was needed. Subjects used an electric side-stick on their right-hand side to give inputs to the CE. The stick was configured to rotate only around its roll axis; its mass and damping were negligible and its gain was 0.133 rad/deg, yielding an input of 1.33 rad to the CE for every 10 deg stick deflection. The task was presented on a display directly in front of the subjects, with bright green lines and indicators on a black background. The radii of the circular display and the CE output marker were 11.5 cm and 0.23 cm, respectively; the target crosshair lines were 0.32 cm long, the preview was scaled to 0.22 s/cm, and yaw angles were displayed at 2.08 deg/cm.



Figure 8.2: SIMONA Research Simulator (SRS).

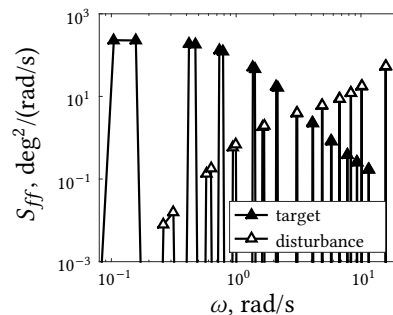


Figure 8.3: Forcing functions power spectra.

8.3.3. FORCING FUNCTIONS

The forcing functions were constructed as multisines to facilitate analysis of the experimental data with frequency-domain system identification techniques:

$$f_{t,d}(t) = \sum_{i=1}^{20} A_{t,d}[i] \sin(\omega_b k_{t,d}[i]t + \phi_{t,d}[i]) \quad (8.7)$$

Here, f is the respective forcing function signal, each the sum of 20 individual sine components i that have frequency $\omega_b k[i]$, amplitude $A[i]$, and phase $\phi[i]$ (see Table 8.1 for their values). To avoid spectral leakage, the frequencies are integer multiples k of the fundamental measurement frequency $\omega_b = 2\pi/120 \approx 0.0524$ rad/s, for the measurement time of 120 s. The frequencies of the two forcing functions were mutually exclusive (yielding two uncorrelated signals) and equal to those in the preview tracking experiments in Parts I and II. To obtain a realistic task, the amplitudes at higher frequencies were attenuated using the magnitude distribution of a second-order low-pass filter [45, 46, 111]:

$$H_A(j\omega) = \frac{(1 + 0.1j\omega)^2}{(1 + 0.8j\omega)^2} \quad (8.8)$$

Moreover, the disturbance signal was prefiltered with the inverse of the CE dynamics, because this signal enters the loop before the CE (see Fig. 8.1). The spectra of the forcing functions are shown in Fig. 8.3. The standard deviation of the target and disturbance

Table 8.1: Amplitudes, frequencies and phases of the target and disturbance forcing function signals.

		target signals f_t						disturbance signal f_d			
k_t	A_t	ω_t	$\phi_{t,1}$	$\phi_{t,2}$	$\phi_{t,3}$	$\phi_{t,4}$	$\phi_{t,5}$	k_d	A_d	ω_d	ϕ_d
-	deg	rad/s	rad	rad	rad	rad	rad	-	deg	rad/s	rad
2	0.308	0.105	0.028	1.156	1.278	4.752	5.105	5	0.002	0.262	4.755
3	0.305	0.157	2.299	1.783	2.651	5.326	5.492	6	0.003	0.314	4.937
8	0.279	0.419	5.953	3.655	2.051	6.104	2.667	11	0.008	0.576	2.393
9	0.272	0.471	3.439	3.364	0.485	2.841	2.400	12	0.009	0.628	3.470
14	0.232	0.733	1.048	3.212	4.286	0.963	4.079	18	0.016	0.942	5.278
15	0.223	0.785	1.400	5.901	1.352	4.758	3.739	19	0.017	0.995	4.326
26	0.144	1.361	1.621	3.074	1.594	0.771	1.172	31	0.028	1.623	4.749
27	0.139	1.414	1.898	1.524	4.749	4.072	6.025	32	0.028	1.676	0.955
40	0.085	2.094	2.102	2.243	3.535	1.349	1.687	58	0.040	3.037	1.814
41	0.082	2.147	5.420	0.597	0.077	1.743	4.791	59	0.040	3.089	4.670
78	0.031	4.084	3.360	5.938	0.100	3.871	4.744	93	0.050	4.869	3.346
79	0.030	4.136	5.704	4.734	5.516	6.049	1.418	94	0.050	4.922	0.692
110	0.019	5.760	5.208	1.430	5.653	3.549	2.992	128	0.060	6.702	2.158
111	0.018	5.812	0.444	4.074	5.578	4.000	3.609	129	0.060	6.754	2.564
148	0.013	7.749	1.701	2.713	5.727	0.166	3.945	158	0.070	8.273	3.903
149	0.012	7.802	5.457	1.973	5.008	4.221	1.730	159	0.071	8.325	3.219
177	0.010	9.268	5.847	4.698	5.807	0.152	3.959	193	0.085	10.105	1.609
178	0.010	9.320	1.693	1.381	1.580	4.410	3.193	194	0.086	10.158	4.606
220	0.008	11.519	6.016	4.907	4.945	2.747	3.365	301	0.148	15.760	0.889
221	0.008	11.572	0.713	3.805	3.827	1.411	2.490	302	0.149	15.813	5.525

signals were 4.5 and 1.8 deg, respectively. Random phases were generated for the individual sine-components, aiming for an average crest factor [175]. Five different target signals were generated, differing only by their phases $\phi[i]$, to avoid subjects from memorizing the signals after repeated exposure. As the disturbance is not explicitly visible, it is impossible for subjects to memorize, so the same signal could be used for all runs.

8.3.4. EXPERIMENTAL PROCEDURE

The experiment was performed by eight male volunteers aged between 22 and 32 years, with no to extensive prior tracking experience. Subjects were briefed before participating, and gave informed consent. They were familiarized with the task before the actual experiment commenced by performing at least one run of each condition. After this, the four conditions were presented to the subjects one by one, in a randomized order according to a balanced Latin-square design. In each condition, subjects performed the task until their performance was comparable and remained approximately the same in the last five runs, which were then used for analysis. A minimum of eight runs was performed for each condition. After every run, subjects were verbally informed of their performance score (root-mean-square of the tracking error) to further motivate them. Each run lasted for 132 s: the first eight and final four seconds were used as run-in and fade-out, respectively; the remaining 120 s of data were used for analysis. Breaks of around 15 minutes were taken between every two conditions, resulting in a total experiment time of approximately three hours per subject.

8.4. DATA ANALYSIS

8

8.4.1. TRACKING PERFORMANCE AND CONTROL ACTIVITY

The variance of the tracking error $e(t)$ was used as measure for the tracking performance. It is defined in the frequency domain by:

$$\sigma_e^2 = \frac{1}{\pi} \int_0^\infty S_{ee}(\omega) d\omega, \quad (8.9)$$

with S the power-spectral density function. S was estimated per measurement run by its periodogram. By integrating Eq. (8.9) only over the respective input frequencies of the target or disturbance signals, their individual contributions to the total error can be estimate, while integrating over the remaining frequencies yields the remnant contribution. Hereby, the small remnant contribution at the target and disturbance input frequencies is neglected. A repeated measures two-way ANOVA was applied to test for significant changes between conditions, based on the five-run average error variance per subject. The variance of the control output $u(t)$ was calculated similarly and was used as measure for control activity.

8.4.2. OPEN-LOOP DYNAMICS

For better insight into the changes in target-tracking and disturbance-rejection performance, FRFs of the open-loop dynamics were estimated, according to [42]:

$$H_{ol,t}(j\omega_t) = \frac{\bar{X}(j\omega_t)}{\bar{E}(j\omega_t)}, \quad H_{ol,d}(j\omega_d) = -\frac{\bar{U}(j\omega_d)}{\bar{U}(j\omega_d) + \bar{F}_d(j\omega_d)}. \quad (8.10)$$

The bars indicates the frequency-domain average of the signals (over each subject's five measurement runs per condition), taking into account the different time-domain realizations of the target signal; for example, $\bar{X}(j\omega_t) = \frac{1}{5} \sum_{n=1}^5 X^n(j\omega_t) e^{-j\angle F_t^n(j\omega_t)}$. In the frequency range where the magnitude of the open-loop dynamics is larger than one, tracking performance is typically good [6, 45]; the upper limit of this range, the crossover frequency ω_c (i.e., $|H_{ol}(j\omega_c)| = 1$) was used as a second measure for task performance. The corresponding phase margin, $\phi_m = 180 + \angle H_{ol}(j\omega_c)$, was used as measure for the stability of the closed-loop system. A repeated measures two-way ANOVA was applied to test for significant changes in ω_c and ϕ_m between conditions.

8.4.3. HUMAN MULTILoop CONTROL DYNAMICS

The two external input signals (target and the disturbance) allow for estimating the dynamics of only two HC responses [86, 190]. Corresponding to the analysis in Parts I and II, a lumped target (feedforward) response $H_{o_t}(j\omega)$ and a lumped CE output (feedback) response $H_{o_x}(j\omega)$ are estimated, see Fig. 8.4. The control output of this model is given by:

$$U(j\omega) = H_{o_t}(j\omega)F_t(j\omega) - H_{o_x}(j\omega)X(j\omega) + N(j\omega). \quad (8.11)$$

Similarly, the control output in the preview model (Fig. 8.1d) can be written as:

$$U(j\omega) = H_{o_{e^*}}(j\omega)H_{o_f}(j\omega)e^{\tau_f j\omega}F_t(j\omega) - (H_{o_{e^*}}(j\omega) + H_{o_m}(j\omega))X(j\omega) + N(j\omega). \quad (8.12)$$

Comparing Eq. (8.12) with Eq. (8.11) yields:

$$\begin{aligned} H_{o_t}(j\omega) &= H_{o_{e^*}}(j\omega)H_{o_f}(j\omega)e^{\tau_f j\omega}, \\ H_{o_x}(j\omega) &= H_{o_{e^*}}(j\omega) + H_{o_m}(j\omega). \end{aligned} \quad (8.13)$$

In compensatory tasks $H_{o_f}(j\omega)e^{\tau_f j\omega}$ drops from Eq. (8.13), which can thus be solved explicitly for the remaining HC dynamics $H_{o_m}(j\omega)$ and $H_{o_{e^*}}(j\omega)$ (note that in this case e^*

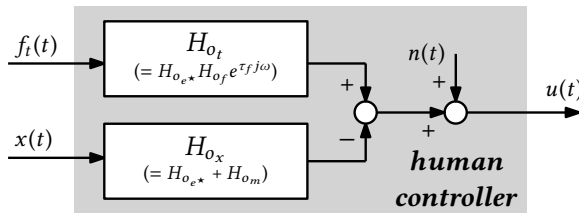


Figure 8.4: Lumped-dynamics HC model with responses to the target (H_{o_t}) and the CE output (H_{o_x}).

reduces to the actual error e , see Section 8.2). Similarly, $H_{o_m}(j\omega)=0$ in visual-only preview tasks also yields explicit expressions for the two remaining HC responses. However, if all three responses are indeed active in preview tasks with motion feedback, it is not possible to solve Eq. (8.13) for all three dynamics, leading to *lumped response estimates*.

FRFs of $H_{o_t}(j\omega)$ and $H_{o_x}(j\omega)$ were estimated using a multiloop, system identification technique based on Fourier coefficients [86, 190]. Eq. (8.11) provides a single equation with three unknowns, namely, $H_{o_t}(j\omega)$, $H_{o_x}(j\omega)$, and the remnant $N(j\omega)$. Due to the multisine forcing function design, the remnant is relatively small at the input frequencies, and can thus be neglected when evaluating Eq. (8.11) only at the target signal input frequencies ω_t . A second equation is obtained by interpolating the averaged signals, $\bar{U}(\omega_d)$, $\bar{F}_t(\omega_d)$, and $\bar{X}(\omega_d)$, in the frequency domain, from the disturbance to the target signal input frequencies, yielding $\tilde{U}(\omega_t)$, $\tilde{F}_t(\omega_t)$, and $\tilde{X}(\omega_t)$:

$$\begin{bmatrix} \tilde{U}(j\omega_t) \\ \tilde{U}(j\omega_t) \end{bmatrix} = \begin{bmatrix} \tilde{F}_t(j\omega_t) & -\tilde{X}(j\omega_t) \\ \tilde{F}_t(j\omega_t) & -\tilde{X}(j\omega_t) \end{bmatrix} \begin{bmatrix} H_{o_t}(j\omega_t) \\ H_{o_x}(j\omega_t) \end{bmatrix} \quad (8.14)$$

This system of two equations can be solved to obtain the nonparametric FRF estimates $H_{o_t}(j\omega_t)$ and $H_{o_x}(j\omega_t)$, at the target signal input frequencies. Similarly, after interpolating all signals from ω_t to ω_d , Eq. (8.14) can also be solved to obtain estimates of $H_{o_t}(j\omega_d)$ and $H_{o_x}(j\omega_d)$ at the disturbance signal input frequencies.

8.4.4. PARAMETER ESTIMATION

The model parameters were estimated by minimizing a frequency-domain, least-squares cost function $J(\Theta)$, based on the modeling errors $\epsilon(\Theta, j\omega_i)$ at all 40 input frequencies ω_i of the two forcing functions combined:

$$\hat{\Theta} = \underset{\Theta}{\operatorname{argmin}} J(\Theta), \quad (8.15)$$

$$J(\Theta) = \frac{1}{2} \sum_{i=1}^{40} |\epsilon(\Theta, \omega_i)|^2, \quad (8.16)$$

$$\epsilon(\Theta, \omega_i) = \bar{U}(j\omega_i) - \hat{U}(\Theta, j\omega_i). \quad (8.17)$$

Here, $\hat{\Theta}$ is the estimated model parameter vector and $\hat{U}(\Theta, j\omega_i)$ is the modeled control output, given by:

$$\hat{U}(\Theta, j\omega_i) = \hat{H}_{o_t}(\Theta, j\omega_i)\bar{F}_t(j\omega_i) - \hat{H}_{o_x}(\Theta, j\omega_i)\bar{X}(j\omega_i). \quad (8.18)$$

Four models were fit to the data. The most elaborate model is the **Visual-Vestibular (VV)** preview model, with parameter vector $\Theta = [K_{e^*} \ T_{L,e^*} \ \tau_v \ \omega_{nms} \ \zeta_{nms} \ K_f \ T_{l,f} \ \tau_f \ K_m \ \tau_m]^T$ (see Fig. 8.1d). The VV compensatory model, given in Fig. 8.1c, is identical, but without the preview parameters K_f , $T_{l,f}$, and τ_f . The other two “**Visual-Only**” (VO) models are identical to the VV compensatory and preview models, but lack the vestibular feedback channel, such that K_m and τ_m are absent from the parameter vector. The VO and VV compensatory models were fit to data obtained in both compensatory conditions (i.e., with

and without motion feedback), and, similarly, the VO and VV preview models were fit to data obtained in both preview conditions, yielding two model fits per experimental condition. A Nelder-Mead simplex algorithm was used to minimize $J(\Theta)$, constrained to non-negative parameters ($\Theta \geq 0$) and, based on literature, “realistic” values of human limitations, that is, τ_v between 0.2 and 0.4 s, τ_m between 0.1 and 0.4 s, and ζ_{nms} higher than 0.05. To avoid the local minimums of the nonlinear cost function, the solution with the lowest cost value was selected from 100 randomly initialized optimizations.

8.4.5. VARIANCE ACCOUNTED FOR

The Variance Accounted For (VAF) was used as a measure for the model quality-of-fit. The VAF quantifies the similarity of two signals, its maximum value of 100% indicates that two signals are equal. To quantify the model’s ability to capture the measured human behavior, the VAF was calculated based on the difference between the measured and modeled HC control output, which corresponds to the modeling error ϵ in Eq. (8.17):

$$\text{VAF} = \left(1 - \frac{\sigma_\epsilon^2}{\sigma_u^2}\right) \times 100\%. \quad (8.19)$$

The signals’ variances were calculated according to Eq. (8.9), so all double-sided power-spectrum frequencies were accounted for, and not just the forcing function frequencies.

8.4.6. PARAMETER CORRELATION MATRIX

Correlation matrices were calculated to assess possible ambiguities in the new visual-vestibular preview model. First, the Fisher information matrix M was estimated, which, for the frequency-domain cost function in Eq. (8.16) and the assumption of zero-mean white modeling errors ϵ , can be approximated as [159]:

$$M_{\Theta\Theta} = \frac{1}{40} \sum_{i=1}^{40} \text{Re} \left\{ \left(\frac{\partial \epsilon^*(\Theta, \omega_i)}{\partial \Theta^T} \right) \left(\frac{\partial \epsilon(\Theta, \omega_i)}{\partial \Theta} \right) \right\}, \quad (8.20)$$

with $*$ the complex conjugate and T the transpose. Substituting Eqs. (8.17) and (8.18) into Eq. (8.20) yields:

$$M_{\Theta\Theta} = \frac{1}{40} \sum_{i=1}^{40} \text{Re} \left\{ \left(-F_t^*(\omega_i) \frac{\partial H_{o_t}^*(\Theta, \omega_i)}{\partial \Theta^T} + X^*(\omega_i) \frac{\partial H_{o_x}^*(\Theta, \omega_i)}{\partial \Theta^T} \right) \left(-F_t(\omega_i) \frac{\partial H_{o_t}(\Theta, \omega_i)}{\partial \Theta} + X(\omega_i) \frac{\partial H_{o_x}(\Theta, \omega_i)}{\partial \Theta} \right) \right\}. \quad (8.21)$$

The partial derivatives were estimated with a numerical balanced finite-difference method, similar as in [53], with a $\pm 10^{-4}$ step in each parameter around $\hat{\Theta}$. Assuming unbiased estimates, the covariance matrix $C = M_{\Theta\Theta}^{-1}$, and the correlation R between two parameters with indices k and l is given by:

$$R_{k,l} = \frac{C_{k,l}}{\sqrt{C_{k,k}C_{l,l}}}. \quad (8.22)$$

8.5. NONPARAMETRIC RESULTS

8.5.1. TRACKING PERFORMANCE AND CONTROL ACTIVITY

Fig. 8.5 shows the variance of the tracking error $e(t)$ and the control output $u(t)$, while Table 8.2 shows the results of the corresponding ANOVA tests. Motion feedback results in a lower tracking error, both in compensatory and in preview tracking tasks, and all input frequencies (target, disturbance and remnant) contribute significantly to this. Subjects thus improve both target-tracking and disturbance-rejection performance, while also generating less tracking errors at the unexcited remnant frequencies. Performance improves markedly from compensatory to preview tasks, especially because of significantly better target-tracking performance, but also due to lower errors at the disturbance and remnant frequencies. Motion feedback yields a smaller performance benefit in preview tasks, compared to compensatory tasks (significant interaction effect at all input frequencies).

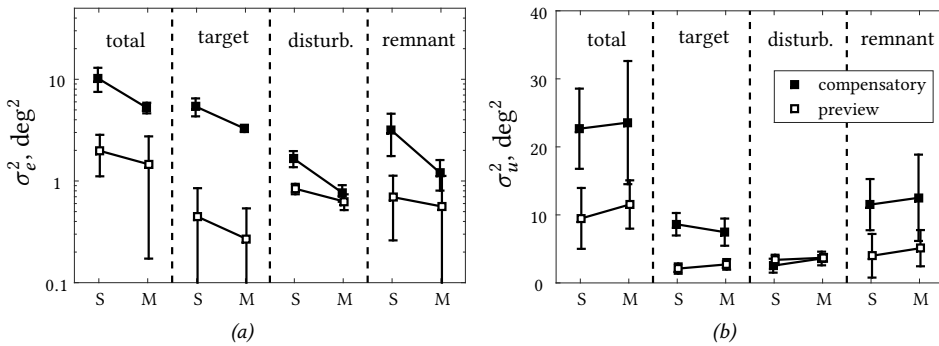


Figure 8.5: Error (a) and control output (b) variances, eight-subject average and 95% confidence intervals (corrected for between-subject variability); S and M indicate static and motion tasks.

Table 8.2: Error and control output ANOVA results. Symbols “**”, “*”, and “-” indicate the result is highly significant ($p < .01$), significant ($p < .05$), and not significant ($p > .05$), respectively.

		error, e			control output, u		
		df	F	sig.	df	F	sig.
σ	motion	(1,7)	12.0	*	(1,7)	0.2	-
	display	(1,7)	44.3	**	(1,7)	14.6	**
	mot. \times disp.	(1,7)	13.1	**	(1,7)	0.1	-
σ_t	motion	(1,7)	15.3	**	(1,7)	0.1	-
	display	(1,7)	90.0	**	(1,7)	84.2	**
	mot. \times disp.	(1,7)	18.8	**	(1,7)	2.1	-
σ_d	motion	(1,7)	30.0	**	(1,7)	3.0	-
	display	(1,7)	35.8	**	(1,7)	0.8	-
	mot. \times disp.	(1,7)	17.3	**	(1,7)	1.8	-
σ_r	motion	(1,7)	6.1	*	(1,7)	0.3	-
	display	(1,7)	12.3	**	(1,7)	9.4	*
	mot. \times disp.	(1,7)	7.5	*	(1,7)	0.0	-

Effects of motion feedback on control activity are small, both in compensatory and preview tasks (no significant motion and interaction effects). Control activity is substantially lower in preview tasks compared to compensatory tasks, due to significantly less activity at the target and remnant input frequencies. As the target is explicitly visible in preview tasks (and not in compensatory tasks), subjects can purposely ignore the higher frequencies that are more difficult to track (as explained in Part II of this thesis), which was captured by the low-pass filter in the preview model, Eq. (8.5). Remnant is known to scale with overall control activity [196], so the lower remnant in preview tasks likely results from the reduced activity at the target input frequencies.

8.5.2. OPEN-LOOP DYNAMICS

Fig. 8.6 shows the crossover frequencies and phase margins, with accompanying ANOVA results in Table 8.3, while Figs. 8.7 and 8.8 show the examples of the estimated target and disturbance open-loop dynamics. Physical motion results in a higher disturbance crossover frequency (significant effect), both in compensatory and preview tracking tasks (no interaction effect). Subjects maintain a disturbance phase margin of around 25 deg, regardless of the task (no significant effects). Fig. 8.8 illustrates that the disturbance open-

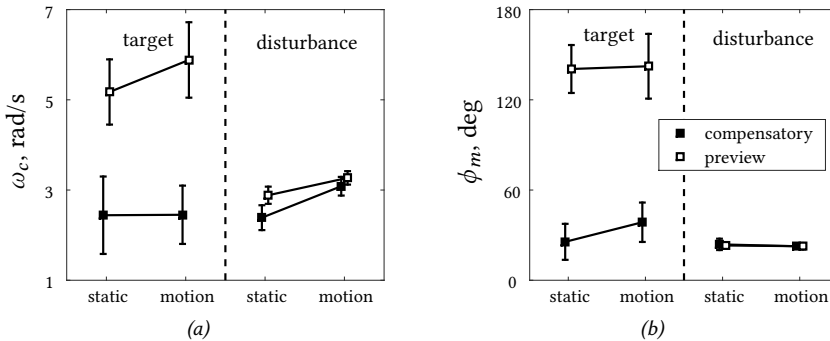


Figure 8.6: Measured crossover frequencies (a) and phase margins (b), eight-subject average and 95% confidence intervals (corrected for between-subject variability).

Table 8.3: Crossover frequencies and phase margins ANOVA results. Symbols “**”, “*”, and “-” indicate the result is highly significant ($p < .01$), significant ($p < .05$), and not significant ($p > .05$).

	target						disturbance					
	crossover frequency			phase margin			crossover frequency			phase margin		
	df	F	sig.	df	F	sig.	df	F	sig.	df	F	sig.
motion	(1,7)	6.6	*	(1,7)	1.4	-	(1,7)	35.0	**	(1,7)	0.4	-
display	(1,7)	23.9	**	(1,7)	112.0	**	(1,7)	6.6	*	(1,7)	0.1	-
mot. × disp.	(1,7)	16.4	**	(1,7)	0.8	-	(1,7)	4.4	-	(1,7)	0.2	-

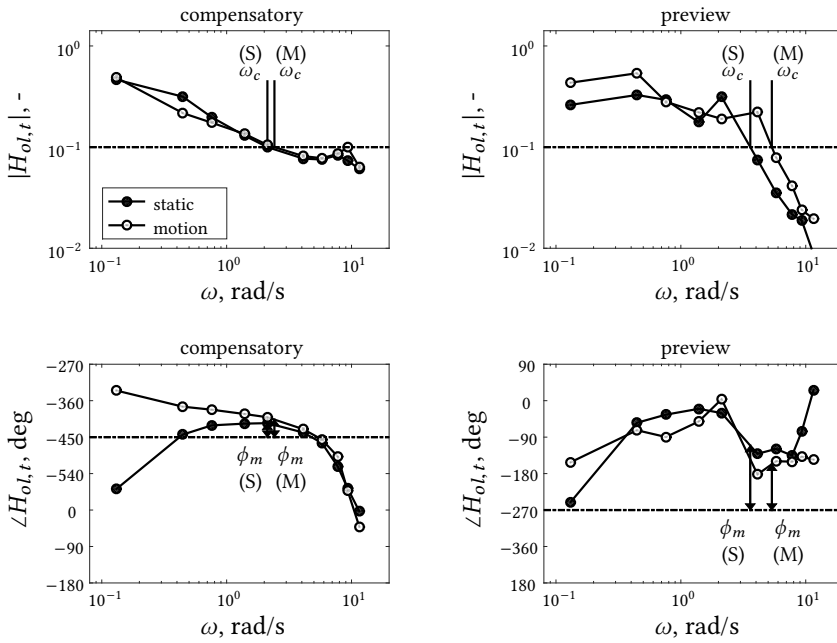


Figure 8.7: Estimated target open-loop dynamics, single-subject data.

8

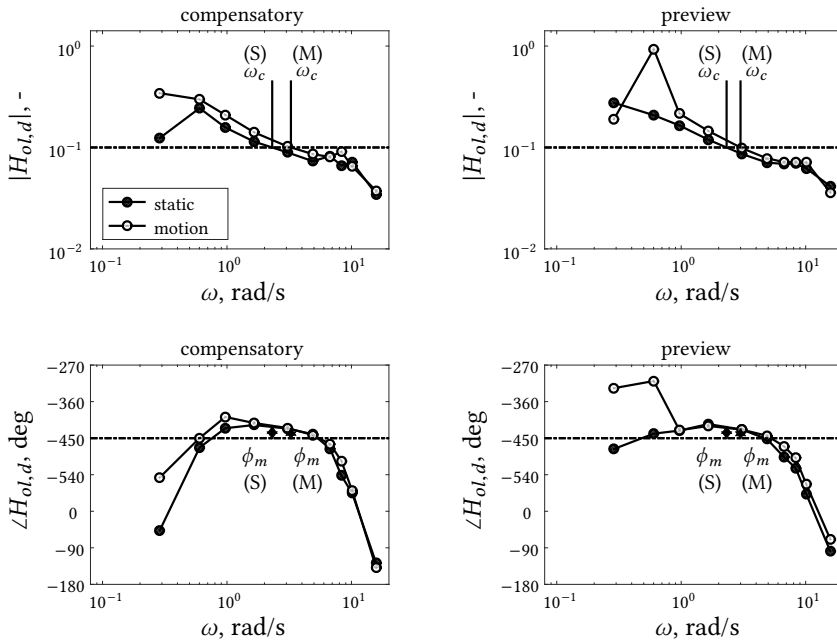


Figure 8.8: Estimated disturbance open-loop dynamics, single-subject data.

loop dynamics are identical in compensatory and preview tasks, both with and without motion feedback. As reflected by the higher crossover frequencies with motion feedback, the open-loop magnitude is higher at low frequencies, which indicates better disturbance-rejection behavior (consistent with the lower tracking error in Fig. 8.5a). In static tasks, preview yields a higher disturbance crossover frequency compared to compensatory tasks (significant effect).

The target crossover frequencies and phase margins are substantially different in compensatory and preview tasks. By responding to the target ahead in preview tasks, HCs generate phase lead, which results in much higher phase margins as compared to compensatory tasks (significant effect). The stability improvement that results allows HCs to steer more aggressively (see Chapter 4), yielding higher crossover frequencies (significant effect). Consequently, the effects of motion feedback are different: in preview tasks the crossover frequency increases, while the phase margin remains constant; in compensatory tasks the phase margin increases while the crossover frequency remains constant (see Figs. 8.6 and 8.7).

8.5.3. HUMAN MULTILoop CONTROL DYNAMICS

Figs. 8.9 and 8.10 show the estimated HC dynamics $H_{o_x}(j\omega)$ and $H_{o_r}(j\omega)$. For $H_{o_x}(j\omega)$, similar effects of motion feedback are visible in compensatory and in preview tasks. First, the phase roll-off at high frequencies in $H_{o_x}(j\omega)$ is smaller with motion feedback. This points to a lower response delay and is strong evidence that the faster vestibular response is indeed activated [45, 111, 190]. Second, with motion feedback, the magnitude of $H_{o_x}(j\omega)$ is higher at the lower and middle frequencies, which corresponds well to the effects of a higher visual gain and lower visual lead time-constant, as has been reported in compensatory tracking tasks when an additional vestibular loop is closed [190, 193].

The estimated $H_{o_r}(j\omega)$ response dynamics (Fig. 8.10) are very similar with and without motion feedback. However, with motion feedback slightly less phase lead is visible around 1-3 rad/s, both in compensatory and preview tasks. The lumped $H_{o_r}(j\omega)$ response was assumed to contain only visual response dynamics (i.e., no H_{o_m}), see Eq. (8.13). The reduced phase lead must therefore originate from the error response, which corresponds to the $H_{o_x}(j\omega)$ dynamics in Fig. 8.9 and previous findings in compensatory tasks [190, 193].

8.6. MODELING RESULTS

8.6.1. VARIANCE ACCOUNTED FOR

The VAFs of the fitted models are generally 80-90% (see Fig. 8.11), indicating that all models reasonably mimic subjects' measured control outputs. In the static conditions (without motion feedback), the visual-only and visual-vestibular models describe the output equally well, as expected, indicating that subjects closed no vestibular feedback-loop. In compensatory tasks with motion feedback, the visual-vestibular model yields VAFs that are about 5% higher as compared to the visual-only model, which indicates that subjects initiated a vestibular response which dynamics could not be captured by the visual-only model.

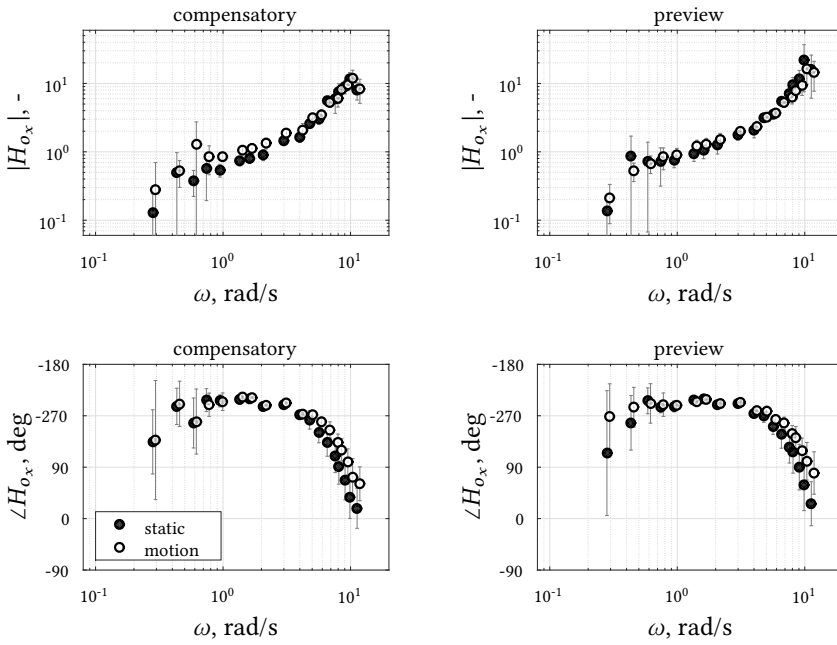


Figure 8.9: Estimated CE output response dynamics, mean of all subjects with standard deviations.

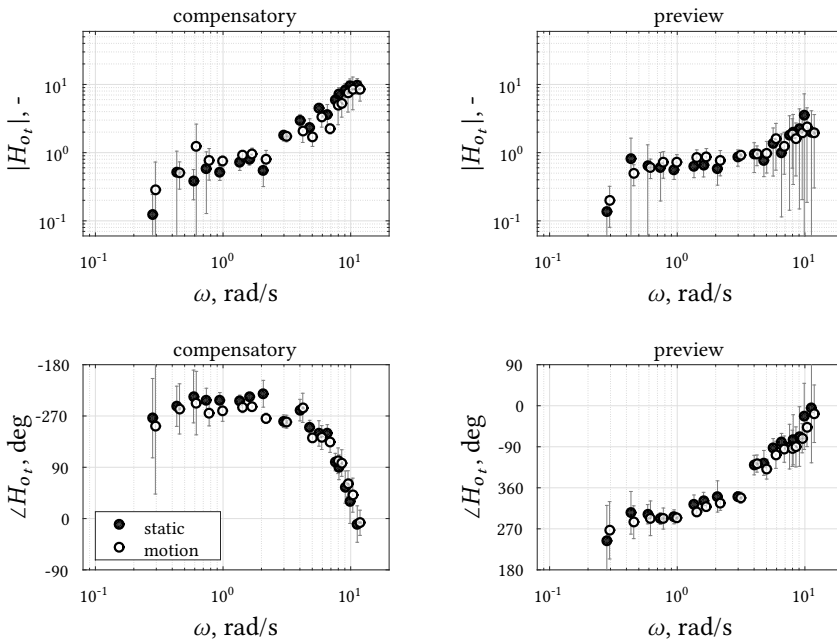


Figure 8.10: Estimated target response dynamics, mean of all subjects with standard deviations.

However, in preview tasks with motion feedback, both models yield identical VAFs, suggesting either that no vestibular channel is active, or that the visual-only preview model has enough flexibility to also capture the HC's combined visual-vestibular dynamics.

8.6.2. VESTIBULAR GAIN AND TIME DELAY

Fig. 8.12 shows the estimated vestibular channel parameters, from visual-vestibular model fits to measurements in tasks both with and without motion feedback. In compensatory tasks *without* motion feedback, as expected, the vestibular response gain K_m (Fig. 8.12a) is estimated to be approximately zero, while K_m is clearly nonzero in the compensatory task *with* motion feedback. In preview tasks with motion feedback, K_m has similar values as in compensatory tasks, which suggest that an identically strong vestibular response is initiated. However, in static preview tasks, the vestibular response gain is also nonzero, and approximately equally large (or even higher) as in preview tasks with motion feedback. Therefore, in preview tasks, the response gain K_m is a poor indicator for whether subjects actually respond to the available motion cues, or not.

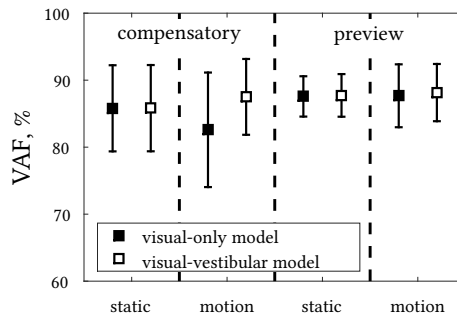


Figure 8.11: VAFs of the model fits, average over eight subjects and standard deviations.

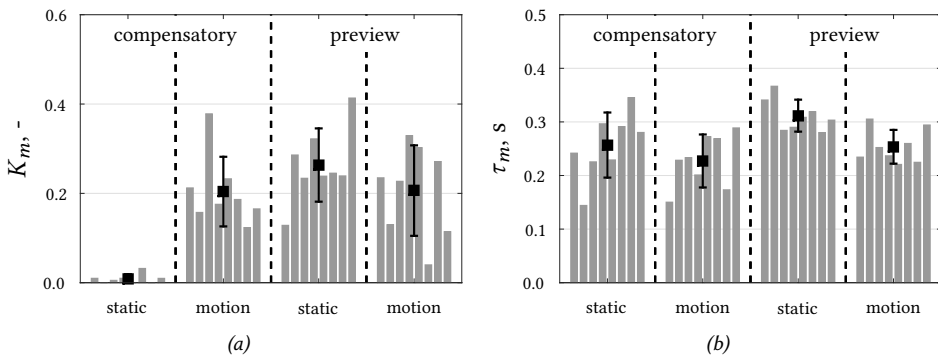


Figure 8.12: Estimated vestibular response parameters, gain K_m (a) and time delay τ_m (b), individual subjects (gray bars), and means with 95% confidence intervals (errorbars).

The vestibular response time delay τ_m (Fig. 8.12b) is estimated to be around 0.25 s in both compensatory and preview tasks with motion feedback, which is consistent with previous findings [111, 112, 193]. In static compensatory tasks, the delay can attain any value between 0.1 and 0.4 s (the estimation constraints) as the low value of the vestibular gain K_m means that the vestibular response has almost no effect on the cost function. In static preview tasks, the vestibular channel does contribute to the cost function and τ_m is approximately 0.3 s, which is even higher than the delay in the visual channel (see Fig. 8.15).

8.6.3. MODELED CONTROL DYNAMICS

Bode plots of the fitted models in tasks with motion feedback are shown in Figs. 8.13 and 8.14. In the compensatory task with motion, the visual-vestibular model has a higher VAF, a lower cost function value, and captures the shape of the nonparametric FRFs better, compared to the visual-only model. This strongly supports that a vestibular response is

model	VO	VV		VO	VV
K_{e^*} , -	0.31	1.15	τ_v , s	0.22	0.27
ω_{nms} , rad/s	11.59	14.16	ζ_{nms} , -	0.12	0.06
T_{L,e^*} , s	1.62	0.30	K_m , -	-	0.38
τ_m , s	-	0.23	VAF, %	79.34	87.20
J, -	3.67	0.27			

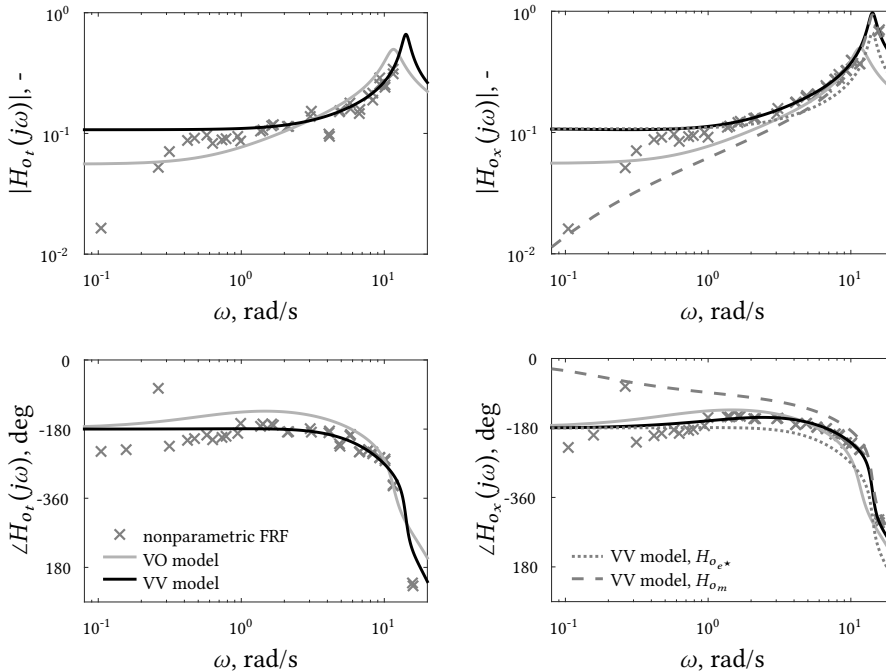


Figure 8.13: Visual-only (VO) and visual-vestibular (VV) model fits for Subject 3 in compensatory task with motion feedback.

initiated. The individual contributions of the visual ($H_{o_{e^*}}$) and vestibular (H_{o_m}) channel dynamics to the $H_{o_x}(j\omega)$ response (see Eq. (8.13)), as estimated in the visual-vestibular model, are also shown in Fig. 8.13. The visual response dominates at low frequencies, while the vestibular response becomes stronger at higher frequencies.

In preview tasks with motion feedback (Fig. 8.14) the visual-only and visual-vestibular model fits are very similar. Both capture the shape of the nonparametric FRFs well, with a slightly higher VAF for the visual-only model, but a slightly lower cost function value for the visual-vestibular model. $H_{o_x}(j\omega)$ shows that the visual-vestibular model fit includes a substantial vestibular response (i.e., the magnitude of $H_{o_m}(j\omega)$ is nonzero), but the overall response is identical to that of the visual-only model. These model fits, without comparison to the results from a static task, thus provide no clear-cut evidence whether this – representative – subject responded to the available vestibular motion cues.

model	VO	VV		VO	VV
K_{e^*} , -	1.01	1.17	τ_v , s	0.20	0.21
ω_{nms} , rad/s	14.30	14.02	ζ_{nms} , -	0.07	0.09
T_{L,e^*} , s	0.62	0.32	K_f , -	1.02	1.00
τ_f , s	0.69	0.74	$T_{l,f}$, s	0.71	0.57
K_m , -	-	0.23	τ_m , s	-	0.25
VAF, %	85.12	84.39	J, -	0.38	0.32

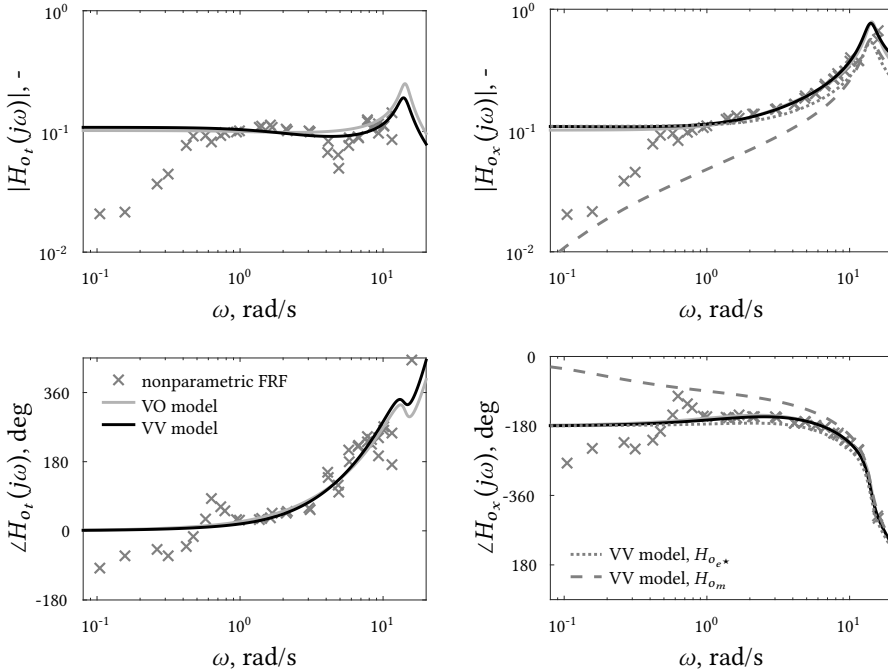


Figure 8.14: Visual-only (VO) and visual-vestibular (VV) model fits for Subject 3 in preview task with motion feedback.

8.6.4. PARAMETER CORRELATION MATRICES

Tables 8.4 and 8.5 show the correlation matrices for the preview task with motion feedback, for the VO and VV model fits in Fig. 8.14, respectively. The visual-only model contains a strong negative correlation between K_{e^*} and T_{L,e^*} , which reflects that a lower K_{e^*} can be compensated for by a higher T_{L,e^*} to yield almost the same model output. Such an exchange only affects the very lowest frequencies of the modeled dynamics, where the magnitude of the subject's response is small, hence limited information is present in the control data about these two parameters. Other correlations in the visual-only model are small, indicating that each parameter has a unique contribution in describing the human's control behavior.

The visual-vestibular model contains many strong correlations, indicating that multiple parameters can capture similar characteristics of the subject's response dynamics. In particular, the three delays in the model (τ_v , τ_m , and τ_f) are strongly correlated, with absolute values above 0.9. Apparently, only *two* input-output delays can be reliably estimated from the data, which is a direct result of having only *two* experimental forcing functions. Tables 8.4 and 8.5 thus shows that the proposed visual-vestibular preview model is *overdetermined* for the obtained measurement data.

Table 8.4: Correlation matrix of the VO model, preview task with motion feedback, Subject 3.

	K_{e^*}	τ_v	ω_{nms}	ζ_{nms}	T_{L,e^*}	K_f	τ_f	$T_{L,f}$
K_{e^*}	1
τ_v	-0.62	1
ω_{nms}	-0.19	0.40	1
ζ_{nms}	-0.34	0.29	0.15	1
T_{L,e^*}	-0.96	0.63	0.20	0.40	1	.	.	.
K_f	0.25	-0.11	-0.03	-0.05	-0.23	1	.	.
τ_f	-0.31	0.32	0.11	0.20	0.27	0.17	1	.
$T_{L,f}$	0.14	0.02	0.01	0.02	-0.16	0.46	0.53	1

Table 8.5: Correlation matrix of the VV model, preview task with motion feedback, Subject 3.

	K_{e^*}	τ_v	ω_{nms}	ζ_{nms}	T_{L,e^*}	K_f	τ_f	$T_{L,f}$	K_m	τ_m
K_{e^*}	1
τ_v	-0.15	1
ω_{nms}	-0.17	-0.61	1
ζ_{nms}	0.11	-0.73	0.43	1
T_{L,e^*}	-0.71	-0.09	0.36	-0.18	1
K_f	0.11	-0.64	0.46	0.32	0.31	1
τ_f	-0.09	0.96	-0.62	-0.63	-0.22	-0.63	1	.	.	.
$T_{L,f}$	0.04	-0.42	0.36	0.03	0.48	0.70	-0.40	1	.	.
K_m	0.10	0.89	-0.67	-0.50	-0.50	-0.72	0.92	-0.64	1	.
τ_m	0.13	-0.99	0.62	0.77	0.05	0.61	-0.94	0.36	-0.86	1

8.6.5. VISUAL RESPONSE AND NEUROMUSCULAR SYSTEM PARAMETERS

Although correlated parameters are difficult to estimate accurately, they may still reveal how HCs adapt their control behavior. Therefore, the remaining model parameters, those of the visual channel and HCs' neuromuscular system, are shown in Fig. 8.15. In compensatory tasks (black markers), introduction of motion feedback leads to a clear increase in the visual response gain K_{e^*} (Fig. 8.15a), and a clear decrease in T_{L,e^*} (Fig. 8.15b), the amount of visual lead generated. These effects are well-known in compensatory tracking tasks [190, 193], and are a direct result of the “lead” generated in the vestibular channel

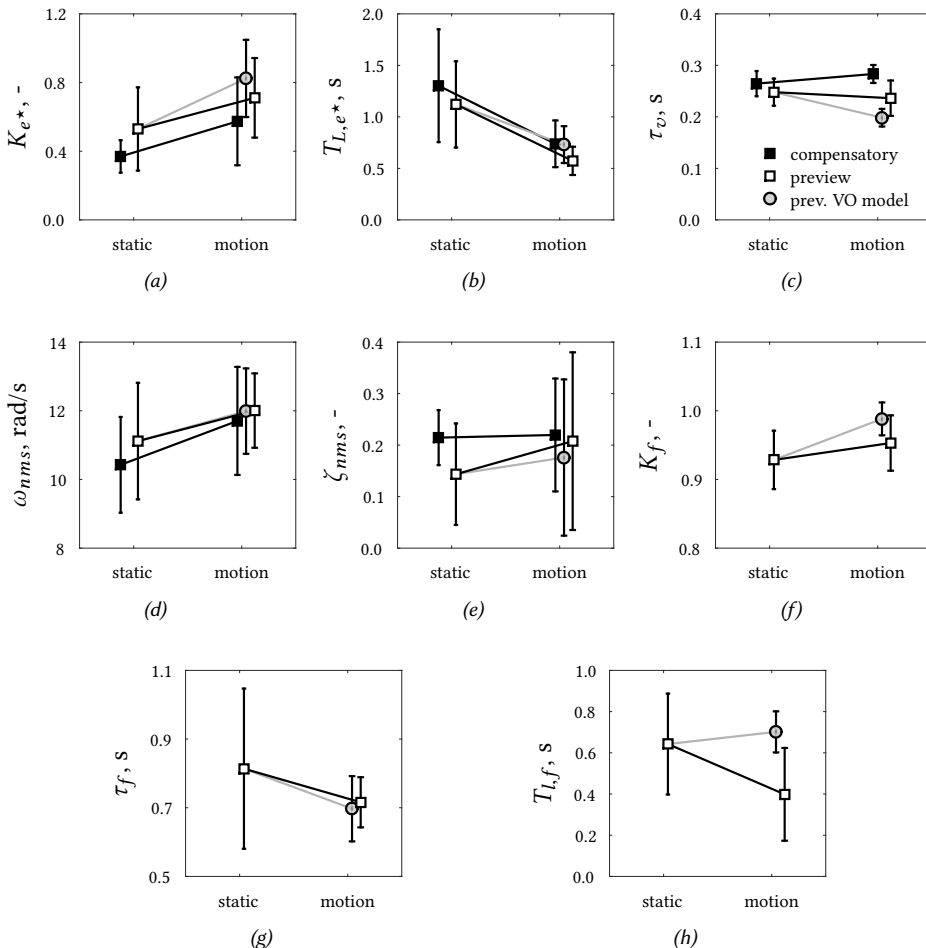


Figure 8.15: Estimated model parameters of the visual response channel. Static conditions show results from visual-only model fits, and motion conditions show results from visual-vestibular model fits. Additional gray markers indicate results of the visual-only (VO) model fit in preview tasks with motion feedback.

(based on the yaw acceleration). Figs. 8.15a and 8.15b reveal an identical trend in preview tracking tasks, that is, K_{e^*} increases and T_{L,e^*} decreases. This suggests that indeed a similar vestibular feedback-loop is closed, and, additionally, that the visual channel adaptation to motion feedback is similar as in compensatory tasks.

In both compensatory and preview tasks, the visual delay τ_v (Fig. 8.15c) is invariant with the introduction of motion feedback. τ_v decreases only when the visual-only model (gray markers) is fitted in preview tasks with motion feedback, which again suggests that the vestibular channel is active, but that this channel's lower delay is now captured by τ_v (τ_m is absent from the visual-only model). In compensatory and preview tasks, availability of motion feedback also leads to a similar increase in subjects' neuromuscular system break frequency ω_{nms} (Fig. 8.15d), while their damping ratio ζ_{nms} is generally invariant.

Fig. 8.15 also shows that the values of the preview parameters K_f , τ_f , and $T_{L,f}$ in tasks without motion feedback correspond closely to those estimated from the visual-only experiments of Part II. The introduction of motion feedback evokes a higher K_f , which approaches unity value, and which is around the value that yields optimal tracking performance in static preview tracking tasks (see Chapters 5 and 6). τ_f appears to be invariant, or decreases slightly, when motion feedback becomes available. Both with and without motion feedback, τ_f is approximately 0.7-0.8 s, confirming that subjects respond to the target trajectory ahead to anticipate the trajectory's changes. $T_{L,f}$ decreases with motion feedback, which indicates that less of the target's high frequencies are cognitively attenuated by subjects, such that these are tracked more aggressively. Note that the visual-only model yields markedly different values of $T_{L,f}$; here the lead generated in the human's vestibular response is captured by $H_{o_{e^*}}(j\omega)$, see Eq. (8.13), the lower $T_{L,f}$ compensates for this artifact in the $H_{o_r}(j\omega)$ response.

8

8.7. DISCUSSION

This chapter tested the hypothesis that, in preview tracking tasks, HCs use physical motion in a very similar way as in compensatory tasks, namely through closure of an additional vestibular feedback channel. A human-in-the-loop tracking experiment was performed, that allowed for separating data according to the target-tracking and disturbance-rejection parts of the task, and also for separating the HC's feedforward and feedback response dynamics using multiloop system identification. It was then attempted to model the human's control behavior in preview tracking tasks with motion feedback, by merging previous models for static preview tracking and visual-vestibular compensatory tracking.

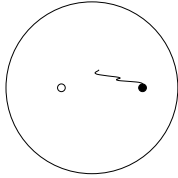
The effects of motion feedback are indeed very similar in compensatory and preview tracking tasks, in particular on task performance and the HC's feedback control dynamics. The presented results provide strong, albeit indirect, evidence that HCs close a similar vestibular feedback-loop in preview tasks as in compensatory tasks, which *confirms* the main hypothesis. With the introduction of motion feedback, lead generation partly shifts from the visual error-response to the vestibular response. Because reduced visual lead in tasks with physical motion feedback already lead to an attenuated target response at high frequencies, less cognitive "smoothing" of the previewed trajectory is required (lower $T_{L,f}$).

It was shown that HCs most likely apply *all three* expected responses in preview tracking tasks with physical motion feedback: feedforward, visual feedback, and vestibular feedback. However, the main evidence for this fact comes from comparing tasks with and without motion feedback, and with and without preview. The data obtained in the preview task with motion feedback, by itself (so without reference results from the other tasks), provided no unambiguous evidence whether or not HCs were responding to the motion cues. To do so, future work can use a third uncorrelated forcing function to disentangle all three response channels. The only possibility for such a forcing function is to additionally perturb the motion cues provided by the simulator (i.e., the input to the H_{om} block in Fig. 8.1d). This perturbation was purposely excluded here, because it leads to incoherent visual and motion cues, which can yield unanticipated HC behavior adaptations or even complete ignorance of the, now *unreliable*, motion cues.

The obtained results emphasize that the roles of motion cues and preview information in manual control tasks are fundamentally different. Both support improved task performance, but through completely different control mechanisms, namely feedback (motion) and feedforward (preview). Strong feedforward control in practical control tasks with preview does not fully replace the benefits of motion feedback, nor does motion feedback reduce the benefits of preview information. These findings are important for the design of flight and driving simulators, because they suggest that providing motion feedback is equally important in practical tasks that involve feedforward control, as in the elaborately studied, and well-understood compensatory tracking task.

8.8. CONCLUSION

This chapter studied the effects of motion feedback on human control behavior in preview tracking tasks, using measurements from a human-in-the-loop experiment. Introduction of motion feedback evokes a very similar vestibular feedback-loop closure in compensatory and preview tasks. Nonetheless, two forcing functions are insufficient to explicitly separate humans' feedforward, visual feedback, and vestibular feedback responses, and the proposed visual-vestibular preview model is thus overdetermined. Measuring human use of motion feedback with these techniques can be expected to be even more challenging in real-world control tasks that involve preview. The fundamental different roles of preview information and physical motion feedback suggest that it is equally important to supply physical motion feedback in flight and driving simulators, both when practical control tasks are performed that support feedforward control, as when performing compensatory tracking tasks.

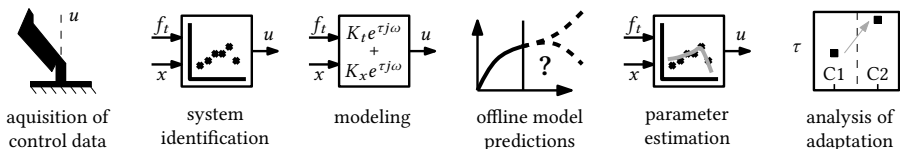


9

MULTIPLE VISUAL FEEDBACKS AND OUTSIDE VISUAL FIELD CONTROL

Chapters 7 and 8 extended our understanding of preview tracking (from Chapters 2–6) to tasks with perspective displays and with physical motion feedback. While already spanning a broad range of tasks, all experimental displays still provided feedback of only a single controlled element output. In contrast, the outside visual field in real-world control tasks provides a wealth of optical cues, from which humans can select multiple features as feedbacks for control. This chapter extends the obtained models – and knowledge – of manual preview control to the task of steering a car along a winding road, which is such a multiloop, outside-visual control task. A human-in-the-loop simulator driving experiment is performed with full 180×40 deg field-of-view visuals. Frequency-response functions are estimated of the human’s inner-loop heading response, in addition to the preview (feedforward) and lateral position feedback responses estimated in previous chapters. The preview tracking model is extended with a heading feedback inner-loop. Estimated model parameters quantify the role of each loop closure, and, most importantly, also quantify the exact optical features that drivers select from the outside visuals as feedbacks for control.

Steps of the cybernetic approach involved:



Parts of this chapter have been published as:

Title Identification and Modeling of Driver Multiloop Feedback and Preview Steering Control
Conference IEEE International Conference on Systems, Man, and Cybernetics, Miyazaki, Japan, 2018
Authors K. van der El, D.M. Pool, M.M. van Paassen, and M. Mulder

9.1. INTRODUCTION

CONSIDERING the task of *steering* a car along a winding road, drivers are known to rely heavily on visual feedback [1, 48, 146]. Two dominant scientific approaches have been adopted to understand driver steering. The *information-centered*, or perceptual approach aims at finding the salient optical cues that drivers use for control, while the *control-theoretic* approach aims at understanding how drivers manipulate the steering wheel to meet the task's guidance and stability requirements [96]. The perceptual approach has shown that drivers use patterns of the optical flow field for control [1, 51, 146, 197, 198], "near" and "far" regions in the visual field [51, 58, 69], and the road's curvature or tangent point [65, 73, 74]. The control-theoretic approach has shown that drivers combine *feedforward* control to follow the road's curves, with *multiloop feedback* control to stabilize the vehicle's relevant degrees-of-freedom (e.g., lateral position, heading) [88, 90, 91, 199].

The perceptual approach relies mostly on experimental occlusion methods, eye-tracking data, and theoretic field analyses, while the control-theoretic approach primarily investigates the humans steering output. One can argue that the perceptual and control-theoretic approaches are complementary, but as of yet poorly integrated [89]. This is perhaps surprising, as perspective geometrical relations directly link the optical features in the human's visual field, the domain of the perceptual approach, to the vehicle's outputs (lateral position, heading, etc.), the stabilization of which is the domain of the control-theoretic approach [96]. By estimating control-theoretic model parameters, such as control gains and delays, from experimental data using *system identification* techniques, the optical cues used by humans have been estimated in helicopter hovering (Grunwald and Merhav [64]), aircraft pitch control (Sweet [98]), and driver steering tasks on straight roads (Weir and McRuer [90, 99]).

For understanding driver steering on *winding* roads, however, it is safe to say that the full potential of the control-theoretic approach has not yet been exploited. This is certainly not because there are no models of driver steering behavior, see [88, 199] for reviews. Instead, we lack empirical data about exactly which control loops are closed by drivers and with what control dynamics. Tentatively, drivers mechanize at least *three* responses while steering, namely, feedback responses based on 1) vehicle heading and 2) lateral position on the road, and 3) a feedforward response based on preview of the road's trajectory ahead. We urgently need a driver model that does not only capture drivers' control *output*, but also their *multiloop control dynamics*. The parameters of such a model (e.g., gains, delays) will have a clear and direct *physical* meaning, and are therefore related to the visual cues used by drivers through perspective geometry.

A well-known model that has been shown to capture the human's control dynamics, is the *crossover model* for single-loop compensatory tracking tasks developed by McRuer *et al.* [6]. The crossover model was extended to preview tracking tasks in Chapter 2 of this thesis, using explicit *multiloop* system identification techniques to measure and model humans' feedforward control response, in addition to their compensatory feedback control behavior. Unfortunately, no equivalent data of multiloop dynamics of the three expected responses in driving have been published to date. This chapter aims to fill this gap in our knowledge of driver steering. Three key innovations are presented:

- Frequency-Response Function (FRF) measurements are obtained of driver steering dynamics in the *three* key hypothesized response channels, namely their feedforward, or *preview* response, as well as their *heading* and *lateral position* feedback responses. Thereby, for the first time, explicit data are available for assessing the control loops closed by the driver, and with what control dynamics.
- A novel driver steering model is proposed that, besides capturing the driver's steering output, also matches the three estimated FRFs of the driver's steering dynamics. The model will be shown to be a direct extension to the well-validated crossover model [6], as well as to proposed models for straight road driving [165] and single-loop preview tracking (Parts I and II of this thesis). Thereby, a unified quasi-linear modeling framework is obtained that spans human control behavior from single-loop compensatory tracking tasks to curve driving.
- The obtained model's parameters are estimated, quantifying: 1) driver control behavior, 2) *which* optical cues are used (using perspective geometrical relations), 3) *how* preview information is processed, and 4) how the control loops are integrated.

In the following, first, the performed simulator driving experiment is explained, after which a separate section is dedicated to each of the three steps above. This chapter ends with a discussion and the main conclusions.

9.2. DATA ACQUISITION

A driving simulator experiment was performed to acquire specific steering data that allow for studying the driver's multiloop response properties.

9.2.1. CONTROL TASK

The considered driving task is illustrated in Figs. 9.1 and 9.2. The driver is to follow the road (the *target* trajectory), for which the centerline lateral position is given by y_c . Simultaneously, the driver must suppress wind-gust disturbances, y_d laterally and ψ_d on heading¹, yielding a total of three external signals, as needed for estimating three FRFs of drivers' steering dynamics [86] (see Section 9.3.1 for details). Only the road's centerline is shown during the experiment, see Fig. 9.2, opposed to a lane of normal width, to limit variability in measured steering behavior. Drivers are effectively tasked to track the road center and thus minimize the lateral position error $y_e = y_c - y$, with y the vehicle's lateral position. A steering wheel is used to provide inputs δ to the vehicle, see Fig. 9.1. The vehicle moves at constant forward velocity U_0 (13.89 m/s or 50 km/h), and the inner- (ψ) and outer-loop (y) vehicle dynamics, $G_\delta^\psi(j\omega)$ and $G_y^\psi(j\omega)$, see Fig. 9.3, are approximated as pure integrators, identical as in [58, 91]. Note that due to the absence of sideslip dynamics in the vehicle model, the lateral position disturbance y_d is directly related to the sideslip angle, $\beta = \arctan(\frac{1}{U_0} \frac{dy_d}{dt})$.

¹Note that different mathematical symbols are adopted than in Chapters 2–7 for consistency with literature on driving (e.g., [50, 52, 90, 165, 200, 201]). Fig. 9.1 summarizes the equivalent symbols.

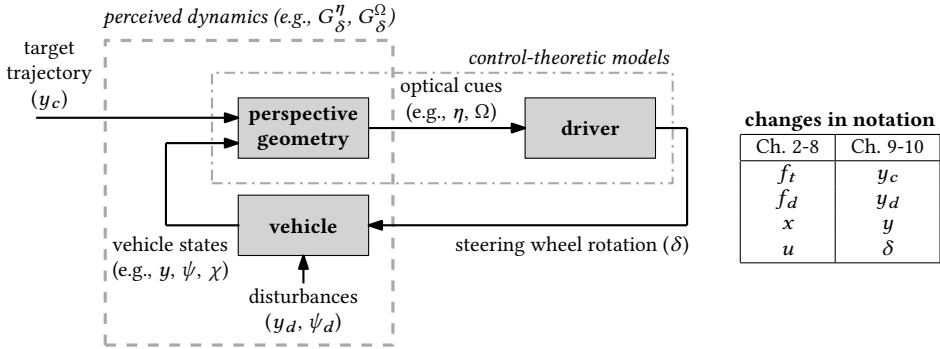


Figure 9.1: Schematic of the driver in a steering task. Control-theoretic models typically lump the perspective geometry and driver blocks, ignoring driver optical cue selection. The change in notation relative to Chapters 2–7 is summarized in the table on the right.

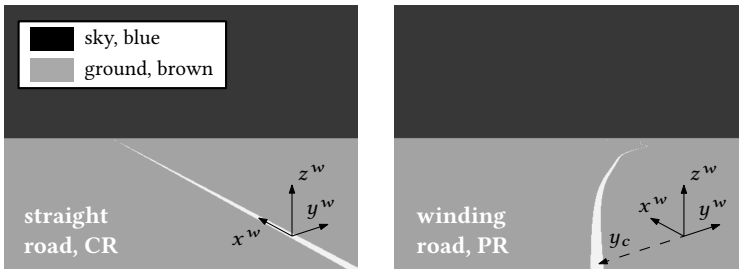


Figure 9.2: Central portion of the experimental visuals presented to the participants.

Fig. 9.3 illustrates the driver’s assumed heading $H_{o_\psi}(j\omega)$ and lateral position $H_{o_y}(j\omega)$ feedback-loop closures, together with the target feedforward response $H_{o_{y_c}}(j\omega)$. Note that the inputs to this control-theoretic model are y_c , y , and ψ , such that the perspective geometry and driver blocks from Fig. 9.1 are effectively lumped together. Only towards the end of this chapter, in Section 9.5, will we separate the characteristics of the driver’s response again from the perspective geometry. That section explains in detail what optical cues (e.g., splay angle Ω , bearing angle η) provide the information required to mechanize the $H_{o_{y_c}}(j\omega)$, $H_{o_\psi}(j\omega)$, and $H_{o_y}(j\omega)$ responses in Fig. 9.3.

9.2.2. INDEPENDENT VARIABLES

To tie in with previous manual control modeling efforts in [90, 200], and Chapters 2–7 of this thesis, the experiment had two independent variables, see Table 9.1. First, driving on straight roads ($y_c=0$) was compared to driving on winding roads ($y_c\neq 0$), see Fig. 9.2. Straight road driving is effectively a compensatory (C) disturbance-rejection task, whereas the winding road yields a pursuit (P) task, combining target-tracking with disturbance-rejection [90]. Second, both tasks were performed both with a naturally rotating (R) view and with a fixed (F) viewing direction. In the “natural”, rotating-view tasks, the virtual

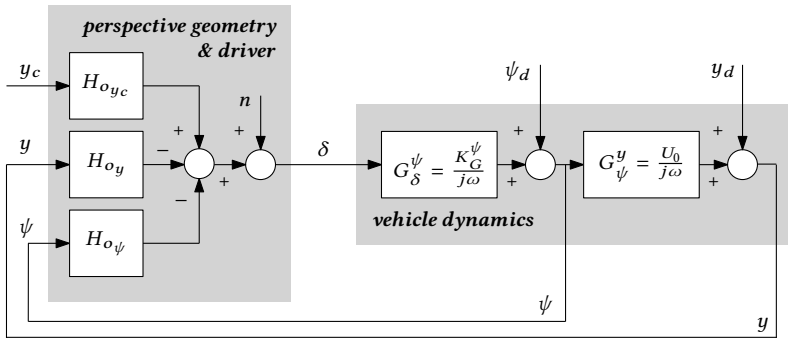


Figure 9.3: Closed-loop control diagram that illustrates drivers’ multiloop control behavior.

camera is aligned with the vehicle’s heading ψ ; in the fixed-view tasks, the camera is always pointed “north”, such that the visuals only reflect the vehicle’s translational lateral movements (information about y) and lack heading information (ψ). In fixed-view tasks, it should thus be impossible for participants to mechanize the inner-loop $H_{o_\psi}(j\omega)$ response in Fig. 9.3. The full factorial of the two independent variables was tested, yielding four experimental conditions, abbreviated as CF, CR, PF, and PR.

In the fixed-view, straight road driving task CF, the lateral position y (or y_e , as $y_c = 0$) is the only available feedback. Humans can be expected to adopt a single-loop compensatory control organization, exhibiting behavior as predicted by the crossover model [6]. The fixed-view, winding road task PF is comparable to the preview tracking task performed in Chapter 7 of this thesis, which invoked two steering responses $H_{o_{y_c}}(j\omega)$ and $H_{o_y}(j\omega)$. In rotating-view tasks, heading information is additionally available, such that humans can be expected to also mechanize $H_{o_\psi}(j\omega)$, leading to a total of either two (in CR tasks) or all three (in PR tasks) tentative responses in Fig. 9.3. This experiment design thereby facilitates direct comparisons of human control dynamics between tasks ranging from single-loop compensatory tracking to curve driving, and to model this behavior in a unifying framework. Table 9.1 summarizes the feedbacks (y_c , y , and ψ) that are available in each task.

Table 9.1: Available feedbacks and expected number of driver responses in the four conditions.

	CF	CR	PF	PR
task	compensatory	compensatory	pursuit	pursuit
view direction	fixed	rotating	fixed	rotating
y feedback	yes	yes	yes	yes
ψ feedback	no	yes	no	yes
y_c	= 0	= 0	≠ 0	≠ 0
# human responses	1	2	2	3

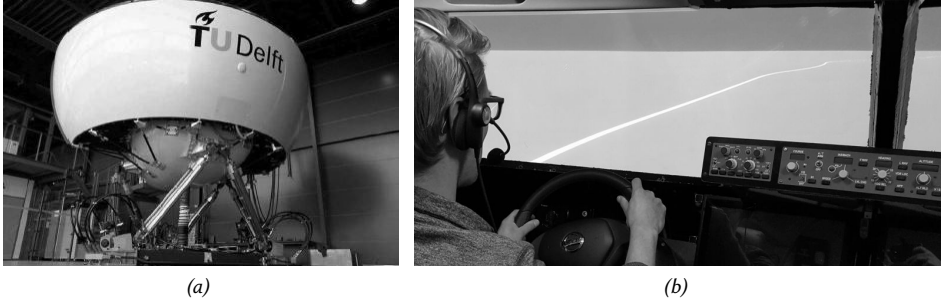


Figure 9.4: The SIMONA research simulator (SRS), outside (a) and inside (b).

9.2.3. APPARATUS

The experiment was performed in the SIMONA Research Simulator (SRS) at TU Delft, Fig. 9.4a, of which the left-hand side was equipped with a customized passenger-car steering wheel. The motion system of the SRS was switched off throughout the experiment. Visuals were presented on the simulator's collimated projection system, which provided participants with a 180×40 deg field of view, see Fig. 9.4b. The road's centerline was white, 10 cm wide, and was viewed from 1 m above the ground plane, corresponding to [50, 52] and the typical eye-height of a driver in a passenger car. Steering wheel rotations were limited to ± 45 deg for safety. The steering gain (K_G^ψ in Fig. 9.3) was manually tuned to provide adequate control authority, while still allowing for accurate steering inputs, yielding a value of 1.33 (deg/s)/deg. The steering wheel stiffness was set to 0.087 Nm/deg within 5.7 deg of the neutral position and to 0.131 Nm/deg otherwise, the damping ratio was 0.007 Nm·s/deg and inertia was 0.2 kg·m².

9.2.4. ROAD TRAJECTORY AND WIND-GUST DISTURBANCES

To estimate drivers' control dynamics without making any *a priori* assumptions about the adopted dynamics, an instrumental-variable system identification technique is adopted (see Section 9.3 for details). To estimate the dynamics of the three response blocks in Fig. 9.3, three instrumental variables are required [86], for which the three applied *forcing functions* are used: the target y_c , and the two disturbances y_d and ψ_d . Corresponding to the common practice in manual control experiments, random-appearing multisine signals are used (e.g., see [44, 86, 165, 175] and Chapters 2 and 7). The road's trajectory is the sum of 10 sinusoids:

$$y_c(a) = \sum_{i=1}^{10} A_{y_c}[i] \sin(\omega_{y_c}[i]a + \phi_{y_c}[i]), \quad (9.1)$$

with amplitude $A_{y_c}[i]$, frequency $\omega_{y_c}[i]$, and phase $\phi_{y_c}[i]$ of the i -th sinusoid, and a the along-track distance [93]. The longitudinal road coordinates are given by $x_c = \int \cos(\psi_c) da$, with the road heading given by $\psi_c = \arcsin(\frac{dy_c}{da})$. The heading and lateral position disturbances y_d and ψ_d are defined identical to Eq. (9.1); the forcing function amplitudes, frequencies, and phases are provided in Table 9.2.

Table 9.2: Amplitudes, frequencies and initial phases of the external forcing function signals.

road centerline, y_c								
RMS(y_c) = 13.1 m, RMS(ψ_c) = 15 deg								
i	k_{y_c}	ω_{y_c}	A_{y_c}	$\phi_{y_c,1}$	$\phi_{y_c,2}$	$\phi_{y_c,3}$	$\phi_{y_c,4}$	$\phi_{y_c,5}$
-	-	rad/m	m	rad	rad	rad	rad	rad
1	3	0.01	17.70	2.92	5.05	4.00	2.66	0.80
2	9	0.04	5.02	1.49	2.99	5.12	2.71	1.08
3	15	0.07	2.33	4.85	5.23	3.73	1.36	0.53
4	27	0.12	0.73	4.26	2.98	0.17	4.08	3.88
5	39	0.18	0.30	6.20	5.00	2.02	5.10	2.74
6	53	0.24	0.14	1.61	2.11	2.51	2.98	3.93
7	71	0.32	0.07	0.83	0.32	3.93	4.92	3.58
8	93	0.42	0.03	1.31	1.03	1.49	5.97	5.21
9	121	0.55	0.02	0.35	4.45	5.88	3.08	4.14
10	155	0.70	0.01	4.21	5.96	0.62	5.75	5.69

disturbance, y_d					disturbance, ψ_d			
RMS(y_d) = 0.3 m, RMS(β) = 1.27 deg					RMS(ψ_d) = 2.2 deg			
i	k_{y_d}	ω_{y_d}	A_{y_d}	ϕ_{y_d}	k_{ψ_d}	ω_{ψ_d}	A_{ψ_d}	ϕ_{ψ_d}
-	-	rad/m	m	rad	-	rad/m	deg	rad
1	5	0.02	0.29	5.98	7	0.03	2.20	5.04
2	11	0.05	0.24	4.04	13	0.06	1.74	6.22
3	19	0.09	0.16	3.05	23	0.10	1.08	4.17
4	31	0.14	0.09	6.11	35	0.16	0.63	4.40
5	43	0.19	0.06	0.99	47	0.21	0.41	4.97
6	59	0.27	0.04	0.01	65	0.29	0.25	4.97
7	77	0.35	0.02	1.78	85	0.38	0.16	4.10
8	101	0.46	0.02	2.28	111	0.50	0.11	5.90
9	131	0.59	0.01	0.41	143	0.65	0.08	5.48
10	169	0.76	0.01	2.41	183	0.83	0.07	0.73

Mutually exclusive input frequencies ω_{y_c} , ω_{ψ_d} , and ω_{y_d} are selected to guarantee that the three forcing functions are uncorrelated, and can thus serve as independent instrumental variables. All frequencies $\omega[i]$ are integer multiples k of the fundamental frequency ($\frac{2\pi}{1389} = 0.0045$ rad/m) that corresponds to the 1389 m long measurement part of the track, which was chosen to be identical to [50, 52]. A reasonably low-frequency driving task was obtained by attenuating the amplitudes $A[i]$ at higher frequencies, see Table 9.2. The amplitudes were further scaled to obtain a task that predominant involves *target tracking*, with RMS(ψ_c) = 15 deg, RMS(ψ_d) = 2.2 deg, and RMS(β) = 1.27 deg. The phases $\phi[i]$ were randomized in accordance with the method in [175]. Five different phase realizations were used for y_c to prevent participants from memorizing (parts of) the road's trajectory. Fig. 9.5 shows a portion of the road trajectory; participants followed the road trajectory reasonably well, and remained clearly closer to the centerline in tasks with a rotating view, due to the availability of heading feedback.

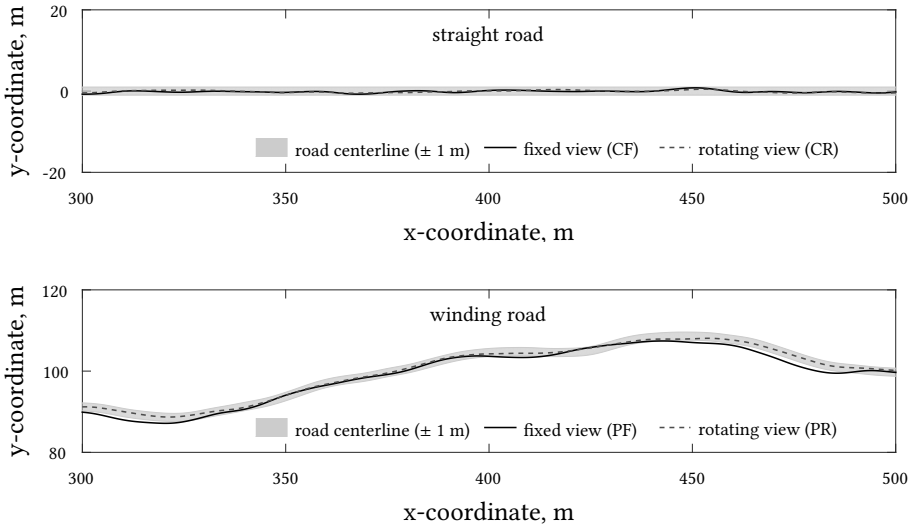


Figure 9.5: A portion of the road trajectory together with the vehicle positions measured for a representative participant. In the figure the road’s centerline is drawn to be 2 m wide to provide a reference for the magnitude of the vehicle’s lateral deviations.

9.2.5. PARTICIPANTS, INSTRUCTIONS, AND PROCEDURES

Eight motivated volunteers participated in the experiment, all students or staff from TU Delft. All participants signed for informed consent prior to the experiment, and were instructed to follow the displayed centerline as accurately as possible.

Participants were seated on the left side of the simulator, with fastened seat belt. First, a single run of each condition was performed to familiarize participants with the steering wheel, the vehicle dynamics, and the display. Then, the four experimental conditions were performed in an order randomized over sets of four participants according to a balanced Latin-square design. A condition was performed at least until tracking performance ($RMS(y_e)$) and control activity ($RMS(\delta)$) were approximately constant in five consecutive runs, which were then used for analysis. A single run was 1806 m, but included 278 m run-in and 139 m run-out; only the steering data in the remaining 1389 m measurement portion of the track were used for analysis.

9.2.6. DATA ANALYSIS

During the experiment, time traces of the applied steering wheel rotations δ and vehicle lateral position y and heading ψ were recorded at 100 Hz. Collected data were interpolated offline to constant along-track distance intervals. The actual time participants took to complete the measurement part of the track was always well within 0.5 s of the nominal time (100.05 s, the time taken when perfectly following the centerline). Therefore, all experimental results are expressed as function of the nominal time (corresponding to

a fundamental frequency of 0.0628 rad/s) instead of the along-track distance, to facilitate comparison with Chapters 2–7 of this thesis, as well as with driver steering data in literature, such as reported in [90, 99].

9.3. MULTILoop DYNAMICS ESTIMATION

9.3.1. SYSTEM IDENTIFICATION TECHNIQUES

Open-loop dynamics

For each forcing function, an open-loop FRF function can be defined to quantify the performance in tracking or rejecting that respective signal. Using Ogata's [202] definition that open-loop dynamics are equal to the negative ratio of the feedback and actuating signals, the heading and lateral position open-loop dynamics are:

$$\begin{aligned} H_{ol}^{\psi_d}(j\omega_{\psi_d}) &= -\frac{\psi(j\omega_{\psi_d}) - \psi_d(j\omega_{\psi_d})}{\psi(j\omega_{\psi_d})} \\ &= G_{\delta}^{\psi}(j\omega_{y_d})[H_{o_{\psi}}(j\omega_{y_d}) + G_{\psi}^y(j\omega_{y_d})H_{o_y}(j\omega_{y_d})], \end{aligned} \quad (9.2)$$

$$\begin{aligned} H_{ol}^{y_d}(j\omega_{y_d}) &= -\frac{Y(j\omega_{y_d}) - Y_d(j\omega_{y_d})}{Y(j\omega_{y_d})} \\ &= \frac{G_{\delta}^y(j\omega_{y_d})H_{o_y}(j\omega_{y_d})}{1 + G_{\delta}^{\psi}(j\omega_{y_d})H_{o_{\psi}}(j\omega_{y_d})}, \end{aligned} \quad (9.3)$$

with $G_{\delta}^y(j\omega) = G_{\delta}^{\psi}(j\omega)G_{\psi}^y(j\omega)$. Good performance is obtained with open-loop dynamics $|H_{ol}(j\omega)| > 1$. The crossover frequency, where $|H_{ol}(j\omega)| = 1$, is therefore a useful indicator of performance; the corresponding phase margin reflects the stability of the closed-loop system. When humans fail to mechanize a heading response, $H_{o_{\psi}}(j\omega)=0$ and Eq. (9.2) equals Eq. (9.3), such that the lateral position and heading open-loop dynamics are equal. Estimated crossover frequencies are used to investigate drivers' control organization, because multiloop controllers are in general organized with decreasing crossover frequencies towards the outer loops [97, 106]. Target-tracking is typically analyzed using the "equivalent" open-loop FRF, given by [90]:

$$\begin{aligned} H_{ol}^{y_c}(j\omega_{y_c}) &= \frac{Y(j\omega_{y_c})}{E(j\omega_{y_c})} \\ &= \frac{G_{\delta}^y(j\omega_{y_c})H_{o_{y_c}}(j\omega_{y_c})}{1 + G_{\delta}^{\psi}(j\omega_{y_c}) \left[H_{o_{\psi}}(j\omega_{y_c}) + G_{\psi}^y(j\omega_{y_c})[H_{o_y}(j\omega_{y_c}) - H_{o_{y_c}}(j\omega_{y_c})] \right]}. \end{aligned} \quad (9.4)$$

Multiloop driver response dynamics

To measure drivers' multiloop response dynamics, the three-channel parallel model structure in Fig. 9.3 is used. It is *not* implied that drivers are internally organized as such; this structure is only used as a convenient tool for measuring driver multiloop steering dynamics. Identical as was done for the single-loop preview tracking tasks in Chapter 2,

the driver's dynamics and control organization (in Section 9.4), and even the visual inputs (in Section 9.5), are eventually obtained by reorganizing the general three-channel control diagram based on the estimated dynamics in each channel. Exploiting the uncorrelated external signals as instrumental variables, FRF measurements of $H_{o_{y_c}}(j\omega)$, $H_{o_{\psi}}(j\omega)$, and $H_{o_y}(j\omega)$ can be obtained directly at the multisine input frequencies ω_{y_c} , ω_{ψ_d} and ω_{y_d} , see [86] and Chapter 2 for details. Although this method has provided accurate estimates of the dynamics of two human response channels in a wide range of tasks (e.g., see [86, 87, 131, 132] and Chapters 2–8), and occasionally of even more than two channels [53, 203], it has not yet been applied to estimate the human's feedforward response together with the two feedback responses that are expected to be simultaneously mechanized in the PR condition.

Perfect target-tracking dynamics

Using Fig. 9.3, the feedforward target response dynamics $H_{o_{y_c}}^P(j\omega)$ that yield perfect target-tracking (i.e., $y = y_c$, or $y_e = 0$) can be derived to be:

$$H_{o_{y_c}}^P(j\omega) = H_{o_y}(j\omega) + \frac{H_{o_{\psi}}(j\omega)}{G_{\psi}^y(j\omega)} + \frac{1}{G_{\delta}^y(j\omega)}, \quad (9.5)$$

where $G_{\delta}^y(j\omega) = G_{\delta}^{\psi}(j\omega)G_{\psi}^y(j\omega)$. The derivation of Eq. (9.5) is identical to that for single-loop tracking tasks, which is given in Chapter 4. Comparison of the actual measured $H_{o_{y_c}}(j\omega)$ with $H_{o_{y_c}}^P(j\omega)$ then shows the extent to which human drivers approach this theoretical optimum.

9.3.2. RESULTS

Open-loop dynamics

Figs. 9.6 and 9.7 show Bode plots of the estimated open-loop dynamics in straight and winding road conditions, respectively. As expected, the disturbance open-loops generally comply with the crossover model [6], with a magnitude response that has a slope of -1 (20 dB/decade) in the crossover region and the phase roll-off at higher frequencies that reflects the participants' time delay. The behavior of the target open-loop is very different (Fig. 9.7c,f), with a magnitude slope of -3 around crossover, which corresponds to the earlier measurements in preview tracking tasks in Chapter 4.

Estimated crossover frequencies and phase margins are summarized in Fig. 9.8. In conditions with a fixed viewing direction, both on straight and winding roads, the crossover frequencies and phase margins are identical for heading and lateral position disturbance-rejection. This confirms that indeed no heading response was mechanized, as explained in Section 9.3.1.1. In rotating-view tasks (CR and PR), the heading and lateral position crossover frequencies are markedly different, indicating that a heading response was active here. Moreover, the heading crossover frequency is higher in rotating-view tasks, while the lateral position crossover frequency is lower (both significant effects, see Table 9.3), suggesting that drivers are indeed organized with heading as an inner control loop for equalizing the lateral position outer loop, as suggested by McRuer *et al.* [90].

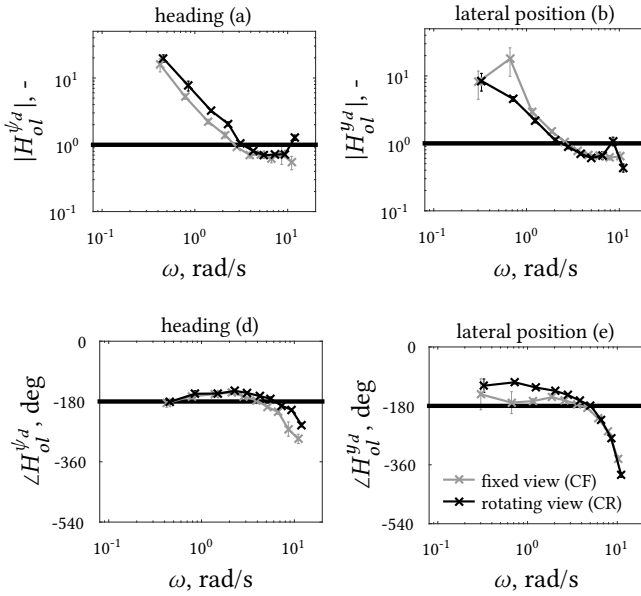


Figure 9.6: Bode plots of estimated open-loop FRFs for a representative participant, straight road conditions (CF, CR); errorbars indicate the standard error.

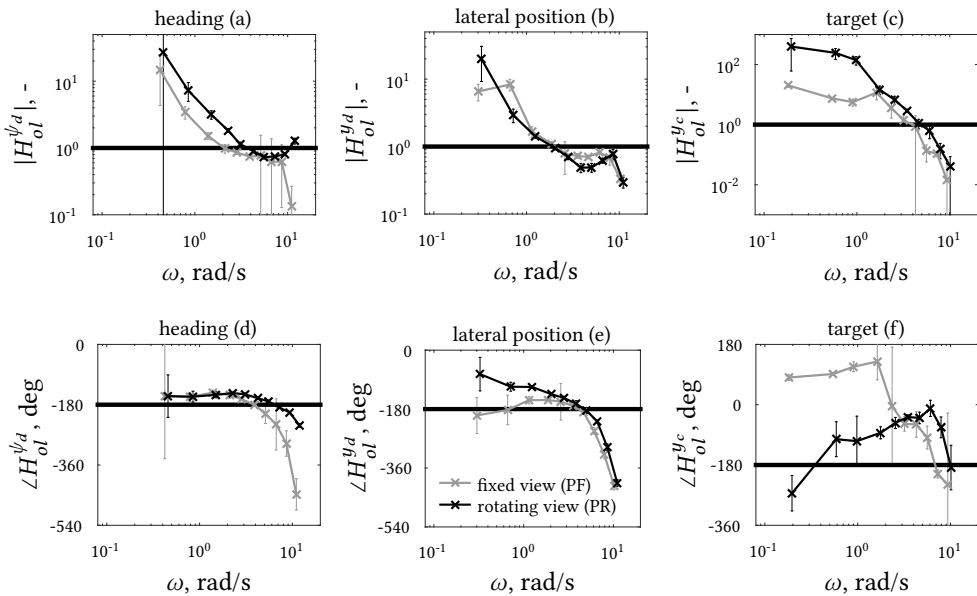


Figure 9.7: Bode plots of estimated open-loop FRFs for a representative participant, winding road conditions (PF, PR); errorbars indicate the standard error.

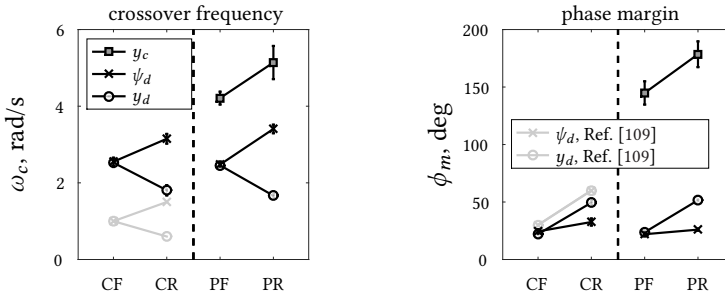


Figure 9.8: Crossover frequencies and phase margins, average of eight participants and standard errors, together with the analytical predictions made by Weir and McRuer [109].

Table 9.3: Results of statistical ANOVA and t-test analyses on the crossover frequencies and phase margins. Significant effects ($p < .05$) are indicated by a “*” symbol.

		crossover freq.			phase margin		
factor		df	F/t	sig.	df	F/t	sig.
y_c	view direction	(7)	2.17	-	(7)	3.35	*
	view direction	(1,7)	186	*	(1,7)	23.4	*
ψ_d	road	(1,7)	1.33	-	(1,7)	4.65	-
	view dir. \times road	(1,7)	4.41	-	(1,7)	2.05	-
y_d	view direction	(1,7)	85.9	*	(1,7)	210	*
	road	(1,7)	1.03	-	(1,7)	1.56	-
	view dir. \times road	(1,7)	0.62	-	(1,7)	0.08	-

Tasks with a rotating view also show significantly higher phase margins, indicating improved stability in all three loops (see Fig. 9.8 and Table 9.3). While the target crossover frequency also increases with rotational feedback, this effect is not statistically significant. There is no significant difference in disturbance-rejection performance and stability between compensatory (straight road) and pursuit tasks (winding roads), which corresponds to single-loop tracking tasks with and without preview, see Chapter 4.

Multiloop FRF estimates

Heading response: The heading FRF estimates $H_{o,\psi}(j\omega)$ in the rotating-view tasks (CR and PR, black markers in Figs. 9.9 and 9.10) are a relatively smooth function of frequency, and variations between the five measurement runs are small (i.e., reasonably small errorbars). In contrast, the estimated FRF components in the fixed-view tasks (CF and PF, gray markers) have a much lower magnitude and show considerable variation between runs, while the estimated phases are an inconsistent function of frequency. Thereby, the FRF estimates in the fixed-view tasks in general appear to reflect only the effect of noise in the loop (due to human remnant) [56, 141], which suggest that no consistent heading response was active. In contrast, the FRF estimates in rotating-view tasks provide strong evidence that participants indeed consistently used heading feedback for controlling their vehicle.

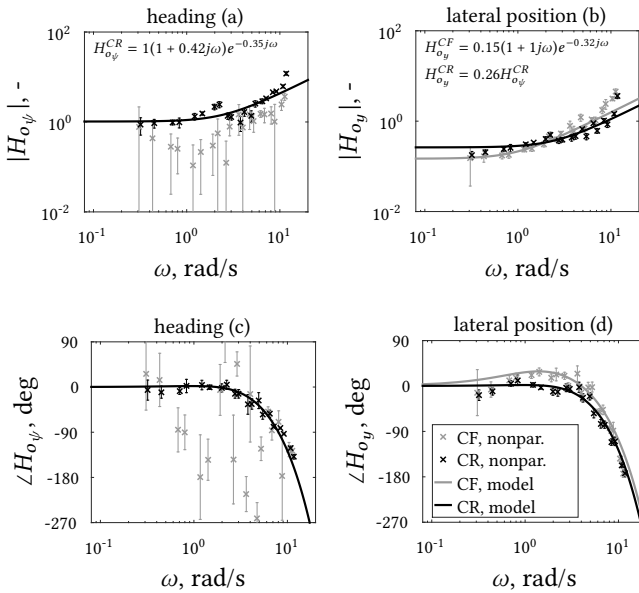


Figure 9.9: Bode plots of the multiloop response dynamics of a representative participant, straight road conditions (CF, CR): FRF estimates with standard errors, and model fits.

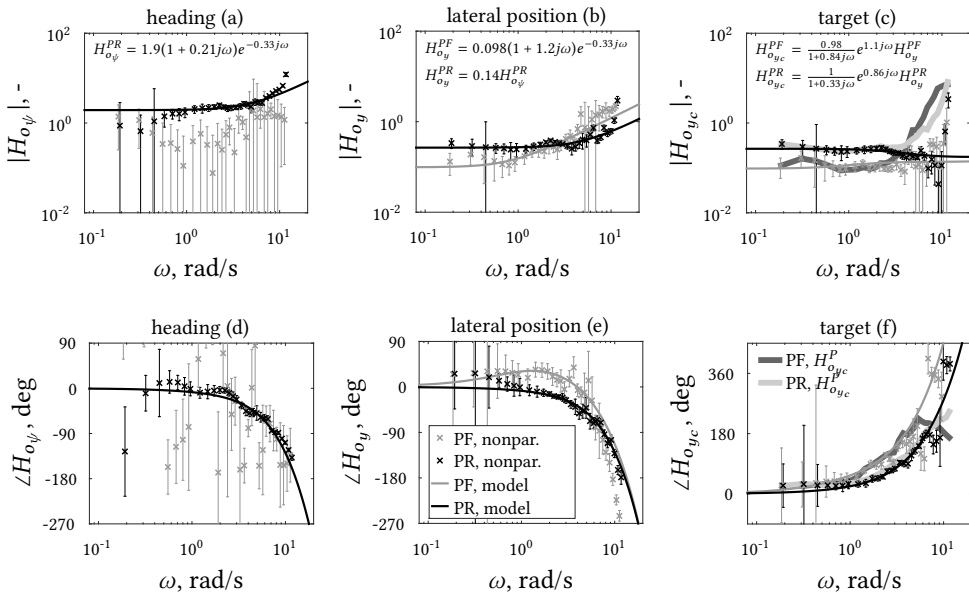


Figure 9.10: Bode plots of the multiloop response dynamics of a representative participant, winding road conditions (PF, PR): FRF estimates with standard errors, perfect target-tracking dynamics, and model fits.

Multiloop feedback dynamics: Figs. 9.9 and 9.10 show that $H_{o_y}(j\omega)$ in fixed-view tasks (CF and PF, gray markers) approximates gain dynamics at low frequencies, and differentiator dynamics at higher frequencies, with notable phase lead for frequencies up to 4 rad/s. This indicates responses proportional to the vehicle's lateral position and lateral velocity (or path angle). Thereby, the double integrator $G_{\delta}^y(j\omega)$ lateral position vehicle dynamics are equalized to an integrator open-loop in the crossover region, yielding a stable system even without a heading-loop closure. In rotating-view tasks (CR and PR, black markers), the required stabilizing lead is instead obtained from the heading-loop closure. Both $H_{o_\psi}(j\omega)$ and $H_{o_y}(j\omega)$ approximate gain dynamics up to frequencies well beyond crossover, indicating inner- and outer-loop responses proportional to the vehicle's heading angle and lateral position, respectively. The slight increase in magnitude at the highest frequencies may indicate lead, that is, relatively weak responses proportional to lateral velocity and heading rate, or oscillatory behavior due to drivers' neuromuscular system dynamics, but it is not possible to know which of these, without measurements at higher frequencies.

Feedforward preview dynamics: In both fixed- and rotating-view tasks, the magnitude of the feedforward response FRF approximates gain dynamics, especially at low frequencies, see Fig. 9.10. This suggests that participants responded to the lateral position of the centerline, so not its heading or curvature. Increasing phase lead is visible at higher frequencies, corresponding to the behavior of a negative time delay, or a *look-ahead time*, similar as observed in single-loop preview tracking tasks (e.g., see Chapter 2). The FRF estimates of $H_{o_{y_c}}(j\omega)$ are relatively noisy at the highest frequencies, because the available preview allows participants to recognize and deliberately ignore much of these fast centerline oscillations, leading to low signal-to-noise ratios at these frequencies (see also Chapter 2).

9.3.3. IMPLICATIONS FOR DRIVERS' CONTROL ORGANIZATION

In summary, the estimated open-loop and multiloop FRFs suggest the following about drivers' control organization and steering dynamics:

- Availability of heading feedback in rotating-view tasks (CR and PR) leads to a heading-loop closure, additional to a lateral position loop; in absence of heading feedback, only the lateral position loop is mechanized in fixed-view tasks (CF and PF).
- When drivers adopt a multiloop feedback organization, the *inner* loop is based on heading feedback and the *outer* loop is based on lateral position feedback, as indicated by the higher bandwidth (ω_c) in suppressing heading disturbances ψ_d compared to lateral position disturbances y_d [97, 106].
- Opposed to the parallel multiloop organization in Fig. 9.3, drivers appear to be organized as series multiloop controllers. The identical shape of the $H_{o_y}(j\omega)$ and $H_{o_\psi}(j\omega)$ FRF estimates, and in particular the equal lead and phase lag in both responses, suggests that *the same* driver steering dynamics are visible in both responses. Moving these identical dynamics to *after* the summation sign of the control diagram in Fig. 9.3, identical as in Chapter 2, yields a series control organization.

- Similarly, the feedforward response also appears to be in series with the other responses, as the low-frequency FRF components in the $H_{o_{y_c}}(j\omega)$ and $H_{o_y}(j\omega)$ responses are identical. This corresponds to observations reported in the single-loop preview tracking tasks in Chapter 2, and suggests that driver feedforward control is effectively a preshaping filter on the previewed target centerline trajectory that, together with the lateral position feedback response, provides the reference for an inner-loop heading response.

9.4. MODELING DRIVER MULTILoop STEERING BEHAVIOR

9.4.1. CONTROL-THEORETIC DRIVER MODEL

Based on the estimated FRF data of Section 9.3, we propose the quasi-linear control model in Fig. 9.11 to describe human control behavior in all four experimental conditions, providing a unifying model for tasks ranging from single-loop compensatory tracking to curve driving. Consistent with the estimated FRFs, the driver is modeled as a *series* multiloop controller with a heading feedback inner-loop, lateral position feedback outer-loop, and a target prefiltering function. The dynamics of the series multiloop model in Fig. 9.11 are related to the estimated FRFs of Fig. 9.3 as follows:

$$H_{o_\psi}(j\omega) = H_o^{comp}(j\omega), \quad (9.6)$$

$$H_{o_y}(j\omega) = K_y^\psi H_o^{comp}(j\omega), \quad (9.7)$$

$$H_{o_{y_c}}(j\omega) = H_{o_f}(j\omega) K_y^\psi H_o^{comp}(j\omega), \quad (9.8)$$

which can be verified by expressing the output δ of both models as a function of the inputs y_c , y , and ψ , and then equating the outputs of the two models. Importantly, the proposed model includes submodels that are identical to well-validated human controller models for tasks were humans mechanize just one or two control channels. First, the central element, or inner loop, is equivalent to the *simplified precision* model for the human's error response $H_o^{comp}(j\omega)$ in single-loop compensatory tracking tasks [6]. Second, the inner- and outer-loop combination for multiloop heading and lateral position feedback is identical to the driver model for disturbance-rejection on straight roads by Weir and McRuer [90, 109, 165]. Finally, the prefilter $H_{o_f}(j\omega)$ provides a low-pass filtered, time-advanced target input to the system, identical to the low-frequency, *far-viewpoint* response in the human controller model for single-loop preview tracking tasks in Chapter 2. For consistency with Chapter 2, the input to series model in Fig. 9.11 is the target τ_f s ahead, opposed to the *current* target in the parallel model in Fig. 9.3.

Inner loop / Single-loop compensatory tracking

Consistent with the estimated inner-loop FRFs (see Figs. 9.9 and 9.10), the *simplified precision model* [6] is adopted for the central compensatory control element $H_o^{comp}(j\omega)$:

$$H_o^{comp}(j\omega) = K_{e^*} (1 + T_{L,e^*} j\omega) e^{-\tau_{e^*} j\omega}. \quad (9.9)$$

The three model parameters are the equalization gain K_{e^*} , equalization lead time-constant T_{L,e^*} , and response time delay τ_{e^*} . In tasks where humans mechanize no heading

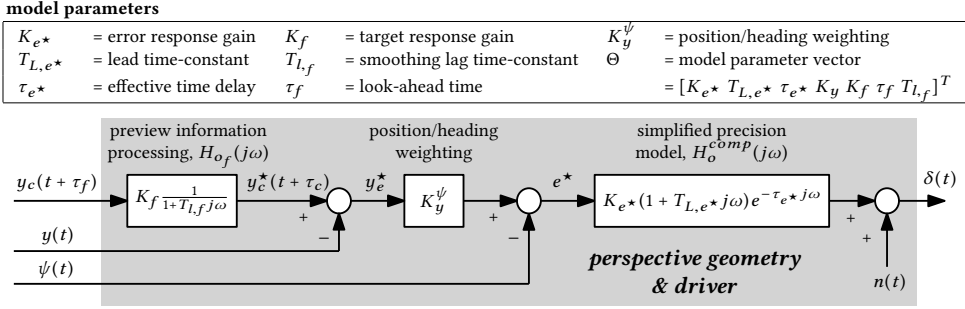


Figure 9.11: Control-theoretic model for driver steering on winding roads, a combination of the simplified precision model [6], the multiloop compensatory driver model for (wind-gust) disturbance-rejection on straight roads [165], and the model for human use of preview in single-loop display tracking tasks (from Chapters 2–7).

inner-loop (e.g., our fixed-view tasks), the remaining lateral position loop closure adopts the compensatory “inner-loop” control dynamics $H_o^{comp}(j\omega)$. In this case, substantial lead equalization is required to attain single-integrator open-loop dynamics, using the crossover model’s verbal adjustment rules [6], because the vehicle has double-integrator characteristics from the steering input to lateral position, given by the dynamics $G_\delta^y(j\omega)$. Depending on the performed control task (e.g., the controlled element dynamics, see Chapter 2), humans may adapt their compensatory control dynamics. More detailed models for $H_o^{comp}(j\omega)$ can include lag equalization or an additional element for the neuromuscular system activation dynamics (e.g., see [44]), but such extensions are not required to capture the current experimental data.

Multiloop feedback / Straight road driving

With rotational feedback, the heading response is the model’s inner-loop, while lateral position feedback becomes the outer-loop. Because the inner-loop closure provides the lead equalization required to obtain a stable integrator magnitude slope around the open-loop crossover frequency [6, 109, 110, 144], drivers can close the lateral position outer-loop using proportional control only, see Fig. 9.11. The model gain K_y^ψ characterizes drivers’ relative weighing of lateral position and heading feedback, and translates the future, filtered error, y_e^* in Fig. 9.11, into a reference angle.

Processing of preview information

In accordance with the target FRF $H_{o_{y_c}}(j\omega)$ in Fig. 9.10, and corresponding to the model for single-loop preview tracking tasks in Chapter 2, the use of preview information is modeled with a prefilter $H_{o_f}(j\omega)$ that outputs a single processed target position $y_c^*(t + \tau_c)$:

$$H_{o_f}(j\omega) = K_f \frac{1}{1 + T_{L,f}j\omega} e^{\tau_f j\omega} = K_f \frac{e^{T_{L,f}j\omega}}{1 + T_{L,f}j\omega} e^{\tau_c j\omega}, \tag{9.10}$$

with $\tau_f = T_{L,f} + \tau_c$, see Fig. 9.12a. Here, τ_f is a look-ahead time that indicates the farthest point ahead on the target trajectory that is used by the human for control and $T_{L,f}$ is the time constant of the low-pass filter, which can be interpreted as the portion of the

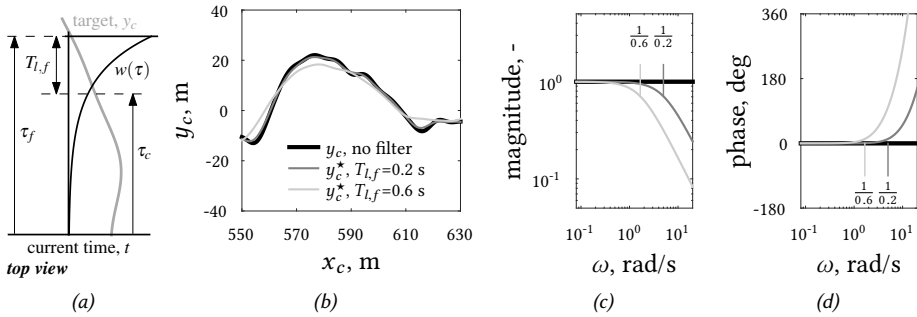


Figure 9.12: Illustration of the impulse response function $w(t)$ that weights the previewed target signal, corresponding to the first-order low-pass filter $(1 + T_{l,f}j\omega)^{-1}e^{T_{l,f}j\omega}$ (a); the effect of this smoothing filter on the processed centerline trajectory y_c^* (b) and Bode plots of the smoothing filter (c,d).

trajectory used for smoothing. As such, τ_c is the effective look-ahead time of the “target” point $y_c^*(t + \tau_c)$ that is the reference for the feedback control loops, see Fig. 9.11. A more intuitive interpretation of the low-pass filter is obtained from its time-domain, impulse response weighting function $w(t)$, see Fig. 9.12a. The smoothed target signal $y_c^*(t + \tau_c)$ is the weighted average, or *convolution*, of the previewed target $y_c(t + \tau_f)$ and the weighting function $w(t)$. As a result y_c^* is identical to the real centerline trajectory y_c at low frequencies, but not at high frequencies, where oscillations of y_c are attenuated, as illustrated in Fig. 9.12b-d. This is consistent with the observed lower magnitude of the target FRF $H_{o_{y_c}}(j\omega)$ at the higher frequencies in Fig. 9.10, and effectively reflects that the road’s tighter corners are cut.

The human’s level of pursuit control is characterized by the gain K_f . A gain $K_f < 1$ indicates that drivers prioritize vehicle stabilization (feedback) over tracking of the target trajectory (feedforward), as explained in Chapter 4. When $K_f=1$ m/m and $\tau_f=T_{l,f}=0$ s, the processed target equals the actual current position of the centerline, $y_c^*(t + \tau_c) = y_c(t)$, and the model reduces to a zero-preview compensatory control strategy, identical to the model for straight road driving (see Fig. 9.11).

9.4.2. MODEL FITS

Parameter estimation

An estimate of the proposed model’s parameter vector $\hat{\Theta}$ (see Fig. 9.11) is obtained by minimizing the least-squares error between the measured (δ) and modeled ($\hat{\delta}$) steering wheel rotations in the frequency-domain, with $\hat{\delta}(j\omega) = H_{o_{y_c}}(j\omega)Y_c(j\omega) - H_{o_\psi}(j\omega)\psi(j\omega) - H_{o_y}(j\omega)Y(j\omega)$, see Fig. 9.3. The Variance Accounted For (VAF) is used as measure for the model quality-of-fit; the maximum VAF is 100% and reflects a model that perfectly replicates the measured control output. Parameter correlations are obtained from the Fisher information matrix, identical as in Chapter 8.

Quality-of-fit

The dynamics of the fitted model are shown in the Bode plots in Figs. 9.9 and 9.10, together with the FRF estimates. The FRF estimates of the driver's lateral position feedback, heading feedback, and feedforward response dynamics are *all* captured well by the model, even though the model was fit by minimizing the error in steering *output*. Only at the very lowest and highest input frequencies there is a small discrepancy between the model and the FRFs, because at these frequencies several FRF components are poorly estimated (obvious from the large errorbars) and because no element for the driver's neuromuscular system dynamics was included in the model.

Table 9.4 shows that the model closely matches the measured steering wheel angles δ in all four conditions, as the average VAFs are well above 90%. Obtained VAFs are slightly higher in rotating-view tasks, indicating that the proposed linear model captures participants' steering output even better than in fixed-view tasks. Likely, this reflects a lower relative contribution of the remnant to the steering output, and relatively more linear control behavior in rotating-view tasks; this corresponds to the data in Chapter 4, where human remnant was larger in double-integrator (fixed view) as compared to single-integrator control tasks (the heading dynamics in rotating-view tasks). In summary, the model captures both the driver's *multiloop control dynamics* and steering *output* well.

Parameter estimates

Table 9.4 also lists the estimated model parameters. Subjects strongly adapt their error equalization dynamics between tasks, see K_{e^*} and T_{L,e^*} in Table 9.4. Tasks with viewing rotations (CR and PR), where equalizing lead is obtained from the heading-loop closure, evoke markedly less explicit lead equalization (lower T_{L,e^*}), but a substantially higher control gain K_{e^*} as compared to fixed-view tasks (CF and PF). Similarly, T_{L,e^*} decreased while K_{e^*} increases from straight to winding road tasks. The product $K_{e^*}T_{L,e^*}$, which can be interpreted as the gain on the *error rate*, is between 0.1 and 0.2 in fixed-view tasks and increases to around 0.4 s in rotating-view tasks, see Fig. 9.13a. The response delay τ_{e^*} is on average between 0.3 and 0.35 s, and increases slightly from fixed- to rotating-

Table 9.4: Estimated model parameters, average over eight subjects and standard deviations.

	CF	CR	PF	PR
VAF, %	92.3±3.33	94.6±1.24	91.2±1.91	94.2±1.10
K_{e^*} , rad/rad	0.11±0.03	1.19±0.40	0.14±0.02	2.06±0.18
T_{L,e^*} , s	1.44±0.40	0.40±0.12	0.90±0.13	0.19±0.02
τ_{e^*} , s	0.33±0.03	0.35±0.02	0.30±0.02	0.34±0.02
K_y^ψ , rad/m	-	0.18±0.04	-	0.12±0.01
K_f , m/m	-	-	0.99±0.01	1.00±0.00
$T_{l,f}$, s	-	-	0.86±0.07	0.26±0.13
τ_f , s	-	-	1.06±0.05	0.89±0.11
$\frac{1}{K_y^\psi U_0}$, s	-	0.41±0.08	-	0.62±0.08
$\tau_f - T_{l,f}$, s	-	-	0.20±0.06	0.63±0.08

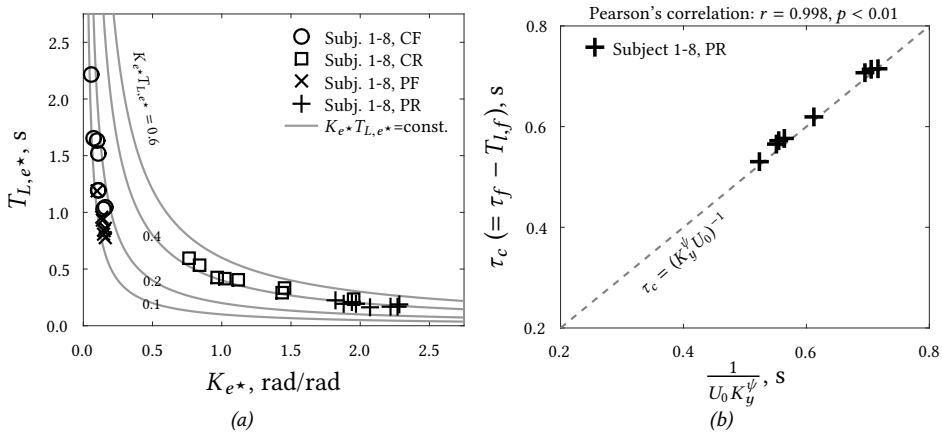


Figure 9.13: The equalization lead time-constant T_{L,e^*} as a function of the equalization gain K_{e^*} (a), and the look-ahead time $\tau_c (= \tau_f - T_{L,f})$ as a function of the feedback weighting gain K_y^ψ , for the PR task only (b).

view tasks, Table 9.4. This contradicts findings in single-loop tracking tasks [6], where lead generation for equalizing double integrator vehicle dynamics (our fixed-view tasks) results in higher response delays than the typical gain response in single integrator tasks, such as our vehicle's heading dynamics in rotating-view tasks. However, a similar increase in visual response delay has been observed when motion feedback is made available in compensatory tracking tasks [111]. Tentatively, with the increased stability provided by an additional loop closure (visual heading or vestibular), there is less incentive for subjects to put effort into reducing their delay.

Subjects' relative weighting of lateral position and heading feedback, K_y^ψ , which is only estimated for rotating view tasks, is slightly higher on straight roads as compared to winding roads, see Table 9.4. Subjects thus minimized lateral position errors more aggressively on straight roads. In winding-road tasks, the estimated target weighting gain K_f approximates unity, for all subjects, both in tasks with and without viewing rotations. Therefore, K_f may in fact be dropped from the proposed model. The farthest preview point of the winding road ahead used for control, characterized by τ_f , is approximately 1.1 s in fixed-view tasks, which matches well with the measurements in double integrator preview tracking tasks in Chapter 5. τ_f drops slightly in rotating-view tasks to around 0.9 s, which is partly because a shorter portion of the previewed trajectory is used for smoothing (lower $T_{L,f}$). The lower $T_{L,f}$ in rotating-view tasks also suggests that subjects cut corners less and follow more of the centerline's higher frequencies when heading feedback is available.

Parameter correlations

Table 9.5 shows the correlations between the estimated parameters of the proposed driver model, but only for the full driving task, condition PR. The inner-loop compensatory control parameters are correlated, as well as the preview processing parameters τ_f and $T_{L,f}$. Strong correlations between these parameters were also found in the model for single-loop

Table 9.5: Model parameter correlations in the PR task, average of eight subjects. Substantial correlations (>0.5) are emphasized in gray.

	K_y^ψ , rad/m	K_{e^*} , rad/rad	T_{L,e^*} , s	τ_{e^*} , s	K_f , m/m	τ_f , s	$T_{L,f}$, s
K_y^ψ , rad/m	1
K_{e^*} , rad/rad	0.46	1
T_{L,e^*} , s	-0.20	-0.72	1
τ_{e^*} , s	-0.45	-0.65	0.81	1	.	.	.
K_f , m/m	0.07	0.09	-0.11	-0.07	1	.	.
τ_f , s	-0.21	-0.64	0.41	0.48	0.14	1	.
$T_{L,f}$, s	0.26	-0.58	0.47	0.34	0.11	0.83	1

preview tracking tasks, see Chapter 8. The “new” parameter as opposed to the single-loop tracking tasks is the weighting of lateral position and heading feedback K_y^ψ . This gain is *not* strongly correlated with any other model parameter, indicating that it can be accurately estimated from the measurement data.

9.4.3. MODEL ANALYSIS

Perfect target-filtering dynamics

With the model, the perfect target-tracking dynamics from Section 9.3.1 can be analyzed in more detail. In fact, an expression for the perfect *prefilter* dynamics $H_{of}^P(j\omega)$ is obtained by substituting the modeled dynamics, Eqs. (9.6)–(9.8), and the vehicle dynamics into Eq. (9.5):

$$H_{of}^P(j\omega) = \underbrace{1}_{\text{low freq.}} + \underbrace{\frac{1}{K_y^\psi U_0} j\omega}_{\text{middle freq.}} + \underbrace{\frac{1}{K_G^\psi U_0 K_y^\psi H_o^{comp}} (j\omega)^2}_{\text{high freq.}} = 1 + \frac{1}{H_{ol}^{yd}(j\omega)}. \tag{9.11}$$

The compact right-most expression can be obtained because the middle and high frequency terms equal the inverse of the lateral position open-loop dynamics in Eq. (9.3). At low frequencies, $H_{of}^P(j\omega)$ is unity such that a direct unfiltered response to the centerline’s lateral position $y_c(t)$ is desirable. At the middle frequencies above $K_y^\psi U_0$ rad/s, Eq. (9.11) shows that the differentiator term dominates $H_{of}^P(j\omega)$, and drivers ideally respond to the centerline’s heading angle $\psi_c(t)$. At the highest frequencies, the double differentiator term $(j\omega)^2$ shows that a response to the centerline’s curvature is required². However, the example $H_{of}^P(j\omega)$ dynamic in the Bode plots in Fig. 9.14 do not fully support these strict frequency distinctions. The low-, middle-, and high-frequency terms of $H_{of}^P(j\omega)$ in fact partially cancel each other due to phase differences. For the model parameter combination shown in Fig. 9.14, a prefilter that approximates gain magnitude dynamics is desirable up to frequencies of almost 7 rad/s.

²Subjects occasionally adopted a two-viewpoint control strategy in the preview tracking tasks in Chapters 2–7. The far-viewpoint response, identical to the target prefilter modeled here, serves to match the low frequencies of $H_{of}^P(j\omega)$, while the model’s “near-viewpoint” response improves the match with the high frequencies of $H_{of}^P(j\omega)$. The FRF estimates in Figs. 9.9 and 9.10 show that all dynamics can be captured by a far-viewpoint-only model, suggesting that a near-viewpoint response is absent. Note that other steering tasks may evoke a near-viewpoint response, for example, when high-frequency tracking is critical.

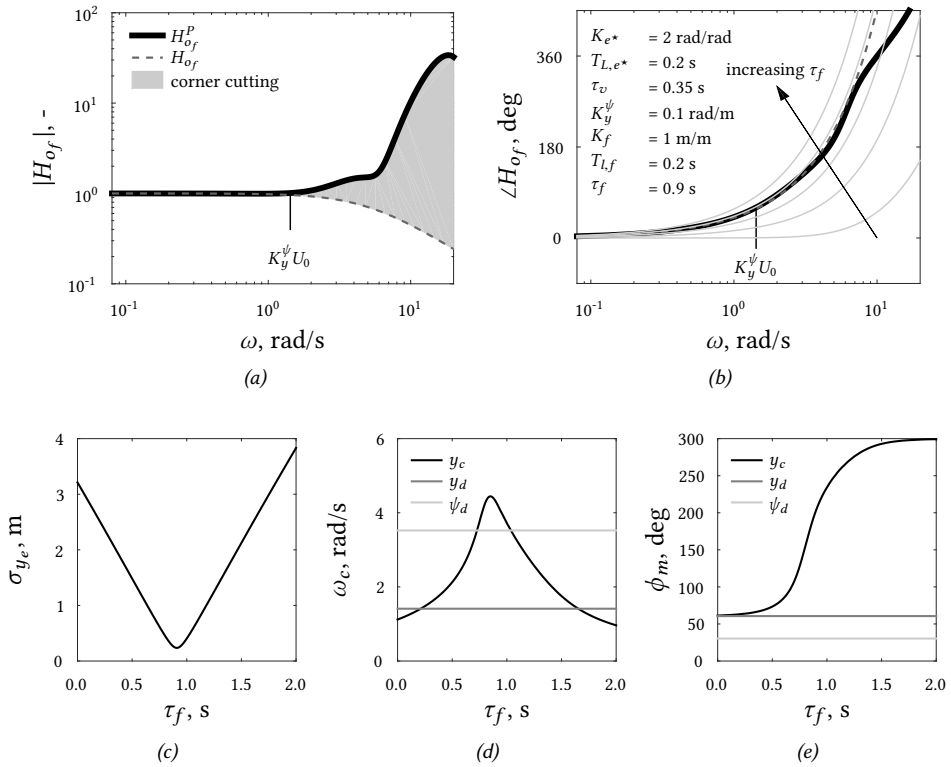


Figure 9.14: Bode plots of preview processing dynamics (a,b), for the approximate average parameters estimates in the full driving condition PR. For look-ahead time $\tau_c = 1/(K_y^\psi U_0)$, here 0.7 s, the phase of the human's dynamics $H_{of}(j\omega)$ is identical to the phase required for perfect target-tracking, $H_{of}^P(j\omega)$, except at very high frequencies. The effect of a suboptimal τ_f value is visible in the standard deviation of the lateral position errors σ_{y_e} (c), the target crossover frequency (d) and the target phase margin (e).

Optimal look-ahead time

Corresponding to the measured FRFs, the target prefilter model $H_{of}(j\omega)$, Eq. (9.8), lacks the lead dynamics required for perfect target-tracking. However, because subjects look ahead at the previewed centerline, $H_{of}(j\omega)$ effectively includes a *negative* time delay, yielding *phase lead*. To match the phase of $H_{of}^P(j\omega)$, the optimal look-ahead time $\tau_c (= \tau_f - T_{l,f})$ can be approximated as the highest time-constant in Eq. (9.11), namely $1/U_0 K_y^\psi$. Fig. 9.13b shows that all subjects indeed adopt a look-ahead time $\tau_c \approx 1/U_0 K_y^\psi$, such that they match the phase of $H_{of}^P(j\omega)$ well in both the low- and middle frequency ranges, as illustrated in detail in Fig. 9.14b.

The near-perfect match of τ_c to $1/U_0 K_y^\psi$ perhaps seems surprising. The *statical* correlation coefficient (so not the *model* parameter correlations that were obtained from the Fisher matrix, discussed before) between τ_c and $1/U_0 K_y^\psi$ for the eight subjects is 0.998,

as indicated in Fig. 9.13b. Often, such a high correlation indicates a redundancy in the model, with multiple parameters – or parameter combinations – that describe the same behavior. However, Table 9.5, the *model* parameter correlations, shows that the measurement data correlate K_y^ψ only weakly to τ_f and $T_{l,f}$, and thus to τ_c . In other words, K_y^ψ , τ_f and $T_{l,f}$ describe *unique* portions of the measured driver behavior, yet participants appear to have trilaterally tuned the specific behaviors reflected by these parameters to obtain a statistically near-perfect match.

A performance perspective clarifies why all participants equalize τ_c almost perfectly to $1/U_0K_y^\psi$. Fig. 9.14b-e show the effect of selecting a suboptimal look-ahead time τ_c ($= \tau_f - T_{l,f}$), in this case by varying τ_f and keeping $T_{l,f}$ constant. The average lateral deviation from the centerline increases markedly when τ_f is suboptimal, see Fig. 9.14c: for a τ_f that is just 0.3 s away from the optimum, the average lateral deviations increase by a factor four. Similarly, Fig. 9.14d shows that a 0.3 s offset in τ_f leads to a crossover frequency that is twice as low. Clearly, the performance penalty for subjects that poorly tune their look-ahead times is large, which explains the strong statistical correlation between τ_c and $1/U_0K_y^\psi$ in Fig. 9.13b.

Corner-cutting behavior

The experimental $H_{o_{y_c}}(j\omega)$ FRF estimate, Fig. 9.10, as well as the modeled $H_{o_f}(j\omega)$ dynamics in Eq. (9.8) indicate that participants exhibit lag or smoothing behavior at high frequencies, and *not* the lead dynamics required for perfect target-tracking, see Eq. (9.11). Fig. 9.14 illustrates that especially the magnitude of the prefilter $H_{o_f}(j\omega)$ is substantially lower at high frequencies than required for perfect target-tracking. Higher time-constants $T_{l,f}$ indicate more smoothing, see Fig. 9.12, or that participants “ignore” even more of the target centerline’s high frequencies. The lower magnitude than required for perfect target-tracking, but matching phase, effectively reflects corner-cutting behavior (see also Chapter 4). The effects of various values of $T_{l,f}$ are further investigated in Section 9.5.

9.5. FROM CONTROL THEORY TO VISUAL CUES

Until now, the *lumped* combination of the perspective geometry and driver blocks in Fig. 9.1 was considered. The implicit assumption then is that drivers can somehow pick up the model inputs from the visual scene: the (previewed) centerline’s lateral position y_c and the vehicle outputs y and ψ . Next, it is investigated what visual cues may provide this information to the driver, by connecting the estimated model parameters to visual cues using perspective geometry. In this section, only the natural, *rotating-view* tasks are considered (CR and PR); an equivalent but simplified analysis could be performed for the fixed-view tasks.

9.5.1. VISUAL CUES AND PERSPECTIVE GEOMETRY

Available visual cues

Fig. 9.15 shows the driver’s view through the front windshield, both for straight and winding roads. Three optical features are visible:

- the horizon line, which is an optical invariant for zero vehicle roll and pitch [47, 96];
- the vehicle's front windshield frame and hood (not explicitly shown in Figs. 9.15a and 9.15b), which are optical invariants assuming steady driver gaze, and provide a reference for the vehicle's lateral position y and heading ψ ;
- the road's centerline, whose bearing angle η and splay angle Ω within the driver's perspective view are *not* invariant, and are thus the only optical cues available for minimizing the lateral position deviations y_e .

Perspective geometry: Straight roads

Consider the centerline of a straight road (Fig. 9.15a), which, by definition, is given by $\psi_c(t + T_{la}) = y_c(t + T_{la}) = 0$ for all times t and look-ahead times T_{la} . Assuming small heading errors, the visual bearing angle of a point A on the centerline T_{la} ahead is [114]:

$$\eta(t, T_{la}) \approx \frac{-y(t)}{U_0 T_{la}} - \dot{\psi}(t) \approx \frac{y_e(t)}{U_0 T_{la}} + \psi_e(t). \quad (9.12)$$

The splay angle Ω for a straight road can be approximated by [96, 114, 204]:

$$\Omega(t) \approx \frac{-y(t)}{h} \approx \frac{y_e(t)}{h}, \quad (9.13)$$

with h the driver's eye-height above the road surface. The splay angle Ω is thus directly proportional to the vehicle's lateral position (error), while the visual angle $\eta(T_{la})$ to the centerline's vanishing point ($T_{la} \rightarrow \infty$) indicates heading (error), see Fig. 9.15a. On straight roads, these two cues thus provide all information required to mechanize the observed multiloop heading and lateral position feedback responses. Differentiating Eqs. (9.12) and (9.13) shows that the rate of change of η and Ω convey information, amongst others, about the vehicle's path angle $\chi = \arctan(\frac{1}{U_0} \frac{dy}{dt})$ and heading rate $\dot{\psi}$ [47, 96]; these signals may play a role in the observed lead steering dynamics at high frequencies, see Fig. 9.9 and Table 9.4.

In fact, drivers can also estimate both the vehicle's heading and lateral position (errors), according to Eq. (9.12), using the visual angles to *any two* aim points on the centerline [114]. Straight roads thus have multiple redundant optical features that can be used by drivers to adopt a multiloop, lateral position and heading control organization. The relation between the optical cues provided by straight roads and control-theoretic model inputs (y and ψ , or y_e and ψ_e) is *overdetermined*, and as a result, knowledge of the control-theoretic model parameters alone are not sufficient to determine which exact optical cues are used by the driver.

Perspective geometry: Winding roads

Sections 9.3 and 9.4 provided evidence that participants also close a heading loop when driving along winding roads. However, from Fig. 9.15b it is clear that winding roads lack a direct optical feature that indicates the vehicle's heading (error), equivalent to the vanishing point of a straight road, see Fig. 9.15a. Using Fig. 9.15c, the visual angle $\eta(T_{la})$ to an

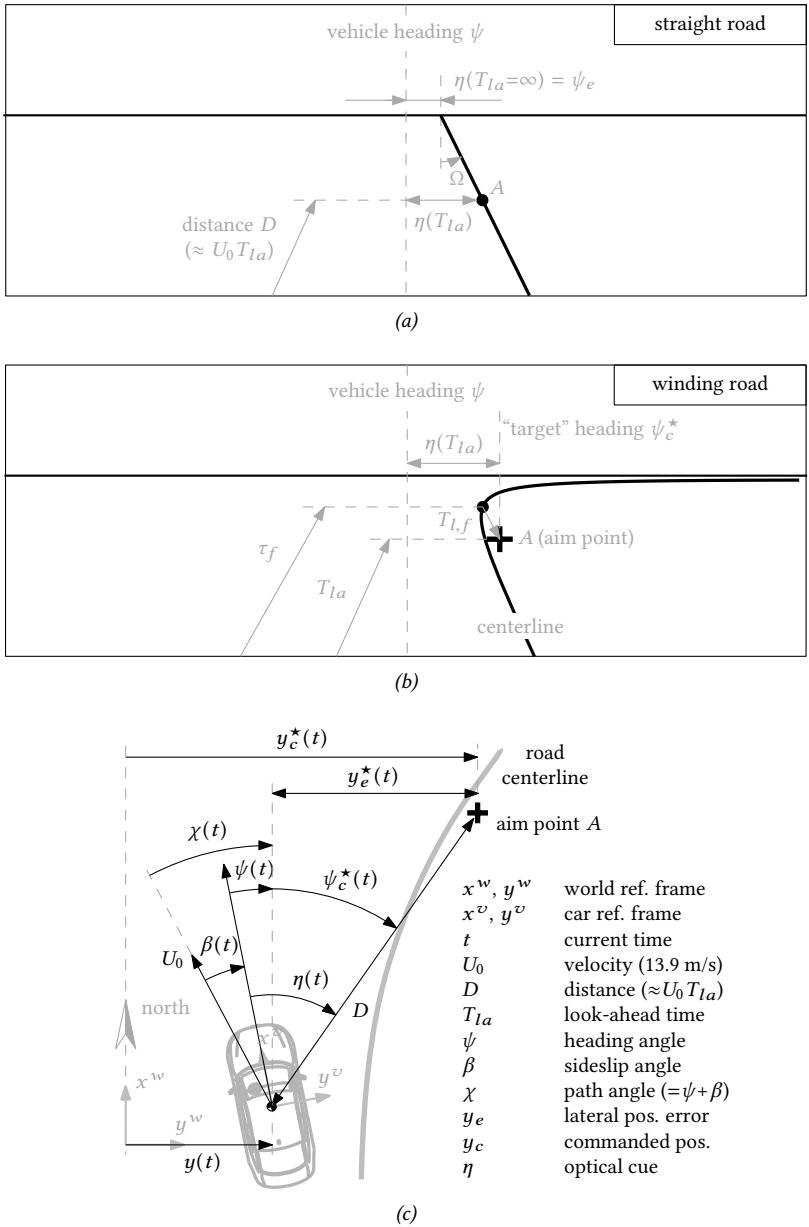


Figure 9.15: A driver's perspective view on the centerline of a straight (a) and winding road (b), and a top view corresponding to the winding road (c) that reveals the geometric relation between the optical cue η , the vehicle lateral position and heading, and the aim-point position.

aim point A at look-ahead time T_{la} (or distance $U_0 T_{la}$) ahead can be expressed as follows:

$$\begin{aligned}\eta(t, T_{la}) &= \psi_c^*(t, T_{la}) - \psi(t) \\ &= \arcsin\left(\frac{y_c^*(t + T_{la}) - y(t)}{U_0 T_{la}}\right) - \psi(t) \\ &\approx \frac{y_c^*(t + T_{la}) - y(t)}{U_0 T_{la}} - \psi(t), \quad \text{for small } \psi.\end{aligned}\quad (9.14)$$

Note that the aim point A in Fig. 9.15b,c is slightly on the inside of the curve and corresponds to the *smoothed* centerline y_c^* (i.e., after low-pass filtering). Eq. (9.14) shows that the visual angle η provides information about *all three* of the control-theoretic model's inputs on winding roads, that is, y , ψ , and y_c^* . However, there is a *fixed* $1/(U_0 T_{la})$ weighting between position and heading information that corresponds to the distance of aim point A ahead of the vehicle in the visual scene. While other information may be obtained from the visual scene (e.g., from the local optical splay angles $\Omega(T_{la})$ of the road ahead [53]), their analysis is beyond the scope of this chapter.

9.5.2. RELATING CONTROL THEORY TO PERSPECTIVE CUES

Using Fig. 9.11, the input to the control-theoretic model's compensatory response, the error $e^*(j\omega)$, can be written in the frequency domain as follows:

$$e^*(j\omega) = K_y^\psi \left[e^{\tau_c j\omega} Y_c^*(j\omega) - Y(j\omega) \right] - \psi(j\omega). \quad (9.15)$$

As is clear from comparing Eq. (9.15) with the Fourier transform of Eq. (9.14), both results are very similar; in fact, $e^*(j\omega) = \eta(j\omega, T_{la})$ when:

$$K_y^\psi = \frac{1}{U_0 T_{la}}, \quad (9.16)$$

$$e^{\tau_c j\omega} = e^{T_{la} j\omega}. \quad (9.17)$$

Eq. (9.16) reflects that the model parameter K_y^ψ , the weighting between heading and lateral position control, can be interpreted as the inverse of the look-ahead distance ($= T_{la} U_0$) at which the aim point is located. Weir and McRuer [90, 99] used this relation in their "aim-point" model for straight road driving. It should be noted that the relation between K_y^ψ and T_{la} is unique only when assuming that drivers minimize a *single* visual angle. If drivers in fact minimize two visual angles $\eta(T_{la,1})$ and $\eta(T_{la,2})$ in a two-channel parallel control organization, K_y^ψ would be related to the two look-ahead times by $K_y^\psi = \frac{1}{2U_0} \left(\frac{1}{T_{la,1}} + \frac{1}{T_{la,2}} \right)$. This indeed confirms that the relation between control-theoretic model parameters and optical cues is overdetermined on straight roads.

For driving on winding roads, Eq. (9.17) provides a crucial second relation: $\tau_c = T_{la}$. There are thus *two* model parameters that characterize the driver's look-ahead time of the visual aim point on winding roads: the gain K_y^ψ that weighs drivers' relative use of heading and lateral position feedback, and the feedforward look-ahead time $\tau_c (= \tau_f - T_{l,f})$. Combining Eqs. (9.16) and (9.17) shows that the feedback and feedforward model parameters

correspond to the same look-ahead time of the visual aim point when:

$$T_{la} = \tau_c = \frac{1}{K_y^\psi U_0}. \quad (9.18)$$

The experimental values of τ_c and $1/(K_y^\psi U_0)$ in Fig. 9.13b indeed confirm that drivers' feedback and feedforward control dynamics are tuned to correspond to the same look-ahead time, for *all eight* subjects. The error minimized by drivers, $e^*(j\omega)$ in the control-theoretic model in Fig. 9.11, is thus the visual angle $\eta(j\omega)$: the difference between the vehicle's current heading and a "target" heading provided by the aim point. Estimated aim points for our eight subjects are located at look-ahead times T_{la} between 0.5 and 0.75 s in winding road tasks PR, and between 0.25 and 0.55 in straight road tasks CR, see Fig. 9.13b and Table 9.4.

9.5.3. IMPLICATIONS FOR DRIVER STEERING

After dropping K_f (≈ 1 m/m) from the model, and substituting T_{la} for both $1/U_0 K_y^\psi$ and τ_c ($= \tau_f - T_{l,f}$), only five parameters are required to capture the measured driving steering behavior (T_{la} , $T_{l,f}$, K_{e^*} , T_{L,e^*} , and τ_{e^*}). In this form, the model suggests that driver steering behavior is the combination of four distinct processes. The following two processes are key, reflecting driver steering at low frequencies:

- *Looking ahead*: selection of an aim point in the visual scene at a look-ahead time T_{la} ahead of the vehicle; the aim point is on or near the road's centerline.
- *Proportional compensatory control*: minimization of the visual angle between the vehicle's heading and the bearing angle of the selected aim point through straight-forward *proportional* compensatory control (K_{e^*}) with a response time delay τ_{e^*} .

Such a control strategy, of compensatory control relative to a *future* target point directly available from visual preview, has been referred to as *prospective* control [89, 205]. In theory, according to the model, these two processes require no visual information except the aim point, suggesting that drivers can exhibit this baseline steering behavior when only a *single* point on the centerline trajectory ahead is visible. This is supported by the seminal occlusion experiment of Land and Horwood [58, 66], in which drivers could steer adequately when only a single, well located, one-deg vertical portion of the visual field was available. Furthermore, this finding was only true for driving at relatively low velocities, evoking the relatively low-frequency control behavior to which the above two baseline processes apply. In addition, drivers can mechanize the following two higher-frequency control mechanisms:

- *Lead equalization*: the generation of high-frequency lead ($T_{L,e^*} > 0$ s) yields an increase in phase margin at crossover, providing improved stability and performance in disturbance-rejection.
- *Target smoothing*: using a $T_{l,f}$ s long portion of the previewed centerline trajectory beyond the aim point to filter the higher frequencies from the centerline trajectory yields a smoothed aim point. Thereby, the road's high-frequency oscillations are

effectively ignored, yielding corner-cutting behavior. The farthest point on the centerline used for control is located $\tau_f = T_{la} + T_{l,f}$ s ahead of the vehicle.

For adopting such high-frequency lead or lag (smoothing) control mechanisms, drivers can benefit from – or even require – visual information in addition to the aim point. To generate high-frequency lead, drivers possibly rely on the global optical flow to obtain heading rate information [47, 197, 200], and for obtaining a smoothed aim point, any portion of the previewed centerline trajectory up to τ_f s ahead may be used. This is again consistent with the experimental results of Land and Horwood [58, 66]: distinct “near” and “far” parts in the visual field are required for adequate steering at higher driving velocities (or in tasks with high-frequency forcing functions, as in the current experiment).

9.5.4. SINGLE-LOOP OPTICAL CUE CONTROL

The proposed driver model provides a novel view on steering behavior. Effectively, steering can be considered as single-loop compensatory control, with the visual angle η as the “error” feedback variable: $\delta(j\omega) = H_o^{comp}(j\omega)\eta(j\omega)$. This single-loop compensatory control strategy is further investigated here.

Optical cue dynamics

The perceived dynamics of the visual angle $G_\delta^\eta(j\omega, T_{la})$, as they appear to the driver, are the lumped combination of the vehicle dynamics and the perspective transformation [64, 96], see Fig. 9.1. Equivalently, $G_\delta^\eta(j\omega, T_{la})$ is obtained by dividing the Fourier transform of Eq. (9.12) by $\delta(j\omega)$:

$$G_\delta^\eta(j\omega, T_{la}) = \frac{\eta(j\omega)}{\delta(j\omega)} = \frac{-G_\delta^y(j\omega)}{U_0 T_{la}} - G_\delta^\psi(j\omega), \quad (9.19)$$

A Bode magnitude plot of these dynamics is given in Fig. 9.16a. Eq. (9.19) and Fig. 9.16a show that the dynamic response of η due to the driver’s steering δ depends explicitly on the look-ahead time T_{la} , that is, how far ahead the aim point is positioned in the visual scene. The optical cue dynamics $G_\delta^\eta(j\omega, T_{la})$ resemble the vehicle’s lateral position dynamics (here, a double integrator) at low frequencies, and the vehicle’s heading dynamics (here, a single integrator) at high frequencies; from Eq. (9.19), it can be derived that the break frequency is at $1/T_{la}$ rad/s. Selecting an aim point $y_c^*(t + T_{la})$ close ahead thus yields a predominantly *double integrator* control task, while an aim point far ahead effective yields a *single integrator* control tasks.

Open-loop dynamics

Assuming that driver behavior is indeed characterized by compensatory control on the optical cue η , as suggested, driver steering can be expected to also comply with the crossover model. Then, according to the crossover model’s verbal adjustment rules [6], the visual angle open-loop dynamics $H_{ol}^{optc}(j\omega) = H_o^{comp}(j\omega)G_\delta^\eta(j\omega, T_{la})$ should resemble integrator dynamics in the crossover region, with a positive phase margin at crossover. In fact, substituting Eq. (9.6) for $H_o^{comp}(j\omega)$ and Eq. (9.19) for $G_\delta^\eta(j\omega, T_{la})$, shows that $H_{ol}^{optc}(j\omega) = H_{ol}^{\psi_d}(j\omega)$, the heading open-loop dynamics in Eq. (9.2). The heading phase margins in Fig. 9.8 are above 20 deg, thus confirming that the visual angle loop is stable.

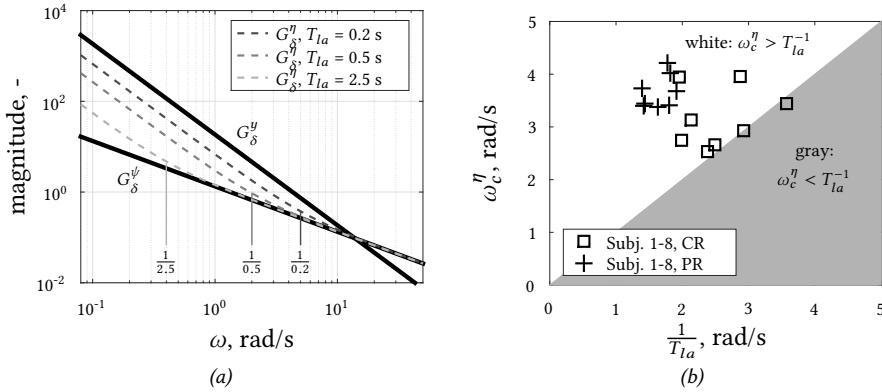


Figure 9.16: Bode magnitude plot of the inner- (heading) and outer-loop (lateral position) vehicle dynamics, together with the visual angle dynamics $G_{\delta}^{\eta}(j\omega, T_{la})$ for various look-ahead times T_{la} (a), and the open-loop optical-cue crossover frequency ω_c^{η} (b), as a function of the break frequency $1/T_{la}$ of $G_{\delta}^{\eta}(j\omega, T_{la})$.

Furthermore, because the measured compensatory control response $H_o^{comp}(j\omega)$ is predominantly a gain in rotating view tasks (see Figs. 9.9 and 9.10), the visual cue dynamics $G_{\delta}^{\eta}(j\omega, T_{la})$ should approximate an integrator around crossover. Fig. 9.16b shows that participants in general indeed adopted a crossover frequency ω_c^{η} that is higher than $1/T_{la}$ rad/s, the frequency beyond which $G_{\delta}^{\eta}(j\omega, T_{la})$ resembles integrator dynamics. However, in the straight road driving task (CR), $\omega_c^{\eta} \approx 1/T_{la}$ for several subjects, hence crossover occurs right where the visual cue dynamics transition from a double to a single integrator. Due to the double integrator magnitude slope right below crossover, the magnitude of the open-loop dynamics $H_{ol}^{optc}(j\omega)$ are much larger than one at low frequencies, providing desirable error-suppression characteristics [6].

Effects of look-ahead time variations

Next, closed-loop model simulations are performed to investigate the effects of varying the look-ahead time T_{la} in the proposed, five parameter visual cue model. These simulations are identical to those performed in Section 9.4 for τ_f variations, so all model parameters except T_{la} were kept fixed at the values shown in Fig. 9.14b. Results of varying T_{la} are shown in Fig. 9.17. The driver-vehicle system becomes unstable (i.e., negative phase margins) when the look-ahead time T_{la} is reduced to below approximately 0.25 s (Fig. 9.17d). Increasing the look-ahead time T_{la} , beyond the optimal value (0.5-1 s ahead), in general leads to larger deviations from the centerline (σ_{y_e} , Fig. 9.17a), lower control activity (σ_{δ} , Fig. 9.17b), lower tracking bandwidth (ω_c , Fig. 9.17c) and larger stability margins (ϕ_m , Fig. 9.17d). These effects all saturate for higher look-ahead times. When a control strategy with a lower compensatory response gain K_{e^*} is adopted (dotted lines in Fig. 9.17), a higher look-ahead time T_{la} is required to achieve optimal performance (the minimum in σ_{y_e} in Fig. 9.17a moves to the right).

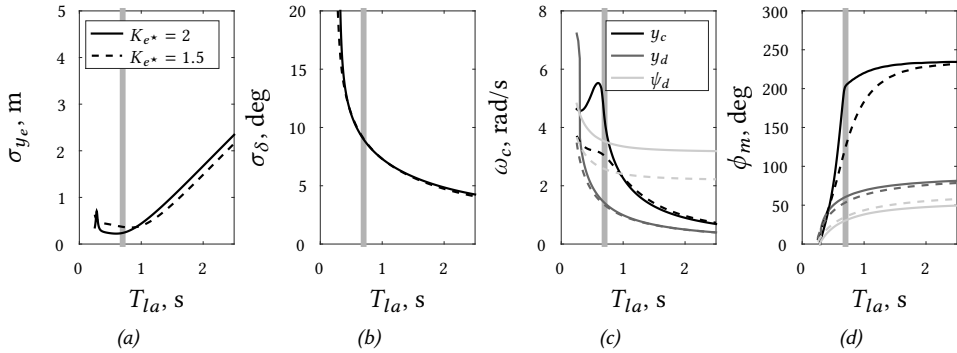


Figure 9.17: Simulated effects of the look-ahead time T_{la} on tracking performance σ_{y_e} (a), control activity σ_{δ} (b), crossover frequency ω_c (c), and phase margin ϕ_m (d). Other model parameters were kept fixed at the values shows in Fig. 9.14. The vertical gray line indicates the average T_{la} estimate of the eight participants from the experiment (the average experimental $K_{e^*} \approx 2$ rad/rad).

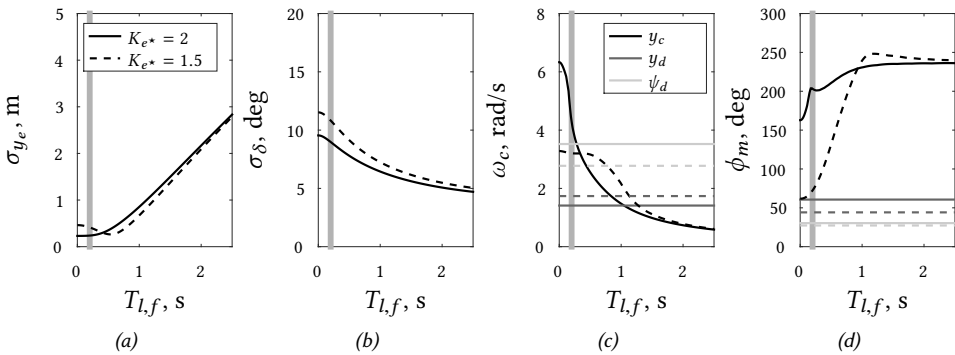


Figure 9.18: Simulated effects of the smoothing filter time-constant $T_{l,f}$ on tracking performance σ_{y_e} (a), control activity σ_{δ} (b), crossover frequency ω_c (c), and phase margin ϕ_m (d). Other model parameters were kept fixed at the values shows in Fig. 9.14, so $T_{la} = 0.7$ s. The vertical gray line indicates the average experimental $T_{l,f}$ estimate.

Effects of smoothing filter variations

Fig. 9.18 shows identical simulations results for smoothing filter time-constant $T_{l,f}$ variations, keeping T_{la} fixed. Increased smoothing behavior (higher $T_{l,f}$) in general leads to a lower target crossover frequency (Fig. 9.18c) and larger deviations y_e from the centerline (Fig. 9.18a), but at the benefit of requiring less control activity (Fig. 9.18b). When steering with a lower gain K_{e^*} , more filtering ($T_{l,f} \approx 0.6$ s) is required to reach optimal performance (compare the solid and dotted lines in Fig. 9.18a). Moreover, for such a low-gain control strategy, increased smoothing benefits the phase margin (Fig. 9.18d), which increases from around 70 deg ($T_{l,f} = 0$ s) to well over 200 deg ($T_{l,f} > 1$ s). The disturbance crossover frequencies and phase margins are lower for a lower K_{e^*} , but are unaffected by $T_{l,f}$.

9.6. DISCUSSION

The aim of this chapter was to improve our understanding of driver steering behavior. We elaborately analyzed and discussed a collected set of steering data, obtained in a dedicated human-in-the-loop simulator experiment. In summary, three key innovations were presented: 1) multiloop FRF measurements of driver steering behavior, 2) control-theoretic modeling of these multiloop FRF data, and 3) physical interpretation of the estimated model parameters in terms of optical cue usage.

Explicit evidence was presented that drivers mechanize an inner-loop based on heading in “natural”, rotating-view tasks, as opposed to fixed-view tasks, where lead on lateral position (or path angle feedback) is used to stabilize the vehicle. In real-life driving tasks, path angle cues may be more salient due to increased visual texture and optic flow; however, Weir and McRuer [90, 99] have suggested that most often the (visually salient) heading angle is used to close a stabilizing inner-loop, which supports our results.

The measured feedforward preview FRF $H_{o_{yc}}(j\omega)$ could be captured well with our *single* preview-point driver model, together with a low-pass smoothing filter. This suggests that drivers do *not* mechanize two distinct responses for tracking the low and high frequencies of the centerline trajectory, in contrast to the control behavior sometimes observed in single-loop preview tracking tasks, see Chapters 2–7 of this thesis. Moreover, the single preview-point model suggests that previously proposed, more complex two-point [94, 95, 139, 206] or multipoint [92, 93] driver models may not be required to capture driver preview steering behavior. Instead, overt trajectory smoothing behavior (i.e., corner cutting), which also results from a weighted response to multiple preview points, could already be produced here by a single first-order low-pass filter and feedback of a single preview point. Only a single lag time-constant ($T_{l,f}$) is then required to quantify the driver’s processing of the relevant segment of the previewed centerline trajectory.

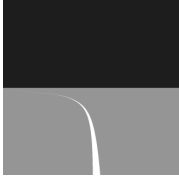
For decades, the prevailing view on driver steering has been that of a dual control strategy [89], much based on the control-theoretical modeling by Donges [91], and the subsequent empirical support by Land and Horwood [58]. However, the presented results suggest that the original “guidance” (feedforward, open-loop control) and “stabilization” (feedback, closed-loop control) levels proposed by Donges [91] may in fact be highly integrated, by direct control of the visual angle η . The selection of an aim point, and adaptation of its look-ahead time T_{la} , simultaneously affects driver feedback control behavior through the relative weighting of lateral position and heading information, as well as the anticipation time in the feedforward control response for target-tracking. Variations in the look-ahead time T_{la} appear to explain the following empirically obtained characteristics about driver steering behavior. Lower T_{la} leads to more emphasis on lateral position control relative to heading control, as well as poorer anticipation of the upcoming curves in the road, and *vice versa*. The order of the visual angle dynamics increases for lower T_{la} , requiring more lead equalization from the driver, which explains the oscillatory or jerky steering that is observed when only the “near visual field” is visible [51, 58, 67–69, 152]. On the contrary, a higher T_{la} yields an emphasis on heading control, leading to lower-order visual angle dynamics, reduced driver lead equalization, and the smoother control behavior associated with the visibility of the “far visual field” [51, 58, 67–69, 152]. Visual features

and patterns besides the aim point could play an important role both in the generation of high-frequency lead (feedback control) and in the smoothing of the target trajectory (feedforward control). As these processes manifest predominantly at high frequencies, they are most critical for driving at high velocities, or, as in the case of this investigation, with relatively high-bandwidth forcing functions.

Simulation of the target-tracking dynamics using the proposed model structure provides a valuable analytic tool for understanding how much preview drivers need in a certain task, and how this varies between drivers. To a first approximation, the optimal look-ahead time $T_{la} = 1/\omega_c^{y_d}$, see Eq. (9.11), indicates that drivers need less preview when steering more aggressively (i.e., with a higher disturbance-rejection crossover frequency). Because higher-order vehicle dynamics typically result in lower crossover frequencies [6], it can thus be expected that drivers of such vehicles need more preview. Moreover, as opposed to the performed centerline *tracking* experiment, the available lane width in realistic driving tasks allows for certain lateral deviations from the road centerline. This means that adequate performance can be achieved with a relatively lower lateral position crossover frequency, as illustrated by the results from Weir and McRuer [109] in Fig. 9.8. Consequently, based on the perfect target-tracking dynamics, drivers in “normal” lane-keeping tasks can be expected to adopt a larger look-ahead time than found in the current tracking experiment.

9.7. CONCLUSION

This chapter improved our understanding of driver steering behavior through three key innovations. First, for the very first time, multiloop Frequency-Response Function (FRF) measurements provided unique evidence that drivers close an inner-loop based on heading feedback, in addition to a lateral position outer-loop. Driver feedforward control processes include *looking ahead* and *smoothing* of the previewed centerline trajectory. Second, the obtained FRF data were modeled using quasi-linear control theory; the resulting model does not only capture the driver steering *output*, but is the first that also captures drivers’ *multiloop control dynamics*. Extending previous models such as the seminal crossover model, a unified framework is now available for analyzing manual control behavior in tasks that range from single-loop compensatory tracking to driving with preview on winding roads. Identifiable and physically-interpretable model parameters exactly quantify how much of the previewed trajectory is used for anticipation and smoothing, and to what extent heading feedback alleviates the need for drivers to explicitly generate lead. Third and finally, estimated model parameters were connected to available optical features in the visual scene using perspective geometry, effectively integrating *control-theory* with *perceptual* models of driver steering behavior. Thereby, it is now possible to estimate the optical cues used by drivers directly from steering data, and to quantitatively predict the effects of degraded visual feedback on driver steering behavior. These results can be instrumental for understanding and avoiding driver-automation interaction issues in modern road vehicles, and to systematically design human-like or individualized driver support systems.

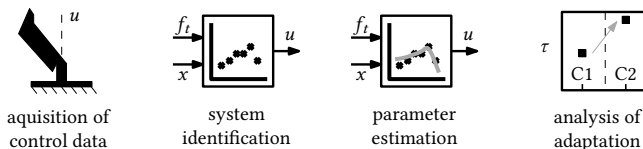


10

BOUNDARY AVOIDANCE AND RESTRICTED PREVIEW IN DRIVING

Chapter 9 proposed a driver steering model that captures the human's multiloop control dynamics, while also quantifying the exact visual angle that drivers select as feedback for control. This chapter investigates to what extent this behavior – and the proposed model – is representative for a range of realistic curve driving tasks, where: 1) deviations from the centerline are not necessarily minimized (as in Chapter 9), but the full width of a road lane can be exploited, and 2) preview available from the road ahead is restricted due to fog. A human-in-the-loop simulator experiment is performed, in which centerline-tracking and lane-keeping (boundary-avoidance) driving tasks are compared, both with unrestricted visibility and with dense, simulated fog that obscures the road beyond 0.5 s ahead. Driver steering behavior and optical cue selection, and adaptation thereof between the different driving scenarios, are explicitly quantified by estimating the parameters of the proposed multiloop preview steering model of Chapter 9. In addition, a variety of time-domain measures are presented to connect the results to other research on driver steering behavior, which do typically not adopt a frequency-domain modeling approach.

Steps of the cybernetic approach involved:



The contents of this chapter will be submitted for publication as:

Title Identification of Driver Boundary-Avoidance and Restricted-Preview Steering Behavior
Journal IEEE Transactions on Human-Machine Systems
Authors K. van der El, D.M. Pool, M.M van Paassen, and M. Mulder

10.1. INTRODUCTION

IN manual control of vehicles or devices, humans can benefit profoundly from the availability of *preview* information about the target trajectory to follow in the near future [59, 207]. Both overt stability and performance metrics deteriorate when preview is restricted, which has been shown, for example, when driving through fog on a winding road [58, 59, 208, 209], and when the available preview is limited on tracking displays (e.g., in Chapter 5 and [49, 54, 55]). In single-loop tracking tasks, quasi-linear human controller models were key to revealing that restricted preview does not only limit the human's abilities to anticipate, but also to smooth the target trajectory ahead (see Chapter 5). Although restricted preview has an identical negative effect on performance in steering of ground vehicles such as passenger cars, it is as of yet unclear whether humans adapt their control behavior identically in these more realistic tasks. Opposed to human behavior in single-loop display tracking tasks, drivers adopt a *multiloop* control organization, exploiting feedback signals about both lateral position and heading, see Chapter 9, and [90, 99]. Moreover, instead of *tracking* an exactly defined target trajectory, a range of lateral positions between the demarcated lane edges is equally acceptable while driving, yielding a *boundary-avoidance* or lane-keeping task [116, 117, 210].

Tracking tasks essentially require continuous attention and control from the human operator. Changes in the target signal, external disturbances, and internal perception or motor noise directly yield errors and thus an incentive to steer [6, 44]. In boundary-avoidance tasks, deviations from the centerline are not considered errors per se; such deviations may accumulate over time, before evoking a control response only after passing a certain threshold. Furthermore, corner cutting is often a manifestation of driving skill, and not control error [117]. Experimental data suggest that drivers aim to keep the *time to line crossing* (TLC), that is, the time before the vehicle would leave the road assuming constant control inputs, above a threshold of 3-4 s [116]. The TLC quantifies the time available to the driver to make a corrective steering action; sufficiently high TLCs evoke no steering response and can even lead to intermittent control [116, 118, 211]. As opposed to tracking, such human behavior has been quite generally referred to as error-neglecting [116], boundary-avoidance [210, 212-214], or – as will be used here – *satisficing* control [117]. It is important to clearly distinguish the control *task* from the human's *behavior*. Boundary-avoidance tasks may still evoke *tracking* behavior, for example, narrower road lanes were shown to lead to smaller deviations from the centerline in driver steering tasks [215], and also from the tunnel center when flying through a displayed tunnel-in-the-sky [97, 216]. Conversely, humans may display *satisficing* behavior in tracking tasks, for example, a substantial priority for low control effort may lead to larger errors [120, 217].

Multiloop system identification and modeling of the driver's steering dynamics in Chapter 9 has led to new insights into driver steering behavior, preview processing and cue utilization, but only in tracking of a winding road's centerline with unrestricted preview. This chapter aims to quantify how drivers adapt their steering behavior between centerline tracking and boundary-avoidance tasks, and between "nominal" tasks with full preview and "off-nominal", safety-critical tasks where preview is severely limited. To do so, new empirical human-in-the-loop steering data is presented, collected in a simulator driv-

ing experiment, with the specific purpose to facilitate analyzing the driver's adaptation both in the time- and frequency-domain, as well as with the multiloop driver model from Chapter 9. The frequency-domain measures and quasi-linear model parameters are identical to those presented throughout this thesis, while the additional time-domain analysis facilitates the explicit comparison of obtained results to driver steering behavior measures as often presented in literature (e.g., [52, 102, 116, 119, 211]). Thereby, this chapter aims to connect the knowledge of how humans use preview in relatively artificial tracking tasks, obtained throughout this thesis, to what is known in the literature of driver steering in realistic curve driving tasks.

10.2. DRIVING EXPERIMENT

10.2.1. INDEPENDENT VARIABLES

Two independent variables were varied in the performed driving experiment, the road presentation and the available preview, see Fig. 10.1. The road was presented either by its centerline only, yielding a tracking task (TR) as considered in Chapter 9, or by a 3.5 m wide lane, extending 1.75 m on each side of the centerline, yielding a lane-keeping task (LK). Preview was either unrestricted (PR) or limited to 7 m (≈ 0.5 s) by fog (FG) ahead of the vehicle. The factorial of the two independent variables was tested, yielding four experimental conditions referred to as TR-FG, LK-FG, TR-PR, and LK-PR.

10.2.2. APPARATUS AND CONTROL VARIABLES

The experiment was performed in a setup identical to that used in Chapter 9, but with slight adaptations to better resemble real-life driving tasks. First, the "bicycle model" was used for the vehicle dynamics [218]; the model parameters were configured to resemble a neutrally steering, typical passenger car, identical to [50]. Second, the ground and sky planes of the outside scenery showed a typical rural road found in The Netherlands. The rich textures for the grass and clouds were absent in the experiment of Chapter 9, but an identical experiment in the same simulator setting by Wolters *et al.* [52] revealed negligible driver behavior adaptations to this optical flow. Third, the control loading of the steering wheel was manually tuned to better match the feel of a typical passenger car, resulting in a stiffness of 10 Nm/rad (≈ 0.17 Nm/deg); the rotational limit was increased, but for safety still limited to ± 2 rad ($\approx \pm 115$ deg). All other experimental settings were equal to Chapter 9, including the road trajectory, the external disturbances, and the vehicle's constant forward velocity (50 km/h).

10.2.3. PARTICIPANTS, INSTRUCTIONS, AND PROCEDURE

Eleven motivated volunteers participated in the experiment, three of which failed to finish the experiment due to emerging signs of motion sickness. The remaining eight participants (five male, three female) were on average 26.4 years old ($\sigma = 2.8$ years), were in possession of a driver's license for 5 years ($\sigma = 2.2$ years), and drove 7,400 km per year



Figure 10.1: Central portion of the experimental visuals as presented to the participants.

($\sigma = 6,000$ km). All participants signed for informed consent before starting the experiment. Participants were instructed to drive as they would normally do in lane-keeping tasks (LK-FG and LK-PR), and to minimize the lateral position error relative to the centerline in tracking tasks (TR-FG and TR-PR).

The participants were then seated in the simulator for an initial five-run training phase to familiarize themselves with the steering wheel, the disturbances, the vehicle dynamics, and the display. The LK-PR task was first performed with the wind-gust disturbances switched off, such that participants could feel their contribution when they were switched on in the second run. Subsequently, the LK-FG, TR-PR, and TR-FG tasks were practiced.

Then, the measurement phase of the experiment commenced. The four experimental conditions were performed in an order randomized according to a balanced Latin-square design. A condition was performed at least until the average deviations from the centerline and steering wheel deflections were approximately constant in five consecutive runs, indicating that the participant's initial learning and adaptation curve had flattened. After each run, participants were given a performance score to motivate them. They were additionally asked to indicate signs of emerging motion sickness on the 11-point misery scale (e.g., see [219]); for comfort of the participants, the experiment was directly terminated when a score of five or higher was given. To reduce fatigue, participants left the simulator after each condition for a 10-20 min break, before moving on to the next condition. The experiment was typically completed in approximately three hours.

10.2.4. DEPENDENT MEASURES

The following dependent measures were calculated from the experimental data:

Position in the lane: Lateral position on the road was used as a measure of performance, and is characterized by the vehicle's deviation y_e from the centerline. The standard deviation σ_{y_e} is used to compare driving performance to literature [50, 52, 66, 209, 220–222]. The contributions due to the external target, lateral position disturbance, and heading disturbance signals, as well as due to the human remnant, are characterized by the standard deviation σ_{y_e} at each respective set of input frequencies, that is, ω_{y_c} , ω_{y_d} , ω_{ψ_d} , and ω_n . These separate contributions were calculated in the frequency domain, following the methodology detailed in Chapter 3. The target-to-error dynamics $Y_e(j\omega)/Y_c(j\omega)$ were estimated to further quantify road following performance, see Chapter 6 for details.

Lateral accelerations: The standard deviation of the lateral vehicle accelerations σ_{a_y} was used to compare the performed driving task with measurements obtained in the real world and other simulator driving tasks [102, 119].

Intermittent control behavior: The level of intermittent control was characterized by the time $T_{\delta \approx 0}$ for which participants have an approximately constant control input. To estimate $T_{\delta \approx 0}$, the control input was assumed to be constant when the steering wheel deflection rate $\dot{\delta} < 3$ deg/s, identical to [116], but only for periods longer than 0.3 s to omit steering reversals. The TLC was used as measure for the incentive for continuous control, opposed to intermittent control [116]. The TLC indicates the time before any side of the vehicle will hit a lane edge, when the current steering wheel angle is maintained, see Fig. 10.2. The *curved* TLC was calculated, by extrapolating both the current heading angle and rate, see [116, 117] for details. The alternative *straight* TLC was not considered, because neglecting the heading rate would yield a poor estimate of the actual time until road departure, due to the relatively high road curvatures. The vehicle was assumed to be 1.5 m wide, identical to [117]. In tracking tasks, a virtual TLC was calculated for comparison with the lane-keeping tasks, by assuming identical road width (3.5 m).

Control activity: The standard deviation of the control output σ_δ was used as measure for control activity. Identical as the lateral position, σ_δ was further separated into contributions due to the target and disturbance signals, and the human remnant. Estimates of the control output spectral density functions $S_{\delta\delta}$ were used to further quantify control activity at different frequencies.

Tracking bandwidth and stability: Open-loop crossover frequencies ($\omega_c^{y_c}$, $\omega_c^{y_d}$, and $\omega_c^{\psi_d}$) were used as frequency-domain measures for the bandwidth with which humans track the centerline trajectory y_c and suppress the external disturbances y_d and ψ_d . The corresponding phase margins ($\phi_m^{y_c}$, $\phi_m^{y_d}$, and $\phi_m^{\psi_d}$) were used as measures for stability. These measures were calculated identically as in Chapter 9.

Human control dynamics: Estimates of the human's multiloop control dynamics were used as an explicit measure for driver visual cue selection, information processing, and control behavior. Measures include multiloop Frequency-Response Function (FRF) estimates ($H_{o_{y_c}}(j\omega)$, $H_{o_y}(j\omega)$, and $H_{o_\psi}(j\omega)$), estimates of the parameters of the multiloop driver

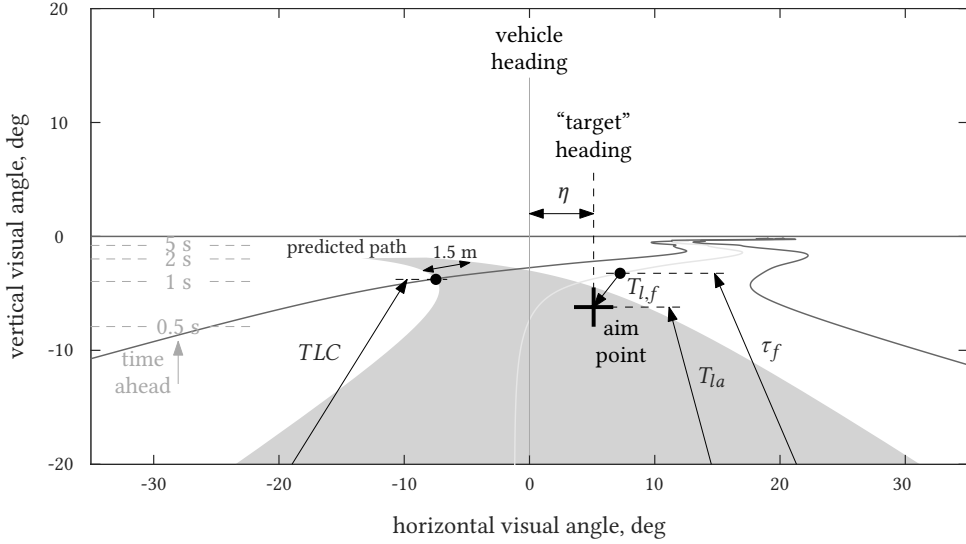


Figure 10.2: A graphical illustration of the TLC and the physical meaning of the model's look-ahead times, together with the visual angle η that is effectively minimized by the driver through compensatory control, see Chapter 9 for details.

model (K_{e^*} , T_{L,e^*} , τ_v , ω_{nms} , ζ_{nms} , T_{la} , τ_f , and $T_{L,f}$), and the estimated visual angle η that is minimized through compensatory control. These measures are obtained according to the methodology described in Chapter 9; in particular, for the model parameter estimates, the multiloop driver model is first fit to the data, before the look-ahead time $T_{la} = 1/(U_0 K_y^\psi)$ is computed from the estimated value of K_y^ψ in a second step. Fig. 10.2 illustrates the physical meaning of the model's look-ahead times and the visual angle η for reference. To quantify human adaptation in even more detail than in Chapter 9, a model for the human's neuromuscular actuation dynamics ($H_{nms}(j\omega)$, identical as in Part II) is also included in the compensatory control response $H_o^{comp}(j\omega)$. The modeled control output as a function of the optical angle η is given by $\hat{\delta}(j\omega) = H_o^{comp}(j\omega)\eta(j\omega) + N(j\omega)$, with:

$$H_o^{comp}(j\omega) = K_{e^*}(1 + T_{L,e^*}j\omega)e^{-\tau_v j\omega} \frac{\omega_{nms}^2}{(j\omega)^2 + 2\zeta_{nms}\omega_{nms}j\omega + \omega_{nms}^2}, \quad (10.1)$$

with ω_{nms} and ζ_{nms} the neuromuscular break frequency and damping ratio, respectively. To avoid obtaining physically unrealistic break frequencies and damping ratios, constraints of $\omega_{nms} < 18$ rad/s and $0.05 < \zeta_{nms} < 0.4$ were applied while estimating the parameters from the data. Note that the modeled delay τ_v now represents *only* the human's visual response delay, opposed to Chapter 9, where τ_{e^*} captures both the human's visual response delay *and* the phase effects of the neuromuscular system.

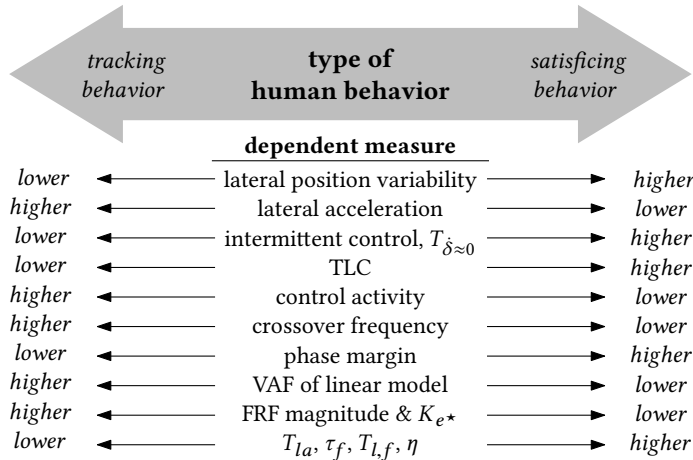


Figure 10.3: Hypothesized qualitative changes in the dependent measures when human behavior shifts between pure tracking and satisficing control.

10.2.5. HYPOTHESES

H.I First, it is hypothesized that restricted preview affects human control behavior identically as in single-loop tracking tasks (Chapter 5), in particular leading to more lateral position variations in the lane (higher σ_{y_e}) and a lower phase margin $\phi_m^{y_e}$. These effects are a direct consequence of limiting the most distant visual trajectory input to the driver (τ_f) to 0.5 s ahead, and, as $\tau_f = T_{la} + T_{l,f}$, this limits the driver’s ability to anticipate (T_{la}) and smooth ($T_{l,f}$) the trajectory’s curves.

H.II Second, it is hypothesized that there is an interactive effect of road presentation and restricted preview on driver steering behavior. Humans are hypothesized to display higher levels of satisficing control behavior in lane-keeping tasks (LK) with full preview, as compared to centerline-tracking (TR) tasks, but *not* when preview is restricted. While available lane width increases the range of acceptable vehicle trajectories, it is expected that drivers can exploit this additional freedom only when there is adequate baseline performance and stability, which may not be attained when fog severely limits the preview of the road ahead. Fig. 10.3 illustrates the changes in the dependent measures that are expected to occur when participants show higher levels of satisficing control behavior in LK-PR tasks.

10.3. RESULTS

10.3.1. NONPARAMETRIC MEASURES

Position on the road

Fig. 10.4a shows a portion of the road, together with the trajectories traveled by a representative participant in the conditions where the average lateral deviation are largest (LK-FG)

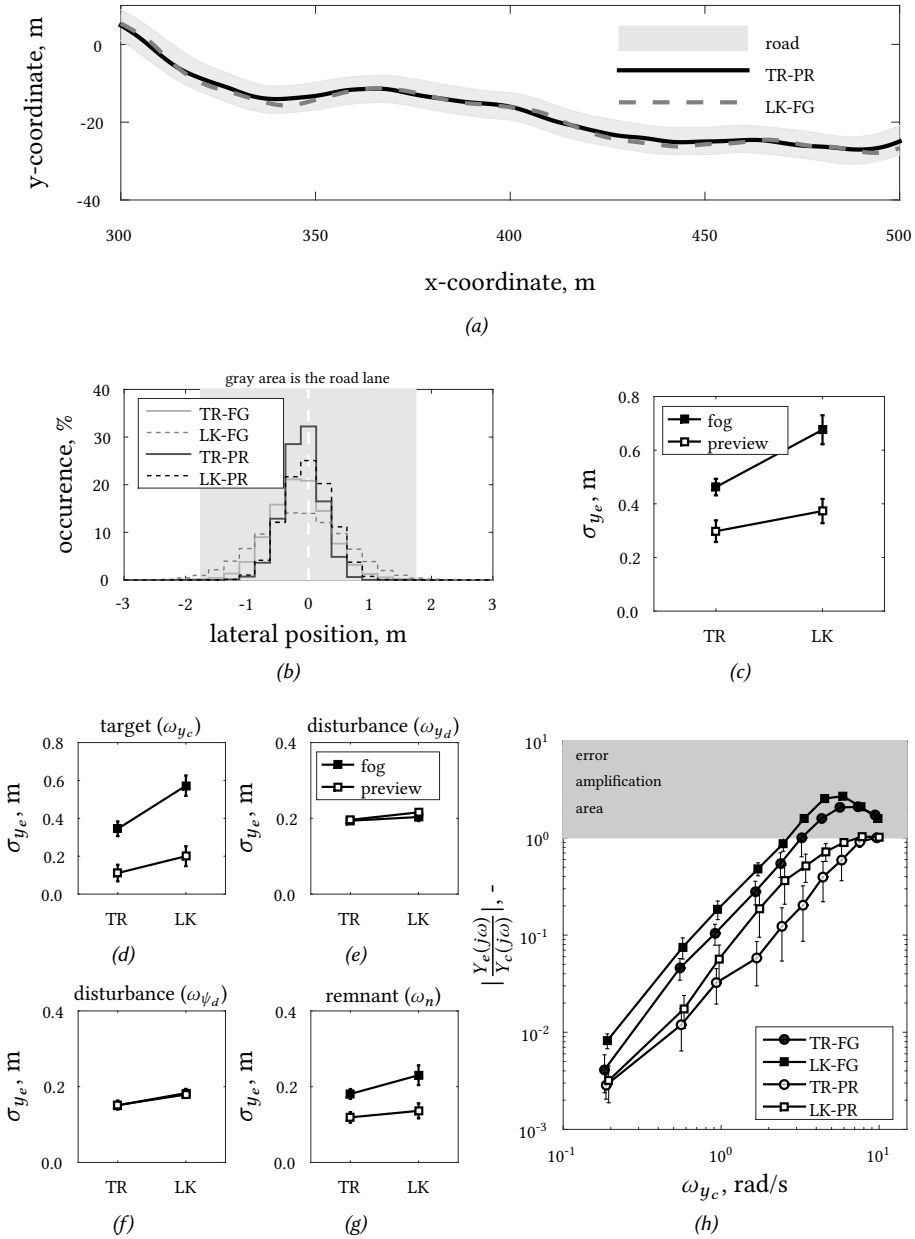


Figure 10.4: Lateral position deviations y_e from the road centerline: a top view of representative traveled paths in single runs of LK-FG and TR-PR tasks (a); the y_e distribution summed over all eight participants (b); the average standard deviations of y_e of the eight participants (c-g), with 95% confidence intervals (corrected for between-participant variability); and the target-to-error dynamics, average of eight participants and standard deviations (h).

and smallest (TR-PR). The vehicle trajectories both approximately match the road trajectory, but the absence of preview in the LK-FG task clearly results in vehicle trajectories that approach the road edges closer and more often. This is confirmed by the lateral position distributions on the road in Fig. 10.4b, which illustrate that the vehicle's center of gravity seldom crosses the road's boundaries, except occasionally in the LK-FG condition. Figs. 10.4b and 10.4c both show that participants keep their vehicle closer to the road's centerline in TR tasks (opposed to LK), and when preview is available (opposed to FG). In the nominal driving task (LK-PR), σ_{y_e} is on average 0.38 m, a value comparable to the similar simulator driving experiment by Wolters *et al.* [52], which also included relatively strong external disturbances, yet higher than typical deviations ($0.1 < \sigma_{y_e} < 0.3$ m) reported throughout literature [50, 66, 209, 220–222].

Figs. 10.4d–10.4g show that all external signals (target y_c , disturbances y_d and ψ_d , and remnant n) contribute to the increase in y_e between TR and LK tasks, but that the increase is largest at the input frequencies of the target signal (i.e., the road trajectory). Restricted preview mainly results in poorer target tracking, similar as in single-loop tracking tasks (see the experiments in Part II of this thesis), by inhibiting participants from anticipating the road's upcoming curves. Disturbance rejection is only marginally affected by restricted preview, both in TR (corresponding to Part II) and LK tasks. Lateral position deviations due to remnant n increase for FG compared to PR tasks, see Fig. 10.4g.

The measured target-to-error dynamics are shown in Fig. 10.4h. In PR tasks, the magnitude of the target-to-error dynamics is always smaller than unity. On the contrary, in FG tasks, the magnitude is larger than unity at frequencies above 2.5 rad/s, indicating that participants' steering increases the vehicle's deviation from the centerline compared to a zero-control strategy. Such error *amplification* results from the human's visual response time delay when performing closed-loop feedback control, and reflects the “jerky” control behavior that is reported in driving experiments where the “far visual field” is occluded [51, 58, 69]. Identical to the single-loop tracking tasks in Chapters 4 and 6, preview allows participants to anticipate the target trajectory to compensate for their own response time delay, which, consequently, eliminates the amplification peak.

Lateral acceleration

The standard deviations of the vehicle lateral accelerations σ_{a_y} are on average between 3 and 6.5 m/s², see Fig. 10.5. The lateral accelerations are 50–100% higher when preview is restricted (compared to PR tasks). Opposed to TR, LK yields lower accelerations when preview is available, but higher accelerations when preview is restricted.

The measured lateral accelerations in the nominal driving task (LK-PR) are typically below 11 m/s² ($= 3\sigma_{a_y}$, 99.7% of the data). This is markedly higher than the maximum $a_y \approx 5$ m/s² reported for real-world driving scenarios in [119], while a_y was shown to peak at around 9 m/s² in other simulator driving experiments (e.g., in [102]). The high accelerations are a direct result of the fixed forward vehicle velocity, lateral wind-gust disturbances (y_d and ψ_d), and relatively high road curvatures ($\sigma = 0.0175$ m⁻¹). Moreover, the performed experiment lacked physical motion feedback, the absence of which is known to evoke more aggressive control behavior [52], and higher lateral accelerations [102].

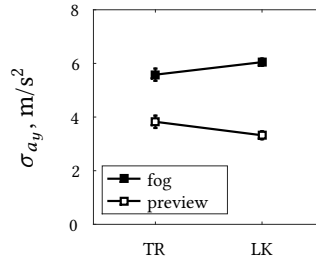


Figure 10.5: Standard deviation of the vehicle lateral accelerations a_y ; average of eight participants and 95% confidence intervals, corrected for between-subject variability.

Intermittent control

Fig. 10.6 shows the time $T_{\delta \approx 0}$ for which control behavior was kept constant, the *intermittent* control output. Overall, Fig. 10.6 shows that participants seldomly kept their control output δ constant for a sustained period of time. Especially when preview is restricted by fog, $T_{\delta \approx 0}$ approaches zero, indicating continuous closed-loop control activity. With preview, $T_{\delta \approx 0}$ is clearly higher and increases further from TR to LK tasks. However, even in LK-PR tasks, the time that participants kept the steering wheel angle approximately constant is below 10% of the total measurement time (Fig. 10.6b). Although no comparable results are available from literature, the $T_{\delta \approx 0}$ measurements are likely relatively low due to the characteristics of the performed driving task, with its constantly varying road curvature and persistent quasi-random external disturbances (ψ_d and y_d).

Time to line crossing

The Time to Line Crossing (TLC) was on average between 0.5 and 1.5 s throughout the experiment, see Fig. 10.7. This is much lower than what is typically observed in curve driving tasks (e.g., $TLC > 3$ s [116]), which is a direct result of the road's constantly varying curvature, as well as the high average curvature, in combination with the vehicle's fixed velocity. Availability of preview leads to a markedly higher TLC (Fig. 10.7b). Compared to the "virtual" TLC in tracking tasks, lane-keeping yields a higher TLC in preview tasks, but a lower TLC in tasks with fog, suggesting that available lane width makes the task more difficult without preview and easier with preview. During the periods where the control output is constant (Fig. 10.6), the TLC is around 0.2 s higher than the average TLC measured throughout the full experiment (see the "x" markers in Fig. 10.7b). Higher TLCs thus indeed appear to evoke less steering corrections, as suggested earlier by Godthelp [116].

Driver control output

The standard deviation of the control activity σ_δ , shown in Fig. 10.8a, is 50-75% higher in tasks with fog (compared to PR). This contradicts single-loop tracking results from Chapter 4, where identical control activity was measured in tasks with and without preview. From TR to LK tasks, participants increase their control activity σ_δ by approximately 10% without preview, but decrease σ_δ by around 20% with full preview. Lane keeping thus evokes less control activity than tracking in PR tasks, supporting the obtained TLCs that the LK task is *easier* and that the higher lateral position variability on the road (Fig. 10.4)

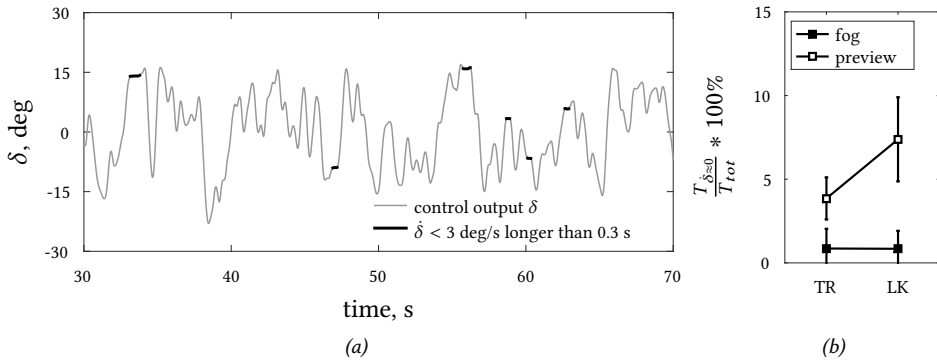


Figure 10.6: Time that the control output is approximately constant, single-run data of a representative participant in the LK-PR condition (a) and the average of eight participants (b), with 95% confidence intervals (corrected for between-participant variability).

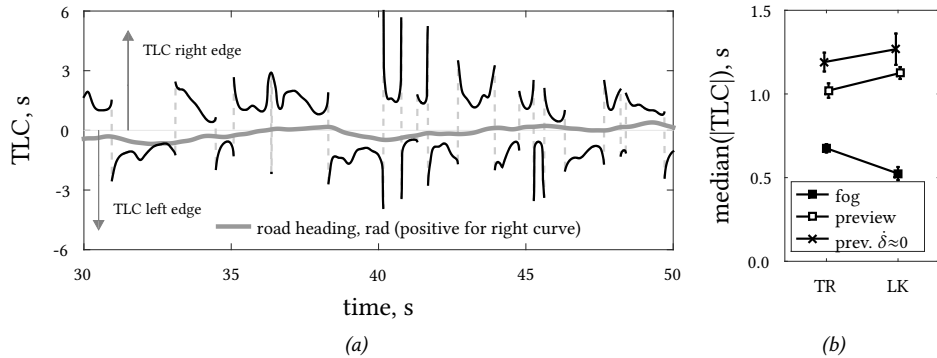


Figure 10.7: The curved TLC, single-run data of a representative participant in the LK-PR condition (a) and the median of eight participants (b), with 95% confidence intervals (corrected for between-participant variability); in tracking, TLC is based on a virtual 3.5 m wide road.

10

is the result of *satisficing* control behavior. On the contrary, the higher lateral position variability in LK-FG tasks (compared to TR-FG) does *not* reflect satisficing behavior, as the accompanying higher control activity suggests that the task is *more difficult*. The increased task difficulty likely results from the visual presentation: comparing Figs. 10.1a and 10.1b shows that the centerline in TR tasks is more salient than the lane edges in LK tasks. Note that changes in σ_δ between conditions correspond directly to changes in the vehicle’s lateral accelerations, see Fig. 10.5.

Figs. 10.8b–10.8e show that the target frequencies account for over 50% of the total σ_δ , such that over 75% of the control output *power* (σ_δ^2) is primarily dedicated to *target tracking*. Neither of the independent variables has a marked effect on the control output power at the frequencies of the disturbance signals y_d (Fig. 10.8c) and ψ_d (Fig. 10.8d). Fig. 10.8e

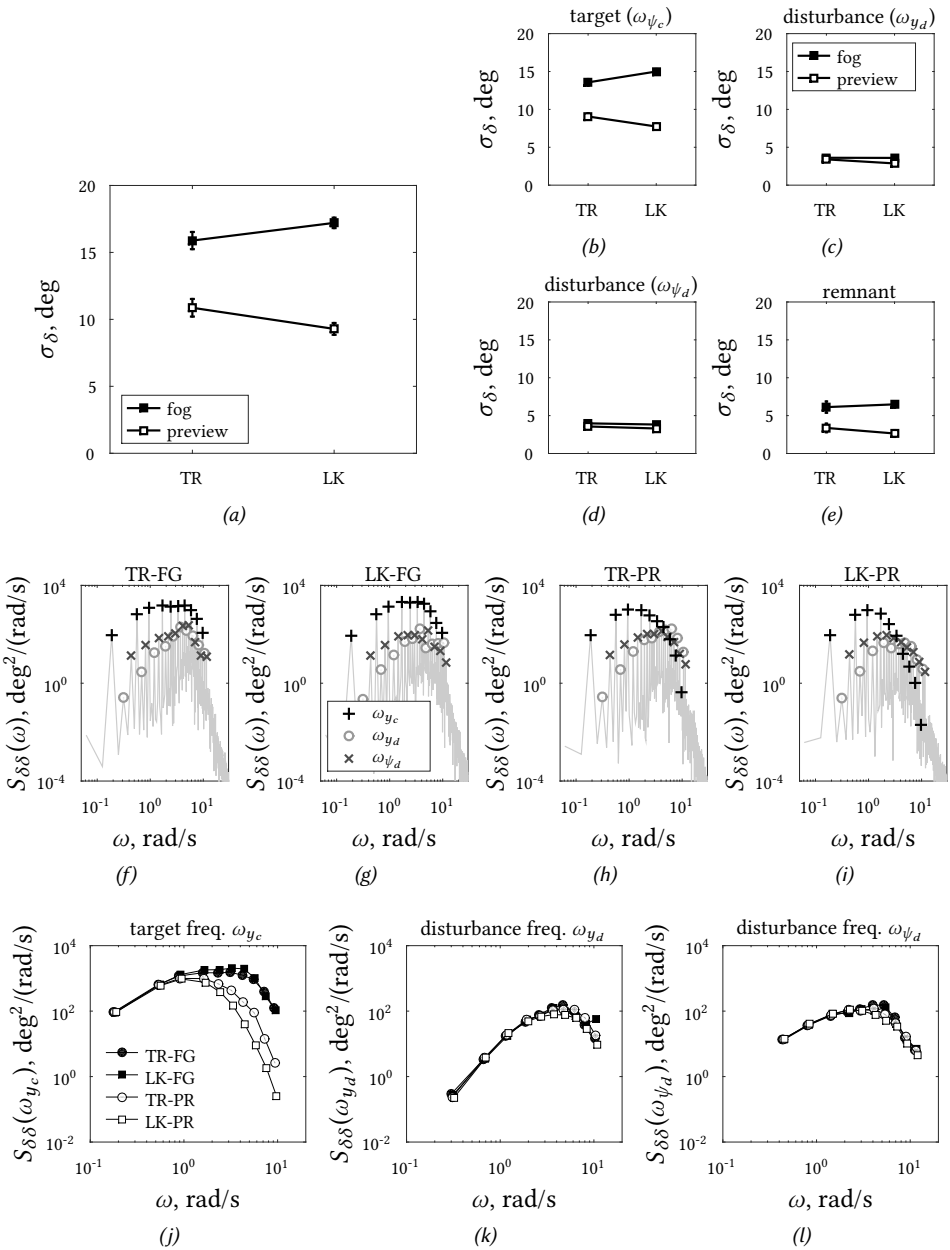


Figure 10.8: Standard deviations of the control output δ (a-e), average of eight participants and 95% confidence intervals (corrected for between-participant variability); the estimated power spectra of the control output $S_{\delta\delta}(\omega)$ for Participant 1 (f-i), and the average $S_{\delta\delta}(\omega)$ of all eight participants at the target (j), lateral position disturbance (k) and heading disturbance (l) input frequencies.

shows that the control activity due to remnant n increases for FG compared to PR tasks, which is a direct consequence of the higher total control activity (Fig. 10.8a) with which remnant typically scales [120, 196]. The increased remnant activity explains why σ_{y_e} at the remnant frequencies was also higher in FG tasks, see Fig. 10.4g.

The estimated power spectra of the control outputs, given in Figs. 10.8f–10.8i, have clear peaks at the input frequencies of the external signals (y_c , y_d , and ψ_d), indicating an accumulation of control activity, as intended. At most of the target frequencies (“+” markers in Figs. 10.8f–10.8i, or see Fig. 10.8j), control power is identical in the two FG tasks. Availability of preview evokes reduced control activity especially at the higher target signal input frequencies, which decreases even further from tracking (TR-PR) to lane-keeping tasks (LK-PR). In TR-PR tasks, the control output power at the highest target frequency is identical to that of the remnant at the surrounding frequencies (Fig. 10.8h); in LK-PR tasks, the same is visible for the *two* highest target frequencies (Fig. 10.8i). This reduced control activity is observed in all participants (Fig. 10.8j) and implies that the target centerline’s higher frequencies are deliberately ignored, facilitated by their visibility through the available preview. This same behavior was observed in the single-loop preview tracking tasks in Part II of this thesis.

Tracking bandwidth and stability

Figs. 10.9a and 10.9d show the measured target crossover frequencies $\omega_c^{y_c}$ and phase margins $\phi_m^{y_c}$. These measures clearly show the effects of both restricted preview and available lane width, as well as their interaction. First, preview yields a large increase in $\phi_m^{y_c}$ from around 25 deg in FG tasks to 125–200 deg in PR tasks, in accordance with measurements in single-loop display tracking tasks, see Chapters 4 and 5. From TR-PR to LK-PR tasks, $\omega_c^{y_c}$ drops from 5.5 to 3.5 rad/s, reflecting that participants follow less of the road’s higher frequencies, corresponding to the lower control activity at these frequencies (Fig. 10.8j). At the same time, $\phi_m^{y_c}$ increases from 125 deg to almost 200 deg, indicating an even further improvement of the already opulent stability margins. In tasks with fog, $\omega_c^{y_c}$ also decreases between tracking and lane keeping (from around 5 to 4 rad/s), but less dramatically, and no accompanying increase in $\phi_m^{y_c}$ is visible. This shows that the LK-FG task was indeed more difficult than the TR-FG tasks, confirming that the higher lateral position variability is *not* a manifestation of satisficing control behavior, as opposed to the PR tasks.

Disturbance-rejection performance and stability are in general only marginally affected by preview and road width, see Fig. 10.9 (b,c,e,f). Most consistent and pronounced is a reduction of the inner-loop, heading crossover frequency $\omega_c^{\psi_d}$ from around 3.5 to 3 rad/s from TR to LK tasks, a clear indication of less aggressive feedback control.

Driver control dynamics

FRF estimates of driver multiloop control dynamics are given by markers in the Bode plots in Figs. 10.10 and 10.11. The shapes of the three measured FRFs are identical in TR and LK tasks, both with and without preview, which indicates that participants adopt a similar control strategy. Restricted preview has some notable effects, in particular on the target feedforward response $H_{o_{y_c}}$. With fog, less phase lead and a higher FRF magnitude is visible at the higher input frequencies of $H_{o_{y_c}}(j\omega)$, indicating less centerline trajectory anticipation and smoothing, respectively. Interestingly, participants adopt a target response

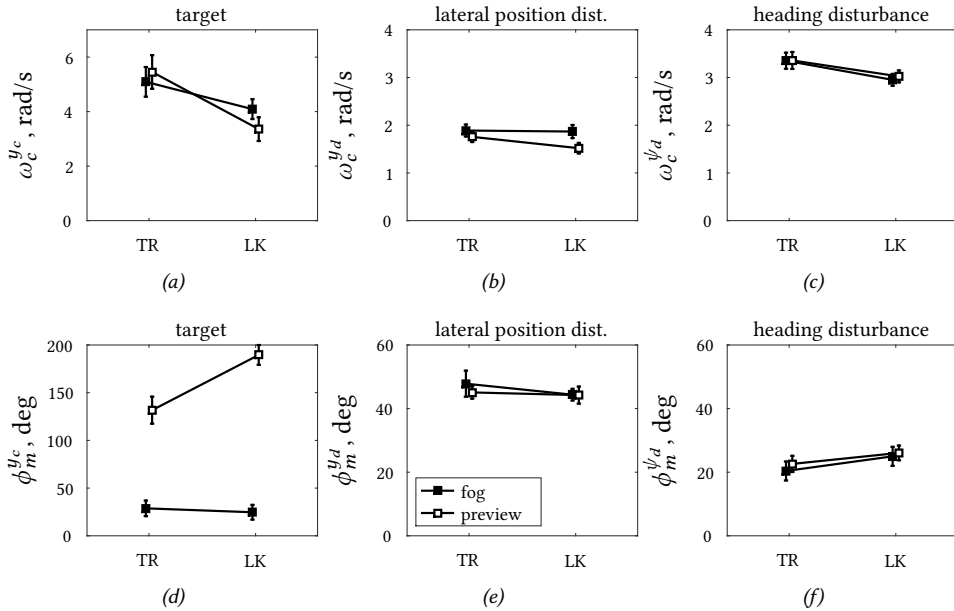


Figure 10.9: Crossover frequencies ω_c and phase margins ϕ_m ; average of eight participants and 95% confidence intervals, corrected for between-participant variability.

$H_{o_{y_c}}(j\omega)$ that approximates the $H_{o_{y_c}}^P(j\omega)$ dynamics required for *perfect* target-tracking; however, they mainly match the *phase* of $H_{o_{y_c}}^P(j\omega)$ in preview tasks and its *magnitude* in tasks with restricted preview, signifying that synchronizing the vehicle with the center-line oscillations is prioritized in PR tasks. These effects correspond to the experimental results in Chapter 5, where available preview was limited in single-loop tracking tasks.

10.3.2. MODELING RESULTS

Model quality-of-fit

The dynamics of the fitted multiloop driver model are also shown in Figs. 10.10 and 10.11, together with the estimated FRFs. In general, the driver model captures the shape of all three FRF estimates well in all four tasks, with the following exceptions:

- The highest frequencies of the feedforward response $H_{o_{y_c}}(j\omega)$, Figs. 10.10 and 10.11 (a,d), especially in preview tasks, because participants ignore the highest frequencies of the target trajectory, see Fig. 10.8.
- The lowest frequencies of the heading response $H_{o_{\psi}}(j\omega)$, Figs. 10.10 and 10.11 (b,e), because, here, control output is dominated by the lateral position outer-loop [223].
- The highest frequencies of all three FRFs in the LK-FG task; here, the neuromuscular system dynamics were difficult to estimate, likely because the break frequency ω_{nms} is beyond the highest forcing function input frequency (11.5 rad/s).

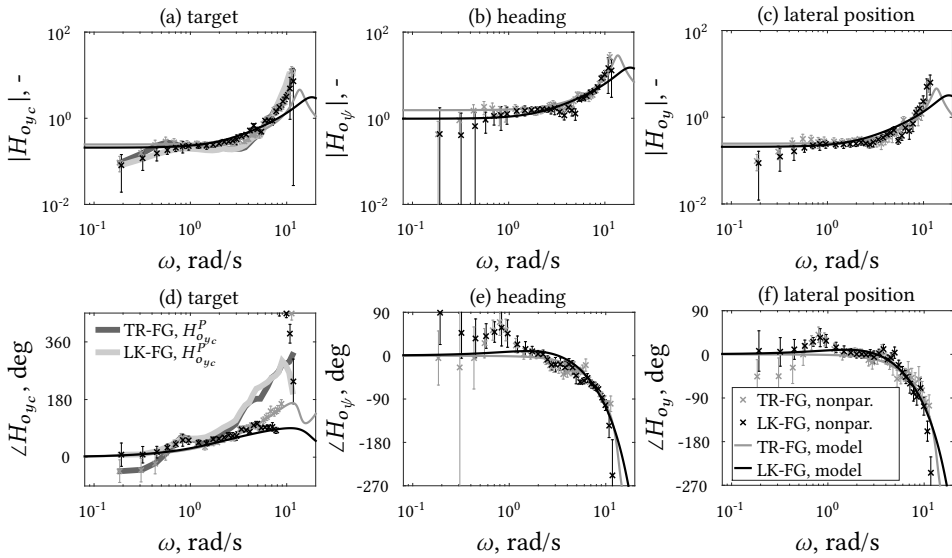


Figure 10.10: Bode plots of the multiloop steering dynamics of a representative participant in conditions with fog (TR-FG and LK-FG): nonparametric FRF estimates with standard errors, perfect target-tracking dynamics, and the model fits.

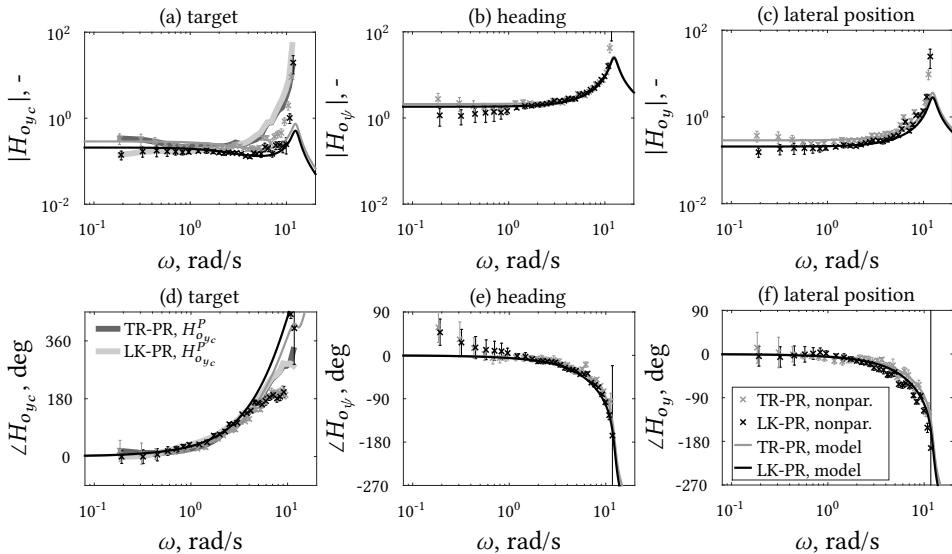


Figure 10.11: Bode plots of the multiloop steering dynamics of a representative participant in conditions with full preview (TR-PR and LK-PR): nonparametric FRF estimates with standard errors, perfect target-tracking dynamics, and the model fits.

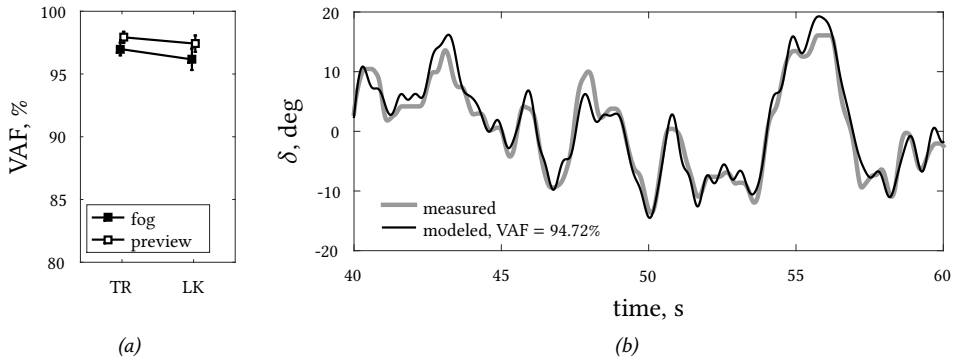


Figure 10.12: Model VAFs, quantifying the quality-of-fit: the average of all eight participants (a) with 95% confidence intervals (corrected for between-participant variability), and representative time-traces of a single run (b); Participant 1, Run 5, LK-PR.

In addition to capturing the estimated FRFs of participants' multiloop steering dynamics, the model also captures participants' steering outputs well, as indicated by the high model VAFs ($> 95\%$) in Fig. 10.12a. In fact, even when considering the measured control outputs (δ) in a single run – opposed to the five-run average considered throughout this thesis – the human's control output is accurately captured, as shown in Fig. 10.12b. Together, these results indicate that the driver model proposed in Chapter 9 can not only capture driver behavior in tracking tasks with full preview (TR-PR), but can also be applied in more realistic lane-keeping tasks, and in tasks with restricted preview. Thereby, the applicability of the quasi-linear driver modeling framework is considerably extended.

Anticipatory control behavior

The estimated feedforward model parameters T_{la} , T_{lf} , and τ_f are shown in Fig. 10.13. In tasks where preview was restricted by fog, the farthest point of the centerline trajectory ahead used for control, characterized by τ_f , is well within the remaining 0.5 s visible region ahead of the vehicle. This supports that the quasi-linear model's look-ahead times indeed have a direct *physical interpretation* and accurately reflect the portion of the previewed trajectory used by drivers for control (see Fig. 10.2), identical as in single-loop preview tracking tasks (see Chapters 3 and 5). In fact, in TR-FG and LK-FG tasks, the most distant target point used for control (τ_f) lies 0.44 s and 0.33 s ahead of the vehicle, respectively, such that *not all* the 0.5 s of available preview information is exploited. This is likely the consequence of the poor contrast of the road trajectory at the 0.5 s limit where it disappears in the fog (see Fig. 10.1); because the white centerline (TR tasks) is visually more salient than the road lane edges (LK), participants can adopt a larger look-ahead time. This explains exactly *why* the LK-FG task was more difficult than the TR-FG task, as suggested before by the lateral position deviations on the road (Fig. 10.4), the TLCs (Fig. 10.7), the control activity (Fig. 10.8a) and the target crossover frequency (Fig. 10.9a): the experimental visuals made it more difficult for participants to use the full 0.5 s of “theoretically” available preview.

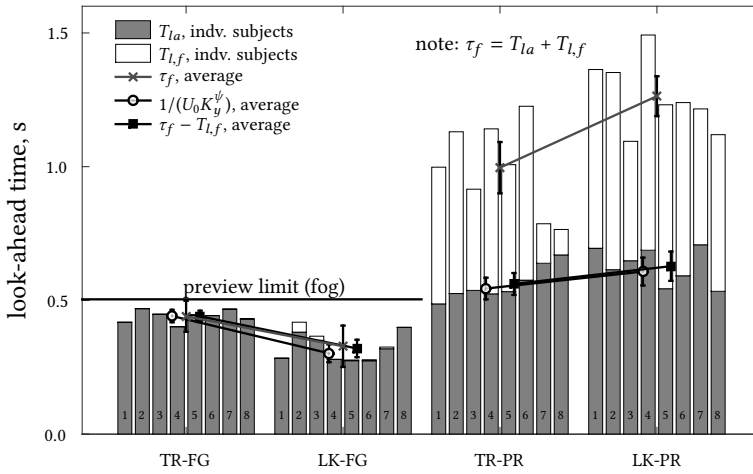


Figure 10.13: Estimated feedforward anticipatory control behavior parameters; individual participants are shown with bars, markers indicate the average and 95% confidence intervals (corrected for between-participant variability). White bars are poorly visible in tasks with fog, as $T_{l,f}$ is approximately zero for most participants. The feedback and feedforward look-ahead time parameters, $1/(U_0 K_y^\psi)$ and $\tau_f - T_{l,f}$, respectively, which correspond to T_{la} , are shown for comparison with Chapter 9.

Fig. 10.13 further shows that restricted preview severely limits participants to both anticipate (T_{la}) and smooth ($T_{l,f}$) the target trajectory. The most distant point on the trajectory ahead that is used for control (τ_f) decreases substantially, from around 1.2 s in tasks with preview to around 0.4 s in tasks with fog. Interestingly, participants do not smooth the target trajectory at all in tasks with fog ($T_{l,f} \approx 0$ s) and use all of the remaining preview for anticipation (T_{la}). The look-ahead time T_{la} is decreased only slightly when preview is restricted, from around 0.6 (PR) to 0.4 s (FG) ahead. A lower T_{la} implies that participants rely relatively more on lateral position feedback and less on heading feedback (as explained in Chapter 9 and [109, 165, 223]), which corresponds with the fact that the (still visible) “near visual field” provides mostly lateral position information [58, 64]. In tasks with preview, lane-keeping (LK-PR) leads to more trajectory smoothing than centerline tracking (TR-PR): $T_{l,f}$ on average increases from 0.43 to 0.64 s. This indicates that the higher-frequency oscillations of the road trajectory are ignored, and agrees with the lack of a control response observed at these frequencies (Fig. 10.8j).

Feedback control behavior

As explained in Chapter 9, the model fits yield *two* independent estimates of the look-ahead time T_{la} , namely $1/(U_0 K_y^\psi)$ for the feedback responses and $\tau_f - T_{l,f}$ for the feedforward response. Fig. 10.13 shows that these two T_{la} estimates are almost identical in all tasks, further supporting the key finding of Chapter 9. The main implication of this fact is that drivers apparently minimize the visual angle η between the vehicle and a “target” heading, obtained by smoothing a portion of the centerline trajectory. Fig. 10.2 illustrates this visual angle, for a look-ahead time that corresponds to the average of the estimated values

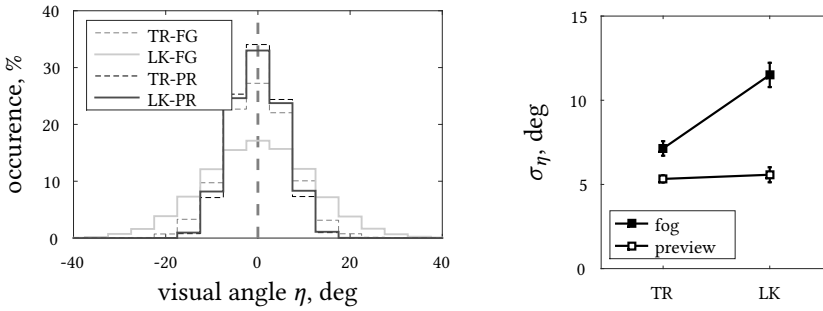


Figure 10.14: The visual angle η that drivers minimize through compensatory control.

in the LK-PR tasks: $T_{la} = 0.6$ s and $\tau_f = 1.25$ s. This η is the signal that is apparently minimized by drivers through compensatory feedback control, see also Chapter 9. Using the estimated look-ahead times in open-loop model simulations, the actual visual angles η were estimated, results of which are shown in Fig. 10.14. The visual angle η is generally below ± 20 deg, so the target heading, or aim point is always relatively in front of the driver in the visual field (and T_{la} s ahead). The magnitude of the visual angle is larger in tasks where the deviations from the centerline are larger (Fig. 10.4), leading to the largest visual angles in LK-FG tasks and the smallest angles in TR-PR tasks.

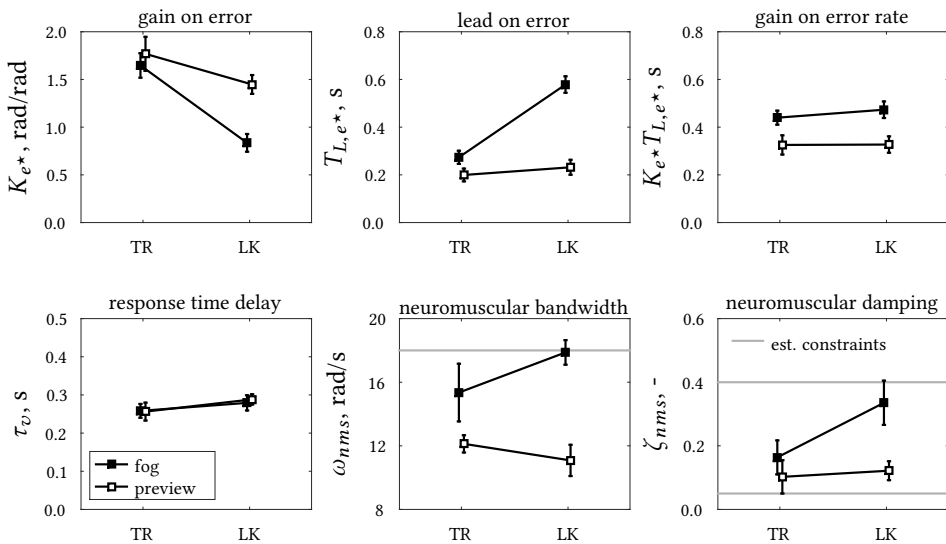


Figure 10.15: Estimated compensatory response parameters; average of eight participants and 95% confidence intervals (corrected for between-participant variability). Gray lines indicate the parameters estimation constraints imposed on ω_{nms} and ζ_{nms} .

Fig. 10.15 shows the estimated parameters of the compensatory submodel, which quantify how participants minimized the visual angle η . Compared to TR tasks, participants reduce their gain K_{e^*} in LK tasks, that is, they minimize η less aggressively. In tasks with restricted preview, in particular in lane-keeping tasks (LK-FG), participants generate markedly more lead (T_{l,e^*}). The fog limits the heading feedback conveyed by the visual scene, leading to a lower T_{la} and reduced stability (see Chapter 9), which is thus compensated for by a stronger reliance on *predictive* behavior (higher T_{L,e^*}). Participants furthermore have a slightly higher visual delay τ_v during LK as compared to TR tasks. Tentatively, the explicit error visible in tracking task motivates participants to put additional effort into reducing their response delay to increase performance. An identical increase in visual response delay was observed when additional motion (Chapter 8) or heading (Chapter 9) feedback was made available in preview tracking tasks. Finally, participants also markedly adapt their neuromuscular system dynamics to the task. The break frequency of the neuromuscular system ω_{nms} strongly resembles the applied control activity in Fig. 10.8a. ω_{nms} increases from lane-keeping to centerline-tracking tasks with preview from 9.5 (LK-PR) to 12 rad/s (TR-PR); then to 15.5 rad/s when preview is restricted in tracking tasks (TR-FG), and finally to 18 rad/s in lane-keeping tasks with fog (LK-FG), where the highest control activity is observed.

10.4. DISCUSSION

It was hypothesized (H.I) that in a (more) realistic driving task, restricted preview affects human control behavior identically as in single-loop display tracking tasks (Chapter 5). Indeed, fog led to increased lateral position deviations from the road's centerline while the target response stability (phase margin) decreased substantially from around 150 to 30 deg. Model fits showed that drivers' main steering adaptation is to use road preview information from less far ahead, below the preview limit of 0.5 s, opposed to using approximately 1.2 s in tasks with full preview. Limiting the available preview mainly inhibits drivers from *smoothing* the road's trajectory, such that the minimized visual angle contains more high-frequency components. With fog, drivers still select an aim point for the visual angle that is positioned as far ahead as possible, so the look-ahead time T_{la} is right below the 0.5 s preview limit, to maintain the feedback performance and stability for disturbance-rejection. These results fully confirm the first hypothesis (H.I).

It was further hypothesized (H.II) that drivers display higher levels of satisficing control behavior in lane-keeping tasks (LK) as compared to centerline-tracking tasks (TR), but only with full preview. This hypothesis is confirmed, because *all* dependent measures reflect a higher level of satisficing control in LK tasks with preview, as compared to TR, see Fig. 10.3. In particular, the lateral deviation from the lane centerline, the TLC, and the intermittent control output increases, while drivers steer less aggressively (lower K_{e^*}), minimize the visual angle farther ahead (higher T_{la}) and ignore more of the road trajectory's higher frequencies (higher $T_{l,f}$). When preview is restricted, lateral deviations also increase from TR to LK tasks; however, this is *not* a manifestation of increasing satisficing behavior, but the result of the smaller look-ahead time, as a consequence of the limited visual contrast between the rendered road lane edges and the fog in LK-FG tasks.

Nonetheless, differences in driver behavior between tracking and lane-keeping tasks are smaller than expected, and no clear, discrete control-mode switch was observed from tracking to satisficing behavior. Instead, it appears to be more appropriate to consider measured steering behavior on a continuous scale between tracking and satisficing control behavior, much like Fig. 10.3, and as suggested by Gray [212, 213]. This is comparable to the notion by Wasicko *et al.* [42] that pursuit displays do not necessarily evoke corresponding “pursuit-type” control behavior, but that human behavior instead decreasingly resembles pure compensatory control behavior. The relative level of satisficing or tracking behavior in a driving task likely depends on driver experience, and task variables such as the vehicle dynamics, road curvature and lane width, and the power of the external (wind-gust) disturbances. The low TLC measurements suggest that participants exhibited only limited levels of satisficing control behavior. Future experiments with realistic road-curvature profiles and without external disturbances could lead to higher TLCs, and may, consequently, evoke more pronounced satisficing behavior. Such future experiments are required to further extend the applicability of the proposed quasi-linear model to explain driver steering in more realistic driving tasks.

The TLC is often considered as a measure for drivers’ incentive to steer: when the TLC drops below a certain threshold, steering corrections are required to avoid lane departures. Estimated control-theoretic model parameters indicate that, in our experiment, participants in fact respond to the road trajectory τ_f s ahead, suggesting that there may be a correlation with the TLC. Fig. 10.16 shows that a correlation between the experimental TLCs and the model’s look-ahead times τ_f indeed appears to exist, especially in tasks with preview. Future experiments should investigate if such a relation holds over a wide range of driver tasks. Larger TLCs in general occur in less demanding driving tasks [116, 211]. Correspondingly, here, less demanding tasks also lead to higher model look-ahead times, as is visible, for example, from the difference between TR-PR and LK-PR in Fig. 10.13.

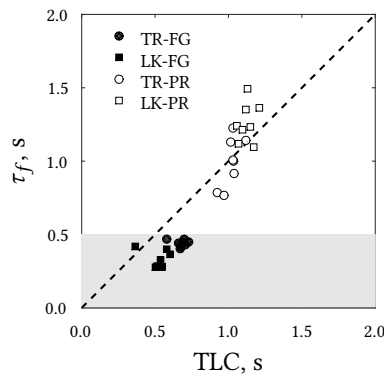


Figure 10.16: Correlation between the TLC and the estimated farthest preview point used for control (τ_f); gray area indicates the available preview in tasks with fog (FG).

10.5. CONCLUSION

In this chapter, human-in-the-loop experimental data were presented to quantify possible differences between driver steering behavior in centerline-tracking and lane-keeping tasks, and how these vary between conditions with full or restricted preview. When preview is restricted, drivers use as much as possible of the remaining preview to anticipate the road's curves, but cease to use preview for smoothing the trajectory (i.e., corner cutting). Steering behavior measured in the experiment mostly resembles tracking and *not* satisficing control, both in tracking *and* lane-keeping tasks, as near-continuous steering was required to follow the constantly varying road curvature and suppress the quasi-random external disturbances. Nonetheless, drivers display signs of emergent satisficing behavior in the “nominal” lane-keeping, curve driving task with preview: they steer less aggressively, more intermittently, and ignore more of the road's fast changes, which leads to a larger lateral position variability within the lane. For the first time, driver multiloop steering dynamics were accurately captured by a quasi-linear control-theoretic model, yielding a unifying framework for manual control that spans from compensatory tracking to curve driving, lane-keeping tasks. The model's physically interpretable parameters provide novel quantitative insights, in particular into drivers' use of visual cues and preview information.

11

CONCLUSION AND RECOMMENDATIONS

Each chapter of this thesis treated a distinct, mostly isolated aspect of manual preview control. This final chapter first recapitulates the main findings of each individual chapter, and then provides a general conclusion that summarizes the implications of this thesis as a whole. Furthermore, five recommendations are given, discussing where the obtained results can either catalyze future research or can be directly applied to improve current automation technology.

THE pioneering work by Sheridan [61] in 1966 set-off the quest to rationalize and quantify human manual preview control. Yet, in the five subsequent decades, exactly *how* humans use available preview information for control has remained puzzling and no *general, widely-accepted* model has been put forward. For the quintessential preview control task of steering a car along a winding road, the most-cited cybernetic models (e.g., [90–95]) have implemented human use of preview in fundamentally different ways. Key unknowns have remained *which portions* of the previewed trajectory humans use for control, *what control dynamics and organization* humans adopt, and how humans *adapt* these behaviors to critical task variables such as the available preview time, the vehicle dynamics, and the trajectory (road) to follow. Therefore, this thesis had the following goal:

Goal of this thesis

Provide a qualitative and quantitative understanding of human behavior and adaptation in manual control with preview, through a cybernetic modeling approach.

Next, the main conclusions are presented, followed by recommendations for future work.

11.1. CONCLUSION

11.1.1. PART 1: FUNDAMENTALS OF MANUAL PREVIEW CONTROL

Chapter 2: Modeling human preview tracking behavior

In Chapter 2, empirical human-in-the-loop data were collected in order to obtain a first *descriptive, control-theoretic model* of human control behavior in pursuit and preview tracking tasks. The experiment’s uncorrelated multisine target and disturbance signals allowed for identifying the dynamics in two of the human’s response channels, without making any *a priori* assumptions. Estimated *feedback* dynamics were found to resemble the human’s control response in compensatory tracking tasks and were modeled in accordance with the *simplified precision model* [6, 80]. Two parallel control responses were found to be required to model the human’s *feedforward* dynamics in preview tasks. The main response is mechanized based on a “far viewpoint” along the previewed trajectory ahead, and provides a scaled and low-pass filtered future reference input to the compensatory (feedback) control loop. The second feedforward channel is an open-loop control response that is based on a “near viewpoint” ahead and is used to track only the higher frequencies of the target trajectory. The resulting model is the first that has not only been shown to capture the human’s control *output* in preview tracking tasks, but also their internal, *multiloop control dynamics*. Additionally, the model has *physically* interpretable parameters that can be instrumental for explaining measured behavior, such as look-ahead times that quantify the near- and far-viewpoint locations (i.e., human *inputs*).

Main finding of Chapter 2

Manual control behavior in preview tracking tasks can be modeled with two parallel feedforward responses, together with a compensatory error-feedback response.

Chapter 3: The portions of preview used for control

Chapter 3 investigated to what extent the estimated near- and far-viewpoint positions of the model derived in Chapter 2 reflect the actual portions of the previewed trajectory that humans use for control. First, it was shown theoretically that humans likely adopt a two-viewpoint parallel feedforward response to match the dual nature of feedforward dynamics $H_{o_t}^P(j\omega)$ that yield *perfect* target-tracking:

$$H_{o_t}^P(j\omega) = \underbrace{H_{o_x}(j\omega)}_{\text{low freq.}} + \underbrace{\frac{1}{H_{ce}(j\omega)}}_{\text{high freq.}}, \quad (11.1)$$

with $H_{o_x}(j\omega)$ the human's compensatory feedback response dynamics and $H_{ce}(j\omega)$ the controlled element dynamics. Second, a similar tracking experiment was performed as in Chapter 2, but the human's visual focus of attention was additionally recorded with an *eye tracker*. Moreover, 0.5 s long portions of preview around the estimated viewpoints were occluded in different experimental conditions, to induce adaptations in human gaze and preview control behavior.

Target-tracking was indeed found to be inferior at higher and lower frequencies when the near- and far-viewpoints were occluded, respectively, confirming the distinct roles of these preview regions in matching the two terms in the dynamics of Eq. (11.1). Data from the occlusion scenarios indicated that humans rely on fair stretches – and thus not *points* – of preview around the estimated model's near- and far-viewpoints to mechanize each feedforward response. Finally, the eye-tracking data indicated that humans predominantly focus their gaze at the *near viewpoint*, suggesting that a direct relation exists between human control and gaze behavior.

Main findings of Chapter 3

1. Portions of preview information around the estimated model's near- and far-viewpoints are essential for high- and low-frequency target-tracking, respectively.
2. Humans seem to focus their gaze mainly at the estimated near viewpoint.

11.1.2. PART 2: HUMAN ADAPTATION TO TASK VARIABLES

A *general* theory of manual preview control requires an understanding of human *adaptation* to critical task variables, in addition to the model from Part I. Part II of this thesis investigated how humans adapt their behavior to three key task variables: the controlled element dynamics, the preview time, and the target trajectory bandwidth. Before drawing conclusions on human adaptation to each individual task variable, first, the observed general mechanisms that underlie human adaptation in preview tasks are summarized.

General principles of adaptation

The proposed control-theoretic model suggests that humans can adapt their behavior along *four* main dimensions in preview tasks. 1) Identical as in compensatory tracking tasks [80], humans first adapt their compensatory feedback response $H_{o_x}(j\omega)$ to attain integrator disturbance-rejection open-loop dynamics, $H_{o_l,d}(j\omega) = H_{o_x}(j\omega)H_{ce}(j\omega)$, around

crossover. 2) Positioning the far viewpoint (characterized by parameter τ_f) farther ahead yields additional *phase lead* in the feedforward, target response. This phase lead is essential in compensating for the lag of both the controlled element and the human's own response, the $1/H_{ce}(j\omega)$ and $H_{ox}(j\omega)$ terms in Eq. (11.1), respectively. 3) By scaling (i.e., parameter K_f) the target at the far viewpoint humans tune the priority for target tracking (feedforward) relative to stabilizing feedback control, while target smoothing (i.e., low-pass filtering, parameter $T_{l,f}$) leads to attenuation of undesirable high-frequency oscillations. 4) The auxiliary, open-loop near-viewpoint response can be reinforced or attenuated (parameter K_n) to adapt the extent of high-frequency target-tracking.

It is not trivial to find systematic behavioral invariants within (combinations of) these interactive degrees of freedom, and to formulate a set of “verbal adjustment rules”, comparable to those by McRuer *et al.* [6, 80] for compensatory tracking. Looking at overt tracking *performance*, Part II showed that humans typically minimize the target-tracking error within their physical limitations; however, only at the lower frequencies where the far-viewpoint response is dominant, and not always at the higher frequencies of the near-viewpoint response. The adopted near-viewpoint response appears to depend strongly on task difficulty, operator experience, and operator motivation, the latter because matching the magnitude of the $1/H_{ce}(j\omega)$ term in Eq. (11.1) requires substantial control effort. Consequently, the characteristics of the far-viewpoint response can be predicted accurately in *offline* computer simulations by optimizing the model parameters for minimal closed-loop tracking errors, but identical predictions for the near-viewpoint response are less accurate.

Fortunately, the far-viewpoint response is often of primary interest, as real-world target trajectories generally lack very high frequencies (e.g., the road in driving tasks). An equation that, when satisfied, yields zero-error, perfect target-tracking, is obtained by substituting the far-viewpoint-only model into Eq. (11.1):

$$K_f \frac{1}{1 + T_{l,f}j\omega} e^{\tau_f j\omega} = \underbrace{1}_{\text{low freq.}} + \underbrace{\frac{1}{H_{ol,d}(j\omega)}}_{\text{high freq.}}. \quad (11.2)$$

Eq. (11.2) shows that the required adaptation of the far-viewpoint preview response (left-hand side) depends on the disturbance open-loop dynamics (right-hand side), that is, the human's feedback control behavior. This equation is probably the closest to an “adjustment rule” as possible for preview tasks, without drastic simplifications. As it is not possible to satisfy Eq. (11.2) in *magnitude* at high-frequencies (at least without a near-viewpoint response), human preview control should primarily aim to equalize the *phases* on both sides of Eq. (11.2). To do so, the far viewpoint position (or look-ahead time, τ_f) must compensate for the phase lags of $H_{ol,d}(j\omega)$ and $1/(1 + T_{l,f}j\omega)$. Amongst others, Eq. (11.2) shows that humans who minimize the error *more aggressively* (higher $|H_{ol,d}(j\omega)|$) should position the far viewpoint *closer ahead*, as the target is intercepted faster.

Chapter 4: Effects of controlled element dynamics

Chapter 4 investigated human adaptation between tasks with gain, single- and double-integrator *controlled element dynamics*, both in offline model simulations and with human-in-the-loop data. It was found that human controllers indeed adapt their feedback

response to obtain integrator-like disturbance open-loop dynamics. Second, humans adopted *higher* near- and far-viewpoint look-ahead times in tasks with *higher-order* controlled element dynamics, to compensate for the larger inherent phase lag. At the same time, the increased task difficulty caused humans to ignore more of the target trajectory's oscillations both by down-scaling and increased smoothing of the far-viewpoint response, and by attenuating (in the extreme case, omitting) the near-viewpoint response.

Main finding of Chapter 4

In tasks with higher-order controlled element dynamics, humans use more preview and ignore more of the target trajectory's (high-frequency) oscillations.

Chapter 5: Effects of preview time

Human adaptation to *preview time* was investigated in Chapter 5. Again, pre-experimental *offline* model predictions were verified with human-in-the-loop data, for eight preview time settings between 0 and 2 s. First, it was shown that a *critical* preview time exists beyond which additional preview information is not used for control. Positioning the far viewpoint beyond the critical preview time is undesirable, as this provides phase lead in excess of the perfect target-tracking dynamics, Eq. (11.1), and hence *suboptimal* performance. Second, restricting the preview time forces humans to adopt a far viewpoint that is closer ahead than the desired, optimal position, so insufficient phase lead can be generated to match the phase of Eq. (11.1). To avoid further undesirable phase lags in the feedforward response when preview is restricted, human controllers reduce the time-constant of the low-pass smoothing filter. In addition, it is no longer possible to move the controlled element output *synchronously* with the target, so humans attenuate the full far-viewpoint response to avoid amplifying the tracking errors. The near-viewpoint response is not systematically adapted to the preview time, but disappears when the available preview becomes too short to recognize full high-frequency oscillations (or patterns in general) in the previewed target trajectory. When the preview time approaches zero, a classical pursuit task is obtained [61]; here, the "far-viewpoint" response is reduced to a direct unfiltered (but possibly scaled) response to the *current* target, and no near-viewpoint response is mechanized.

Main finding of Chapter 5

Restricted preview inhibits humans from using the optimal viewpoints ahead for control, yielding inferior performance, but only below the critical preview time.

Chapter 6: Effects of target trajectory bandwidth

Chapter 6 investigated human adaptation to the *target trajectory bandwidth*. This bandwidth has no direct effect on the perfect target-tracking dynamics of Eq. (11.1), yet the target trajectory spectrum determines the frequency range in which the human's feedforward response should optimally match Eq. (11.1). Offline model simulations showed that no structural adaptation of the human's feedforward dynamics is required in preview tasks when the target bandwidth is varied from 1.5 to 2 and 4 rad/s. This is in stark contrast

to compensatory and pursuit tracking tasks, where *crossover regression* is beneficial when the target trajectory bandwidth approaches the open-loop crossover frequency [6]. In a human-in-the-loop experiment, the predicted (lack of) adaptation was indeed confirmed for a preview task with a double-integrator controlled element.

Main finding of Chapter 6

Humans do not systematically adapt their control behavior to the target trajectory bandwidth (between 1.5-4 rad/s) in preview tracking tasks.

11.1.3. PART 3: FROM PREVIEW TRACKING TO CURVE DRIVING

With a control-theoretic model and a solid understanding of human adaptation in preview tracking tasks, obtained in Parts I and II of this thesis, Part III focused on human use of preview in *more realistic* control tasks. Consecutive experiments introduced the viewing perspective, additional feedbacks (motion and visual rotations), and target trajectory boundary-width that characterize real-life control tasks such as curve driving. The obtained model was augmented in accordance with each new finding.

Chapter 7: Effects of linear perspective

Chapter 7 investigated how the linear perspective of real-world outside visuals affects the way humans use preview for control. As opposed to preview information on plan-view tracking displays (used in Parts I and II), the previewed trajectory on perspective displays is presented with increasingly smaller resolution as a nonlinear function of time (or distance) ahead. Experiment data showed that humans nearly perfectly invert both the vertical and the horizontal perspective compressions, for both the near-viewpoint and the far-viewpoint responses. Control outputs were found to be equivalent with plan-view and perspective preview displays, indicating that humans adapt their control gains to the perspective transformations such that their combination is generally *invariant*. The model for plan-view preview tracking tasks from Parts I and II was thus concluded to be equally applicable to perspective preview tracking tasks.

Main finding of Chapter 7

Humans use preview identically in plan-view and perspective tracking tasks; near- and far-viewpoint responses guide high- and low-frequency tracking, respectively.

Chapter 8: Effects of vestibular feedback

Chapter 8 investigated how physical motion feedback affects the way humans use preview for control. As in Parts I and II, human-in-the-loop data were gathered with *two* uncorrelated perturbations, the target and disturbance. Therefore, not all *three* human response channels – feedforward, visual feedback, and motion feedback – could be separately measured with instrumental-variable, system identification techniques. Nonetheless, strong yet indirect evidence indicated that humans do use physical motion to mechanize an additional (inner) feedback loop, identical to the response observed in compensatory tracking

tasks with motion [83, 111, 193]. As a consequence of the additional loop closure, errors are more aggressively minimized and, in accordance with Eq. (11.2), the far viewpoint is positioned closer ahead as compared to visual-only preview tasks. Extending the proposed preview control model with an explicit vestibular response channel, however, leads to overparameterization, which corresponds with the fact that the visual and vestibular sensory modalities provide redundant information about the controlled element output.

Main finding of Chapter 8

Human controllers use motion feedback equivalently, as an inner-loop feedback signal, in tracking tasks with and without preview; the adopted far-viewpoint preview response is equivalent in preview tasks with and without motion feedback.

Chapter 9: Multiple visual feedbacks and outside visual field control

Chapter 9 introduced two innovations, which led to a task that closely resembles the tracking of a winding road's centerline in a passenger car. First, rotational visual cues were introduced, and second, instead of a (perspective) display tracking task, the previewed trajectory was shown on a outside visual screen that provides a 180×40 deg field-of-view, equivalent to the (first-person) view through the front windshield of a car.

For the first time in this thesis, human-in-the-loop data were gathered with *three* external perturbations (target, lateral position disturbance, and heading disturbance), so that the dynamics of *three* human control responses could be identified. Thereby, direct evidence was obtained of the fact that humans use available heading information to close an inner feedback-loop, in addition to a lateral-position outer-loop. The heading loop equalizes the vehicle dynamics such that a proportional control response suffices to close the outer loop, as previously suggested in [90, 99]. This behavior was incorporated in the preview model through an additional gain that weights the human's relative use of heading and lateral position feedback. When organized as these *multiloop* feedback controllers, the filtered far-viewpoint provides the reference input to the lateral position outer-loop, identical as in single-axis tracking tasks. No evidence for a near-viewpoint response was found in these multiloop preview control tasks.

Whereas an explicit marker indicated the relevant controlled element output in the displays in Chapters 2–7, the human's forward view (outside) in the curve driving tasks of Chapter 9 provided no direct, unambiguous visual cues for the vehicle's lateral position and heading. The second innovation of Chapter 9 was to use perspective geometry to mathematically relate the estimated model control gains and look-ahead times to optical features in the driver's visual field. This showed that the minimized "internal" error in the preview model in fact corresponds to the visual angle between the vehicle's heading and the smoothed far-viewpoint, or *aim point*. Although comparable control models have been proposed before (e.g., see [65, 94, 95, 109]), Chapter 9 provided the first *direct evidence* that humans seem to respond to a salient visual angle. In addition, the model parameters quantifying exactly *which* visual angle is minimized by drivers.

Main findings of Chapter 9

1. Humans use rotational visual cues to mechanize an additional inner-loop feedback response based on heading; the smoothed far-viewpoint is still used as reference input (i.e., as aim point) to the lateral position outer-loop.
2. Driver steering in tracking a winding road's centerline can be represented as a compensatory control response, based on a single visual angle that is available from the perspective view ahead.

Chapter 10: Boundary avoidance and restricted preview in driving

Chapter 10 investigated the difference in driver steering behavior between centerline-tracking and *boundary-avoidance* (or lane-keeping) tasks, both with unrestricted and restricted preview. In a human-in-the-loop experiment, evidence was found that boundary-avoidance tasks evoke less aggressive error-minimization, and even some *intermittent* control behavior. Estimated feedforward dynamics indicated that humans use preview identically in both cases. Nonetheless, the far viewpoint is filtered (i.e., smoothed) more in boundary-avoidance tasks to exploit the available lane width. Restricted preview, due to severe simulated fog, was found to force drivers to position their far viewpoint closer ahead, at the limit where the road disappears into the fog. Furthermore, fog inhibits drivers from smoothing the target trajectory due to the lack of anticipating phase lead from the far viewpoint. These behavior adaptations are identical as found in the plan-view, pre-view tracking tasks of Part II, which thus prove instrumental for studying manual control (adaptation) in general real-world control tasks with preview.

Main findings of Chapter 10

1. Humans adopt an equivalent far-viewpoint preview response in tracking and boundary-avoidance tasks, but the latter evoke less aggressive error minimization, and a more smoothed far viewpoint that is positioned farther ahead.
2. Restricted preview forces human controllers to select a far viewpoint at a sub-optimal (closer) position and inhibits smoothing of the target trajectory, similarly in boundary-avoidance and tracking tasks.

11.1.4. GENERAL CONCLUSION

In conclusion, this thesis provided additional quantitative and qualitative insight into human manual preview control, through a cybernetic, control-theoretic modeling approach [6, 44]. The roadmap followed throughout this thesis is repeated in Fig. 11.1. Before the writing of this thesis, the simplified precision and crossover models were the state-of-the-art cybernetic manual control models. These models captured human control behavior only in the extremely limited compensatory tracking tasks, where a single-channel, error-minimizing, feedback control organization must be adopted. Corresponding to Step 1 in Fig. 11.1, this thesis first extended the cybernetic modeling framework to also capture humans' *feedback* and *feedforward* control behavior in tracking tasks with *preview* (Part I

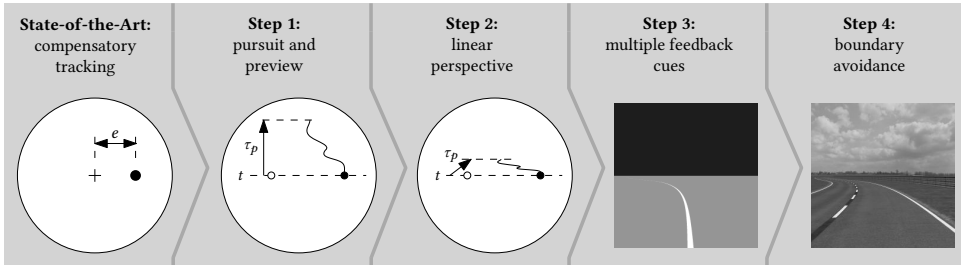


Figure 11.1: The roadmap followed throughout the thesis, adapted from the introduction (Chapter 1).

of this thesis), including their adaptation to key task variables (Part II). Then, in Part III, this thesis extended the proposed preview model to accommodate newly gained insight of human adaptation to important elements of *real-world* control tasks, such as linear perspective (Step 2 in Fig. 11.1), motion and visual rotational feedback (Step 3), and previewed target boundaries (Step 4).

As a result of the adopted bottom-up, stepwise approach, a *unifying* model could be proposed that captures human manual control behavior in a wide variety of preview control tasks. It was found that human controllers in all cases minimize a certain error variable, equally so in compensatory tracking tasks and in realistic lane-keeping tasks on winding roads (this key finding is illustrated on the cover of this thesis). The proposed models' *central* element is therefore an error-minimizing feedback response, which matches the seminal *precision model* for compensatory tracking tasks [6]. The commonality between all control tasks with preview is that humans minimize a time-advanced error relative to the (filtered) far viewpoint. Optionally, humans can mechanize an auxiliary, open-loop near-viewpoint response in parallel to the error response, to improve high-frequency target-tracking.

This proposed control-theoretic model has physically interpretable parameters that allow for quantifying (otherwise lumped) control processes within the human, to an extent that is not currently matched by any other method. The defining characteristics of the human's *compensatory control dynamics* can be estimated directly from measurement data, as well as how the human controller *integrates* multiple (visual or other) feedbacks, *what portions* of the previewed trajectory are used, and how the previewed trajectory is *processed*. The model naturally accommodates human controllers' strong *adaptive capabilities* through parameter adaptations, and consequently allows for rationalizing and quantitatively predicting human control behavior in a broad range of manual control tasks with preview.

11.2. RECOMMENDATIONS

In the following, five main recommendations are provided to indicate where the results of this thesis can be applied, or where further research is most needed.

11.2.1. SYSTEM IDENTIFICATION OF REAL-WORLD PREVIEW CONTROL

In this thesis, dedicated experiments were performed with *multisine* target and disturbance signals, which are sufficiently exciting over a wide range of frequencies to estimate the key characteristics of the human controller. While *multisine* target trajectories resemble certain winding real-world roads, they lack the step, ramp, or clothoid patterns that define many other roads and curve onsets. Additionally, (side-wind) disturbances are not always present in everyday driving tasks. It is currently not clear whether driving tasks that lack *multisine* perturbations are sufficiently exciting to estimate the parameters of the proposed driver model, and thus the key characteristics of the human controller. To obtain accurate *online* estimates that can be used, for example, in driver monitoring or support technology, it is recommended that future research investigates the proposed model's identifiability in real-world driving scenarios, where less steering is required (e.g., see [224]).

The lack of *multisine* perturbations in real-world driving tasks has the additional drawback that it is difficult to obtain multiloop frequency-response functions of the driver's *internal control dynamics*. These were the primary measure for validating the model fits in this thesis. The Variance Accounted For (VAF) can be used as an alternative measure, but quantifies only the match of the human and model *outputs*. Unfortunately, this thesis also showed that the obtained VAFs vary substantially (approximately between 65 and 95%), and depend strongly on the experimental control task and each individual person's control behavior. The value of the VAF thus provides no *absolute* measure for the model's quality-of-fit. It is recommended that future work searches for a more general, absolute measure to assess the model's fit to an individual's control behavior.

Finally, to avoid over-fitting the data, it is a common system identification practice to separate an obtained data set into a part for *estimating* the model parameters and a part for model *validation*. This thesis fitted the models to *all* obtained measurement data, because of the substantial time involved to collect human-in-the-loop measurement data. Future work may obtain models that better reflect an individual human's manual control behavior by using a dedicated portion of the measurement data *only* for validation.

11.2.2. TWO-LEVEL DRIVER STEERING BEHAVIOR

Ever since the publication of the seminal paper by Land and Horwood [58] in 1995, the generally accepted view on driver steering is that of a dual-mode controller (although the term *two-level* control was coined already in 1978 [91]). Land and Horwood showed that a "near" and a "far" portion of the visual field must be visible to achieve accurate steering when driving along winding roads, for velocities above 61 km/h. At the lower velocity of 45 km/h, a single, well positioned one-deg portion of the visual field was shown to facilitate accurate steering. These findings have been rationalized with some success using model-based analyses (e.g., see [94]), but, unfortunately, multiple replication experiments [67, 68] could not (fully) reproduce the results of Land and Horwood. One of the fundamental shortcomings has remained our limited understanding of human preview control and, in particular, human *adaptation* thereof to road curvature, width, and driving velocity.

The driver model developed in Chapters 9 and 10 of this thesis may provide the much-

needed tool to finally systematically address whether, and under what conditions, humans rely on a single or multiple portions of preview for control. For example, the proposed model suggests that at low target frequencies, corresponding to a low-velocity, low-curvature driving task, the human's steering behavior is characterized by minimization of the *single* visual angle to the unfiltered far viewpoint. Low-pass smoothing behavior, for which visibility of a substantial *portion* of the previewed trajectory may be required, manifests only at higher target frequencies (i.e., higher driving velocities or road curvatures). The critical next step that is currently (as of 2018) being investigated at our group, is whether the proposed driver steering model can explain and predict when one or two portion of a previewed road must be visible for accurate steering, and how this depends on (combinations of) critical task variables such as driving velocity and road curvature.

11.2.3. TIME-VARYING USE OF PREVIEW INFORMATION

This thesis studied manual preview control behavior as a *time-invariant* process. Time-varying behavior was purposely suppressed in the performed human-in-the-loop experiments by holding the task variables constant throughout a 100-120 s measurement run. As a consequence, amongst others, the far viewpoint selected by a human controller is implicitly assumed to be located at a fixed distance (or time) ahead of the vehicle. The position of this point may in fact be *time-varying* in many practical control tasks, for two reasons. First, neither the task variables (e.g., road curvature, available preview) nor the operator-centered variables (e.g., motivation, fatigue) are truly “invariant” for prolonged periods of time. Steady-state variations in these variables are known to cause human adaptation (e.g., see Chapters 9 and 10 and [59, 67, 102, 119, 215, 225, 226]), so temporal variations likely induce a time-varying far-viewpoint position. Second, as opposed to a *travel* point at a fixed time ahead, which moves forward through space as if tethered to the vehicle, humans may instead rely on *waypoints*, which are fixed in space [89]. For example, a waypoint could be placed on the inside of an upcoming curve in the road, which thus *approaches* the vehicle when the curve is negotiated (unlike a travel point), and is eventually replaced by a new waypoint farther ahead along the road.

To study to whether the previewed portions that are used for control are *time-varying*, system identification techniques are required that explicitly account for time-variations, as opposed to the time-averaging (frequency-domain) techniques adopted in this thesis. Such techniques have already been applied with success to study time-varying manual control behavior in various tracking tasks [133, 227–229]. Techniques based on Kalman filtering (e.g., see [133]) are particularly promising for quantifying the extent to which the far viewpoint – and thus the preview used by human controllers – is time-varying, because these techniques directly provide time-varying estimates of a model's parameters.

11.2.4. CONNECTING HUMAN GAZE TO PREVIEW CONTROL BEHAVIOR

The modeled far-viewpoint position was shown in this thesis to be strongly related to the farthest point ahead along the previewed trajectory that a human uses for control. The viewpoint positions were estimated with high precision directly from measurement

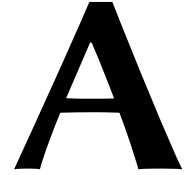
data using system identification techniques. In contrast, most researchers to date have relied on eye-tracking data instead of system identification techniques to quantify the visual information used by humans, in particular in driving (e.g., see [63, 65, 70, 73, 89]). It has been suggested that human gaze and control behavior are in fact related [71, 72, 89]: a salient optical feature may first attract the human's gaze before the information is used for control. In Chapter 3, a first attempt was made to explicitly correlate human gaze to the estimated model viewpoint positions, but only for *averaged* data in single-axis preview tracking tasks with integrator controlled element dynamics. It would be extremely valuable to relate the estimated far viewpoint (or aim point) in the driving model of Chapters 9 and 10 to human gaze data in a curve driving task. If such a relation exists, it would link the currently rather disconnected theories of human manual control and human gaze behavior, which could eventually lead to a more integrated theory of human locomotion altogether [89].

11.2.5. ENGINEERING APPLICATIONS

Besides propelling further research to increase our understanding of human use of preview, the results from this thesis can be applied directly to improve cutting-edge technology. At the moment, Advanced Driver Assistance Systems (ADAS) are rather haphazardly being introduced to support manual control in road vehicles. An example is the lane-keeping assist system, which *shares* control with the human driver, and typically communicates with the human through torques on the steering wheel. Such systems are currently manually tuned, one-size-fits-all automatic controllers. Mismatches between the intentions of the human driver and the automatic controller lead to conflicting torques and lacking confidence in the novel automated support systems [32, 33, 224, 230]. Replacing the automatic part of a shared controller with the driver model proposed in this thesis may help to resolve such conflicts, as the automatic controller's torques will better resemble those of the human driver. Thereby, the human's acceptance of the system will potentially improve. The parameters of the driver model could even be identified *online* from steering data to *intelligently adapt* the automatic controller to an individual driver's temporal control behavior.

Tentatively, more of tomorrow's vehicles will drive fully autonomously between two locations, without any human intervention. It is not difficult to imagine that passenger confidence in such systems will also increase when the automatic controllers resemble *human* control behavior, of which we have well-developed internal models and expectations. The proposed driver model could be used to synthesize an automatic controller that provides human-like steering. In fact, due to the model's ability to capture human *adaptation*, it can even provide robust human-like steering for a wide range of road curvatures, widths, and preview times.

APPENDICES



TWO INTERPRETATIONS OF FEEDFORWARD IN MANUAL CONTROL

Preview information allows humans to mechanize an anticipatory feedforward response in addition to a stabilizing feedback response. Throughout this thesis, the human's feedforward response dynamics are estimated and modeled using a parallel two-channel control organization with controlled element output feedback. The possible error feedback response that humans may in practice also mechanize is thereby ignored. Most researchers have in fact used a two-channel parallel control organization with such an error feedback response (instead of controlled element output feedback) to measure and model the human's feedforward dynamics in preview control tasks. This appendix explains the implications of the choice for either two-channel organization for identifying and modeling the feedforward response of a human manual controller.

The contents of this appendix will be submitted for publication as:

Title Two Interpretations of Feedforward in Manual Control
Journal IEEE Transactions on Human-Machine Systems
Authors K. van der El, D.M. Pool, and M. Mulder

A.1. MULTI-CHANNEL MANUAL CONTROL IN PURSUIT TASKS

A.1.1. MULTI-CHANNEL PURSUIT CONTROL BEHAVIOR

Consider a general manual control task, in which the human manipulates a control interface (signal u) to guide a certain output of a vehicle or device, $x(t)$, to the target value $f_t(t)$, at current time t . Both $x(t)$ and $f_t(t)$ are assumed to be known to the human from visual feedback. The human’s task is to minimize the error $e(t)$:

$$e(t) = f_t(t) - x(t). \tag{A.1}$$

This task corresponds to the pursuit and preview control tasks that are investigated in Chapters 2–7 of this thesis. The most general control diagram of the human in such a single-axis visual-only control task is shown in Fig. A.1a. Humans can mechanize control responses to the three available signals: 1) feedforward $H_{o_t}(j\omega)$ on the *target trajectory* $f_t(t)$, 2) feedback $H_{o_x}(j\omega)$ on the *controlled element output* $x(t)$, and 3) feedback $H_{o_e}(j\omega)$ on the *error* $e(t)$. Although this general, three-channel control diagram has occasionally

(a) general three-channel model

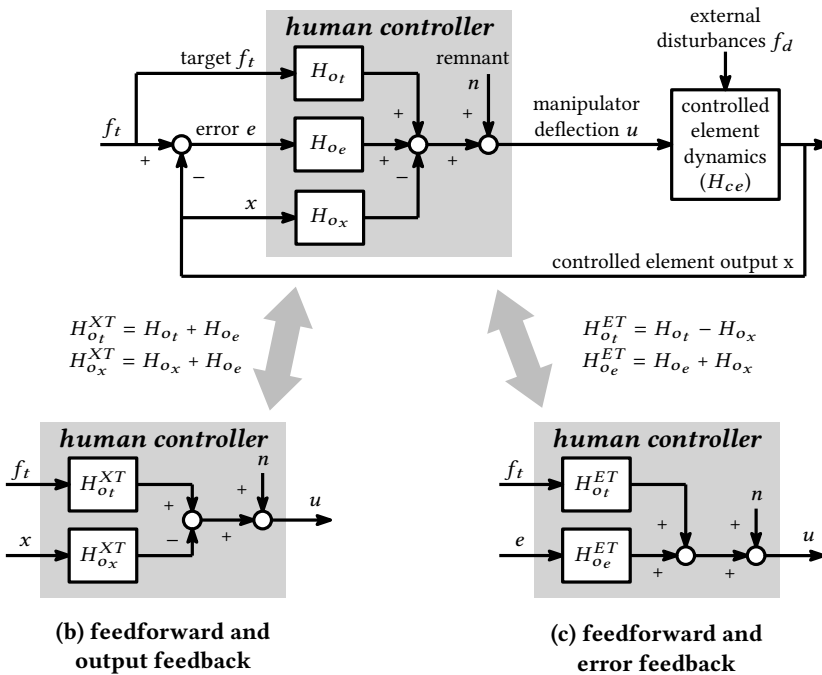


Figure A.1: A general, three-channel control diagram of the human in a visual pursuit control task, with feedforward response $H_{o_t}(j\omega)$, error feedback response $H_{o_e}(j\omega)$, and output feedback response $H_{o_x}(j\omega)$. The human’s feedforward control dynamics have been estimated in two-channel control organizations with either an output feedback response and with an error feedback response.

been discussed in literature [42, 62, 84, 85], directly measuring the dynamics of all three control responses is impossible for two reasons:

- The general three-channel response structure is *overdetermined*, due to the linear relation between the three inputs, $f_t(t)$, $x(t)$, and $e(t)$.
- *Three* uncorrelated external perturbation signals are required to measure the frequency responses of all three control dynamics [86], but only two meaningful perturbations can be applied: the target $f_t(t)$ and the disturbance $f_d(t)$, see Fig. A.1a.

A

Consequently, only two out of the three possible control responses can, and have been, directly measured. The following three two-channel control organizations are available for analyzing human control behavior:

XT: A parallel *feedforward* and *output* feedback organization, see Fig. A.1b, such that the error feedback block is omitted. This is the control organization that is used throughout this thesis, and has occasionally been used before (e.g., by Tomizuka [217] in an optimal preview control model).

ET: A parallel *feedforward* and *error* feedback organization, see Fig. A.1c, without output feedback response. This model is most commonly used throughout literature to study feedforward behavior in manual control (e.g., see [42, 56, 61, 90, 91, 125–130]).

EX: A parallel *error* and *output* feedback organization (not shown in Fig. A.1). Due to the absence of an explicit feedforward response, this organization has only seldom been used to investigate human behavior in control tasks other than compensatory tracking (see [141] for an exception).

As will be shown in the following, the three two-channel control organizations can all be used to study pursuit control behavior, as each is equally capable of capturing the human's full three-channel control dynamics. However, it has been poorly recognized that the two actually obtained estimates of the human's control dynamics *depend directly on the chosen two-channel structure*. The *a priori* choice for any of the three structures can have profound implications for the extent to which obtained control behavior data is observable and interpretable.

A.1.2. MODEL EQUIVALENCE

Given the general three-channel control diagram in Fig. A.1a, the Fourier transform of the human's control output $U(j\omega)$ can be written as follows:

$$U = H_{o_t}F_t + H_{o_e}E - H_{o_x}X + N. \quad (\text{A.2})$$

Here and in the following, the dependency of the signals and dynamics on $j\omega$ is dropped for brevity, and capitals indicate the Fourier transform of the respective signals. Substituting $E = F_t - X$, Eq. (A.1), into Eq. (A.2) yields:

$$\begin{aligned} U &= H_{o_t}F_t + H_{o_e}(F_t - X) - H_{o_x}X + N \\ &= (H_{o_t} + H_{o_e})F_t - (H_{o_x} + H_{o_e})X + N. \end{aligned} \quad (\text{A.3})$$

Comparing Eq. (A.3) with the expression for the human’s output in the two-channel *XT* control organization, given by $U = H_{o_t}^{XT}F_t - H_{o_x}^{XT}X + N$ (see Fig. A.1b), shows that:

$$H_{o_t}^{XT} = H_{o_t} + H_{o_e}, \tag{A.4}$$

$$H_{o_x}^{XT} = H_{o_x} + H_{o_e}. \tag{A.5}$$

The key implication of Eq. (A.4) is that the feedforward dynamics $H_{o_t}^{XT}(j\omega)$, as estimated in an *XT* structure, are *not the human’s true feedforward dynamics* $H_{o_t}(j\omega)$, but the *lumped combination* of $H_{o_t}(j\omega)$ and $H_{o_e}(j\omega)$. Equivalently, the estimated controlled element output response in Eq. (A.5) is the lumped combination of $H_{o_x}(j\omega)$ and $H_{o_e}(j\omega)$.

Using similar derivations, the responses in the *ET* and *EX* two-channel organizations can also be expressed as a function of the true human responses in the general three-channel structure. Moreover, expressions can be obtained that relate the responses of each of the two-channel organizations; these relations are all summarized in Table A.1. As is clear from this table, the response dynamics of the *ET* and *EX* structures are also the lumped combination of two *true* human’ responses, for instance, the feedforward $H_{o_t}^{ET} = H_{o_t}(j\omega) - H_{o_x}(j\omega)$. Regardless of the selected two-channel model structure, the remaining two responses are thus “contaminated” by the dynamics of the omitted third response, *if* the human in fact mechanizes this third response.

A.1.3. PERFECT TARGET-TRACKING

Focusing on the two-channel control organizations that include an explicit feedforward response, *XT* (Fig. A.1b) and *ET* (Fig. A.1c), it can be shown that the *desirable* feedforward dynamics are fundamentally different in both cases. Humans track the target trajectory perfectly when $e(t) = 0$ for all time t , or equivalently, when $x(t) = f_t(t)$, see Eq. (A.1). In the frequency domain, perfect target-tracking is thus given by $X(j\omega) = F_t(j\omega)$ for all ω . Assuming zero remnant $N(j\omega) = 0$ and external disturbance $F_d(j\omega) = 0$, Fig. A.1a shows

Table A.1: Relations between the equivalent multi-channel models.

		original organization			
		general	<i>XT</i>	<i>EX</i>	<i>ET</i>
<i>XT</i>	$H_{o_t}^{XT}$	$H_{o_t} + H_{o_e}$	-	$H_{o_e}^{EX}$	$H_{o_t}^{ET} + H_{o_e}^{ET}$
	$H_{o_x}^{XT}$	$H_{o_x} + H_{o_e}$	-	$H_{o_x}^{EX} + H_{o_e}^{EX}$	$H_{o_e}^{ET}$
<i>EX</i>	$H_{o_e}^{EX}$	$H_{o_e} + H_{o_t}$	$H_{o_t}^{XT}$	-	$H_{o_t}^{ET} + H_{o_e}^{ET}$
	$H_{o_x}^{EX}$	$H_{o_x} - H_{o_t}$	$H_{o_x}^{XT} - H_{o_t}^{XT}$	-	$-H_{o_t}^{ET}$
<i>ET</i>	$H_{o_e}^{ET}$	$H_{o_e} + H_{o_x}$	$H_{o_x}^{XT}$	$H_{o_e}^{EX} + H_{o_x}^{EX}$	-
	$H_{o_t}^{ET}$	$H_{o_t} - H_{o_x}$	$H_{o_t}^{XT} - H_{o_x}^{XT}$	$-H_{o_x}^{EX}$	-



that the following expressions hold for the XT two-channel organization:

$$\begin{aligned}
 X &= H_{ce}U, \\
 X &= H_{ce}(H_{o_t}^{XT}F_t - H_{o_x}^{XT}X), \\
 (1 + H_{ce}H_{o_x}^{XT})X &= H_{ce}H_{o_t}^{XT}F_t, \\
 \left(\frac{1}{H_{ce}} + H_{o_x}^{XT}\right)X &= H_{o_t}^{XT}F_t.
 \end{aligned} \tag{A.6}$$

Again, all elements' dependency on $j\omega$ in Eq. (A.6) are dropped for brevity. Substituting $X(j\omega) = F_t(j\omega)$ in Eq. (A.6) yields the following expression for the perfect target-tracking dynamics $H_{o_t}^{P,XT}$ in the XT structure:

$$H_{o_t}^{P,XT} = \frac{1}{H_{ce}} + H_{o_x}^{XT}. \tag{A.7}$$

A similar derivation for the two-channel ET organization yields [125]:

$$H_{o_t}^{P,ET} = \frac{1}{H_{ce}}. \tag{A.8}$$

Comparison of Eqs. (A.7) and (A.8) clearly shows that the *desired* human feedforward dynamics are different in a two-channel control organization with error or output feedback. Consequently, it can be expected that different feedforward dynamics are obtained when estimating the human's control dynamics using an ET or XT two-channel control organization (except when $H_{o_x}(j\omega) = 0$).

A.2. EXAMPLE MEASUREMENT DATA: PREVIEW TRACKING

A.2.1. CONTROL TASK AND SYSTEM IDENTIFICATION TECHNIQUES

To illustrate the implications of selecting an XT or ET control organization for analyzing feedforward control behavior, human-in-the-loop data from the preview tracking experiment of Chapter 5 are re-used here. These data were collected in a visual-only single-axis preview tracking task, where the preview time τ_p was varied in eight conditions between 0 and 2 s. Only the data from the tasks with double-integrator controlled element dynamics are considered here.

First, Frequency-Response Function (FRF) estimates are obtained of the human's two-channel control dynamics, using the same instrumental-variable, multiloop system identification technique that is used in the main chapters of this thesis, see Chapter 2 for details. The human's dynamics are estimated twice, in the XT control organization, yielding $H_{o_t}^{XT}(j\omega)$ and $H_{o_x}^{XT}(j\omega)$, and in the ET control organization, yielding $H_{o_t}^{ET}(j\omega)$ and $H_{o_e}^{ET}(j\omega)$. These estimates facilitate comparing the feedforward dynamics in both model structures.

Second, two models are fit to the same measurement data. One of these models is the *preview tracking* model proposed in this thesis, which follows from analysis of the FRF estimates in the XT organization. The other model is based on *inverse feedforward* models

that are commonly used in literature (e.g., in [42, 61, 90, 91, 125, 126, 128, 130]), which follow from analysis of the FRF estimates in the *ET* organization. The models are explained in detail later. The model fitting routine is identical to that applied in Chapter 5. The Variance Accounted For (VAF) is used as measure for the quality-of-fit, quantifying the models' capability to capture the human's control output (see Chapter 5 for details).

A.2.2. FREQUENCY-RESPONSE FUNCTION ESTIMATES

The estimated FRFs are shown in the Bode plots in Fig. A.2. The error feedback response $H_{o_e}^{ET}(j\omega)$ in the *ET* organization (Fig. A.2c,d) is identical to the output feedback response $H_{o_x}^{XT}(j\omega)$ in the *XT* organization (Fig. A.2e,f), which is in accordance with the model equivalence equations in Table A.1. Most importantly, however, Fig. A.2a,b shows that the feedforward dynamics are very different when estimated in an organization together with error or output feedback, as expected. In the *ET* organization, the human's feedforward dynamics approximate a double differentiator, both in magnitude and in phase, up to frequencies around 7 rad/s. These dynamics thus match well with the inverse of the controlled element dynamics $1/H_{c_e}(j\omega)$ that lead to perfect target-tracking in the *ET* organization, see Eq. (A.8). At higher frequencies, both the magnitude and phase of $H_{o_e}^{ET}(j\omega)$ increasingly deviate from the perfect target-tracking dynamics $H_{o_i}^{P,ET}$.

In contrast to the double differentiator behavior in the *ET* organization, the feedforward dynamics $H_{o_i}^{XT}(j\omega)$ in the *XT* organization, the "cross" markers in Fig. A.2a,b, resemble gain dynamics. In addition, substantial phase lead is visible, which increases towards higher frequencies, indicating the presence of a negative response delay, or *look-ahead* time, in the human's feedforward dynamics. Identical as in the *ET* organization, the perfect target-tracking dynamics in the *XT* organization are also matched well up to frequencies around 7 rad/s. However, at higher frequencies, the *XT* FRF estimates suggest that predominantly the *magnitude* of the human's response is inadequate for perfect target-tracking, whereas the *ET* FRF estimates instead suggests that the *phase* of the feedforward response is inadequate. Analysis of feedforward behavior using *XT* or *ET* two-channel organizations thus yields a fundamentally different interpretation of the human's control limitations.

A.2.3. CYBERNETIC MODELING

The first model that will be considered is the preview tracking model from this thesis. This model, abbreviated here as PR, was proposed in Chapter 2 to capture the estimated FRFs in the *XT* control organization. For simplicity, only the dominant *far-viewpoint* preview response is considered here, such that the PR model is given by:

$$H_{o_x}^{XT}(j\omega) = K_{e^*}(1 + T_{L,e^*}j\omega)e^{-\tau_v j\omega}H_{nms}(j\omega), \quad (\text{A.9})$$

$$H_{o_i}^{XT}(j\omega) = K_f \frac{1}{1 + T_{L,f}j\omega} e^{\tau_f j\omega} K_{e^*}(1 + T_{L,e^*}j\omega)e^{-\tau_v j\omega}H_{nms}(j\omega), \quad (\text{A.10})$$

with equalization gain and lead time-constant K_{e^*} and T_{L,e^*} , respectively, and feedback response time delay τ_v . Use of preview is captured by the target weighting gain K_f , lag

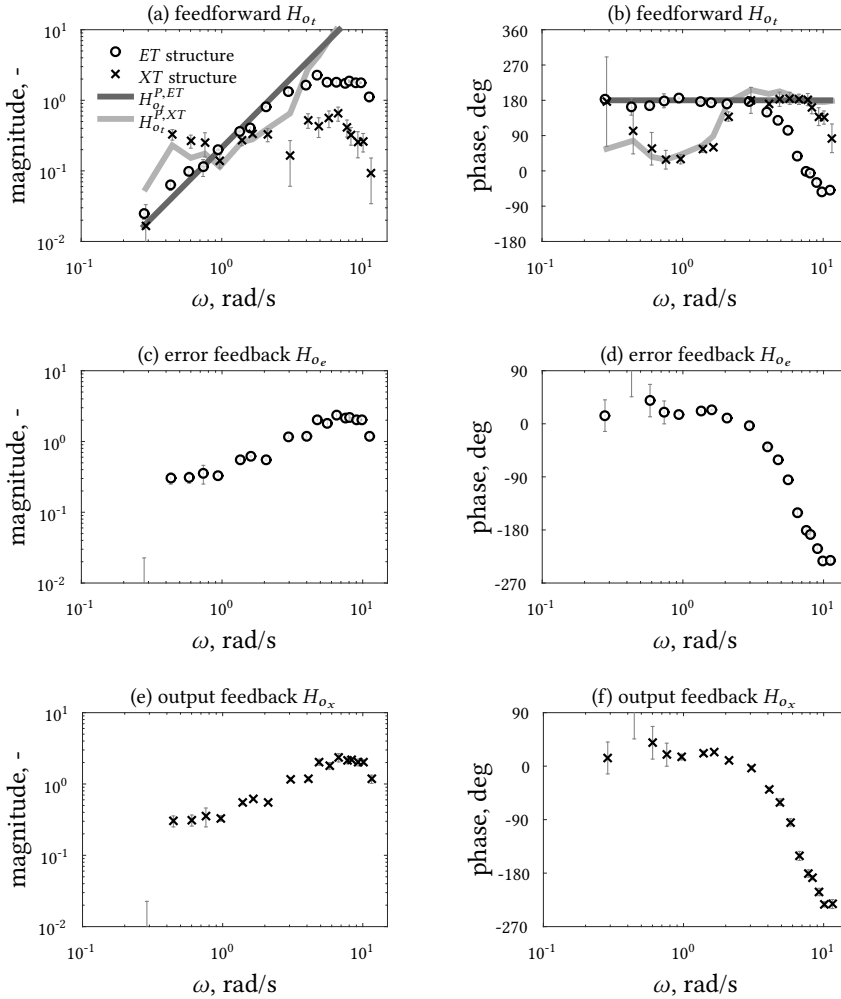


Figure A.2: Bode plots of human multiloop control dynamics in a preview tracking tasks ($\tau_p = 2$ s) with double integrator controlled element dynamics, estimated using ET and XT model structures; data are the five-run average of Subject 1, with standard errors.

time-constant T_{lf} , and look-ahead time τ_f , see Chapter 2 for details. The neuromuscular dynamics are given by:

$$H_{nms}(j\omega) = \frac{\omega_{nms}^2}{(j\omega)^2 + 2\omega_{nms}\zeta_{nms}j\omega + \omega_{nms}^2}, \quad (\text{A.11})$$

with neuromuscular break frequency ω_{nms} and damping ratio ζ_{nms} .

The second model that will be considered follows from modeling the FRF estimates in the ET control organization. Van Lunteren [56], who published the only multiloop ET data

for preview tracking task (besides this thesis), proposed to model the feedforward channel as the inverse of the controlled element dynamics, without any elements for the human's limitations. Other *ET*-based feedforward models have been proposed that do include dynamics for the human's limitations [125, 126, 128, 130], but these models described human feedforward behavior in (zero-preview) pursuit tracking tasks with predictable target signals. Here, the inverse feedforward model from Drop *et al.* [126] will be used, abbreviated as IFF, and not the simpler model proposed by Van Lunteren [56]. The IFF by Drop *et al.* facilitates a direct comparison with the PR model for two reasons; first, it has an equal number of parameters, and second, the meaning of the parameters roughly correspond between the two models. The IFF model is given by:

$$H_{o_e}^{ET}(j\omega) = K_e(1 + T_{L,e}j\omega)e^{-\tau_v j\omega}H_{nms}(j\omega), \quad (\text{A.12})$$

$$H_{o_t}^{ET}(j\omega) = K_t \frac{1}{1 + T_{L,t}j\omega} e^{\tau_l j\omega} \frac{1}{H_{ce}(j\omega)} H_{nms}(j\omega), \quad (\text{A.13})$$

with target response gain K_t , lag time-constant $T_{L,t}$, and look-ahead time τ_l . Note that Drop *et al.* [126] modeled τ_l as a *delay*, that is $e^{-\tau_l j\omega}$, but that this is changed here to a *negative* delay, or look-ahead time, for easier comparison with the PR model. While the meaning of the feedback parameters is identical as in the PR model, the “*” superscript is dropped from the error response gain and lead time-constant, as the compensatory response in the *ET* model is with respect to the *true* current tracking error $e(t)$, opposed to the filtered, time-advanced error $e^*(t)$ in the PR model.

A.2.4. MODELING RESULTS

Fig. A.3 shows the dynamics of the fitted PR and IFF models, together with the nonparametric FRF estimates, for the same data as in Fig. A.2. The models match the estimated FRF reasonably well, both in feedforward and feedback, especially below 5 rad/s. However, at higher frequencies, the PR model arguably outperforms the IFF model in describing the respective FRF data. Whereas the feedback $H_{o_x}^{XT}(j\omega)$ FRF is captured almost perfectly by the PR model (Fig. A.3e,f), the IFF model fit deviates from the $H_{o_e}^{ET}(j\omega)$ FRF at frequencies beyond 5 rad/s (Fig. A.3c,d). Moreover, while both models fail to fully capture the high frequencies of the respective feedforward FRF estimates, the PR model provides a better match with the $H_{o_t}^{XT}(j\omega)$ than the IFF model with the $H_{o_t}^{ET}(j\omega)$ dynamics, especially in magnitude (see Fig. A.3a).

The corresponding model VAFs in Fig. A.4a show that both models capture the measured humans' control output approximately equally well in zero-preview, pursuit tasks. The quality of the PR model fit remains constant when the preview time increases from zero to two seconds, but, in contrast, the IFF model quality-of-fit deteriorates markedly for $\tau_p > 0.5$ s. The PR model is thus more capable than the IFF model to capture the human's control output in tasks with ample preview.

Fig. A.4 also shows the estimated parameters for the two model fits, which quantify *how* humans adapt their control behavior to the preview time. While both models contain the same number of parameters, which, in addition, have a similar physical meaning, the estimated parameter adaptations to preview time are *very different*. For example, whereas the

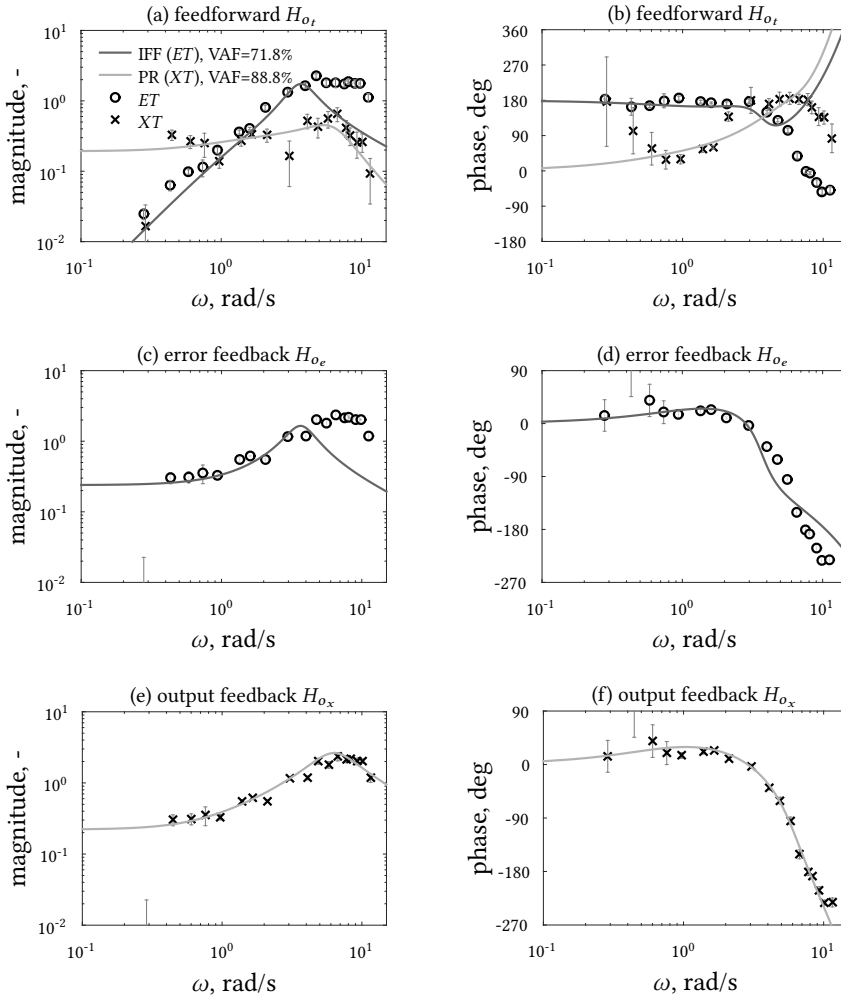


Figure A.3: Bode plots of the fitted IFF and PR models, which are based on the ET (IFF) and XT (PR) FRF data, respectively. Corresponding to Fig. A.2, presented data are from Subject 1 in tasks with 2 s of preview.

PR model fits suggest that the human's response delay τ_v remains approximately constant for all preview times τ_p between 0 and 2 s, the IFF model suggests that humans severely reduce their delay, from 0.3 to around 0.12 s.

Perhaps the most interesting result from the estimated parameters is in the look-ahead time in Fig. A.4i, given by τ_f in the PR model and τ_t in the IFF model. With increasing preview, the estimated look-ahead time increases in both models. In the PR model, the value of the look-ahead time is roughly equal to the preview time, $\tau_f \approx \tau_p$, for preview times below 1 s. This suggests that the human controllers were responding to the *end*

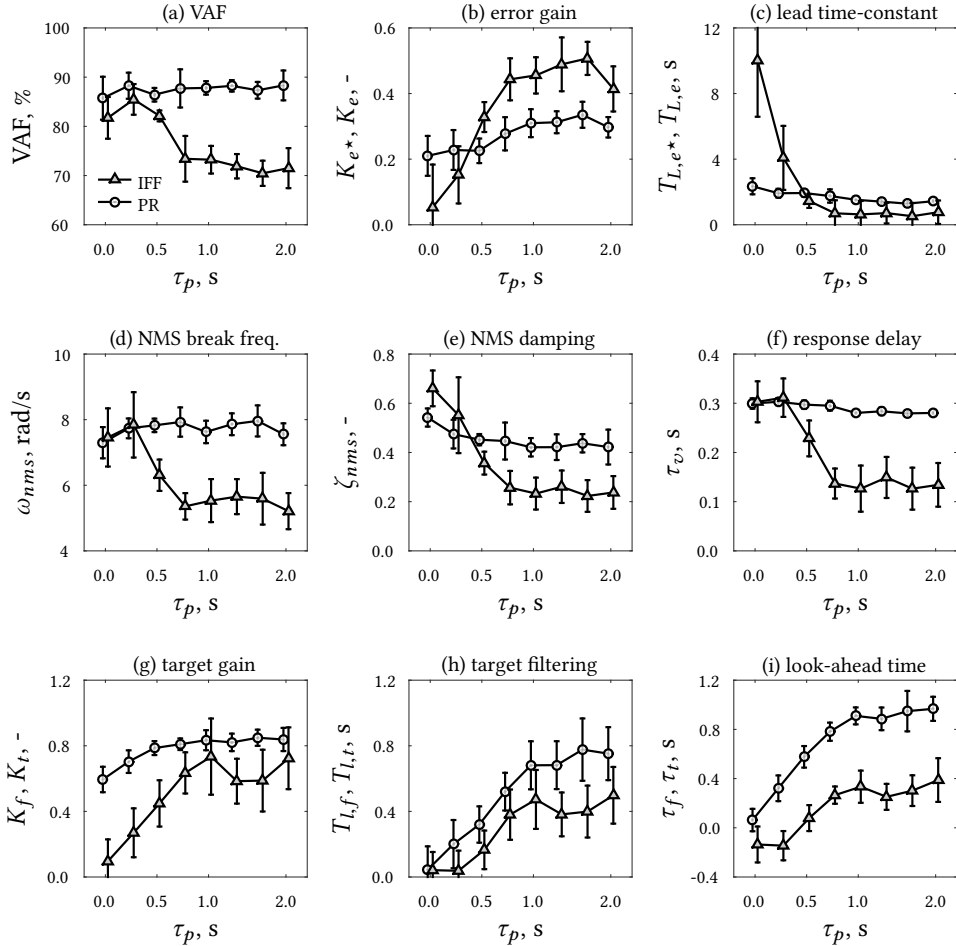


Figure A.4: Quality-of-fit (VAF) and the estimated parameters of the IFF and PR models; average of eight subjects and 95% confidence intervals (corrected for between-subject variability).

point of the displayed preview line, as discussed in detail in Chapter 5. However, in the IFF model, the look-ahead time is much lower, indicating that the experimental participants used less of the previewed trajectory. It is likely that humans use *all* of the available preview to anticipate the target trajectory when the preview time is restricted. As such, the model parameters of the PR model appear to have a more direct physical meaning than the parameters of the IFF model.



A.3. CONCLUSION

This appendix investigated the implications of measuring the human's feedforward dynamics in manual control tasks using different two-channel control organizations. Estimated feedforward dynamics are very different when the feedback channel is based on the tracking error or the controlled element output, because estimated control dynamics are contaminated by the neglected other response. Consequently, when using multiloop system identification techniques to measure the human's behavior in *any* task that allows for more than one response channel, extreme care should be taken when physically interpreting the estimated dynamics and the thereon based model parameters.

A

For the human's control behavior in preview tracking tasks, modeling the two-channel control organization with feedforward and controlled element output feedback (yielding the preview model as used throughout this thesis) provides a more useful model than the "traditional" feedforward models that are based on inverse controlled element dynamics. The preview model from this thesis, even without a near-viewpoint response, captures both the human's control output and the multiloop frequency-response function estimates better than an inverse feedforward model. In contrast to the inverse feedforward model, the preview model's parameters appear to be directly physically interpretable, with a far viewpoint that is linked strongly to the preview time for tasks where the available preview is limited. These conclusions, while based on single-axis pursuit and preview tracking tasks, apply equally to tasks with multiloop heading and lateral position feedback, such as the driving tasks of Chapters 9 and 10.

B

REMNANT DATA AND MODELING

The main focus of this thesis is to understand the linear, time-invariant dynamics of human manual preview control, which determine most of the human's control output. In the adopted quasi-linear modeling framework, control behavior that is not linear and time-invariant is not explicitly modeled; examples include time-varying and nonlinear control behavior, and internal noise sources such as motor or perception noise. The lumped combination of all human behavior that is not linear, time-invariant is referred to as remnant [6, 196]. Remnant models have occasionally been used to improve predictions of human control behavior beyond fully linear, time-invariant simulations, see [83, 131–133] for examples. To facilitate similar predictions in pursuit and preview tracking tasks, this appendix provides remnant data, together with remnant models that can be used in computer simulations.

B.1. REMNANT POWER

The data presented in this appendix are taken from the experiment discussed in Chapters 2 and 4. The experiment included conditions with gain (GN), single-integrator (SI) and double-integrator (DI) controlled element dynamics, all of which were performed with a pursuit (PS) and a preview (PR) display, the latter with 1 s of preview. All conditions were performed by twelve subjects. For reference, a control diagram of the human in such a control task is reproduced from Chapters 2 and 4 in Fig. B.1.

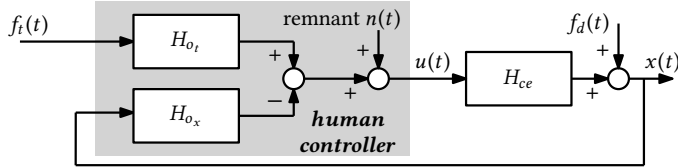


Figure B.1: Illustration of the human in a pursuit or preview tracking task with controlled element dynamics $H_{ce}(j\omega)$. The human's linear responses to the target and the controlled element output are given by $H_{o_t}(j\omega)$ and $H_{o_x}(j\omega)$, respectively, and n is the remnant.

Fig. B.1 shows that the human control output is the sum of the linear responses to the external target signal f_t and disturbance signal f_d , and the remnant $n(t)$ [196]: $u(t) = u_t(t) + u_d(t) + u_n(t)$. This is clear by writing the control output as a function of the external inputs in the frequency domain, using Fig. B.1:

$$U(j\omega) = \frac{H_{o_t}(j\omega)F_t(j\omega) - H_{o_x}(j\omega)F_d(j\omega) + N(j\omega)}{1 + H_{o_x}(j\omega)H_{ce}(j\omega)}, \quad (\text{B.1})$$

with $H_{o_t}(j\omega)$ and $H_{o_x}(j\omega)$ the human's linear feedforward and feedback responses, respectively, and $H_{ce}(j\omega)$ the controlled element dynamics. The capitals in Eq. (B.1) denote the discrete Fourier transforms of the respective signals.

The periodogram can be used as estimate for the control output power-spectral density function: $\hat{S}_{uu}(j\omega) = \frac{1}{f_s L} |U(j\omega)|^2$, with L the number of samples and f_s the sampling frequency. Fig. B.2 shows the estimated control output spectra for the five runs of a single participant in the SIPR condition. The target and disturbance are multisine signals that have power only at a discrete number of frequencies (20 each), ω_t for the target and ω_d for the disturbance. Fig. B.2 shows distinct peaks in the control output spectra at these frequencies, indicating that the participant clearly acted to track the target and suppress the disturbance. At these frequencies, the control output spectral-density has contributions both due to the remnant and due to the human's linear response to the forcing functions. At all other frequencies, the human *remnant* is the only contributor to the control output, see Eq. (B.1), hence these are referred to as the remnant frequencies ω_n .

In the main chapters of this thesis, the remnant contribution to the control output $u(t)$ is estimated as the sum of the power of $u(t)$ at the remnant frequencies ω_n . Thereby, the remnant contribution at the target and disturbance frequencies is effectively ignored and the true remnant contribution is underestimated. One method to estimate the remnant

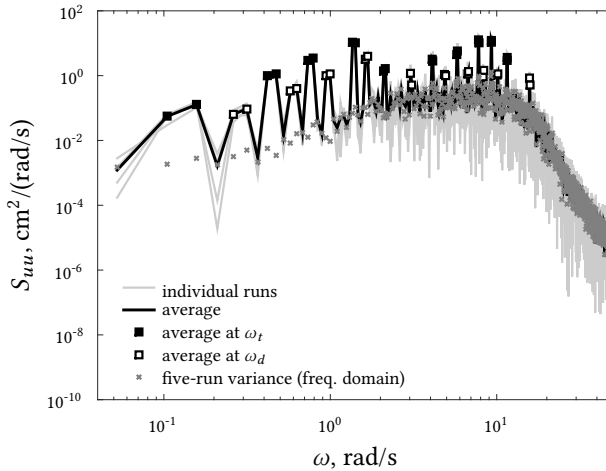


Figure B.2: Control output spectrum for Subject 2 in the SIPR condition: the data of the five measurement runs, the frequency-domain average per frequency, and the frequency-domain variance per frequency. The control output is shown in cm for consistency with Chapter 4, the rotations at the side-stick are obtained by mapping with a gain of 0.445 cm/deg.

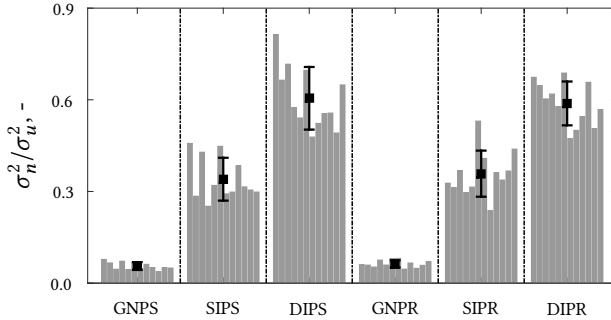
contribution at the target and disturbance input frequencies, here referred to as M1, uses the data from the adjacent, non-excited frequencies [87]. The average of the remnant data over a number of neighboring non-excited frequencies yields an estimate for the remnant power at ω_t or ω_d , assuming that the remnant is a smooth function of frequency. Unfortunately, quite a few of the lower frequencies are occupied by the target and disturbance signals in the performed experiment, as is visible in Fig. B.2. The remnant at these frequencies is typically not a problem for adequate task performance, as errors due to control inaccuracies are well-attenuated due to the high loop gain (e.g., see [6, 80]). Nonetheless, few *input-free* frequencies remain for estimating the remnant at ω_t or ω_d .

Another estimate for the remnant at the target and disturbance input frequencies can be obtained from the variance of the Fourier transform of the control output $U(j\omega)$ of the five runs per input frequency [231]. Fig. B.2 shows that this estimate, in the remainder referred to as M2, indeed reasonably matches with the average control output spectrum at the remnant frequencies, which verifies the method. The variance-based method yields a remnant estimate that is a reasonably smooth function of frequency, also at the lower frequencies, where almost all frequencies are excited by a target or disturbance sinusoid. Note that between 3-10 rad/s (see Fig. B.2), the variance-based method yields a relatively high estimate of the remnant contribution, especially as compared to the remnant at neighboring, non-excited frequencies.

For comparison, Table B.1 gives the total remnant power, as estimated with the two methods. When considering only the remnant frequencies ω_n (as done throughout this thesis), the power of the control output signal is almost equal to the power as estimated with the variance-based method. Both methods thus provide equal estimates of the remnant

Table B.1: Estimated remnant as a fraction of the control output power (σ_n^2/σ_u^2).

	GNPS	SIPS	DIPS	GNPR	SIPR	DIPR
M1: average power (ω_n)	0.041	0.292	0.527	0.051	0.309	0.509
M2a: variance over five runs (ω_n)	0.041	0.288	0.515	0.050	0.306	0.501
(M2a/M1)*100%	97.776	98.733	97.768	99.110	98.917	98.499
M2b: variance over five runs (all ω)	0.056	0.340	0.605	0.063	0.358	0.588
(M2b/M2a)*100%	137.888	118.166	117.428	125.782	117.065	117.374

**Figure B.3:** Relative remnant contribution to the control output, estimated over all frequencies using the frequency-domain variance-based method (M2b).

power at the non-excited frequencies. However, the variance-based method also allows for estimating the remnant at the target and disturbance frequencies. With *all* frequencies included, the estimated remnant contribution to the control output is typically a striking 17% higher than for the remnant frequencies only (see Table B.1), and this percentage is even higher (but less relevant) when the remnant contribution is small. The remnant contribution estimates presented in this thesis thus *underestimate* the true remnant. The remnant contributions, as estimated with the variance-based method at all frequencies, are given for all twelve participants in Fig. B.3.

B.2. REMNANT MODELING

The remnant spectrum in Fig. B.2 does not resemble the flat amplitude spectrum of Gaussian white noise. Therefore, the characterization of the remnant can be improved beyond only calculating its power. In literature, this is often done by *modeling* the spectrum of the injected remnant $n(t)$ [131, 132, 196]. From Fig. B.1 and Eq. (B.1), it follows that the injected remnant $N(j\omega)$ is related to the remnant contribution to the control output *in the loop* $U_n(j\omega)$ as follows:

$$N(j\omega) = (1 + H_{o_x}(j\omega)H_{c_e}(j\omega))U_n(j\omega). \quad (\text{B.2})$$

Example remnant spectra estimates obtained with Eq. (B.2) are shown in Fig. B.4. To quantify the remnant characteristics, and to facilitate *quantitative* simulations, the following

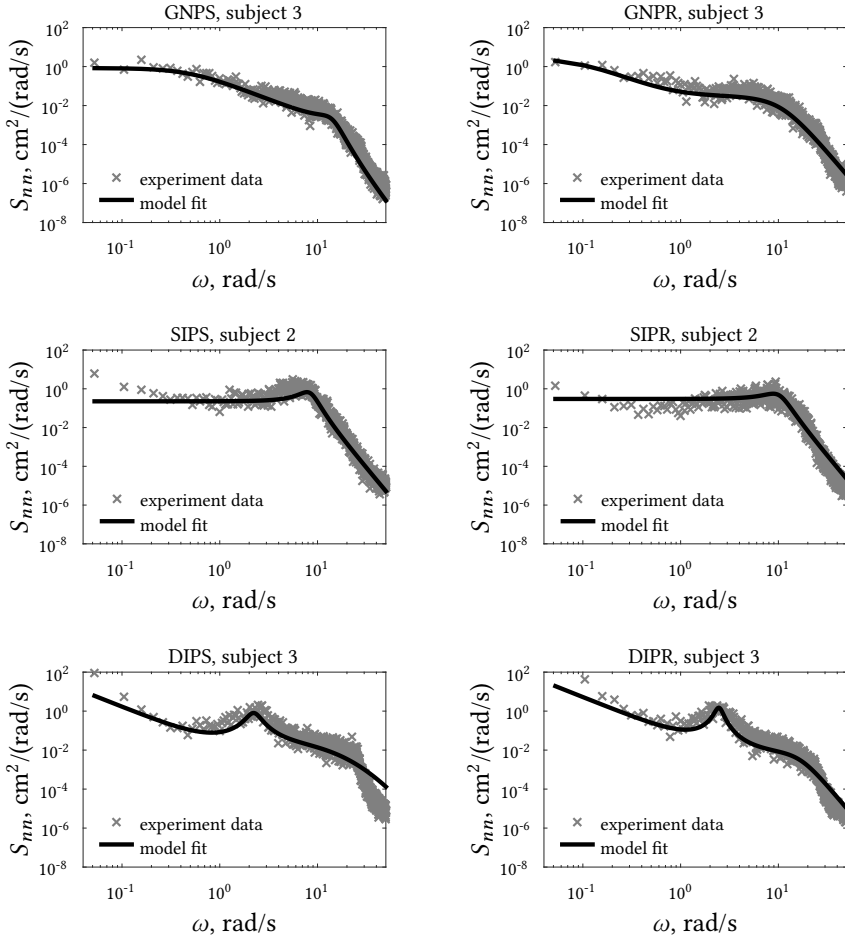


Figure B.4: Remnant spectra and remnant model fits, for the same (representative) participants and conditions as presented in Chapter 2.

remnant filter is fit to the remnant data, partly based on the model in [132]:

$$H_n(j\omega) = \underbrace{\frac{1 + T_{L,n}j\omega}{1 + T_{I,n}j\omega}}_{\text{lead-lag}} \underbrace{\frac{\omega_{n,1}^3}{(j\omega^2 + 2\omega_{n,1}\zeta_{n,1}j\omega + \omega_{n,1}^2)(\omega_{n,1} + j\omega)}}_{\text{third-order filter}} \underbrace{\frac{\omega_{n,2}^2}{j\omega^2 + 2\omega_{n,2}\zeta_{n,2}j\omega + \omega_{n,2}^2}}_{\text{second-order filter}} \quad (\text{B.3})$$

In single-integrator tasks, neither the lead-lag nor the second-order filter are required for a good fit of the remnant shape. In gain tasks, the second-order filter is not required, while in DI tasks, the second order filter is required, but the lag term from the lead-lag filter can be omitted. Fig. B.5 shows the resulting estimates of the remnant filter parameters.

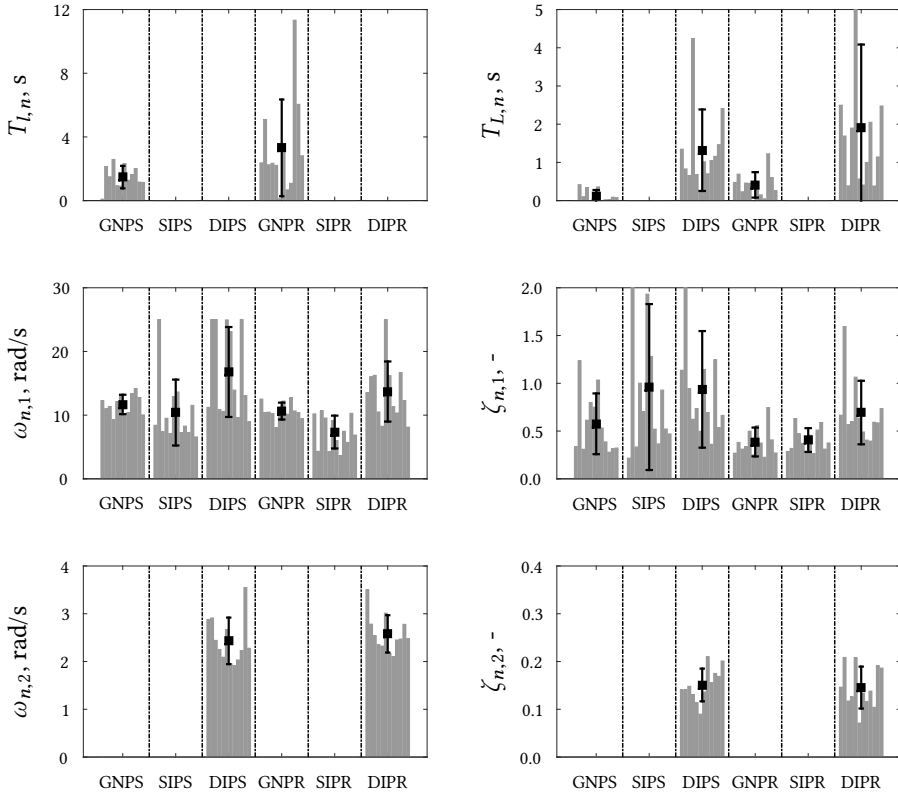


Figure B.5: Estimated remnant filter parameters for pursuit and preview tracking tasks with gain, single- and double-integrator controlled element dynamics. Gray bars reflect the individual participants, errorbars are the means with standard deviations.

B.3. CONCLUSION

This appendix provided remnant data of twelve participants in pursuit and preview tracking tasks with gain, single-, and double-integrator controller element dynamics. The remnant power and spectra were quantified, so that these can be used to improve predictions of human control behavior beyond simulations with only the linear, time-invariant models, as proposed throughout this thesis. A method was presented for quantifying the remnant power at the input frequencies of multisine target and disturbance signals, which, for the experiment of Chapters 2 and 4, account for a substantial portion of the total remnant power. The remnant contribution estimates presented in the main chapters of this thesis, which neglect the remnant at the target and disturbance input frequencies, thus underestimate the true remnant. The data presented in this appendix are representative for human remnant in the pursuit and preview tracking tasks of Parts I and II, but not necessarily as well for the more realistic control tasks investigated in Part III, where the remnant generally contributes much less to the total control output.

REFERENCES

- [1] J. J. Gibson and L. E. Crooks, "A theoretical field-analysis of automobile-driving," *The American Journal of Psychology*, vol. 51, no. 3, pp. 453–471, Jul. 1938.
- [2] R. S. Sharp, "Motorcycle steering control by road preview," *Journal of Dynamic Systems, Measurement, and Control*, vol. 129, pp. 373–381, Jul. 2007.
- [3] R. A. Hess, J. K. Moore, and M. Hubbard, "Modeling the manually controlled bicycle," *IEEE Trans. on Systems, Man, and Cybernetics, Part A: Systems and Humans*, vol. 42, no. 3, pp. 545–557, May 2012.
- [4] B. Shyrokau, J. De Winter, O. Stroosma, C. Dijksterhuis, J. Loof, M. M. Van Paassen, and R. Happee, "The effect of steering-system linearity, simulator motion, and truck driving experience on steering of an articulated tractor-semitrailer combination," *Applied Ergonomics*, vol. 71, pp. 17–28, Sep. 2018.
- [5] I. L. Ashkenas and D. T. McRuer, "A theory of handling qualities derived from pilot-vehicle system considerations," *Aerospace Engineering*, vol. 21, no. 2, pp. 60–102, 1962.
- [6] D. T. McRuer and H. R. Jex, "A review of quasi-linear pilot models," *IEEE Trans. on Human Factors in Electronics*, vol. 8, no. 3, pp. 231–249, May 1967.
- [7] T. B. Sheridan, W. L. Verplanck, and T. L. Brooks, "Human/computer control of undersea teleoperators," in *Proc. 14th Ann. Conf. on Manual Control*, Los Angeles, CA, 1978, pp. 343–357.
- [8] W. Veldhuyzen and H. G. Stassen, "The internal model concept: An application to modeling human control of large ships," *Human Factors*, vol. 19, no. 4, pp. 367–380, 1979.
- [9] S. Bennett, *A History of Control Engineering 1930-1955*. Hertfordshire, UK: Peter Peregrinus Hitchin, 1993.
- [10] F. B. Bjørneset, M. D. Dunlop, and E. Hornecker, "Assessing the effectiveness of direct gesture interaction for a safety critical maritime application," *International Journal of Human-Computer Studies*, vol. 70, no. 10, pp. 729–745, 2012.
- [11] A. K. Bejczy, "Sensors, controls, and man-machine interface for advanced teleoperation," *Science*, vol. 208, no. 4450, pp. 1327–1335, Jun. 1980.
- [12] T. B. Sheridan, *Telerobotics, Automation, and Human Supervisory Control*. MIT Press Cambridge, 1992.

- [13] D. A. Mindell, *Our Robots, Ourselves: Robotics and the Myths of Autonomy*. Penguin Publishing Group, 2015.
- [14] J. Smisek, "Systematic framework for teleoperation with haptic shared control," Ph.D. dissertation, Aerospace Engineering, TU Delft, Delft, The Netherlands, 2017.
- [15] A. Hufschmidt and C.-H. Lücking, "Abnormalities of tracking behavior in Parkinson's disease," *Movement Disorders*, vol. 10, no. 3, pp. 267–276, 1995.
- [16] R. D. Jones, I. M. Donaldson, and N. B. Sharman, "A technique for removal of the visuoperceptual component from tracking performance and its application to Parkinson's disease," *IEEE Trans. on Biomedical Engineering*, vol. 43, no. 10, pp. 1001–1010, Oct. 1996.
- [17] P. Soliveri, R. G. Brown, M. Jahanshahi, T. Caraceni, and C. D. Marsden, "Learning manual pursuit tracking skills in patients with Parkinson's disease," *Brain*, vol. 120, no. 8, pp. 1325–1337, 1997.
- [18] M. M. K. Oishi, P. TalebiFard, and M. J. McKeown, "Assessing manual pursuit tracking in Parkinson's disease via linear dynamical systems," *Annals of Biomedical Engineering*, vol. 39, no. 8, Aug. 2011.
- [19] R. D. Jones, "Measurement and analysis of sensory-motor performance: Tracking tasks," in *Medical Devices and Human Engineering*. CRC Press LLC, 2014.
- [20] *Global Status Report on Road Safety 2015*. World Health Organization, 2015.
- [21] L. Evans, "The dominant role of driver behavior in traffic safety," *American Journal of Public Health*, vol. 86, pp. 784–786, 1996.
- [22] A. DeNisco Rayome. (2018, Feb.) Dossier: The leaders in self-driving cars. [Online]. Available: <https://www.zdnet.com/article/dossier-the-leaders-in-self-driving-cars/>
- [23] H. Mantakos. Is GA flying safer than driving? Consulted: 14/09/2017. [Online]. Available: <http://www.meretrrix.com/~harry/flying/notes/safetyvsdriving.html>
- [24] R. Parasuraman, T. B. Sheridan, and C. D. Wickens, "A model for types and levels of human interaction with automation," *IEEE Trans. on Systems, Man, and Cybernetics, Part A: Systems and Humans*, vol. 30, no. 3, pp. 286–297, May 2000.
- [25] T. Gordon and M. Lidberg, "Automated driving and autonomous functions on road vehicles," *Vehicle System Dynamics*, vol. 53, no. 7, pp. 958–994, 2015.
- [26] B. Strauch, "Ironies of automation: Still unresolved after all these years," *IEEE Trans. on Human-Machine Systems*, vol. 48, no. 5, pp. 419–433, Oct. 2018.
- [27] T. Miyashita, T. Tajika, H. Ishiguro, K. Kogure, and N. Hagita, "Haptic communication between humans and robots," in *Robotics Research: Results of the 12th International Symposium, ISRR*, San Francisco, CA, 2005, pp. 525–536.

- [28] J. Smisek, E. Sunil, M. M. van Paassen, D. A. Abbink, and M. Mulder, "Neuromuscular-system-based tuning of a haptic shared control interface for UAV teleoperation," *IEEE Trans. on Human-Machine Systems*, vol. 47, no. 4, pp. 449–461, Aug. 2017.
- [29] K. Korosec. (2018, Jun.) Why self-driving car companies are eyeing this remote driving startup. [Online]. Available: <http://fortune.com/2018/06/12/phantom-auto-self-driving-cars/>
- [30] R. W. Howard, "Automatic flight controls in fixed wing aircraft: The first 100 years," *Aeronautical Journal*, 1973.
- [31] D. T. McRuer and D. Graham, "A flight control century: Triumphs of the systems approach," *Journal of Guidance, Control and Dynamics*, vol. 27, no. 2, pp. 161–173, 2003.
- [32] D. A. Abbink, M. Mulder, and E. R. Boer, "Haptic shared control: Smoothly shifting control authority?" *Cognition, Technology & Work*, vol. 14, no. 1, pp. 19–28, Mar. 2012.
- [33] F. Flemisch, M. Heesen, T. Hesse, J. Kelsch, A. Schieben, and J. Beller, "Towards a dynamic balance between humans and automation: Authority, ability, responsibility and control in shared and cooperative control situations," *Cognition, Technology & Work*, vol. 14, no. 1, pp. 3–18, Mar 2012.
- [34] F. Mars, M. Deroo, and J.-M. Hoc, "Analysis of human-machine cooperation when driving with different degrees of haptic shared control," *IEEE Trans. on Haptics*, vol. 7, no. 3, pp. 324–333, Jul. 2014.
- [35] F. Mars and P. Chevrel, "Modelling human control of steering for the design of advanced driver assistance systems," *Annual Reviews in Control*, vol. 44, pp. 292–302, 2017.
- [36] M. M. van Paassen, R. P. Boink, D. A. Abbink, M. Mulder, and M. Mulder, *Advances in Aviation Psychology*. Routledge, 2017, vol. 2, ch. Four design choices for haptic shared control, pp. 237–254.
- [37] D. A. Abbink, T. Carlson, M. M., J. C. F. de Winter, F. Aminravan, T. L. Gibo, and E. R. Boer, "A topology of shared control systems - Finding common ground in diversity," *IEEE Trans. on Human-Machine Systems*, vol. 48, no. 5, pp. 509–525, Oct. 2018.
- [38] G. Baxter, J. Rooksby, Y. Wang, and A. Khajeh-Hosseini, "The ironies of automation, still going strong at 30?" in *ECCE 2012 Proceedings of the 30th European Conference on Cognitive Ergonomics*, 2012, pp. 65–71.
- [39] L. Bainbridge, "Ironies of automation," *Automatica*, vol. 19, no. 6, pp. 775–779, 1983.
- [40] N. Merat, A. H. Jamson, F. C. H. Lai, M. Daly, and O. M. J. Carsten, "Transition to manual: Driver behaviour when resuming control from a highly automated vehicle," *Transportation Research Part F: Traffic Psychology and Behaviour*, vol. 27, no. B, pp. 274–282, Nov. 2014.

- [41] F. J. Valero-Cuevas, *Fundamentals of Neuromechanics*. Springer-Verlag London, 2015.
- [42] R. J. Wasicko, D. T. McRuer, and R. E. Magdaleno, "Human pilot dynamic response in single-loop systems with compensatory and pursuit displays," Air Force Flight Dynamics Laboratory, Wright-Patterson Air Force Base, OH, Tech. Rep. AFFDL-TR-66-137, 1966.
- [43] D. T. McRuer and E. S. Krendel, "Mathematical models of human pilot behavior," Advisory Group for Aerospace Research and Development, AGARDograph AGARD-AG-188, Jan. 1974.
- [44] M. Mulder, D. M. Pool, D. A. Abbink, E. R. Boer, P. M. T. Zaal, F. M. Drop, K. van der El, and M. M. van Paassen, "Manual control cybernetics: State-of-the-art and current trends," *IEEE Trans. on Human-Machine Systems*, vol. 48, no. 5, pp. 468–485, Oct. 2018.
- [45] D. M. Pool, M. Mulder, M. M. van Paassen, and J. C. van der Vaart, "Effects of peripheral visual and physical motion cues in roll-axis tracking tasks," *Journal of Guidance, Control, and Dynamics*, vol. 31, no. 6, pp. 1608–1622, Nov.-Dec. 2008.
- [46] T. Lu, D. M. Pool, M. M. van Paassen, and M. Mulder, "Use of simulator motion feedback for different classes of vehicle dynamics in manual control tasks," in *Proc. 5th CEAS Air & Space Conference, Delft, The Netherlands*, no. 52, Sep. 2015.
- [47] J. J. Gibson, "Visually controlled locomotion and visual orientation in animals," *British Journal of Psychology*, vol. 49, no. 3, pp. 182–194, Aug. 1958.
- [48] M. Sivak, "The information that drivers use: Is it indeed 90% visual?" *Perception*, vol. 25, no. 9, pp. 1081–1089, 1996.
- [49] M. Tomizuka and D. E. Whitney, "The human operator in manual preview tracking (an experiment and its modeling via optimal control)," *Journal of Dynamic Systems, Measurement, and Control*, vol. 98, no. 4, pp. 407–413, Dec. 1976.
- [50] P. R. Lakerveld, H. J. Damveld, D. M. Pool, K. van der El, M. M. van Paassen, and M. Mulder, "The effects of yaw and sway motion cues in curve driving simulation," in *Proceedings of the 13th IFAC/IFIP/IFORS/IEA Symposium on Analysis, Design and Evaluation of Man-Machine Systems*, Kyoto, Japan, 2016, pp. 500–505.
- [51] C. D. Mole, G. Kountouriotis, J. Billington, and R. M. Wilkie, "Optic flow speed modulates guidance level control: New insights into two-level steering," *Journal of Experimental Psychology: Human Perception and Performance*, vol. 42, no. 11, pp. 1818–1838, Nov. 2016.
- [52] J. P. M. A. Wolters, K. van der El, H. J. Damveld, D. M. Pool, M. M. van Paassen, and M. Mulder, "Effects of simulator motion on driver steering performance with various visual degradations," in *IEEE International Conference on Systems, Man, and Cybernetics*, Miyazaki, Japan, 2018.

- [53] M. Mulder, "Cybernetics of tunnel-in-the-sky displays," Ph.D. dissertation, Aerospace Engineering, TU Delft, Delft, The Netherlands, 1999.
- [54] L. D. Reid and N. H. Drewell, "A pilot model for tracking with preview," in *Proc. 8th Ann. Conf. on Manual Control*, Ann Arbor, MI, 1972, pp. 191–204.
- [55] K. Ito and M. Ito, "Tracking behavior of human operators in preview control systems," *Electrical Eng. in Japan*, vol. 95, no. 1, pp. 120–127, 1975, (Transl.: D.K. Ronbunshi, vol. 95C, no. 2, Feb. 1975, pp 30-36).
- [56] A. van Lunteren, "Identification of human operator describing function models with one or two inputs in closed loop systems," Ph.D. dissertation, Mechanical Engineering, TU Delft, Delft, The Netherlands, 1979.
- [57] K. van der El, S. Barendswaard, D. M. Pool, and M. Mulder, "Effects of preview time on human control behavior in rate tracking tasks," in *Proc. 13th IFAC/IFIP/IFORS/IEA Symposium on Analysis, Design and Evaluation of Man-Machine Systems*, vol. 49, no. 19, Kyoto, Japan, 2016, pp. 108–113.
- [58] M. F. Land and J. Horwood, "Which parts of the road guide steering?" *Nature*, vol. 377, pp. 339–340, Sep. 1995.
- [59] J. R. McLean and E. R. Hoffmann, "The effects of restricted preview on driver steering control and performance," *Human Factors*, vol. 15, no. 4, pp. 421–430, 1973.
- [60] R. A. Miller, "On the finite preview problem in manual control," *International Journal of Systems Science*, vol. 7, no. 6, pp. 667–672, 1976.
- [61] T. B. Sheridan, "Three models of preview control," *IEEE Trans. on Human Factors in Electronics*, vol. 7, no. 2, pp. 91–102, Jun. 1966.
- [62] R. A. Hess, "Pursuit tracking and higher levels of skill development in the human pilot," *IEEE Trans. on Systems, Man, and Cybernetics*, vol. 11, no. 4, pp. 262–273, Apr. 1981.
- [63] M. Kondo and A. Ajimine, "Driver's sight point and dynamics of the driver-vehicle-system related to it," in *Proc. SAE Automotive Eng. Congr.*, Detroit, MI, 1968.
- [64] A. J. Grunwald and S. J. Merhav, "Vehicular control by visual field cues – Analytical model and experimental validation," *IEEE Trans. on Systems, Man, and Cybernetics*, vol. 6, no. 12, pp. 835–845, Dec. 1976.
- [65] M. F. Land and D. N. Lee, "Where we look when we steer," *Nature*, vol. 369, pp. 742–744, Jun. 1994.
- [66] M. F. Land and J. Horwood, "How speed affects the way visual information is used in steering," in *Vision in Vehicles VI*, A. G. Gale, Ed., Amsterdam, North Holland, 1998, pp. 43–50.

- [67] A. Chatziastros, G. M. Wallis, and H. H. Bülthoff, "The effect of field of view and surface texture on driver steering performance," in *Vision in Vehicles VII*, A. G. Gale, Ed., Amsterdam, North Holland, 1999, pp. 253–259.
- [68] S. Cloete and G. Wallis, "Visuomotor control of steering: The artefact of the matter," *Experimental Brain Research*, vol. 208, no. 4, pp. 475–489, 2011.
- [69] I. Frissen and F. Mars, "The effect of visual degradation on anticipatory and compensatory steering control," *The Quarterly Journal of Experimental Psychology*, vol. 67, no. 3, pp. 499–507, 2014.
- [70] O. Lappi, J. Pekkanen, and T. H. Itkonen, "Pursuit eye-movements in curve driving differentiate between future path and tangent point models," *PLoS ONE*, vol. 8, no. 7, Jul. 2013.
- [71] J. P. Wann and D. Swapp, "Why you should look where you are going," *Nature Neuroscience*, vol. 3, no. 7, pp. 647–648, Jul. 2000.
- [72] M. F. Land and B. W. Tatler, *Looking and acting: Vision and eye movements in natural behaviour*. Oxford University Press, Oxford, UK, 2009.
- [73] F. I. Kandil, A. Rotter, and M. Lappe, "Driving is smoother and more stable when using the tangent point," *Journal of Vision*, vol. 9, no. 1, pp. 1–11, 2009.
- [74] O. Lappi, "Future path and tangent point models in the visual control of locomotion in curve driving," *Journal of Vision*, vol. 14, no. 12, pp. 1–22, Oct. 2014.
- [75] L. R. Young, "On adaptive manual control," *IEEE Trans. on Man-Machine Systems*, vol. 10, no. 4, pp. 292–331, Dec. 1969.
- [76] M. Mulder, M. M. van Paassen, J. M. Flach, and R. J. Jagacinski, *The Occupational Ergonomics Handbook*. Taylor and Francis, 2006, ch. 12 - Fundamentals of Manual Control, 2nd edition.
- [77] M. M. van Paassen and M. Mulder, *International Encyclopedia of Ergonomics and Human Factors*. Taylor and Francis, 2006, ch. Identification of Human Control Behavior, pp. 400–407, 2nd edition.
- [78] J. Rasmussen, "Skills, rules, and knowledge; signals, signs, and symbols, and other distinctions in human performance models," *IEEE Trans. Systems, Man, and Cybernetics*, vol. 13, no. 3, pp. 257–266, 1983.
- [79] E. S. Krendel and D. T. McRuer, "A servomechanics approach to skill development," *Journal of the Franklin Institute*, vol. 269, no. 1, pp. 24–42, Jan. 1960.
- [80] D. T. McRuer, D. Graham, E. S. Krendel, and W. J. Reisener, "Human pilot dynamics in compensatory systems, theory models and experiments with controlled element and forcing function variations," Air Force Flight Dynamics Laboratory, Wright-Patterson Air Force Base, OH, Tech. Rep. AFFDL-TR-65-15, 1965.

- [81] H. J. Damveld, "A cybernetic approach to assess the longitudinal handling qualities of aeroelastic aircraft," Ph.D. dissertation, Aerospace Engineering, TU Delft, Delft, The Netherlands, 2009.
- [82] D. M. Pool, "Objective evaluation of flight simulator motion cueing fidelity through a cybernetic approach," Ph.D. dissertation, Aerospace Engineering, TU Delft, Delft, The Netherlands, 2012.
- [83] T. Lu, "Objective evaluation of human manual control adaptation boundaries using a cybernetic approach," Ph.D. dissertation, Aerospace Engineering, TU Delft, Delft, The Netherlands, 2018.
- [84] R. W. Allen and D. T. McRuer, "The man/machine control interface - Pursuit control," *Automatica*, vol. 15, no. 6, pp. 683–686, Nov. 1979.
- [85] D. T. McRuer, "Human dynamics in man-machine systems," *Automatica*, vol. 16, no. 3, pp. 237–253, 1980.
- [86] R. L. Stapleford, D. T. McRuer, and R. E. Magdaleno, "Pilot describing function measurements in a multiloop task," *IEEE Trans. on Human Factors in Electronics*, vol. 8, no. 2, pp. 113–125, Jun. 1967.
- [87] M. M. van Paassen and M. Mulder, "Identification of human operator control behaviour in multiple-loop tracking tasks," in *Proc. 7th IFAC/IFIP/IFORS/IEA Symposium on Analysis, Design and Evaluation of Man-Machine Systems*, Kyoto, Japan, 1998, pp. 515–520.
- [88] J. Steen, H. J. Damveld, R. Happee, M. M. van Paassen, and M. Mulder, "A review of visual driver models for system identification purposes," in *IEEE International Conference on Systems, Man, and Cybernetics*, Anchorage, AK, 2011, pp. 2093–2100.
- [89] O. Lappi and C. D. Mole, "Visuomotor control, eye movements, and steering: A unified approach for incorporating feedback, feedforward, and internal models," *Psychological Bulletin*, vol. 144, no. 10, pp. 981–1001, Oct. 2018.
- [90] D. T. McRuer, R. W. Allen, D. H. Weir, and R. H. Klein, "New results in driver steering control models," *Human Factors*, vol. 19, no. 4, pp. 381–397, Aug. 1977.
- [91] E. Donges, "A two-level model of driver steering behavior," *Human Factors*, vol. 20, no. 6, pp. 691–707, Dec. 1978.
- [92] C. C. MacAdam, "Application of an optimal preview control for simulation of closed-loop automobile driving," *IEEE Trans. on Systems, Man, and Cybernetics*, vol. 11, no. 6, pp. 393–399, Jun. 1981.
- [93] R. S. Sharp, D. Casanova, and P. Symonds, "A mathematical model for driver steering control, with design, tuning and performance results," *Vehicle System Dynamics*, vol. 33, no. 5, pp. 289–326, May 2000.

- [94] D. D. Salvucci and R. Gray, "A two-point visual control model of steering," *Perception*, vol. 33, no. 10, pp. 1233–1248, Dec. 2004.
- [95] L. Saleh, P. Chevrel, F. Claveau, J. F. Lafay, and F. Mars, "Shared steering control between a driver and an automation: Stability in the presence of driver behavior uncertainty," *IEEE Trans. on Intelligent Transportation Systems*, vol. 14, no. 2, pp. 974–983, 2013.
- [96] M. Mulder, M. M. van Paassen, and E. R. Boer, "Exploring the roles of information in the control of vehicular locomotion: From kinematics and dynamics to cybernetics," *Presence: Teleoperators and Virtual Environments*, vol. 13, no. 5, pp. 535–548, 2004.
- [97] M. Mulder and J. A. Mulder, "Cybernetic analysis of perspective flight-path display dimensions," *Journal of Guidance, Control, and Dynamics*, vol. 28, no. 3, pp. 398–411, May–Jun. 2005.
- [98] B. T. Sweet, "The identification and modeling of visual cue usage in manual control task experiments," Ph.D. dissertation, Department of Aeronautics and Astronautics, Stanford University, Stanford, CA, 1999.
- [99] D. H. Weir and D. T. McRuer, "Measurement and interpretation of driver/vehicle system dynamic response," *Human Factors*, vol. 15, no. 4, pp. 367–378, Aug. 1973.
- [100] B. S. Repa, P. M. Leucht, and W. W. Wierwille, "The influence of motion cues on driver-vehicle performance in a simulator," in *Proc. 17th Ann. Conf. on Manual Control*, Los Angeles, CA, Oct. 1981, pp. 157–169.
- [101] W. W. Wierwille, J. G. Casali, and B. S. Repa, "Driver steering reaction time to abrupt-onset crosswinds, as measured in a moving-base driving simulator," *Human Factors*, vol. 25, no. 1, pp. 103–116, 1983.
- [102] G. Reymond, A. Kemeny, J. Droulez, and A. Berthoz, "Role of lateral acceleration in curve driving: Driver model and experiments on a real vehicle and a driving simulator," *Human Factors*, vol. 43, no. 3, pp. 483–495, Sep. 2001.
- [103] J. Greenberg, B. Artz, and L. Cathey, "The effect of lateral motion cues during simulated driving," in *DSC North America Proc.*, Dearborn, MI, 2003.
- [104] A. R. Valente Pais, M. Wentink, M. M. van Paassen, and M. Mulder, "Comparison of three motion cueing algorithms for curve driving in an urban environment," *Presence: Teleoperators & Virtual Environments*, vol. 18, no. 3, pp. 200–221, Jun. 2009.
- [105] B. J. Correia Grácio, M. Wentink, A. R. Valente Pais, M. M. Van Paassen, and M. Mulder, "Driver behavior comparison between static and dynamic simulation for advanced driving maneuvers," *Presence: Teleoperators & Virtual Environments*, vol. 20, no. 2, pp. 143–161, Apr. 2011.
- [106] D. T. McRuer, I. L. Ashkenas, and H. R. Pass, "Analysis of multiloop vehicular control systems," Air Force Flight Dynamics Laboratory, Wright-Patterson Air Force Base, OH, Tech. Rep. ASD-TDR-62-1014, Mar. 1964.

- [107] D. T. McRuer, L. G. Hofmann, H. R. Jex, G. P. Moore, A. V. Phatak, D. H. Weir, and J. Wolkovitch, "New approaches to human-pilot/vehicle dynamic analysis," Air Force Flight Dynamics Laboratory, Wright-Patterson Air Force Base (OH), Tech. Rep. AFFDL-TR-67-150, 1968.
- [108] E. W. Vinje, "An analysis of pilot adaptation in a simulated multiloop VTOL hovering task," *IEEE Trans. on Man-Machine Systems*, vol. 9, no. 4, pp. 110–120, Dec. 1968.
- [109] D. H. Weir and D. T. McRuer, "Dynamics of driver vehicle steering control," *Automatica*, vol. 6, no. 1, pp. 87–98, Jan. 1970.
- [110] R. A. Hess, "Simplified approach for modelling pilot pursuit control behaviour in multi-loop flight control tasks," *Proceedings of the Institution of Mechanical Engineers, Part G: Journal of Aerospace Engineering*, vol. 220, no. 2, pp. 85–102, 2006.
- [111] P. M. T. Zaal, D. M. Pool, J. de Bruin, M. Mulder, and M. M. van Paassen, "Use of pitch and heave motion cues in a pitch control task," *Journal of Guidance, Control, and Dynamics*, vol. 32, no. 2, pp. 366–377, Mar.-Apr. 2009.
- [112] D. M. Pool, G. A. Harder, and M. M. van Paassen, "Effects of simulator motion feedback on training of skill-based control behavior," *Journal of Guidance, Control, and Dynamics*, vol. 39, no. 4, pp. 889–902, 2016.
- [113] J. P. Wann and R. M. Wilkie, *Optic Flow and Beyond*. Springer, 2004, ch. How do we Control High Speed Steering?, pp. 401–419.
- [114] L. Li and J. Chen, "Relative contributions of optic flow, bearing, and splay angle information to lane keeping," *Journal of Vision*, vol. 10, no. 11, Sep. 2010.
- [115] P. M. T. Zaal, F. M. Nieuwenhuizen, M. M. van Paassen, and M. Mulder, "Modeling human control of self-motion direction with optic flow and vestibular motion," *IEEE Trans. on Cybernetics*, vol. 43, no. 2, pp. 544–556, Apr. 2013.
- [116] H. Godthelp, "Vehicle control during curve driving," *Human Factors*, vol. 28, no. 2, pp. 211–221, Apr. 1986.
- [117] E. R. Boer, "Satisficing curve negotiation: Explaining drivers' situated lateral position variability," in *Proceedings of the 13th IFAC/IFIP/IFORS/IEA Symposium on Analysis, Design and Evaluation of Man-Machine Systems*, vol. 49, no. 19, Kyoto, Japan, 2016, pp. 183–188.
- [118] G. Markkula, E. R. Boer, R. Romano, and N. Merat, "Sustained sensorimotor control as intermittent decisions about prediction errors: Computational framework and application to ground vehicle steering," *Biological Cybernetics*, vol. 112, no. 3, pp. 181–207, Jun. 2018.
- [119] J. Xu, K. Yang, Y. Shao, and G. Lu, "An experimental study on lateral acceleration of cars in different environments in Sichuan, southwest China," *Discrete Dynamics in Nature and Society*, 2015, online publication.

- [120] D. L. Kleinman, "Optimal control of linear systems with time-delay and observation noise," *IEEE Trans. on Automatic Control*, vol. 14, no. 5, pp. 524–527, Oct. 1969.
- [121] S. Baron and D. L. Kleinman, "The human as an optimal controller and information processor," *IEEE Trans. on Man-Machine Systems*, vol. 10, no. 1, pp. 9–17, Mar. 1969.
- [122] C. C. MacAdam, "An optimal preview control for linear systems," *Journal of Dynamic Systems, Measurement, and Control*, vol. 102, pp. 188–190, Sep. 1980.
- [123] A. M. C. Odhams and D. J. Cole, "Application of linear preview control to modelling human steering control," *Proceedings of the Institution of Mechanical Engineers, Part D: Journal of Automobile Engineering*, vol. 223, no. 7, pp. 835–853, Jul. 2009.
- [124] J. Kok and R. van Wijk, "Evaluation of models describing human operator control of slowly responding complex systems," Ph.D. dissertation, Mechanical Engineering, TU Delft, Delft, The Netherlands, 1978.
- [125] F. M. Drop, D. M. Pool, H. J. Damveld, M. M. van Paassen, H. H. Bülthoff, and M. Mulder, "Identification of the transition from compensatory to feedforward behavior in manual control," in *IEEE Int. Conf. Systems, Man, and Cybernetics*, 2012, pp. 2008–2013.
- [126] F. M. Drop, D. M. Pool, H. J. Damveld, M. M. van Paassen, and M. Mulder, "Identification of the feedforward component in manual control with predictable target signals," *IEEE Trans. on Cybernetics*, vol. 43, no. 6, pp. 1936–1949, Dec. 2013.
- [127] B. Yu, J. S. Freudenberg, and R. B. Gillespie, "Human control strategies in pursuit tracking with a disturbance input," in *Proc. 53rd IEEE Conf. on Decision and Control*, Los Angeles, CA, 2014, pp. 3795–3800.
- [128] V. A. Laurence, D. M. Pool, H. J. Damveld, M. M. van Paassen, and M. Mulder, "Effects of controlled element dynamics on human feedforward behavior in ramp-tracking tasks," *IEEE Trans. on Cybernetics*, vol. 45, no. 2, pp. 253–265, Feb. 2015.
- [129] R. J. Jagacinski, G. M. Hammond, and E. Rizzi, "Measuring memory and attention to preview in motion," *Human Factors*, vol. 59, no. 5, pp. 796–810, Aug. 2017.
- [130] F. M. Drop, D. M. Pool, M. M. van Paassen, M. Mulder, and H. H. Bülthoff, "Effects of target signal shape and system dynamics on feedforward in manual control," *IEEE Trans. on Cybernetics*, 2018, in press.
- [131] F. M. Nieuwenhuizen, P. M. T. Zaal, M. Mulder, M. M. van Paassen, and J. A. Mulder, "Modeling human multichannel perception and control using linear time-invariant models," *Journal of Guidance, Control, and Dynamics*, vol. 31, no. 4, pp. 999–1013, Jul.-Aug. 2008.
- [132] P. M. T. Zaal, D. M. Pool, Q. P. Chu, M. M. van Paassen, M. Mulder, and J. A. Mulder, "Modeling human multimodal perception and control using genetic maximum likelihood estimation," *Journal of Guidance, Control, and Dynamics*, vol. 32, no. 4, pp. 1089–1099, Jul.-Aug. 2009.

- [133] A. Popovici, P. M. T. Zaal, and D. M. Pool, "Dual extended kalman filter for the identification of time-varying human manual control behavior," in *Proceedings of the AIAA Modeling and Simulation Technologies Conference, Denver (CO)*, no. AIAA-2017-3666, 2017.
- [134] M. Tomizuka and D. E. Whitney, "The preview control problem with application to man-machine system analysis," in *Proc. 9th Ann. Conf. on Manual Control*, Cambridge, MA, 1973, pp. 429–441.
- [135] J. G. Kreifeldt, "An analysis of the human as a predictor model," in *IEEE Conf. Adaptive Processes*, Fort Lauderdale, FL, 1979, pp. 1074–1077.
- [136] W. W. Wierwille, J. R. Knight, and G. A. Gagne, "An experimental study of human operator models and closed-loop analysis methods for high-speed automobile driving," *IEEE Trans. on Human Factors in Electronics*, vol. 8, no. 3, pp. 187–201, Sep. 1967.
- [137] R. A. Hess and A. Modjtahedzadeh, "A preview control model of driver steering behavior," in *Proc. 1989 IEEE Int. Conf. on Systems, Man, and Cybernetics*, Cambridge, MA, 1989, pp. 504–509.
- [138] G. Prokop, "Modeling human vehicle driving by model predictive online optimization," *Vehicle System Dynamics*, vol. 35, no. 1, pp. 19–53, 2001.
- [139] C. Sentouh, P. Chevrel, F. Mars, and F. Claveau, "A sensorimotor driver model for steering control," in *Proc. 2009 IEEE Int. Conf. Systems, Man, and Cybernetics*, San Antonio, TX, 2009, pp. 2462–2467.
- [140] S. D. Keen and D. J. Cole, "Bias-free identification of a linear model-predictive steering controller from measured driver steering behavior," *IEEE Trans. on Systems, Man, and Cybernetics - Part B: Cybernetics*, vol. 42, no. 2, pp. 434–443, Apr. 2012.
- [141] M. C. Vos, D. M. Pool, H. J. Damveld, M. M. van Paassen, and M. Mulder, "Identification of multimodal control behavior in pursuit tracking tasks," in *Proc. 2014 IEEE Int. Conf. on Systems, Man, and Cybernetics*, San Diego, CA, 2014, pp. 69–74.
- [142] T. Yamashita, "Effects of sine wave combinations on the development of precognitive mode in pursuit tracking," *The Quarterly Journal of Experimental Psychology*, vol. 42A, no. 4, pp. 791–810, 1990.
- [143] L. Ljung, *System Identification: Theory for the User*, 2nd ed. Upper Saddle River, NJ: Prentice Hall, Inc., 1999.
- [144] R. A. Hess and A. Modjtahedzadeh, "A control theoretic model of driver steering behavior," *IEEE Control Systems Magazine*, vol. 10, no. 5, pp. 3–8, Aug. 1990.
- [145] D. A. Abbink, M. Mulder, F. C. T. van der Helm, M. Mulder, and E. R. Boer, "Measuring neuromuscular control dynamics during car following with continuous haptic feedback," *IEEE Trans. on Systems, Man, and Cybernetics, Part B: Cybernetics*, vol. 41, no. 5, pp. 1239–1249, Oct. 2011.

- [146] D. A. Gordon, "Perceptual basis of vehicular guidance: IV," *Public Roads*, vol. 34, no. 3, pp. 53–68, 1966.
- [147] K. Rayner, "Eye movements in reading and information processing: 20 years of research," *Psychological Bulletin*, vol. 124, no. 3, pp. 372–422, Nov. 1998.
- [148] M. F. Land, "Eye movements and the control of actions in everyday life," *Progress in Retinal and Eye Research*, vol. 25, no. 3, pp. 296–324, May 2006.
- [149] D. Panchuk and J. N. Vickers, "Using spatial occlusion to explore the control strategies used in rapid interceptive actions: Predictive or prospective control?" *Journal of Sports Sciences*, vol. 27, no. 12, pp. 1249–1260, Oct. 2009.
- [150] H. Strasburger, I. Rentschler, and M. Jüttner, "Peripheral vision and pattern recognition: A review," *Journal of Vision*, vol. 11, no. 5, pp. 1–82, Dec. 2011.
- [151] E. R. Schotter, B. Angele, and K. Rayner, "Parafoveal processing in reading," *Attention, Perception and Psychophysics*, vol. 74, no. 1, pp. 5–35, Jan. 2012.
- [152] P. M. van Leeuwen, R. Happee, and J. C. F. de Winter, "Vertical field of view restriction in driver training: A simulator-based evaluation," *Transportation Research Part F: Traffic Psychology and Behaviour*, vol. 24, pp. 169–182, May 2014.
- [153] D. C. Niehorster, W. W. F. Siu, and L. Li, "Manual tracking enhances smooth pursuit eye movements," *Journal of Vision*, vol. 15, no. 15, pp. 1–14, 2015.
- [154] R. Zheng, K. Nakano, H. Ishiko, K. Hagita, M. Kihira, and T. Yokozeki, "Eye-gaze tracking analysis of driver behavior while interacting with navigation systems in an urban area," *IEEE Trans. on Human-Machine Systems*, vol. 46, no. 4, pp. 546–556, Dec. 2016.
- [155] B. A. Wandell, *Foundations of Vision*, 1st ed. Sinauer Associates Inc., 1995.
- [156] R. W. Allen and H. R. Jex, "A simple fourier analysis technique for measuring the dynamic response of manual control systems," *IEEE Trans. on Systems, Man and Cybernetics*, vol. 2, no. 5, pp. 638–643, Sep. 1972.
- [157] H. R. Jex, R. E. Magdaleno, and A. M. Junker, "Roll tracking effects of G-vector tilt and various types of motion washout," in *Proc. 14th Ann. Conf. on Manual Control*, 1978, pp. 463–502.
- [158] T. A. Bahill and J. D. McDonald, "Smooth pursuit eye movements in response to predictable target motions," *Vision Research*, vol. 23, no. 12, pp. 1573–1583, 1983.
- [159] R. Pintelon and J. Schoukens, *System Identification - A Frequency Domain Approach*, 2nd ed. John Wiley & Sons, 2012.
- [160] A. E. Patla and S. Rietdyk, "Visual control of limb trajectory over obstacles during locomotion: Effect of obstacle height and width," *Gait & Posture*, vol. 1, pp. 45–60, 1993.

- [161] R. A. Scheidt and C. Ghez, "Separate adaptive mechanisms for controlling trajectory and final position in reaching," *Journal Neurophysiology*, vol. 98, pp. 3600–3613, 2007.
- [162] R. A. Hess, "A model-based theory for analyzing human control behavior," in *Advances in Man-Machine Research*. JAI Press, 1985, vol. 2, pp. 129–176.
- [163] R. W. Allen and H. R. Jex, "An experimental investigation of compensatory and pursuit tracking displays with rate and acceleration control dynamics and a disturbance input," National Aeronautics and Space Administration, Washington, D.C., Tech. Rep. NASA CR-1082, 1968.
- [164] G. C. Beerens, H. J. Damveld, M. Mulder, M. M. van Paassen, and J. C. van der Vaart, "Investigation into crossover regression in compensatory manual tracking tasks," *Journal of Guidance, Control, and Dynamics*, vol. 32, no. 5, pp. 1429–1445, Sep.–Oct. 2009.
- [165] D. T. McRuer, D. H. Weir, H. R. Jex, R. E. Magdaleno, and R. W. Allen, "Measurement of driver-vehicle multiloop response properties with a single disturbance input," *IEEE Trans. on Systems, Man, and Cybernetics*, vol. 5, no. 5, pp. 490–497, Sep. 1975.
- [166] D. T. McRuer, R. E. Magdaleno, and G. P. Moore, "A neuromuscular actuation system model," *IEEE Trans. on Man-Machine Systems*, vol. 9, no. 3, pp. 61–71, Sep. 1968.
- [167] F. M. Drop, D. M. Pool, M. M. van Paassen, M. Mulder, and H. H. Bülthoff, "Objective model selection for identifying the human feedforward response in manual control," *IEEE Trans. on Cybernetics*, vol. 48, no. 1, pp. 2–15, Jan. 2018.
- [168] R. W. Roig, "A comparison between human operator and optimum linear controller RMS-error performance," *IRE Trans. on Human Factors in Electronics*, vol. 3, no. 1, pp. 18–21, Mar. 1962.
- [169] M. Olivari, F. M. Nieuwenhuizen, J. Venrooij, H. H. Bülthoff, and L. Pollini, "Methods for multiloop identification of visual and neuromuscular pilot responses," *IEEE Trans. on Cybernetics*, vol. 45, no. 12, pp. 2780–2791, Dec. 2015.
- [170] J. Venrooij, D. A. Abbink, M. Mulder, M. M. van Paassen, M. Mulder, F. C. T. van der Helm, and H. H. Bülthoff, "A biodynamic feedthrough model based on neuromuscular principles," *IEEE Trans. on Cybernetics*, vol. 44, no. 7, pp. 1141–1154, Jul. 2013.
- [171] R. W. Pew, J. C. Duffendack, and L. K. Fensch, "Sine-wave tracking revisited," *IEEE Trans. on Human Factors in Electronics*, vol. 8, no. 2, pp. 130–134, Jun. 1967.
- [172] R. E. Magdaleno, H. R. Jex, and W. A. Johnson, "Tracking quasi-predictable displays subjective predictability gradations, pilot models for periodic and narrowband inputs," in *5th Ann. NASA-University Conf. on Manual Control*, 1969, pp. 391–428.
- [173] H. G. H. Zollner, D. M. Pool, H. J. Damveld, M. M. van Paassen, and M. Mulder, "The effects of controlled element break frequency on pilot dynamics during compensatory target-following," in *Proc. AIAA Guidance, Navigation, and Control Conference*, Toronto, Canada, 2010, pp. 1–12.

- [174] H. Gerisch, G. Staude, W. Wolf, and G. Bauch, "A three-component model of the control error in manual tracking of continuous random signals," *Human Factors*, vol. 55, no. 5, pp. 985–1000, Oct. 2013.
- [175] H. J. Damveld, G. C. Beerens, M. M. van Paassen, and M. Mulder, "Design of forcing functions for the identification of human control behavior," *Journal of Guidance, Control, and Dynamics*, vol. 33, no. 4, pp. 1064–1081, Jul. 2010.
- [176] W. Mugge, D. A. Abbink, and C. Van der Helm, "Reduced power method: How to evoke low-bandwidth behaviour while estimating full-bandwidth dynamics," in *Proc. IEEE 10th International Conference on Rehabilitation Robotics*, Noordwijk, The Netherlands, Jun. 2007, pp. 575–581.
- [177] A. J. Grunwald, J. B. Robertson, and J. J. Hatfield, "Experimental evaluation of a perspective tunnel display for three-dimensional helicopter approaches," *Journal of Guidance, Control, and Dynamics*, vol. 4, no. 5, pp. 623–631, 1981.
- [178] W. H. Levison and R. Warren, "Use of linear perspective scene cues in a simulated height regulation task," in *Proc. 20th Ann. Conf. Manual Control*, Sunnyvale, CA, June 1984.
- [179] S. W. Breur, D. M. Pool, M. M. van Paassen, and M. Mulder, "Effects of displayed error scaling in compensatory roll-axis tracking tasks," in *Proc. AIAA Guidance, Navigation, and Control Conf.*, no. AIAA-2010-8091, Toronto, Canada, Aug. 2-5 2010.
- [180] S. Murray, H. Boyaci, and D. Kersten, "The representation of perceived angular size in human primary visual cortex," *Nature Neuroscience*, vol. 9, no. 3, pp. 429–434, Mar. 2006.
- [181] W. S. Kim, S. R. Ellis, M. E. Tyler, B. Hannaford, and L. W. Stark, "Quantitative evaluation of perspective and stereoscopic displays in three-axis manual tracking tasks," *IEEE Trans. on Systems, Man, and Cybernetics*, vol. 17, no. 1, pp. 61–72, Jan. 1987.
- [182] I. D. Haskell and C. D. Wickens, "Two- and three-dimensional displays for aviation: A theoretical and empirical comparison," *The International Journal of Aviation Psychology*, vol. 3, no. 2, pp. 87–109, 1993.
- [183] S. Zhai, P. Milgram, and A. Rastogi, "Anisotropic human performance in six degree-of-freedom tracking: An evaluation of three-dimensional display and control interfaces," *IEEE Trans. on Systems, Man, and Cybernetics - Part A: Systems and Humans*, vol. 27, no. 4, pp. 518–528, Jul. 1997.
- [184] B. T. Sweet, "A model of manual control with perspective scene viewing," in *AIAA Modeling and Simulation Technologies (MST) Conf.*, Boston, MA, Aug. 2013.
- [185] J. D. Foley, A. van Dam, S. K. Feiner, and J. F. Hughes, *Computer Graphics. Principle and Practice.*, 2nd ed. Reading, MA: Addison-Wesley, 1992.

- [186] A. Modjtahedzadeh and R. A. Hess, "A model of driver steering control behavior for use in assessing vehicle handling qualities," *Journal of Dynamic Systems, Measurement, and Control*, vol. 115, no. 3, pp. 456–464, 1993.
- [187] F. C. T. Van der Helm, A. C. Schouten, E. De Vlugt, and G. G. Brouwn, "Identification of intrinsic and reflexive components of human arm dynamics during postural control," *Journal of Neuroscience Methods*, vol. 119, no. 1, pp. 1–14, Sep. 2002.
- [188] E. Schmider, M. Ziegler, E. Danay, L. Beyer, and M. Böhner, "Is it really robust? Reinvestigating the robustness of ANOVA against violations of the normal distribution assumption," *Methodology*, vol. 6, no. 4, pp. 147–151, 2010.
- [189] R. J. A. W. Hosman and J. C. van der Vaart, "Effects of vestibular and visual motion perception on task performance," *Acta Psychologica*, vol. 48, no. 1-3, pp. 271–287, Aug. 1981.
- [190] R. L. Stapleford, R. A. Peters, and F. R. Alex, "Experiments and a model for pilot dynamics with visual and motion inputs," Systems Technology, Inc., Hawthorne (CA), Tech. Rep. NASA CR-1325, 1969.
- [191] F. M. Drop, "Control-theoretic models of feedforward in manual control," Ph.D. dissertation, Aerospace Engineering, TU Delft, Delft, The Netherlands, 2016.
- [192] J. A. Schroeder, "Simulation motion effects on single axis compensatory tracking," in *Proc. AIAA Flight Simulation Technologies Conference, Monterey (CA)*, no. AIAA-1993-3579, 1993, pp. 202–213.
- [193] R. J. A. W. Hosman, "Pilot's perception and control of aircraft motions," Ph.D. dissertation, Aerospace Engineering, TU Delft, Delft, The Netherlands, 1996.
- [194] J. Ellerbroek, O. Stroosma, M. Mulder, and M. M. van Paassen, "Role identification of yaw and sway motion in helicopter yaw control tasks," *Journal of Aircraft*, vol. 45, no. 4, pp. 1275–1289, Jul.-Aug. 2008.
- [195] D. M. Pool, H. J. Damveld, M. M. van Paassen, and M. Mulder, "Tuning models of pilot tracking behavior for a specific simulator motion cueing setting," in *Proc. AIAA Modeling and Simulation Technologies Conference*, no. AIAA-2011-6322, Portland, OR, Aug. 8-11 2011.
- [196] W. H. Levison, S. Baron, and D. L. Kleinman, "A model for human controller remnant," *IEEE Trans. on Man-Machine Systems*, vol. 10, no. 4, pp. 101–108, Dec. 1969.
- [197] J. P. Wann and M. F. Land, "Steering with or without the flow: Is the retrieval of heading necessary?" *Trends in Cognitive Sciences*, vol. 4, no. 8, pp. 319–324, Aug. 2000.
- [198] R. M. Wilkie and J. P. Wann, "Judgments of path, not heading, guide locomotion," *Journal of Experimental Psychology: Human Perception and Performance*, vol. 32, no. 1, pp. 88–96, Feb. 2006.

- [199] C. C. MacAdam, "Understanding and modeling the human driver," *Vehicle System Dynamics*, vol. 40, no. 1-3, pp. 101–143, Jan. 2003.
- [200] D. T. McRuer and D. H. Weir, "Theory of manual vehicular control," *Ergonomics*, vol. 12, no. 4, pp. 599 – 633, 1969.
- [201] H. J. Damveld, M. Wentink, P. M. van Leeuwen, and R. Happee, "Effects of motion cueing on curve driving," in *Proceedings of the Driving Simulation Conference 2012*, Sep. 2012, pp. 1–9.
- [202] K. Ogata, *Modern Control Engineering*, 5th ed. Upper Saddle River, NJ: Prentice Hall, 2010.
- [203] S. Barendswaard, D. M. Pool, and M. Mulder, "Human crossfeed in dual-axis manual control with motion feedback," in *Proc. 13th IFAC/IFIP/IFORS/IEA Symposium on Analysis, Design and Evaluation of Man-Machine Systems*, vol. 49, no. 19, Kyoto, Japan, 2016, pp. 189–194.
- [204] J. M. Flach, B. A. Hagen, and J. F. Larish, "Active regulation of altitude as a function of optical texture," *Perception & Psychophysics*, vol. 51, no. 6, pp. 557–568, Jul. 1992.
- [205] H. Zhao and W. H. Warren, "On-line and model-based approaches to the visual control of action," *Vision Research*, vol. 110, pp. 190–202, May 2015.
- [206] E. R. Boer, "What preview elements do drivers need?" in *Proceedings of the 13th IFAC/IFIP/IFORS/IEA Symposium on Analysis, Design and Evaluation of Man-Machine Systems*, vol. 49, no. 19, Kyoto, Japan, 2016, pp. 201–107.
- [207] R. Hess and K. K. Chan, "Preview control pilot model for near-earth maneuvering helicopter flight," *Journal of Guidance, Control, and Dynamics*, vol. 11, no. 2, pp. 146–152, Mar.-Apr. 1988.
- [208] R. W. Allen, D. T. McRuer, J. R. Hogge, R. W. Humes, A. C. Stein, J. F. O'hanlon, R. T. Hennessy, G. R. Kelley, and G. V. Bailey, "Drivers' visibility requirements for roadway delineation, Volume I: Effects of contrast and configuration on driver performance and behavior," Systems Technology, Inc., Tech. Rep. FHWA-RD-77-165, Nov. 1977.
- [209] R. W. Allen and J. F. O'hanlon, "Effects of roadway delineation and visibility conditions on driver steering performance," *Transportation research record*, vol. 739, pp. 5–8, 1979.
- [210] S. Mammer, S. Glaser, and M. Netto, "Time to line crossing for lane departure avoidance: A theoretical study and an experimental setting," *IEEE Trans. on Intelligent Transportation Systems*, vol. 7, no. 2, pp. 226–241, May 2006.
- [211] H. Godthelp, P. Milgram, and G. J. Blaauw, "The development of a time-related measure to describe driving strategy," *Human Factors*, vol. 26, no. 3, pp. 257–268, Jun. 1984.

- [212] W. R. Gray, III, "Boundary-avoidance tracking: A new pilot tracking model," in *Proc. AIAA Atmospheric Flight Mechanics Conference and Exhibit*, San Francisco (CA), Aug. 2005, pp. 1–12.
- [213] —, "A generalized handling qualities flight test technique utilizing boundary avoidance tracking," in *Proc. U.S. Air Force T&E Days*, Los Angeles (CA), Feb. 2008, pp. 1–19.
- [214] G. D. Padfield, L. Lu, and M. Jump, "Tau guidance in boundary-avoidance tracking: New perspectives on pilot-induced oscillations," *Journal of Guidance, Control and Dynamics*, vol. 35, no. 1, pp. 80–92, Jan.-Feb. 2012.
- [215] J. R. McLean and E. R. Hoffmann, "The effects of lane width on driver steering control and performance," in *Australian Road Research Board (ARRB) Conference, 6th, Volume 6, Issue 6*, Canberra, Australia, 1972, pp. 418–439.
- [216] V. Wilckens, "Improvements in pilot/aircraft-integration by advanced contact analog displays," in *Proc. 9th Annual Conference on Manual Control*, 1973, pp. 175–193.
- [217] M. Tomizuka, "The optimal finite preview problem and its application to man-machine systems," Ph.D. dissertation, Mech. Eng., MIT, Feb. 1974.
- [218] R. Rajamani, *Vehicle Dynamics and Control*, ser. Mechanical Engineering Series. Springer Science & Business Media, 2011.
- [219] J. E. Bos, "Less sickness with more motion and/or mental distraction," *Journal of Vestibular Research*, vol. 25, no. 1, pp. 23–33, 2015.
- [220] R. W. Allen, H. R. Jex, D. T. McRuer, and R. J. DiMarco, "Alcohol effects on driving behavior and performance in a car simulator," *IEEE Trans. on Systems Man and Cybernetics*, vol. 5, no. 5, pp. 498–505, Sep. 1975.
- [221] E. C. Hildreth, J. M. H. Beusmans, E. R. Boer, and C. S. Royden, "From vision to action: Experiments and models of steering control during driving," *Journal of Experimental Psychology: Human Perception and Performance*, vol. 26, no. 3, pp. 1106–1132, Jun. 2000.
- [222] F. Mars, "Driving around bends with manipulated eye-steering coordination," *Journal of Vision*, vol. 8, no. 11, pp. 1–11, Aug. 2008.
- [223] R. W. Allen, "Stability analysis of automobile driver steering control," in *Proc. 17th Ann. Conf. on Manual Control*, 1981, pp. 597–609.
- [224] S. Barendswaard, D. M. Pool, and D. A. Abbink, "A method to assess individualized driver models: Descriptiveness, identifiability and realism," *Transportation Research Part F: Traffic Psychology and Behaviour*, 2018, available online.
- [225] K. Guo, H. Ding, J. Zhang, J. Lu, and R. Wang, "Development of a longitudinal and lateral driver model for autonomous vehicle control," *International Journal of Vehicle Design*, vol. 36, no. 1, pp. 50–65, 2004.

- [226] T. Melman, D. A. Abbink, M. M. van Paassen, E. R. Boer, and J. C. F. de Winter, "What determines drivers' speed? A replication of three behavioural adaptation experiments in a single driving simulator study," *Ergonomics*, vol. 61, no. 7, pp. 966–987, 2018.
- [227] E. R. Boer and R. V. Kenyon, "Estimation of time-varying delay time in nonstationary linear systems: An approach to monitor human operator adaptation in manual tracking tasks," *IEEE Trans. on Systems, Man, and Cybernetics, Part A: Systems and Humans*, vol. 28, no. 1, pp. 89–99, Jan. 1998.
- [228] P. M. Thompson, D. H. Klyde, and M. J. Brenner, "Wavelet-based time-varying human operator models," in *Proceedings of the AIAA Atmospheric Flight Mechanics Conference and Exhibit, Montreal (CA)*, no. AIAA-2001-4009, 2001.
- [229] A. van Grootheest, D. M. Pool, M. M. van Paassen, and M. Mulder, "Identification of time-varying manual control adaptations with recursive ARX models," in *Proceedings of the AIAA Modeling and Simulation Technologies Conference, Kissimmee (FL)*, no. AIAA-2018-0118, 2018.
- [230] W. M. Scholtens, S. Barendswaard, D. M. Pool, M. M. van Paassen, and D. A. Abbink, "A new haptic shared controller reducing steering conflicts," in *IEEE International Conference on Systems, Man, and Cybernetics*, 2018.
- [231] J. Schoukens, R. Pintelon, and Y. Rolain, *Mastering System Identification in 100 Exercises*. Wiley-IEEE Press, 2012.

ACKNOWLEDGEMENTS

A thesis is supposed to have a single author, and only one corresponding Ph.D. title is awarded. As author I receive these honors, but this does not do justice to the many people without whom this thesis would not be here. I am grateful to all who contributed.

First of all, I would like to thank Max Mulder, my promotor. Max, you gave me the opportunity to pursue a Ph.D. *and* to do so in my favorite topic. Without your trust in me this thesis would not be here, and in fact no thesis would ever carry my name. I cannot think of a more supportive, motivating, and approachable promotor. You explained the things I struggled with for months in several enlightening minutes, always including a couple (soccer-related) jokes along the way. Max, thank you for everything.

If possible, the second author on this thesis should be my copromotor, Daan Pool. Daan, I consider myself lucky that you were my supervisor. This section is too short to thank you for all your patient explanations, support, motivational speeches, famous red-pencil improvements, and even many hints to new bands. This section is also too short to make up for the countless times I stormed uninvited into your office with new questions, never to be expelled without an ingenious answer. You clarified the most complex problems with a simple drawing (many of the illustrations in this thesis were inspired by you), and then let me free again to make my own mistakes. Thank you Daan, for helping me with so much more than just the technical content of this thesis.

Two other people that contributed greatly to this thesis are René and Herman. René, thank you for solving many seemingly unsolvable problems, and for all the improvements on my papers. Herman, your help with the first chapters of this thesis have also shaped the following chapters, written long after you left TU Delft. Moreover, René, Herman, and Olaf, the simulation software that you developed for this thesis is perhaps less visible, but not less valuable. I cannot image how much time you have spend in its development and maintenance; the time that I could consequently save and spend on technical challenges undoubtedly brought this thesis to a much higher level. I would also like to thank all the technicians who maintained the simulators at the C&S Section, and in particular Alwin, Andries, and Harold; you facilitated the experiments that proved crucial to this thesis.

Furthermore, I am very thankful to Sharon, João, Evgeny, Maurice, and Casper. Supervising you during your M.Sc. theses on manual preview control has been incredibly motivating and educational. Your enthusiasm made these four years so much more fun and rewarding. I am especially indebted to Sharon, João, and Evgeny: as you can see, without your contributions this thesis would be almost half as thick (and not nearly half as good).

I am also extremely grateful to the participants of my experiments, who spend hours in dark laboratory rooms performing boring, often frustrating control tasks, all *fully voluntary*. Without your sacrifices, this thesis simply wouldn't be here. While you are supposed

to remain anonymous, a special thanks to Ivan: by participating in *all* the experiments presented in this thesis you have contributed a staggering *34 hours* of steering data.

I also like to thank all my C&S colleagues at the Faculty of Aerospace Engineering. We have had numerous talks, coffees, barbeques, laughs, sailing trips, drinks, conferences, and many other things that shaped me, and therefore also helped to shape this thesis. In particular I would like to thank Sarah, all the great discussions, courses and conferences we had were invaluable. Tao, Yingzi, and Daniel, having you as roommates was both fun and educational (indeed, you *almost* managed to teach me Chinese and German). Dirk, your revival coffees, incomprehensible programming solutions, and even your memes were incredibly beneficial to this thesis.

Of course, I have saved the most important people for last: my friends and family. You make me realize everyday that there are more important things in life than writing a thesis. Somewhat paradoxically, I do believe that this greatly contributed to this thesis' quality, as you often helped me to take some distance from the research, so I could later plunge in again with a refreshed view. Clearly, all the people I have met in the past years have played their part and I am grateful to all. But I am especially grateful to "Le Poisson Noire", Kim and Carlo, Jeroen and Esther, and "the minis". You were, and are, invaluable for everything from a simple chat, drink, laugh, and a free meal, to full-blown holidays abroad. And finally, pap, mam, even though you must have wandered so many times what the purpose is of all these weird formulas, you never stopped to support me. The book in your hands is also yours, as it certainly would not be here without your belief in me, and you motivating me to pursue my dreams.

Kasper van der El

Capelle aan den IJssel, December 2018

CURRICULUM VITÆ

KASPER VAN DER EL

Kasper van der El was born on June 4th, 1990, in Capelle aan den IJssel, the Netherlands. Here, he attended the Comenius College from 2002 to eventually obtain his VWO diploma in 2008, with a specialization in the “Nature and Technique” course profile.

In 2008, Kasper started as a bachelor’s student with the Faculty of Aerospace Engineering at Delft University of Technology. He studied Sustainable Energy Technologies for his minor, an interfaculty program at Delft University of Technology. For his bachelor’s graduation project, he designed a race buggy in a team of ten students, the first that could complete the famous Dakar rally purely on battery power. Despite its novel design, the buggy was never constructed. In 2011, he obtained the bachelor’s degree in Aerospace Engineering, finishing the curriculum in nominal time.



In 2011, Kasper continued his education at the Faculty of Aerospace Engineering to pursue the master’s degree in the field of Control and Simulation. In 2012, he was three months in Singapore for an internship, at the School of Mechanical and Aerospace Engineering, Nanyang Technological University, during which he worked on the control algorithm for a perched landing of a bio-inspired Unmanned Aerial Vehicle (UAV). On his return to the Netherlands, he began writing his master’s thesis, titled “*An Empirical Human Operator Model for Preview Tracking Tasks*”. For this work, he obtained the master’s degree in Aerospace Engineering, *cum laude*, in November 2013.

Kasper then took a two-month backpack trip through New Zealand. He started his new job in the beginning of 2014 at the Plan Approval Office of Bureau Veritas in Rotterdam, the Netherlands, where he worked for ten months. He was then offered a Ph.D. position at the Control and Simulation section of the Faculty of Aerospace Engineering, Delft University of Technology. From December 2014, he has been expanding the research initiated during his master’s thesis, that is, the study of how humans use preview information in manual control. After his promotion in December 2018, he will continue his career as a researcher at Damen Shipyards, Gorinchem, focusing on automation in the maritime domain.

LIST OF PUBLICATIONS

JOURNAL PUBLICATIONS

1. **K. van der El**, D.M. Pool, H.J. Damveld, M.M. van Paassen, and M. Mulder, "An Empirical Human Controller Model for Preview Tracking Tasks," *IEEE Transactions on Cybernetics*, vol. 46, no. 11, pp. 2609-2621, Nov. 2016.
2. **K. van der El**, D.M. Pool, M.M. van Paassen, and M. Mulder, "Effects of Preview on Human Control Behavior in Tracking Tasks With Various Controlled Elements," *IEEE Transactions on Cybernetics*, vol. 48, no. 4, pp. 1242-1252, Apr. 2018.
3. **K. van der El**, D.M. Pool, M.M. van Paassen, and M. Mulder, "Effects of Linear Perspective on Human Use of Preview in Manual Control," *IEEE Transactions on Human-Machine Systems*, vol. 48, no. 5, pp. 496-508, Oct. 2018.
4. **K. van der El**, S. Padmos, D.M. Pool, M.M. van Paassen, and M. Mulder, "Effects of Preview Time in Manual Tracking Tasks," *IEEE Transactions on Human-Machine Systems*, vol. 48, no. 5, pp. 486-495, Oct. 2018.
5. M. Mulder, D.M. Pool, D.A. Abbink, E.R. Boer, P.M.T. Zaal, F.M. Drop, **K. van der El**, and M.M. van Paassen, "Manual Control Cybernetics: State-of-the-Art and Current Trends," *IEEE Transactions on Human-Machine Systems*, vol. 48, no. 5, pp. 468-485, Oct. 2018.
6. **K. van der El**, D.M. Pool, and M. Mulder, "Measuring and Modeling Driver Steering Behavior: From Compensatory Tracking to Curve Driving," *Transportation Research Part F: Traffic Psychology and Behaviour*, accepted, pre-print available online.
7. **K. van der El**, D.M. Pool, M.M. van Paassen, and M. Mulder, "Effects of Target Trajectory Bandwidth on Manual Control Behavior in Pursuit and Preview Tracking," *IEEE Transactions on Human-Machine Systems*, under review.
8. **K. van der El**, D.M. Pool, M.M. van Paassen, and M. Mulder, "Unifying Perception and Control in Driver Steering Models through an Empirical Approach," *IEEE Transactions on Human-Machine Systems*, under review.
9. J.W.G. Wildenbeest, R.J. Kuiper, **K. van der El**, F.C.T. van der Helm, and D.A. Abbink, "A Cybernetic Approach to Quantify the Effect of Haptic Feedback on Operator Control Behavior in Free-Space Telemanipulation," *IEEE Transactions on Human-Machine Systems*, to be submitted.
10. **K. van der El**, D.M. Pool, M.M. van Paassen, and M. Mulder, "Identification of Driver Boundary-Avoidance and Restricted-Preview Steering Behavior," *IEEE Transactions on Human-Machine Systems*, to be submitted.

11. **K. van der El**, D.M. Pool, and M. Mulder, "Two Interpretation of Feedforward in Manual Control," *IEEE Transactions on Human-Machine Systems*, to be submitted.
12. **K. van der El**, J. Morais Almeida, D.M. Pool, M.M. van Paassen, and M. Mulder, "The Effects of Motion Feedback in Manual Preview Tracking Tasks," *Journal of Guidance, Control, and Dynamics*, to be submitted.

CONFERENCE PUBLICATIONS

1. P.R. Lakerveld, H.J. Damveld, D.M. Pool, **K. van der El**, M.M. van Paassen, and M. Mulder, "The Effects of Yaw and Sway Motion Cues in Curve Driving Simulation," *Proceedings of the 13th IFAC/IFIP/IFORS/IEA Symposium on Analysis, Design, and Evaluation of Human-Machine Systems, Kyoto, Japan, 2016*.
2. **K. van der El**, S. Barendswaard, D.M. Pool, and M. Mulder, "Effects of Preview Time on Human Control Behavior in Rate Tracking Tasks," *Proceedings of the 13th IFAC/IFIP/IFORS/IEA Symposium on Analysis, Design, and Evaluation of Human-Machine Systems, Kyoto, Japan, 2016*.
3. **K. van der El**, J. Morais Almeida, D.M. Pool, M.M. van Paassen, and M. Mulder, "The Effects of Motion Feedback in Manual Preview Tracking Tasks," *Proceedings of the AIAA Modeling and Simulation Technologies Conference, Denver (CO), USA, 2017*.
4. **K. van der El**, D.M. Pool, and M. Mulder, "Measuring and Modeling Driver Steering Behavior: From Compensatory Tracking to Curve Driving," *Proceedings of the Driving Simulation Conference, Stuttgart, Germany, 2017*.
5. **K. van der El**, D.M. Pool, M.M. van Paassen, and M. Mulder, "Identification and Modeling of Driver Multiloop Feedback and Preview Steering Control," *Proceedings of the IEEE International Conference on Systems, Man, and Cybernetics, Miyazaki, Japan, 2018*.
6. E. Rezunenko, **K. van der El**, D.M. Pool, M.M. van Paassen, and M. Mulder, "Relating Human Gaze and Manual Control Behavior in Preview Tracking Tasks with Spatial Occlusion," *Proceedings of the IEEE International Conference on Systems, Man, and Cybernetics, Miyazaki, Japan, 2018*.
7. J.P.M.A. Wolters, **K. van der El**, H.J. Damveld, D.M. Pool, M.M. van Paassen, and M. Mulder, "Effects of Simulator Motion on Driver Steering Performance with Various Visual Degradations," *Proceedings of the IEEE International Conference on Systems, Man, and Cybernetics, Miyazaki, Japan, 2018*.
8. M. Willems, D.M. Pool, **K. van der El**, H.J. Damveld, M.M. van Paassen, and M. Mulder, "Analysis of Skill Development in Manual Ramp-Tracking Tasks," *Proceedings of the 14th IFAC/IFIP/IFORS/IEA Symposium on Analysis, Design, and Evaluation of Human-Machine Systems, Tallinn, Estonia, 2019*.

The introduction of ever-advancing automatic control systems is rapidly changing traditional manual control tasks such as piloting of aircraft and steering of cars. In order to predict how human controllers will interact with new technology, a thorough understanding of the human's adaptive manual control *capabilities* and *limitations* is essential. This thesis investigates human manual control behavior in control tasks with *preview*, where information is available about the trajectory to follow *in the future*; an example is the road that is visible ahead while driving. Human control behavior is measured in tasks that range from basic display tracking (yellow grid on this cover) to realistic car curve driving. A unifying control-theoretic model is developed, which captures the measured human control behavior in *all* preview tasks. The proposed theoretical advancements do not only improve our understanding of manual preview control, but also pave the way for an objective model-based approach to optimize the design of tomorrow's *intelligent* automation technology.

